Talanta

The International Journal of Pure and Applied Analytical Chemistry

Publication information: *Talanta* (ISSN 0039-9140). For 2008, volumes 74–76 are scheduled for publication. Subscription prices are available upon request from the Publisher or from the Regional Sales Office nearest you or from this journal's website (http://www.elsevier.com/locate/talanta). Further information is available on this journal and other Elsevier products through Elsevier's website: (http://www.elsevier.com). Subscriptions are accepted on a prepaid basis only and are entered on a calendar year basis. Issues are sent by standard mail (surface within Europe, air delivery outside Europe). Priority rates are available upon request. Claims for missing issues should be made within six months of the date of dispatch.

Orders, claims, and journal enquiries: please contact the Customer Service Department at the Regional Sales Office nearest you:
Orlando: Elsevier, Customer Service Department, 6277 Sea Harbor Drive, Orlando, FL 32887-480 USA; phone: (+1) (877) 8397126 [toll free number for US customers], or (+1) (407) 3454020 [customers outside US]; fax: (+1) (407) 3631354; e-mail: usjcs@elsevier.com
Amsterdam: Elsevier, Customer Service Department, PO Box 211, 1000 AE Amsterdam, The Netherlands; phone: (+31) (20) 4853757; fax: (+31) (20) 4853432; e-mail: nlinfo-f@elsevier.com
Tokyo: Elsevier, Customer Service Department, 4F Higashi-Azabu, 1-Chome Bldg, 1-9-15 Higashi-Azabu, Minato-ku, Tokyo 106-0044, Japan; phone: (+81) (3) 5561 5037; fax: (+81) (3) 5561 5047; e-mail: jp.info@elsevier.com
Singapore: Elsevier, Customer Service Department, 3 Killiney Road, #08-01 Winsland House I, Singapore 239519; phone: (+65) 63490222; fax: (+65) 67331510; e-mail: asiainfo@elsevier.com

USA mailing notice: *Talanta* (ISSN 0039-9140) is published monthly by Elsevier B.V. (P.O. Box 211, 1000 AE Amsterdam, The Netherlands). Annual subscription price in the USA US$ 4,085 (valid in North, Central and South America), including air speed delivery. Application to mail at periodical postage rate is paid at Rathway, NJ and additional mailing offices.
USA POSTMASTER: Send address changes to *Talanta*, Publications Expediting Inc., 200 Meacham Avenue, Elmont, NY 11003.
AIRFREIGHT AND MAILING in the USA by Publications Expediting Inc., 200 Meacham Avenue, Elmont, NY 11003.

Available online at www.sciencedirect.com

ScienceDirect

Talanta 75 (2008) 786–791

Talanta

www.elsevier.com/locate/talanta

Direct detection of formaldehyde in air by a novel NAD$^+$- and glutathione-independent formaldehyde dehydrogenase-based biosensor

S. Achmann[a,*], M. Hermann[b], F. Hilbrig[b], V. Jérôme[b], M. Hämmerle[a], R. Freitag[b], R. Moos[a]

[a] *Chair of Functional Materials, University of Bayreuth, 95440 Bayreuth, Germany*
[b] *Chair for Process Biotechnology, University of Bayreuth, 95440 Bayreuth, Germany*

Received 30 July 2007; received in revised form 29 November 2007; accepted 7 December 2007
Available online 23 December 2007

Abstract

An amperometric enzyme-based sensor-system for the direct detection of formaldehyde in air is under investigation. The biosensor is based on a native bacterial NAD$^+$- and glutathione-independent formaldehyde dehydrogenase as biorecognition element. The enzyme was isolated from *Hyphomicrobium zavarzinii strain ZV 580*, grown on methylamine hydrochloride in a fed-batch process. The sensor depends on the enzymatic conversion of the analyte to formic acid. Released electrons are detected in an amperometric measurement at 0.2 V vs. Ag/AgCl reference electrode by means of a redox-mediator. To optimize the sensing device, Ca^{2+} and pyrroloquinoline quinone (PQQ) were added to the buffer solution as reconstitutional substances.

At this stage, the sensor shows linear response in the tested ppm-range with a sensitivity of 0.39 μA/ppm. The signal is highly reproducible with respect to sensitivity and base line signal. Reproducibility of sensitivity is more than 90% within the same bacterial batch and even when enzyme of different bacterial batches is used.

Keywords: Enzyme sensor; Gas-phase; Gas sensor; Amperometric biosensor; Dye-linked formaldehyde dehydrogenase; *Hyphomicrobium zavarzinii*

1. Introduction

In spite of their high sensitivity and selectivity the use of biosensors for industrial or medical analysis is still restricted. Enzyme-based sensor-systems still suffer from their low long-time stability often provoked by the low stability of their biological components [1]. They are also often restricted to analytes in solvent or fluidic analysis-systems, because an appropriate medium (solvent or gel) adjusted to the used enzymatic system [2] is needed, to gain optimum activity and stability of the enzyme and other biological components. Thus, for gas phase analysis additional sampling and accumulation steps have to be incorporated prior to the real measurement, showing a few drawbacks such as high cost for technical equipment, longer sampling time and sometimes reduction of measuring-range.

The enzyme-based sensor-system investigated here is designed to avoid some of the difficulties mentioned above. In contrast to existing systems [3–5], the amperometric biosensor detects the analyte formaldehyde directly from the gas phase without prior accumulation or sampling steps. So, it can be used as an online detection system to monitor the formaldehyde concentration in ambient air.

Unlike other biosensors detecting formaldehyde, which often use commercially available formaldehyde dehydrogenase from *P. putida* [6,7], or another NAD$^+$- and/or glutathione-dependent formaldehyde dehydrogenase [8], the novel biosensor uses a dye-linked formaldehyde dehydrogenase from *H. zavarzinii strain ZV 580* as biorecognition element. This enzyme catalyses the conversion of the analyte without the need of NAD$^+$, a cofactor which is very well known in the literature [9] for its instability in different buffers, its high over potential for direct re-oxidation, and a proposed radical reaction mechanisms during re-oxidation [10]. Therefore, a NAD-independent system is expected to show a better long-term stability than the available systems.

---

[*] Corresponding author at: Chair of Functional Materials, University of Bayreuth, FAN-A Room A 0.09, 95440 Bayreuth, Germany.
Tel.: +49 921 557412; fax: +49 921 557405.
E-mail address: Sabine.Achmann@uni-bayreuth.de (S. Achmann).

0039-9140/$ – see front matter © 2007 Elsevier B.V. All rights reserved.
doi:10.1016/j.talanta.2007.12.015

A dye-linked formaldehyde dehydrogenase (DL-FDH) from *H. zavarzinii strain ZV 580* was earlier described by Klein et al. [11] and further characterized by Schwartz et al. [12]. Also not yet verified, pyrroloquinoline quinone (PQQ) may be the bound cofactor, and it is generally assumed that Ca^{2+} ions are required for the stabilization of the tetrameric structure of DL-FDH and for its optimal functionality [13].

In this study, the sensitivity of partially purified DL-FDH from *H. zavarzinii strain ZV 580* on formaldehyde in an amperometric biosensor system, the cross-sensitivity and the effect of adding Ca^{2+} ions and PQQ on the sensor signal are investigated.

2. Materials and methods

2.1. Chemicals

1,2-Naphthoquinone-4-sulfonic acid (sodium salt, approx. 97%, NQS) was purchased from Sigma, NAD^+ (free acid, approx. 95%) from Merck. Formaldehyde sample solutions were prepared from a 36.5% stock solution (formalin solution, Riedel-de-Haen), containing 10% methanol as stabilizer, by dilution. All other chemicals were of analytical grade. Distilled water was used to prepare standard and buffer solutions.

2.2. Organism and growth

The α-proteobacterium *H. zavarzinii strain ZV 580* was cultivated as described previously [14]. The strain *H. zavarzinii ZV 580* was from the collection of the “Institut für Allgemeine Mikrobiologie” (University of Kiel, Germany) and a generous gift from Dr. Vorholt (INRA/CNRS, Castanet-Tolosan, France).

Briefly, bacteria were grown in a mineral medium in a fully automated fed-batch process in a NLF22 bioreactor from Bioengineering (Wald, Switzerland) with 10 mM methylamine hydrochloride supplemented to the culture medium as C-source. The mineral medium contained 10 mM K_2HPO_4, 14 mM Na_2HPO_4, 10 mM $MgSO_4$, 15 mM $(NH_4)_2SO_4$, 4 μM $FeSO_4$, 1 μM $ZnSO_4$, 10 μM $CaCl_2$, 1 μM $CuSO_4$, 1 μM $CoCl_2$, 186 μM $(NH_4)_6Mo_7O_{24}$, 5 μM $MnCl_2$ and 4 μM EDTA and was kept at a pH of 6.9 ± 0.1.

2.3. Preparation of active DL-FDH

To receive active DL-FDH for application in the biosensor device, cell-free extract from the cultivated *H. zavarzinii* was prepared as described previously [14].

In short, the cell lysate was first saturated to 40% with ammonium sulfate, stirred for 60 min at 4 °C and the resulting precipitate was discarded. Subsequently the ammonium sulfate concentration was raised to 60% and the precipitate obtained after 60 min stirring at 4 °C (later called P60 or P60-fraction) containing the DL-FDH was collected by centrifugation and resuspended in a minimal volume of buffer (50 mM potassium phosphate buffer pH 8.0). The P60 sample was desalted using a “Zeba™ desalt” spin column (Pierce, Bonn, Germany) and the final enzyme concentration was determined using a micro-BCA protein assay (Pierce, Bonn, Germany), both according to the manufacturer’s instructions.

Table 1
Formaldehyde concentration in the aqueous phase and the corresponding equilibrium gas phase concentrations at 20 °C according to the equation given by Dong and Dasgupta [15]

Concentration of CH_2O in the aqueous phase (mM)	Concentration of CH_2O in the gas phase (vppm)
2.62	0.5
11.69	2
31.4	5
66.4	10
103	15

2.4. Sensor set-up

The sensor is based on the enzymatic conversion of the analyte by DL-FDH from *H. zavarzinii strain ZV 580* and subsequent electrochemical detection of released electrons with the aid of 1,2-naphtoquinone-4-sulfonic acid (NQS) as mediator (Fig. 1). The flux of electrons was recorded in an amperometric measurement at +200 mV vs. Ag/AgCl reference (3 M KCl, 210 mV vs. NHE) using a potentiostat (PGSTAT 12, Eco Chemie, The Netherlands).

The sensor device consists of a 3-electrode configuration with disks of woven graphite gauze (Alfa Aesar, Ø = 15 mm) as working and counter electrode included in a plastic housing (Fig. 2). Both electrodes were contacted with Pt-wire (Ø = 0.2 mm). The gas diffuses into the liquid phase via a 15 mm diameter Teflon membrane (FALP02500, Millipore, France). Loss of enzyme is restricted by a dialyses membrane with a MWCO of 12,000–14,000 Da (Medicell International, London, Great Britain).

Gaseous formaldehyde samples were collected from the head space above aqueous solutions of known concentration. The CH_2O concentration in the gas phase above the solution was calculated according to the equation given by Dong and Dasgupta [15] as shown in Table 1.

The buffer within the sensor contained 0.1 M KCl with 80 mM phosphate at pH 8. The mediator NQS was added in a concentration of 5 mM to the phosphate buffer. Experiments were conducted with varying formaldehyde concentrations as stated in Table 1 at room temperature and the sensing device was freshly prepared before each measurement.

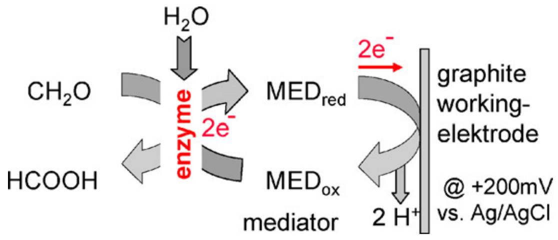

Fig. 1. Mechanism of the measurement of released electrons in the enzyme catalyzed conversion step of formaldehyde to formic acid.

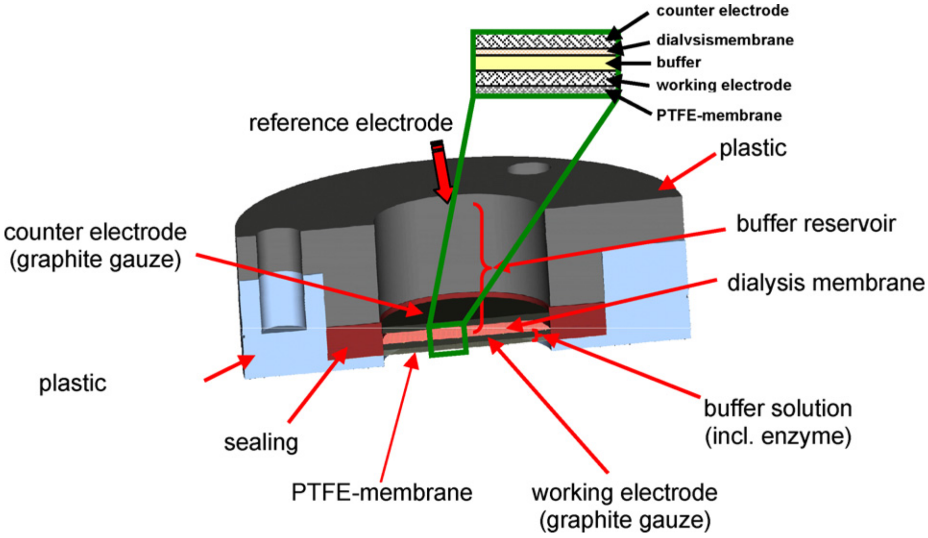

Fig. 2. Sensor set-up: plastic housing with different membranes and electrodes for the detection of the gaseous analyte formaldehyde.

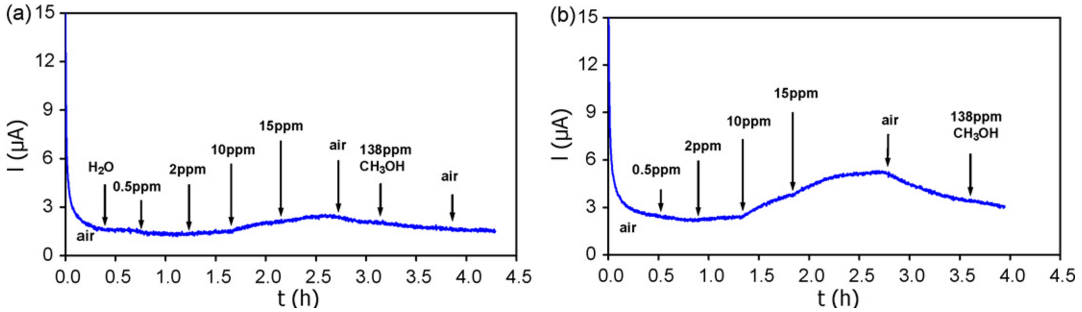

Fig. 3. Sensitivity enhancement by quantitative increase of the enzyme load in use. (a) 300 µg protein included in P60-fraction in 200 µl buffer, (b) 600 µg protein in P60-fraction in 200 µl buffer. Sensor response to formaldehyde and methanol vapor above aqueous sample solutions. Potential applied: +200 mV vs. Ag/AgCl. Buffer composition: 0.1 M KCl, 80 mM KH_2PO_4, pH 8, 5 mM NQS. $c(CH_2O) = 0.5–15$ vppm, $c(CH_3OH) = 30$ mM (138 vppm in the gas phase [16,17]), both as indicated.

3. Results and discussion

3.1. Sensor characteristics

In order to optimize the sensitivity of the sensor, two different possibilities were examined: first, the enzyme load was gradually increased by enhancing the amount of P60-fraction in use. For sensor tests a P60-fraction with a final enzyme concentration, determined from micro-BCA protein assay, of 18 mg/ml was used with a specific activity of 0.023 U/mg protein (one unit is defined as the amount of enzyme required for reduction of 1 µmol of dichlorphenolindophenol (DCPIP) per minute). In detail, the enzyme load was increased from 300 µg to 1200 µg of protein included in the P60-fraction.

The sensitivity was enhanced by doubling the enzyme load in use from 76 nA/ppm to 200 nA/ppm when 300 µg or 600 µg protein in P60-fraction were tested, respectively (Figs. 3a, b and 4). Obviously, enzyme saturation is not reached for the amount of formaldehyde that has to be converted and the reaction is quantitatively limited by the enzymatic conversion rate. So in a range, current is also a function of the enzyme load not only of the concentration of the analyte.

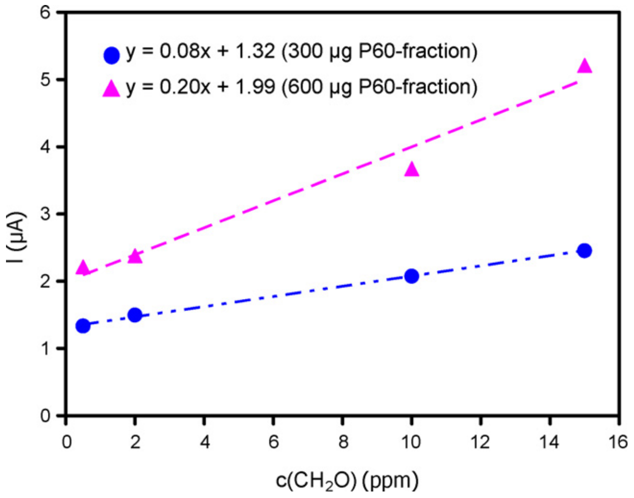

Fig. 4. Characteristic response curve of a sensor with an enzyme load of (●) 300 µg protein included in P60-fraction and (▲) 600 µg protein of P60-fraction in 200 µl buffer. Potential applied: +200 mV vs. Ag/AgCl. Buffer composition: 0.1 M KCl, 80 mM KH_2PO_4, pH 8, 5 mM NQS.

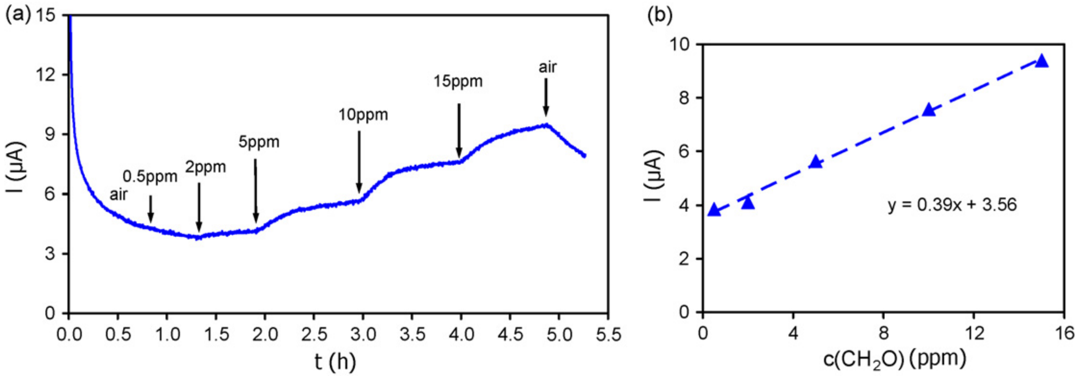

Fig. 5. (a) Response of the sensor to the vapor above aqueous sample solutions of formaldehyde and methanol when an enzyme load of 1200 μg protein in P60-fraction is used and PQQ and Ca^{2+} was added. Potential applied: +200 mV vs. Ag/AgCl. Buffer composition: 0.1 M KCl, 80 mM KH_2PO_4, pH 8, 5 mM NQS, 1 μM PQQ, 50 μM $CaCl_2$. Enzyme loading: 1200 μg protein in P60-fraction in 200 μl buffer. (b) Linear response curve of the sensor in the tested range of 0.5–15 vppm CH_2O.

Another possibility to enhance the sensor sensitivity is to improve the activity of the enzyme itself by adding PQQ (1 μM) and Ca^{2+} ions by means of 50 μM $CaCl_2$ to the buffer solution as previously reported in Ref. [14]. This so called reconstitution of the active form of the enzyme increases the sensor sensitivity from 200 nA/ppm to 270 nA/ppm in the case of 600 μg un-reconstituted and reconstituted protein in P60-fraction, respectively, i.e. approximately 25% higher sensitivity (results not shown). That is again due to the fact that higher enzyme activity leads to higher enzymatic conversion rates, resulting in a higher sensor signal.

At present, highest sensitivity is realized by adding PQQ and Ca^{2+} to 1200 μg protein in P60-fraction and implementing this for biorecognition. A characteristic signal is shown in Fig. 5(a, b) with a sensitivity of 390 nA/ppm, a t_{90}-time of about 15 min and a linear response curve in the tested range.

3.2. *Selectivity of the sensing device*

To evaluate the selectivity of the sensing device, interference from methanol and the influence of water vapor were of special interest.

Methanol is used in a concentration of 10% as a stabilizing agent in the formalin solution, from which gaseous formaldehyde samples were prepared. Furthermore, methanol is also a possible C-source for *H. zavarzinii* growth, so that the enzyme preparation may contain a methanol metabolizing enzyme, too.

Aqueous solutions of methanol in the range of 3–60 mM were prepared and tested, to rule out the possibility that methanol instead of formaldehyde is responsible for the sensor signal or that there are any interferences by methanol. For comparison, an aqueous solution of 103 mM CH_2O, corresponding to 15 vppm CH_2O in the gas phase, contains about 19 mM methanol. So, the range mentioned above exceeds the amount of methanol included in the formaldehyde samples by far.

Gaseous methanol for interference tests were again sampled above the head space of the mentioned aqueous solutions. Gas phase concentrations as shown in Table 2 were calculated by Henry's law with a Henry's law constant given by Sander [16] and Snider and Dawson [17].

Table 2
Methanol concentration in the gas phase above aqueous methanol sample solutions calculated by an Henry's law constant at standard conditions (298.15 K) given by Sander [16] and Snider and Dawson [17]

Concentration of CH_3OH in the aqueous phase (mM)	Concentration of CH_3OH in the gas phase (vppm)
3	13.8
30	138
60	276

The sensor showed no sensitivity to gaseous methanol in the tested range, at all (Fig. 6) so that it can be stated, that there is no influence of methanol on the sensor signal and that the signal does not result from any conversion of methanol included in the test samples

Due to the fact that all gaseous samples are derived from aqueous solutions, interferences from water vapor were also evaluated but it was found that water vapor did not affect the base signal of the senor (results not shown).

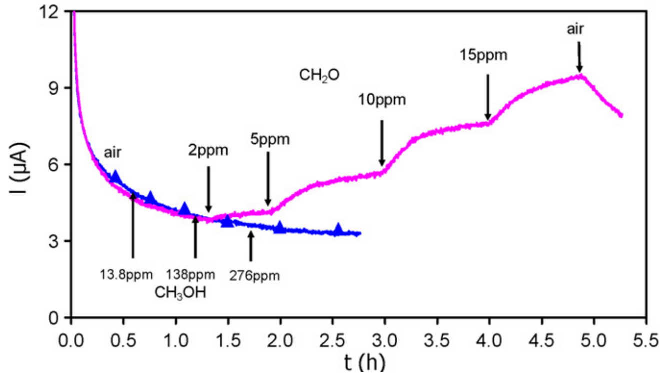

Fig. 6. Selectivity data of the sensing device. Methanol was used as possible interfering substance in the range of 3–60 mM in solution. (▲) Gaseous methanol samples generated by aqueous solutions; (—) gaseous formaldehyde samples. Potential applied: +200 mV vs. Ag/AgCl. Buffer composition: 0.1 M KCl, 80 mM KH_2PO_4, pH 8, 5 mM NQS, 1 μM PQQ, 50 μM $CaCl_2$. Data received from two freshly prepared sensors with an enzyme load of 1200 μg protein in P60-fraction in 200 μl buffer.

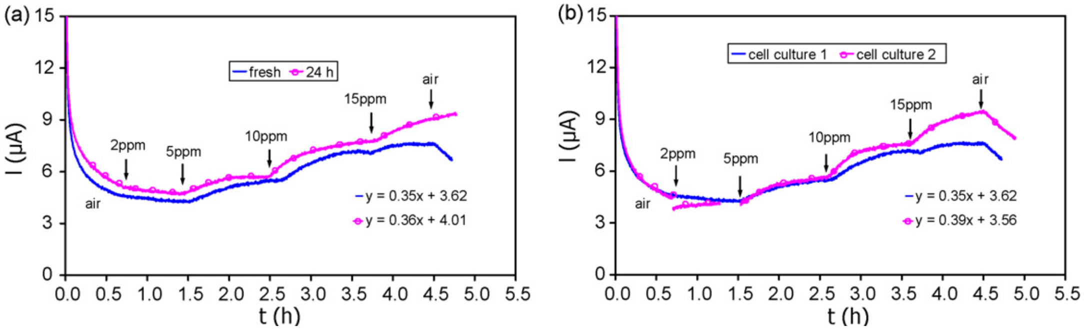

Fig. 7. Reproducibility of the sensor. Different 1200 μg P60-fraction enzyme samples in 200 μl buffer are used. (a) Effect of deterioration during storage for 24 h at 4 °C: (—) freshly prepared enzyme samples as biorecognition element; (◯) enzyme stored at 4 °C for 24 h. (b) Enzyme samples of diverse *Hyphomicrobium zavarzinii* batch cultures: (—) culture 1; (◯) culture 2. Potential applied: +200 mV vs. Ag/AgCl. Buffer composition: 0.1 M KCl, 80 mM KH_2PO_4, pH 8, 5 mM NQS, 1 μM PQQ, 50 μM $CaCl_2$. c(CH_2O) = 2–15 vppm.

3.3. Reproducibility of the sensor signal

Reproducibility of the sensor signal was especially evaluated with regard to deterioration of the enzyme sample and influences of microbial enzyme production.

Therefore, enzyme samples isolated from *H. zavarzinii* grown in different bioreactor batches were examined. Deterioration was reviewed after the enzyme sample was kept at 4 °C for 24 h.

The signal was highly reproducible when enzyme of the same bacterial batch was used and the influence of deterioration during storage was quite low. After 24 h at 4 °C the reproducibility of the sensor signal is about 98.5% related to freshly prepared enzyme (Fig. 7a, 350 nA/ppm and 360 nA/ppm, respectively). Even when enzyme samples isolated from *H. zavarzinii* cells grown in different bioreactor batches were used, the signal was very repeatable. As can be seen from Fig. 7b, the sensitivity of the sensing device is altered from 350 nA/ppm to 390 nA/ppm for two different cell cultures, meaning a reproducibility of about 92%. In this case the linear range of the sensor prepared with cell culture 1 from 0 vppm up to 10 vppm was taken into account.

Reproducibility data after storage are quite promising. After optimizing the storage procedure there will be hardly any disadvantages of producing the enzyme samples in greater amount in one bioreactor process and store them for later use.

3.4. Cofactor mediated biosensor

In order to reduce the number of components involved in the reaction chain, PQQ which is a possible mediator for dehydrogenase enzymes [18,19], was used as mediating cofactor and reconstitution element simultaneously. The cofactor was used in concentrations of 1 μM and 10 μM, added to the buffer solution.

The sensor shows a formaldehyde concentration dependent signal, when 1 μM PQQ is used. The sensitivity of the sensor is 140 nA/ppm meaning about 35% of the sensitivity of a reconstituted sensor with an enzyme load of 1200 μg protein in P60-fraction (cp. Fig. 5, sensitivity 390 nA/ppm). Increasing the PQQ concentration to 10 μM does not lead to higher sensitivity of the sensor (results not shown).

Without the addition of any mediator or of PQQ, a very low electron transfer rate to the electrode was detected (Fig. 8). A possible reason for this low current are not yet identified redox-active substances in the protein fraction that can be converted at the electrode producing an amperometric signal. It is also possible, that the enzyme itself is directly re-oxidized at the electrode surface. For this possibility the sensitivity decline or may be loss at 10 vppm would indicate an electron transfer limitation for higher analyte concentrations.

Further investigations have to be done to clarify this phenomenon.

3.5. Complexation of Ca^{2+}

A quasi-negative control was prepared by complexation of the structurally important Ca^{2+} by the addition of 1 mM EDTA to the buffer solution. In that case, only 1 μM PQQ was added to the buffer solution without $CaCl_2$.

The sensor response to formaldehyde is almost completely lost when Ca^{2+} is complexed by EDTA (Fig. 9, time gaps result from inconsistent measurement periods of the two experiments).

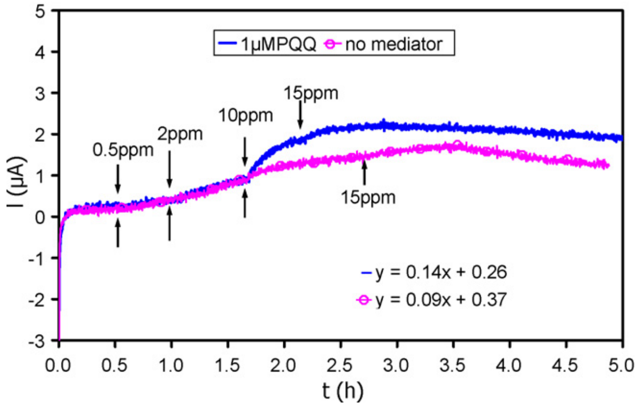

Fig. 8. Sensor signal for a PQQ mediated biosensor and a biosensor where no mediator was added, enzyme load: 1200 μg protein in P60-fraction in 200 μl buffer. (—) 1 μM PQQ is added to a buffer solution (0.1 M KCl, 80 mM KH_2PO_4, 55 μM $CaCl_2$, pH 8) (◯) no mediator is added to the buffer solution (0.1 M KCl, 80 mM KH_2PO_4, 50 μM $CaCl_2$, pH 8). Potential applied: +200 mV vs. Ag/AgCl. c(CH_2O) = 0.5–15 vppm.

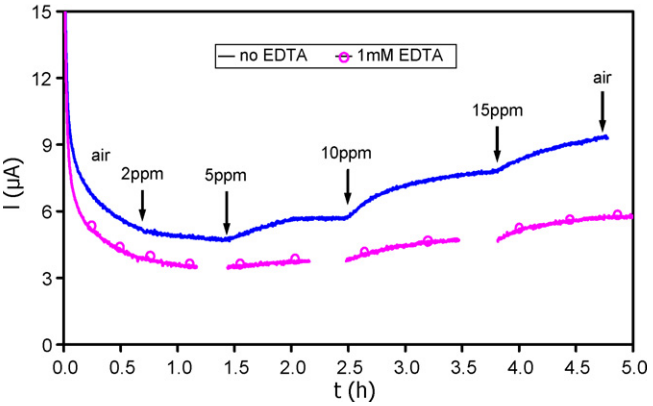

Fig. 9. Complexation of Ca^{2+} by EDTA: comparison of a sensor signal characteristic for a (—) PQQ and $CaCl_2$ reconstituted enzyme sample (buffer: 0.1 M KCl, 80 mM KH_2PO_4, pH 8, 5 mM NQS, 1 µM PQQ, 50 µM $CaCl_2$) and (○) an enzyme sample where Ca^{2+} is complexed by the addition of 1 mM EDTA to the buffer solution (buffer: 0.1 M KCl, 80 mM KH_2PO_4, pH 8, 5 mM NQS, 1 µM PQQ). Potential applied: +200 mV vs. Ag/AgCl. Enzyme load: 1200 µg protein in P60-fraction in 200 µl buffer. $c(CH_2O) = 2–15$ vppm.

As it was corroborated by the loss of sensitivity through complexation, Ca^{2+} plays an important role in the active centre of DL-FDH and for the sensing purpose.

It is likely that Ca^{2+} already embedded in the enzyme structure cannot be complexed by the added EDTA in solution and so a negligible amount of enzyme is still possible to convert formaldehyde causing the marginal signal shown in Fig. 9.

4. Conclusion and perspectives

In the studies presented above, native DL-FDH isolated from *H. zavarzinii strain ZV 580* was successfully implemented in a sensing device. Using the DL-FDH it was possible to detect gaseous formaldehyde with a dehydrogenase enzyme without the addition of the unstable, unbound cofactor NAD^+ directly from the gas phase. With the elimination of NAD^+ it is much more promising to obtain a sensor device with higher long-term stability.

Further on, it was demonstrated that the detection of gaseous formaldehyde by DL-FDH is selective against methanol and that water vapor does not influence the measurement result at the air saturation point at room temperature.

Reproducibility of the measured signal was over 90% when the sensitivities of deteriorated enzyme samples and even of enzyme samples isolated from different *H. zavarzinii* cultures were compared to freshly prepared protein fractions.

Reconstitution with PQQ and Ca^{2+} improved the sensitivity of the device and showed the importance of these substances for the activity of the enzyme.

First experiments with a cofactor mediated reaction chain were very promising. Using a PQQ-functionalized electrode, much more effective electrical contact between enzyme and electrode might be possible. Anyway, the elimination of another additional substance, in this case the additional mediator NQS, will again enhance the feasibility to get a more stable sensor device.

For this, further work is under investigation to determine the dependence of the sensor stability from different factors and to evaluate the benefit of the formerly stated improvements.

Acknowledgement

Financial support by the *Deutsche Forschungsgemeinschaft* (Ha 4424/1-1).

References

[1] S. Achmann, M. Hämmerle, R. Moos, in: G. Gerlach, H. Kaden (Eds.), Dresdner Beiträge zur Sensorik, vol. 24, TUDpress, Dresden, 2005, pp. 177–180.
[2] S. Achmann, M. Hämmerle, R. Moos, Electroanal. 20 (2007) 410–417.
[3] R. Kataky, M.R. Bryce, L. Goldenberg, S. Hayes, A. Nowak, Talanta 56 (2002) 451.
[4] F. Vianello, A. Stefani, M.L. Paolo, A. Rigo, A. Lui, B. Margesin, M. Zen, M. Scarpa, G. Sonicini, Sens. Actuator B:-Chem. 37 (1996) 49.
[5] Y. Herschkovitz, I. Eshkenazi, C.E. Campbell, J. Rishpon, J. Electroanal. Chem. 491 (2000) 182.
[6] K. Mitsubayashi, G. Nishio, Y. Nakayama, H. Amagai, H. Watanabe, N. Jaffrezic-Renault, T. Noguer, J.-L. Marty, Int. J. Environ. Anal. Chem. 85 (12–13) (2005) 917.
[7] M. Hämmerle, E.A.H. Hall, Biosens. Bioelectron. 11 (1996) 239.
[8] M.B. Ali, Y. Korpan, M. Gonchar, A.V. Elľskaya, M.A. Maaref, N. Jaffrezic-Renault, C. Martelet, Biosens. Bioelectron. 22 (2006) 575.
[9] L. Rover Jr., J.C.B. Fernandes, G. de Oliveira Neto, L.T. Kubota, E. Katekawa, S.H.P. Serrano, Anal. Biochem. 260 (1998) 50.
[10] I. Katakis, E. Dominguez, Mikrochim. Acta 126 (1–2) (1997) 11.
[11] C.R. Klein, F.P. Kessler, C. Perrei, J. Frank, J.A. Duine, A.C. Schwartz, Biochem. J. 301 (1994) 289.
[12] A.C. Schwartz, G. Gockel, J. Groß, B. Moritz, H.E. Meyer, Arch. Microbiol. 182 (6) (2004) 458.
[13] M.O. Lueg, A.C. Schwartz, Biol. Chem. H-S 378 (1997) 72.
[14] V. Jérôme, M. Hermann, F. Hilbrig, R. Freitag, Appl. Microbiol. Biotechnol. 77 (4) (2007) 779.
[15] S. Dong, P.K. Dasgupta, Environ. Sci. Technol. 20 (6) (1986) 637.
[16] R. Sander, Compilation of Henry's Law Constants for Inorganic and Organic Species of Potential Importance in Environmental Chemistry, Version 3, 1999, www.henrys-law.org.
[17] J.R. Snider, G.A. Dawson, J. Geophys. Res. 90D (1985) 3797.
[18] I. Willner, R. Baron, B. Willner, Biosens. Bioelectron. 22 (9–10) (2007) 1841.
[19] A. Bardea, E. Katz, A.F. Bückmann, I. Willner, J. Am. Chem. Soc. 119 (1997) 9114.

Available online at www.sciencedirect.com

ScienceDirect

Talanta 75 (2008) 717–724

Talanta

www.elsevier.com/locate/talanta

Determination of the herbicide benfuresate by its photo-induced chemiluminescence using flow multicommutation methodology

J.R. Albert-García, J. Martínez Calatayud*

Department of Analytical Chemistry, University of Valencia, Valencia, Spain

Received 6 July 2007; received in revised form 15 November 2007; accepted 7 December 2007
Available online 15 December 2007

Abstract

The present paper deals with an analytical strategy based on coupling photo-induced chemiluminescence in a multicommutation continuous-flow methodology for the determination of the herbicide benfuresate. The solenoid valve inserted as small segments of the analyte solution was sequentially alternated with segments of the NaOH solution for adjusting the medium for the photodegradation. Both flow rates (sample and medium) were adjusted to required time for photodegradation, 90 s; and then, the resulting solution was also sequentially inserted as segments alternated with segments of the oxidizing solution system, hexacyanoferrate (III) in alkaline medium. The calibration range from 1 μg L^{-1} to 95 mg L^{-1}, resulted in a linear behaviour over the range 1 μg L^{-1} to 4 mg L^{-1} and fitting the linear equation: $I = 4555.7x + 284.2$, correlation coefficient 0.9999. The limit of detection was 0.1 μg L^{-1} ($n = 5$, criteria 3σ) and the sample throughput was 22 h^{-1}. The consumption of solutions was very small; per peak were 0.66 mL, 0.16 mL and 0. 32 mL sample, medium and oxidant, respectively. Inter- and intra-day reproducibility resulted in a R.S.D. of 3.9% and 3.4%, respectively.

After testing the influence of a large series of potential interferents the method is applied to water samples obtained from different places, human urine and to one formulation.

Keywords: Herbicides; Photo-induced chemiluminescence; Multicommutation; Benfuresate

1. Introduction

Benfuresate (2,3-dihydro-3,3-dimethylbenzofuran-5-yl ethanesulphonate) is a viscous brown-coloured liquid, which can solidify at ambient temperature. Its average photolysis time in an aqueous solution exposed to the sunlight is 7 days. The compound is soluble in water (0.261 g L^{-1}) and in organic solvents such as methanol, acetone, dichloromethane, toluene and ethyl acetate. Its molecular structure is shown in Fig. 1.

Benfuresate is a herbicide against weeds widely used on cotton, tobacco, sugarcane, rice, maize and bean crops. The compound acts by inhibiting fat synthesis—it is specially efficient against *Digitaria*, *Sectaria*, *Cyperus*, *Portulaca*, *Solanum* and *Gallium*; also, it is moderately toxic, and an eye and skin irritant. Pursuant to current regulations, it is available as emulsifying concentrates, liquids and wettable powders for use in low or ultra-low volumes [1].

Benfuresate is moderately toxic by ingestion and virtually harmless when absorbed through the skin. A study involving three generations of mice that were given a dose of a few mg kg^{-1} day^{-1} exposed no adverse effect on reproduction (fertility, pregnancy and nursing). Also, no teratogenic effects on rats or mice, or mutagenic effects on cell cultures, have been detected. As regards animal metabolism, the herbicide has never been detected in urine or milk. This suggests that it is absorbed into the blood stream via the gastrointestinal tract and metabolized for release via urine.

The earliest determination of benfuresate was reported in 2000, when Nemoto et al. [2] quantified it together with 110 other pesticides in vegetables by GC–MS (SIM) following preconcentration on a silica column. Also in 2000, Kaihara et al. [3] determined benfuresate and 27 other pesticides in fruits and vegetables by supercritical fluid extraction following separation on an HPLC column. In 2002, the same authors [4] determined

---

* Corresponding author at: Departamento de Quimica Analitica, Universidad de Valencia. c/ Moliner 50, Burjassot, Valencia 46100, Spain.
Tel.: +34 96 354 40 62; fax: +34 96 354 40 62.
E-mail address: jose.martinez@uv.es (J.M. Calatayud).

0039-9140/$ – see front matter © 2008 Elsevier B.V. All rights reserved.
doi:10.1016/j.talanta.2007.12.003

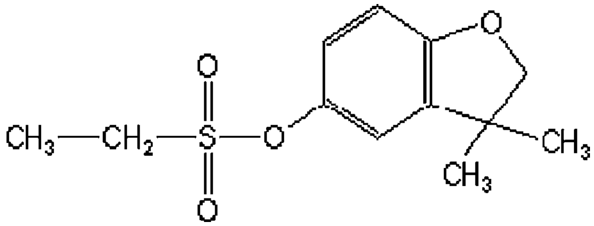

Fig. 1. Molecular structure of the benfureaste.

18 pesticides including benfuresate in rice, fruit and vegetable samples by using supercritical fluid extraction in combination with HPLC–MS. Also in 2002, Ueno et al. [5] determined 87 nitrogen- and sulphur-containing pesticides – benfuresate included – in vegetables by using GC-NPD/FPD. The most recent determinations of benfuresate were reported by Sakamoto and Tsutsumi [6] who used solid-phase micro-extraction in 2004 to determine 174 pesticides in water samples; Chu et al. [7] who employed GC–MS in 2005 to determine 266 pesticides in apple juice, and our own group [8] who determined benfuresate and ethofumesate in water, commercial formulations, soil and urine by their native fluorescence.

Based on the foregoing, the pesticide has never been determined on the basis of its chemiluminescence or using multicommutation methodology [9–11]. In this work, we used the photo-induced chemiluminescence of benfuresate to determine it in a multicommutated continuous-flow system. Advantages of this emergent methodology have been discussed elsewhere [10].

2. Experimental

2.1. Reagents and apparatus

All solutions were prepared in purified water by reverse osmosis and then deionised (18 MΩ cm) with a Sybron/Barnstead Nanopure II water purification system provided with a fibber filter of 0.2-μm pore size. All reagents used were analytically pure unless stated otherwise.

The benfuresate was from Dr. Ehrenstorfer GmbH (97.3%, Ausburg, Germany). Another pesticide tested as interferent ethofumesate was also from the same manufacturer (98.5%, Dr. Ehrenstorfer GmbH). Other chemicals were strong inorganic acids and alkalis, oxidants as $KMnO_4$, $Ce(NH_4)_2(NO_3)_6$, H_2O_2 and $K_3Fe(CN)_6$ (all of them from Panreac, Spain); organized media reagents and sensitizers: formic acid, acetonitrile, 2-propanol, *N*,*N*-dimethylformamide, arabig gum, resorcine, *o*-acetotoluidine, sodium dodecyl sulphate, hexadecylpyridinium chloride, β-cyclodextrine (Fluka), benzalconium chloride, Tween 80 (Guinama), quinine sulphate, Rhodamine B and Rhodamine 6G (Sigma–Aldrich), Triton X-100 (Scharlau), ethanol, *N*-cetyl-*N*,*N*,*N*-trimethylammonium bromide, cumarine and fluorescein (Panreac); as photodegradation media were used $Fe(NO_3)_3{\cdot}7H_2O$ (Probus) and $FeSO_4{\cdot}9H_2O$ (Merck).

The experimental set-up (Fig. 2) consisted of PTFE tubing of 0.8 mm i.d. and a Minipuls-2 pump from Gilson (Worthington, OH), and was completely automated by using three model 161T031 solenoid valves from NResearch (Northboro, MA) that were connected to a custom-made KSP interface. The whole system was governed via software developed by the authors under the Microsoft Windows 98 operating system and run on a Pentium PC. The software and interface allowed each valve, the insertion sequence and the number of cycles to be controlled as a function of the number of samples, reagents and standards to be used. The photoreactor was a PTFE tube 150 cm long × 0.8 mm i.d. that was helically coiled around a commercial low-pressure Sylvania 15 W mercury lamp. The flow-cell was a spirally coiled quartz tube behind which a reflecting surface was placed in order to maximize light collection. The cell was placed next to the window of the photomultiplier tube (a P30CWAD5F-29 type 9215 model from Electron Tubes that was operated at 1180 V) and the body of elements (last solenoid valve, cell and photomultiplier) was accommodated in a specially designed black box in order to

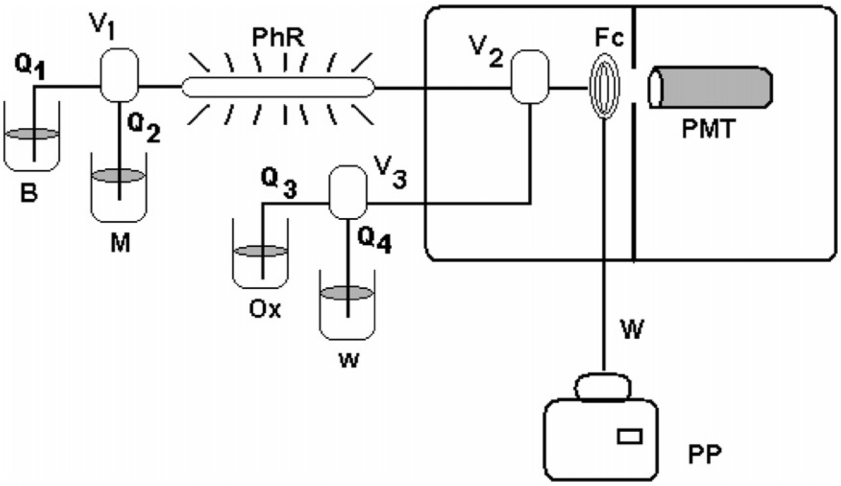

Fig. 2. Continuous-flow manifold of the multicommutation type B, benfuresate solution; M, medium solution for photodegradation; PhR, photoreactor; Ox, oxidant solution; w, water; V_1, V_2 and V_3; solenoid valves; Qn, flowing channels, 1 benfuresate solution, 2, photodegradation medium, 3 oxidant solution and 4 water; Fc, flow-cell; PMT, photomultiplier tube; W, waste; and, PP, peristaltic pump.

completely block ambient light. The output of the photomultiplier tube was connected to a computer equipped with a counter, which was also supplied by Electron Tubes.

2.2. Flow assembly

The manifold used throughout is depicted in Fig. 2. The peristaltic pump was placed behind the detector in order to aspirate the sample and reagents into the flow-cell at an overall rate of $10\,\mathrm{mL\,min^{-1}}$. Had the pump been placed in front of the valve, pressure building within the system might have caused connectors to dislodge. The valve operational sequence for inserting alternated segments of two different solutions, can be described with the expression $N^*(t_1, t_2)$, where t_1 and t_2 are the times during which the valve is ON and OFF (ON when inserting one solution and OFF the other), respectively, and N is the number of ON/OFF cycles used (the number of total inserted segments). The previous assembly was used both for preliminary testing and for the proper determinations. Only the number of pulses (N) and their length (t_1 and t_2) for each solenoid valve changed between tests.

The assembly included three solenoid valves and four PTFE tubing channels: valve V_1 allows alternating solution segments from the analyte (Q_1) and the medium to the photoreactor. Valve V_3 alternate the oxidant solution (through channel Q_3) and water (Q_4) flowing to wash manifold between two consecutive cycles. The chemiluminescent reaction is performed when valve V_2 alternate micro-segments oxidant and the resulting solution from the photoreactor. The operating sequence was as follows. The valve ON/OFF sequence used in the optimization tests started with 50 alternate microinsertions of pesticide and photodegradation medium. During each microinsertion, V_1 was kept ON for 0.4 s to aspirate benfuresate via Q_1 and then OFF for 0.2 s to aspirate photodegradation medium via Q_2. During the 30 s where the sample was inserted, V_2 was kept ON in order to allow the photoreactor to be loaded with benfuresate–photodegradation medium mixture. Then, V_1 and V_2 were switched OFF and the flow was stopped for 150 s in order to irradiate the sample with UV light. During that interval, Q_4 was used to circulate water in order to remove any excess benfuresate-photodegradation medium mixture potentially reaching the flow-cell. After 165 s, V_3 was switched ON to insert the oxidant. Once the flow was stopped, V_2 was switched ON to have 30 alternate micro-segments of photo-degraded pesticide and oxidant inserted. This valve was placed 2 cm from the flow-cell in order to maximize the resulting signal. Once the chemiluminescence response was obtained and the baseline restored, a new cycle was started.

3. Results and discussion

3.1. Preliminary tests

Initial tests involved screening for pesticides giving a chemiluminescent product. To this end, we used various types of media including H_2O, 0.05% H_2O_2, 6×10^{-5} M Fe^{3+}, 6×10^{-5} M Fe^{2+} and 10^{-3} M NaOH; a photodegradation time (stopped-flow) of 2.5 min, and reaction with 7×10^{-4} M $KMnO_4$ in 2 M H_2SO_4. Based on the results, we chose benfuresate for further testing, as it was one of the pesticides best performing in the tests.

Subsequent tests were conducted with a $8\,\mathrm{mg\,L^{-1}}$ concentration of benfuresate and various oxidants including 6×10^{-3} M Ce(IV) and 7×10^{-4} M MnO_4^- (both in 2 M H_2SO_4), and also $Fe(CN)_6^{3-}$ in 1.5 M NaOH. The use of ceric and ferricyanide ions in their respective media as oxidants in conjunction with Fe(II) and H_2O as photodegradation media was found to provide the highest outputs (see Fig. 3).

In order to choose the most suitable medium and oxidant, we performed additional, pre-calibration tests using analyte concentrations from $0.5\,\mathrm{mg\,L^{-1}}$ to $5\,\mathrm{mg\,L^{-1}}$. Such tests revealed ferricyanide as an oxidant and water as degradation medium to give a greater slope (2139.9) than did Ce(IV) in combination with water (1393.9) or aqueous ferrous ion (1175.7). Based on

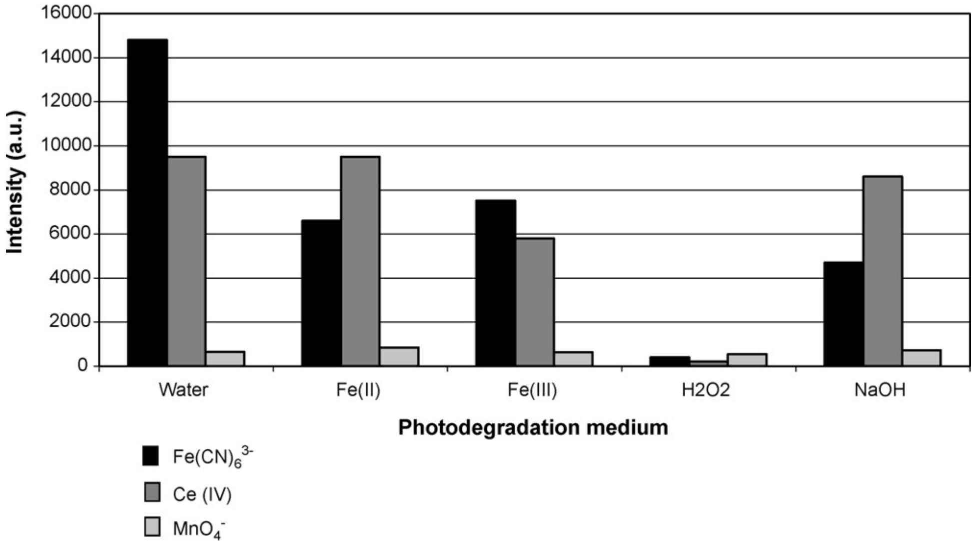

Fig. 3. Influence of the oxidant system and photodegradation media and the emission output of benfuresate ($8\,\mathrm{mg\,L^{-1}}$ benfuresate).

Table 1
Study of different media and photodegradation time intervals (1 $mg L^{-1}$ benfuresate)

Time (s)	Medium [pH]						
	$HClO_4$ 5×10^{-2} M [1.5]	$HClO_4$ ($\times 10^{-4}$ M) [2.95]	$HClO_4$ ($\times 10^{-6}$ M) [4.4]	Deionized water [6.1]	NaOH ($\times 10^{-6}$ M) [6.6]	NaOH ($\times 10^{-4}$ M) [8.8]	NaOH ($\times 10^{-2}$ M) [11.3]
0	87	46	68	67	140	56	71
30	1028	1597	2707	3784	2564	2481	1055
60	1203	2250	3762	**4400**	3687	3268	1179
90	1148	2643	**4050**	3984	3751	3641	1350
120	804	2391	4021	2751	3222	3337	1300
150	734	2262	3846	1950	2941	2641	1290
180	630	1784	3184	1627	2134	2157	1240
240	453	1057	2900	1352	1945	1954	1003

In bold the highest emission outputs.

these results, $Fe(CN)_6{}^{3-}$ was selected as an oxidant and H_2O as photodegradation medium.

The nature of the photodegradation medium can influence the specific photoproducts obtained and/or their concentrations, and also the photodegradation time required. We thus examined the effects of both variables at once, using 6×10^{-3} M $Fe(CN)_6{}^{3-}$ in 1.5 M NaOH as an oxidant and a benfuresate concentration of 1 $mg L^{-1}$. The specific media and photodegradation times used, and the results they provided, are shown in Table 1.

The optimum photodegradation time was always 60–90 s. In fact, longer times (more than 120 s) resulted in decreased signals, possibly by effect of the formation of other, non-chemiluminescent photodegradation products. The greatest emission intensity was that obtained in the aqueous medium; however, the analytical signals obtained in 10^{-6} M $HClO_4$ were also quite substantial, so both media were considered in subsequent tests.

The UV–vis spectra for the photodegraded solutions exhibited an identical profile but differences in absorptivity in the maximum absorption region. Benfuresate was photodegraded by using variable irradiation times in order to examine their effect.

3.2. Influence of the alkaline medium, the oxidant concentration in it and the type of acid used as photodegradation medium

The oxidant concentration is a critical variable for chemiluminescent systems [12]; in fact, too low concentrations can result in very small or even undetectable signals, whereas too high levels can lead to self-absorption of the chemiluminescence by the oxidant. This led us to conduct a comprehensive study of the influence of the oxidant concentration on the chemiluminescent system. We examined the effects of the oxidant and NaOH concentrations. As can be seen from Fig. 4, the analytical signal peaked at an oxidant concentration of 5×10^{-4} M, which was thus chosen to study the effect of the NaOH concentration. This was examined over the range 0.1–2.5 M, using a benfuresate concentration of 1.5 $mg L^{-1}$ in both photodegradation media (water and perchloric acid). As can be seen from Fig. 5, using 10^{-6} M $HClO_4$ as photodegradation medium resulted in substantially increased signals.

The previous study was extended to the influence of the specific alkali used as oxidation medium (NaOH and KOH) and the acid employed as photodegradation medium (water, HCl,

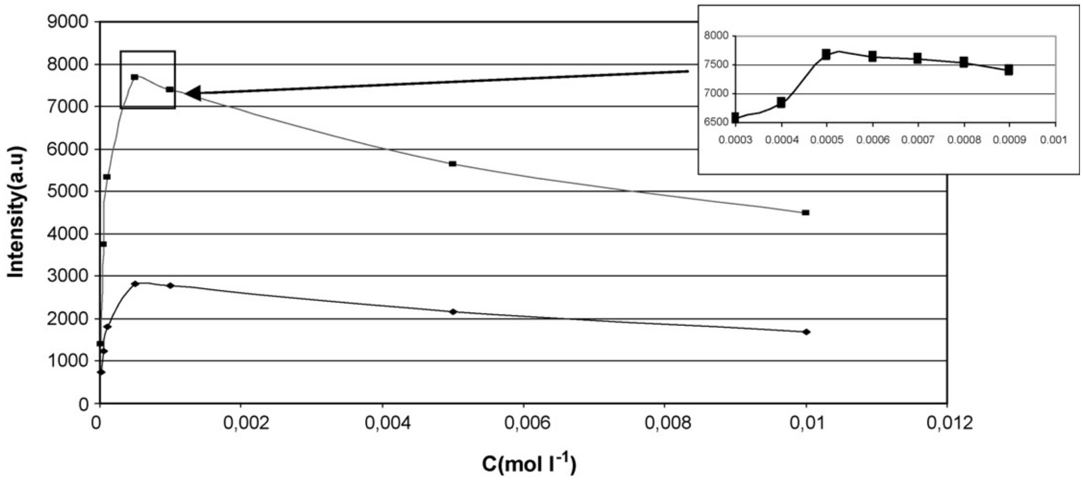

Fig. 4. Influence of the $Fe(CN)_6{}^{3-}$ concentration in two different media (1.5 $mg L^{-1}$ benfuresate). Upper curve, perchloric acid and lower curve, water.

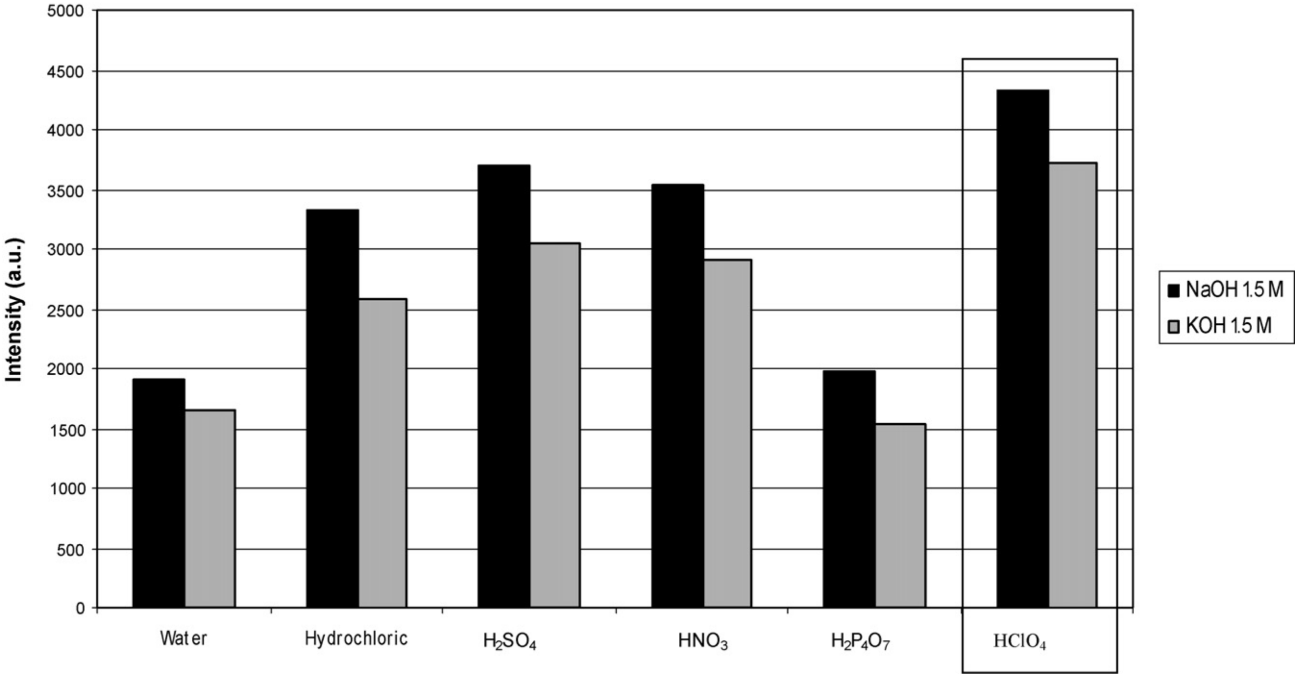

Fig. 5. Influence of the acid and alkali for photodegradation and chemiluminometric oxidation, respectively.

H_2SO_4, HNO_3, $H_2P_4O_7$ and $HClO_4$), using a fixed concentration for both the former (1.5 M) and the latter (10^{-6} M). The best oxidation medium with all acids used as photodegradation media was found to be NaOH, which was adopted for further work. Also, $HClO_4$ was found to provide a signal 15% taller than that obtained with H_2SO_4, so the former was kept as the photodegradation medium of choice (Fig. 6).

3.3. *Influence of surfactants and sensitizers*

Chemiluminescent reactions [13,14] can be benefited from the use of organized media (usually surfactants); in fact, such media can boost the emission intensity [15] by protecting the excited species from interactions with its closest environment, thereby avoiding radiationless losses of energy. On the other hand, sensitizers (fluorophores) facilitate energy transfers by acting as chemiluminescent acceptors and, ultimately, as the light emitters; in this way, they facilitate indirect chemiluminescence-based determinations. Based on the foregoing, we tested various sensitizers and surfactants.

Experimental results demonstrated using 20% acetonitrile as sensitizer increased the net analytical signal by up to 450%. Also, acetonitrile exhibited a much lower blank signal – which is important with a view to obtaining good detection limits – than did the other sensitizers and surfactants studied. The optimum amount of acetonitrile was determined by using a proportion from 1% to 20%. Based on the results, a 2.5% concentration resulted in the maximum possible net signal (*i.e.* the largest possible difference from the blank signal), so no more acetonitrile need to be added to the medium (Table 2).

Photochemical pathways (primary and secondary reactions) for the sensitized oxidations depend on its state of ionization that can be modified by the solvent used and properties of solvent. The influence of the acetonitrile on irradiation processes has been discussed in some few papers [16–19]. The photochemical process was found to depend markedly on solvent polarity; on the photosensitized oxidation of phenylthioacetic acid, changing the solvent from acetonitrile to water led to a dramatic change in the primary photochemical pathways. In the photosensitized oxida-

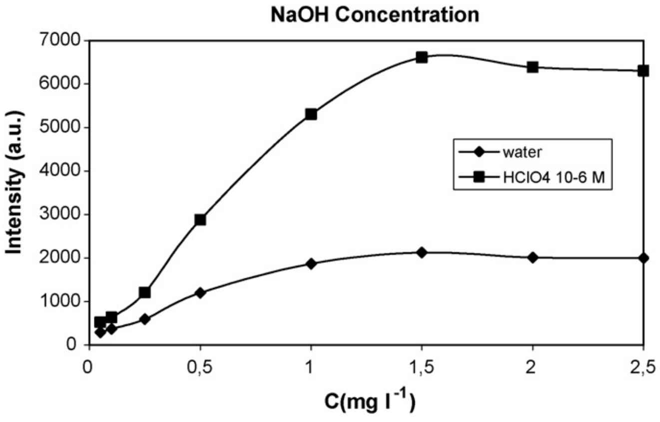

Fig. 6. Influence of the NaOH concentration (1.5 mg L^{-1} of benfuresate).

Table 2

Study of the influence of the acetonitrile concentration (photodegradation medium) on the outputs (0.25 mg L^{-1} benfuresate)

Acetonitrile concentration (in %)	Blank signal	Pesticide signal	Output
1	43	3818	3771
2.5	46	6137	**6091**
5	47	5774	5727
10	148	6025	5877
20	150	6112	5962

In bold the highest emission outputs.

tive degradation of some pesticides in which the mixture was also used acetonitrile/water; the photoproducts obtained and the reduction potential of the photo-excited sensitizer were in agreement with a primary mechanism involving an electron-transfer from the pesticide to the excited photo-sensitizer. These results showed that an electron-acceptor photo-sensitizer may increase the rate of photodegradation. A non-singlet-oxygen mechanism is proposed, in which an excited sensitizer is quenched by oxygen to produce a sensitizer radical cation and a superoxide ion ($O_2^{\bullet -}$), the former of which oxidizes, while $O_2^{\bullet -}$reacts with the resulting $^{\bullet +}$ to give the major oxidation products.

3.4. Combined effect of the photodegradation and oxidation temperatures

The influence of the two temperatures was initially examined separately. Temperature can have a relatively complex effect on chemiluminescence. As is usually the case with fluorescent systems, an increased temperature should result in decreased emission through an increased likelihood of deactivation via external conversions leading to an increased frequency of collisions with other molecules. However, chemiluminescent systems additionally involve a chemical reaction, which can be favored by an increased temperature. Therefore, the net result can be the acceleration of the chemiluminescent reaction.

The effect of the photodegradation temperature was studied by placing the vessels containing the sample, photodegradation medium and water in a Tectron 200 analogue immersion bath from J.P. Selecta at temperatures from 20 °C to 80 °C. In order to study the influence of the oxidation temperature in isolation, the vessels containing 10^{-4} M $KMnO_4$ and water were also immersed in the previous bath at temperatures from 25 °C to 80 °C. In both cases, raising the temperature resulted in a gradual decrease in emission intensity; thus, the intensity at 80 °C was only 66% of that obtained at room temperature, the latter being chosen for subsequent tests.

3.5. Multivariate optimization

The last step in the optimization process involved using the modified simplex method (MSM), a multiparametric mathematical model, to examine the combined effect of flow rates over the range 7.0–11.0 mL min^{-1}; a number of segments of 20–40 for V_2; ON and OFF times of 0.4–0.8 s and 0.1–0.4 s, respectively, for the same valve; and ON and OFF times of 0.1–0.5 s for V_1. The MSM uses a simple algorithm to construct polyhedra in a multi-dimensional space from the different intervals, which constitute the vertices of the polyhedra. The algorithm seeks to identify the optimum vertices (*viz.* those resulting the highest possible analytical signals) [20,21].

Subsequently, the intervals were fitted to the optimum region defined by the first simplex. The new intervals studied were 750–1000 pump display; 24–30 segments for V_2; ON and OFF times of 0.4–0.7 s and 0.2–0.2 s, respectively, for V_2; ON and OFF times of 0.4–0.6 s and 0.1–0.2 s, respectively, for V_1. Based on the results of the simplex, the new dynamic parameters for

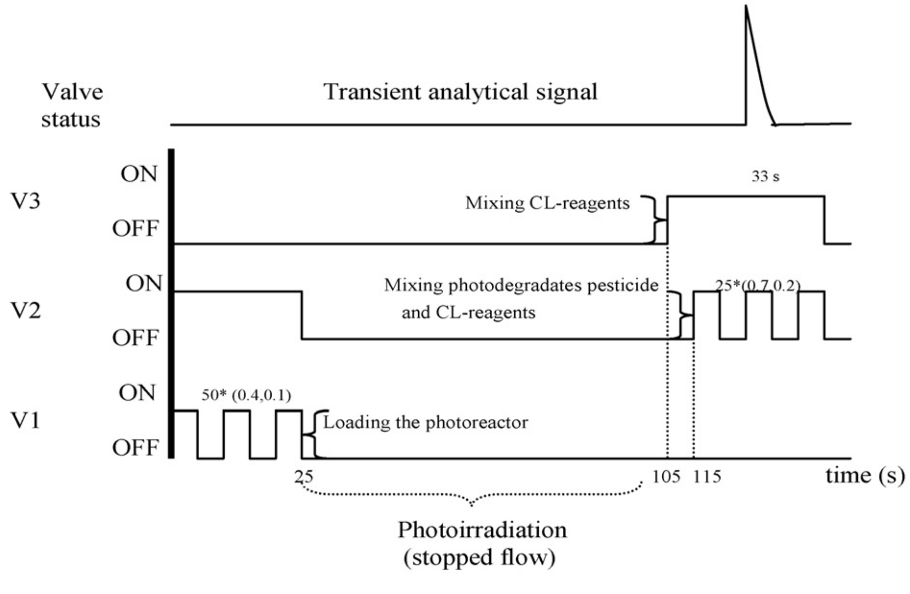

V_1= 0,50*(0.4,0.1),0.5

V_2 = 0,25,90,25*(0.7,0.2),0.5

V_3 = 105,33

t_{cycle} = 160 s

Fig. 7. Working optimized program for the solenoid valve set (figure and data). The working preliminary set (previous to optimization) was as follows: $V_1 = 0$, 50(0.4, 0.2), 0.5; $V_2 = 0$, 30, 150, 30(0.6, 0.2), 0.5; $V_3 = 165$, 39; $t_{cycle} = 240$ s.

the solenoid valves corresponded to the configuration defined in Fig. 7, and a total flow rate of 10 mL min^{-1}.

4. Analytical applications

The optimum operational conditions identified in previous tests were used in combination with benfuresate concentrations over the range 1–95 mg L^{-1} ($n = 9$) in order to obtain a calibration curve that was linear over the concentration range 1 µg L^{-1}–4 mg L^{-1} ($n = 6$) and conformed to the equation $I = 4555.7x + 284.2$, where I is the emission intensity and x is the analyte concentration. The correlation coefficient was 0.9999.

The limit of detection was calculated as the lowest pesticide concentration giving a signal equal to that of the blank plus three times its standard deviation (σ). The value thus obtained was 0.1 µg L^{-1} ($n = 5$).

Within-day deviations were estimated by using 11 insertions of a sample containing a 0.15 mg L^{-1} analyte concentration and between-day deviations from five aliquots of a sample containing 0.2 mg L^{-1} benfuresate that was inserted on non-consecutive days. Both types of deviation were calculated to be 3.4%. According to this series of insertions of the analyte dissolution a sample throughput was 22 h^{-1} and being the sample and reagents consumption was 0.66 mL, 0.16 mL and 0.32 mL sample, photodegradation medium and oxidant, respectively.

The potential interferents studied included both inorganic cations and anions, and a pesticide of the benfuresate family. To this end, we used a 0.5 mg L^{-1} concentration of analyte and a 0.1–500 mg L^{-1} concentration of each interferent. The resulting signals were compared with that provided by a 0.5-mg L^{-1} solution of the analyte containing none of the studied interferents. A potential interferent was assumed not to interfere when it altered the analytical signal by less than 5%. See Table 3.

Using a bond Elut C_{18} solid-phase extraction cartridge from Varian [8] allowed the interferences of Fe^{2+}, Fe^{3+}, Mn^{2+}, Cd^{2+}, Cu^{2+}, Co^{2+}, Pb^{2+}, Cr^{3+}, $CrO_4{}^{2-}$, CN^-, CH_3COO^-, $NO_3{}^-$ and $NO_2{}^-$ to be avoided. A solution containing the previous ions at a 500 mg L^{-1} concentration and the analyte at 0.5 mg L^{-1} in a final volume of 25 mL was passed through the cartridge, which was washed with 20 mL of deionized water. Then, the analyte was eluted with 0.625 mL of acetonitrile (2.5% in the final volume) and the eluate was made to 25 mL with deionized water. The error thus obtained in the benfuresate concentration was 3.1%. Therefore, all interferents were successfully removed as per the above-described criterion.

4.1. *Application to water, human urine and commercial formulations*

The water samples required prior passage through a C_{18} solid-phase extraction cartridge, which was then washed with 20 mL of deionized water, dried and eluted with 0.625 mL of acetonitrile (2.5% in the final volume), the eluate being made to 25 mL with deionised water.

Commercial pesticide formulations contain both the active compound and other ingredients including emulsifiers, dispersants and adjuvants (inert compounds) intended to improve spreading and availability in the target medium.

Table 3
Influence of foreign compounds

Interferent	C (mg L^{-1})	Er (%)
Fe^{3+}	0.25	−4.5
Fe^{2+}	1	−3.2
$NH_4{}^+$	500	−2.5
Mn^{2+}	5	3.8
K^+	500	−5
Na^+	500	4.8
Zn^{2+}	100	−1.8
Mg^{2+}	500	1.0
Cd^{2+}	10	3.2
Cu^{2+}	0.5	−4.1
Ca^{2+}	100	3.0
Ni^{2+}	50	1.1
Co^{2+}	2	−4.6
Pb^{2+}	2	4.4
Cr^{3+}	2	−1.0
CN^-	2	4.3
$H_2PO_4{}^-$	250	−3.3
CH_3COO^-	5	0.6
I^-	50	2.2
$NO_2{}^-$	5	−3.7
$NO_3{}^-$	1	−4.3
Cl^-	500	0.2
$HCO_3{}^-$	500	3.5
$CO_3{}^{2-}$	100	3.3
$CrO_4{}^{2-}$	2	−0.8
$SO_4{}^{2-}$	500	−7.4
Urea	100	4.2
Ethofumesate	3	1.9

Maximum assayed concentration (0.5 mg L^{-1} benfuresate). Anion and cation solutions were prepared from sodium and chloride salts, respectively.

Because no commercial formulations of benfuresate were available from registered local pesticide manufacturers, we prepared a laboratory formulation containing the inert ingredients included by the US Environmental Protection Agency among the allowed compounds for pesticide formulations [22]. The formulation was of the type typically used in Spain (emulsionable concentrations, GCPF code) [23] and contained 40% benfuresate and 60% acetone.

The urine sample was collected from a healthy male and spiked with benfuresate at a 0.5 mg L^{-1} concentration prior to passage through a C_{18} cartridge that was washed with 20 mL of deionised water and eluted with 0.625 mL of acetonitrile, the eluate being made to 25 mL with deionised water for analysis. Obtained results (recoveries) were as follows: residual water (Xirivella, Spain) 103.5 ± 4.5; tap water (Burjassot, Spain) 98.4 ± 2.3; bottled water (Bejis, Spain) 97.1 ± 4.0.

5. Conclusions

A new method based on the photo-induced chemiluminescence of benfuresate was developed for its determination in a multicommutated flow analysis system using alkaline potassium ferricyanide to generate the chemiluminescence in a direct manner.

Multicommutated flow analysis allows manifolds to be miniaturized, reproducibility to be increased by effect of the need for minimal operator intervention, and consumption of sample and reagents to be reduced relative to FIA as the two are only circulated for the time strictly needed.

The proposed method was successfully used to determine the pesticide benfuresate in various types of environmental (mineral, supply and waste waters) and biological samples (human urine), as well as in commercial formulations. The method is more easily automated, uses less sample and reagent per analysis, and is better suited to small amounts of analyte and more reproducible than its fluorescence-based counterpart.

References

[1] http://www.agro-biz.com.ar/uso_seguro/glosario.html.

[2] S. Nemoto, K. Sasaki, S. Eto, I. Saito, H. Sakai, T. Takahasi, Y. Tonogai, T. Nagayama, S. Hori, Y. Maekawa, M. Toyoda, Shokuhin Eiseigaku Zasshi 41 (2000) 233.

[3] A. Kaihara, K. Yoshii, Y. Tsumara, Y. Nakamura, S. Ishimitsu, Y. Tonogai, J. Health Sci. 46 (2000) 336.

[4] A. Kaihara, K. Yoshii, Y. Tsumara, Y. Nakamura, S. Ishimitsu, Y. Tonogai, J. Health Sci. 48 (2002) 173.

[5] E. Ueno, H. Oshima, I. Saito, H. Matsumoto, Shokuhin Eiseigaku Zasshi 43 (2002) 80.

[6] M. Sakamoto, T. Tsutsumi, J. Chromatogr. A 1028 (2004) 63.

[7] X.-G. Chu, X.-Z. Hu, H.-Y. Yao, J. Chromatogr. A 1063 (2005) 201.

[8] J.R. Albert-Garcia, J. Martínez Calatayud, J. Flow Injection Anal. 23 (2006) 19.

[9] J. Martínez Calatayud, J. Flow Injection Anal. 24 (2007) 1.

[10] M. Catalá Icardo, J.V. García Mateo, J. Martínez Calatayud, Trends Anal. Chem. 21 (2002) 366.

[11] http://www.uv.es/martinej/Flow-Analysis/JVicente-MULTICOMMUTATION.htm.

[12] M. Palomeque, J.A. García Bautista, M. Catalá Icardo, J.V. García Mateo, J. Martínez Calatayud, Anal. Chim. Acta 512 (2004) 149.

[13] Y. Zhao, W. Baeyens, X. Zhang, A. Calokerinos, K. Nakashima, G. Van der Waken, Analyst 122 (1997) 103.

[14] H. Pasekova, M. Polasek, Talanta 52 (2000) 67.

[15] Z. Zhu, Q. Yang, Z. Hao, L. Jianyan, Huaxue Fence 36 (2000) 60.

[16] T. Pigot, J.C. Dupin, H. Martínez, C. Cantau, M. Simon, S. Lacombe, Micropor. Mesopor. Mater. 84 (2005) 343.

[17] T. Mori, M. Takamoto, Y. Tate, J. Shinkuma, T. Wada, Y. Inoue, Tetrahedron Lett. 42 (2001) 2505.

[18] V. Latour, T. Pigot, M. Simon, H. Cardy, S. Lacombe, Photochem. Photobiol. Sci. 4 (2005) 221.

[19] P. Filipiak, J. Bartoszewicz, G.L. Hug, H. Kozubek, J. Paczkowski, B. Marciniak, J. Photochem. Photobiol. A: Chem. 191 (2007) 167.

[20] W. Spendley, G.R. Hext, F.R. Himsworth, Technometrics 4 (1962) 441.

[21] S.N. Deming, L.R. Parker, CRC Crit. Rev. Anal. Chem. 7 (1978) 187.

[22] http://www.epa.gov/opprd001/inerts/lists.html.

[23] http://www.agriculture.com.

Available online at www.sciencedirect.com
ScienceDirect

Talanta 75 (2008) 691–696

Talanta

www.elsevier.com/locate/talanta

Voltammetric reduction of finasteride at mercury electrode and its determination in tablets

A. Álvarez-Lueje*, S. Brain-Isasi, L.J. Núñez-Vergara, J.A. Squella

Bioelectrochemistry Laboratory, Chemical and Pharmaceutical Sciences Faculty, University of Chile, P.O. Box 233, Santiago 1, Chile

Received 7 August 2007; received in revised form 4 December 2007; accepted 6 December 2007
Available online 15 December 2007

Abstract

Finasteride in hydroalcoholic solutions (ethanol/Britton-Robinson buffer, 30/70) exhibits cathodic response in a wide range of pH (−0.5 to 12) using differential pulse (DPP) and tast polarography (TP). The reduction peak of finasteride at acidic pH, is a catalytic proton peak resulting from a mechanism involving a first protonation of finasteride followed by the reduction of the protons combined with finasteride in order to regenerate finasteride and liberate hydrogen. Based on the catalytic hydrogen wave, a novel method for the determination of finasteride can be proposed. For analytical purposes we selected DPP technique in an ethanol/0.0625 mol L^{-1} H_2SO_4 (30/70) solution medium. In this condition the I_p varied linearly with finasteride concentration between 5×10^{-5} and 5×10^{-4} mol L^{-1}. Within-day and inter-day reproducibility's were adequate with R.S.D. values lower than 2%. The selectivity of the method was checked with both accelerated degradation trials and typical excipients formulations. The developed method was applied to the assay and the uniformity content of finasteride tablets and compared with the standard HPLC method. The DPP-developed method was adequate for the finasteride determination in pharmaceutical forms as that exhibited an adequate accuracy, reproducibility and selectivity. Furthermore, treatment of the sample was not required as in HPLC; the method is not time-consuming and less expensive than the HPLC ones.

Keywords: Finasteride; Differential pulse voltammetry; Reduction; Tablets

1. Introduction

Finasteride (*N*-(1,1-dimethylethyl)-3-oxo-4-aza-5α-androst-1-ene-17α-carboxamide) (Fig. 1) is an inhibitor of the 5α-reductase cellular type 2 and it is used to treat prostatic alterations and androgenetic alopecia in men [1,2]. The drug is a member of the family of compounds known as 4-azasteroids [3]. Today the most accepted mechanism brings over the interaction of finasteride with the NADP-5α reductase complex which is related with the redox properties of finasteride, and corresponds to a reduction of the drug in the double bond between the carbons 1 and 2 of the androstane ring; the dihydrofinasteride has been identified by mass spectrometry [4].

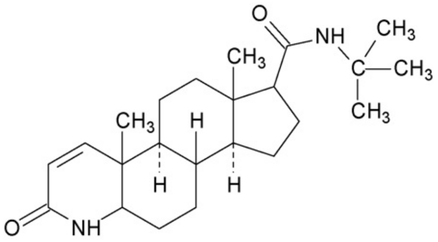

Fig. 1. Chemical structure of finasteride.

HPLC has been used to quantify finasteride in biological fluids [5–10] and also applied to bioequivalence studies [11,12]. The determination of finasteride in tablets has been carried out by using HPLC–UV [13,14], GC–FID [15] and recently a spectrophotometric method based on the formation of ion-pair complexes between the drug with a colorant and measured at the maximum wavelength has been published [16]. In addition, the LC determination of finasteride and its application to storage stability studies had been also described [17].

From the electrochemical point of view, Amer has described the polarographic behaviour of finasteride [18]. The results of the electrochemical behaviour described in that paper differ substantially from our findings. A detailed discussion is included.

---

* Corresponding author. Fax: +56 7378920.
E-mail address: aalvarez@ciq.uchile.cl (A. Álvarez-Lueje).

0039-9140/$ – see front matter © 2007 Elsevier B.V. All rights reserved.
doi:10.1016/j.talanta.2007.12.004

2. Experimental

2.1. Reagents and drugs

Finasteride (99.8% chromatographically pure) was supplied by Sanitas Laboratories (Santiago, Chile). Commercial capsules of Saniprosto® (declared amount per tablet 5.0 mg finasteride, Sanitas Laboratories. Santiago, Chile) were obtained commercially. Spironolactone (≥97%, Sigma–Aldrich).

All reagents were of analytical grade unless indicated otherwise. Phosphoric acid and acetonitrile HPLC grade (Merck) were used. Deionized water was obtained in the laboratory, using ionic interchanged columns (Milli-Q).

2.2. Solutions preparation

2.2.1. Buffer solutions

0.1 mol L^{-1} Britton-Robinson buffer (acetic acid–boric acid–phosphoric acid) for polarographic experiments was used, and desired pH was adjusted with concentrated solutions of NaOH. An ionic strength of 0.3 mol L^{-1} was adjusted with KCl.

2.2.2. H_0 scale

A modified Hammett's acidity scale (H_0) for solutions below pH 1.5 (using H_2SO_4–H_2O) was employed [19].

2.2.3. Stock drug solution

15.54 mg finasteride was dissolved and diluted up to 25 mL with ethanol, to obtain a final concentration around of 1.67×10^{-3} mol L^{-1} finasteride. The solution was protected from light by using amber glass material.

2.2.4. Work solution

A 3-mL aliquot of the stock solution was taken and then diluted to 10 mL with mobile phase or Britton-Robinson buffer solution, for HPLC or DPP, respectively.

2.3. Apparatus

2.3.1. Voltammetric analyzer

Differential pulse polarographic (DPP), tast polarographic (TP) experiments were performed with an automatized assembly BioAnalytical System, composed by a CV-50 W potentiostat polarographic system (CGME), coupled to a GATEWAY 2000 PC and acquisition and treatment data system BAS CV-50 W v. 2.0

A dropping mercury electrode (BAS) as the working electrode, a platinum wire (Metrohm type 6.0322.000) counter electrode and an Ag/AgCl (BAS) reference electrode were employed. The operating conditions were: sensitivity between 1 and 10 μA; drop time 300 ms; potential range 0 to −1700 mV; pulse retard 17 ms; pulse height 50 mV.

2.3.2. HPLC

Measurements were carried out using a Waters assembly equipped with a model 600 Controller pump and a model 996 Photodiode Array Detector. The acquisition and treatment of data were made with the Millenium v. 2.1 software. As chromatographic column a Bondapak/Porasil C18 column of 3.9 mm × 150 mm was used. As column guard a C18 Bondapak (30 mm × 4.6 mm) was employed. The injector was a 20 μL Rheodyne valve. UV detection at 240 nm was employed and the column was kept at constant temperature using a Waters column heater cartridge model 600.

An isocratic elution composed of a solution consisting of acetonitrile/2.5 mmol L^{-1} phosphoric acid (50/50, v/v) mobile phase was used. The flow was 1.5 mL min^{-1} and the working temperature was kept constant at 45 ± 1 °C. In these conditions, finasteride exhibited a retention time of 3.94 ± 0.04 min. This chromatographic system was based on USP assay for finasteride [13].

2.4. Analytical procedure

2.4.1. Calibration curve preparation

2.4.1.1. Polarography. By diluting the finasteride stock solution with ethanol/0.0625 mol L^{-1} sulfuric acid (30/70, v/v), working solutions ranging between 1×10^{-5} and 5×10^{-4} mol L^{-1} were prepared.

2.4.1.2. HPLC. By diluting the finasteride stock solution with mobile phase, working solutions ranging between 3×10^{-6} and 3×10^{-5} mol L^{-1} were prepared. The solutions were injected and chromatographed according to the working conditions previously given. UV detector was operated at $\lambda = 240$ nm.

2.4.2. Synthetic samples

Excipients (Indigo Carmine, sodium lauryl sulfate, magnesium stearate, starch sodium glycolate, lactose spray dried, carboxymethylcellulose PA 102, talc, titanium dioxide, microcrystalline cellulose, red iron oxide, yellow iron oxide, hydroxypropylcellulose and pregelanitizated starch) were added to the drug for recovery studies, according to manufacturer's batch formulas for finasteride tablets.

2.4.3. Composite assay for finasteride tablets

Not less than 15 finasteride tablets were weighed and finely powder and then an accurately weighed quantity of the powder, equivalent to about 5 mg of finasteride were transferred to a 25-mL volumetric flask with aid of ethanol, sonicated and fill to volume with ethanol. The solution was divided into two; one for DPP assay and the second one centrifuged for 10 min at 4000 rpm, and the clear liquid was used for HPLC assay.

2.4.4. Individual tablet assay procedure

2.4.4.1. Polarography. For this study no less than 10 commercial tablets of finasteride (Saniprosto®, amount declared 5.0 mg finasteride per tablet) were used. Each tablet was independently suspended in 10-mL ethanol with sonication to assure the complete dissolution of the drug and diluted to a final volume of 25.0 mL with the same solvent. A 3-mL aliquot of each solution was taken and diluted to 10 mL with 0.0625 mol L^{-1} sulfuric acid, to obtain a finasteride concentration of 1.6×10^{-4} mol L^{-1}. Each sample solution was transferred to a polarographic cell, bubbled with nitrogen during 5 min and recorded at least twice from −900 to −1400 mV. The mg amount of finasteride in the sample solution was calculated from the prepared standard calibration curve.

2.4.4.2. HPLC. For this study no less than 10 commercial tablets of finasteride (Saniprosto®, amount declared 5.0 mg finasteride per tablet) were used. The content of each tablet was independently suspended in 10-mL ethanol with sonication to assure the complete dissolution of the drug and diluted to a final volume of 25.0 mL with the same solvent. Each one of the above solutions was centrifuged by 10 min at 4000 rpm, and then an aliquot of 0.5-mL supernatant was taken and diluted to a 10-mL volume with mobile phase. The mg amount of finasteride in the sample solution was calculated from the corresponding prepared standard calibration curve. This procedure was adapted from the finasteride assay on Pharmacopoeia [13].

2.4.5. Selectivity studies [20]

2.4.5.1. Degradation trials. Hydrolysis. 3 mL of finasteride stock solution were transferred to a 10-mL distillation flask and adding (a) 7-mL water for neutral hydrolysis, (b) 1 mL 1 mol L^{-1} HCl for acid hydrolysis, or (c) 1 mL 1 mol L^{-1} NaOH for alkaline hydrolysis. Then each solution was completed to 10-mL volume with water and boiled for 1 h at reflux.

Photolysis. 10 mL of 1×10^{-3} mol L^{-1} finasteride ethanol solution was bubbled for 2 min with nitrogen and transferred to a black box and then irradiated with UV light (UV Black–Ray long wave ultraviolet lamp, UVP model B 100 AP (50 Hz, 2.0 A) with a 100 W Par 38 Mercury lamp equipped with a 366 nm filter) at a distance of 15 cm for 8 h (1.2×10^{19} quanta s^{-1}, determined by using the potassium ferrioxalate chemical actinometer) [21].

Thermolysis: Circa 2.1 mg was heated at 105 °C for 5 h.

Appropriate volumes of each obtained solution from the degradation trials or the corresponding mg from thermolysis in raw material assay were taken and completed to a final volume with ethanol and 0.0625 mol L^{-1} sulfuric acid to obtain a theoretical concentration of 6×10^{-5} mol L^{-1} finasteride (30% ethanol in final solution). Samples from these studies were stored at −20 °C and protected from light prior to polarographic analysis. Each sample was analyzed by duplicate.

2.4.6. Statistic analysis

Comparison between different techniques, as well as the comparison with standard deviations was carried out by means of the Student's *t*-test, and using significance limits between 95% and 99% of confidence [22,23].

3. Results and discussion

Finasteride in hydroalcoholic solutions (ethanol/Britton Robinson buffer, 30/70) exhibits cathodic response in a wide range of pH (2–12) using DPP and TP (Fig. 2A). As can be seen, the polarographic response in DPP mode at pH 2 is very well defined and peak currents are notoriously higher than the peak currents at pH > 3. With the aim to investigate the possibility to obtain better resolution of the polarographic peak, H_0 scale was explored. In super acid media (Fig. 2B), well-resolved peaks and high peak current values were obtained. On the other hand, at pH > 2, both the peak shape changes and peak current diminishes. As can be seen in Fig. 2A, the DP polarogram evidences a shoulder in alkaline pH and in TP a new wave appears (insert in Fig. 2A).

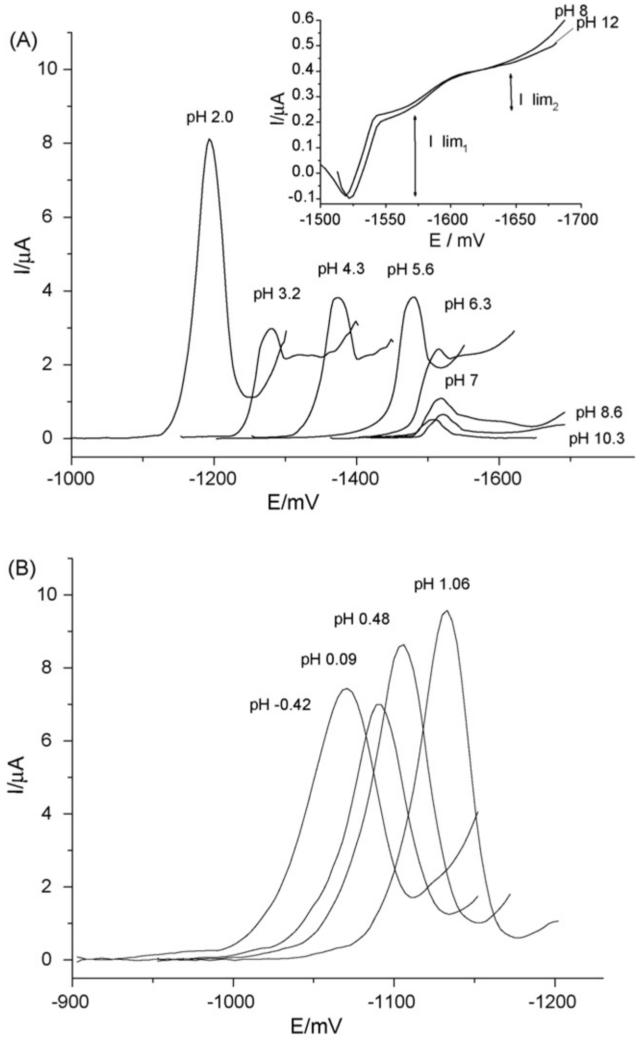

Fig. 2. DPP and TP (A) 5×10^{-4} mol L^{-1} finasteride solution at different pH. (A) pH 2–12, ethanol/Britton-Robinson buffer, 30/70. (B) pH < 2, ethanol/0.0625 mol L^{-1} sulfuric acid, 30/70.

From the DPP curves we can study the dependence of peak potentials and peak current with pH. E_p–pH plots exhibit three main zones. The first two, between pH −0.5 and 2 and pH 2 and 6, are pH-dependent. The third zone, above pH 6, is pH independent. As can be seen in Fig. 3A, the peak potential remains stable between pH 6 and 12. Furthermore, peak current dramatically decreases while the pH increases (Fig. 3B).

From the pH behaviour it is possible to conclude that the peak current is extraordinarily pH sensitive, changing about eight folds between pH 2 and 7. On the other hand, the value of

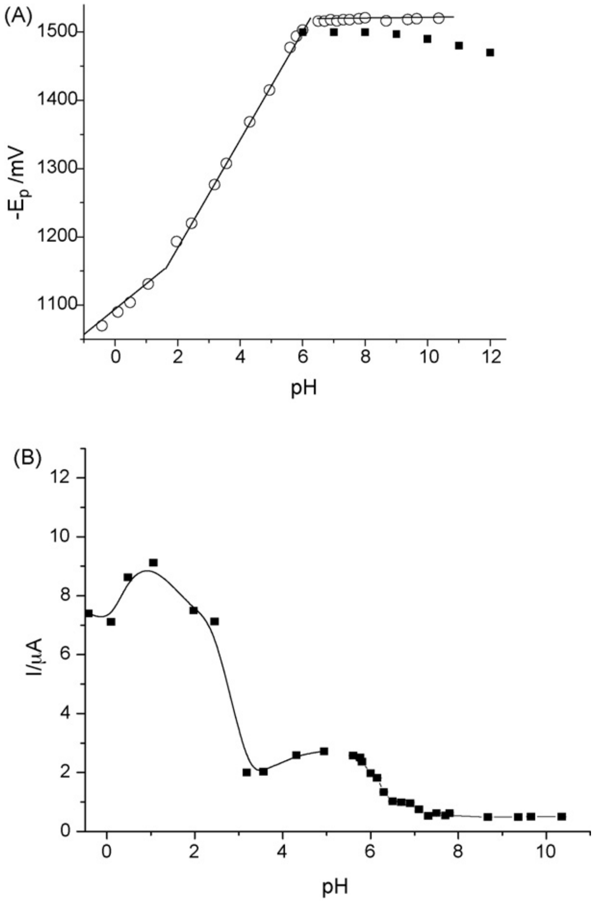

Fig. 3. (A) Peak potential evolution of 5×10^{-4} mol L^{-1} finasteride solution with pH ((◯) our results; (■)Amer' results). (B) Peak current evolution with pH.

the peak potential is very near the hydrogen discharge. Both of these aspects are strongly indicative that the process obeys the catalytic hydrogen wave [24].

Furthermore, in order to deep in the elucidation of the process involved in the reduction peak; finasteride was compared with a drug with similar structure such as spironolactone [24]. This drug produces a polarographic response via the 2e$^-$ and 2H$^+$ reduction of the carbonyl group. As can be seen in Fig. 4, the limiting currents of equimolar solutions of both compounds only are equal at pH > 9. At pH 2, the finasteride limiting current is about eight folds higher than spironolactone's one, which indicates that the electrochemical reduction of finasteride does not involve 2e$^-$ and 2H$^+$ in all pH range, such as was erroneously concluded in the previous work of Amer [18]. Securely, the increase of the limiting current of finasteride solutions at acidic pH indicates that at acidic pH the catalytic wave of protons is occurring. From the first work of Mairanovskii it is well known that sulfur- and nitrogen-containing organic compounds can act as catalyst diminishing hydrogen overpotential, thus, promoting a catalytic wave before the hydrogen of the medium [24].

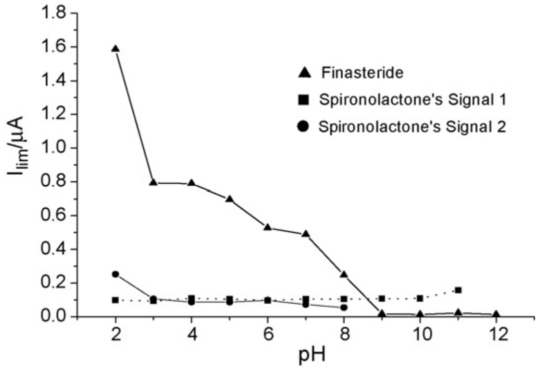

Fig. 4. Limiting current evolution with pH of finasteride and spironolactone (5×10^{-4} mol L^{-1} concentration solutions, ethanol/Britton-Robinson buffer, 30/70).

Consequently, in the case of finasteride, the catalytic wave is generated by the following steps. In a first step, finasteride (F) interacts with proton to form the protonated finasteride (FH$^+$), probably in the nitrogen at 4-position in the ring A. Then FH$^+$ was polarographically reduced to produce FH which in a bimolecular interaction regenerated finasteride and molecular hydrogen according to:

$$\mathrm{F} + \mathrm{H}^+ \rightleftarrows \mathrm{FH}^+$$

$$\mathrm{FH}^+ + \mathrm{e}^- \rightarrow \mathrm{FH}$$

$$2\mathrm{FH} \rightarrow 2\mathrm{F} + \mathrm{H}_2$$

Our results differ substantially from those previously described by Amer, who reported that the polarographic response of finasteride appears only between pH 6 and 12, and obviously he did not see the catalytic wave. Moreover, the ΔE_p reported by Amer between pH 6 and 12 is only about 30 mV (Fig. 3A). Likewise, in our results the peak current behaviour with pH is also in opposition with the Amer's description.

Based on the catalytic hydrogen wave, a novel method for the determination of finasteride can be proposed. For analytical purposes, we have selected the DPP technique working in ethanol/0.0625 mol L^{-1} H$_2$SO$_4$ (30/70) hydroalcoholic medium. In this condition the I_p varied linearly with finasteride concentration between 5×10^{-5} and 5×10^{-4} mol L^{-1}. Within-day and inter-day reproducibility's were adequate with R.S.D. values lower than 2%. In Table 1 the analytical parameters are summarized.

Table 1
Analytical parameters for the developed DPP method

Parameter	DPP
Within-day reproducibility, CV (%)[a]	0.17
Inter-day reproducibility, CV (%)[a]	1.06
Recovery (%)[b] ± S.D.	98.21 ± 1.84
Concentration range (mol L^{-1})	5×10^{-5}–5×10^{-4}
Calibration curve	$I_p = 19921.62[\mathrm{C}] - 0.0857$ ($n = 9$, $r = 0.9993$)
Detection limit (mol L^{-1})	7.59×10^{-6}
Quantitation limit (mol L^{-1})	1.53×10^{-5}

[a] Concentration level of 3.5×10^{-4} mol L^{-1}.

[b] Average on a concentration level of 1×10^{-4} mol L^{-1}.

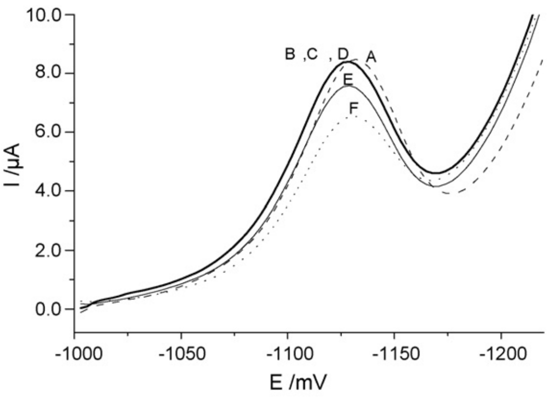

Fig. 5. DPP of selectivity trials: (A) 6×10^{-5} mol L^{-1} finasteride standard solution, (B) neutral hydrolysis, (C) thermolysis, (D) photolysis, (E) acid hydrolysis and (F) alkaline hydrolysis (ethanol/0.0625 mol L^{-1} sulfuric acid, 30/70).

Table 2
Individual tablet assay of finasteride[a]

Tablet	HPLC–UV		DPP	
	Found (mg)	Found (%)	Found (mg)	Found (%)
1	4.75	95	4.88	97.6
2	4.83	96.6	4.79	95.8
3	4.91	98.2	4.88	97.6
4	4.99	99.8	4.91	98.2
5	4.76	95.2	4.94	98.8
6	4.99	99.8	5.15	103.0
7	4.66	93.2	4.75	95.0
8	4.69	93.8	4.85	97.0
9	4.88	97.6	4.86	97.2
10	4.79	95.8	4.98	99.6
Average	4.83	96.5	4.89	98.0
S.D.	0.12	2.32	0.11	2.21
CV (%)	2.5	2.4	2.3	2.3

[a] Declared amount/tablet: 5.0 mg finasteride.

In order to check our proposed method for selectivity, we tried different degradation pathways for finasteride. Selectivity is a parameter that gives account of the capacity of the method of producing a signal due to only the presence of the analyte (finasteride) and consequently free of other interferences such as degradation products, metabolites or pollutants. We have used the following trials in order to prove the selectivity: hydrolysis (acidic, alkaline and neutral), photolysis and thermolysis [20].

When a finasteride solution was exposed to either acid or alkaline hydrolysis, the polarographic peak diminishes and no new signals appear in the polarograms (Fig. 5). Actually, hydrolysis of finasteride in acid media for 1 h produces a peak current reduction in approximately 17% and in alkaline media, about 40%. Furthermore, in order to check the selectivity of possible photodecomposition products, finasteride was exposed to 366-nm UV for 8 h. In this experiment, the finasteride's peak remains unaltered. Similar behaviour was obtained when finasteride was submitted to thermolysis or neutral hydrolysis test. According to the described results obtained in the selectivity trials, it can be concluded that the proposed differential pulse polarographic method is sufficiently selective, in order to be applied to finasteride quantification and also can be applied for further stability studies.

In order to obtain the precision and accuracy of the developed method, a recovery study was performed. These results (Table 1) reveal that the method has an adequate precision and accuracy and consequently, can be applied to the determination of finasteride in commercial dosage (tablets). Also, we can conclude from these experiments that typical excipients included in the drug formulation (Indigo Carmine, sodium lauryl sulfate, magnesium stearate, starch sodium glycolate, lactose spray dried, carboxymethylcellulose PA 102, talc, titanium dioxide, microcrystalline cellulose, red iron oxide, yellow iron oxide, hydroxypropylcellulose and pregelanitizated starch) do not interfere with the selectivity of the method, and previous separation or extractions are not necessary.

The proposed DPP method was applied successfully to both a composite assay and an individual tablet assay, in order to verify the uniformity content of finasteride. With comparative purposes a HPLC analysis was also carried out (Table 2). In the composite assay 98.5% and 99.6% of the label claimed for DPP and HPLC, respectively were found, which fall within the percentages accepted by United Sates Pharmacopoeia (95.0–105.0%). Also, the content for all assayed tablets in the individual tablet assay fall in the range of 85.0–115.0% of label claim and no unit is outside the range of 75.0–125.0% of label claim, fulfilling the Pharmacopoeia requirement for uniformity content of tablets [13]. The results obtained in the uniformity content test by each applied method were compared by applying Snedecor *F*-test (variance proportion) and then the Student's *t*-test ($p < 0.05$, $n = 10$), and it was concluded that no significant differences exist between them and that they were statistically equivalent.

Finally, we can conclude that the DPP-developed method is enough for the finasteride determination in pharmaceutical forms, as it exhibits an adequate accuracy, reproducibility and selectivity. Furthermore, treatment of the sample is not required as in HPLC; the method is not time-consuming and less expensive than the HPLC ones.

References

[1] J.D. McConnell, R. Bruskewitz, P. Walsh, G. Andriole, M. Lieber, H.L. Holtgrewe, P. Albertsen, C.G. Roehrborn, J.C. Nickel, D.Z. Wang, A.M. Taylor, J. Waldstreicher, N. Engl. J. Med. 338 (1998) 557.
[2] V.H. Price, N. Engl. J. Med. 341 (1999) 964.
[3] A. Guarna, E.G. Occhiato, G. Danza, A. Conti, M. Serio, Steroids 63 (1998) 355.
[4] H. Bull, M. García-Calvo, J. Am. Chem. Soc. 118 (1996) 2359.
[5] B. Matuszewski, M. Constanzer, Anal. Chem. 70 (1998) 882.
[6] C. Cendrowska, B. Buszewski, J. Liq. Chromatogr. Relat. Technol. 22 (1999) 2259.
[7] M. Constanzer, C. Chavez-Eng, J. Chromatogr. B 693 (1997) 117.
[8] F.Q. Guo, L.F. Huanga, K.P. Wong, Y. Daí, Y.W. Li, Y.Z. Liang, K.L. Huang, K.J. Zhong, M.J. Wu, J. Pharm. Biomed. Anal. 43 (2007) 1507.
[9] M. Thevis, H. Geyer, U. Mareck, U. Flenker, W. Schanzer, Ther. Drug Monit. 29 (2007) 236.
[10] M. Mazzarino, F. Botre, Rapid Commun. Mass Spectrom. 20 (2006) 3465.
[11] F.G. de Menezes, W. Ribeiro, D.R. Ifa, M.E. de Moraes, M.O. de Moraes, G. de Nucci, Arzneimittel-Forschung 51 (2001) 145.

[12] A. Almeida, S. Almeida, A. Filipe, S. Gagnon, A. Mirapeix, B. Girard, M. Tanguay, Arzneimittel-Forschung 55 (2005) 218.
[13] USP 27-NF 22. United States Pharmacopoeial Convention, Inc., Rockville, MD, USA, 2004.
[14] H. Demir, A. Cucu, S. Sakarya, Anal. Chim. Acta 557 (2006) 252.
[15] S. Sağlık, S.T. Ulu, Anal. Biochem. 352 (2006) 260.
[16] S.T. Ulu, Spectrochim. Acta A. Mol. Biomol. Spectrosc. 67 (2007) 778.
[17] A.A. Syed, M.K. Amshumali, J. Pharm. Biomed. Anal. 25 (2001) 1015.
[18] S. Amer, Il Farmaco 58 (2003) 159.
[19] M.J. Jorgenson, D.A. Hartter, J. Am. Chem. Soc. 85 (1963) 878.
[20] O.A. Quattrochi, S.A. De Andrizzi, R.F. Laba, Introducción a la HPLC, aplicación y práctica, Artes Gráficas Farro SA, Argentina, 1992.
[21] K. Akimoto, H. Kurosaka, I. Nakagawa, K. Sugimoto, Chem. Pharm. Bull. 36 (1988) 1483.
[22] R.C. Graham, Data Analysis for the Chemical Sciences. A Guide to Statistical Techniques, VHC Publishers, Inc., New York, 1993.
[23] J.K. Taylor, Statistical Techniques for Data Analysis, Lewis Publishers, Inc., New York, 1990.
[24] S.G. Mairanovskii, J. Electroanal. Chem. 6 (1963) 77.

Available online at www.sciencedirect.com
ScienceDirect
Talanta 75 (2008) 629–635
Talanta
www.elsevier.com/locate/talanta

Beyond potentiometry: Robust electrochemical ion sensor concepts in view of remote chemical sensing

Eric Bakker[a,b,*], Vishnupriya Bhakthavatsalam[a], Kebede L. Gemene[a]

[a] *Department of Chemistry, 560 Oval Drive, Purdue University, West Lafayette, IN 47907, USA*
[b] *Nanochemistry Research Institute, Department of Applied Chemistry, Curtin University of Technology, Perth, Western Australia 6845*

Received 9 March 2007; accepted 11 October 2007
Available online 18 October 2007

Abstract

For about 100 years, potentiometry with ion-selective electrodes has been one of the dominating electroanalytical techniques. While great advances in terms of selective chemistries and materials have been achieved in recent years, the basic manner in which ion-selective membranes are used has not fundamentally changed. The potential readings are directly co-dependent on the potential at the reference electrode, which requires maintenance and for which very few accepted alternatives have been proposed. Fouling or clogging of the exposed electrode surfaces will lead to changes in the observed potential. At the same time, the Nernst equation predicts quite small potential changes, on the order of millivolts for concentration changes on the order of a factor two, making frequent recalibration, accurate temperature control and electrode maintenance key requirements of routine analytical measurements. While the relatively advanced selective materials developed for ion-selective sensors would be highly attractive for low power remote sensing application, one should consider solutions beyond classical potentiometry to make this technology practically feasible. This paper evaluates some recent examples that may be attractive solutions to the stated problems that face potentiometric measurements. These include high-amplitude sensing approaches, with sensitivities that are an order of magnitude larger than predicted by the Nernst equation; backside calibration potentiometry, where knowledge of the magnitude of the potential is irrelevant and the system is evaluated from the backside of the membrane; controlled current coulometry with ion-selective membranes, an attractive technique for calibration-free reagent delivery without the need for standards or volumetry; localized electrochemical titrations at ion-selective membranes, making it possible to design sensors that directly monitor parameters such as total acidity for which volumetric techniques were traditionally used; and controlled potential coulometry, where all ions of interest are selectively transferred into the ion-selective organic phase, forming a calibration-free technique that would be exquisitely suitable for remote sensing applications.

Keywords: Ion-selective electrodes; Chemical sensors; Reference electrode; Calibration-free; Coulometry; Remote sensing

1. Direct potentiometry: the state of the art and promise for remote sensing

Ion-selective electrodes are among the oldest known types of chemical sensors [1]. In most cases, an ion-selective membrane separates the sample from an inner solution, and the electromotive force between reference electrodes in the aqueous sample and the inner solution is measured under zero current conditions (see Fig. 1). The inherent promise of this arrangement in view of remote sensing is multifold. It is an extremely simple and direct form of converting chemical into electrical information. The logarithmic activity of the ion of interest is directly proportional to the observed electromotive force, or potential. In so-called direct potentiometry, this measurement is performed directly on the sample, ideally without any sample preparation steps that are often impossible in remote sensing situations. Zero current potential measurements are also among the least power intensive measurements possible, making membrane electrodes quite promising candidates for the stated application. Ion-selective electrodes based on polymeric membranes are today the most intensively studied systems, and synthetic receptors (ionophores) that selectively bind to the target analytes have been reported for over 60 analytes [2,3].

In recent years, the field of potentiometric sensing with ion-selective electrodes has undergone a steady transformation. Perhaps most importantly, it was found that such sensors often exhibit vastly better ion selectivities than traditionally reported

---

[*] Corresponding author. Tel. +61 8 9266 2743.

0039-9140/$ – see front matter © 2007 Elsevier B.V. All rights reserved.
doi:10.1016/j.talanta.2007.10.021

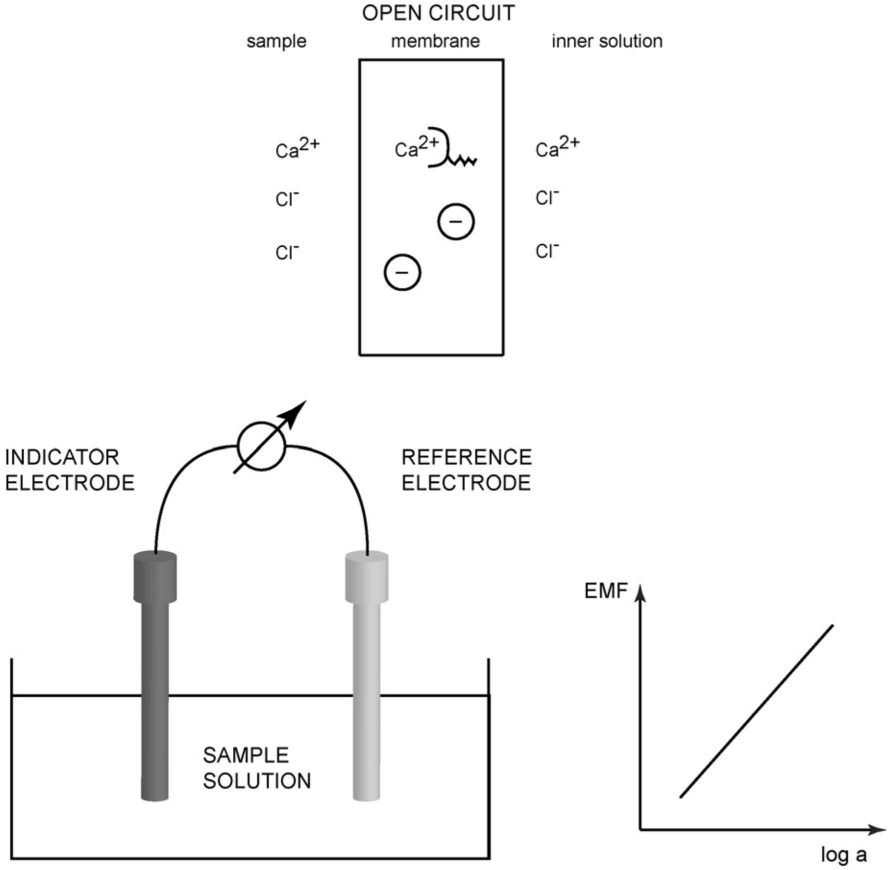

Fig. 1. Classical direct potentiometry with polymeric membrane ion-selective electrodes is widely used for the direct detection of electrolytes in clinical analysis. The potential is measured across a suitably formulated membrane that is contacted with two aqueous solutions, of which one is the sample (top). It is ideally a direct function of the ion activity on either side of the membrane, which leads to a log-linear relationship between the sample activity and the observed potential (bottom right). Since the measurement is equally dependent on the potential at the reference electrode (left), this technique requires careful maintenance, temperature control and frequent recalibrations.

[4–6], and this knowledge has allowed research teams to greatly improve on the detection limits of these electrodes [7–10]. Today, measurements at concentrations as low as nanomolar levels are not uncommon, and ion detection in small sample volumes on the order of 1 μl showed that total ion quantities as low as 300 attomol can be potentiometrically observed without any sample accumulation steps [11]. Indeed, potentiometry is a technique that, in principle, lacks so-called scaling laws [12]. A reduction in the sample or sensor size should not have an effect on the sensor output signal.

2. The trouble of direct potentiometry

One would think that the relatively low production costs, the simple required instrumentation and the long and established history of ion-selective electrodes would make them prime candidates for the measurement of ions in a number of situations. Indeed, these sensors are routinely used in all types of clinical analyzers to determine electrolyte concentrations in blood and other physiological samples [13,14]. Potentiometric microelectrodes are used in physiology for single cell electrolyte detection [15]. Environmental applications are also routinely known. But widespread applications in remote sensing, requiring no human intervention, no temperature control and very little fluidic recalibration, turns out to be extremely difficult with the current state of the art. Why is this so?

Let us have a closer look at the Nernst equation, according to which ion-selective electrodes are supposed to function if all works as expected:

$$\mathrm{emf} = K + \frac{2.303RT}{zF}\log a_{\mathrm{I}} \qquad (1)$$

The electromotive force, emf, depends on the logarithmic activity, a_{I}, of the analyte ion of interest. The sensitivity (slope) of this relationship primarily depends on the temperature and on the charge, z, of the ion I^z. The symbol K is, hopefully, a constant potential term, and R and F are the universal gas constant and the Faraday constant.

The logarithmic relationship between the observed potential and the sample activity means that small concentration changes translate into extremely small potential changes. Consider a 10% activity change of calcium ions at 25 °C. Eq. (1) predicts a mere 1.2 mV change in the emf. A twofold activity change gives an 8.9 mV signal change. In clinical analysis, this level of repeatability is accomplished by careful control of the temperature (T), frequent recalibrations (compensating for potential drifts) and the use of reliable reference electrodes (keeping *K* as constant as possible). Needless to say, such level of control and recalibration is neither desired nor possible in a miniature remote sensing environment. Temperature compensation is, of course, possible by simultaneous measurement with temperature probes. Potential drifts will, however, lead to analytically inacceptable inaccuracies after prolonged lack of recalibration steps, which are a serious limitation of the technology.

The second principal problem is the reference electrode. To this day, established reference electrodes still require a liquid junction and an electrolyte reservoir of constant composition. This design is most likely unacceptable for remote sensing applications, and direct potentiometric sensing will only be possible with pseudo-reference electrodes, such as a second ion-selective electrode selective for a background ion whose concentration remains sufficiently constant in the course of the measurement. Overall, current technology appears to be ill suited for prolonged use of miniature sensing systems that are supposed to give reliable measuring results over prolonged periods of time on the order of days or even months.

Very similar problems have also been major stumbling blocks in the realization of implantable sensing devices that can be left inside the body for prolonged periods of times, even after decades of active research in the field [16]. Perhaps the idea of using direct potentiometry as the readout principle for sensor devices that cannot be recalibrated has been flawed all along. In this article we discuss a few innovative measurement principles involving the same type of materials used in ion-selective electrodes that may help to overcome these long standing limitations.

3. High-amplitude sensing: chemical alarm systems without reliable reference electrodes

The above-mentioned limitation of the low sensitivity imposed by the Nernst equation and the accompanied stringent stability requirements for the reference electrode have been conceptually addressed by making use of ion fluxes [17]. Ion-selective membranes may be engineered to induce a zero-current flux of analyte ions from the sample in the direction of the membrane. This may be accomplished with electrodes containing inner solutions that exchange the analyte ion by a secondary ion at the inner membrane side. The resulting counterdiffusion flux transports the secondary ions to the sample and siphons the analyte ions away from the sample to the membrane phase. At a critical ion concentration in the sample, the imposed flux is sufficient to deplete these ions locally at the membrane surface, and a very large potential change is observed akin to a titration

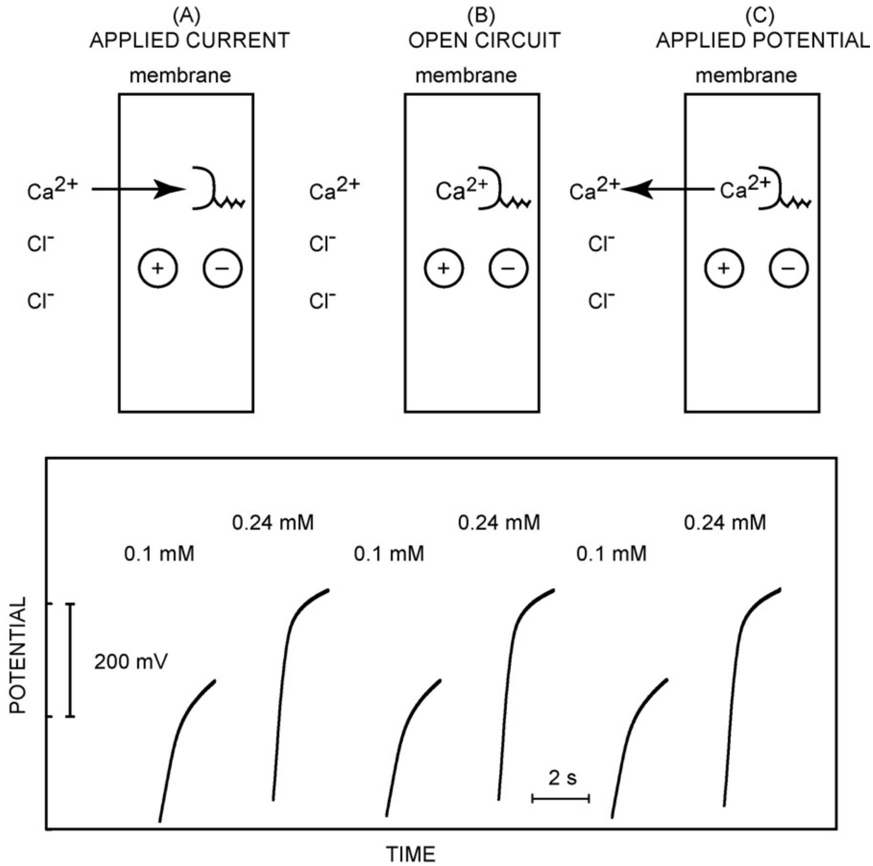

Fig. 2. High amplitude-pulsed chronopotentiometry with ion-selective membranes [19]. This technique yields sensitivities that are drastically larger than predicted by the Nernst equation. This is accomplished by localized sample depletion at the ion-selective membrane in a three-pulse experiment (top): an applied current pulse of variable magnitude extracts ions into the membrane and may lead to localized depletion near the membrane surface (A). This may be followed by an open circuit measurement pulse to give potential readings that are independent of the sample or membrane resistance (B). The system is subsequently regenerated by a potential pulse (C). Bottom: large, nearly 200 mV observed potential responses upon changing the calcium sample concentration from 0.1 to 0.24 mM [19].

endpoint. If two ion-selective electrodes are measured against each other, each engineered to exhibit slightly different fluxes, a very large peak-shaped potential response may be observed at a critical concentration. This concept does not require a traditional reference electrode and gives much larger sensitivities than allowed by the Nernst equation [17].

This promising concept still has a number of potential limitations. The adjustment of inward ion fluxes by chemical means is relatively difficult because they are only accurately stable if the system is at steady state and the concentration gradients are linear. The countertransport process that drives the inward analyte flux will eventually change the composition of the inner solution, which in turn will alter the fluxes over time. This becomes more problematic with ultraminiaturized systems where the inner solution reservoir cannot be very large. Membrane surface fouling/adsorption processes may change the magnitude of the observed fluxes, limiting accuracy. Lastly, this concept demands a relatively high selectivity over the secondary ion and a relatively limited concentration range.

A number of the above-mentioned limitations have been recently addressed by moving to an instrumentally controlled system [18,19], illustrated in Fig. 2 (top). Here, the membrane contains no added ion-exchanger, and spontaneous extraction of hydrophilic ions into the membrane is suppressed. The measurement occurs in three distinct stages (Fig. 2). In step A, a short current pulse drives ions from the sample into the membrane. The current amplitude is directly proportional to the ion flux, and may now be much more accurately controlled than in the chemical mode mentioned above. In step B, the potential is measured under zero-current conditions in complete analogy to traditional emf measurements. This avoids problems associated with resistance changes in the solution, which may bias the observed potential if measured during the first pulse. In step C, a potential is applied that drives all previously extracted ions back into the aqueous solution, essentially resetting the membrane. Differential measurements may be easily accomplished with the same membrane, by either using pulses of varying magnitudes or, more simply, subtracting potentials measured at different times within a single pulse. Fig. 2 (bottom) shows with a calcium-selective membrane that such a technique may yield orders of magnitude higher sensitivities than predicted on the basis of the Nernst equation. A calcium concentration change

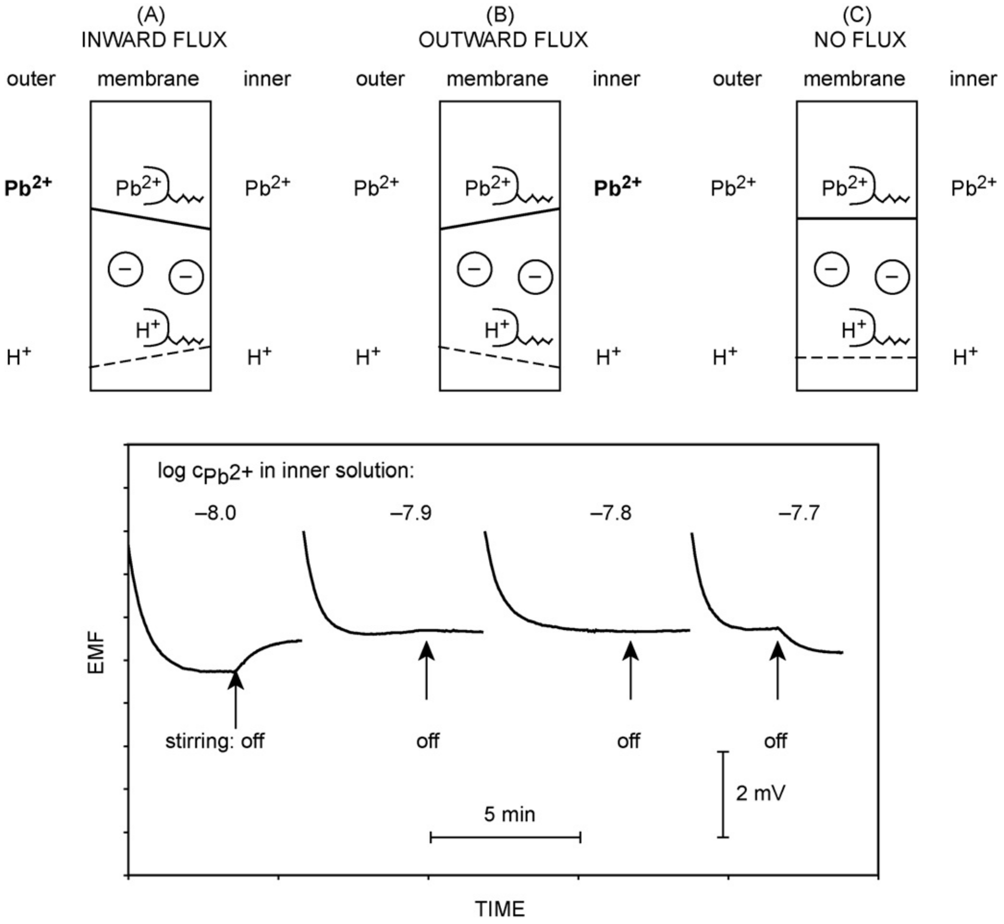

Fig. 3. Backside calibration potentiometry [20]. This novel technique utilizes thin supported membranes where concentration gradients reach their steady state in a matter of seconds [21]. The composition at the backside of the membrane may be altered and the effect of aqueous solution stirring evaluated. The stir effect disappears when the steady-state concentration gradient becomes negligibly small. Under these conditions information on the sample composition is obtained without the need for the magnitude of the potential and without requiring any alterations of the sample composition. It gives information on sample activity ratios on the basis of the underlying ion-exchange processes. Bottom: determination of lead concentrations at pH 4 by varying the composition at the backside and evaluating the stir effect with such thin suppported membranes [20].

from 0.1 mM to just 0.24 mM, measured during pulse B at open circuit, gives a potential change of close to 200 mV [19]. The Nernst equation would predict just 11.3 mV under equilibrium conditions. In differential measurements, the reference electrode is now only utilized to adjust the baseline potential at step C, which may also be accomplished with a second ion-selective electrode if needed. Some of the other limitations stated above still remain: a high selectivity is required, the measuring range cannot be shifted to extremely high concentrations, and surface fouling may influence the mass transport kinetics. And of course, the required instrumentation is somewhat more elaborate than in traditional potentiometry.

4. Backside calibration potentiometry

Very recently, a new measurement principle for ion-selective membranes has been introduced. Here, the magnitude of the observed potential is unimportant and the technique does not rely on the Nernst equation. Moreover, changes in the sample composition for calibration or standard addition purposes are, ideally avoided as well. This principle is termed backside calibration potentiometry [20].

In backside calibration potentiometry, as the name implies, the sample side of the sensor is never altered for calibration purposes and reference electrodes are, in some cases, unimportant as well. The concept utilizes relatively thin supported ion-selective membranes across which steady-state concentration gradients are established in a matter of seconds [21] as illustrated in Fig. 3. In this experiment, the inner solution composition is altered until the concentration gradient across the membrane reduces to zero, which can be likened to the zeroing of a Wheatstone bridge. Here, it is accomplished by changing the stirring rate of the two aqueous solutions and monitoring the potential: no influence of stirring on the emf is observed once the ion concentration gradients disappear. What makes this technique unique is that the magnitude of the potential is unimportant in this experiment. Of course, the approach alone does not allow one to determine single ion activities, which would be thermodynamically impossible. Instead, it has been shown that one determines the activity ratio of analyte ion to its dominant interferent because the concentration gradients are dictated by ion-exchange equilibrium processes [20]. If the activity of the interferent is known, the analyte ion activity may be determined. Fig. 3 (bottom) shows how this concept can be used to determine lead ions in samples buffered at pH 4, with hydrogen ions the dominant interferents [20]. Indeed, the lead concentrations found by this technique in environmental water samples corresponded well to independently measured values.

5. Constant current coulometry: calibration-free reagent delivery

One may easily envision the accurate delivery of ionic reagents from an ion-selective membrane by current control. If spontaneous zero current ion fluxes are negligibly small, an imposed current pulse will deliver a defined quantity of material into the sample without any need for titrimetric standards or calibration procedures, with a very high degree of selectivity. This concept has just recently been demonstrated with a polymeric ion-selective membrane for the purpose of accurately delivering reagents [22]. Fig. 4 demonstrates the coulometric delivery of calcium for the titration of EDTA. Here, one ion-selective membrane was electrochemically controlled to deliver calcium ions, and a second ion-selective membrane of similar composition was used as the detector electrode [22]. The simple relationship between applied number of coulombs and expelled amount of ions (Faraday's law) coupled with the high ion selectivity of such membranes makes this a very promising technique to deliver reagents without the need for maintaining accurate standard solutions.

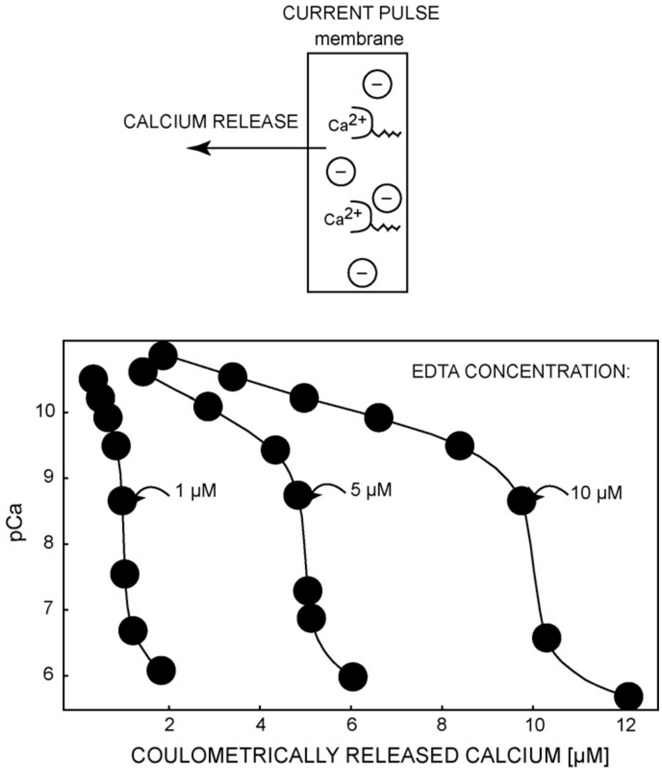

Fig. 4. Chemically selective controlled potential coulometry with ion-selective membranes [22]. An imposed current translates into the release of a defined quantity of ions from the membrane into the sample. Unlike classical coulometry with metal electrodes, this is a chemically selective technique. It alleviates the need for standardization of titrants and volumetric delivery and is attractive for remote sensing applications. Bottom: titration of low concentrations of EDTA with coulometrically released calcium [22]. The free calcium was measured with a second calcium-selective electrode.

The concept of perturbing the sample by galvanostatic control has recently been extended to allow localized titration measurements without the need for standard solutions or bulk sample perturbations [23]. Here, pulsed galvanostatic perturbation and potential measurement are performed at the very same interface. The approach is illustrated in Fig. 5 with H^+-selective membranes for the determination of total acidity. A constant current pulse is imposed across an ion-selective membrane free of added lipophilic cation-exchanger, and results in a defined flux of hydrogen ions from the sample in direction of the membrane. The resulting increase in the unstirred diffusion layer thickness

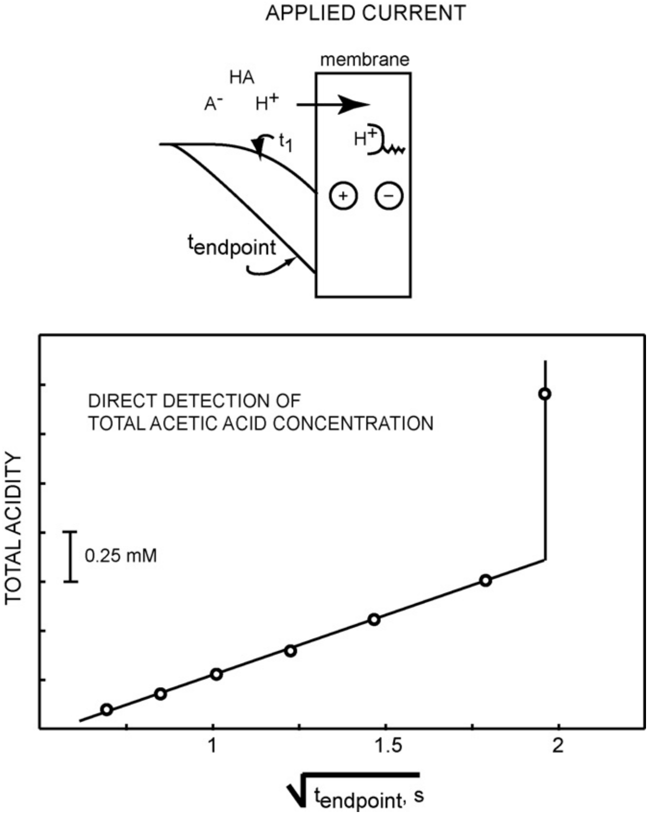

Fig. 5. Direct sensing of total acidity without sample perturbation or bulk sample titration [23]. In this example, a constant current pulse is imposed across a polymeric H^+-selective membrane and the potential is observed at the very same electrode, yielding an elegant actuator/sensor combination. The current pulse results in an imposed H^+ flux in direction of the membrane, which is supported by any acid dissociation equilibria. As the diffusion layer thickness expands in the first few seconds of this experiment, the potential is monitored for the endpoint time. As shown in the bottom plot, this endpoint time is a direct function of the total acidity of the sample [23].

as a function of time forces the acidity gradient to increase to maintain the imposed ion flux. Once the acid is locally depleted at the ion-selective membrane, a well-defined potential change is observed that indicates the localized titration endpoint in just a few seconds [23]. The key limitations of such localized titrations relative to classical titrimetric analysis concern the kinetic nature of the measurement. Measurements on low ionic strength solutions may be affected by migration, rather than pure diffusion processes, and changes in diffusion coefficients will also give variations in the observed endpoint. Nonetheless, such principles are highly attractive for continuous monitoring purposes because they are fast, automated, make use of selective chemistry, do not require reagents or the need to collect sample aliquots. Many potential applications exist where the use of such direct sensing techniques may far outweigh their fundamental limitations.

6. Coulometric ion transfer: calibration-free sensing

Controlled current coulometry was discussed above to accurately deliver reactants from ion-selective membranes. Recently, controlled potential coulometry was introduced by the group of Kihara as a very promising calibration-free analysis method in the field of ion sensing [24]. The principle is illustrated in Fig. 6. A suitable potential applied between a Ag/AgCl electrode placed in the sample and a reference electrode in contact with an organic solvent containing a calcium ionophore and an inert lipophilic salt drives calcium ions from the sample solution into the organic solvent. The current associated with this process is monitored and integrated over the entire analysis time. The coulometric analysis of calcium is possible, for instance, if most calcium ions have been selectively transferred and non-Faradaic processes (charging currents) are kept insignificant [24]. To make this promising technique even more practical for routine use, the system may need to be further miniaturized for reduced analysis times and sample volumes, the direct sample contact of Ag/AgCl will have to be avoided and, perhaps most important, the simple solvent 1,2-dichloroethane used in this work may need to be replaced by a more robust and inert sensing material. While more work is certainly required to make this direction a practical approach, coulometry may be the key solution to many of the stability problems that plague the field of ion sensing in non-traditional applications today.

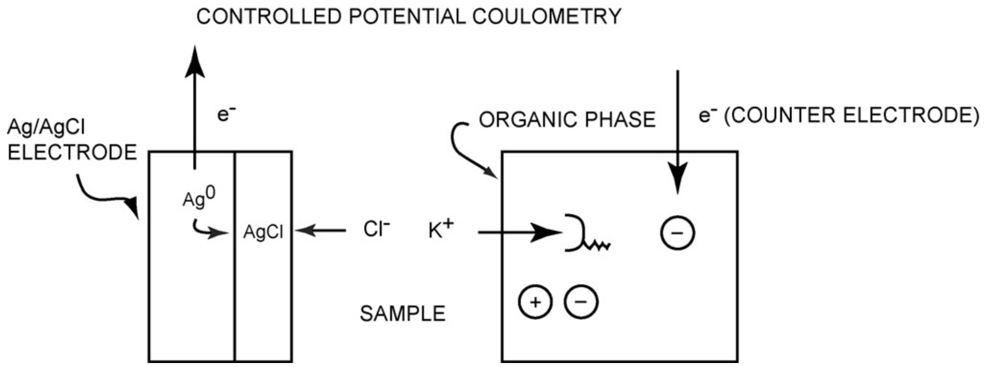

Fig. 6. Controlled potential coulometry with ion-selective organic phases [24]. In this new technique, all ions are exhaustively and selectively extracted from the aqueous sample to an organic phase doped with a selective receptor. The observed current is integrated over the entire experiment and yields the total number of moles of the ion of interest. This technique is inherently calibration-free and scientifically robust, and may eventually be highly suited for miniaturized, remote sensing systems.

Acknowledgements

The authors wish to thank the National Institutes of Health through grants EB002189 and GM 07178 in support of their electrochemical sensor research.

References

[1] M. Cremer, Z. Biol. 47 (1906) 562.
[2] E. Bakker, P. Bühlmann, E. Pretsch, Chem. Rev. 97 (1997) 3083.
[3] P. Bühlmann, E. Pretsch, E. Bakker, Chem. Rev. 98 (1998) 1593.
[4] T. Sokalski, M. Maj-Zurawska, A. Hulanicki, Mikrochim. Acta 1 (1991) 285.
[5] E. Bakker, Anal. Chem. 69 (1997) 1061.
[6] E. Bakker, E. Pretsch, P. Bühlmann, Anal. Chem. 72 (2000) 1127.
[7] T. Sokalski, A. Ceresa, T. Zwickl, E. Pretsch, J. Am. Chem. Soc. 119 (1997) 11347.
[8] E. Bakker, E. Pretsch, Trends Anal. Chem. 20 (2001) 11.
[9] E. Bakker, E. Pretsch, Trends Anal. Chem. 24 (2005) 199.
[10] E. Bakker, E. Pretsch, Angew. Chem. Int. Ed. 46 (2007) 5660.
[11] A. Malon, T. Vigassy, E. Bakker, E. Pretsch, J. Am. Chem. Soc. 128 (2006) 8154.
[12] A. Manz, N. Graber, H.M. Widmer, Sens. Actuator B1 (1990) 244.
[13] M.E. Collison, M.E. Meyerhoff, Anal. Chem. 62 (1990) A425.
[14] M.E. Meyerhoff, Clin. Chem. 36 (1990) 1567.
[15] D. Ammann, F. Lanter, R.A. Steiner, P. Schulthess, Y. Shijo, W. Simon, Anal. Chem. 53 (1981) 2267.
[16] E. Lindner, R.P. Buck, Anal. Chem. 72 (2000) 336A.
[17] T. Vigassy, A. Ceresa, M. Badertscher, W.E. Morf, N.F. de Rooij, E. Pretsch, Sens. Actuator B 76 (2001) 476.
[18] S. Makarychev-Mikhailov, A. Shvarev, E. Bakker, J. Am. Chem. Soc. 126 (2004) 10548.
[19] S. Makarychev-Mikhailov, A. Shvarev, E. Bakker, Anal. Chem. 78 (2006) 2744.
[20] A. Malon, E. Bakker, E. Pretsch, Anal. Chem. 79 (2007) 632.
[21] K. Tompa, K. Birbaum, A. Malon, T. Vigassy, E. Bakker, E. Pretsch, Anal. Chem. 77 (2005) 7801.
[22] V. Bhakthavatsalam, A. Shvarev, E. Bakker, Analyst 131 (2006) 895.
[23] K.L. Gemene, E. Bakker, Anal. Chem., in review.
[24] A. Yoshizumi, A. Uehara, M. Kasuno, Y. Kitatsuhi, Z. Yoshida, S. Kihara, J. Electroanal. Chem. 581 (2005) 275.

Available online at www.sciencedirect.com

ScienceDirect

Talanta 75 (2008) 705–709

Talanta

www.elsevier.com/locate/talanta

Antioxidant activity of whey protein fractions isolated by gel exclusion chromatography and protease treatment

Tuğba Bayram[a], Murat Pekmez[b], Nazlı Arda[b], A. Süha Yalçın[a,*]

[a] Department of Biochemistry, School of Medicine, Marmara University, 34668 Haydarpaşa, İstanbul, Turkey
[b] Department of Molecular Biology and Genetics, Faculty of Science, İstanbul University, 34118 Vezneciler, İstanbul, Turkey

Received 19 June 2007; received in revised form 22 November 2007; accepted 7 December 2007
Available online 23 December 2007

Abstract

Whey proteins were isolated from whey powder by a combination of gel exclusion chromatography and protease (pepsin or trypsin) treatment. Whey solution (6 g/dl) was applied to Sephadex G-200 column chromatography and three fractions were obtained. Gel electrophoresis (SDS-PAGE) was used to identify the fractions; the first one contained immunoglobulins and bovine serum albumin, the second contained β-lactoglobulin and α-lactalbumin whereas the third fraction contained small peptides. We have also subjected the whey filtrate to proteases (pepsin and trypsin). Treatment with proteases showed that β-lactoglobulin can be obtained after hydrolysis of the second fraction with pepsin. When the whey filtrate was treated with pepsin and then applied to Sephadex G-200 column chromatography three fractions were obtained; the first one was bovine serum albumin, the second was β-lactoglobulin and the third fraction contained small peptides. After trypsin treatment only two fractions were obtained; the first one was serum albumin and the second fraction was an α-lactalbumin rich fraction. We have determined the antioxidant activity of the fractions using an assay based on the measurement of superoxide radical scavenging activity. Our results showed that among the three fractions, the first fraction had the highest superoxide radical scavenging activity. Also, protease treatment of the second fraction resulted in an increase in the antioxidant activity.

Keywords: Antioxidant activity; Gel chromatography; α-Lactalbumin; β-Lactoglobulin; Whey

1. Introduction

Milk is a complex mixture of proteins, lipids, carbohydrates, vitamins, and minerals structured to provide a complete diet for infants in mammals. Whey protein is a term often used as a synonym for milk-serum proteins. Sweet whey is produced in large amounts worldwide from milk using the enzymatic action of chymosin (also called rennet enzyme) on the casein fraction [1]. Whey represents a rich and heterogeneous mixture of secreted proteins with wide ranging nutritional, biological and functional-food attributes [2]. Whey proteins include α-lactalbumin (α-La), β-lactoglobulin (β-Lg), bovine serum albumin (BSA), immunoglobulins (Ig), and a number of minor proteins and enzymes [3]. Main constituents of whey are β-lactoglobulin and α-lactalbumin, two small globular proteins that account for approximately 70–80% of total whey protein. Historically, whey has either been considered a waste product and disposed of in the most cost-effective manner, or processed into relatively low-value commodities such as whey powder and various grades of whey protein concentrate/isolate [4].

β-Lg is a small, soluble globular protein with a monomer mass of 18 kDa. Between pH 3 and 7, it exists in solution as a dimer with an effective molecular mass of about 36 kDa [5]. It has a variety of useful nutritional and functional-food characteristics that have made it an ingredient of choice in the formulation of modern foods and beverages. β-Lg exhibits a growing number of biological effects including anti-hypertensive, anti-cancer, hypocholesterolemic, opiodergic, and anti-microbial activities [2,4]. α-La is another major whey protein that makes up 25% of total bovine whey protein. It is one of the few proteins that remains intact upon pasteurization, and is a calcium binding protein that enhances calcium absorption. It is also a rich source of the amino acids lysine, leucine, threonine, tryptophan and cysteine [6].

---

* Corresponding author. Tel.: +90 216 4144733; fax: +90 216 4181047.
E-mail address: asyalcin@marmara.edu.tr (A.S. Yalçın).

0039-9140/$ – see front matter © 2007 Elsevier B.V. All rights reserved.
doi:10.1016/j.talanta.2007.12.007

In this study, we have isolated whey proteins from whey powder, an industrial by-product. We have also determined the antioxidant activities of the fractions obtained.

2. Experimental

2.1. Sample preparation

Whey powder was obtained from a commercial milk and milk products company (Sütaş, Bursa-Turkey). Whey solution (6%, w/v) was prepared in ultra pure water and was centrifuged at 4000 × *g* and 4 °C for 60 min. The supernatant was filtered through a 0.45 μm syringe filter.

2.2. Size exclusion chromatography

Size exclusion chromatography was performed using a Sephadex G-200 column (1.5 cm × 30 cm). The column was equilibrated and eluted with 0.02 M phosphate buffer, pH 8.6. The flow rate was set as 0.3 ml/min, and fractions of 1–1.5 ml were collected. Absorbances were measured at 280 nm to estimate their protein content. Additionally, quantitative protein analysis was performed according to Lowry et al. [7].

2.3. Hydrolysis of whey proteins

Pepsin (Sigma-P7012; 2500–3500 Units/mg) and trypsin (Fluka-93610; ∼9000 Units/mg) were used for the hydrolysis of whey proteins. For pepsin hydrolysis, the pH of the sample was adjusted to 1.5 with 1.0 M HCl. The enzymatic reaction was carried out at 37 °C for 30 min with a protein to enzyme ratio of 1:100 (w/w). The reaction was ended by adjusting the pH to 7.8 with 1.0 M NaOH. For trypsin hydrolysis, the pH of the sample was adjusted to 9.0 with 1.0 M NaOH. The enzymatic reaction was carried out at 37 °C for 30 min with a protein to enzyme ratio of 1:50 (w/w). The reaction was stopped by adding 150 mM Na_2CO_3.

2.4. Electrophoretic analysis

Gel electrophoresis (SDS-PAGE) was carried out at a constant voltage of 200 mV using 18% separating gel and 4% stacking gel. Samples were loaded to different lanes and protein standards were used to identify individual proteins according to their molecular mass. Gels were stained with 0.05% Coomassie Brilliant Blue R-250. Destaining was carried out with a solution of isopropanol and acetic acid [3].

2.5. Antioxidant activity

Antioxidant activities of different fractions were determined by an assay based on scavenging of superoxide radicals [8]. One ml of the sample (or ultra pure water for control) was added to 3 ml of the reaction mixture made up of 50 mM phosphate buffer (pH 7.8), 13 mM methionine, 2 μM riboflavin, 100 μM EDTA and 75 μM nitro blue tetrazolium (NBT). After incubation under fluorescent light for 10 min, absorbance of the blue colored formazan was measured spectrophotometrically at 560 nm. Per-

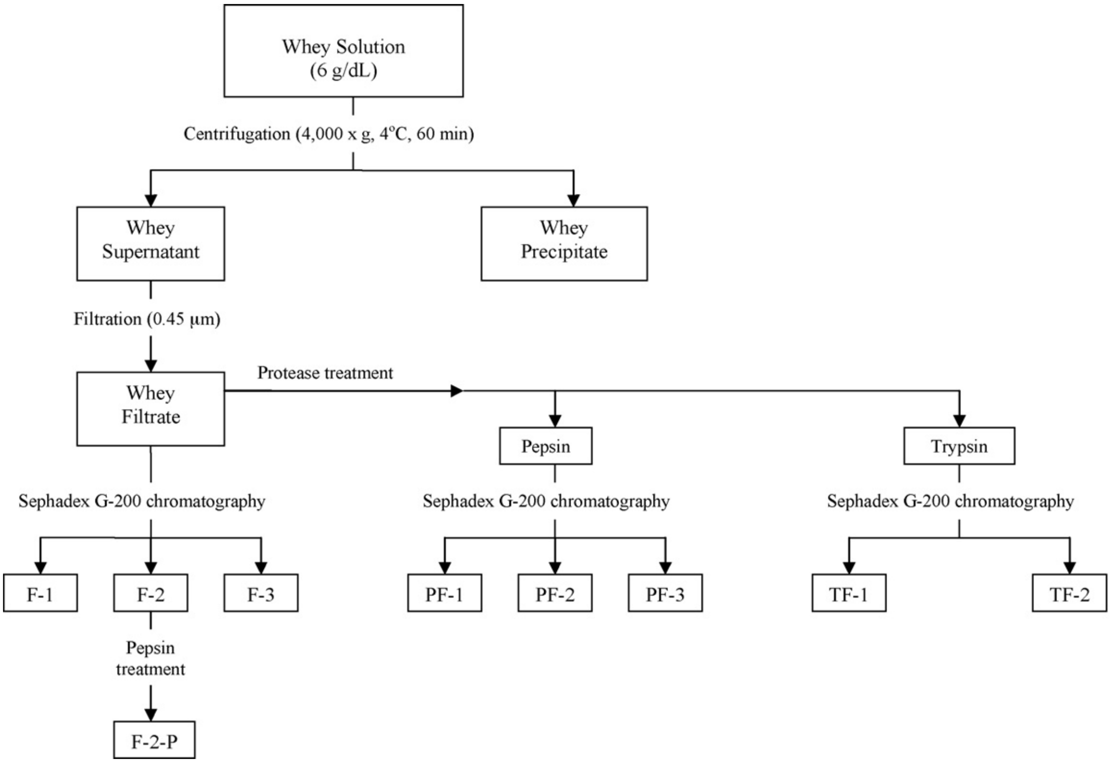

Fig. 1. A schematic overview of the isolation procedure used to obtain the fractions.

centage inhibition of superoxide anion formation was calculated using the following formula.

$$\%\text{Inhibition} = \left[\frac{A_0 - A_1}{A_0}\right] \times 100,$$

A_0=Absorbance of the control; A_1=Absorbance of the sample

The results were expressed as the protein concentration (mg/ml) leading to 50% inhibition (IC_{50}).

3. Results and discussion

Preparative chromatographic separation techniques are of importance to the biopharmaceutical industry because they can deliver high-purity products, are relatively easy to develop, and can readily be scaled from the laboratory scale to the desired production level [9]. One reason for the ubiquity of chromatographic steps in preparative protein purification is that they provide a relatively efficient means to meet manufacturing goals of the biopharmaceutical industry [10]. Several processes have been proposed for commercial-scale production of whey protein fractions. These fall into three main categories: selective precipitation induced by adjustment of the solution physical properties, membrane filtration based primarily on differences in size and charge, and selective adsorption [11,12].

A schematic overview of the isolation procedure used in our study is presented in Fig. 1. We have first prepared a whey solution (6%, w/v) which was centrifuged (4000 × *g*, at 4 °C for 60 min) to remove large particles and coagulated material. The supernatant was filtered through a microfilter (0.45 μm) and applied to a Sephadex G-200 column (Fig. 2). The three fractions recovered were identified by gel electrophoresis (SDS-PAGE). Immunoglobulins (Ig) and bovine serum albumin (BSA) were eluted in the first peak, β-lactoglobulin (β-Lg) and α-lactalbumin (α-La) in the second peak and small peptides in the third peak (Fig. 3).

We have also subjected whey filtrate to proteases (pepsin or trypsin). The results are shown in Fig. 4. Three fractions were obtained after pepsin treatment, while trypsin treatment gave two fractions. Further analysis of the fractions obtained by gel electrophoresis following pepsin treatment showed that the first fraction was BSA; the second was β-Lg and the third fraction contained small peptides. After trypsin hydrolysis the first fraction was BSA and the second was a fraction rich in α-La. The second fraction obtained from Sephadex G-200 column chromatography was hydrolyzed by pepsin in another set of experiments. As shown in Fig. 5, hydrolysis of the second fraction by pepsin yielded β-Lg near homogeneity suggesting the possibility of isolating purified β-Lg after treatment of the second fraction with pepsin.

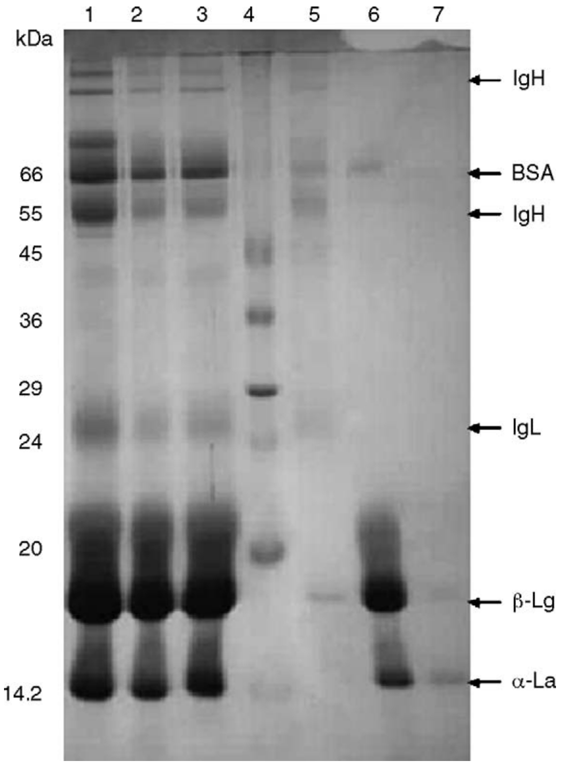

Fig. 3. Gel electrophoresis (SDS-PAGE) of Sephadex G-200 fractions. Lane 1: whey solution; Lane 2: whey supernatant; Lane 3: whey filtrate; Lane 4: molecular weight markers; Lane 5: F-1; Lane 6: F-2; Lane 7: F-3.

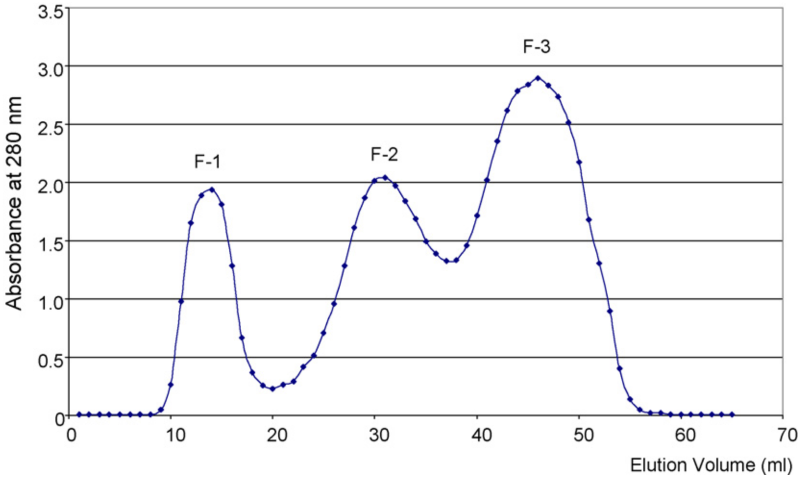

Fig. 2. Sephadex G-200 chromatography of whey filtrate.

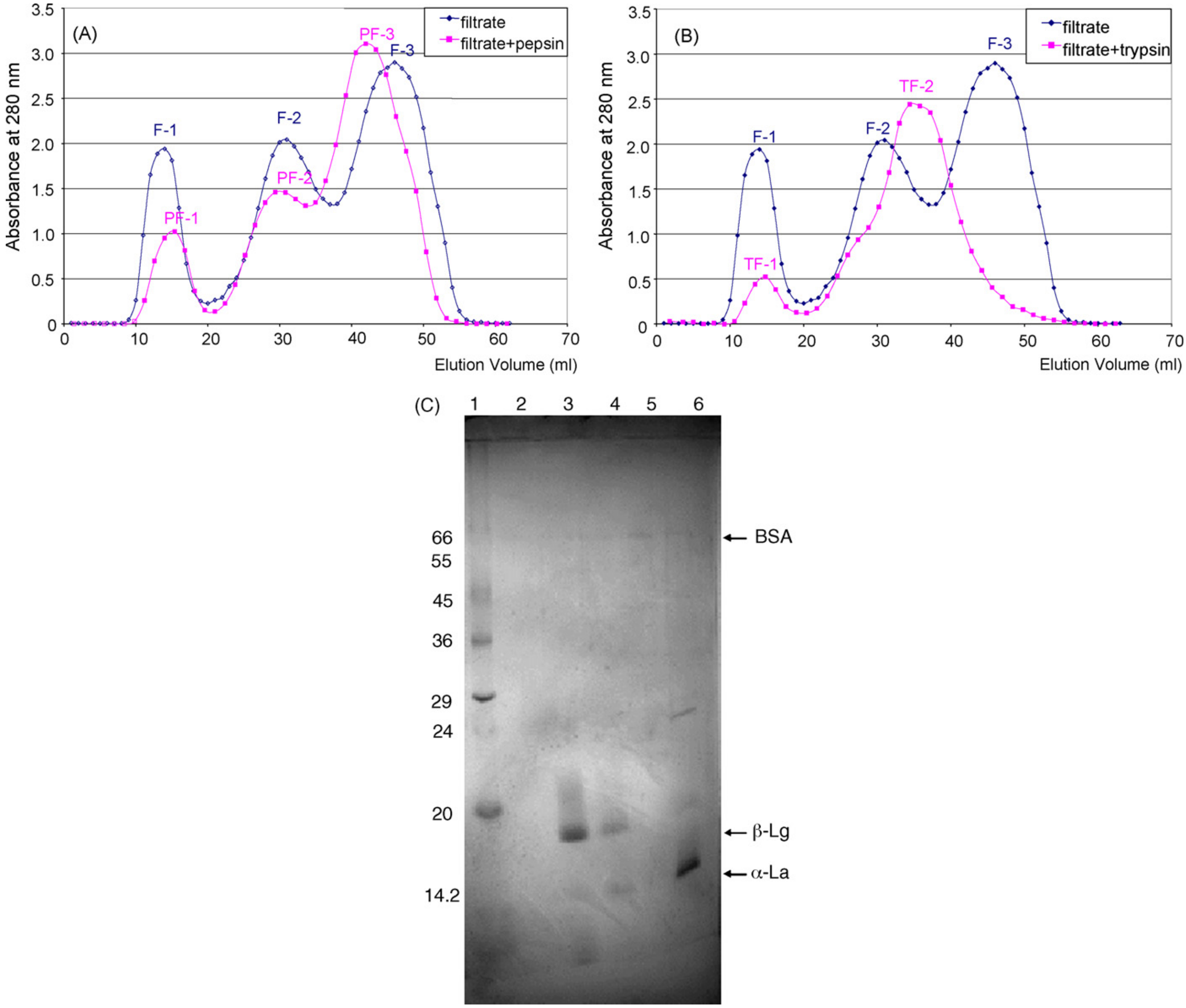

Fig. 4. Sephadex G-200 chromatography of whey filtrate before and after protease treatment. (A) Pepsin treatment; (B) trypsin treatment; (C) gel electrophoresis (SDS-PAGE). Lane 1: MW markers; Lane 2: PF-1; Lane 3: PF-2; Lane 4: PF-3; Lane 5: TF-1; Lane 6: TF-2.

Milk contains several antioxidant factors like vitamins and enzymes. Possible antioxidant activity of milk proteins and hydrolysates has also been reported [13]. Accordingly, several investigators have tried to isolate antioxidant proteins and peptides from milk, whey and whey protein hydrolysates [13–15]. Antioxidant activity of the hydrolysates seems be inherent to the characteristic amino acid sequences of peptides derived depending on the protease specificity.

Our ultimate aim is to perform a variety of biological activity analyses on whey protein fractions. In this study we have used an antioxidant assay based on superoxide radical scavenging activity. Among the three fractions obtained from Sephadex G-200 chromatography, highest superoxide radical scavenging activity was present in the first fraction (Tables 1 and 2). Also, protease treatment of the fractions resulted in an increase in the antioxidant activity. This was particularly evident for the second fraction which contains α-La and β-Lg. These results suggest that the superoxide radical scavenging antioxidant activity is inherent in the peptide sequence of β-Lg in accordance with recent reports on the antioxidant activity of both β-Lg and its hydrolysates [16,17]. The antioxidant activity demonstrated by whey proteins and their hydrolysates suggests that these have potential to enhance product stability by preventing oxidative deterioration. Thus, whey proteins can be readily utilized as functional ingredients in food products.

In conclusion, in the present study, we have compared the antioxidant activities of whey proteins and their hydrolysates. We have also observed that β-lactoglobulin was resistant to pepsin while α-lactalbumin was resistant to trypsin cleavage. Accordingly, β-Lg can be easily purified using a combination of Sephadex G-200 size exclusion chromatography and pepsin treatment, whereas an α-lactalbumin rich fraction can be obtained after tryptic hydrolysis. Isolating milk-serum

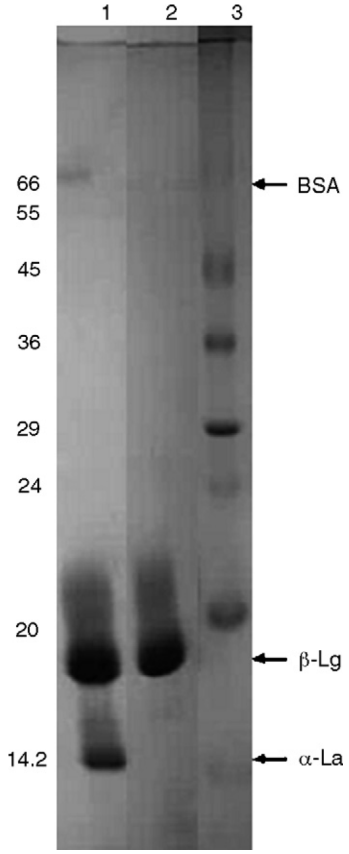

Fig. 5. Gel electrophoresis (SDS-PAGE) of the second fraction before (F-2) and after (F-2P) pepsin treatment. Lane 1: F-2; Lane 2: F-2-P Lane 3: MW markers.

Table 1
Protein concentration of different fractions obtained as described in Fig. 1

Fraction	Protein (mg/ml)	Volume (ml)	Total protein (mg)
Whey solution	9.32	52.0	484.64
Whey precipitate	16.42	2.7	44.33
Whey supernatant	7.82	49.0	383.18
Whey filtrate	7.48	44.1	329.87
F-1	0.38	6.0	2.28
F-2	1.65	7.2	11.88
F-3	2.00	9.6	19.20
Pepsin	6.48	10.0	64.80
Trypsin	6.73	10.0	67.30
F-2-P	1.42	4.0	5.68
PF-1	0.13	8.4	1.09
PF-2	0.43	7.0	3.01
PF-3	1.82	14.0	25.48
TF-1	0.13	5.0	0.65
TF-2	1.68	21.0	35.28

The fractions used were obtained as described in Fig. 1.

Table 2
Antioxidant activities of different fractions obtained as described in Fig. 1

Fraction[a]	Antioxidant activity[b]
Whey solution	n.d.
Whey precipitate	n.d.
Whey supernatant	33 ± 1
Whey filtrate	43 ± 3
F-1	9.3 ± 0.9
F-2	176 ± 7
F-3	91 ± 2
Pepsin	101 ± 8
Trypsin	54 ± 1
F-2-P	16 ± 3
PF-1	21 ± 4
PF-2	88 ± 3
PF-3	143 ± 10
TF-1	n.d.[c]
TF-2	60 ± 13

[a] The fractions were obtained and designated as described in Fig. 1.

[b] Antioxidant activity was assayed as superoxide scavenging activity and expressed as the protein concentration (IC_{50}) leading to 50% inhibition of superoxide radical formation under the conditions described in the methods. Results are given as the mean ± S.D. of three different determinations.

[c] n.d. = not determined.

proteins by a procedure combining gel exclusion chromatography and proteases seems to be an easy method of obtaining whey proteins for further characterization and functional analysis. We are presently carrying out experiments on whey protein fractions to determine their biological activities and to identify different bioactive proteins/peptides.

Acknowledgements

This work was supported by Marmara University Research Fund (SAG-YLS-290506-0092 and SAG-YYP-290906-0208) and Turkish Scientific and Technological Research Council (SBAG-2972/104S507).

References

[1] A. Tolkach, U. Kulozik, J. Food Eng. 67 (2005) 13.
[2] A.S. Yalçın, Curr. Pharm. Des. 12 (2006) 1637.
[3] R. Burr, in: S. Roe (Ed.), Protein Purification Applications, Oxford University Press, USA, 2001, pp. 87–115.
[4] D.E.W. Chatterton, G. Smithers, P. Roupas, A. Brodkorb, Int. Dairy J. 16 (2006) 1229.
[5] H. Roginski, J.W. Fuquay, P.F. Fox (Eds.), Encyclopedia of Dairy Sciences, Academic Press, New York, 2003.
[6] E.A. Permyakov, L.J. Berliner, FEBS Lett. 473 (2000) 269.
[7] O. Lowry, N.J. Rosebrough, A.L. Farr, R.J. Randall, J. Biol. Chem. 193 (1951) 265.
[8] C.A. Martinez, M.E. Loureiro, M. Oliva, M. Maestri, Plant Sci. 160 (2001) 505.
[9] E.N. Lightfoot, Ind. Eng. Chem. Res. 38 (1999) 3628.
[10] L. Pedersen, J. Mollerup, E. Hansen, A. Jungbauer, J. Chromatogr. B 790 (2003) 161.
[11] S. Doultani, K.N. Turhan, M.R. Etzel, Process Biochem. 39 (2004) 1737.
[12] A.L. Zydney, Int. Dairy J. 8 (1998) 243.
[13] A. Pihlanto, Int. Dairy J. 16 (2006) 1306.
[14] G. Ünal, A.S. Akalın, Agro Food Ind. Hi-Tech. 17 (2006) 4.
[15] S.C. Cheison, Z. Wang, S.-Y. Xu, J. Agric. Food Chem. 55 (2007) 3896.
[16] H.C. Liu, W.L. Chen, S.J.T. Mao, J. Dairy Sci. 90 (2007) 547.
[17] R.J. Elias, J.D. Bridgewater, R.W. Vachet, T. Waraho, D.J. McClements, E.E. Decker, J. Agric. Food Chem. 54 (2006) 9565.

Available online at www.sciencedirect.com

ScienceDirect

Talanta 75 (2008) 734–739

Talanta

www.elsevier.com/locate/talanta

Determination of sulfonic acids and alkylsulfates by ion chromatography in water

Maria Concetta Bruzzoniti *, Rosa Maria De Carlo, Corrado Sarzanini

Department of Analytical Chemistry, University of Torino, Via P. Giuria 5, 10125 Torino, Italy

Received 19 July 2007; received in revised form 23 November 2007; accepted 7 December 2007
Available online 27 December 2007

Abstract

A fast ion chromatographic method with suppressed conductivity detection has been developed for the simultaneous determination of methane-, ethane-, 1-propane-, 1-butane-, 1-pentane-, 1-hexane-, 1-heptane-, 1-octane-, 1-nonane-, 1-decane-, 1-dodecane-, dodecylbenzene-, *p*-toluene-, benzenesulfonic acids, octylsulfate and dodecylsulfate in water samples. Due to the high number of analytes and their heterogeneity, the effect of the mobile phase parameters (NaOH, CH_3OH and CH_3CN concentration) on the retention factors has been studied in detail, so achieving, for the first time, the separation among 15 of these analytes by a gradient elution. Detection limits included within 0.06–0.16 μM have been obtained.

Interferences from Cl^-, NO_3^- and SO_4^{2-}, possible anions present in water samples, have been considered and a SPE procedure has been developed for analytes enrichment and matrix removal in a seawater sample. This is the first application of an ion-exchange chromatographic method to a seawater sample for this kind of analytes.

Keywords: Alkylsulfonic acids; Arylsulfonic acids; Anionic surfactants; Ion chromatography; Preconcentration; Seawater

1. Introduction

The use of surfactants is widespread in several human activities. According to their chemical characteristics, they are classified into four groups: anionic, non-ionic, cationic and amphoteric surfactants. Among the anionic surfactants, alkanesulfonates, alkylsulfate and alkylbenzenesulfonate are commonly employed as cleaning agents, laundry detergents and cosmetics and personal care products. The extensive use of these compounds leads also to their discharge into the environment, mainly into the water compartment.

A hazard of surfactants to aquatic ecosystems primarily consists in the adsorption on the cell surface of microorganisms at the lowest trophic level, which affects the production–degradation characteristics of the ecosystem and the parameters of water body self-purification [1,2].

The approved analytical methods for anionic surfactants are based on colorimetric methylene blue reaction [3,4] but are known to suffer both from positive and negative interferences. Other analytical methods such as liquid chromatography allow the characterization of individual surfactants in complex mixtures [5]. Analytical methods, mainly chromatographic and electrophoretic, for trace analysis of ionic and neutral surfactants, including sample preparation steps, have been reviewed by Vogt and Heinig [6]. More recently, as a result of increased LC/MS applications, reversed phase chromatography has been coupled to ESI ion trap mass spectrometry for the determination of anionic, amphoteric and non-ionic surfactants [7].

HPLC separation methods coupled to evaporative light-scattering detection (ELSD) [8] detection have been developed in surfactants analysis, but with DL as high as, e.g. 5 μg (for sodium lauryl sulfate by a 20 μL loop). The same detection technique has been employed to show the performance of a new column for surfactant determination based on mixed mechanisms: reversed-phase, anion-exchange and dipole–dipole interactions [9]. The ELSD detection proves to be effective for the detection of the non-UV-absorbing surfactants. Suppressed

---

Abbreviations: C_1 sulfonic, methanesulfonic acid; C_2 sulfonic, ethanesulfonic acid; C_3 sulfonic, 1-propanesulfonic acid; C_4 sulfonic, 1-butanesulfonic acid; C_5 sulfonic, 1-pentanesulfonic acid; C_6 sulfonic, 1-hexanesulfonic acid; C_7 sulfonic, 1-heptanesulfonic acid; C_8 sulfonic, 1-octanesulfonic acid; C_9 sulfonic, 1-nonanesulfonic acid; C_{10} sulfonic, 1-decanesulfonic acid; C_8 sulfate, octylsulfate; C_{12} sulfonic, 1-dodecanesulfonic acid; C_{12} sulfate, dodecylsulfate.

* Corresponding author. Tel.: +39 011 6707844; fax: +39 011 6707615.
E-mail address: mariaconcetta.bruzzoniti@unito.it (M.C. Bruzzoniti).

0039-9140/$ – see front matter © 2007 Elsevier B.V. All rights reserved.
doi:10.1016/j.talanta.2007.12.026

conductivity detection is optimal for ionic surfactants and is often coupled to ion-exchange separation mechanisms. It is noteworthy mentioning that suppressed conductivity has been coupled to reversed phase [10] or ion-pair reversed-phase mechanism, being this technique developed for the determination of sulfonated and sulfated anionic surfactants, providing linear ranges, e.g. for sodium laureth sulfate of 2.5–500 μg mL^{-1} [11].

Few anion-exchange methods with suppressed conductivity detection for the separation of surfactants are present [10,12,13] but they suffer of poor baseline resolution among analytes, relevant gradient baseline disturbance and moreover, just a limited number of analytes can be separated. Furthermore, applications in environmental samples are lacking.

The aim of this work was the development of a chromatographic method for the separation and the enrichment from water samples of sulfated and sulfonated surfactants based on anion-exchange and suppressed conductimetric detection. Sixteen analytes, including short chain alkylsulfonic acids, have been considered, namely: methanesulfonic, ethanesulfonic, 1-propanesulfonic, 1-butanesulfonic, 1-pentanesulfonic, 1-hexanesulfonic, 1-heptanesulfonic, 1-octanesulfonic, 1-nonanesulfonic, 1-decanesulfonic, 1-dodecanesulfonic, dodecylbenzenesulfonic, *p*-toluenesulfonic, benzenesulfonic acids, octylsulfate and dodecylsulfate.

The separation of 15 species has been achieved in less than 16 min throughout a detailed study of the effect of mobile phase parameters (NaOH, CH_3OH, CH_3CN concentration) on retention factors and the optimization of a gradient elution. To the best of our knowledge, this is the first report on the separation of such a large number of analytes. Detection limits included within 0.06–0.16 μM have been obtained. When possible to be compared, these values are lower than those reported in literature.

For environmental application of the method developed, the main inorganic interferences (Cl^-, $NO_3{}^-$, $SO_4{}^{2-}$) potentially occurring in water compartments have been evaluated.

Since surfactants are among the most important components in the group of highly toxic substances that affect environmental conditions in marine ecosystems [1], the method developed has been applied on a seawater sample for which a preconcentration/matrix removal step has been optimized. This is the first application of an ion-exchange chromatographic method to a seawater sample for this kind of analytes.

2. Experimental

2.1. Chromatographic apparatus

A quaternary gradient pump Model GP 40 (Dionex Co., Sunnyvale, CA, USA), equipped with automatic membrane eluent degassing, a Rheodyne 7125 injection valve (sample loop 200 μL) and a conductivity detector was used. For eluent conductivity suppression, an AMMS III-4 mm anionic micromembrane suppressor, with 25 mM sulfuric acid as regenerant (5 mL min^{-1}) has been used. Eluent flow rate was 1 mL min^{-1}. A chromatographic data system (AI-450, Dionex) was used for data collection and for the integration of peak areas. Separation was performed at room temperature.

2.2. Stationary phase

A Dionex IonPac AS11 (250 mm × 4 mm, particle diameter 13 μm, ethylvinylbenzene cross-linked with 55% divinylbenzene, functionalized with alkanol quaternary ammonium groups; 0–100% solvent compatible; capacity 45 μequiv.) has been used as analytical column. A 50 mm × 4 mm Dionex IonPac AG11 (9 μequiv. capacity) has been used as guard column.

2.3. Chemicals

Deionized water (18 MΩ cm^{-1} resistivity) from a Milli-Q water purification system (Millipore, USA), has been used for eluent and standard solutions preparation.

Sulfuric acid (95–97%, Riedel de-Haen, Seelze, Germany), HPLC grade methanol (Riedel de-Haen) and NaOH solution (49.5–50.5%, Mallinckrodt Baker B.V., Deventer, Netherlands) were used.

All analyte standards were from Merck (Darmstadt, Germany), except ethanesulfonic acid and dodecylsulfate (Acros Organics, Geel, Belgium) and methanesulfonic acid (Aldrich, St. Louis, MO, USA).

Eluents were filtered through mixed cellulose ester 0.22 μm-filters (Advantec MFS, Inc., Pleasanton, CA, USA) before use.

2.4. Preconcentration procedure

For preconcentration, polystyrene-divinylbenzene SDB-1 cartridges (Bakerbond SDB-1, 3 ml, 200 mg, J.T. Baker, Nova Chimica, Milano) have been used.

The cartridges have been connected with a Minipuls 3 peristaltic pump (Gilson Inc., Middleton, WI, USA) set at 1.5 rpm, conditioned as recommended by the producer (two aliquots of 3 mL methanol, followed by 6 mL H_2O) and finally loaded with the sample (10 mL). The cartridge has then been rinsed twice with 3 mL H_2O, dried up, and, finally, the sample has been eluted by five aliquots of 0.5 mL CH_3OH each. The organic solvent has been evaporated (water bath) and the residual reconstituted with 2 mL H_2O, and finally injected into the chromatographic system. The seawater sample has been collected in Mar Tirreno (South Italy) in dark glass bottle and refrigerated.

3. Results and discussion

3.1. Effect of NaOH concentration

Due to the hydroxide selectivity exhibited by the analytical column, a NaOH-based eluent has been initially chosen. In Fig. 1, the behavior of *k* is shown for the analytes in the range 0.31–90 mM NaOH. In agreement with the anion-exchange mechanism, retention decreases with the increase of eluent concentration for all the analytes. A great difference in retention between the C_1–C_4 sulfonic acids and the other analytes has been observed.

Alkanesulfonates are the first eluting analytes with a retention order depending upon their alkyl chain length. Since even at the highest NaOH concentrations evaluated, 1-dodecanesulfonic

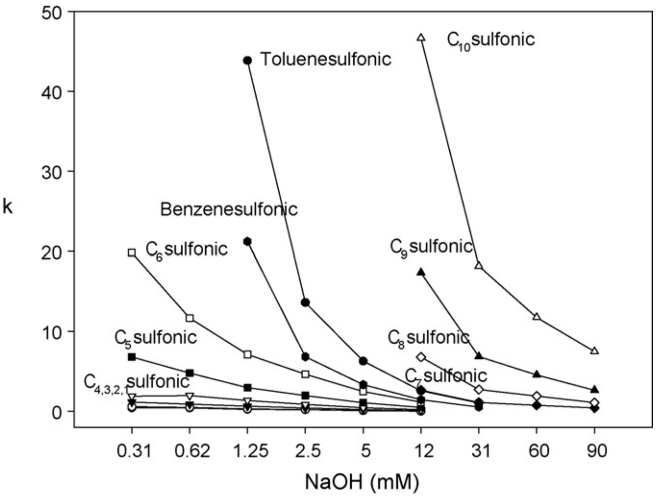

Fig. 1. Effect of NaOH concentration on retention factors for the analytes studied. Column: IonPac AG11 and AS11 (250 mm × 4 mm). Note that the abscissa scale type is category.

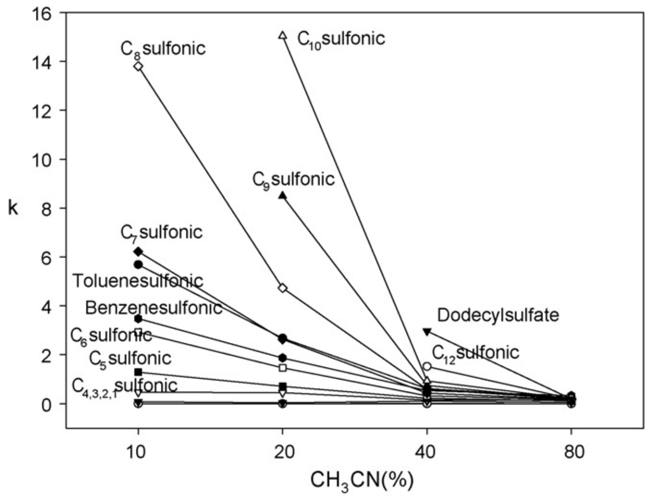

Fig. 2. Effect of CH_3CN concentration on retention factors for the analytes studied. Column: IonPac AG11 and AS11 (250 mm × 4 mm). Eluent: 2 mM NaOH, CH_3CN as shown. Note that the abscissa scale type is category.

acid, dodecylsulfate and dodecylbenzenesulfonic acids do not elute, it is reasonable to presume the presence of hydrophobic interactions for these analytes with the stationary phase. This hypothesis is also supported by the behavior of *p*-toluenesulfonic acid that is more retained than benzenesulfonic acid and by the tailed and asymmetric peaks obtained for, e.g. 1-decanesulfonic acid at the highest NaOH concentrations (90 mM). Interestingly, the aromatic sulfonic acids are more retained than C_6 sulfonic, but less than C_8–C_{10} sulfonic acids.

To reduce the hydrophobic interactions and to achieve lower retention times, the effects of organic modifiers on *k* have been studied.

3.2. *Effect of organic solvents*

The effect of the organic solvents has been evaluated at 2 mM NaOH, where the separation of the shortest chain analytes also occurs.

The increase of acetonitrile percentage in the eluent reduces the retention factors for all the analytes (Fig. 2). Differently from what observed with methanol (see further), the increase of acetonitrile does not alter the selectivity of the separation (i.e. the elution order for the analytes). For CH_3CN content higher than 40%, it is possible to elute also dodecylsulfate and 1-dodecanesulfonic acid, previously retained at 90 mM NaOH. Dodecylbenzenesulfonic acid is not eluted.

The elution of dodecylsulfate and 1-dodecanesulfonic acid allows us to make some considerations about their retention interactions. Since the two analytes have the same alkyl chain length, hydrophobic interactions of similar entity with the stationary phase should be expected (actually rather minimized by the presence of the organic solvent). The difference in the chromatographic behavior must be ascribed to the polar head which carries, for 1-dodecanesulfonic acid and for dodecylsulfate, one and two negative charges, respectively, supporting that the dominant mechanism is the anion-exchange one.

Differently from acetonitrile, methanol does not provide a monotone trend for *k* and causes selectivity inversions at different percentages as a function of the surfactant family (arylsulfonates: 60%, alkylsulfonates: 80%).

The effect of the presence of the organic solvent in the eluent in an ion-exchange system is of difficult interpretation and prediction, as deeply discussed in a previous work [14], but the solvated radius of analyte ions, eluent ions and functional groups of the stationary phase, determined also by hydrogen bonding properties and dispersive (London) forces, greatly influence the retention mechanism in the presence of different organic solvents. Nevertheless, the effect of methanol in decreasing the hydrophobic interactions is evident (compare Figs. 1 and 3) and proves to be effective in eluting also dodecylbenzenesulfonic acid, at CH_3OH >80%, that up to now was still retained in the column. For further experiments, methanol has been chosen as organic modifier.

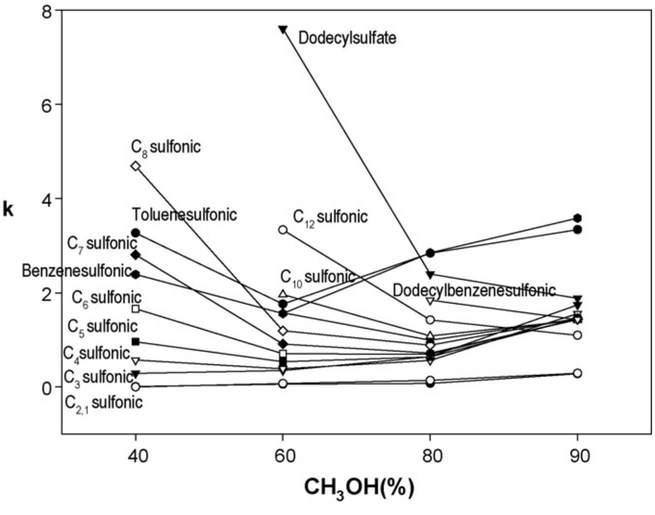

Fig. 3. Effect of CH_3OH concentration on retention factors for the analytes studied. Column: IonPac AG11 and AS11 (250 mm × 4 mm). Eluent: 2 mM NaOH, CH_3OH as shown. Note that the abscissa scale type is category.

Table 1
Composition of the mobile phase at the different times of the gradient elution programs employed in the study, and related chromatographic retention of selected analytes

	Time (min)	0	5	7	10	11	12	15	30	Main results for the analytes injected
Gradient 1	NaOH (mM)	0	0.31		0.62			31	60	Elution of C_2–C_9 within 30 min C_3–C_5 unresolved
Gradient 2	NaOH (mM)	0							15	Elution and complete separation of C_2–C_7 within 23 min
Gradient 3	NaOH (mM)	0	7.5	60						Elution and complete separation of C_2–C_7 within 10 min
Gradient 4	NaOH (mM)	0	6	6						Elution and complete separation of C_2–C_7 and benzenesulfonic acid within 12 min
	CH_3OH (%)	0	0	40						Coelution C_7-*p*-toluenesulfonic acid
Gradient 5	NaOH (mM)	0	6	6						Elution and complete separation of C_7, benzenesulfonic and *p*-toluenesulfonic acids within 11 min
	CH_3OH (%)	0	0	60						
Gradient 6	NaOH (mM)	0	6	6	6		6			Elution and complete separation of C_2–C_{10}, benzenesulfonic, *p*-toluenesulfonic acids and octylsulfate within 14 min
	CH_3OH (%)	0	0	60	60		80			
Gradient 7	NaOH (mM)	0	6	6		6	6			Elution and separation of 15 analytes (see Fig. 4). Partial coelution of C_1-C_2
	CH_3OH (%)	0	0	60		60	80			

3.3. Optimization of separation by linear gradient elution

The number of the analytes and their similar structure make the optimization of the separation a difficult task. From the isocratic experiments, it appeared necessary to include also the organic modifier in the gradient optimization. About 40 gradient compositions have been tested, acting on the following parameters: NaOH concentration, steepness and duration of the gradient, methanol content and time of introduction of methanol in the gradient. The main results achieved by the most effective gradient compositions have been collected in Table 1.

Data shown in Fig. 1 show that the elution of the surfactants can be feasible in reasonable times by increasing the competing ion in the mobile phase. Therefore, the first experiments were aimed to optimize the NaOH content in the gradient program. As a first attempt, NaOH concentration was increased within 30 min but, in order to enhance the separation among the first eluting analytes, a preliminary step at NaOH = 0 was introduced (gradient 1). Since this multi-step gradient composition gave rise to coelution of C_3–C_5 peaks at about 15 min, a gradient with a simplified composition (gradient 2) and a lower elution power within the first 15 min of run has been tested. This gradient well resolved the previous coelutions but gave broad peaks, so the elution power has been significantly increased (gradient 3) in a shorter period of time.

This approach reduces the elution times of C_2–C_7 to about 10 min without any coelution. By gradient 4, the decrease (compared to the previous gradients) of NaOH concentration within the first 7 min has been balanced with the increase in methanol percentage. This composition resulted in the elution of benzenesulfonic acid, but also in a coelution between C_7 and toluenesulfonic acid, that can be solved by the increase of CH_3OH content (gradient 5), thanks to the different trend of selectivity *vs.* CH_3OH (Fig. 3). Keeping constant the condition so far optimized until the elution of the last analyte (toluenesulfonic acid), an increase of methanol content to 80% (as indicated by the isocratic elutions previously shown), allowed us to go through gradients 6 and 7, being the last one the most efficacious for the simultaneous separation of the selected analytes within about 16 min (Fig. 4). It should be remarked that dodecylbenzenesulfonic acid that would be eluted at isocratic conditions (2 mM NaOH, 80% CH_3OH) at $t_r = 4.9$ min is not eluted by the gradient.

3.4. Evaluation of interferences

The inorganic anions Cl^-, $NO_3{}^-$ and $SO_4{}^{2-}$ have been injected as possible interferences in aqueous samples. Referring to Fig. 4, Cl^- corresponds to peak 4. The $SO_4{}^{2-}$ ion does not elute within the chromatographic run and therefore, a final washing step of the column (60 mM NaOH for 20 min and 100% CH_3OH for 20 min) is recommended. The $NO_3{}^-$ ion partially coelutes with 1-pentanesulfonic acid (peak 6).

3.5. Linearity and detection limits

Linearity has been evaluated within the range 0.93–11.4 μM ($n = 4$). Coefficients of determination r^2 were included within 0.9695 (1-nonanesulfonic acid) and 0.9997 (ethanesulfonic acid).

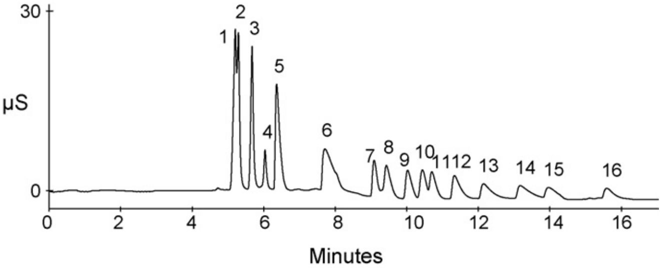

Fig. 4. Optimized separation; elution by gradient 7 (see Table 1). Peaks: 1, C_1 sulfonic; 2, C_2 sulfonic; 3, C_3 sulfonic; 4, Cl^-; 5, C_4 sulfonic; 6, C_5 sulfonic + $NO_3{}^-$; 7, C_6 sulfonic; 8, benzenesulfonic acid; 9, C_7 sulfonic; 10, toluenesulfonic acid; 11, C_8 sulfonic; 12, C_9 sulfonic; 13, C_{10} sulfonic; 14, C_8 sulfate; 15, C_{12} sulfonic; 16, C_{12} sulfate. Analyte concentrations: 50 μM each.

Table 2
Detection limits for the species evaluated

Analyte	Detection limits	
	μM	$\mu g\,L^{-1}$
Methanesulfonic acid	0.06	5.8
Ethanesulfonic acid	0.10	11
1-Propanesulfonic acid	0.13	16
1-Hexanesulfonic acid	0.05	8.3
Benzenesulfonic acid	0.07	11
1-Heptanesulfonic acid	0.07	12
p-Toluenesulfonic acid	0.09	17
1-Octanesulfonic acid	0.10	19
Octylsulfate	0.15	31
1-Nonanesulfonic acid	0.10	21
1-Decanesulfonic acid	0.14	31
1-Dodecanesulfonic acid	0.16	40

The detection limits, calculated as the concentration corresponding to three times the standard deviation of the blank, are shown in Table 2. When available, these values have been compared with those from literature, resulting to be lower (e.g. for 100 μL injection volume: 1-hexanesulfonic acid: 60 $\mu g\,L^{-1}$, 1-heptanesulfonic acid: 80 $\mu g\,L^{-1}$, 1-octanesulfonic acid: 80 $\mu g\,L^{-1}$, octylsulfate: 850 $\mu g\,L^{-1}$, 1-decanesulfonic acid: 900 $\mu g\,L^{-1}$, 1-dodecanesulfonic acid: 660 $\mu g\,L^{-1}$, [10], or comparable [12].

The standard deviation of the blank has been calculated as the average of 10 different injections. The DL values for 1-butanesulfonic acid (1.0 μM) and dodecylsulfate (1.7 μM) are much higher due to a significant background noise.

3.6. *Preconcentration: real sample analysis and matrix removal*

Coastal ecosystems can receive large quantities of surfactants, due to wastewaters and sewage sludge discharge to the sea [15]; therefore, it can be of interest to test the suitability of the method developed for this kind of matrix. The highly saline content in an ion-exchange chromatographic analysis can strongly interfere with analyte determination; in particular, when a sea water sample has to be analyzed by anion-exchange, the most important problem is the Cl^- content (about 0.5 M), so the first purpose was the reduction of matrix interference.

An ion-interaction mechanism (ion-pair reagent: tetrabutylammonium hydroxide, TBAOH) has been chosen and a SDB-1 phase has been used.

The TBAOH plays a very important role in analytes preconcentration, since TBA^+ has electrostatic interactions with hydrophobic anions such as surfactants, and can ion-pair in the polystyrene-divinylbenzene substrate, allowing retention of charged analytes that, otherwise, would be eluted unretained by the cartridge. On the contrary, inorganic anions should exhibit lower pairing ion interactions and elute unretained by the SDB-1.

To evaluate surfactants recoveries, four different preconcentration conditions have been preliminarily compared using C_9 sulfonic as test solute: (i) precoating of SDB-1 cartridge with TBA^+ and addition of TBA^+ in the sample solution to be loaded; (ii) precoating of SDB-1 cartridge with TBA^+ and loading of the sample solution; (iii) loading of the sample solution on the unfunctionalized SDB-1 cartridge; (iv) loading of the sample solution added with TBA^+ on the unfunctionalized SDB-1 cartridge. Since the recoveries obtained were respectively: 33.9%, 42.8%, 94.5% and 99.8%, the last approach was subsequently followed and TBAOH has been added into the sample solution, without any precoating of the SDB-1 support.

To evaluate the efficacy of this approach, 25 mL of a synthetic solution containing 0.5 M (17726 $mg\,L^{-1}$) Cl^-, 50 μM of each of the 14 analytes, 1 mM TBAOH (pH 6.0 by HCl) has been prepared. The amount of ion interaction reagent is in excess with respect to the total amount of analytes. An aliquot of 10 mL of the solution has been loaded into the SDB-1 cartridge by a peristaltic pump. The cartridge (activated as described) has been rinsed twice with aliquots of 3 mL H_2O to improve the removal of inorganic anions. The recovery of analytes from the SDB-1 has been performed by five aliquots of 0.5 mL CH_3OH. The organic solvent has been evaporated (water bath) and the residual was reconstituted with 2 mL H_2O, and finally injected with an in-line filter, into the chromatographic system. It should be remarked that the IC injection of the solution proved the Cl^- content to be lower than 20 $mg\,L^{-1}$ and hence do not interfere with the determination of the surfactants. At the light of the preliminary results obtained, the same procedure has been followed to evaluate analytes recovery and reproducibility in the seawater sample.

The sample has been filtered on a 0.22 μm filter and divided into two aliquots. The first aliquot has been added with 250 μM TBAOH, pH 6 (blank); the second one has been added with 250 μM TBAOH, pH 6 and 12.5 μM of each of the 14 analytes. These solutions have been prepared and processed in triplicate according to the procedure previously detailed. The results obtained (recoveries and R.S.D.) are shown in Table 3.

The short-chain analytes (methane-, ethane-, propanesulfonic acids) are not retained (<2%), while retention for the

Table 3
Preconcentration of analytes from a seawater sample (10 mL) by SDB-1 cartridges

Analyte	Recovery (%)	R.S.D. (%)[a]
1-Butanesulfonic acid	16	4.2
1-Pentanesulfonic acid	37	19
1-Hexanesulfonic acid	104	2.1
Benzenesulfonic acid	54	1.9
1-Heptanesulfonic acid	100	2.7
p-Toluenesulfonic acid	133	8.9
1-Octanesulfonic acid	119	4.1
1-Nonanesulfonic acid	103	1.1
1-Decanesulfonic acid	101	0.9
Octylsulfate	113	3.0
1-Dodecanesulfonic acid	94	4.0
Dodecylsulfate	60	12.0

Preconcentration: seawater in 250 μM TBAOH, pH 6, spiked with 12.5 μM of each analyte; recovery: 5 aliquots of 0.5 mL CH_3OH, evaporation and reconstitution with 2 mL H_2O.

[a] *n* = 3.

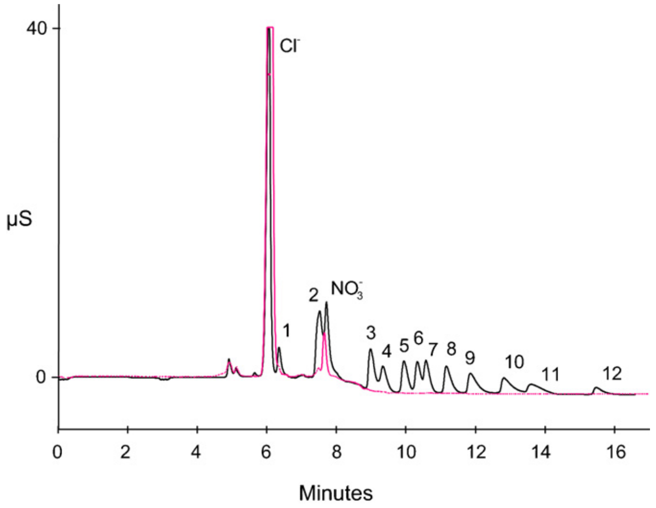

Fig. 5. Preconcentration and separation of surfactants from a seawater sample. Overlay chromatograms of the as such sample (dotted line) and of the spiked (12.5 μM of each analyte) sample. Preconcentration conditions as in Table 3. Separation conditions as in Fig. 4. Peaks: 1, C_4 sulfonic; 2, C_5 sulfonic; 3, C_6 sulfonic; 4, benzenesulfonic acid; 5, C_7 sulfonic; 6, toluenesulfonic acid; 7, C_8 sulfonic; 8, C_9 sulfonic; 9, C_{10} sulfonic; 10, C_8 sulfate; 11, C_{12} sulfonic; 12, C_{12} sulfate.

homologues sulfonic acids increases with the length of the alkyl chain and it is quantitative from 1-hexanesulfonic acid. Interestingly, the higher retention of *p*-toluenesulfonic acid in respect to the benzenesufonic acid, indicates a contribute of $–CH_3$ group to the adsorption in the SDB-1 phase. These behaviors are in agreement with the reversed phase ion interaction mechanism.

The chromatograms obtained after preconcentration are shown in Fig. 5. It should be remarked that the NO_3^- ion hampered the calculation of C_5 sulfonate recovery which is affected by the highest R.S.D.

4. Conclusions

The optimization of a fast anion-exchange chromatographic method for the simultaneous separation of 15 analytes belonging to sulfonic acids and alkylsulfates classes has been shown (analysis run about 16 min).

The separation has been achieved after a gradient elution which has been optimized after a detailed study of the effect of mobile phase parameters (NaOH, CH_3OH, CH_3CN) on *k*, which has indicated that CH_3OH greatly affects the selectivity of the separation and is the key parameter to be tuned.

After the evaluation of the main interferences occurring in aqueous samples (Cl^-, NO_3^- and SO_4^{2-}), the chromatographic method has been applied to a seawater sample for which an optimization of preconcentration/matrix removal step has been performed. This is the first report on the use of ion chromatoraphy for the determination of these analytes in a seawater sample.

Acknowledgements

The authors would like to thank Dr. F. Benso for his support and fruitful discussions and Dr. Angelo Dossena (Nova Chimica srl, Italy) for the supply of test SDB-1 cartridges and for useful information about this product. The financial contribution (PRIN 2004) from MIUR (Ministero dell'Istruzione, dell'Università e della Ricerca), Italy, is gratefully acknowledged.

References

[1] O.V. Stepanets, G.Y. Solov'eva, A.M. Mikhailova, A.I. Kulapin, J. Anal. Chem. 56 (2001) 290.
[2] M.A. Lewis, Ecotoxicol. Environ. Saf. 20 (2) (1990) 123.
[3] EPA Report # 600/4-79-020, Methods for chemical analysis of water and wastes (MCAWW), method 425.1, 1983.
[4] APHA (American Public Health Association), Standard Methods, Method 5540 C, 19th ed., APHA (American Public Health Association), Washington, DC, USA, 1995, pp. 5–42.
[5] P.A. Lara-Martin, A. Gomez-Parra, E. Gonzalez-Mazo, J. Chromatogr. A 1137 (2006) 188.
[6] C. Vogt, K. Heinig, Fresen. J. Anal. Chem. 363 (1999) 612.
[7] L.H. Levine, J.L. Garland, J.V. Johnson, J. Chromatogr. A 1062 (2005) 217.
[8] H.S. Park, C.K. Rhee, J. Chromatogr. A 1046 (2004) 289.
[9] X. Liu, C.A. Pohl, J. Weiss, J. Chromatogr. A 1118 (2006) 29.
[10] L.M. Nair, R. Saari-Nordhaus, J. Chromatogr. A 804 (1998) 233.
[11] L.H. Levine, J.E. Judkins, J.L. Garland, J. Chromatogr. A 874 (2000) 207.
[12] N. Pan, D.J. Pietrzyk, J. Chromatogr. A 706 (1995) 327.
[13] M. Aceto, C. Sarzanini, O. Abollino, E. Mentasti, Chromatographia 41 (1995) 445.
[14] M.C. Bruzzoniti, E. Mentasti, C.A. Pohl, J.M. Riviello, C. Sarzanini, J. Chromatogr. A 925 (2001) 99.
[15] M. Petrovic, A.R. Fernández-Alba, F. Borrull, R.M. Marce, E. González Mazo, D. Barceló, Environ. Toxicol. Chem. 21 (2002) 37.

Available online at www.sciencedirect.com

ScienceDirect

Talanta 75 (2008) 697–704

Talanta

www.elsevier.com/locate/talanta

Comparison between traditional strategies and classification technique (SIMCA) in the identification of old proteinaceous binders

R. Checa-Moreno [a], E. Manzano [b], G. Mirón [b], L.F. Capitan-Vallvey [b,*]

[a] Laboratorio Central de Sanidad Animal, M.A.P.A., c/Camino del Jau s/n, Santa Fe, Granada E-18320, Spain
[b] Solid Phase Spectrometry Research Group, Department of Analytical Chemistry, Campus Fuentenueva, Faculty of Sciences, University of Granada, Granada E-18071, Spain

Received 25 April 2007; received in revised form 4 December 2007; accepted 7 December 2007
Available online 26 December 2007

Abstract

In this paper, we performed a comparison between commonly used strategies amino acid ratios (Aa ratios), two-dimensional ratio plots (2D-Plot) and statistical correlation factor (SCF) and a classification technique, soft independent modelling of class analogy (SIMCA), to identify protein binders present in old artwork samples. To do this, we used a natural standard collection of proteinaceous binders prepared in our laboratory using old recipes and eleven samples coming from Cultural Heritage, such as mural and easel paintings, manuscripts and polychrome sculptures from the 15–18th centuries. Protein binder samples were hydrolyzed and their constitutive amino acids were determined as PITC-derivatives using HPLC-DAD. Amino acid profile data were used to perform the comparison between the four different strategies mentioned above. Traditional strategies can lead to ambiguous or non-conclusive results. With SIMCA, it is possible to provide a more robust and less subjective identification knowing the confidence level of identification. As a standard, we used proteinaceous albumin (whole egg, yolk and glair); casein (goat, cow and sheep) and collagen (mammalian and fish). The process results in a more robust understanding of proteinaceous binding media in old artworks that makes it possible to distinguish them according to their origin.

Keywords: Proteinaceous binders; HPLC-DAD; PITC-amino acids derivatization; Classification technique; Characterisation strategies comparison

1. Introduction

In paintings, the characterisation of organic binders used because of their pigment fixative and dispersing qualities is crucial since it is an important source of information both for reconstructing the working techniques used in a particular painting and for defining a programme for the restoration and conservation of the artwork itself. Organic materials used in art generally need special attention in the conservation of paintings, due to the relatively increased tendency of the inorganic constituent to undergo degradation, transformation and oxidation processes [1]. Egg, animal glue, milk or casein, drying oils, plant resins, animal resins and waxes are the most common natural organic media historically used in Europe and in the Mediterranean Basin [2]. Their chemical composition and physical properties are considerably influenced by many factors, among them the artist's technique of using a wide variety of binder recipes in order to improve the painting properties and many formulations have not been documented. Furthermore, different binding media can be used for different parts of a painting. Other factors to be taken into account are the heterogeneity of the binder, the possible interferences caused by inorganic pigments, the effect of aging and the environment and the complex mixtures of other organic materials used in several picture layers [3]. Clearly, the identification of organic matter in ancient artworks is not a totally resolved issue [4,5].

In this paper, we are interested in the three types of proteinaceous matter – casein, egg and animal glue – that are usually used as binders in particular pictorial techniques like tempera. To know their specific identification and their degradation compounds, various techniques have been adopted. Staining techniques in paint cross-sections like visible-light [6–8], and fluorescent stains [9], infrared spectrometry (IR) [10], Fourier-transform infrared spectrometry (FT-IR) microspectrometry applied on cross-sections [11], differential thermal analysis (DTA) [12] and immunological techniques [13] have

---

[*] Corresponding author.
E-mail address: lcapitan@ugr.es (L.F. Capitan-Vallvey).

0039-9140/$ – see front matter © 2007 Elsevier B.V. All rights reserved.
doi:10.1016/j.talanta.2007.12.020

been used. Nevertheless the techniques that are most commonly used at this time in the identification of proteinaceous paint media are chromatographic techniques [14,15]. Since proteins are polymers with high molecular weight, hydrolysis methods able to break the peptidic bonds and liberate the amino acids are required. The individual amino acids can be subsequently labelled for identification by derivatization and analyzed by chromatography. Initially, paper chromatography [16] and thin layer chromatography (TLC) [17] were used, but later, to achieve the required specificity and sensitivity, high-performance liquid chromatography (HPLC) [4,18–20] and gas chromatography (GC) [21–26] were used. The coupling of GC with MS as the detection system (GC–MS), makes it possible to obtain structural information regarding unknown components as well as the simultaneous determination of amino acids and fatty acids using capillary GC–MS [14,24,26–28]. Pyrolysis-gas chromatography–mass spectrometry (Py-GC–MS) [24], direct pyrolysis mass spectrometry (DPMS) [29] and direct temperature resolved mass spectrometry (DTMS) [30], capillary zone electrophoresis (CZE) [31], HPLC with electron spray ionisation-time of flight mass spectrometry (ESI-TOF MS) and matrix assisted laser desorption ionisation-mass spectrometry (MALDI-MS) [32] are techniques that promise an important contribution to the study of old proteinaceous paint media, their mixtures and their degradation processes.

The HPLC method that has been extensively used for these kind of samples used the derivatization agent phenylisothiocyanate (PITC), which reacts with amino acids to form phenylthiocarbamyl-amino acids followed by HPLC analysis with UV detection [4,15,19,20]. The characterisation of proteinaceous media in micro-samples of artworks by HPLC and even GC procedures is generally based on the determination of their amino acidic composition, because different proteins have a different percentage profile of their constitutive amino acids. Nevertheless, the identification of protein binders through their amino acid composition is a problem not yet resolved. In the field of Cultural Heritage, the characterisation of proteinaceous binders from the data of amino acidic profiles has been processed by different methods and several strategies have been developed to obtain the final goal: (a) amino acid ratio flow charts, (b) bidimensional plots of amino acid ratios, (c) using a correlation index estimated with amino acid profiles of samples and standard databases and (d) multivariate statistical analysis such as principal components analysis (PCA). All strategies use reference proteinaceous standards. The simplest and very subjective procedure is a visual comparison of amino acid compositional data against a protein standard [33]. Another strategy described consists of using characteristic amino acid ratio (Aa ratios) values which differentiate the three main proteinaceous media, i.e., egg, animal glue and casein [15,21,34–38]. Casolli et al. [39] have developed a flow chart using amino acid ratio data (flowchart), where the nature of the binder is identified depending on the choice based on the chart flow; others have proposed using the bidimensional plotting of amino acid ratios (2D-Plot) [40]. Another strategy uses the statistical correlation factor (SCF) [22] which indicates the degree of similarity between the amino acid composition data of samples coming from artworks and the data for selected proteinaceous reference materials. Finally, strategies that use techniques of multivariate data processing such as PCA [19,22,24,27,34] or factor analysis (FA) [26,28,34] have been described. Nevertheless, the representation of principal components is biased by the subjectivity of the researcher, since PCA is only a projection or dimensionality reduction technique but not a classification technique.

In this work, we use the soft independent modelling of class analogy classification technique (SIMCA) [41] on the profile of amino acids collected by HPLC-DAD analysis using phenylisothiocyanate (PITC) as the derivating agent [42]. These profiles were obtained from a collection of reference proteinaceous binders prepared by us [43] and a sample set coming from paintings, manuscripts and sculptures from the 15–18th centuries. With SIMCA, more than traditional strategies, it is possible to use software to learn the confidence level for each classification made. This is performed by an appropriate statistical *F*-test.

This paper aims to provide a critical comparison of the traditional strategies and SIMCA for characterisation of proteinaceous binders in real Spanish Cultural Heritage samples.

1.1. Objectives

Our objective in this paper is to compare traditional strategies previously used in the bibliography and SIMCA to identify proteinaceous binders present in painting samples. Amino acid compositional profiles obtained by HPLC-DAD in artworks and reference samples will be used here to compare three classical identification strategies and SIMCA. In this work, the SIMCA classification technique is used because it offers the confidence level of identifying or discarding the binder present, without the subjectivity of the other three strategies. These four strategies will be applied to eleven samples coming from ten pieces of art from Cultural Heritage and their results are critically discussed.

2. Experimental

2.1. Instrumentation

A Hewlett-Packard HP 1090 liquid chromatograph (Palo Alto, CA, USA) and an Aminoquant ODS column (5 μm 200 mm × 2.1 mm i.d.), were used for the separation. The PITC derivatives were identified using a diode array detector (DAD) selected at 254 nm. The chromatographic method for amino acid determination as PITC-derivatives is a modification of the Bidlingmeyer procedure [42], the conditions of which were previously optimized [43] to the Microbore column mentioned above. Column temperature 40 °C; flow-rate 0.5 ml/min; buffer A: 0.28 M sodium acetate, 0.075 TEA and 6% acetonitrile (pH 6.38); buffer B: 60% acetonitrile; mobile phase gradient was: 0% B at 0 min, first linear gradient 2% B at 2 min, second linear gradient 43% B at 9 min; 50% B at 13 min. For treatment and later data analysis the software packages Excel spreadsheet (Microsoft Office 2002) and SIMCA-S for Windows ver. 5.1 (1994) by Umetri AB (Umea, Sweden) were used in a Pentium 300 MHz personal computer.

Table 1
Collection of protein binder standard produced (training set)

Albumins	Poultry whites, yolks and whole eggs	Chicken *Gallus gallus*
		Dwarf chicken *Gallus gallus*, *Holland bredd*
		Pheasant *Phasianus colchicus* (2)*
		Goose *Anser anser*
		Turkey *Meleagris gallopavo* (2)
		Peacock *Pavo cristatus* (2)
		Pigeon *Columba livia domestica*
		Duck *Cairina moschata*
		Mallard *Anas platyrhynchos*
Caseins (milks)	Spanish breeds of Caprine *Capra aegagrus hircus*	Granadina (3)
		Granadino-Murciana
		Capra pyrenaica hispanica (2)
		Malagueña (2)
		Manchega (2)
	Spanish breeds of Bovine *Bos Taurus*	Friesian (2)
		Holstein (2)
		Brown Swiss (2)
		Jersey
	Spanish breeds of Ovine *Ovis aries*	Segureña (2)
		Merino (3)
		Red
		Red Majorcan
		Manchega
		Lacha (2)
		Churro (2)
		Castellana (2)
		Awassi (2)
		Black-eye
Collagens	Fish: skins, backbones, and air bladders	Flounder *Platichthys flesus* (5)
		Cod *Gadus morruha* (6)
		Sturgeon *Acipenser sturio* (8)
		Sole *Solea solea* (8)
		Hake *Merluccius merluccius* (6)
		Blue whiting *Micromesistius poutassou* (10)
		Turbot *Psetta maxima* (5)
	Mammalian: skins, bones and cartilages	Rabbit *Oryctolagus cuniculus* (5)
		Pigs *Sus* (7)
		Bovine *Bos primigenius* (8)
		Ovine *Ovis aries* (8)
		Caprine *Capra hircus* (5)

* The number of replicated samples coming from different origins likes farms, supermarkets, etc. appears between brackets.

2.2. *Reference materials*

For this study, a collection of natural proteinaceous binder standards (Table 1) was used to develop SIMCA models. These calibration standards (training set) were used to perform the protein identification from artwork materials. This collection has the variability inherent in different animal species and sample origins. We prepared a natural reference material collection of 127 traditionally employed binders (egg albumin, milk casein and collagen-like substances). Eggs and natural milks were obtained from local farmhouses while collagen-like substances came from different parts of fish and mammalian animals that had been previously purchased in different supermarkets in Granada (Spain). The protein standard preparation was carried out according to old recipes and in this way we obtained standard substances very similar to those used by ancient artists. Current knowledge about the techniques used over the centuries in the creation of artworks comes mainly from historical treatises that contribute a global view of the techniques used in different places and ages. *Il Libro dell'Arte* by Cenini [44] (written at the beginning of the 15th century), was consulted in the preparation of reference samples.

2.3. *Artwork samples*

Eleven samples coming from Cultural Heritage, artworks belonging to the 15–18th centuries such as manuscripts, polychrome sculptures and mural and easel paintings were used in this study (test set). All available information about them is shown in Table 2. Pigments and other interference substances were not determined in the artwork samples.

2.4. *Sample treatment*

Protein present in paint samples (0.5–1 mg) were extracted in 200 μL of 0.5 M phosphate buffer solution pH 12.0 and

Table 2
Samples belonging to Cultural Heritage artworks analyzed (test set)

Sample 1: Parchment. Located at Royal Chancery of Granada-Spain (Signature: ARCHGR: parchment no. 70) Identification: *Catholic King's Diploma*. It dates from the century second half of 15th century and before 1492. Sample coming from the red side of the stamp.

Sample 2: Parchment. Identification: *Nobility Accomplishment* in favour of Mrs. Bartolomé and Diego de Hontiveros in their lawsuit with the Council of Manzanares. Parchment containing a capital letter with a Virgin and Child image. Located at Royal Chancery of Granada-Spain (Signature: ARCHGR: parchment no. 39). Sample coming from the Virgin's face side (brown).

Sample 3: Parchment. Identification: *Nobility Accomplishment* in favour of Mrs. Antón Ruiz and Gonzalo Ruiz, neighbours of Socuéllamos, dated in Granada the 7 September, 1535. Located at Royal Chancery of Granada-Spain (Signature: ARCHGR: parchment no. 51). Sample coming from the coat of arms blue side.

Samples 4 and 5: Parchment. Identification: *Nobility Certification* in favour of Mrs. Francisco Fernández de Bastida and Alarcón, Juan, Pedro and Ginés Fernández de Bastida in the village of Librilla (Murcia). Dated the 27 June, 1579. Located at Royal Chancery of Granada-Spain (Signature: ARCHGR: parchment no. 47). Two samples taken of black ink.

Sample 6: Easel painting. Identification: *Madonna with Child*, unknown author. 13th century. Located in the Cathedral Museum of Guadix (Granada). Unknown author. Sample coming from the child's knee.

Sample 7: Sculpture. Identification: *S. Sebastian* sculpture. 17th century. Located at Parish/parochial Church of Villanueva de Mesía (Granada). Unknown author. Sample taken from S. Sebastian's arm.

Sample 8: Easel painting. Identification: *Eucharist exaltation* 18th century. Located in the Cathedral Museum of Guadix (Granada). Sample taken from chalice side. Unknown author

Sample 9: Easel painting. Identification: *Jesus Christ* 16–17th century. Private collection Granada (Spain) Unknown author

Sample 10: Easel painting. Identification: *Eucharist exaltation* 18th century. Located in the Cathedral Museum of Guadix (Granada). Unknown author. Sample taken from the shaded right part of the Centurion's face.

Sample 11: Wall painting. Identification: Decorative motifs of Ancient Convent of Santa Paula, today Hotel Palacio de Santa Paula (AC Hotels), Granada. Unknown author. Sample taken from the wall painting motif.

5% in 3-(cyclohexylamino)-1-propanesulfonic acid (CAPS) for 2 h at 60 °C and then purified by Microcon unit from Millipore—Amicon© and kept in 50 μL 0.0025 M phosphate buffer solution, pH 12.3 and 10^{-5} M norleucine (internal standard). Protein reference samples were solved in the buffer solution.

2.5. Analytical procedure

Both reference standards and artwork samples were hydrolyzed in 6N HCl acid vapour-phase at previously optimized conditions, 115 °C for 15 h, derivatized with PITC, and finally, analyzed by HPLC in order to determine their amino acidic profile. The total amount of each amino acid (in picomoles) in samples was determined by a weighted calibration based on peak area to internal standard ratio.

2.6. Statistical treatment

To identify the protein material present in the Cultural Heritage samples, amino acid ratios Gly/Glu, Gly/Asp, Pro/Asp and Glu/Pro were calculated from the profile data and a flow chart was then applied according to the Aa-ratios strategy [34]. The 2D-Plot strategy requires another ratio calculation to build the plots described [40], these were: Pro/Phe versus Asp/Ala, Pro/Ile versus Glu/Ser and Gly/Phe versus Glu/Ala. For this second strategy, ratios for several reference samples were additionally calculated in order to simultaneously project reference and artwork samples. For the third traditional strategy considered here, SCF [45], each artwork sample was correlated with a representative specimen of each group of reference samples in order to obtain the appropriate correlation coefficient [46]. This coefficient, as is well known, is defined by the following equation:

$$r = \frac{\sum XY - (\sum X \sum Y/n)}{\sqrt{\left[\sum X^2 - \left((\sum X)^2/n\right)\right]}\sqrt{\left[\sum Y^2 - \left((\sum Y)^2/n\right)\right]}}$$

where X and Y are the concentrations for each amino acid, n is the number of amino acids measured and r is the correlation coefficient. By definition, sample data are represented by X, and reference data by Y. A correlation coefficient of 1.0 indicates a perfect correlation; a value of 0.0 indicates that no correlation exists.

To apply the SIMCA strategy, we first did an exploratory multivariable analysis performing a principal component projection using the amino acid profile data of the protein reference samples. The previously autoscaled profiles (127 protein binder standards × 17 amino acids) were used to do an exploratory multivariable analysis using PCA. PCA showed that three large groups of standards corresponding to the three different origins of the protein binder reference standards considered, e.g., albumins, caseins and collagens (Fig. 1a) appeared well separated. Individualised PC projections for each group showed that it was possible to distinguish new classes inside of each one. Therefore, SIMCA models on principal components were developed for all of them: class (albumin, casein and collagen) and subclass (glair, yolk, whole egg, caprine, ovine, bovine, mammalian and fish). All these models were validated by crossvalidation. Table 3 shows a short summary of the class and subclass models developed.

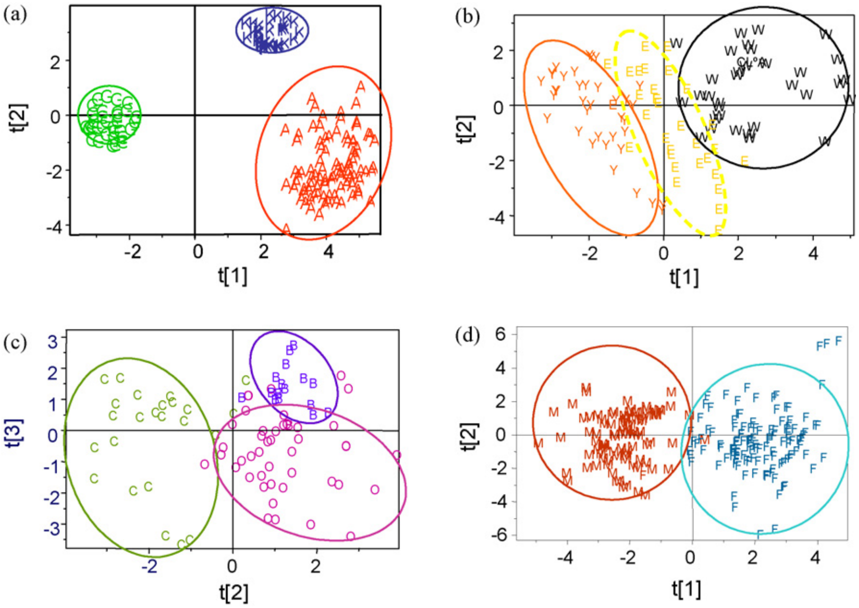

Fig. 1. Projections in principal components of the collection of reference samples. Principal component projection of full data set. A: albumins, K: caseins and G: glues; individual PC projection for albumin class: W: whites, Y: yolks and E: egg whole; individual PC projection for casein class: B: bovine, C: caprine and O: ovine; (d) individual PC projection for glue class: M: mammalian and F: fishes.

2.7. *Results and discussion*

Reference standard and artwork samples were analyzed according to the sample preparation and chromatographic procedures previously described. Typically, around 1–5 mg of dry frozen reference standards previously prepared by us were dissolved in 0.0025 M phosphate buffer solution, pH 12.3, and 10^{-5} M norleucine (internal standard) solution. The artwork samples were treated as is described in Section 2.4. Then both types of samples were subjected to vapour-phase hydrolysis, derivation and chromatographic separation processes. Table 4 shows the amino acid profile data obtained for the samples, i.e., artworks and several reference standards belonging to each kind of protein considered selected from the collection. The amino acid content indicated was obtained by extrapolating the peak area to internal standard ratios on a weighted calibration curve for each amino acid. For reasons of brevity, only one compositional profile of the reference standard binder is shown belonging to every group or subgroup of the reference standard considered in this work [43].

Common strategies such as amino acid ratios (Aa ratios), 2D-Plots and SCF were compared with the SIMCA classification technique. This was carried out using the eleven samples coming from ten Cultural Heritage works of art, selected from murals and easel paintings, manuscripts and polychrome sculptures from the 15–18th centuries.

The ratios needed for performing the identification using the previously described flow chart [39] were calculated from the amino acid profiles of each sample (Fig. 2). These were Gly/Glu, Gly/Asp, Pro/Asp and Glu/Pro. Thus, it was concluded that in samples 1–4 the protein binder present was casein, with collagen in the rest (5–11).

With the second strategy, 2D-Plots, samples and several protein binder standards were simultaneously projected in three

Table 3
Model characteristics at class and subclass levels

Model	Number of objects	A	Number of variables	Variance explained (%)	Sensibility $(1-\alpha)$ (%)	Specificity $(1-\beta)$ (%)
Albumin	36	2	10 (Ser, Gly, Arg, Ala, Pro, Tyr, Met, Ile, Leu and Lys)	65	92	100
White	12	2	14 (Ser, Gly, His, Arg, Thr, Ala, Pro, Tyr, Val, Met, Ile, Leu, Phe, Lys)	61	92	75
Whole egg	12	3	15 (Asp, Glu, HOpr, Ser, Gly, Arg, Ala, Pro, Tyr, Val, Met, Ile, Leu, Phe, Lys)	76	92	92
Yolk	12	2	12 (Asp, Glu, HOpr, Ser, Arg, Tyr, Val, Met, Ile, Leu, Phe, Lys)	60	92	100
Casein	34	3	14 (Asp, Glu, Ser, His, Arg, Thr, Ala, Pro, Tyr, Val, Met, Ile, Leu and Phe)	68	88	100
Goat	10	2	9 (Asp, Glu, HOpr, Arg, Thr, Ala, Pro, Tyr, Lys)	74	90	80
Sheep	17	2	9 (Asp, Glu, Ser, Thr, Ala, Pro, Tyr, Phe, Lys)	70	95	82
Cow	7	1	8 (Asp, Glu, Thr, Ala, Pro, Tyr, Leu, Phe)	61	85	85
Collagen	80	2	15 (Asp, Glu, HOpr, Ser, Gly, His, Arg, Thr, Pro, Tyr, Val, Met, Ile, Leu and Phe)	60	90	100
Mammalian	33	1	8 (Glu, HOpr, Ser, Gly, Ala, Met, Ile, Phe)	33	91	100
Fish	47	2	8 (Glu, HOpr, Ser, Gly, Ala, Met, Ile, Phe)	64	96	98

A: number of principal components of the model. α: α error and β: β error.

Table 4
Amino acid profiles (in pmol) of the samples and standards that are under study[a]

Sample number	Asp	Glu	HOpr	Ser	Gly	His	Arg	Thr	Ala	Pro	Tyr	Val	Met	Ile	Leu	Phe	Lys
1	6.0	9.6	1.5	9.9	16.2	2.3	2.3	4.5	7.3	7.7	3.0	4.9	1.5	9.3	6.2	4.6	3.1
2	7.2	9.6	3.3	9.5	18.3	1.6	4.1	3.8	8.9	8.2	2.0	5.1	1.4	4.3	6.3	3.4	2.9
3	7.1	11.3	2.0	8.1	13.0	3.0	3.0	5.0	3.0	10.3	2.0	5.1	2.0	8.5	6.8	5.9	4.0
4	7.9	12.1	2.6	6.6	15.6	1.3	4.8	4.4	9.7	9.0	2.3	5.2	1.9	4.4	6.9	3.0	2.3
5	5.3	7.9	6.2	3.0	36.4	0.3	5.0	2.0	12.1	12.3	0.4	2.1	0.4	1.1	2.6	1.5	1.4
6	4.7	7.8	9.1	3.0	33.4	0.2	4.2	1.5	12.6	13.7	0.3	2.1	0.4	1.3	2.8	1.6	1.1
7	3.7	6.0	6.1	3.3	35.4	0.3	4.9	2.8	12.9	13.3	0.5	3.1	0.2	1.3	3.7	1.5	1.1
8	4.6	7.3	6.5	2.6	34.3	0.4	5.1	0.9	12.3	12.3	0.6	1.9	0.2	1.3	2.7	2.0	4.9
9	6.1	7.4	6.7	3.9	35.3	0.2	3.9	2.3	12.2	12.2	0.1	2.2	0.1	1.5	2.7	1.5	1.8
10	4.5	7.2	7.4	2.9	31.3	0.9	4.6	1.8	11.4	13.6	0.9	3.0	1.3	1.8	3.2	2.3	2.0
11	3.7	6.6	5.4	4.0	39.3	0.5	4.9	2.0	12.3	10.8	0.4	0.9	0.7	1.1	2.4	2.1	3.0
Reference samples:																	
Albumin	9.2	11.8	0.2	7.8	6.6	2.3	4.8	5.5	8.0	6.6	2.6	6.9	3.0	5.3	8.7	4.6	6.1
Casein	8.3	21.7	0.2	5.7	2.8	2.3	2.3	4.4	4.0	12.8	3.3	6.8	1.7	4.6	8.7	3.8	6.4
Collagen	4.8	8.0	7.5	3.6	35.3	0.7	4.9	1.8	10.9	12.0	0.4	1.7	0.9	1.0	2.3	1.6	2.7
Glair	9.3	12.6	0.2	8.5	6.9	2.0	4.1	5.6	7.5	6.3	3.2	6.8	3.4	4.9	7.8	5.3	5.7
Whole egg	9.5	12.2	0.2	8.0	6.5	2.3	4.5	5.6	8.0	6.2	1.8	7.6	3.0	5.5	8.9	4.6	5.7
Egg yolk	8.9	10.8	0.2	7.0	6.4	2.7	5.8	5.3	8.4	7.3	2.8	6.3	2.4	5.4	9.3	3.9	7.1
Goat casein	8.4	21.4	0.2	5.5	2.4	2.3	2.1	5.1	4.0	13.6	2.8	7.3	1.8	4.5	8.6	3.9	6.3
Sheep casein	8.8	21.5	0.1	5.9	3.2	2.4	2.5	4.3	4.3	12.1	3.3	6.6	1.6	4.4	8.5	3.7	6.8
Cow casein	7.9	22.3	0.2	5.8	2.7	2.3	2.3	4.0	3.8	12.7	3.8	6.6	1.8	4.9	8.8	3.9	6.2
Mammalian collagen	5.1	8.3	8.7	2.6	34.1	0.5	4.6	1.5	10.5	13.3	0.2	1.6	0.4	1.1	2.6	1.6	3.1
Fish collagen	4.5	7.7	6.3	4.7	36.5	0.9	5.2	2.2	11.3	10.6	0.5	1.7	1.4	1.0	1.9	1.5	2.3

[a] For those amino acids not present in protein or whose content is insignificant the L.D. of the method is indicated. Asp: aspartic acid; Glu: glutamic acid; HOpr: hydroxyproline; Ser: serine; Gly: glycine; His: histidine; Arg: arginine; Thr: threonine; Ala: alanine; Pro: proline; Tyr: tyrosine; Val: valine; Met: methionine; Ile: isoleucine; Leu: leucine; Phe: phenylalanine; Lys: lysine.

bidimensional plots. The plots were built using the same amino acid ratios indicated by Pancella and Bart [40]. Identification of the protein binder present in the samples was performed by evaluating the proximity of the samples to the three main standard groups. The plots built were: Pro/Phe versus Asp/Ala, Pro/Ile versus Glu/Ser and Gly/Phe versus Glu/Ala (Fig. 3).

The projection Pro/Phe versus Asp/Ala (Fig. 3a) shows that sample 1, 2 and 4 contain albumin, sample 3 casein and the rest of samples (5–11) collagen. The projection Pro/Ile versus Glu/Ser (Fig. 3b) shows that samples 1–4 contain albumin, although the identification of samples 1 and 2 is less clear than that of samples 3 and 4. Moreover samples 5–11 contain collagen. The last projection considered, Gly/Phe versus Glu/Ala (Fig. 3c), shows the same results as the first projection. In this case, sample 3 is clearly considered as a casein binder and samples 5–11 are collagen. The 2D-Plot strategy is unanimous in classifying samples 5–11 as collagens; nevertheless the conclusions for samples 1–4 were very ambiguous. Sample 1 is considered. The results for sample 4 are similar and it is clearly considered as albumin by plot 3b whereas plots 3a and 3c are not as conclusive. Sample 2 is not clearly identified as albumin by any plot used. The results for sample 3 are very interesting, while plot 3c showed clearly casein; plot 3a is not so categorical in classifying it as casein and finally plot 3b conclusively indicates that the protein binder present is albumin.

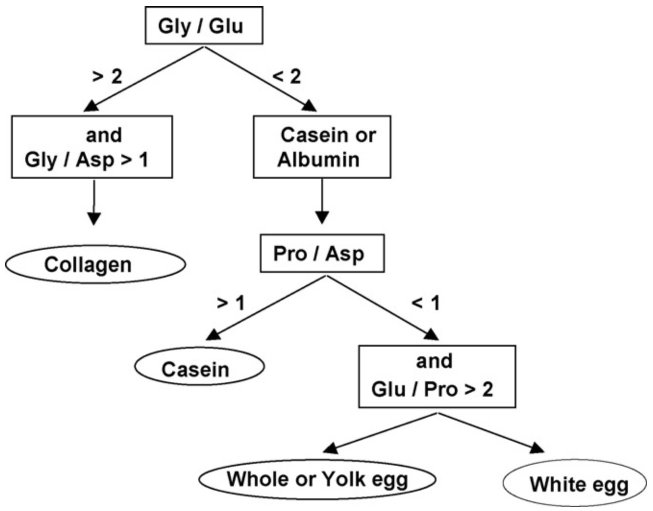

Fig. 2. Flow chart for the identification of protein binders based on ratios of constituent amino acids.

The third strategy considered and previously described [22,45] used SCF. The correlation factors between each amino acid profile of the samples and each protein binder standard are shown in Table 5. Only samples 5–11 show a good correlation ($r > 0.98$) with the collagen standard. The rest of the samples (1–4) are not assigned to any other type of protein binder considered here.

Finally, the SIMCA strategy was applied to identify the proteinaceous binder in the artwork samples as described in (Table 6). The binder present in samples 1–4 cannot be considered as belonging to any of the classes or subclasses considered here ($P < 95–99\%$). Samples 5–11 contain collagen as binder. Additionally, this strategy made it possible to identify binders

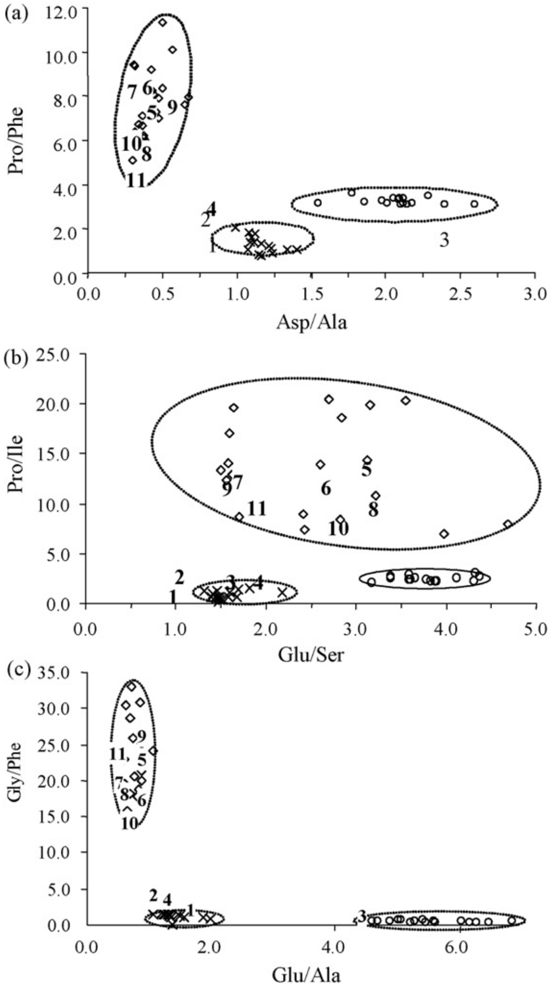

Fig. 3. Identification of the samples coming from Cultural Heritage according to the strategy of bidimensional projections of the ratios of amino acids: (×) albumins; (◯) caseins and (◊) collagens.

at the subclass level. Thus, in samples 6 and 10, collagen binder coming from mammals was identified, whereas samples 5, 7, 8, 9 and 11 contain collagen coming from fish.

The results obtained using SIMCA methodology were compared to those obtained using the traditional strategies for binder identification. It was observed that classical strategies can lead to ambiguous results. In the case of sample 1, the Aa ratio and 2D-Plot strategies would consider it as casein or egg, respectively. Something similar occurs with sample 3, which could contain casein or collagen binder. Sample 2 is a more unclear case because the same strategy, 2D-Plot, leads to different conclusions; a projection plot concludes that it is casein, the other shows egg. The great differences in classification obtained with traditional strategies can be attributed to the fact that identification is based only on the small amount of information contained in a few amino acid ratios employed whereas SIMCA methodology uses the greater information latent in the full amino acid profile. On the other hand, SCF strategy led to similar results to SIMCA, that is, protein present in samples 1–4 could not be identified as belonging to any kind of protein considered here whereas samples 5–11 were identified as collagen binder. But this strategy was not able to distinguish the origin of the collagen, that is, mammalian or fish. In short, classical strategies have been shown to lead to unclear results against a probabilistic and statistical-based method such as SIMCA. Thus, identification is based now on statistical tests where decisions about the protein present are taken at an appropriated level of confidence ($P > 95\%$). In samples 1–4, the available tools (strategies) including SIMCA can only state that a protein binder different from those considered here is present. The presence of some other kind of protein or perhaps mixtures of them can be hypothesized, but there is no statistical support to specify this.

Table 5
Sample origin and protein binder identification according to the four identification strategies considered

Sample	R^2_{Albumin}	R^2_{Casein}	R^2_{Collagen}
1	0.347	0.125	0.539
2	0.337	0.099	0.768
3	0.418	0.370	0.358
4	0.495	0.254	0.652
5	0.052	0.002	0.995
6	0.038	0.003	0.985
7	0.043	0.000	0.982
8	0.048	0.002	0.989
9	0.057	0.002	0.993
10	0.040	0.003	0.987
11	0.037	0.000	0.988

Table 6
Correlation coefficients found (R^2) between the samples of the Cultural Heritage and protein standards

Number	Aa ratios	2D-Plot	SCF	SIMCA ($P > 95$–99%)	
				Class	Subclass
1	Casein	Egg	–	None	–
2	Casein	Casein and egg	–	None	–
3	Casein	Collagen	–	None	–
4	Collagen	Collagen	Collagen	None	–
5	Collagen	Collagen	Collagen	Collagen	Fish
6	Collagen	Collagen	Collagen	Collagen	Mammalian
7	Collagen	Collagen	Collagen	Collagen	Fish
8	Collagen	Collagen	Collagen	Collagen	Fish
9	Collagen	Collagen	Collagen	Collagen	Fish
10	Collagen	Collagen	Collagen	Collagen	Mammalian
11	Collagen	Collagen	Collagen	Collagen	Fish

3. Conclusions

We carried out a comparison between traditional strategies and a classification technique, namely SIMCA. SIMCA analysis makes it possible to identify the protein binder present in eleven samples coming from Cultural Heritage artwork such as wall and easel paintings, manuscripts and polychrome sculptures from the 15–18th centuries.

Three previously described strategies were selected for carrying out the identification of protein binders present in artwork samples through their amino acid content and were compared with SIMCA. Classical strategies can produce ambiguous results in some cases and different results in other cases according to the strategy used. Thus, the classification performed is based on latent information based only on a few amino acids or ratios and it is supported by the subjectivity of the researcher because s/he decides the last resort. Moreover, with none of classical strategies is it possible to know the confidence level of the classification carried out.

Collagen was identified in seven samples (5–11) and it was possible to identify the origin. It was concluded that the rest of the samples (1–4) did not contain any of the proteins considered at a confidence level of 95%. Nevertheless, the presence of an amino acid in these samples could suggest the presence of another protein binder, for example: another kind of protein not considered here or it could be some kind of mixture or may be a simple environmental or fingerprint contamination. The question of mixtures is not considered in this work, but it will be treated in future studies.

The applicability of the SIMCA classification technique as a tool to identify the proteinaceous binders present in Cultural Heritage artworks has been shown. Moreover, with SIMCA it is possible to know what the proteinaceous binders are, not only at a class level but at a subclass level as well. If the protein binder present is albumin, it is possible to distinguish whether it comes from glair, yolk or whole egg, between ovine, caprine and bovine for caseins and between mammals and fish for collagens. A more robust and less subjective identification has been performed than with traditional strategies with which it is possible to know the confidence level of acceptance.

Acknowledgements

We acknowledge financial support from the *Ministerio de Educación y Cultura, Dirección General de Enseñanza Superior* (Spain) from Project BHA2003-08671, coordinated by Dr. L.R. Rodríguez Simón. Acknowledgements to the conservation and restoration repair shop *Escuela de Flandes* from Granada, to the Royal Chancery Archive of Granada and the *Laboratorio Central de Sanidad Animal* (Ministry of Agriculture, Food and Fisheries) Santa Fe (Granada), Spain.

References

[1] D.W. Grattan, J. Int. Inst. Conser-Can. Group 4 (1979) 17.
[2] J.S. Mills, R. White, The Organic Chemistry of Museum Objects, 2nd ed., Butterworth, Heinemann, 2003 (Reprinted 2003).
[3] A. Karpowicz, Stud. Conserv. 26 (1981) 153.
[4] S.M. Halpine, Stud. Conserv. 37 (1992) 22.
[5] L. Masschelein-Kleiner, in: N. Brommelle, P. Smith (Eds.), Contribution to the Study of Aged Proteinaceous Media, en Conservation and Restoration of Pictorial Art, Butterworth, London, 1976.
[6] M. Johnson, E. Packard, Stud. Conserv. 16 (1971) 145.
[7] E. Martin, Stud. Conserv. 22 (1977) 63.
[8] M.C. Gay, Ann. Lab. Rech. Mus. France 8 (1970).
[9] R. Wolberrs, G. Landrey, AIC Preprints: 15th Annual Meeting, American Institute for Conservation, Vancouver, British Columbia, Washington, DC.
[10] R.J. Meilunas, J.G. Bentsen, A. Steinberg, Stud. Conserv. 35 (1990) 33.
[11] M.R. Derrick, J.M. Landry, D.C. Stulik, Methods in Scientific Examination of Artworks of Art: Infrared Microspectroscopy, Getty Conservation Institute, 1991.
[12] M. Odlyha, Thermochim. Acta 269–270 (1995) 705.
[13] B. Ramirez-Barata, S. de la Vina, Stud. Conserv. 46 (2001) 282.
[14] M.P. Colombini, F. Modugno, J. Sep. Sci. 27 (2004) 147.
[15] S.L. Vallance, Analyst 122 (1997) 75R.
[16] M. Hey, Stud. Conserv. 3 (1958) 183.
[17] L. Masschelein-Kleiner, Stud. Conserv. 1 (1974) 207.
[18] S.L. Vallance, B.W. Singer, S.M. Hitchen, J. Townsend, LC–GC Int. 10 (1997) 48.
[19] C.M. Grzywacz, J. Chromatogr. A 676 (1994) 177.
[20] F. Ronca, Stud. Conserv. 39 (1994) 100.
[21] R. White, National Gallery Tech. Bull. 8 (1984) 5.
[22] M.R. Schilling, H.P. Khanjian, ICOM, 11th Trienal Meeting, Edinburgh, 1996.
[23] V. Pitthard, M. Griedder, S. Stanek, Ann. Chim. 96 (2006) 561.
[24] M.P. Colombini, I. Bonaduce, G. Gautier, Chromatographia 58 (2003) 1.
[25] W. Nowik, Stud. Conserv. 40 (1995) 120.
[26] M.P. Colombini, F. Modugno, A. Giacomelli, J. Chromatogr. A 846 (1999) 101.
[27] M.P. Colombini, F. Modugno, E. Menicagli, R. Fuoco, A. Giacomelli, Microchem. J. 67 (2000) 291.
[28] M.P. Colombini, R. Fuoco, A. Giacomelli, B. Muscatello, N. Fanelli, Sci. Tech. Cult. Herit. 7 (1998) 49.
[29] A. Ballistreri, M. Fichera, P. Fifi, G. Musumarra, Sci. Tech. Cult. Herit. 7 (1998) 27.
[30] O.F. van den Brink, G.B. Eijke, J.J. Boon, Thermochim. Acta 365 (2000) 1.
[31] S.N. Krylov, N.J. Dovichi, Anal. Chem. 72 (2000) 111R.
[32] K. Dif, C. Pepe, J. Peduzzi, B. Lavedrine, C. Chahine, J. Cult. Herit. 3 (2002) 317.
[33] Halpine S.M. Studies in the History of Art, 51, Monograph Series II, National Gallery of Art, Washington, 1995.
[34] R. Aruga, P. Mirti, A. Casoli, G. Palla, Fresenius J. Anal. Chem. 365 (1999) 559.
[35] C.W. Gehrke, L.L. Wall, J.S. Absheer, F.E. Kaise, R.W. Zumwalt, J. Assoc. Off. Anal. Chem. 68 (1985) 811.
[36] A.H. Woods, P.R. O'Bar, Science 167 (1970) 79.
[37] G.L. Peterson, Anal. Biochem. 201 (1979) 113.
[38] E.E. Hartree, Anal. Biochem. 48 (1972) 422.
[39] A. Casoli, P.C. Musini, G. Palla, Chromatographia 42 (1996) 421.
[40] R. Pancella, R. Bart, Zeitschrift fur Kunsttechnologie, vol. 3, Laboratoire de Conservation de la Pierre, Lausanne, 1989, pp. 101–111.
[41] S. Wold, Pattern Recognit. 8 (1976) 151.
[42] B.A. Bidlingmeyer, B.A. Cohen, T.L. Tarvin, J. Chromatogr. 336 (1984) 93.
[43] R. Checa-Moreno, Identificación de aglutinantes proteicos pictóricos mediante cromatografía líquida y técnicas de reconocimiento de pautas, Tesis Doctoral, Universidad de Granada, 2003.
[44] C. Cenini, The Craftsman's Handbook. 'Il Libro dell'Arte, Dover Publications, Inc., New York, 1960.
[45] M.R. Schilling, H.P. Khanjian, J. Am. Inst. Conserv. 35 (1996) 123.
[46] P.C. Meier, R.E. Zünd, Statistical Methods in Analytical Chemistry, John Wiley & Sons Inc., New York, 1977.

Available online at www.sciencedirect.com
ScienceDirect
Talanta
Talanta 75 (2008) 765–769
www.elsevier.com/locate/talanta

Analytical method for authentication of Traditional Balsamic Vinegar of Modena

Roberto Consonni[a,*], Laura R. Cagliani[a], Silvia Rinaldini[b], Antonia Incerti[b]

[a] *Istituto per lo Studio delle Macromolecole, Lab. NMR, CNR, v. Bassini 15, 20133 Milan, Italy*
[b] *Agenzia Regionale Prevenzione e Ambiente dell'Emilia Romagna, sez. Reggio Emilia, v. Amendola 2, 42100 Reggio Emilia, Italy*

Received 28 August 2007; received in revised form 16 November 2007; accepted 7 December 2007

Abstract

^{13}C NMR spectroscopy was employed for evaluating glucose and fructose isoforms content in Traditional Balsamic Vinegar of Modena. With the use of reference spectra recorded in water for samples obtained with respect to set rules, a shift determination method for fructose carbon isoforms was introduced to determine the frauds present in unknown Traditional Balsamic Vinegar of Modena samples. No sample preparation yields this approach highly reliable and time saving. Following this approach, for the first time, an objective analytical technique can be used alternatively to the actual procedures for Traditional Balsamic Vinegar certification.

Keywords: Traditional Balsamic Vinegar of Modena; ^{13}C NMR; Vinegar; Authentication; Ageing

1. Introduction

Nowadays, the most emerging request in food science is the authenticity determination of dairy products; robust and reproducible analytical methods are required to address this question. In the recent years, different analytical techniques were presented in the literature: FT-IR spectroscopy [1–4], isotope ratio mass spectrometry, also coupled with separation techniques [5–10] and Raman spectroscopy [11–13]. Recently, different techniques in food authenticity have been reviewed [14–16]. Analytical techniques were often combined with statistical methods, which were growing rapidly during the last years. NMR applications in food authenticity were instead quitely isolated, even though the potentiality of this technique is really outstanding. Examples of NMR applications, mainly concerning the use of the isotope technique (SNIF-NMR) are present in the literature [17–21], while other non-specific natural isotopic fractionation techniques were applied in food authenticity and made use of high resolution NMR techniques [22–26]; interestingly few of them concern the employment of ^{13}C NMR spectroscopy. NMR technique is generally devoted to analyze samples without manipulation with high reproducibility and it is considered as a "fingerprint" method for authentication analysis. In this respect, a quite updated but exhaustive example [27] was reported concerning the carbohydrate determination with high-resolution ^{13}C NMR technique, applied to honey characterization. Here is reported a combined use of high-resolution ^{13}C NMR spectroscopy and a fructose carbon isoforms measurement method for quality assessment and authentication for Traditional Balsamic Vinegar of Modena (TBVM), a very well known Italian product. Traditional Balsamic Vinegar of Modena is an original and PDO product (Reg. CEE no. 813/2000 of 17 April 2000) highly appreciated all over the world.

Its economical value is particularly quoted on the market because of the ageing process that can reach more than 25 years; cooked must and "traditional procedures" are the only allowed ingredients and no additional products can be added. These procedures imply a natural fermentation of cooked grape must, followed by its progressive concentration during the ageing process, that takes place into a series of casks of different wood and size for at least 12 years. Set rules (G.U. no. 124, 30 May 2000) regulate the correct production procedure, which is unique from every point of view; traditionally making process, topping procedure, taste and aroma characterize this product. Different analytical studies were applied on TBVM [28–36] but

---

[*] Corresponding author. Tel.: +39 02 23699578; fax: +39 02 23699620.
E-mail address: roberto.consonni@ismac.cnr.it (R. Consonni).

0039-9140/$ – see front matter © 2007 Elsevier B.V. All rights reserved.
doi:10.1016/j.talanta.2007.12.005

none of them were focused on the authentication evaluation. In the Italian market, another largely consumed flavoring is Balsamic Vinegar of Modena (BVM), which is a different product: it is made from wine vinegar with the addition of caramel and eventually a small quantity of aged wine vinegar, as described in the set rules (D.M. 3 December 1965) for preparation procedure. BVM samples can experience a further ageing process, thus reaching higher quality parameters, but always far away from TBVM peculiarity. Both BVM and TBVM certifications are nowadays obtained by means of sensorial analysis and by very simple physiochemical properties determination like total acidity, density and dry residual.

Analysis of food products should require the use of non-invasive techniques because sensorial and safety properties are related to the structural and compositional complexity and heterogeneity of the matrix, which must be preserved as much as possible in its original state. This work describes the use of ^{13}C NMR spectroscopy with a particular data elaboration emerged from a critical evaluation of several carbon spectra of TBVM and BVM samples. This application gave rise the possibility of a rapid and unequivocal identification of fraud in such very evaluated foods, with no sample preparation.

2. Experimental

2.1. NMR sample and experimental procedures

72 samples of both BVM and TBVM from different producers have been used. Among them, 8 were BVM of known ageing, 22 were TBVM potentially adulterated (named N.D.) while 42 were highly trusted TBVM of known ageing, and used as reference. ^{13}C NMR spectra were recorded on Bruker DMX spectrometer operating at 11.7 T and equipped with a 5-mm reverse probe with *z*-gradient. Samples were prepared by dissolving 100 μL of each sample into 400 μL of DMSO-^{2}H$_6$. Spectra were acquired with 65,500 points covering 30,000 Hz; pulse width of 13 μs (90° pulse) and 5 s for relaxation between each of 512 scans were chosen. Standard inverse-gated decoupling pulse sequence from Bruker library was adopted to avoid the heteronuclear NOE derived from proton decoupling. Spectra were processed by applying an exponential line broadening of 1 Hz for sensitivity enhancement before Fourier transformation and were accurately phased, baseline adjusted and referenced by using the solvent signal as chemical shift standard (TOPSPIN 1.2®). Intensities were scaled with regard to the central line of solvent signal.

3. Results and discussion

3.1. TBVM and BVM samples

A primary condition for quantitative ^{13}C NMR spectroscopy is to avoid the carbon intensity distortion due to the decoupling of proton resonances. The method used, in combination with long relaxation times, recovers the correct intensity of the carbon signals, thus resulting in a correct quantitative spectrum. Analysis of ^{13}C NMR spectrum of TBVM sample, revealed dominant signals from glucose and fructose together with signals from other components (like acetate, furanic derivatives, etc.). Fig. 1A reports the anomeric sugar region of ^{13}C spectrum for TBVM samples dissolved in organic solvent. In particular, as already reported [27], only α and β pyranosidic forms (αGP and βGP, respectively) were observed for glucose, while both pyranosidic and furanosidic α and β forms can be observed for fructose (αFP, βFP, αFF and βFF).

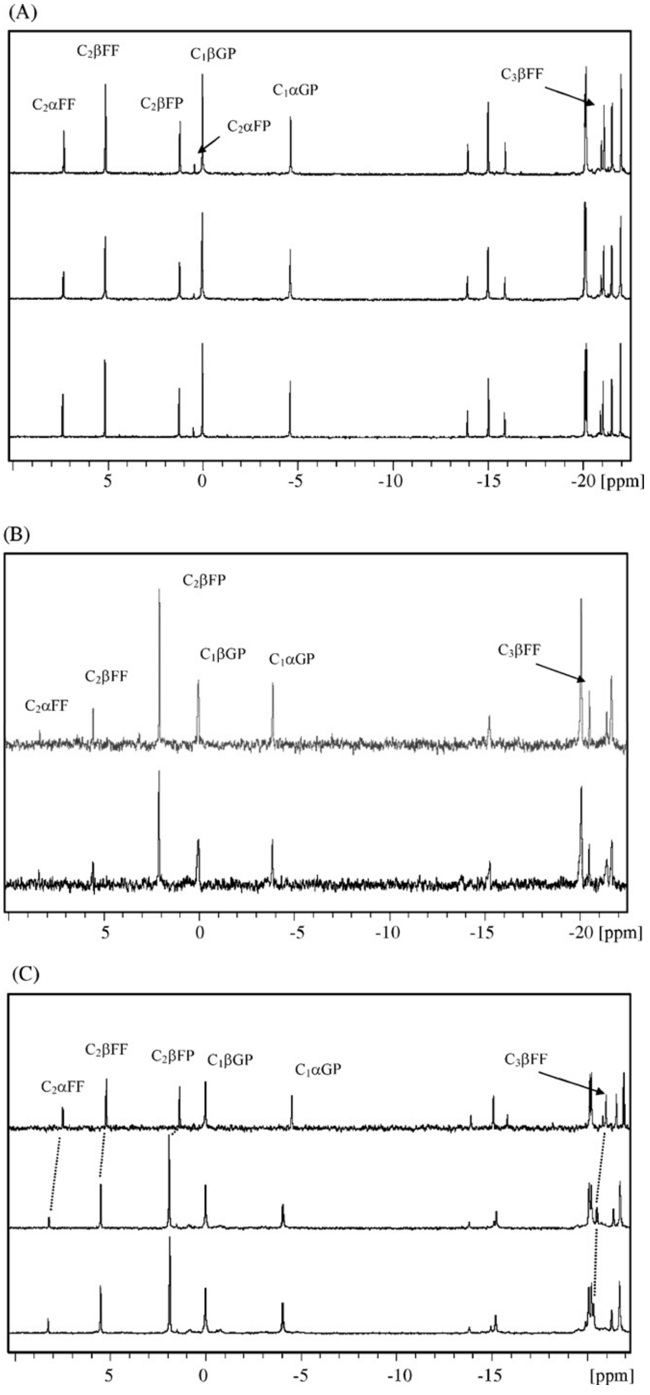

Fig. 1. Anomeric sugar region of the ^{13}C spectrum relative to three TBVM samples (A), two BVM samples (B) and three unknown declared TBVM samples differently defrauded (C). Dotted lines in (C) indicate the shift of fructose isoforms due to different degrees of adulteration.

Table 1
Chemical shift values for standard water solutions (tab) for TBVM sample dissolved in organic solvent (exp) and mean values for observable tautomeric isoforms of fructose in highly trusted TBVM of known ageing samples dissolved in water, obtained after calibration with $C_1\beta GP$ as internal reference ($\Delta\sigma$)

	tab[a]	exp	$\Delta\sigma$
Furanosidic			
αFF			
C1	63.7	64.0	−32.5
C2	105.5	104.4	8.5
C3	82.9	83.2	−13.9
C4	77	76.1	−19.9
C5	82.2	81.2	−14.6
C6	61.9	61.4	−35.3
βFF			
C1	63.6	63.2	n.d.
C2	102.6	102.2	5.6
C3	76.4	76.0	−20.5
C4	75.4	75.6	−21.4
C5	81.6	82.1	−15.2
C6	63.2	63.2	n.d.
Pyranosidic			
βFP			
C1	64.7	64.6	−32.0
C2	99.1	98.3	2.2
C3	68.4	68.1	−28.3
C4	70.5	70.2	n.d.
C5	70	69.5	−26.7
C6	64.1	63.3	n.d.
αFP			
C1	65.9	n.d.	n.d.
C2	99.1	97.6	n.d.
C3	70.9	70.8	n.d.
C4	71.3	71.7	n.d.
C5	62	61.5	n.d.
C6	61.9	59.9	n.d.

n.d. stands for not univocally determined values.
[a] E. Breitmaier, W. Voelter, VCH editors, 1987, 381–384.

Resonance assignment of tautomeric forms for glucose and fructose of TBVM sample dissolved in organic solvent can be easily performed; only fructose values were reported in Table 1, in comparison with the published fructose–water solution values.

Water solution of glucose and fructose showed the tautomeric forms in their “naturally” occurring distribution, in according to the reported value [27]: in particular, fructose presents 4.8%, 23%, 2.4%, and 69.8% of abundance for αFF, βFF, αFP and βFP forms, respectively, while glucose presents only the pyranose tautomeric forms with 37% and 63% of abundance for αGP and βGP forms, respectively.

The analysis of must samples performed in organic solvent (data not shown) revealed the presence of the “natural” distribution for tautomeric forms of both glucose and fructose, due to the large water content. During the cooking process, must sugars were subjected to thermal degradation giving rise to heterocyclic compounds (mainly furfurales) and, as a consequence, the sugar isoforms experienced a redistribution accordingly. In particular, the most abundant form of fructose, βFP, will experience the thermal degradation in the largest extent. This fundamental sugar concentration process of the must, resulted also in a large water loss, which was no longer available in vast bulk, thus not allowing the tautomeric equilibration process. In other words, sugars in TBVM kept their tautomeric distribution in such a way constituting the “traditional labeling” that can be used for TBVM authentication. This observation could be preserved by the use of organic solvent; as a matter of fact, by dissolving TBVM or aged BVM in water, sugars reordered the tautomeric isoforms, reaching again their “naturally” occurring distribution. Glucose isoforms revealed to maintain this “naturally” occurring distribution in organic solvent in both TBVM and BVM samples and thus they were not taken into account. Concerning fructose isoforms, TBVM showed the less abundant one, namely αFP, as well as the intensity ratio value for $C_2\beta FP/C_2\beta FF$ signals largely below one (Fig. 1A). Both these situations were verified for all the highly trusted TBVM samples analyzed. On the contrary, for BVM samples the intensity ratio value was largely over the value of one, as shown in Fig. 1B and the presence of the tautomeric isoform αFP was missed, most likely overlapped with $C_1\beta GP$.

Furthermore, BVM samples revealed different chemical shift values for sugar isoforms with respect to TBVM samples, due to the larger residual water present in BVM. In particular, fructose isoforms showed the largest chemical shift deviations with respect to glucose isoforms. For this reason, in this work, we decided to monitor the fructose isoforms and in particular their shifts by calibrating them with respect to the chemical shift of $C_1\beta GP$ resonance, chosen as internal chemical shift reference; we named this procedure as “shift determination method”.

Water solution of highly trusted TBVM samples of known age were chosen as reference and the $\Delta\sigma$ values obtained for carbons of three out of four observable tautomeric isoforms of fructose were reported in Table 1. The same procedure was then applied to all TBVM and BVM samples in organic solvent.

Finally, chemical shift deviations were calculated with respect to the carbon shifts observed in organic solvent and the mean values measured for reference samples analyzed in water. Inspection of the main chemical shifts deviations obtained for all TBVM revealed that the most sensible carbons were $C_2\alpha FF$ and $C_3\beta FF$ (Fig. 2): on the other hand, some carbons of the four isoforms were partially overlapped or totally missed in some spectra, and for these reasons those were not selected for monitoring shifts. The shifts values observed for highly trusted TBVM were ranging between 1.23 and 1.05 for $C_2\alpha FF$ and between 0.64 and 0.52 for $C_3\beta FF$, but never below 1 and 0.5. For this reason we assumed 1 and 0.5 as reference values.

On the basis of these data, three parameters were assumed to be used for sample classification: (1) the presence of the αFP isoform, indicative for initial discrimination of TBVM samples, (2) the intensity ratio for $C_2\beta FP/C_2\beta FF$ signals, whose upper limit of one was chosen as adulteration alert level (ADUAL) and (3) measurement of the $C_2\alpha FF$ and $C_3\beta FF$ chemical shift deviations, whose values of 1 and 0.5, respectively, were chosen for authentication alert level (AUTAL).

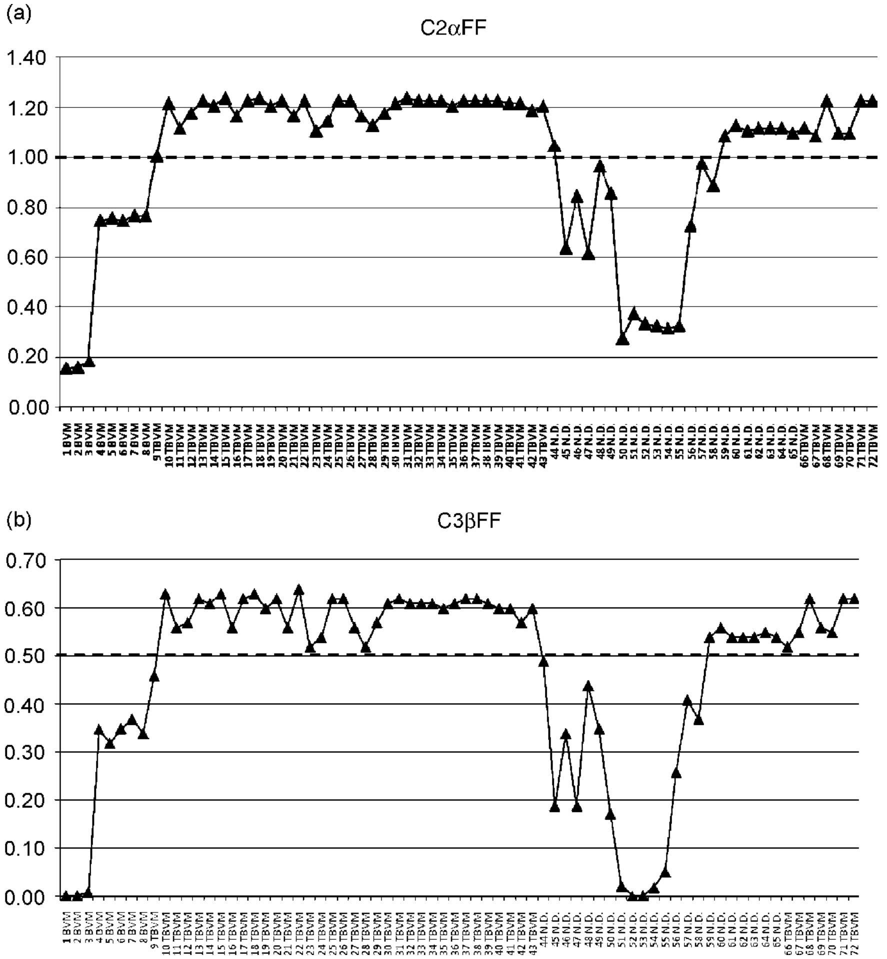

Fig. 2. $C_2\alpha FF$ and $C_3\beta FF$ shift deviations measured for all samples with AUTAL reference values indicated with dotted line.

3.1.1. *Analysis of unknown samples*

When unknown TBVM samples were investigated, the primary indication was the evaluation of the requirement expressed at point (1) followed by ADUAL evaluation, as previously described in point (2). If the sample did not fit the first two points, it can be considered as not obtained in agreement with set rules. If the sample showed ambiguous value for ADUAL value (i.e. very close to one), the AUTAL value needs to be checked. In this sense, AUTAL is considered the authentication factor that validates the previous evaluation. For example, in Fig. 1C ^{13}C NMR spectra of three unknown samples, declared to be TBVM, were reported: only the sample at the top trace reported ambiguous ADUAL value; in the middle and at the bottom trace spectra clearly indicated adulterated samples, obtained not in agreement with set rules, and, additionally, all spectra did not show the presence of αFP tautomeric form. Fig. 2 reports both real and potentially adulterated TBVM as well as BVM samples, either aged or not aged. BVM spectra represented in Fig. 2 were largely below the AUTAL reference values but also N.D. samples (from no. 45 up to no. 58) showed largely distorted shifts for both $C_2\alpha FF$ and $C_3\beta FF$ values, thus indicating large fraud presence. Some other N.D. sample (from no. 59 up to no. 65) resulted not adulterated, thus indicating the observation of set rules. This result was compared with the classical analyses performed on N.D. samples, confirming that other parameters were out of the standard range, suggesting that samples (no. 45–58) were not prepared in according to the correct procedures. In particular, total sulphorous anhydride determination evidenced an average amount of 30 mg/L while it was expected to be absent in TBVM. Another important parameter, named “R Ratio” (°Brix/Total Acidity) [37], indicates the balance among sweet and acid tones and it is used as a synthetic index for TBVM. This parameter was found to be 11.8–16.9, being 7–10 the range for TBVM produced according to set rules.

4. Conclusion

The ^{13}C NMR spectroscopy is here presented as a powerful analytical tool in TBVM characterization. Previously, quantitative carbon determinations, obtained with polarization transfer experiments was successfully applied for olive oil authentication [24]. In this work, the same aim is obtained for TBVM by using the simple carbon decoupled experiment. Dissolving samples in organic solvent, the possibility to monitor the tautomeric isoform ratio of the main present sugars, like glucose and fructose, is available. The most important point and the novelty of this work is the possibility to observe these isoforms, in particular for fructose, that reports the memory of the degradation process experienced, by using organic solvent. This simple trick, in this respect, makes other approaches unsuccessful, like water sample solution. Furthermore, the introduction of reference values, i.e. ADUAL and AUTAL, leads to control two different fructose isoforms, thus preventing eventually sophisticated frauds. This technique showed a new application in the field of food authentication, and on the basis of our results, this methodology is advantageous for this aim and in particular with no need of sample derivatization or manipulation, like other techniques required. On the basis of our knowledge acquired on TBVM samples, we can now safely propose this new approach to determine the authenticity of this very expensive vinegar [37,38].

Acknowledgements

Prof. Vincenzo Ferrari Amorotti and Prof. Francesco Saccani of Consorteria di Spilamberto of Modena are acknowledged for their kind availability and scientific supporting.

References

[1] J. He, L.E. Rodriguez-Saona, M.M. Giusti, J. Agric. Food Chem. 55 (2007) 4443.
[2] D.C. Perez-Marin, A. Garrido-Varo, J.E. Guerrero, Appl. Spectrosc. 60 (2006) 1432.
[3] K. Ruoff, W. Luginbuhl, R. Kunzli, M.T. Iglesias, S. Bogdanov, J.O. Bosset, K. von der Ohe, W. von der Ohe, R. Amado, J. Agric. Food Chem. 54 (2006) 6873.
[4] A. Edelmann, J. Diewok, K.C. Schuster, B. Lendl, J. Agric. Food Chem. 49 (2001) 1139.
[5] F.F. Bensaid, K. Wietzerbin, G.J. Martin, J. Agric. Food Chem. 50 (2002) 6271.
[6] G. Calderone, C. Guillou, F. Reniero, N. Naulet, Food Res. Int. 40 (2007) 324.
[7] E. Jamin, K. Wietzerbin, Am. Lab. 35 (2003) 24.
[8] G.G. Martin, Y.L. Martin, N. Naulet, H.J.D. McManus, J. Agric. Food Chem. 44 (1996) 3206.
[9] P.S. Belton, I. Delgadillo, A.M. Gil, P. Roma, F. Casuscelli, I.J. Colquhoun, M.J. Dennis, M. Spraul, Magn. Reson. Chem. 35 (1997) S52.
[10] G. Fronza, C. Fuganti, P. Grasselli, S. Serra, F. Reniero, C. Guillou, Rapid Commun. Mass Spectrom. 15 (2001) 763.
[11] A.N. Davies, P. McIntyre, E. Morgan, Appl. Spectrosc. 54 (2000) 1864.
[12] H.M. Heise, U. Damm, P. Lampen, A.N. Davies, P.S. McIntyre, Appl. Spectrosc. 59 (2005) 1286.
[13] E.C. Lopez-Diez, G. Bianchi, R. Goodacre, J. Agric. Food Chem. 51 (2003) 6145.
[14] R. Karoui, J. De Baerdemaeker, Food Chem. 102 (2007) 621.
[15] L.M. Reid, C.P. O'Donnell, G. Downey, Trends Food Sci. Technol. 17 (2006) 344.
[16] M.J. Dennis, Analyst 123 (1998) 151R.
[17] J.F. Cotte, H. Casabianca, J. Lhéritier, C. Perrucchietti, C. Sanglar, H. Waton, M.F. Grenier-Loustalot, Anal. Chim. Acta 582 (2007) 125.
[18] I.S. Arvanitoyannis, C. Chalhoub, P. Gotsiou, N. Lydakis-Simantiris, P. Kefalas, Crit. Rev. Food Sci. Nutr. 45 (2005) 193.
[19] E. Jamin, R. Guérin, M. Rétif, M. Lees, G.J. Martin, J. Agric. Food Chem. 51 (2003) 5202.
[20] A.J. Charlton, W.H. Farrington, P. Brereton, J. Agric. Food Chem. 50 (2002) 3098.
[21] P. Petrakis, I. Touris, M. Liouni, M. Zervou, I. Kyrikou, R. Kokkinofta, C.R. Theocharis, T.M. Mavromoustakos, J. Agric. Food Chem. 53 (2005) 5293.
[22] M. Aursand, I.B. Standal, D.E. Axelson, J. Agric. Food Chem. 55 (2007) 38.
[23] G. Vlahov, P. Del Re, N. Simone, J. Agric. Food Chem. 51 (2003) 5612.
[24] G. Vlahov, Magn. Reson. Chem. 35 (1997) S8.
[25] L. Shintu, S. Caldarelli, B.M. Franke, Meat Sci. 76 (2007) 700.
[26] L. Shintu, F. Ziarelli, S. Caldarelli, Magn. Reson. Chem. 42 (2004) 396.
[27] V. Mazzoni, P. Bradesi, F. Tomi, J. Casanova, Magn. Reson. Chem. 35 (1997) S81.
[28] M. Plessi, D. Bertelli, F. Miglietta, J. Food Compos. Anal. 19 (2006) 49.
[29] M. Cocchi, C. Durante, M. Grandi, P. Lambertini, D. Manzini, A. Marchetti, Talanta 69 (2006) 1166.
[30] D. Sanarico, S. Motta, L. Bertolini, A. Antonelli, J. Liq. Chromatogr. R. T. 26 (2003) 2177.
[31] D. Carlavilla, M.V. Moreno-Arribas, S. Fanali, A. Cifuentes, Electrophoresis 27 (2006) 2551.
[32] R. Consonni, A. Gatti, J. Agric. Food Chem. 52 (2004) 3446.
[33] A. Hermann, Eur. Food Res. Technol. 212 (2001) 683.
[34] G. Remaud, C. Guillou, C. Vallet, G.J. Martin, Fresen. J. Anal. Chem. 342 (1992) 457.
[35] M. Gullo, C. Caggia, L. De Vero, P. Giudici, Int. J. Food Microbiol. 106 (2006) 209.
[36] L. Solieri, S. Landi, L. De Vero, P. Giudici, J. Appl. Microbiol. 101 (2006) 63.
[37] M. Gullo, L. De Vero, Ricerche finalizzate alla tutela della tipicità dell'Aceto Balsamico Tradizionale di Reggio Emilia, 2004, 93–107.
[38] R. Consonni, Italy Patent MI2007A001489, (2007).

Available online at www.sciencedirect.com
ScienceDirect

Talanta 75 (2008) 775–785

Talanta

www.elsevier.com/locate/talanta

Sequestering ability of polycarboxylic ligands towards dioxouranium(VI)

Francesco Crea*, Claudia Foti, Silvio Sammartano

Dipartimento di Chimica Inorganica, Chimica Analitica e Chimica Fisica, Università di Messina,
Salita Sperone 31, 98166 Messina (Vill. S. Agata), Italy

Received 30 July 2007; received in revised form 29 November 2007; accepted 7 December 2007

Abstract

In this paper we report a comparison on the sequestering ability of some polycarboxylic ligands towards dioxouranium(VI) (UO_2^{2+}, uranyl). Ligands taken into account are mono- (acetate), di- (oxalate, malonate, succinate and azelate), tri- (1,2,3-propanetricarboxylate) and hexa-carboxylate (1,2,3,4,5,6-benzenehexacarboxylate). The sequestering ability of polycarboxylic ligands towards UO_2^{2+} was quantified by a new approach expressed by means of a sigmoid Boltzman type equation and of a empirical parameters (pL_{50}) which defines the amount of ligand necessary to sequester 50% of the total UO_2^{2+} concentration. A fairly linear correlation was obtained between pL_{50} or $\log K_{110}$ ($\log K_{110}$ refers to the equilibrium: $UO_2^{2+} + L^{z-} = UO_2L^{(2-z)}$; L = generic ligand) and the polyanion charges. In order to complete the picture, a tetra-carboxylate ligand (1,2,3,4-butanetetracarboxylate) was studied in NaCl aqueous solutions at $0 \le I$ ($\mathrm{mol\,L^{-1}}$) ≤ 1.0 and $t = 25\,°C$, by potentiometry, ISE-[H$^+$] glass electrode. The formation of ML^{2-}, MLH^-, MLH_2^0 and $MLOH^{3-}$ species ($M = UO_2^{2+}$ and L = 1,2,3,4-butanetetracarboxylate) was found, with $\log\beta_{110} = 7.937 \pm 0.028$, $\log\beta_{111} = 13.066 \pm 0.027$, $\log\beta_{112} = 17.401 \pm 0.013$, $\log\beta_{11-1} = 2.062 \pm 0.040$ at $I = 0\,\mathrm{mol\,L^{-1}}$ and $t = 25\,°C$ [β_{pqr} refer to reaction: $p\mathrm{UO_2}^{2+} + q\mathrm{L}^{4-} + r\mathrm{H}^+ = (\mathrm{UO_2}^{2+})_p\mathrm{L}_q\mathrm{H}_r^{(2p-4q+r)}$]. The dependence on ionic strength of all ligand protonation constants and of the complex formation constants of UO_2^{2+}–polycarboxylate systems was modelled by the SIT (specific ion interaction theory) approach and by the Pitzer equations.

Keywords: Dioxouranium(VI)–polycarboxylate complexes; Speciation; Sequestering ability; Dependence on ionic strength; SIT equation; Pitzer equations

1. Introduction

Studies on the coordination chemistry of uranium in aqueous solution are increasingly important for understanding the behaviour of uranium in the environment [1–7]. Actinide speciation information is essential for assessing strategies addressing problems such as migration of nuclear waste and materials. If uranium is complexed by mobile organic matter molecules and forms stable complexes, the transport of uranium may be enhanced. The ability of uranium to form complexes with organic compounds has been extensively utilised for cleaning up uranium contamination in soils and in the nuclear industry where chelating agents are common constituents of fluids used to clean reactors [8]. The resultant uranyl-organic chelated species can be highly mobile and potentially highly bioavailable within environment [9]. Commonly, the chelating agents used in the cleaning processes and widely present in geologic environments including surface waters and sedimentary basin fluids, are represented by polycarboxylic ligands whose concentrations can vary from μg/L to mg/L. Literature reports many papers on the acid-base and complexing ability of dioxouranium(VI) towards *O*-donor ligands published in the past five decades; some of them are reported in Refs. [10–25], and reference therein. In recent years the scientific community has shown wide interest on radioactive element speciation and, in particular, the NEA (Nuclear Energy Agency) [26] has collected fundamental data about uranium, neptunium, plutonium, americium and technetium chemistry, in order to develop a specific database. Many thermodynamic data are also reported in databases [27–30]. Our aim is to give a contribution to the knowledge of the uranium chemistry. For these reasons, our group has undertaken studies on the acid-base properties of UO_2^{2+} [31–34] and on

---

* Corresponding author. Fax: +39 090 392827.
E-mail address: fcrea@unime.it (F. Crea).

0039-9140/$ – see front matter © 2007 Elsevier B.V. All rights reserved.
doi:10.1016/j.talanta.2007.12.009

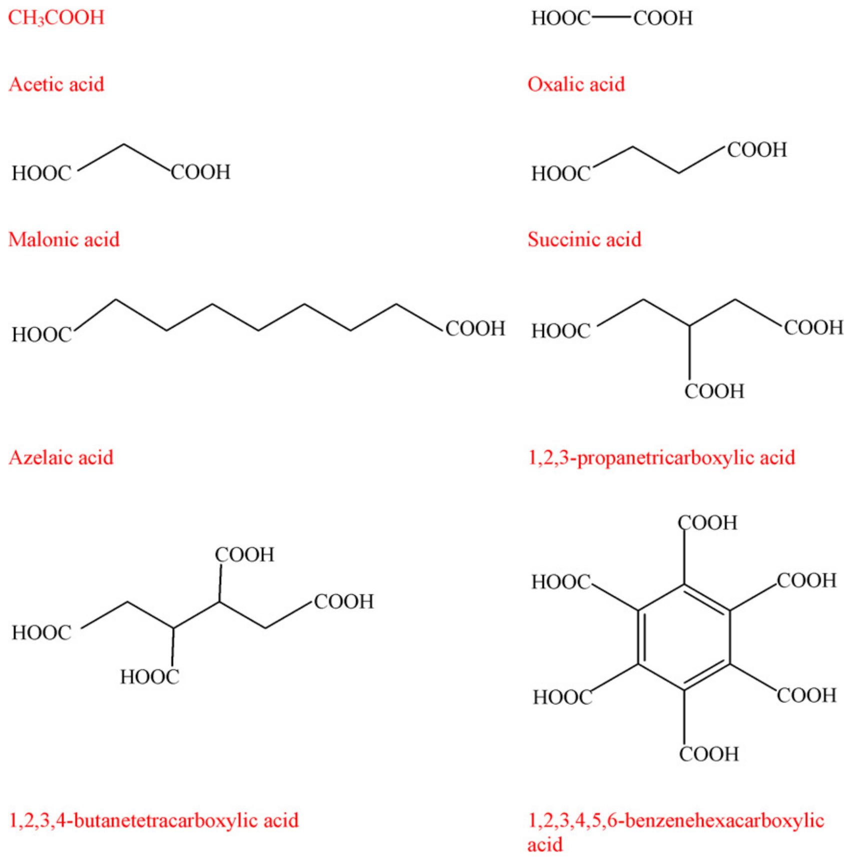

Scheme 1. Structure of ligands.

the sequestering ability of polyfunctional *O*-donor ligands (see Scheme 1) [acetate (*ac*), oxalate (*ox*), malonate (*mal*), succinate (*suc*), azelate (*aze*), 1,2,3-propanetricarboxylate (tricarballylate, *tca*) and 1,2,3,4,5,6-benzenehexacarboxylate (mellitate, *mlt*)] towards uranyl [35–40], in different ionic media and at different ionic strengths values at $t = 25\,^\circ\mathrm{C}$. Here, in order to complete the picture from mono- to esa-carboxylate, we report a potentiometric study on $\mathrm{UO_2}^{2+}$–butanetetracarboxylic acid (*btc*) system, in NaCl aqueous solutions at $0 \leq I\,(\mathrm{mol\,L^{-1}}) \leq 1.0$ and $t = 25\,^\circ\mathrm{C}$.

The results obtained in this paper are consistent with those reported in previous works [35–40], in which it was pointed out that the stability of the $\mathrm{UO_2}^{2+}$–polycarboxylate species and the speciation model may depend on some factors, such as: (a) the coordination number and number of chelate rings; (b) the complex charge; (c) the charge density of the polyanions; (d) the number of –OH groups present in the molecule; (e) the interaction of negatively charged complex species with the cation of the supporting electrolyte (medium stabilisation). The sequestering ability of ligands here investigated towards $\mathrm{UO_2}^{2+}$ can be modelled by using an approach already introduced [38,39]; this method takes into account a Boltzman type equation by which the sum of formation percentages of all metal–ligand complexes, $\Sigma(\%)$ were fitted vs. pL, where $\mathrm{p}L \equiv -\log\,[L]_{\mathrm{tot}}$ ($[L]_{\mathrm{tot}}$ is the total ligand concentration). The pL value at $\Sigma(\%) = 50$, indicates the ligand concentration necessary to sequester 50% of total $\mathrm{UO_2}^{2+}$ in the different experimental conditions. The dependence of $\mathrm{p}L_{50}$ on pH and on the ligand charges was studied.

As further contribute to the study of $\mathrm{UO_2}^{2+}$–polycarboxylate systems, in Appendix A the dependence on ionic strength of molal protonation and complex formation constants was modelled by SIT (specific ion interaction theory) [41,42] and Pitzer [43,44] approaches.

2. Experimental

2.1. Chemicals

Solutions of uranyl nitrate hexahydrate (puriss. >99.5%) were prepared from corresponding Fluka products. Stock solutions of uranyl nitrate were standardized by the gravimetric determination of uranium after oxide $\mathrm{U_3O_8}$ ignition. Stock solutions of 1,2,3,4-butanetetracarboxylic acid (*btc*) (Fluka p.a.) were prepared by weighing the solid products without further purification; the *btc* purity was checked by alkalimetric titration with a standard solution of NaOH, and proved to be ≥99.5%. Standard carbonate-free NaOH solutions were prepared by diluting concentrated (Fluka, puriss.) ampoules, under a stream of purified nitrogen and standardized against potassium hydrogenphthalate (Fluka, puriss.), whilst HCl solutions were standardized against sodium carbonate (Fluka, puriss.). NaCl (Fluka, puriss.) was used after stove drying at 140 °C. All solutions were daily prepared using grade A glassware and ultrapure water (conductivity <0.1 μS). The solutions were preserved from atmospheric $\mathrm{CO_2}$ by means of soda lime traps.

2.2. e.m.f. measurements

Potentiometric measurements on the uranyl–1,2,3,4-butanetetracarboxylate system were carried out following procedures described in previous works [35–40]; instrumental apparatus consisting of a Metrohm (mod. E654) potentiometer equipped with an Orion (Ross mod. 8101) glass electrode coupled with a standard calomel electrode. Instrumental resolution was 0.1 mV. The potentiometric system was controlled by a suitable computer program for data acquisition and e.m.f. stability checks. Pre-established volumes of titrant were delivered to the measurement cell by an automatic Metrohm Dosimat (mod. 665) burette (minimum reading of 0.001 mL). The experiments were carried out in NaCl aqueous solutions at different ionic strength values ($0.1 \leq I$ (mol L^{-1}) ≤ 1.0 mol L^{-1}), at $t = 25 \pm 0.1$ °C. The solutions containing different concentrations of uranyl ion ($0.5 \leq C_{UO_2}{}^{2+} \leq 1.5$ mmol L^{-1}), *btc* ($0.5 \leq C_{btc} \leq 3$ mmol L^{-1}) and NaCl (in order to obtain the pre-established ionic strength values), at different metal/ligand ratios (from $C_M/C_L = 1.2$ to 0.3; $M = UO_2{}^{2+}$ and L = 1,2,3,4-butanetetracarboxylate), were titrated with standard carbonate-free NaOH solutions ($C_{NaOH} = 0.1209$ or 0.4947 mol L^{-1}) until precipitation occurred (pH ≈ 7.5). The experimental conditions used in studying other uranyl–polycarboxylic systems were already reported [35–39]. The sodium hydroxide standard solutions used as titrant were prepared at the same ionic strength of the solutions under study by addition of NaCl, in order to maintain fairly constant the ionic strength values during the titration. In all the experiments a stream of purified nitrogen was bubbled through the solution in order to avoid atmospheric O_2 and CO_2 interference. For all the potentiometric measurements the electrode couple was standardized, in terms of pH = −log [H$^+$], by titrating HCl 10 mmol L^{-1} solution (at the same ionic strength value as the solution under study) with standard NaOH to determine the standard potential E° before each experiment.

2.3. Data analysis and calculations

All the parameters of the acid-base titration were determined using the non-linear least squares computer program ESAB2M [45]. This program allows us to refine the analytical concentration of reagents, formal electrode potential E°, coefficient j_a relative to junction potential (according to the equation: $E_j = j_a$ [H$^+$]) and the ionic product of water K_W; it was also used to determine *btc* purity. The formation constant values were refined by the computer program BSTAC [45] which minimizes the sum of squares error in electromotive force values. In all the least squares calculations weights were obtained from variance propagation. The ES4ECI [45] program was used to draw speciation diagrams and to calculate species formation percentages. All the formation constants are expressed according to the equilibrium:

$$p\mathrm{UO_2}^{2+} + q\mathrm{L}^{z-} + r\mathrm{H}^+ = (\mathrm{UO_2}^{2+})_p\mathrm{L}_q\mathrm{H}_r{}^{(2p-qz+r)} \quad \beta_{pqr}$$

Table 1
Thermodynamic equilibrium constants (molal concentration scale) of hydrolytic species of $UO_2{}^{2+}$, at $t = 25$ °C

p	$-r$[a]	$-\log {}^T\beta_{pr}$[b]
1	1	5.19
2	2	5.76
3	4	11.82
3	5	15.90
3	7	29.27

[a] According to equilibrium: $p\mathrm{UO_2}^{2+} + r\mathrm{H_2O} = (\mathrm{UO_2})_p(\mathrm{OH})_r{}^{(2p-r)} + r\mathrm{H}^+$.

[b] Ref. [31].

$\log {}^T\beta_{pqr}$ values at $I = 0$ mol L^{-1} were calculated from potentiometric data using a simple Debye–Hückel type equation for extrapolation purposes:

$$\log \beta_{pqr} = \log {}^T\beta_{pqr} - z * \frac{AI^{1/2}}{1 + 1.5I^{1/2}} + CI \tag{1}$$

where $z* = \Sigma z^2_{\text{reactants}} - \Sigma z^2_{\text{products}}$ (z = charge); A = Debye–Hückel constant = 0.51 at $t = 25$ °C and C is the only adjustable parameter for the dependence of formation constants on ionic strength. In the paper, errors are expressed as ±S.D., and for the ionic strengths we reported their mean values (±1%).

3. Results and discussion

3.1. Hydrolysis of dioxouranium(VI) and protonation of 1,2,3,4-butanetetracarboxylate

In previous papers [31–34] we already reported the hydrolytic constants of dioxouranium(VI) in different ionic media and at different ionic strengths. Thermodynamic equilibrium constants are reported in Table 1.

As regards 1,2,3,4-butanetetracarboxylate, here we carried out investigations on the protonation constants in NaCl aqueous solutions at $0 \leq I$ (mol L^{-1}) ≤ 1.0. The experimental protonation constants of *btc* are reported in Table 2 in both molar and molal concentration scales. In the same table, the thermodynamic protonation constants [46] and the C parameter for the dependence of protonation constants on ionic strength, calculated by using Eq. (1), are reported.

3.2. Speciation model for the dioxouranium(VI)–carboxylate systems

In defining the best speciation model for the $UO_2{}^{2+}$–polycarboxylate systems, we followed some criteria [36–39] that can be listed as follows: (1) the simplicity of the model; (2) the agreement with similar uranyl–carboxylate systems; (3) the significant formation percentages of each species in all the experimental conditions; (4) the differences in variance between the accepted model and other checked ones.

Following these criteria, the best speciation models proposed [35–39] are resumed in Table 3, with the complex formation constant values at $I = 0$ mol L^{-1}. The speciation mod-

Table 2
Protonation constants of 1,2,3,4-butanetetracarboxylate in NaCl aqueous solution, at different ionic strengths and $t = 25\,°\mathrm{C}$

I (mol L^{-1})	log β_1[a]	log β_2[a]	log β_3[a]	log β_4[a]
0	7.18[b]	13.01[b]	17.54[b]	20.92[b]
0.12	6.26 ± 0.01[c]	11.41 ± 0.01[c]	15.49 ± 0.01[c]	18.64 ± 0.01[c]
0.48	5.88 ± 0.01	10.75 ± 0.01	14.67 ± 0.01	17.75 ± 0.01
0.74	5.78 ± 0.01	10.58 ± 0.01	14.48 ± 0.01	17.54 ± 0.01
0.97	5.73 ± 0.01	10.50 ± 0.01	14.39 ± 0.01	17.46 ± 0.02
C[d]	0.17 ± 0.01	0.34 ± 0.01	0.52 ± 0.01	0.61 ± 0.02
I (mol kg^{-1})	log β_1	log β_2	log β_3	log β_4
0	7.18	13.01	17.54	20.92
0.13	6.26	11.40	15.48	18.63
0.49	5.87	10.74	14.65	17.73
0.75	5.77	10.57	14.45	17.51
0.99	5.72	10.48	14.36	17.42

[a] β_i refers to reaction: $(btc)^{4-} + i\,\mathrm{H}^+ = (btc)\mathrm{H}_i^{(i-4)}$.
[b] Protonation constants at infinite dilution obtained from Ref. [46].
[c] ±S.D.
[d] Empirical parameters of Eq. (1).

els include for acetate [35]: $\mathrm{M}(ac)^+$, $\mathrm{M}(ac)_2^0$, $\mathrm{M}(ac)_3^-$ and $\mathrm{M}(ac)_3\mathrm{OH}^{2-}$; for oxalate [37]: $\mathrm{M}(ox)^0$, $\mathrm{M}(ox)_2^{2-}$, $\mathrm{M}(ox)_3^{4-}$, $\mathrm{M}(ox)\mathrm{OH}^-$, $\mathrm{M}(ox)(\mathrm{OH})_2^{2-}$, $\mathrm{M}(ox)_2\mathrm{OH}^{3-}$, $\mathrm{M}(ox)_3\mathrm{OH}^{5-}$, $\mathrm{M}(ox)_3\mathrm{H}^{3-}$ and $\mathrm{M}_2(ox)_5^{6-}$; for malonate [36]: $\mathrm{M}(mal)^0$, $\mathrm{M}(mal)_2^{2-}$ and $\mathrm{M}_2(mal)_2(\mathrm{OH})_2^{2-}$; for succinate [36]: $\mathrm{M}(suc)^0$, $\mathrm{M}(suc)_2^{2-}$, $\mathrm{M}(suc)_2\mathrm{H}^-$ and $\mathrm{M}_2(suc)_2(\mathrm{OH})_2^{2-}$; for azelate [36]: $\mathrm{M}(aze)^0$, $\mathrm{M}(aze)_2^{2-}$, $\mathrm{M}(aze)\mathrm{H}^+$, $\mathrm{M}_2(aze)_2^0$ and $\mathrm{M}_2(aze)(\mathrm{OH})_2^0$; for 1,2,3-propanetricarboxylate [38]: $\mathrm{M}(tca)^-$, $\mathrm{M}(tca)\mathrm{H}^0$, $\mathrm{M}(tca)_2^{4-}$ and $\mathrm{M}(tca)_2\mathrm{H}^{3-}$; for mellitate [39]: $\mathrm{M}(mlt)^{4-}$, $\mathrm{M}(mlt)\mathrm{H}^{3-}$, $\mathrm{M}(mlt)\mathrm{H}_2^{2-}$, $\mathrm{M}(mlt)\mathrm{H}_3^-$, $\mathrm{M}_2(mlt)^{2-}$, $\mathrm{M}(mlt)\mathrm{OH}^{5-}$ and $\mathrm{M}(mlt)(\mathrm{OH})_2^{6-}$ species. In the same table, the speciation model proposed for 1,2,3,4-butanetetracarboxylate is reported: this is defined by the species: $\mathrm{M}(btc)^{2-}$, $\mathrm{M}(btc)\mathrm{H}^-$, $\mathrm{M}(btc)\mathrm{H}_2^0$ and $\mathrm{M}(btc)\mathrm{OH}^{3-}$. The different speciation models obtained for the $\mathrm{UO_2}^{2+}$–polycarboxylic systems can be explained taking into account some factors: (a) the charge of the ligand; (b) the length of the alkyl chain and the possibility to form chelate rings and uranyl polynuclear species also at low metal/ligand ratios; (c) the interaction of negatively charged complex species with the ions of the supporting electrolyte (medium stabilisation); (d) the pH value where precipitation occurs. Extensive discussions on this topic were carried out in our previous paper [35–39].

The formation constants of $\mathrm{UO_2}^{2+}$–btc species, in the ionic strength range $0 \le I\ (\mathrm{NaCl}) \le 1\ \mathrm{mol\,L^{-1}}$, in both molar and molal concentration scale, are reported in Table 4, together with their corresponding values at infinite dilution calculated by means of Eq. (1). Complex formation constants were calculated without taking into account the formation of Na^+–btc [46]

Table 3
Formation constants in molar concentration scale of $\mathrm{UO_2}^{2+}$–polycarboxylate complexes at infinite dilution and $t = 25\,°\mathrm{C}$

L	log β				Other species[a,b]
	ML[a]	ML$_2$[a]	MLH[a]	MLOH[a]	
ac[c]	2.86	4.62			ML$_3$ (7.22), ML$_3$OH (2.14)
ox[d]	7.05	11.45		1.03	$\mathrm{ML_3}^{4-}$ (11.92), $\mathrm{ML(OH)_2}^{2-}$ (−6.9), $\mathrm{ML_2OH}^{3-}$ (3.41), $\mathrm{ML_3OH}^{5-}$ (4.1), $\mathrm{ML_3H}^{3-}$ (17.08), $\mathrm{M_2L_5}^{6-}$ (24.98)
mal[e]	6.569	10.551			M$_2$L$_2$(OH)$_2$ (4.36)
suc[e]	5.091	7.61			ML$_2$H (11.98), M$_2$L$_2$(OH)$_2$ (2.38)
aze[e]	4.27	7.78	8.641		M$_2$L$_2$ (12.00), M$_2$L(OH)$_2$ (−1.43)
tca[f]	6.222	7.75	11.251		ML$_2$H (14.33)
btc[g]	7.937		13.066	2.062	MLH$_2$ (17.401)
mlt[h]	10.164		16.123	2.328	MLH$_2$ (20.784), MLH$_3$ (24.059), M$_2$L (17.952), ML(OH)$_2$ (−6.816)

[a] Charges omitted for simplicity.
[b] In parentheses log β_{pqr} at infinite dilution.
[c] Ref. [35].
[d] Ref. [37].
[e] Ref. [36].
[f] Ref. [38].
[g] This work.
[h] Ref. [39].

Table 4
Formation constants of UO_2^{2+}–1,2,3,4-butanetetracarboxylate complexes in NaCl aqueous solution, at different ionic strengths and $t = 25\,°C$

I (mol L^{-1})	$\log\beta_{110}$[a]	$\log\beta_{111}$[a]	$\log\beta_{112}$[a]	$\log\beta_{11-1}$[a]
Experimental values				
0	7.94 ± 0.03[b]	13.07 ± 0.03[b]	17.40 ± 0.01[b]	2.06 ± 0.04[b]
0.12	6.20 ± 0.02	10.85 ± 0.02	14.91 ± 0.01	0.97 ± 0.04
0.48	5.39 ± 0.02	9.89 ± 0.02	13.70 ± 0.02	0.34 ± 0.02
0.73	5.32 ± 0.03	9.69 ± 0.01	13.48 ± 0.03	0.16 ± 0.02
0.97	5.28 ± 0.04	9.60 ± 0.01	13.33 ± 0.04	−0.02 ± 0.03
Calculated values[c]				
0	7.94 ± 0.03	13.08 ± 0.03	17.40 ± 0.01	2.11 ± 0.04
0.10	6.25 ± 0.03	10.95 ± 0.02	15.03 ± 0.01	1.01 ± 0.04
0.25	5.76 ± 0.02	10.32 ± 0.02	14.29 ± 0.01	0.63 ± 0.03
0.50	5.44 ± 0.02	9.88 ± 0.01	13.75 ± 0.02	0.32 ± 0.02
0.75	5.31 ± 0.03	9.68 ± 0.01	13.47 ± 0.03	0.13 ± 0.02
1.00	5.27 ± 0.04	9.59 ± 0.01	13.30 ± 0.04	−0.02 ± 0.03

I (mol kg^{-1})	$\log\beta_{110}$	$\log\beta_{111}$	$\log\beta_{112}$	$\log\beta_{11-1}$
0	7.94	13.06	17.40	2.06
0.13	6.20	10.84	14.90	0.97
0.49	5.38	9.88	13.68	0.34
0.75	5.31	9.68	13.46	0.16
0.99	5.27	9.58	13.30	−0.02

[a] β_{pqr} refers to reaction: $p\mathrm{UO_2}^{2+} + q(btc)^{4-} + r\mathrm{H}^+ = (\mathrm{UO_2})_p(btc)_q\mathrm{H}_r^{(2p-4q+r)}$.
[b] ±S.D.
[c] Formation constants calculated from Eq. (1).

and UO_2^{2+}–Cl^- weak species [31], as already done for the other uranyl–polycarboxylate systems [35–39].

In Figs. 1 and 2 two distribution diagrams, for the UO_2^{2+}–1,2,3,4-butanetetracarboxylate system at $I = 0.50$ mol L^{-1}, are reported at a dioxouranium(VI) concentration of 0.5 mmol L^{-1} and two different *btc* concentrations, namely, 0.5 and 1.5 mmol L^{-1}. As can be seen, when high *btc* concentrations are used, low formation percentages of the hydrolytic species of uranyl are observed (with exception of the $M_3(OH)_7^-$), owing to the sequestering ability of *btc* which inhibits the hydrolysis of uranyl. Moreover at high-ligand concentrations the ternary $MLOH^{3-}$ species reaches high formation percentages between $5 \leq pH \leq 7$, and maximum value (about 90%) at $pH \approx 6.5$. Analysing the speciation diagrams, two main features can be observed: (i) in the acidic region, the yields of the different species follows the trend: $M(btc)^{2-} > M(btc)H^+ > M(btc)H_2^0$ (which is a very reasonable trend); (ii) in the pH range 6–7 the mixed hydrolytic species of UO_2^{2+} [$M(btc)OH^{3-}$] is the predominant one, whilst at $pH > 7$, the speciation is regulated by the simple hydrolytic species $M_3(OH)_7^-$ [38,39]. These features are in agreement with the ones observed for other uranyl–polycarboxylate systems. Note that the distribution diagrams were drawn up to $pH \approx 8.1$ (outside the experimental pH range) that is the mean pH value

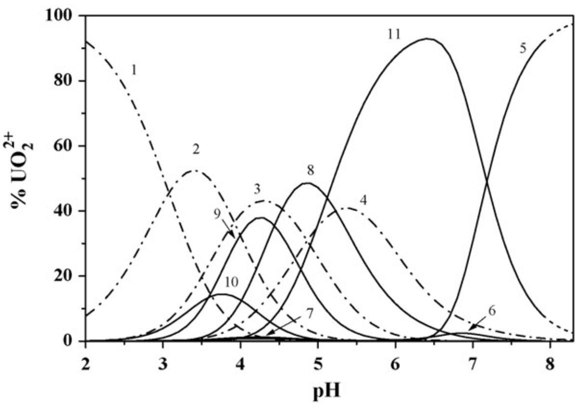

Fig. 1. Speciation diagram of UO_2^{2+}–1,2,3,4-butanetetracarboxylate system in $NaCl_{aq}$ at $I = 0.50$ mol L^{-1} and $t = 25\,°C$. *Concentration*: $C_{UO_2^{2+}} = 0.5$, $C_{btc} = 1.5$ mmol L^{-1}. *Species*: (1) LH_4; (2) LH_3; (3) LH_2; (4) LH; (5) $M_3(OH)_7$; (6) $M_3(OH)_5$; (7) $M_2(OH)_2$; (8) ML; (9) MLH; (10) MLH_2; (11) MLOH (charge omitted for simplicity); short dash line: outside the experimental pH range; dash dot line: ligand speciation.

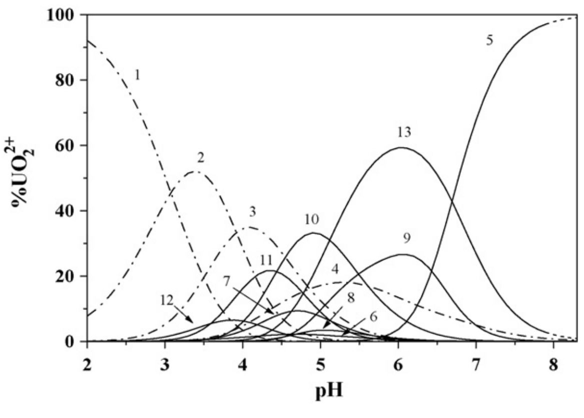

Fig. 2. Speciation diagram of UO_2^{2+}–1,2,3,4-butanetetracarboxylate system in $NaCl_{aq}$ at $I = 0.50$ mol L^{-1} and $t = 25\,°C$. *Concentration*: $C_{UO_2^{2+}} = C_{btc} = 0.5$ mmol L^{-1}. *Species*: (1) LH_4; (2) LH_3; (3) LH_2; (4) LH; (5) $M_3(OH)_7$; (6) MOH; (7) $M_2(OH)_2$; (8) $M_3(OH)_4$; (9) $M_3(OH)_5$; (10) ML; (11) MLH; (12) MLH_2; (13) MLOH (charge omitted for simplicity); short dash line: outside the experimental pH range; dash dot line: ligand speciation.

of seawater, in order to have information about the speciation of the system here investigated in this natural water.

3.3. Sequestering ability of polycarboxylates towards dioxouranium(VI)

In previous papers [38,39], we proposed a Boltzman type equation able to define the sequestering ability of a ligand towards a metal by means of a function of the sum of formation percentages of all metal–ligand complexes, Σ(%), vs. pL, where p$L \equiv -\log [L]_{\text{tot}}$ ($[L]_{\text{tot}}$ is the total ligand concentration). This function is assimilable to a sigmoid curve (or a dose response curve) with asymptotes of 100 for p$L \to -\infty$ and 0 for p$L \to +\infty$:

$$\Sigma(\%) = 100\left[\frac{1}{1+\exp[(\mathrm{p}L - \mathrm{p}L_{50})]/S} - 1\right] \qquad (2)$$

where pL_{50} and S are empirical parameters. In particular, pL_{50} represents the ligand concentration necessary to sequester 50% of metal ion; therefore this parameter can be used as a measure of the sequestering abilities of different ligands. The parameter S is a measure of the slope in the flex of the function Σ(%) vs. pL, and it not influences the model. In order to evidence the different sequestering ability of carboxylic ligands towards UO_2^{2+}, we calculated the pL_{50} values for each uranyl–polycarboxylate system by means of the function Σ(%) vs. pL in the experimental conditions: $C_{UO_2^{2+}} = 10^{-9}\,\text{mol L}^{-1}$ (trace) and pL ranging from 2 to 9. This function is shown in Fig. 3 for *ac*, *ox*, *suc*, *tca*, *btc* and *mlt*, at pH 5.0; in these experimental conditions we obtained for S, taking into account all the uranyl–polycarboxylate systems, a mean value of 0.42 ± 0.01. In order to complete the picture on the sequestering ability of polycarboxylates towards UO_2^{2+}, the pL_{50} values were also calculated at pH 7.0 and 8.1 (mean pH value of seawater). The results are reported in Table 5. The influence of pH on the sequestering ability of ligands towards UO_2^{2+} is shown in Fig. 4 where as example, the sum of percentage of metal–ligand species vs. pL is drawn for UO_2^{2+}–*btc* system at three different pH values (namely: pH 5.0, 7.0 and 8.1) and $C_{UO_2^{2+}} = 10^{-9}\,\text{mol L}^{-1}$ (trace). As can be seen, at pH 5.0 (pL_{50} = 4.52) a greater *btc* concentration is necessary to sequester 50% of UO_2^{2+}, owing to the proton interference, whilst the lower pL_{50} value at pH 8.1 (pL_{50} = 5.40), with respect to the one at pH 7.0 (pL_{50} = 5.99), is due to the fact that at this pH, an high percentage of uranyl is present as hydrolytic species $(UO_2)_3(OH)_7^-$ (see Figs. 1 and 2). The trends observed also depend on the different uranyl–polycarboxylate speciation models. For example, we observed for *ox* and *mlt* an increasing sequestering ability (fairly linear) with pH owing to the formation of some ternary hydrolytic species that reach high formation percentages at pH > 7. For *suc*, *aze* and *tca* at pH 8.1, the UO_2^{2+} percentage sequestered by ligands is <10%, probably because in this experimental condition uranyl is mainly present as $(UO_2)_3(OH)_7^-$ hydrolytic species. The pL_{50} values calculated at pH 8.1 must be considered rough values, because the metal–ligand speciation was studied up to pH lower than 8.1 (pH ≈ 7–7.50), to exception of the oxalate that has been studied up to pH 8.5, owing to the formation of solid phase. Nevertheless, the pL_{50} values obtained can be indicative of the sequestering ability of the different ligands in a natural system such as seawater.

Table 5
pL_{50} values (Eq. (2)) for UO_2^{2+}–carboxylate systems at different pH values and t = 25 °C

L	pL_{50}		
	pH 5.0	pH 7.0	pH 8.1
ac	2.41	2.50	2.28
ox	5.92	6.44	6.74
mal	4.90	4.15	2.98
suc	3.29	2.73	–[a]
aze	3.15	2.71	–[a]
tca	3.86	3.34	–[a]
btc	4.52	5.99	5.40
mlt	5.75	6.35	6.51

[a] pL_{50} have not been calculated owing to the low Σ(%) value.

If we consider the carboxylates belonging to the series $(CH)_n$–$(COOH)_n$ (*ac*, *suc*, *tca*, *btc* and *mlt*) pL_{50} value (Table 5) increases increasing the number of carboxylate groups. The

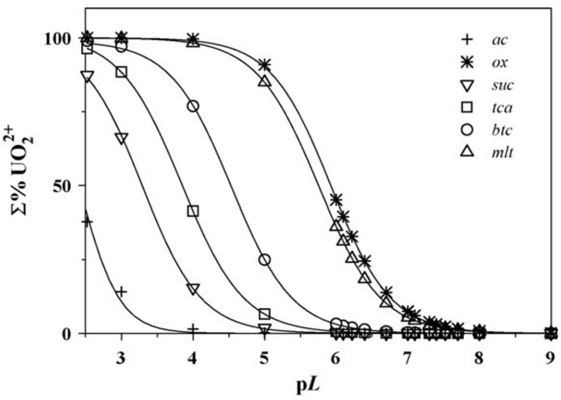

Fig. 3. Sum of percentages of metal–ligand species (for the UO_2^{2+}–*ac*, *ox*, *suc*, *tca*, *btc* and *mlt* systems) vs. pL at pH 5.0. *Conditions*: I = 0.5 mol L^{-1} (NaCl$_{aq}$), $C_{UO_2^{2+}} = 1 \times 10^{-9}$ mol L^{-1} (trace), t = 25 °C. *Symbols*: (+) *ac*; (✱) *ox*; (▽) *suc*; (□) *tca*; (○) *btc*; (△) *mlt*.

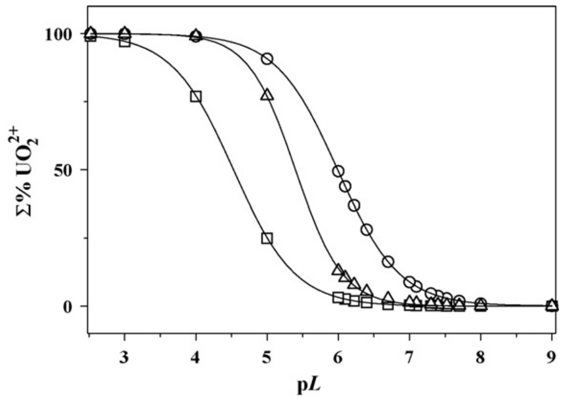

Fig. 4. Sum of percentages of metal–ligand species (for the UO_2^{2+}–1,2,3,4-butanetetracarboxylate system) vs. pL in NaCl$_{aq}$ at I = 0.5 mol L^{-1} and t = 25 °C. *Concentration*: $C_{UO_2^{2+}} = 1 \times 10^{-9}$ mol L^{-1} (trace). *Symbol*: (□) pH 5.0; (○) pH 7.0; (△) pH 8.1.

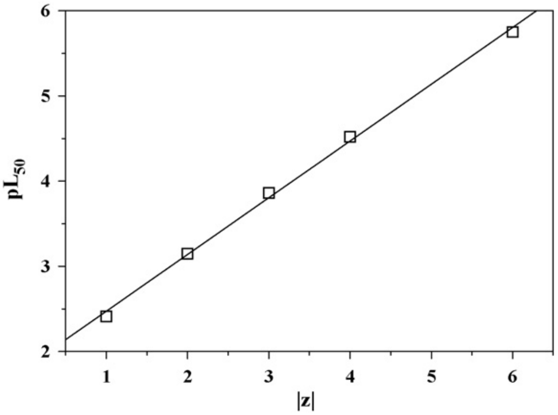

Fig. 5. Correlation between pL_{50} and the charge of anions (z = charge), at pH 5.0. $z = 1$: *ac*; $z = 2$: *suc*; $z = 3$: *tca*; $z = 4$: *btc*; $z = 6$: *mlt*.

dependence of sequestering ability on the charge of anion is shown in Fig. 5, where the relation pL_{50} vs. $|z|$ (z = charge of anion) from acetate to 1,2,3,4,5,6-benzenehexacarboxylate, is plotted at pH 5.0. From Fig. 5, we observed a linear dependence between these two parameters with a linear correlation coefficient $R = 0.9991$ and a standard deviation of 0.064. An analogous correlation is observed for the formation constants (infinite dilution) of the UO_2L species (L = *ac* [35]; *suc* [36]; *tca* [38]; *btc*; *mlt* [39]) and $|z|$; in this case we observed a fairly linear fit with a standard deviation of 0.42. This higher values of standard deviation is due to the fact that when we consider this last correlation, the sequestering ability of the ligands is expressed taking into account only a single species (UO_2L in this case), whilst if we consider the pL_{50} value the sequestering ability is quantitatively expressed taking into

Table A.1
SIT (Eq. (A.2)) and Pitzer (Eqs. (A.5)–(A.13)) parameters for the hydrolysis of dioxouranium(VI), at $t = 25\,°C$

Interaction	ε[a]	$\beta^{(0)}$[b]	$\beta^{(1)}$[b]
UO_2^{2+}, Cl^-	0.25		
$UO_2(OH)^+$, Cl^-	0.46	0.5689	0.5785
$(UO_2)_2(OH)_2^{2+}$, Cl^-	0.30	0.4291	2.1173
$(UO_2)_3(OH)_4^{2+}$, Cl^-	−0.04	0.06649	2.2839
$(UO_2)_3(OH)_5^+$, Cl^-	0.06	0.07369	1.2522
$(UO_2)_3(OH)_7^-$, Na^+	−0.48	−0.5798	1.0034

[a] Ref. [35].
[b] Ref. [32].

Table A.2
SIT (Eq. (A.2)) and Pitzer (Eqs. (A.5)–(A.13)) parameters for the protonation of polycarboxylic ligands in NaCl at $t = 25\,°C$

Interaction	ε	σ_{fit}[a]	$\beta^{(0)}$	$\beta^{(1)}$	σ_{fit}[b]
$(ac)^-$, Na^+	0.156[c]		0.0924 ± 0.0004[d]	0.351 ± 0.001[d]	0.0007
$(mal)^{2-}$, Na^+	0.219 ± 0.007[d]	0.035	0.191 ± 0.004	1.618 ± 0.019	0.026
$(mal)H^-$, Na^+	0.198 ± 0.006	0.038	0.113 ± 0.003	0.727 ± 0.016	0.020
$(suc)^{2-}$, Na^+	0.273 ± 0.001	0.014	0.261 ± 0.001	1.622 ± 0.008	0.015
$(suc)H^-$, Na^+	0.190 ± 0.001	0.010	0.147 ± 0.001	0.451 ± 0.007	0.006
$(aze)^{2-}$, Na^+	0.295 ± 0.006	0.054	0.425[e]	1.643[e]	
$(aze)H^-$, Na^+	0.177 ± 0.004	0.033	0.23[e]	0.185[e]	
$(tca)^{3-}$, Na^+	0.275[f]		0.36[f]	3.40[f]	
$(tca)H^{2-}$, Na^+	0.216[f]		0.23[f]	1.53[f]	
$(tca)H_2^-$, Na^+	0.119[f]		0.11[f]	0.40[f]	
$(btc)^{4-}$, Na^+	0.298 ± 0.017	0.079	0.533 ± 0.040	5.776 ± 0.115	0.002
$(btc)H^{3-}$, Na^+	0.238 ± 0.012	0.040	0.271 ± 0.037	3.437 ± 0.105	0.011
$(btc)H_2^{2-}$, Na^+	0.188 ± 0.010	0.019	0.257 ± 0.011	1.369 ± 0.034	0.001
$(btc)H_3^-$, Na^+	0.127 ± 0.006	0.033	0.134 ± 0.008	0.348 ± 0.023	0.001
$(mlt)^{6-}$, Na^+	0.336[g]		0.726 ± 0.013	13.98 ± 0.04	0.007
$(mlt)H^{5-}$, Na^+	0.341[g]		0.544 ± 0.015	9.881 ± 0.042	0.010
$(mlt)H_2^{4-}$, Na^+	0.344[g]		0.354 ± 0.016	6.651 ± 0.044	0.011
$(mlt)H_3^{3-}$, Na^+	0.348[g]		0.243 ± 0.016	4.086 ± 0.044	0.014
$(mlt)H_4^{2-}$, Na^+	0.273[g]		0.147 ± 0.017	2.029 ± 0.047	0.021
$(mlt)H_5^-$, Na^+	0.234[g]		0.084 ± 0.018	0.907 ± 0.050	0.025

[a] S.D. on the fit of Eq. (A.2).
[b] S.D. on the fit of Eqs. (A.5)–(A.13).
[c] Ref. [14].
[d] ±S.D.
[e] Ref. [52].
[f] Ref. [38].
[g] Ref. [39].

Table A.3
SIT (Eq. (A.2)) parameters of UO_2^{2+}–polycarboxylate species in NaCl at $t = 25\,°C$

Interaction	ε	k_m	σ_{fit}[a]
ac[b]			
ML^+, Cl^-	0.01		
ML_2^0, NaCl		0.41	
ML_3^-, Na^+	0.07		
ML_3OH^{2-}, Na^+	0.45		
mal[c]			
ML^0, NaCl		0.186	
ML_2^{2-}, Na^+	0.436		
$M_2L_2(OH)_2^{2-}$, Na^+	0.939		
suc[c]			
ML^0, NaCl		0.033	
ML_2^{2-}, Na^+	0.322		
ML_2H^-, Na^+	−0.386		
$M_2L_2(OH)_2^{2-}$, Na^+	−0.628		
aze[c]			
ML^0, NaCl		−0.064	
ML_2^{2-}, Na^+	0.002		
MLH^+, Cl^-	−0.052		
$M_2L_2^0$, NaCl		−0.223	
$M_2L(OH)_2^0$		−0.052	
ox[d]			
ML^0, NaCl		0.163	
ML_2^{2-}, Na^+	0.335		
ML_3^{4-}, Na^+	0.317		
$MLOH^-$, Na^+	0.648		
$ML(OH)_2^{2-}$, Na^+	1.015		
ML_2OH^{3-}, Na^+	0.720		
ML_3OH^{5-}, Na^+	−1.037		
ML_3H^{3-}, Na^+	0.091		
$M_2L_5^{6-}$, Na^+	−1.734		
tca[e]			
ML^-, Na^+	−0.305		
ML_2^{4-}, Na^+	−0.204		
MLH^0, NaCl		0.340	
ML_2H^{3-}, Na^+	1.274		
btc			
ML^{2-}, Na^+	−0.043 ± 0.031[f]		0.053
MLH^-, Na^+	−0.051 ± 0.011		0.034
MLH_2^0, NaCl		0.173 ± 0.038[f]	0.049
$MLOH^{3-}$, Na^+	0.440 ± 0.034[f]		0.057

[a] S.D. on the fit of Eq. (A.2).
[b] Ref. [35].
[c] Ref. [36].
[d] Ref. [37] (calculated at $I = 1.02\,mol\,kg^{-1}$).
[e] Ref. [38].
[f] ±S.D.

Table A.4
SIT parameters of UO_2^{2+}–*btc* and *mlt* species in NaCl at $t = 25\,°C$, calculated from Eq. (A.4)

Interaction	ε_0	ε_∞	σ_{fit}[a]
btc			
ML^{2-}, Na^+	−0.140±0.026[b]	0.036±0.021[b]	0.045
MLH^-, Na^+	0.052±0.012	−0.141±0.006	0.026
MLH_2^0, NaCl	−0.02±0.022	0.341±0.020	0.040
$MLOH^{3-}$, Na^+	0.898±0.022	0.043±0.017	0.032
mlt[c]			
ML^{4-}, Na^+	0.781	−1.978	
MLH^{3-}, Na^+	0.888	−1.491	
MLH_2^{2-}, Na^+	1.823	−0.598	
MLH_3^-, Na^+	3.131	−1.702	
M_2L^{2-}, Na^+	2.139	−2.013	
$MLOH^{5-}$, Na^+	0.505	−1.156	
$ML(OH)_2^{6-}$, Na^+	0.375	−0.910	

[a] S.D. on the fit of Eq. (A.4).
[b] ±S.D.
[c] Ref. [39].

account all the metal–ligand species. The knowledge of pL_{50} is essential, because it give a measure of the effective sequestering ability of ligands in different experimental conditions, such as ionic strength, pH, metal–ligand concentration, temperature.

Nevertheless, sequestering abilities of carboxylate ligands towards UO_2^{2+} do not depend only on the ligand charge. Values of Table 5 evidence that a low molecular weight carboxylic ligand such as oxalate (charge −2) has a sequestering ability towards UO_2^{2+} of the same order of magnitude of that presented from mellitate (charge −6). In this case probably other factors play an important role such as the number of chelate rings or the charge density of the polyanions, as pointed out in Section 1, and in a previous work [39].

Acknowledgement

We thank University of Messina (PRA) for financial support.

Appendix A. Dependence on ionic strength

The stoichiometric formation constants of UO_2^{2+}–polycarboxylates species, can be expressed by (charges omitted for simplicity):

$$\log \beta_{pqr} = \log {}^{T}\beta_{pqr} + p \log \gamma_{UO_2} + q \log \gamma_L + r \log \gamma_H - \log \gamma_{(UO_2)_pL_qH_r} \tag{A.1}$$

where γ_i is the activity coefficient of the i-th component and ${}^{T}\beta_{pqr}$ is the formation constant at infinite dilution. The determination of thermodynamic formation constants requires a suitable equation for the dependence of activity coefficients on ionic strength. In this work, the dependence of molal protonation constants and UO_2^{2+}–polycarboxylates formation constants on ionic strength was investigated by means of SIT [41,42] and Pitzer approaches [43,44]; calculations were carried out by using LIANA computer program [45].

According to the SIT equation [41,42], the activity coefficients of a cation or an anion can be expressed as

$$\log \gamma = -z^2 \frac{AI^{1/2}}{1 + 1.5I^{1/2}} + \sum \varepsilon m_i \tag{A.2}$$

and for a neutral species:

$$\log \gamma = k_m I \tag{A.3}$$

where ε is the interaction coefficient and the sum is extended to the interactions between the ion under examination and all

Table A.5
Pitzer (Eqs. (A.5)–(A.13)) parameters of UO_2^{2+}–polycarboxylate species in NaCl at $t = 25\,^\circ C$

Interaction	$\beta^{(0)}$	$\beta^{(1)}$	λ	σ_{fit}[a]
ac				
ML^+, Cl^-	0.45 ± 0.01[b]	-0.65 ± 0.03[b]	–	0.024
ML_2^0, NaCl	–	–	-0.43 ± 0.02[b]	0.056
ML_3^-, Na^+	0.37 ± 0.01	-0.37 ± 0.04	–	0.021
ML_3OH^{2-}, Na^+	0.24 ± 0.01	2.18 ± 0.03	–	0.013
mal				
ML^0, NaCl	–	–	0.329 ± 0.007	0.020
ML_2^{2-}, Na^+	0.698 ± 0.001	2.262 ± 0.003	–	0.001
$M_2L_2(OH)_2^{2-}$, Na^+	1.324 ± 0.001	2.713 ± 0.001	–	0.001
suc				
ML^0, NaCl	–	–	0.140 ± 0.004	0.022
ML_2^{2-}, Na^+	0.497 ± 0.001	2.288 ± 0.004	–	0.001
ML_2H^-, Na^+	-0.381 ± 0.002	1.198 ± 0.005	–	0.003
$M_2L_2(OH)_2^{2-}$, Na^+	-0.698 ± 0.002	2.640 ± 0.004	–	0.002
aze				
ML^0, NaCl	–	–	0.238 ± 0.001	0.002
ML_2^{2-}, Na^+	0.270 ± 0.001	2.390 ± 0.002	–	0.001
MLH^+, Cl^-	0.0777 ± 0.0004	0.998 ± 0.002	–	0.001
$M_2L_2^0$, NaCl	–	–	0.335 ± 0.002	0.003
$M_2L(OH)_2^0$, NaCl	–	–	0.293 ± 0.004	0.015
tca[c]				
ML^-, Na^+	-0.63	1.25	–	
ML_2^{4-}, Na^+	-0.17	6.3	–	
MLH^0, NaCl	–	–	0.55	
ML_2H^{3-}, Na^+	0.38	7.1	–	
btc				
ML^{2-}, Na^+	-0.35 ± 0.02	2.38 ± 0.05	–	0.070
MLH^-, Na^+	-0.10 ± 0.01	0.79 ± 0.03	–	0.038
MLH_2^0, NaCl	–	–	0.459 ± 0.002	0.067
$MLOH^{3-}$, Na^+	0.87 ± 0.01	2.39 ± 0.04	–	0.042
mlt				
ML^{4-}, Na^+	0.21 ± 0.01	3.47 ± 0.04	–	0.027
MLH^{3-}, Na^+	0.22 ± 0.03	2.00 ± 0.08	–	0.057
MLH_2^{2-}, Na^+	1.47 ± 0.03	-0.28 ± 0.08	–	0.051
MLH_3^-, Na^+	2.67 ± 0.04	-4.75 ± 0.05	–	0.048
M_2L^{2-}, Na^+	1.06 ± 0.02	-1.89 ± 0.06	–	0.053
$MLOH^{5-}$, Na^+	0.27 ± 0.01	8.28 ± 0.04	–	0.020
$ML(OH)_2^{6-}$, Na^+	0.61 ± 0.03	12.21 ± 0.08	–	0.030

[a] S.D. on the fit of Eqs. (A.5)–(A.13).
[b] ±S.D.
[c] Ref. [38].

the ions i of opposite charge at the molality m_i, while k_m is the Setschenow coefficient for neutral species. Recently [47–52], we used a modified version of the SIT equation, in which interaction coefficients ε are not constant but depend on ionic strength according to the simple relationship:

$$\varepsilon = \varepsilon_\infty + \frac{\varepsilon_0 - \varepsilon_\infty}{I + 1} \tag{A.4}$$

where ε_0 and ε_∞ are the values of ε at $I \to 0$ and $I \to \infty$, respectively. The goodness of this model was widely tested in previous papers [47–52].

According to specific interaction theory, the Pitzer equation [43,44] estimates activity coefficients in terms of interactions between ions. In the presence of a 1:1 salt MX, the activity coefficients of Eq. (A.1) are given for a cationic species by

$$\begin{aligned}\ln \gamma_c = {} & z_c^2 f^\gamma + 2I(B_{cX} + IC_{cX}) \\ & + I^2(z_c^2 B'_{cX} + z_c C_{cX}) + I(2\theta_{cM} + I\psi_{cMX})\end{aligned} \tag{A.5}$$

for an anionic species by

$$\begin{aligned}\ln \gamma_a = {} & z_a^2 f^\gamma + 2I(B_{Ma} + IC_{Ma}) + I^2(z_a^2 B'_{MX} \\ & + z_a C_{MX}) + I(2\theta_{aX} + I\psi_{aMX})\end{aligned} \tag{A.6}$$

and for neutral species by

$$\ln \gamma = 2\lambda I \tag{A.7}$$

where I is the ionic strength in the molal concentration scale, and

$$B_{\mathrm{ca}} = \beta_{\mathrm{ca}}^{(0)} + \frac{\beta_{\mathrm{ca}}^{(1)}}{2I} f_1 \tag{A.8}$$

$$B'_{\mathrm{ca}} = \frac{\beta_{\mathrm{ca}}^{(1)}}{2I^2} f_2 \tag{A.9}$$

$$C_{\mathrm{ca}} = \frac{C_{\mathrm{ca}}^{(\phi)}}{2|z_c z_a|^{1/2}} \tag{A.10}$$

$$f^{\gamma} = -A_{\phi}[I^{\,1/2}(1+1.2I^{1/2})^{-1} + 1.667\,\ln(1+1.2I^{1/2})] \tag{A.11}$$

$$f_1 = 1-(1+2I^{1/2})\exp(-2I^{1/2}) \tag{A.12}$$

$$f_2 = -1+(1+2I^{1/2}+2I)\exp(-2I^{1/2}) \tag{A.13}$$

with c and a generic cation and anion, respectively, $\beta^{(0)}$, $\beta^{(1)}$ and $C^{(\phi)}$ interaction parameters between two ions of opposite sign, θ interaction parameter between two ions of the same sign (+ +, − − interactions), ψ triplet interaction parameter (+ − +, − + −) and λ interaction parameter of neutral species; A_{ϕ} is the Debye–Hückel coefficient ($A_{\phi} = 0.3912$ at $t = 25\,°\mathrm{C}$). At $I < 3\ \mathrm{mol\,kg^{-1}}$, θ and ψ parameters can generally be neglected.

Calculations were performed by using molal formation constants. The conversion from molar to molal concentration scale was obtained following procedures already proposed [50]. In Tables A.1 and A.2 SIT and Pitzer interaction parameters for hydrolysis of $\mathrm{UO_2}^{2+}$ and for polycarboxylate protonations are reported. As interaction parameter of the neutral species the estimated values $k_{\mathrm{m}} = 0.150$ and $\lambda = 0.173$ [52] were used for all polycarboxylates, but for acetate ($k_{\mathrm{m}} = 0.054$ and $\lambda = 0.062$ [35]). In the SIT equations, we used as interaction coefficients of HCl values already published ($\varepsilon = 0.11$ [47]). In the Pitzer equations, we took into account the interactions between ion of opposite sign ($\beta^{(0)}$ and $\beta^{(1)}$). Since the measurements were made up to $I = 1.0\ \mathrm{mol\,L^{-1}}$, other higher terms were neglected, as well as the quadratic term C^{ϕ}, except for azelate ($C^{\phi} = -0.0253$ and 0.00093 for $(aze)^{2-}$, $\mathrm{Na^+}$ and $(aze)\mathrm{H^-}$, $\mathrm{Na^+}$ interactions, respectively [52]).

SIT and Pitzer parameters for $\mathrm{UO_2}^{2+}$–polycarboxylate systems are reported in Tables A.3–A.5. By using one parameters SIT equation (Eq. (A.2)), good fit was obtained for most of systems, but the use of Eq. (A.4) is necessary when the charge of interaction ions is high such as for *btc*(4−) and *mlt*(6−) (see Table A.4). In this case we used as interaction coefficients of HCl $\varepsilon_{\infty} = 0.136$ and $\varepsilon_0 = 0.0848$ [47].

References

[1] D.L. Clark, D.E. Hobart, M.P. Neu, Chem. Rev. 95 (1995) 25.
[2] L. Couston, D. Pouyat, C. Moulin, P. Decambox, Appl. Spectrosc. 49 (1995) 349.
[3] J.E. Bollinger, D.M. Roundhill, Inorg. Chem. 33 (1994) 6421.
[4] S.A. Sayed, A.T. Kandil, G.R. Choppin, J. Radioanal. Nucl. Chem. 188 (1994) 377.
[5] K.R. Czerwinski, G. Buckau, F. Scherbaum, J.I. Kim, Radiochim. Acta 65 (1994) 111.
[6] G. Meinrath, Y. Kato, Z. Yoshida, J. Radioanal. Nucl. Chem. 174 (1993) 299.
[7] E. Faulques, R.E. Russo, D.L. Perry, Spectrochim. Acta. Part A 50 (1994) 757.
[8] R.M. Sellers, Radiat. Phys. Chem. 21 (1983) 295.
[9] K.G. Robinson, R. Ganesh, G.D. Reed, Water Sci. Technol. 37 (1998) 73.
[10] J. Jiang, L. Rao, P. Di Bernardo, P. Zanonato, A. Bismondo, J. Chem. Soc. Dalton Trans. (2002) 1832.
[11] S. Ahrland, Acta Chem. Scand. 5 (1951) 199.
[12] S. Ahrland, L. Kullberg, Acta Chem. Scand. 25 (1971) 3677.
[13] C. Miyake, H.W. Nürnberg, J. Inorg. Nucl. Chem. 29 (1967) 2411.
[14] C. Nguyen-Trung, G.M. Begun, D.A. Palmer, Inorg. Chem. 31 (1992) 5280.
[15] C. Manfredi, D. Ferri, E. Vasca, T. Caruso, V. Caruso, C. Fontanella, G. Palladino, S. Vero, Ann. Chim. (Rome) 95 (2005) 313.
[16] J. Havel, J. Soto-Guerrero, P. Lubal, Polyhedron 21 (2002) 1411.
[17] E. Vasca, T. Caruso, M. Iuliano, C. Manfredi, C. Fontanella, M. Trifuoggi, Ann. Chim. (Rome) 90 (2000) 181.
[18] D. Ferri, M. Iuliano, C. Manfredi, E. Vasca, T. Caruso, M. Clemente, C. Fontanella, J. Chem. Soc. Dalton Trans. 19 (2000) 3460.
[19] G.R. Choppin, H.N. Erten, A.K. Mohammed, Radiochim. Acta 66/67 (1994) 123.
[20] M. Borkowski, R.C. Moore, M.G. Bronikowski, J.F. Chen, O.S. Pokrovsky, Y.X. Xia, G.R. Choppin, J. Radioanal. Nucl. Chem. 248 (2001) 467.
[21] M. Borkowski, S. Lis, G.R. Choppin, Radiochim. Acta 74 (1996) 117.
[22] B. Arbad, J. Indian Chem. Soc. 62 (1985) 566.
[23] A. Vanni, G. Ostacoli, E. Riletto, Ann. Chim. (Rome) 59 (1969) 847.
[24] A. Bismondo, A. Cassol, P. Di Bernardo, L. Magon, G. Tomat, Inorg. Nucl. Lett. 17 (1981) 79.
[25] V. Andhare, V. Katkar, K. Munsi, J. Indian Chem. Soc. 64 (1987) 589.
[26] F. Mompean, M. Illemassène, J. Perrone, W. Hummel (Eds.), Chemical Thermodynamics of Compounds and Complexes of U, Np, Pu, Am, Tc, Se, Ni and Zr with Selected Organic Ligands, vol. 9, Hardcover ed., Elsevier Science Ltd, 2005.
[27] B.M. May, K. Murray, Joint Expert Speciation System, JESS Primer, Murdoch Western Australia, 2000.
[28] D. Pettit, K.K. Powell, Stability constants database, in: Academic Software, IUPAC, Otley, UK, 1997.
[29] A.E. Martell, R.M. Smith, Critical Stability Constants, vol. 3, 1977, 2nd suppl., vol. 6. Plenum Press, New York, 1989.
[30] A.E. Martell, R.J. Motokaitis, R.M. Smith, NIST-Database 46, Gaithersburg, 1997.
[31] C. De Stefano, A. Gianguzza, T. Leggio, S. Sammartano, J. Chem. Eng. Data 47 (2002) 533.
[32] D. Gianguzza, F.J. Milea, S. Millero, Sammartano, Mar. Chem. 85 (2004) 103.
[33] F. Crea, D. Milea, S. Sammartano, Talanta 65 (2005) 229.
[34] F. Crea, D. Milea, S. Sammartano, Ann. Chim. (Rome) 95 (2005) 767.
[35] F. Crea, A. De Robertis, S. Sammartano, Ann. Chim. (Rome) 93 (2003) 1027.
[36] S. Berto, F. Crea, P.G. Daniele, C. De Stefano, E. Prenesti, S. Sammartano, Ann. Chim. (Rome) 96 (2006) 399.
[37] F. Crea, A. De Robertis, C. De Stefano, S. Sammartano, Talanta 71 (2007) 948.
[38] F. Crea, C. De Stefano, D. Milea, S. Sammartano, Ann. Chim. (Rome) 97 (2007) 163.
[39] F. Crea, A. De Robertis, C. De Stefano, S. Sammartano, J. Solution Chem. 36 (2007) 479.
[40] C. De Stefano, A. Gianguzza, D. Milea, A. Pettignano, S. Sammartano, J. Alloys Compd. 424 (2006) 93.
[41] G. Biedermann, Ionic media, in: Dahlem Workshop on the Nature of Seawater, Dahlem Konferenzen, Berlin, 1975, pp. 339–362.
[42] L. Ciavatta, Ann. Chim. (Rome) 70 (1980) 551.
[43] K.S. Pitzer, J. Phys. Chem. 77 (1973) 268.
[44] K.S. Pitzer, Activity Coefficients in Electrolyte Solutions, 2nd ed., CRC Press, Boca Raton, FL, 1991.

[45] C. De Stefano, P. Mineo, C. Rigano, S. Sammartano, Computer tools for the speciation of natural fluids, in: A. Gianguzza, E. Pelizzetti, S. Sammartano (Eds.), Marine Chemistry—An Environmental Analytical Chemistry Approach, Kluwer Academic Publishers, Amsterdam, 1997, pp. 71–83.

[46] A. De Robertis, C. Foti, A. Gianguzza, Ann. Chim. (Rome) 83 (1993) 485.

[47] C. Bretti, C. Foti, S. Sammartano, Chem. Speciation Bioavailability 16 (2004) 105.

[48] F. Crea, A. De Robertis, S. Sammartano, J. Solution Chem. 33 (2004) 499.

[49] F. Crea, C. De Stefano, O. Giuffrè, S. Sammartano, J. Chem. Eng. Data 49 (2004) 109.

[50] F. Crea, C. De Stefano, A. Gianguzza, D. Piazzese, S. Sammartano, Talanta 68 (2006) 1102.

[51] C. Bretti, F. Crea, C. Foti, S. Sammartano, J. Chem. Eng. Data 50 (2005) 1761.

[52] C. Bretti, F. Crea, C. Foti, S. Sammartano, J. Chem. Eng. Data 51 (2006) 1660.

Available online at www.sciencedirect.com
ScienceDirect
Talanta 75 (2008) 606–612
Talanta
www.elsevier.com/locate/talanta

Integration of analytical measurements and wireless communications—Current issues and future strategies

Dermot Diamond*, King Tong Lau, Sarah Brady, John Cleary

Adaptive Sensors Group, National Centre for Sensor Research, School of Chemical Sciences, Dublin City University, Dublin 9, Ireland

Abstract

Rapid developments in wireless communications are opening up opportunities for new ways to perform many types of analytical measurements that up to now have been restricted in scope due to the need to have access to centralised facilities. This paper will address both the potential for new applications and the challenges that currently inhibit more widespread integration of wireless communications with autonomous sensors and analytical devices. Key issues are identified and strategies for closer integration of analytical information and wireless communications systems discussed.

Keywords: Wireless sensor networks; Chemical sensors; Environmental monitoring; Personal health; Wearable sensors

1. Introduction

1.1. General background

Analytical instruments are becoming ever more automated, with many sophisticated features such as sampling, sample processing, calibration, data generation, and reporting/results analysis controlled by the instrument. Increasingly, operators can control instruments remotely, for example to change or modify the selected method, or to obtain results and reports. Over the past 20 years or so, the concept of μTAS or lab-on-a-chip (LOAC) has evolved, through which it is envisaged that many of these features could be replicated on a microscaled equivalent to bench instruments [1]. The key building block of these devices from the analytical perspective is the microfluidic manifold, through which samples are accessed, reagents added, measurements made, and calibration performed [2]. In its ultimate manifestation, μTAS/LOAC provides a route to the generation of micro-dimensioned analytical instruments that could be deployed remotely, and operate autonomously over relatively long periods of time (years) [3,4].

In parallel, the area of wireless communications has also been evolving towards devices that are increasingly smaller and capable of long-term operation. The availability of low power, reliable wireless communications platforms that can be linked to sensors and analytical devices is an attractive proposition. These devices, known as 'Motes' offer features like adhoc networking, wireless communications, signal acquisition and processing and battery power [5]. The integration of sensing and wireless networking capabilities provides the basic building block of 'wireless sensor networks' (WSNs) concept, which envisages large numbers of autonomous sensors working collaboratively to monitor specific target parameters. In its ultimate manifestation, this happens at 'internet-scale' with sensors functioning as nodes in local-area networks that are themselves linked into wide-area networks, through existing communications infrastructure [6]. These dynamic sensor data streams are fed through to web-based integration hubs that aggregate diverse sources, identify and classify significant events, and feed personalised information back to the relevant destination (individuals, specialists, groups, companies, agencies, etc.).

However, despite the obvious needs and opportunities that exist in areas like environmental and personal health monitoring, integration of *analytical* sensing (e.g. with chemo/biosensors) and mote-based wireless communications has not really happened [7]. High profile deployments of mote-based sensor networks have employed almost entirely relatively simple sensors for temperature, light density, vibration, and so on [8]. For an excellent review of the issues and opportunities related to low-power wireless sensor networks, see Ref. [9].

---

* Corresponding author.
E-mail address: dermot.diamond@dcu.ie (D. Diamond).

0039-9140/$ – see front matter © 2007 Elsevier B.V. All rights reserved.
doi:10.1016/j.talanta.2007.11.022

It is now clear that without the capability of long-term (years) autonomous operation, even rather modest deployments are not feasible. Not surprisingly, significant effort has been directed at developing routes to enable motes to operate indefinitely in terms of power by scavenging from local sources [10]. A recent example is a deployment comprising 557 solar-powered motes, seven gateway nodes, and a root server covering an outdoor test-bed area of approximately 50,000 square meters which was in continuous operation during the last 4 months of 2005. However, the authors mention that taking the deployment outside controlled laboratory conditions gave rise to significant issues with respect to networking protocols and system management tools that could not be predicted on the basis of extrapolation from smaller laboratory deployments [11].

Clearly there are considerable issues in terms of the supporting infrastructure to enable large-scale wireless sensor network deployments involving many thousands of devices, and this is without the added complexity of chemo/bio-sensing layered on top. However, the integration of chemo/bio-information with other networked information is intuitively an attractive proposition with tremendous market potential in environmental sensing, threat detection and personal health monitoring. Currently, in situations where access to real-time chemo/bio information from distributed sources is critical, very sophisticated platforms are the norm. One example is rapid detection of the release of chemo/bio warfare agents in crowded locations such as subways and metros. In the USA, a system known as 'PROTECT' has been installed in a number of locations including Grand Central Terminal and Penn Station. Each sensor unit costs $15,000–$25,000, with the Penn Station deployment costing $1.5 million plus maintenance costs of $1.7 million over 3 years [12]. Clearly, distributed real-time chemo/bio sensing is possible, but at a huge price for relatively small deployments. Interest is growing rapidly, and coupled with the importance of climate change, it is not surprising that large-scale projects that seek to develop distributed sensor networks for environmental monitoring have begun to appear, such as the Beacon Institute, a joint initiative between IBM, State and Federal Agencies, Universities and local communities to instrument the Hudson river [13].

Clearly there is a growing demand for low-cost, low maintenance chemo/bio sensing devices that can be integrated with mote-type communications platforms to provide the basic building blocks of more widely distributed sensor networks. The analytical community has much to offer in terms of making this integration happen, although clearly this will not be easy, as chemo/bio-sensor technology will also have to mature significantly before significant progress can be made. And while we are still a considerable distance away from low cost, reliable, self-sustaining chemo/bio-sensing devices, there are grounds for optimism. In this paper, we will outline the current status of autonomous chemical sensing platforms and discuss performance characteristics and strategies for realising low cost devices that could play a role in future wireless (chemical) sensor networks. We also describe one route to low-cost chemical sensing using very simple coated LEDs that we have investigated, and applied to the detection of gas plumes. Even with small numbers of these relatively simple sensors, it is clear that the *pattern* of response can provide insights into plume source detection, as well as plume extent, direction and velocity. Furthermore, the response pattern can also provide a degree of cross-validation, which enhances the accuracy of decision-making, and compensates for the lack of sophisticated calibration at regular intervals, which is the normal operating paradigm for autonomous chemo/bio sensing devices.

2. Experimental

2.1. Light emitting diode (LED) based chemo-sensors

Dye formulation consisting of Bromocresol green BCG ($pK_a = 4.8$), ethyl cellulose, dibutyl sebacate dissolved in ethanol was coated onto an LED by manual dip-coating (see inset, Fig. 4), as described previously [14]. This LED was reverse biased to enable it to sense the light density passing through the dye coating, and was illuminated by a second LED ($\lambda_{max} = 610$ nm). The emitter LED was selected to give a strong interaction with the spectral changes associated with the dye colour change [15]. In this configuration, the dye coating serves as a chemo-responsive filter that modulates the light density reaching the reverse-biased LED. The light density was monitored using an in-house designed circuit that measures the photo-current through the time taken to discharge of a fixed capacitive voltage (5 V) as described elsewhere [16–21]. The entire device costs ca. $1 and is capable of very sensitive measurements due to the integrating nature of the measurement. The output signal from the LED sensor was passed to a Mica2dot Mote (MPR500), which transmitted the signals to a remote basestation which was a MICA2 series (MPR400) mote attached to a laptop. The motes were obtained from Crossbow Technologies (San Jose, California).

2.2. Conductometric sensors based on carbon black polymer composite

Carbon-polymer inks were made up with carbon black microparticles (∼5–20 μm) and a polymer substrate dissolved in appropriate organic solvents. The ink was then coated onto screen-printed electrodes Ag/AgCl by either spin-coating or manually by using a brush. The final conductivity of the sensors was around 45 kΩ.

Silver-carbon ink based electrodes were fabricated using a DEK 247 semi-automatic screen-printing machine (DEK, UK). The ink used was a Du Pont 5075 silver-carbon ink and was used as received. Printing was carried out on 100 μm PET substrates, pre-baked for 3 h at 90 °C and washed with water, to prevent shrinkage at the curing stage. The composite sensor paste was prepared using a polymer base (PIB, 1 g dissolved in 100 mL cyclohexane) to which carbon black was added (graphite power, Aldrich, Dublin, used as received). Ten microliters of the 1% (m/v) stock polymer solution was transferred to a sample vial and 0.1 g of carbon black added to give a 1:1 polymer-carbon mass ratio in the sample. The mixture was stirred at room temperature as the solvent evaporated until a thick paste formed. A lithographic coating technique was used to produce a polymer film of uniform thickness of ca. 5–20 μm across the gap on the sensor. This was done by applying a mask, made of PET substrate, over the sensor and painting the polymer film across by using a brush, and then allowing the solvent to evaporate before removing the mask. The substrate was cured post-printing for 10 min at 100 °C.

2.3. *Sensing foam for 'smart insole'*

The pressure response foam inserts were generated by depositing polypyrrole on polyeuthethane (PU) foam (Foam Engineers Ltd., England) substrates and integrated with the exercise trainer insole, electrical connections and wireless communications as described previously [22,23]. Samples of approximately 2 cm × 1 cm × 1 cm were cut from this material and positioned into each insole prototype.

The wireless communications platform used was based on Crossbow Motes as for the LED sensors mentioned above. Signals from the foam sensors were integrated into simple voltage divider circuits. The voltage outputs from the sensors were passed into separate 10-bit ADC channels on the mote platform. The ADC values were recorded for each trial and relayed to the base station for observation and processing. A Mica2Dot (MPR500) mote was used as the wearable sensor mote and a MICA2 series (MPR400) mote attached to a laptop functioned as the base-station.

3. Results and discussion

3.1.1. *Field deployable analysers*

Fig. 1 shows a typical conventional field deployable chemical sensing system or remote analyser that basically automates all aspects of an analytical measurement within a reasonably compact, robust container. In this case, the device is configured to monitor phosphate levels in water (lakes, rivers, treatment plant outlets, etc.) but the design considerations are generic and apply to any autonomous analytical device. It contains reagent reservoirs, waste storage, sampling port (filter), a microfluidic manifold, LED-based optical detection, solenoid valves, fluid control, electronics, GPS location tracking system and GSM wireless communications [24].

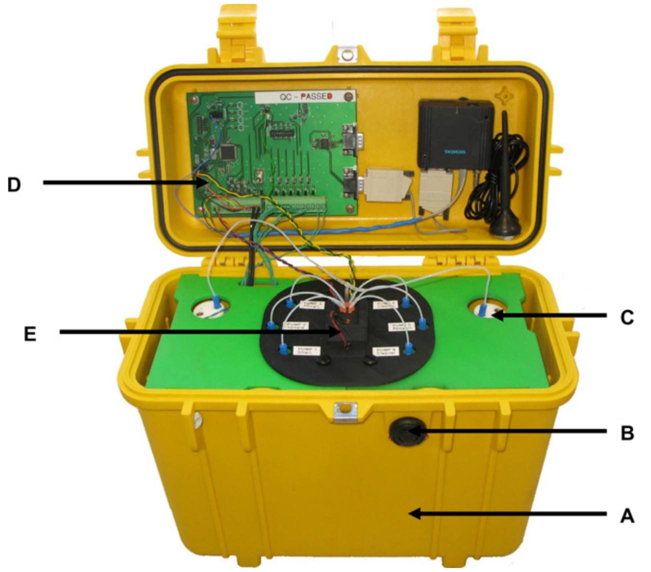

Fig. 1. Typical field deployable chemical sensing system showing (A) tough protective case, (B) sampling port, (C) reagents and waste storage, (D) electronics and (E) microfluidics manifold and optical detector housing. This particular system is configured to monitor dissolved phosphate using the yellow method.

With reagent based systems, issues related to changes in sensor surface characteristics, for example, through biofouling or leaching of active components into the sample, are avoided. The sample is drawn into the microfluidics manifold via a filtered sampling port, where it is mixed with an appropriate reagent and a reaction occurs leading, in this case, to the formation of a coloured product which is detected by an integrated optical detector. The reagent used depends on the analyte, and ideally the analyte-reagent reaction produces a highly coloured product with a large extinction coefficient at a wavelength that matches the emission waveband of the LED, as this allows sensitive and selective measurements to be made with relatively low power consumption. Using a microfluidic manifold allows the sample and reagent volumes required to be drastically reduced, and this, coupled with low power demand, opens the way to producing field-deployable analytical instruments that can operate autonomously for long periods of time (weeks to months).

However, even these relatively sophisticated devices are subject to signal drift as illustrated in Fig. 2, which shows the performance of this relatively sophisticated device during a 3-week field trial at a waste water treatment plant outlet. Initially there is a reasonably good correlation between the prototype phosphate analyser, and reference data generated by the plant monitoring system. However, by the third week, a significant bias between the analyser and the reference data is apparent, which is most likely due to the gradual coating of the optical sensor flow cell in the phosphate analyzer, as it can be completely alleviated by a combination of cleaning cycles and calibration, enabling the system to be used reliably for many months. The system contains enough reagent for 12 months operation and is completely self-sufficient in terms of power consumption and supply. Power is obtained from a lead acid cell which is charged by an external solar panel (10 W solar array, from SunWize Technologies Inc., Kingston, New York). Battery power alone allows for over 6 months operation based on a sampling frequency of 4 per day, with data download once daily via GSM modem. The solar panel theoretically allows for indefinite operation of the system assuming just over 2 h sunlight per day. However, the actual operation lifetime can be greatly reduced by increasing the transmission frequency. The achievement of this reliability requires a sophisticated device incorporating pumps, liquid handling, storage of reagents, and waste. Wireless communications is via GSM text messages which enable remote control of the operating parameters (e.g. sampling rate) as well as transmission of analytical data. This results in a platform that is relatively expensive (ca. €2–10 K typically) and therefore is not suitable for very large-scale deployments.

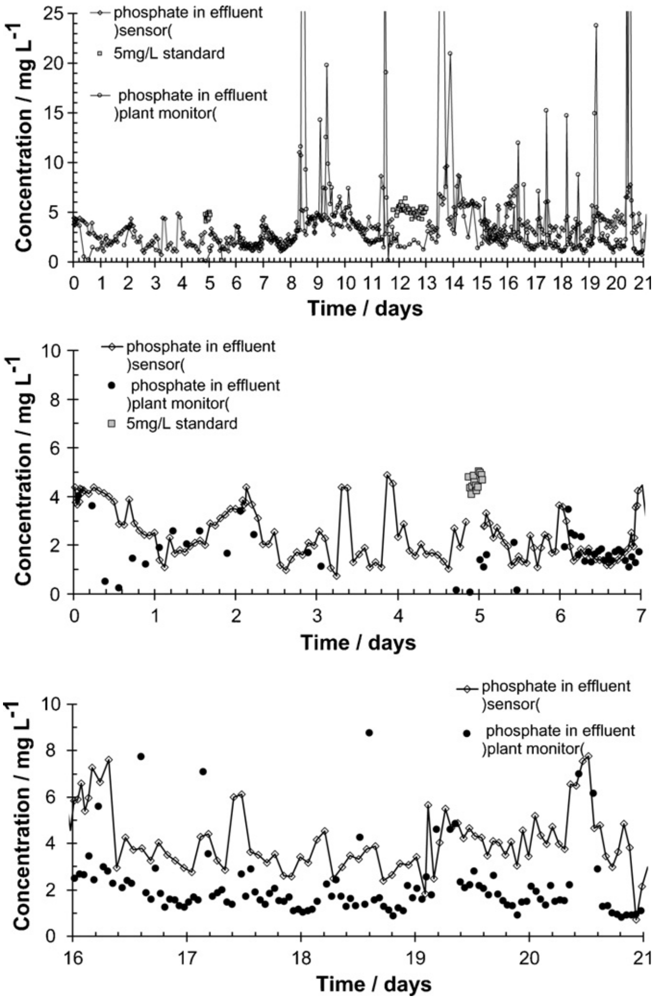

Fig. 2. (Top) Results obtained with the system shown in Fig. 1 over a 3-week deployment at a waste water treatment plant. Reference measurements from the plant phosphate monitoring system data are also shown for comparison. (Middle) Close up of the data over the initial 7 days showing reasonably good correlation between the sensor and the plant monitoring system data. (Bottom) Close up of the final 5 days of the trial showing the emergence of a systematic bias between the two methods, with the sensor signal now clearly indicating higher levels than the plant monitoring system.

However, for most environmental applications involving water and air quality monitoring, the distances between sampling locations can be relatively large (km) and platforms similar to this are probably suitable for most current needs, but they do require a certain level of maintenance (e.g. reagent changes, waste collection, general repairs) and therefore cannot be considered by very large scale deployments involving many thousands or millions of devices.

3.1.2. Matching of hierarchies

Within the world of sensors, it is possible to construct a hierarchy of devices that ranges from very simple, low cost physical/chemical transducers like thermistors, vibration detectors, photodiodes or pregnancy test strips to the much more sophisticated and complex sensing systems described above. In the near future, sensor networks will be heterogeneous in nature, constructed from layers of sensing devices of similar complexity, with a matched level of sophistication in the communications environment [6]. At the lowest level of complexity will be the most densely deployed devices consisting of relatively simple sensors linked to a wireless platform of limited capability. These will feed information through to more sophisticated levels of sensing that are more expensive to deploy and maintain, and therefore less densely distributed. This information will be used to provide early warning of events, and will be used to modify the operating characteristics of the more sophisticated devices (e.g. wake up, or sample more often), and the data from the more sophisticated layers will provide much more reliable information that will be used to confirm the early indicators emerging from the less sophisticated layer. Motes are one building block for these more densely distributed layers, but as described above, deployments of these devices are still relatively small (hundreds typically at the large end) and there are still considerable difficulties in optimising the power consumption/supply and communications capabilities (distance typically up to 100 m, bandwidth typically several kHz) of these devices. However, they do offer a wireless communications platform on which to place sensors, and begin to explore the attractive area of pervasive chemical/biosensors. What is needed is access to very low cost, relatively unsophisticated chemo/bio-sensing devices that match the complexity of the communication platform. A key question is whether, niche applications can be identified with constraints that may provide early wins for researches. For example, applications that do not require communications over long distances (limited to a few metres) and involve only relatively short term deployments (hours, days)? In the following sections, we will attempt to chart a way forward through these issues.

3.2. Low-cost chemosensing platforms

It is relatively easy to build low cost chemo-sensing devices, both electrochemical and optical. For example, Fig. 3 shows an example of a simple screen printed chemoresistor that can be used to detect various gas phase analytes, at a cost of less than one cent per device. A sensitive response to the presence of ethyl acetate is evident in this case. These days electrochemical sensors are mass produced for clinical diagnostics (e.g. blood electrolyte profiling, blood glucose monitoring), but these are essentially single shot devices design to be used once and then discarded. Nevertheless, very low cost electrochemical sensors can be produced and could in principle be linked to a mote platform for remote deployment.

Similarly, low cost optical sensors can also be generated. Fig. 4 shows the response to changes in gas phase pH obtained with a pH-responsive dye coated onto a reverse biased LED (functions as a very low cost photodiode). The signal is obtained by integrating the time over which a capacitance is discharged by the photocurrent generated by light passing through the chemo-responsive dye. As the dye changes colour, the discharge time changes and this can be related to the pH of the sample.

But can such low-cost chemosensors be used in a collaborative manner to compensate for a lower levels of reliability in

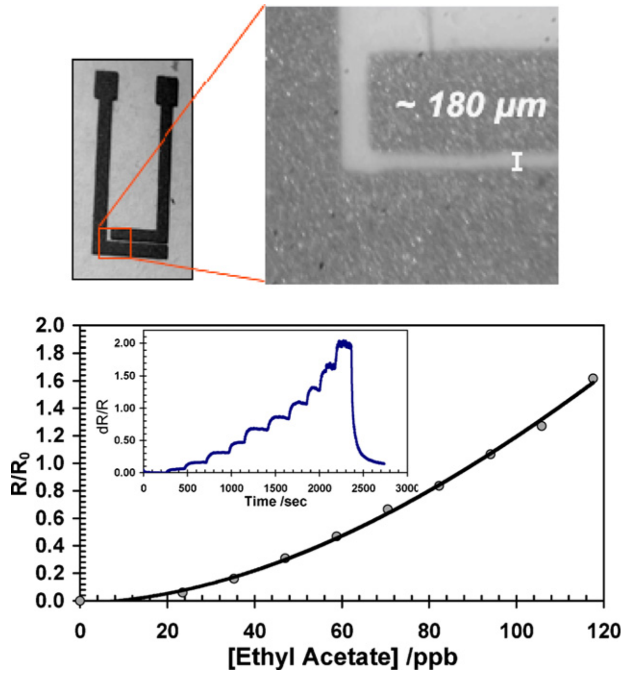

Fig. 3. Low cost screen printed carbon black gas sensors. Top (Left): Design of the sensors with electrical contact pads at the top and sensing area highlighted. Top (Right): Close up of the sensing region of the device illustrating the gap between the electrodes over which the sensing polymer is deposited. (Bottom) Calibration curve of the device response to ethyl acetate and (inset) the dynamic responses obtained to additions of the sample from which the calibration curve was constructed.

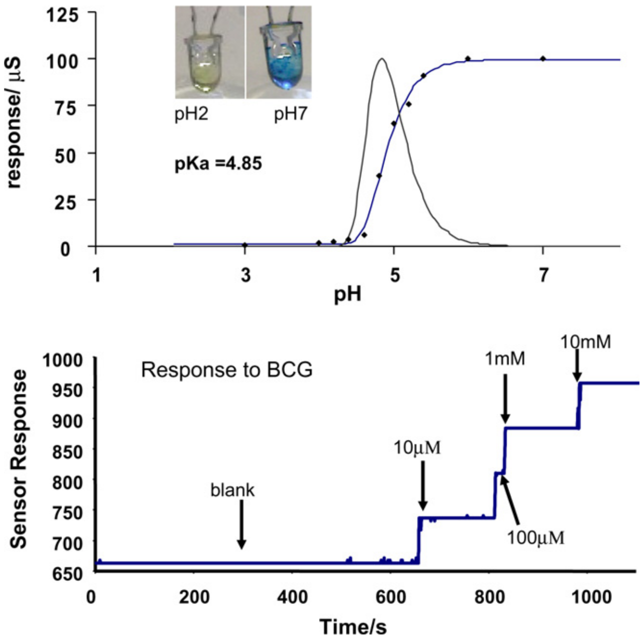

Fig. 4. Low cost optical sensors based on bromocresol green coated LEDs. (Top) Response of reverse biased LEDs coated with BCG showing the response to samples spanning the range pH 2–7. There is a clear inflection as expected and from the 1st derivative plot (shown) the pK_a is estimated to be 4.85 which is close to the literature value of 4.8. The response is based on changes in the dye colour due to pH changes (Inset). This modulates the photocurrent generated by the LED which is detected through variations in the discharge time of a capacitor. (Bottom) Examples of responses obtained with the coated LED sensor showing very stable baseline, coupled with a very rapid and sensitive response. LODs in the nano-molar region can be routinely achieved with this device.

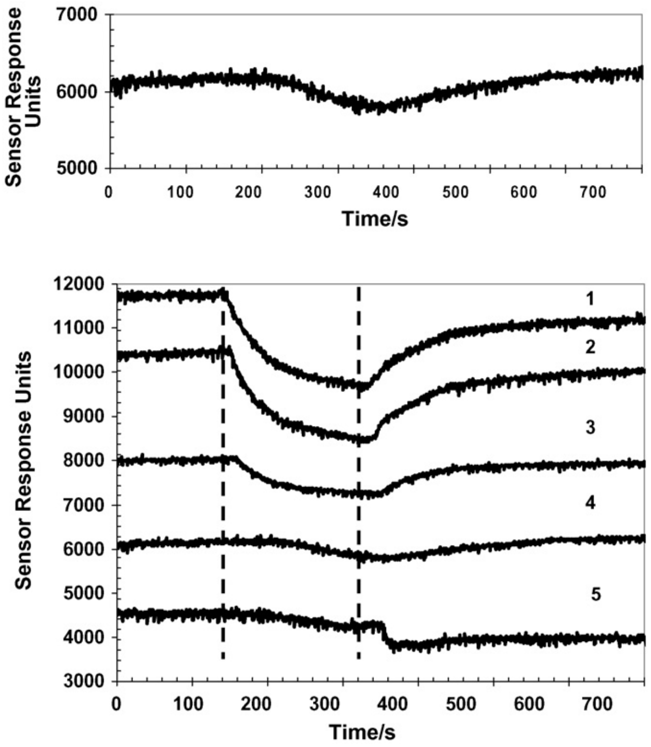

Fig. 5. Comparison of single sensor vs. multisensor information content. Sensors were coated LEDs as shown in Fig. 4. Five sensors were distributed in an environmental chamber along the path of an acid plume which was added at time = 140 s, numbered in order of distance from the plume source 1–5. (Top) Signal from sensor 4. A feature appears to be present over the time 200–500 s, but it is difficult to make a definitive conclusion. (Bottom) The sensor output can be understood more clearly when viewed in context with signals from neighbouring sensors. Sensors 1 and 2 (closest to the plume source) have very definite responses beginning around 150 s. Sensor 3 also shows a definite response but less so than 1 and 2, indicating that the plume is dispersing along its path of propagation. Sensor 4 can now be seen to continue this trend, reinforcing the conclusion that a plume is in progress and dispersing. For additional details see text.

the information content obtained from a single device compared say to the phosphate analyser described above? The indications are that they can. Fig. 5 (top) shows the response of a single dye coated LED sensor which suggests there is a possible ‘event’ happening over the period 200–400 s. However, it is difficult to make a definitive decision about this, as the variation could be due to baseline drift. The traditional approach would be to recalibrate the device and check for baseline drift before making a judgement. However, in this case, we are able to observe and compare to the output of similar sensors in nearby locations, and the conclusion is very definite that there is a real event occurring which began at around 240–250 s. There is a progressive signal delay and also decrease in signal strength from sensors 1 to sensor 5, which indicates the direction of plume movement [14].

Even from this relatively simple deployment of a small number of sensors it is clear that reliability in decision making is considerably enhanced by using the sensor collaboratively. Information about the likely source of an event, its trajectory and area of effect can be estimated, but perhaps most important is the reliability in decision making (has an event happened), as levels of false negatives and positives must be kept to an absolute minimum if this type of collaborative sensor reasoning is to become adopted, for example, for pollution tracking, detection of hazardous fumes at industrial sites or release of chemical warfare agents.

3.3. Wearable sensors

One niche area where sensor networks are likely to make a large impact in the near future is in wearable sensors. Fig. 6 shows an example of wearable sensors incorporated into an exercise trainer. The sensors are produced by coating polyurethane foam with a conducting polymer (polypyrrole) which enables the modified foam to sense pressure [23,25]. In this study, the guiding principle has been to make the wearable material the sensor, rather than attach sensors to the material. From the output, it is possible to detect and classify wearer activity. For example, the number of steps, step frequency, distance moved, activity type (walking, shuffling, jumping, etc.) can be monitored. Using similar approaches it is relatively easy to monitor breathing and heart rate and by combining these signals, an activity profile for a wearer can be built up over time, along with vital signs status. This information can be aggregated with similar information gathered from other wearers, and the resulting data analysed in terms of lifestyle, general wellness or early indications of disease. For example, changes in the walking profile may indicate the onset of Parkinson's disease, whereas breathing and heart rate coupled with activity profile could provide a powerful tool for tracking populations as diverse as people recovering from long-term illness, or optimisation of athlete performance.

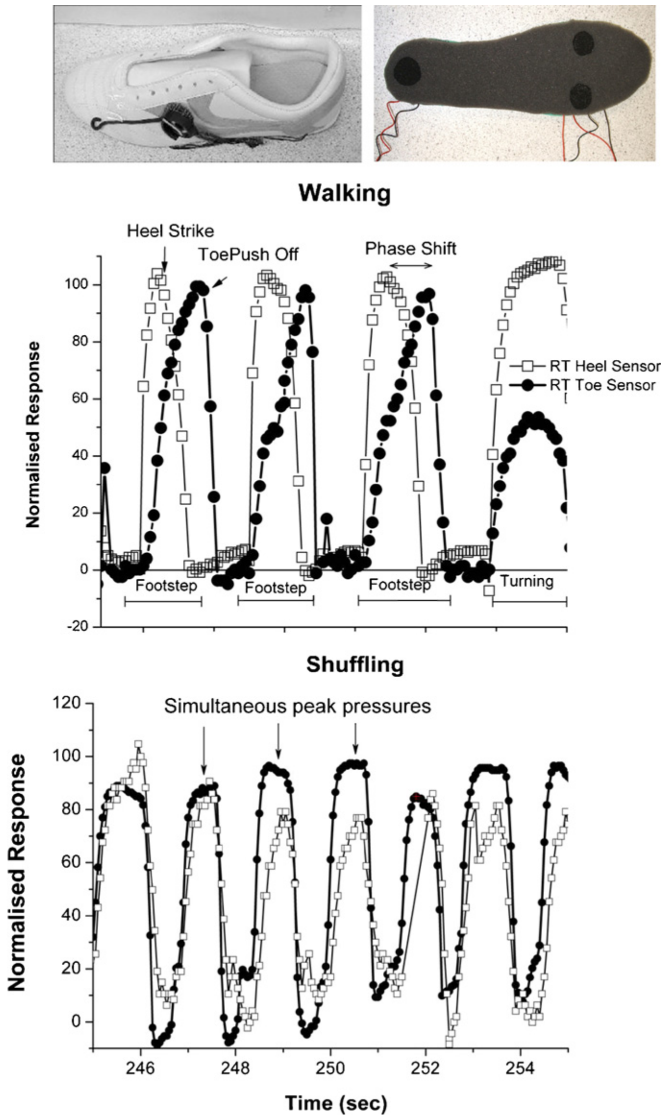

Fig. 6. Monitoring personal activity using wearable sensors. Left (Top): Foam insole of exercise trainer showing pressure sensor inserts based on functionalised polyurethane (PU) foam. Left (bottom): Assembled shoe showing position of wireless mote communications platform. Right (Top): Signals obtained during walking showing a sequence of steps followed by turning movement. The phase shift between the heel strike followed by toe enables the type of movement to be easily identified (walking) and distinguished from turning. Right (Bottom): Pattern obtained from a shuffling movement. The heel-toe phase shift is no longer distinguishable indicating that 'normal' walking pattern is not happening.

Wearable sensors in some ways are an attractive option for chemo/bio-sensing—deployments are generally short term (days at most), and the system is normally recharged by the wearer at regular intervals. However, the major issue is what sample to analyse in order to obtain information on specific markers? The sample of choice is typically blood or urine, but for wearable sensors, the sample that is probably easiest to access is sweat, but relatively little is known about sweat as a diagnostic medium. Coupled with this is the lack of a wearable chemo/bio-sensor platform that is comfortable to wear and operate. However, in recent years, progress in the development of wearable fluidic systems capable of performing tasks similar to conventional flow analysis system has begun to happen [26]. The availability of such platforms will enable sampling, addition of reagents and calibration to be performed in a wearable format that is fully integrated with garments. Integration of this with wearable electronics and communications systems is already well advanced, and these systems should be able to detect threatening external environments (for example, in emergency-disaster scenarios, sensors that 'look out' into the environment through which the wearer is moving will be important) and track key chemo/bio-markers (for example, sensors that 'look in' and track markers like lactate, sodium ions, and pH that are present in an athlete's sweat).

The area of wearable sensors will expand very rapidly over the next 1–2 years, driven by developments like the Nike-Apple launch of the Nike-iPod Sport Kit which tracks the number of steps and step frequency of the wearer using a sensor insert into a Nike trainer that communicates wirelessly to the wearer's iPod. This consumer product is already generating a significant user base, and is likely to generate rapid growth in related products in terms of wearable sensors, and in terms of the information analysis tools that extract fitness/wellness information from the wearer's personal database.

4. Conclusions

The emergence of large-scale widely deployed chemo/bio-sensing networks for environmental monitoring (air, water quality) will grow from the top-down, with initial activity focusing on relatively sophisticated platforms deployed at relatively large distances (km). Clusters of these devices may be located at particular pollution hotspots, but the realisation of a densely deployed heterogeneous sensor network requires significant effort to understand the level of information content that can be acquired from relatively dumb sensors used in a collaborative manner. On the other hand, developments in wearable sensors will happen much more quickly, as issues like power maintenance, length of deployment, communication distance and availability of a reliable platform infrastructure are more solvable. While there are immediate niche opportunities for wearable chemo-sensors that can detect external threats or hazards, wearable chemo-sensors for personal health/wellness will require the development and integration of wearable fluid handling capabilities with wearable electronics and communications.

Acknowledgements

We wish to acknowledge funding from the European Union for research on wearable sensors (ProeTEX FP6-2004-IST-4-026987 and BioTex FP6-2004-IST-NMP-2 projects), as well as National funding obtained from the Irish Environmental Protection Agency (EPA 2004-RS-AIC-M4) and Marine Institute (grant AT/04/01/06) for environmental sensor research, as well as core research support from Science Foundation Ireland under the Adaptive Information Cluster (SFI 03/IN.3/1361).

References

[1] A. Manz, N. Graber, H.M. Widmer, Sens. Actuators B 1 (1990) 244.

[2] D.R. Reyes, D. Iossifidis, P.A. Auroux, A. Manz, Anal. Chem. 74 (2002) 2623.

[3] M. Sequeira, M. Bowden, E. Minogue, D. Diamond, Talanta 56 (2002) 355.

[4] T. Boone, Z.H. Fan, H. Hooper, A. Ricco, H.D. Tan, S. Williams, Anal. Chem. 74 (2002) 78A.

[5] S.J. Bellis, K. Delaney, B. O'Flynn, J. Barton, K.M. Razeeb, C. O'Mathuna, Computer Commun. 28 (2005) 1531.

[6] D. Diamond, Anal. Chem. 76 (2004) 278A.

[7] R. Byrne, D. Diamond, Nat. Mater. 5 (2006) 421.

[8] J. Kumagai, W. Sweet, Spectrum IEEE 41 (2004) 42.

[9] D. Culler, D. Estrin, M. Srivastava, Computer 37 (2004) 41.

[10] X. Jiang, J. Polastre, D. Culler, Fourth International Symposium on Information Processing in Sensor Networks (IPSN), 2005, p. 463.

[11] P. Dutta, J. Hui, J. Jeong, S. Kim, C. Sharp, J. Taneja, G. Tolle, K. Whitehouse, D. Culler, Trio: Enabling Sustainable and Scalable Outdoor Wireless Sensor Network Deployments, ACM Press, Nashville, Tennessee, USA, 2006.

[12] W. Neuman, October 16, 2007. http://www.nytimes.com/2006/10/03/nyregion/03security.html.

[13] The Beacon Institute, October 16, 2007. http://www.thebeaconinstitute.org/institute.

[14] R. Shepherd, S. Beirne, K.T. Lau, B. Corcoran, D. Diamond, Sens. Actuators B 121 (2007) 142.

[15] R.L. Shepherd, W.S. Yerazunis, K.T. Lau, D. Diamond, IEEE Sens. J. 6 (2006) 861.

[16] K.T. Lau, R. Shepherd, D. Diamond, D. Diamond, Sensors 6 (2006) 848.

[17] M. O'Toole, K.T. Lau, D. Diamond, Talanta 66 (2005) 1340.

[18] M. O'Toole, K.T. Lau, B. Schazmann, R. Shepherd, P.N. Nesterenko, B. Paull, D. Diamond, Analyst 131 (2006) 938.

[19] K.T. Lau, W.S. Yerazunis, R.L. Shepherd, D. Diamond, Sens. Actuators B 114 (2006) 819.

[20] K.T. Lau, E. McHugh, S. Baldwin, D. Diamond, Anal. Chim. Acta 569 (2006) 221.

[21] K.T. Lau, S. Baldwin, M. O'Toole, R. Shepherd, W.J. Yerazunis, S. Izuo, S. Ueyama, D. Diamond, Anal. Chim. Acta 557 (2006) 111.

[22] S. Brady, K.T. Lau, W. Megill, G.G. Wallace, D. Diamond, Synth. Met. 154 (2005) 25.

[23] S. Brady, B. Carson, D. O'Gorman, N. Moyna, D. Diamond, International Workshop on Wearable and Implantable Body Sensor Networks (BSN) Boston, (2006), p. 4.

[24] Christina M. McGraw, Shannon E. Stitzel, John Cleary, Conor Slater, Dermot Diamond, Autonomous microfluidic system for phosphate detection, Talanta 71 (2007) 1180.

[25] S. Brady, D. Diamond, K.T. Lau, Sens. Actuators A 119 (2005) 398.

[26] S. Coyle, Y. Wu, K.-T. Lau, D. De Rossi, G.G. Wallace, D. Diamond, MRS Bull. 32 (2007) 434.

Available online at www.sciencedirect.com
ScienceDirect
ELSEVIER
Talanta 75 (2008) 605
Talanta
www.elsevier.com/locate/talanta

Editorial

Special section on wireless sensor networks

The motivation for gathering these papers together goes back to a workshop entitled ‘Energy and Materials: Critical Issues for Wireless Sensor Networks’ which was held in Dublin City University, on the 30th June 2006. Guest of honour at the meeting was noble laureate, Prof. Alan MacDiarmid, from the University of Pennsylvania. At the meeting, Prof. MacDiarmid spoke passionately about the need to understand more about ourselves, and the world we live in, and of the importance of emerging autonomous sensor technology that will provide access to exciting new sources of information about our personal health, and our environment.

In this collection of papers, authored by specialists from a variety of backgrounds, we provide some insight into the enormous potential of autonomous chemo/bio-sensors devices to impact positively on society, and the critical challenges that currently inhibit large-scale adoption and deployment of these devices.

Specifically, Joe Wang and Mark Meyerhoff examine implantable chemo/bio-sensors. The potential for implantable technology to dramatically improve peoples’ lives is evidenced by devices like pacemakers and artificial cochlear implants. They consider ways to make chemo/bio-sensing devices fully implantable and capable of functioning for many years. Mark Meyerhoff’s ‘Nitric Oxide-Releasing/Generating Polymers for the Development of Implantable Chemical Sensors with Enhanced Biocompatibility’ looks at the critical issue of biocompatibility, arguably the most important obstacle inhibiting the broader adoption of implantable chemo/bio-sensors, whereas Joe Wang’s paper focuses on how to power implantable sensors over long periods of time.

Radislav Potyrailo looks at new, low power approaches to communicate with remote chemo/bio-sensors, while Eric Bakker presents a novel approach to using low-limit of detection ion-selective electrodes that could open up many new applications in areas such as environmental monitoring. Cian O’Mahuna examines the whole issue of how to make autonomous sensors self-sufficient in terms of power, while my own paper considers how to make low-cost chemo/bio-sensors, and how we may be able to extract more reliable information from groups of sensors than from a single sensor, because of the relative spatial and temporal information that is inherently coded in data obtained from multiple sources.

In conclusion, Alan’s passing in 2007 is a great loss to the international scientific community. We need more leaders like him who can highlight the need for good science to impact positively on people’s lives, and to show in a simple and convincing manner that scientific breakthroughs can profoundly change society, and make the world a better place to live in.

Ar dheis Dé go raibh a anam.

(A gaelic saying—may he rest in peace).

Dermot Diamond
National Centre for Sensor Research, Dublin City University,
Dublin 9, Ireland
E-mail address: dermot.diamond@dcu.ie

doi:10.1016/j.talanta.2008.01.020

Available online at www.sciencedirect.com

ScienceDirect

Talanta 75 (2008) 832–840

Talanta

www.elsevier.com/locate/talanta

Optimization of dispersive liquid–liquid microextraction of copper (II) by atomic absorption spectrometry as its oxinate chelate: Application to determination of copper in different water samples

Mir Ali Farajzadeh[a,*], Morteza Bahram[b], Behzad Ghorbani Mehr[b], Jan Åke Jönsson[c]

[a] *Department of Analytical Chemistry, Faculty of Chemistry, Tabriz University, Tabriz, Iran*
[b] *Department of Chemistry, Faculty of Science, Urmia University, Beheshti Street, Urmia, Iran*
[c] *Department of Analytical Chemistry, University of Lund, PO Box 124, 221 00 Lund, Sweden*

Received 25 August 2007; received in revised form 11 November 2007; accepted 18 December 2007
Available online 4 January 2008

Abstract

In this study a dispersive liquid–liquid microextraction (DLLME) method based on the dispersion of an extraction solvent into aqueous phase in the presence of a dispersive solvent was investigated for the preconcentration of Cu^{2+} ions. 8-Hydroxy quinoline was used as a chelating agent prior to extraction. Flame atomic absorption spectrometry using an acetylene-air flame was used for quantitation of the analyte after preconcentration. The effect of various experimental parameters on the extraction was investigated using two optimization methods, one variable at a time and central composite design. The experimental design was performed at five levels of the operating parameters. Nearly the same results for optimization were obtained using both methods: sample size 5 mL; volume of dispersive solvent 1.5 mL; dispersive solvent methanol; extracting solvent chloroform; extracting solvent volume 250 μL; 8-hydroxy quinoline concentration and salt amount do not affect significantly the extraction. Under the optimum conditions the calibration graph was linear over the range 50–2000 $\mu g\,L^{-1}$. The relative standard deviation was 5.1% for six repeated determinations at a concentration of 500 $\mu g\,L^{-1}$. The limit of detection (S/N = 3) was 3 $\mu g\,L^{-1}$.

Keywords: Dispersive liquid–liquid microextraction; Optimization; One variable at a time; Central composite design; Atomic absorption spectrometry; Copper ion determination

1. Introduction

Traditional solvent extraction has been used as a basic and powerful method of concentrating for a long time. However, it requires extensive amounts of organic solvents. A special attention is nowadays focused on techniques, which are characterized by a considerable reduction or complete elimination of organic solvents. Such techniques protect the environment against additional quantities of solvents and reduce the cost of analysis. The solvent-free techniques such as gas phase extraction, membrane extraction and solid phase extraction are limited to volatile and relatively volatile organic compounds, volatile nonpolar compounds and relatively low volatile compounds [1], respectively. In 1996, Liu and Dasgupta used 1.3 μL chloroform as extraction reagent, thus decreased the environmental pollution greatly throughout the analytical procedure [2]. Meanwhile, Jeannot and Cantwell introduced the single-drop microextraction (SDME) technique [3] and these authors investigated a convective–diffusive mass transfer model to interpret the kinetic procedure in the novel SDME technique [4]. Pedersen-Bjergaard and Rasmussen reported a microextraction method with a polypropylene hollow fiber as support for the extraction of methamphetamine from urine and plasma. The acceptor solution (0.1 $mol\,L^{-1}$ HCl) inside the hollow fiber was analyzed by capillary electrophoresis (CE) [5]. The enrichment factor (EF) reached 75 times. Lee and co-workers combined the hollow fiber membrane–liquid phase microextraction (HFM–LPME) with GC [6] or HPLC [7] to separate and determine aromatic compounds in various samples. Wu and co-workers developed a method that combined SDME with ETV-ICP-OES/MS for the

---

[*] Corresponding author. Tel.: +98 441 2335943; fax: +98 441 2776707.
E-mail address: farajzade@yahoo.com (M.A. Farajzadeh).

0039-9140/$ – see front matter © 2007 Elsevier B.V. All rights reserved.
doi:10.1016/j.talanta.2007.12.035

determination of trace La [8], Be, Co, Pb and Cd [9] and for speciation of Al [10]. Li and co-workers determined trace Cd and Pb in environmental and biological samples by ETV-ICP-MS after single-drop microextraction [11]. Another extraction procedure, namely homogeneous liquid–liquid extraction, which extracts the target analyte in the homogeneous aqueous solution into a water-immiscible phase, was used by each kind of phase separation phenomenon [12]. The methods, which used phase separation principle, depending on the temperature of the water–propylene carbonate system [13] or the salt effect in the water–acetonitrile system have already been reported [14,15]. Igarashi and co-workers reported a pH-dependent phase separation and used it in determination of copper and palladium as 5,10,15,20-tetrakis (4*n*-pyridyl) porphine chelate by HPLC and spectrophotometric techniques [16]. This method was mainly studied as a highly efficient preconcentration method for the separation of the target analyte before instrumental analysis [17–21].

Another microextraction technique, which uses extraction solvent at μL volume, is dispersive liquid–liquid microextraction (DLLME). It is simple, rapid, efficient and has a higher EF and recovery (R). It was first reported in 2006 by Assadi and co-workers [22,23]. This method uses an extracting solvent dissolved in a dispersive solvent, which is miscible with both extraction solvent and water. Methanol, acetone, acetonitrile, etc., have been used as dispersive solvents. Recently we reported a DLLME method to preconcentrate some polymer additives followed by their determination by HPLC-DAD [24].

In this work preconcentration of Cu^{2+} by dispersive liquid–liquid microextraction was optimized using one variable at a time as well as simultaneous optimization method. No applications of dispersive liquid–liquid microextraction of metallic cations have been previously presented and considerable work is still required to optimize its efficiency. The method of optimization chosen was a chemometric method using a central composite design (CCD) for obtaining the optimal conditions. The goal of the proposed work was to describe in details the effects of various parameters by modeling enrichment factor, recovery and sedimented phase volume as three antagonist responses. The influence of each of the parameters and their interactions could be well identified for different responses screened. The use of an experimental design enabled a subsequent benefit in terms of labor time and number of experience to optimize the conditions. This optimization study investigated the volumes of dispersion solvent, extracting solvent ($CHCl_3$) and Cu^{2+} solution, pH and salt (NaCl) amount in order to build a model to achieve high enrichment factor and recovery and useful amount of sedimented phase volume as responses.

2. Experimental

2.1. Chemicals and solutions

All chemicals such as $CuSO_4{\cdot}5H_2O$, 8-hydroxy quinoline, methanol, chloroform, carbon tetrachloride, dichloromethane, sodium chloride and nitric acid were high-purity grade reagents from Merck Co. (Darmstadt, Germany). A stock solution of 1000 mg L^{-1} Cu^{2+} was prepared in distilled water. A standard solution of 1 mg L^{-1} Cu^{2+} was prepared daily by a suitable dilution of the stock solution with distilled water. 8-Hydroxy quinoline 0.05 mol L^{-1} was prepared in methanol. Acetate buffer (1 mol L^{-1}, pH 6) and nitric acid 0.1 mol L^{-1} were used for pH adjustment and dissolution of residue after evaporation of extract, respectively, before absorbance measurements.

Tap water was collected from our laboratory just before determination of the Cu^{2+} content by either the proposed or by standard methods. River waters (Dozal and Aras Rivers, East Azerbaijan Province, Iran) were picked up a few days before analysis. Two milliliters concentrated nitric acid per liter was added to stabilize the analyte. Sampling locations from Aras River were in the near of Djolfa City (East Azerbaijan Province, Iran) (point 1) and Nodooz (East Azerbaijan Province, Iran) (point 2). Sampling from Dozal River (one branch of Aras River) was carried out about 200 m before its conjunction to Aras River. Sampling was performed directly (without using special apparatus) in polyethylene bottles, which were rinsed with concentrated nitric acid and washed with distilled water. Mineral water was purchased from a local store (Urmia, Iran). All water samples were used without filtration.

2.2. Apparatus

A Shimadzu atomic absorption spectrometer (Model AA-670G) was used for the determination of copper using the manufacturer recommendations.

2.3. Procedure

To 5 mL of 1 mg L^{-1} Cu^{2+} solution in a 12-mL test tube with conical bottom, 1 mL acetate buffer and 0.5 mL 8-hydroxy quinoline solution were added. By using a 5-mL syringe, 1.5 mL methanol containing 250 μL chloroform was added to the above solution. Chloroform was dispersed in all parts of sample and no need to homogenize the sample. The mixture was immediately centrifuged for 5 min at 1000 rpm. The volume of the sedimented phase (chloroform) was determined using a 250-μL HPLC syringe. The sedimented phase was quantitatively transferred to another test tube and allowed to evaporate at room temperature. Finally the residue was dissolved into 0.5 mL 0.1 mol L^{-1} nitric acid and the copper concentration was determined by flame atomic absorption spectrometry. All experiments were performed in triplicate and the mean of results was used in plotting curves or preparation of tables for optimization. Copper standard solutions (0.1–10 mg L^{-1}) in 0.1 mol L^{-1} nitric acid were prepared daily and their absorbance was read along with samples.

2.4. Statistical software

Essential Regression and Experimental Design for Chemists and Engineers, EREGRESS, as a Microsoft Excel Add-In software [25,26] was used to design the experiments and to model and analyze the results.

2.5. Experimental design

Central composite design was used to optimize the preconcentration of Cu^{2+} by dispersive liquid–liquid microextraction. Five independent variables, namely the volume of dispersion solvent ($F1$), extracting solvent $CHCl_3$ ($F2$), Cu^{2+} solution ($F3$), pH ($F4$) and salt (NaCl) amount ($F5$) were studied at five levels with four repeats at the central point, using a circumscribed central composite design. The 8-hydroxy quinoline concentration was selected $0.05\,\mathrm{mol\,L^{-1}}$ in all experiments. For each of the five studied variables, high (coded value: +2) and low (coded value: −2) set points were selected as shown in Table 1. Also Table 2 shows the coded values of designed experiments based on CCD methodology achieved using EREGRESS software.

By the use of EREGRESS, polynomial equations, response surface and central plots for a particular response are produced. For an experimental design with five factors, the model including linear, quadratic, and cross terms can be expressed as the following equation:

$$\begin{aligned}\text{response} = {} & b0 + b1F1 + b2F2 + b3F3 + b4F4 + b5F5 \\ & + b6F1 \times F1 + b7F2 \times F2 + b8F3 \times F3 \\ & + b9F4 \times F4 + b10F5 \times F5 + b11F1 \times F2 \\ & + b12F1 \times F3 + b13F1 \times F4 + b14F1 \times F5 \\ & + b15F2 \times F3 + b16F2 \times F4 + b17F2 \times F5 \\ & + b18F3 \times F4 + b19F3 \times F5 + b20F4 \times F5 \end{aligned} \tag{1}$$

Within Eq. (1), $F1$–$F5$ are the variable parameters, and $b0$–$b20$ are the coefficient values obtained through multiple linear regression (MLR) using EREGRESS. The response surface plots were obtained through a statistical process that described the design and the modeled CCD data. Response surface methodologies graphically illustrate relationships between parameters and responses and are the way to obtain an exact optimum [25,27–29].

As stated a complete central composite experiment design allows estimation of a full quadratic model such as Eq. (1) for each response, namely enrichment factor, recovery and sedimented phase volume. These kind of designs are easy to construct since they are based on multi-level factorials that have been augmented with the center point and $2n$ (n is the number of studied variables) extra star points [30]. The repeatability of the method can be assessed using the optimum obtained through a CCD.

The statistical significance of the full quadratic models predicted was evaluated by the analysis of variance (ANOVA) and least squares techniques. The ANOVA results in determination of which factors significantly affect the response variables in study, using a Fisher's statistical test (F-test). The significance and the magnitude of the estimated coefficients of each variable and all their possible linear and quadratic interactions on the response variables were determined. Such coefficient for each variable represents the expected increase in the response as the variable setting is changed from low to high. Effects with less than 95% of significance, i.e. effects with a p-value higher than 0.05, were discarded and pooled into the error term (often called residual error) and a new analysis of variance was performed for the reduced model. Note that the p-value represents a decreasing index of the reliability of a result [25]. Replicates ($n = 4$) of the central points were performed to estimate the experimental error.

3. Results and discussion

In this study a recently presented microextraction method, dispersive liquid–liquid microextraction, was investigated for enrichment of Cu^{2+} ions from aqueous samples followed by their determination by flame atomic absorption spectrometry. During DLLME, a μL volume of an extracting solvent is dissolved into a dispersive solvent at the mL level. The extracting solvent must have a density higher than that of the aqueous sample and the dispersive solvent must be miscible with both the organic extracting solvent and water. To extract the analyte, the dispersive solvent containing the extracting solvent is added to the analyte solution by a syringe. Thereby the extracting solvent is dispersed into the aqueous phase as tiny droplets. If a pipette is used for adding extraction solvent, the upper part of sample will be cloudy while by using a syringe the extraction solvent is added to the sample under pressure and it dispersed in all parts of sample. This technique is very rapid and efficient but there are many factors that should be optimized before its application. In this work, optimization was performed both via one variable at a time and with central composite design methods. Factors such as selection of the dispersive and extracting solvents and their volumes, sample size, pH, salting out effect, etc., were studied and the optimum conditions were selected. Enrichment factor was calculated using ratio of the analyte concentration in the sedimented phase to the analyte concentration in the aqueous sample. The analyte concentration in the sedimented phase was calculated from the direct calibration graph (0.1–$10\,\mathrm{mg\,L^{-1}}$ Cu^{2+} in $0.1\,\mathrm{mol\,L^{-1}}$ nitric acid) after dissolving residue into nitric acid.

3.1. One variable at a time method

3.1.1. Selection of dispersive and extracting solvents

Four solvents: methanol, acetone, tetrahydrofuran and acetonitrile, were studied as a dispersive solvent in this work. The selection of the extracting solvent is critical and should meet the following criteria: (1) it should dissolve the analyte better than water, (2) it should be heavier than water and (3) it should form tiny droplets when it is added to the aqueous solution of analyte along with a dispersive solvent. Almost all of the suitable extracting solvents are chlorinated. In this work, chloroform, carbon tetrachloride and dichloromethane were investigated. In Fig. 1 the EF is shown for all combinations of dispersive and extracting solvents. Regarding the EF, the combination of chloroform as extracting solvent with methanol as dispersive solvent is the best one and an EF higher than 60 is attainable. On the other hand, regarding recovery, the combination of chloroform

Table 1
The variables and values used for central composite design (CCD)

Variable name	Coded factor levels				
	−2 (low)	−1	0	+1	+2 (high)
Dispersion solvent volume, *F*1 (mL)	0	1	1.5	2	3
$CHCl_3$ volume, *F*2 (μL)	100	200	300	400	500
Cu^{2+} solution volume, *F*3 (mL)	5	10	15	20	25
pH, *F*4	2	4	6	8	10
NaCl amount per 5 mL, *F*5 (g)	0	0.1	0.3	0.5	1.0

Table 2
List of experiments in the CCD for model optimization (coded values) and the responses

Design points	Factors levels					Response		
	*F*1	*F*2	*F*3	*F*4	*F*5	Enrichment factor	Recovery (%)	Sedimented phase volume (μL)
1	−1	−1	−1	1	−1	63.6	49.3	94.3
2 (cp)[a]	0	0	0	0	0	50.8	48.8	169
3	−1	1	−1	1	1	27.2	65.1	295
4	1	1	1	1	1	68.5	66.2	228
5	−2	0	0	0	0	19.2	22.7	196
6 (cp)[a]	0	0	0	0	0	52.7	50.7	170
7	−1	−1	1	1	1	103	33.5	72
8	0	0	0	0	−2	49.4	44.3	158
9	1	−1	−1	−1	−1	131	61.3	64
10	0	0	2	0	0	66.9	29.9	118
11	−1	−1	−1	−1	1	51.7	47.6	112
12	0	−2	0	0	0	0	0	0
13	1	−1	1	1	−1	238	29.3	28
14	1	1	−1	−1	1	38.3	73.6	263
15	2	0	0	0	0	80.7	51.2	126
16	−1	1	1	−1	1	39.3	44.5	252
17	0	0	0	2	0	59.8	56.8	163
18	−1	1	1	1	−1	49.4	54.8	245
19	0	2	0	0	0	30.9	58.8	337
20	−1	1	−1	−1	−1	24.6	56.1	278
21 (cp)[a]	0	0	0	0	0	52.3	49.9	168
22 (cp)[a]	0	0	0	0	0	49.5	47.9	171
23	−1	−1	1	−1	−1	87.5	31.4	80
24	1	1	1	−1	−1	57.2	48.5	202
25	1	1	−1	1	−1	50.1	94	257
26	1	−1	−1	1	1	123	75.7	83
27	0	0	0	−2	0	43.3	45.1	183
28	0	0	0	0	2	34.2	32.7	176
29	0	0	−2	0	0	28.9	77.6	207
30	1	−1	1	−1	1	196	26.3	34

[a] Four center points.

and THF is optional (recovery is more than 70%). Considering the sedimented phase volume it was found that with the combination of chloroform and methanol the sedimented phase volume was about 90 μL whereas in the case of chloroform and THF it was about 650 μL. Therefore, the combination of chloroform and methanol was selected for further studies. Note that in the case of dichloromethane as extraction solvent and either THF or acetonitrile as dispersive solvents no sedimented phase was obtained and hence these conditions are useless.

3.1.2. Dispersive solvent volume

Methanol as a dispersive solvent in different volumes in the range 0–2.5 mL along with 200 μL chloroform as an extracting solvent was used for extraction of copper ions as its oxinate complex using the DLLME procedure. The obtained results (Fig. 2) show that in the case of 1.5 mL methanol the highest recovery and a reasonable EF and sedimented phase volume are attainable. With 3 mL or higher volume of methanol no sedimented organic phase was achieved.

3.1.3. Extracting solvent volume

Extracting solvent (chloroform) volumes on the EF and recovery of analyte, in the range of 50–500 μL were tested. As can be seen from the Fig. 3 there was no sedimented organic phase in the cases of 50 and 100 μL and the system became useless. By using 150 μL chloroform on the other hand, EF 84 and recovery 48% were obtained. The volume of sedimented phase was 43 μL in this condition. Therefore, we chose initially 150 μL

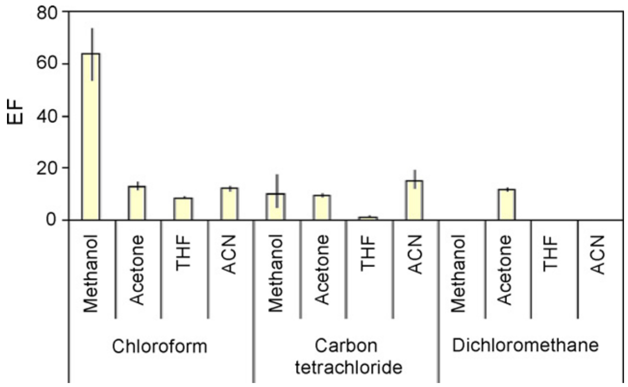

Fig. 1. Selection of extracting and dispersive solvents in DLLME. Conditions: sample, 5 mL Cu^{2+} 1 mg L^{-1}; volume of dispersive solvent, 2 mL; volume of extracting solvent, 200 μL; buffer, 1 mL acetate buffer ($C = 1$ mol L^{-1}, pH 6) and 8-hydroxy quinoline solution, 0.5 mL 0.05 mol L^{-1} in methanol. The bars show the maximum and minimum levels of determinations.

as an optimum volume of chloroform as extracting solvent for further study (optimization of sample size). But it was found that by using 150 μL chloroform, the system became useless at sample sizes larger than 15 mL owing to lack of sedimented phase. Hence, the volume of chloroform was chosen as 250 μL to permit investigation of lager sample sizes. Also recovery of more than 70% and sedimented phase volume about 140 μL were obtained by using 250 μL extracting solvent.

3.1.4. Sample volume

Different volumes of analyte solution (5–50 mL) were used to study the effect of sample size with a constant volume of extracting solvent (250 μL) and dispersive solvent (1.5 mL). The results (Fig. 4) show that with a large sample size (50 mL) no sedimented organic phase was obtained. By increasing the sample size from 5 to 40 mL, the volume of sedimented phase and recovery decreased whereas EF increased. In another study we selected a constant ratio of sample size to the volume of dispersive solvent (methanol). For this purpose, the methanol volume was selected 1.5, 3, 4.5, 6, 7.5, 9, 12 and 15 mL when the volume of sample was 5, 10, 15, 20, 25, 30, 40 and 50 mL, respectively. By this combination no sedimented phase was obtained at the sample volumes higher than 15 mL. We used 1.5 mL methanol and a sample size of 5 mL in the further studies due to higher recovery and reasonable EF and sedimented phase volume.

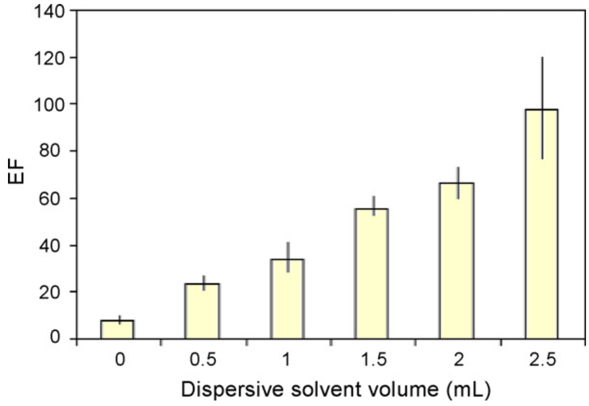

Fig. 2. Dispersive solvent volume study. Other conditions are the same as Fig. 1.

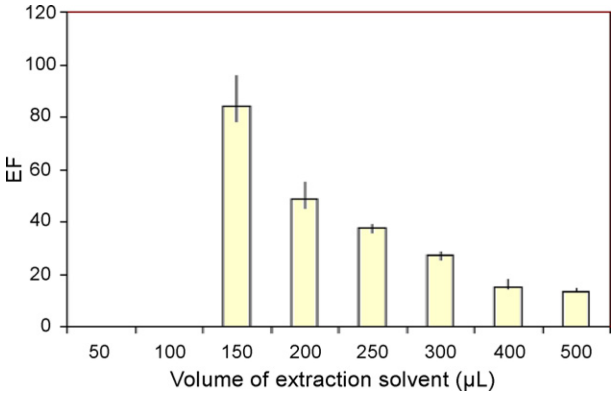

Fig. 3. Selection of extracting solvent volume. Other conditions are the same as Fig. 1.

3.1.5. Influence of pH

pH can play an important role in the producing extractable species from ionic analytes prior to extraction by DLLME. In this study 8-hydroxy quinoline was used as a complexing agent for Cu^{2+} ions to produce a neutral oxinate chelate, which is extractable into chloroform. Because the production of oxinate chelate is pH-dependent, DLLME was performed at different pH values in the range 2–12. The obtained results show that the pH does not influence the sedimented phase volume. The production of oxinate chelate and its extraction is pH-independent between pH 6 and 10. In this range the highest EF and recovery are obtained. Therefore, pH 6 was selected for the following studies.

3.1.6. Study of other parameters

Other parameters such as 8-hydroxy quinoline concentration, salting out effect and reaction time were studied. 8-hydroxy quinoline concentrations in the range of 0.001–0.1 mol L^{-1} in

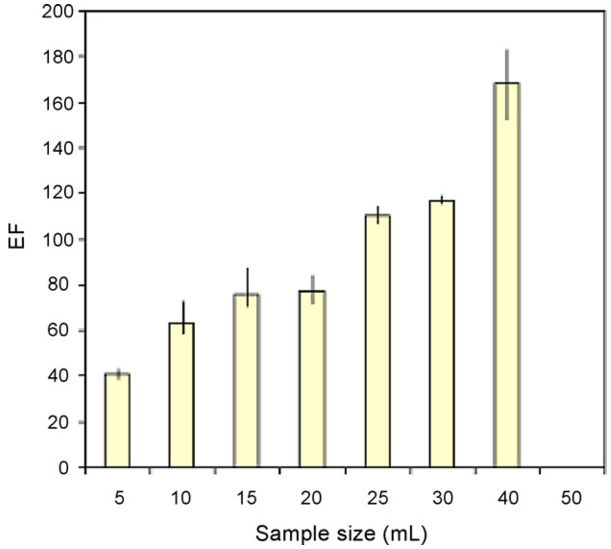

Fig. 4. Effect of sample size on the EF in the extraction of Cu^{2+} ions by DLLME. Other conditions are the same as Fig. 1.

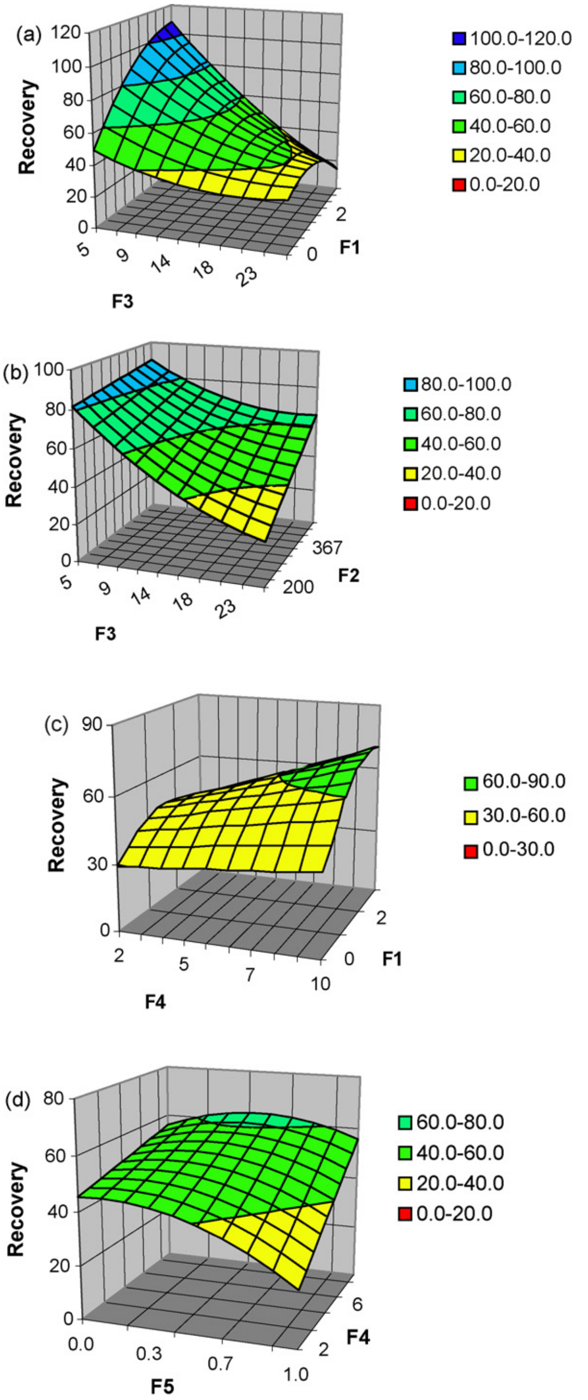

Fig. 5. Response surface of recovery modeling: dispersion solvent ($F1$), extracting solvent, $CHCl_3$ ($F2$), Cu^{2+} solution ($F3$), pH ($F4$) and salt (NaCl) amount ($F5$).

methanol did not influence the EF, recovery and sedimented phase volume.

Also, the influence of ionic strength on the extraction was studied with sodium chloride as a salting out agent at the concentrations of 0.02–0.2 g mL^{-1} and it was found that it has very little effect on the EF and recovery. However, by increasing sodium chloride concentration from 0.02 to 0.2 g mL^{-1}, the volume of sedimented phase was increased from 147 to 175 μL.

Reaction time also was studied over the range 0–10 min. It was defined as the time spent between addition of 8-hydroxy quinoline solution and the addition of extraction solvent (chloroform) dissolved in dispersive solvent (methanol). It was found that both the reaction and the extraction procedures are rapid and time did not affect on the EF, recovery and sedimented phase volume.

3.2. *Experimental design*

Three antagonist criteria namely enrichment factor, recovery and sedimented phase volume were investigated as responses in order to optimize five variables, namely the volumes of dispersion solvent ($F1$), extracting solvent ($F2$), Cu^{2+} solution volume ($F3$), the pH ($F4$) and the salt (NaCl) amount ($F5$). These five parameters were chosen to be optimized simultaneously among all parameters based on their importance and their probably interaction. Tables 1 and 2 present the levels of coded and actual experimental variables that were tested. Also Table 2 presents the corresponding responses.

The aims of the CCD strategy were: (i) to maximize the EF and recovery and give the optimum conditions to obtain a suitable volume of sedimented phase; (ii) to determine which variables have a higher impact on extraction recovery and enrichment factor; (iii) to give an insight on the robustness of the method close to the optimum conditions and (iv) show possible variable interactions.

In order to find the important factors and build a model to optimize the procedure, we start with a full quadratic model including all terms as in Eq. (1). To obtain a simple and yet a realistic model, the insignificant terms ($P > 0.05$) were eliminated from the model through the 'backward elimination' process. The main characteristics of the reduced models are given in Tables 3 and 4.

In the present study, the adjusted R^2 were well within the acceptable limits of $R^2 \geq 0.9$ and there is not too large differences between R^2s which revealed that the experimental data shows a good fit with the second-order polynomial equations (see Table 4).

The plots of predicted responses versus calculated ones showed that the residual values are significantly low (for example the regression equation for predicted recovery versus calculated ones are obtained as $Y = 0.9224X + 3.9413$, $R^2 = 0.9224$). This allows us to further use the response surface as a predictive tool to obtain responses over the whole parameter uncertainty range.

From the constructed models the following results could be obtained (Tables 3 and 4):

- Dispersion solvent ($F1$) and Cu^{2+} solution ($F3$) volumes, affect significantly the recovery modeling by both linear and quadratic variables. Also NaCl amount ($F5$), has a slight quadratic effect in this model. The main interaction variables for recovery modeling were obtained as $F1 \times F3$, $F1 \times F4$, $F2 \times F3$ and $F4 \times F5$.
- When using EF as model response, dispersion solvent ($F1$) and Cu^{2+} solution ($F3$) affect the model by only linear

Table 3
Some characteristics of the constructed models

Response	R^2	R^2 adjustment	R^2 for prediction	Regression equations
Enrichment factor (EF)	0.965	0.932	0.778	$\text{EF} = b0 + b1F1 + b2F2 + b3F3 + b4F1 \times F2 + b5F1 \times F3 + b6F2 \times F2 + b7F2 \times F3 + b8F3 \times F4$
Recovery	0.960	0.922	0.708	$\text{Recovery} = b0 + b1F1 + b2F3 + b3F1 \times F1 + b4F1 \times F3 + b5F1 \times F4 + b6F2 \times F3 + b7F3 \times F3 + b8F4 \times F5 + b9F5 \times F5$
Sedimented phase volume	0.997	0.995	0.989	$\text{Sedimented phase volume} = b0 + b1F1 + b2F2 + b3F4 + b4F1 \times F3 + b5F1 \times F4 + b6F2 \times F5 + b7F3 \times F3$

Table 4
Constants and coefficients for the constructed quadratic models (equations presented in Table 3) for each response

	Recovery		Enrichment factor (EF)		Sedimented phase volume	
	Uncoded values	Coded values	Uncoded values	Coded values	Uncoded values	Coded values
*b*0	60.67	50.81	106.64	67.83	−32.78	169.98
*b*1	36.34	25.82	75.77	53.84	−25.72	−18.27
*b*2	−4.861	−22.50	−0.903	−76.05	0.874	73.61
*b*3	−5.704	−11.81	6.657	30.82	−3.262	−6.041
*b*4	−1.288	−15.83	−0.245	−59.05	−0.743	−9.128
*b*5	1.133	5.571	2.008	24.68	2.391	11.76
*b*6	0.00543	10.39	0.00187	100.63	0.06536	4.655
*b*7	0.07905	11.16	−0.02262	−43.33	−0.104	−14.69
*b*8	3.022	4.363	0.194	7.779		
*b*9	−30.33	−5.833				

variables. The model shows that extracting solvent, $CHCl_3$ ($F2$) has significant linear and quadratic effects. Also the main interaction variables for this model were found as $F1 \times F2$, $F1 \times F3$, $F2 \times F3$, $F3 \times F4$. As results show, the NaCl amount ($F5$), has no significant effect on the enrichment factor modeling.

- For the sedimented phase volume as response an abstract model has been obtained that shows the important linear, quadratic and interacting variables are $F1$, $F2$, $F4$, $F3 \times F3$, $F1 \times F3$, $F1 \times F4$ and $F2 \times F5$. It is clear from the results and the coefficient values $F2 \times F5$ is one of the most significant variables for the sedimented phase volume response modeling. From chemical aspect this is due to salting effect of NaCl ($F5$) on the extraction the analyte into $CHCl_3$ ($F2$).

3.3. Response surface and selection of optimum conditions

The obtained regression models were used to calculate the response surface for each variable separately. Fig. 5 shows response surface plots for recovery, EF and sedimented phase volume, respectively. This figure shows the interaction between the interacting factors when the remaining factors have been kept on the fixed amount using the constructed model by EREGRESS software.

The surface plot of recovery response (Fig. 5a) showed a pronounced decrease as the volume of Cu^{2+} ($F3$) is increased. Oppositely the response surface of EF (not shown) showed a pronounced increase as the volume of Cu^{2+} ($F3$) is increased. Also increasing the extracting solvent volume ($F2$) has antagonist effect. That is increasing will increase recovery (Fig. 5) while decrease the enrichment factor (not shown).

The selection of optimum conditions is possible from the response surface plots. The results demonstrated that most of the response surfaces have nearly flat optimum areas. Therefore, a range of variations for the investigated factors can be chosen simply. For example if the criteria are set as follows: recovery near to 100%, sedimented phase volume more than 50 μL and enrichment factor as high as possible, the conditions that meet these requirements are presented in Table 5.

3.4. Analytical features of DLLME of Cu^{2+} ions

Under the optimum conditions obtained by one variable at a time optimization; sample size, 5 mL; volume of dispersive solvent (methanol), 1.5 mL; extracting solvent (chloroform) volume, 250 μL; buffer, 1 mL acetate buffer ($C = 1\ \text{mol L}^{-1}$, pH 6) and volume of 8-hydroxy quinoline solution, 0.5 mL $0.05\ \text{mol L}^{-1}$ in methanol, some analytical characteristics of the proposed DLLME method were obtained. Calibration curve is linear ($A = 2.8 \times 10^{-4} C + 1.87 \times 10^{-3}$, A = absorbance and C = concentration of Cu^{2+} in $\mu\text{g L}^{-1}$) over the range 10–2000 $\mu\text{g L}^{-1}$. Square of correlation coefficient (R^2) is 0.998. The limit of detection (LOD) (S/N = 3), limit of quantification (S/N = 10) and the relative standard deviation (R.S.D.%) ($n = 6$, $C = 500\ \mu\text{g L}^{-1}$) are 3, 10 $\mu\text{g L}^{-1}$ and 5.1%, respectively. In another study EF, relative enrichment factor (REF) (EF/EF_{max}, EF_{max} is the ratio of sample volume to sedimented phase volume) and recovery were obtained in three different concentrations of analyte and the results summarized in Table 6. EF, REF and recovery were obtained in the ranges 42–48, 0.76–0.86 and 76–87%, respectively. It can be observed that the recovery and the relative enrichment factor agree well, as expected.

Table 5
Optimum conditions obtained by response surface modeling

Variable name	Optimum values			
	Recovery[a] (%)	Enrichment factor[b]	Sedimented phase volume[c]	Selected optimum value[d]
Dispersion solvent volume, *F*1 (mL)	1.5–2.5	3	As low as possible	1.5
$CHCl_3$ volume, *F*2 (μL)	>200	<300	>100 depending to F5	200–300
Cu^{2+} solution volume, *F*3 (mL)	5	>20	<30	20–30
pH, *F*4	6–10	Low effect	Low effect	6–10
NaCl amount per 5 mL, *F*5 (g)	0.2–0.5	No effect	>0.2 depending to F2	0.2–0.5

[a,b,c] The criteria are set as the recovery near to 100%, the enrichment factor as high as possible and the sedimented phase volume more than 50 μL.
[d] The compromise conditions that meet requirements as much as possible.

Table 6
Repeatability study in different concentrations of analyte

Concentration (μg mL^{-1})	Mean EF ± S.D.[a]	REF ± S.D.[a]	Mean recovery ± S.D.[a] (%)
0.50	48 ± 3	0.857 ± 0.062	87 ± 5
1.00	42 ± 2	0.785 ± 0.037	78 ± 4
2.00	42 ± 1	0.761 ± 0.022	76 ± 2

[a] Standard deviation with *n* = 3.

Table 7
Study of interfering ions

Interfering ions	Tolerable concentration (analyte:interfering ion)[a]
Ni^{2+}, Zn^{2+}, Fe^{2+}	1:1
–	1:10
PO_4^{3-}, SO_4^{2-}, NO_3^-, Mg^{2+}, Ca^{2+}, Cr^{3+}, K^+, Hg^{2+}, Fe^{3+}, Pb^{2+}	1:100

Concentration of analyte is 0.5 μg mL^{-1}.
[a] At this ratio no interfering effect was observed.

3.5. Study of interferences

Interferences were studied in the presence of a constant concentration of analyte (0.5 μg mL^{-1}) and different amounts of foreign ions (analyte:foreign ion ratio 1:1, 1:10 and 1:100). Tolerable concentration of foreign ions was considered that concentration in which less than 10% deviation in absorbance reading was observed in comparison with the case in which interfering ion was absent. The obtained results are given in Table 7. As can be seen most ions studied do not have interfering effect at 1:100 ratio. Nickel (II), zinc (II) and iron (II) do not interfere at 1:1 ratio but have serious interference effect at 1:10 ratio.

3.6. Application of the proposed DLLME method to real samples and comparison with a standard method

To evaluate the efficiency of the proposed DLLME method, five water samples including tap water, two river waters (Dozal river and Aras river taken at two points) and mineral water were selected and the proposed DLLME method as well as a standard method [31] were applied to determine the copper content. In the DLLME method standard addition technique was used. For the standard method Cu^{2+} ions were extracted as the pyrrolidine chelate into methyl isobutyl ketone and then the absorbance of organic phase was read using flame atomic absorption spectrometry at atomic line of copper. The obtained results are summarized in Table 8. In three samples, tap water, Dozal river water and mineral water, analyte was not detected by any of the methods. In Aras river water sampled in two points, the obtained concentrations by both methods are in agreement.

A recovery test performed on the samples showed that in all cases the obtained relative recoveries (in comparison with recoveries in distilled water) are between 91 and 107% with R.S.D.% less than 12%, which indicate that no matrix effect was observed. The added concentrations were in the range of 100–500 μg L^{-1}.

Table 8
Cu^{2+} content of different water samples obtained by the proposed method and standard flame atomic absorption spectrometry performed on the samples after extraction of copper as its pyrrolidine complex into methyl isobutyl ketone

Sample	Cu^{2+} concentration (μg L^{-1}) obtained by	
	This method[a]	Standard method[b]
Tap water	ND[c]	ND
Dozal river water	ND	ND
Aras river water (point 1)	131	117 ± 10.9
Aras river water (point 2)	97.2	106 ± 12.9
Mineral water	ND	ND

[a] Obtained by standard addition method.
[b] Mean ± standard deviation (*n* = 3).
[c] Not detected.

4. Conclusion

A dispersive liquid–liquid microextraction method was used for preconcentration of Cu^{2+} ions prior to determination by flame atomic absorption spectrophotometric technique. Enrichment factor and recovery for the target analyte were obtained about 42 and 78%, respectively. The proposed extraction method was used for the quantitation of Cu^{2+} ions in different water samples and the obtained results were compared to those obtained by a standard method. A relatively good agreement was observed between them. The method is simple, efficient and very rapid and it uses extracting solvent at a μL level.

References

[1] B. Zygmunt, A. Jastrzebska, J. Crit. Rev. Anal. Chem. 31 (2001) 1.
[2] H.G. Liu, P.K. Dasgupta, Anal. Chem. 68 (1996) 1817.
[3] M.A. Jeannot, F.F. Cantwell, Anal. Chem. 68 (1996) 2236.
[4] M.A. Jeannot, F.F. Cantwell, Anal. Chem. 69 (1997) 235.
[5] S. Pedersen-Bjergaard, K.E. Rasmussen, Anal. Chem. 71 (1999) 2650.
[6] Y. He, H.K. Lee, Anal. Chem. 69 (1997) 4634.
[7] L.M. Zhao, L.Y. Zhu, H.K. Lee, J. Chromatogr. A 963 (2002) 239.
[8] Y.L. Wu, Z.C. Jiang, B. Hu, Chem. J. Chin. Univ. 24 (2003) 1793.
[9] L.B. Xia, B. Hu, Z.C. Jiang, Y.L. Wu, Y. Liang, Anal. Chem. 76 (2004) 2910.
[10] L.B. Xia, B. Hu, Z.C. Jiang, Y.L. Wu, L. Li, R. Chen, J. Anal. At. Spectrom. 20 (2005) 441.
[11] L. Li, B. Hu, L. Xia, Z.C. Jiang, Talanta 70 (2006) 468.
[12] S. Igarashi, S. Oshite, Bunseki 2 (1997) 702.
[13] K. Murata, S. Ikeda, Bunseki Kagaku 18 (1969) 1137.
[14] C.E. Matkovich, G.D. Christian, Anal. Chem. 45 (1973) 1915.
[15] L.H.M. da Silva, W. Loh, J. Chem. Soc., Chem. Commun. 4 (1998) 1189.
[16] S. Igarashi, N. Ide, Y. Takagai, Anal. Chim. Acta 424 (2000) 263.
[17] T. Sudo, S. Igarashi, Talanta 43 (1996) 233.
[18] S. Igarashi, A. Takahashi, Y. Ueki, H. Yamaguchi, Analyst (Communications) 125 (2000) 797.
[19] A. Takahashi, S. Igarashi, Solv. Extr. Res. Dev. Jpn. 6 (1999) 61.
[20] A. Takahashi, Y. Ueki, S. Igarashi, Anal. Chim. Acta 387 (1999) 71.
[21] S. Oshite, S. Igarashi, J. Chem. Technol. Biotechnol. 74 (1999) 1183.
[22] S. Berijani, Y. Assadi, M. Anbia, M.R. Milani-Hosseini, E. Aghaee, J. Chromatogr. A 1123 (2006) 1.
[23] M. Rezaee, Y. Assadi, M.R. Milani-Hosseini, E. Aghaee, F. Ahmadi, S. Berijani, J. Chromatogr. A 1116 (2006) 1.
[24] M.A. Farajzadeh, M. Bahram, J.Å. Jönsson, Anal. Chim. Acta 591 (2007) 69.
[25] D.D. Stephan, J. Werner, R.P. Yeater, Essential regression and experimental design for chemists and engineers, MS Excel Add-in Software Package, 1998–2001.
[26] J. Bulacov, J. Jirkovsky, M. Muller, R.B. Heimann, Surf. Coat. Technol. 201 (2006) 255.
[27] A.M. Siouffi, R. Phan-Tan-Luu, J. Chromatogr. A 892 (2000) 75.
[28] T. Lundstedt, E. Seifert, L. Abramo, B. Thelin, A. Nystrom, J. Pettersen, R. Bergman, Intell. Lab. Syst. 42 (1998) 3.
[29] P.W. Araujo, R.G. Brereton, Trend Anal. Chem. 15 (1996) 63.
[30] P.A.J. Rosa, A.M. Azevedo, M.R. Aires-Barros, J. Chromatogr. A 1141 (2007) 50.
[31] Standard Methods for the Examination of Water and Wastewater, 20th ed., American Public Health Association, Washington, DC, USA, 1998.

Available online at www.sciencedirect.com

ScienceDirect

Talanta 75 (2008) 804–810

Talanta

www.elsevier.com/locate/talanta

Simultaneous determination of methanol and ethanol in gasoline using NIR spectroscopy: Effect of gasoline composition

Heitor L. Fernandes, Ivo M. Raimundo Jr, Celio Pasquini, Jarbas J.R. Rohwedder*

Instituto de Química, UNICAMP, CP 6154, CEP 13084-971, Campinas, Brazil

Received 18 August 2007; received in revised form 10 December 2007; accepted 12 December 2007
Available online 27 December 2007

Abstract

Near infrared (NIR) spectroscopy was employed for simultaneous determination of methanol and ethanol contents in gasoline. Spectra were collected in the range from 714 to 2500 nm and were used to construct quantitative models based on partial least squares (PLS) regression. Samples were prepared in the laboratory and the PLS regression models were developed using the spectral range from 1105 to 1682 nm, showing a root mean square error of prediction (RMSEP) of 0.28% (v/v) for ethanol for both PLS-1 and PLS-2 models and of 0.31 and 0.32% (v/v) for methanol for the PLS-1 and PLS-2 models, respectively. A RMSEP of 0.83% (v/v) was obtained for commercial samples. The effect of the gasoline composition was investigated, it being verified that some solvents, such as toluene and *o*-xylene, interfere in ethanol content prediction, while isooctane, *o*-xylene, *m*-xylene and *p*-xylene interfere in the methanol content prediction. Other spectral ranges were investigated and the range 1449–1611 nm showed the best results.

Keywords: Alcohol; Methanol; Ethanol; Gasoline; Near infrared spectroscopy; Multivariate calibration; PLS

1. Introduction

Gasoline is a sub-product from the fractional distillation of petroleum, being a complex mixture of hydrocarbons containing from 4 to 12 carbon atoms [1,2]. The gasoline produced at the beginning of the 20th century was composed of hydrocarbons having 10–16 carbon atoms, which was a low octane number fuel. During the last century, new production processes were developed to obtain fuel with higher octane numbers that could be used in vehicles with high compression engines. Aiming to increase the octane number, additives are often added to the gasoline. Some additives, such as tetraethyl lead, contribute to increase atmospheric pollution, while methyl-*tert*-butyl-ether (MTBE) has caused contamination of underground waters [3,4].

In recent last decades, gasoline having the addition of methanol or ethanol has been produced, resulting in a less polluting fuel, while keeping the octane number at the appropriate level for the current necessities of engines of light vehicles. Moreover, another advantage of these additives is that they could be obtained from renewable sources, such as sugarcane (ethanol) and cellulose (methanol) [5].

Methanol and ethanol, both anhydrous, are added to the gasoline in many countries around the world, generally in the ratio of 10% (v/v). In Brazil, the percentage of ethanol is officially established [6], usually varying between 20 and 25% (v/v), although lower concentrations are admitted, depending on the regional difficulties of obtaining this product from the national market.

During the ethanol crisis of 1989 in Brazil, alternative additives were investigated to be incorporated into the gasoline, such as, the oxygenated compounds from petroleum (MTBE, ethyl-*tert*-butyl-ether and TAME, *tert*-amyl-methyl-ether). At that time, in addition to a reduction of the amount of anhydrous ethanol added to the gasoline, a new fuel called MEG (33%, v/v of methanol + 60%, v/v of ethanol + 7%, v/v of gasoline) was proposed. Although its production had been authorized, its commercialization was considered dangerous due to methanol manipulation, finally being abandoned [7]. The addition of methanol to gasoline is currently forbidden in Brazil, however in some countries, such as the USA, it is still used [8].

Although methanol has not been the most used compound for gasoline adulteration, its addition is not detected if only the extraction test based on the volume increase of the aque-

---

* Corresponding author.
E-mail address: jarbas@iqm.unicamp.br (J.J.R. Rohwedder).

0039-9140/$ – see front matter © 2007 Elsevier B.V. All rights reserved.
doi:10.1016/j.talanta.2007.12.025

ous phase (ABNT-NBR 13992) is carried out [9]. Although simple and efficient for the determination of the ethanol content in the gasoline, the extraction test cannot distinguish between methanol and ethanol, making this type of adulteration practically undetected at the moment of the inspection, if part or all of ethanol content in gasoline is substituted by methanol.

Due to the high fuel consumption, it has became more and more necessary to develop fast analytical methods that allow determination of different quality parameters by means of a single analysis. Among several instrumental analytical techniques, near infrared (NIR) spectroscopy has been revealed as promising for the quantitative determination of a great variety of chemical species. This fact is associated with its main characteristics, such as speed of attaining of the results, minimum sample preparation, low residue generation, easy adaptation to a production line and direct application in the field. Moreover, a single spectrum can give simultaneous information about the sample properties and its constituents [10].

Various studies have demonstrated the possibility of applying NIR spectroscopy for quality control of fuels [11–26]. Physical parameters, such as motor octane number (MON) and research octane number (RON), density, distillation temperature and vapor pressure Reid (VPR) can be determined by NIR spectroscopy, in many cases with precision and accuracy comparable to the standard method [17]. Other studies show the possibility of simultaneous determination of aromatic, unsaturated and saturated hydrocarbons content [24], MTBE [25] and sulfur [17,26]. Methanol [14] and ethanol [25,27] have been determined separately in gasoline using NIR spectroscopy. However, there are no studies demonstrating the possibility of simultaneous determination of methanol and ethanol in gasoline or how the gasoline composition can affect the determination of these alcohols.

Thus, this work is aimed at applying NIR spectroscopy, together with multivariate calibration (partial least squares, PLS), for the simultaneous determination of methanol and ethanol, verifying the robustness of the calibration models when confronted with alterations in the gasoline composition.

2. Experimental

2.1. Instrumentation and procedure for spectra acquisition

A FT-NIR spectrometer (Bomem, model MD-160) provided with a flow cuvette of 10 mm pathlength and 80 μL internal volume (Hellma, model 178.710-QS) was used for spectra acquisition between 14000 and 4000 cm^{-1} (714 and 2500 nm), with resolution of 8 cm^{-1}. The sample was pumped into the interior of the cuvette by a peristaltic-pump (Ismatec, model 7331-00) using Viton® tubing and Teflon® conduction tubing (0.8 mm i.d.). To prevent contamination between samples, before acquisition of each spectrum the cuvette was cleaned by initially pumping air and then 5 mL of gasoline sample. The pumping was interrupted during spectra acquisition. The spectrum of the empty cuvette was used as reference for absorbance measurements.

2.2. Sample set

A set formed by 120 samples containing methanol and ethanol, both in the concentration range from 0 to 30% (v/v), was prepared by the addition of known aliquots of methanol (Vetec 99.8%, v/v) and ethanol (Santa Cruz 99.5%, v/v) in to alcohol-free gasoline (gasoline type A, Petrobras). A multivariate calibration model was constructed with 80 samples, while 40 samples were used to verify the prediction capacity of the model (external validation set). To evaluate the precision of the proposed method, four replicates of type A gasoline samples were prepared containing methanol and ethanol mixtures in concentration of 2.5:2.5; 2.5:20.0; 15.0:12.5; 25.0:25.0 and 30.0:2.5% (v/v), respectively.

The proposed method was evaluated for the determination of the alcohol contents in 15 commercial gasoline samples containing ethanol (type C gasoline), commercialized in the Campinas Metropolitan Region, SP. The results were compared with the values of alcohol content determined by the standard method ABNT-NBR 13992 [9]. The procedure for NIR spectra acquisition of these samples was identical to those described above.

2.3. Gasoline composition alteration

The composition of type A gasoline was modified by addition of different hydrocarbons normally present in this fuel. Thus, *n*-hexane (Acros, 95.0%, HPLC grade), isooctane (Aldrich, 99.0%, HPLC grade), *o*-xylene (Acros, 98.0%, HPLC grade), *m*-xylene (Acros, 99.0%, HPLC grade), *p*-xylene (Acros, 99.0%, HPLC grade) and toluene (Acros, 99.0%, HPLC grade) in the concentration range from 1.0 to 8.0% (v/v) were added to type A gasoline. Later, methanol and ethanol were added to these mixtures in the concentrations of 10.0 and 25.0% (v/v), respectively.

2.4. Pre-processing and construction of calibration models

For the construction of the multivariate calibration model, using partial least squares (PLS-1 and PLS-2), initially all sample spectra were evaluated by Principal Component Analysis (PCA) with the purpose of observing their distribution and the existence of clusters and outliers. Pre-processing procedures based on baseline correction and first derivative were evaluated. Calculations were performed with Unscrambler® 9.2 (CAMO, Oslo, Norway).

3. Results and discussion

3.1. Construction of the calibration model and external validation

Fig. 1 shows the spectra of samples of gasoline containing methanol and ethanol, both in the concentration range of 0–30% (v/v), for the spectral range between 1105 and 1682 nm. In the inset of Fig. 1, it is possible to observe the full spectral range from 714 to 2500 nm. Under the experimental conditions employed, below 1105 nm absorption signals are practically inexistent, whereas above 1682 nm high absorption values are observed.

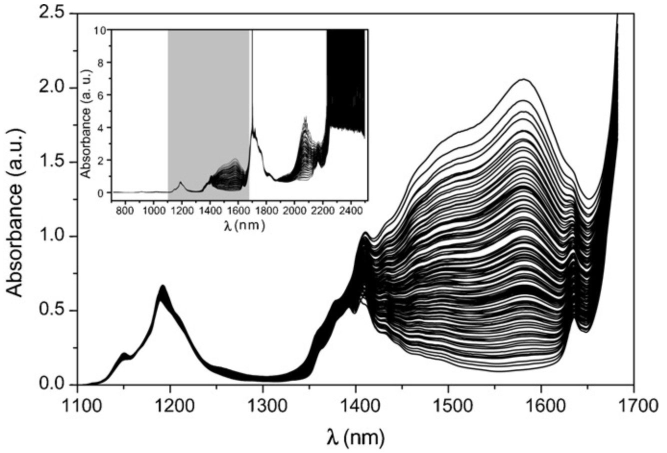

Fig. 1. Spectra of 120 gasoline samples with different methanol and ethanol contents in the spectral range from 1105 to 1682 nm. In the inset, the spectra in the range from 714 to 2500 nm are represented, and the range used is shaded. The range above 2200 nm presents high absorption, due to the use of a 10 mm pathlength cell.

Thus, the spectral range between 1105 and 1682 nm was selected for the construction of the calibration models. In this range, an intense absorption band between 1120 and 1270 nm is observed, referring to the 2nd overtone of the C–H bond stretching from the diverse hydrocarbons and the alcohols that compose the samples. Another band, also wide, between 1350 and 1670 nm, results from the overlapping of two absorption bands. The first, located between 1350 and 1550 nm, is related to first overtone of the combination band from C–H + C–H and C–H + C–C stretching and, the second, between 1400 and 1670 nm, is related to the first overtone of O–H stretching from the alcohols (methanol and ethanol). It is also possible to observe, above of 1650 nm, the beginning of the first overtone from aromatic C–H stretching.

Before initiating the construction of the calibration models, the presence of anomalous samples was verified by means of Principal Component Analysis (PCA). The results showed the existence of two samples, which presented distinct spectral behavior after baseline correction and, therefore, they were removed from the sample set. Several possible causes may contribute for the appearance of an anomalous sample, the most common coming from errors in sample preparation or problems that occurred at the moment of spectra acquisition, such as the presence of air bubbles in the optical path.

After outlier elimination, the 118 remaining samples were used, initially, to evaluate the best spectral data pre-processing technique for the construction of the calibration model. Table 1 shows the results found for methanol and ethanol calibration models. The constructed models involved the use of spectra without any type of pre-processing and spectra whose baseline was corrected and/or to which first derivative was applied. In all procedures of construction of the calibration models, data were mean centered and full cross validation was employed for internal validation.

It was observed that calibration models for methanol and ethanol presented the lowest values of the root mean square error of cross validation (RMSECV) for the spectra set when the first derivative was applied with or without baseline correction. For these models, a maximum number of 4 latent variables (LV) was necessary to explain at least 99% of the spectral. Thus, these results demonstrate that optimum pre-processing is obtained by the application of first derivative in the original spectral signals, and that the prior correction of the baseline before the application of the derivative does not improve the quality of the models.

Then, the 118 samples were divided into two sets, where 2/3 (78 samples) were used for the construction of the calibration models for methanol and ethanol and 1/3 (40 samples) were used in the external validation set. In this last set, samples were selected carefully to represent all the concentration range without, however, including samples whose concentration of either alcohol was at the minimum or at the maximum. Moreover, they also included the samples prepared in replicates ($n = 4$) aiming to evaluate the precision of the model.

Calibration models using PLS-1 (individual calibrations for methanol and ethanol) and PLS-2 (simultaneous calibration for both alcohols) were constructed. The models employed the first derivative of the original spectra, mean centering and full cross-validation. Table 2 shows the results for predictions of the methanol and ethanol contents of 40 samples of the external validation set. The values of root mean square error of prediction (RMSEP) obtained for ethanol for PLS-1 and PLS-2 were equal 0.28% (v/v), whereas for methanol this value was 0.31% (v/v) for PLS-1 and 0.32% (v/v) for PLS-2. These results indicate that both procedures can be used for methanol and ethanol determination when both or only one alcohol is present in gasoline. For the constructed models, a maximum of four latent variables was used.

The accepted absolute error for the determination of alcohol content in gasoline is ±1% (v/v) (relative error of ±4%, considering the concentration of 25% (v/v) of alcohol in the gasoline). In this way, it can be observed that the accuracy in

Table 1
Results obtained by calibration models (PLS-1) for methanol (0–30%, v/v) and ethanol (0–30%, v/v) in gasoline, employing different types of pre-processed NIR spectra (gasoline C samples prepared in the laboratory; spectral range from 1105 to 1682 nm; RMSEC, root mean square error of calibration; R, correlation between the predicted and expected values; LV, number of latent variables)

Type of pre-processing	Methanol			Ethanol		
	RMSECV (%, v/v)	R	LV	RMSECV (%, v/v)	R	LV
No pre-processing	0.650	0.998	4	0.787	0.993	3
Base line correction	0.573	0.998	3	0.814	0.993	2
First derivative	0.297	0.999	3	0.459	0.998	3
Base line correction and first derivative	0.297	0.999	3	0.459	0.998	3

Table 2
Results obtained for determination of methanol and ethanol in samples of the external validation set using the calibration models constructed with PLS-1 and PLS-2 (spectral range from 1105 to 1682 nm and first derivative spectra; RMSEP, root mean square error of prediction, *R*, correlation between predicted and expected values)

Alcohol	Model	RMSEP	Slope	Intercept	*R*
Methanol	PLS-1	0.31	0.9988	0.1740	0.9996
	PLS-2	0.32	0.9989	0.1769	0.9996
Ethanol	PLS-1	0.28	0.9935	0.0044	0.9996
	PLS-2	0.28	0.9933	0.0111	0.9996

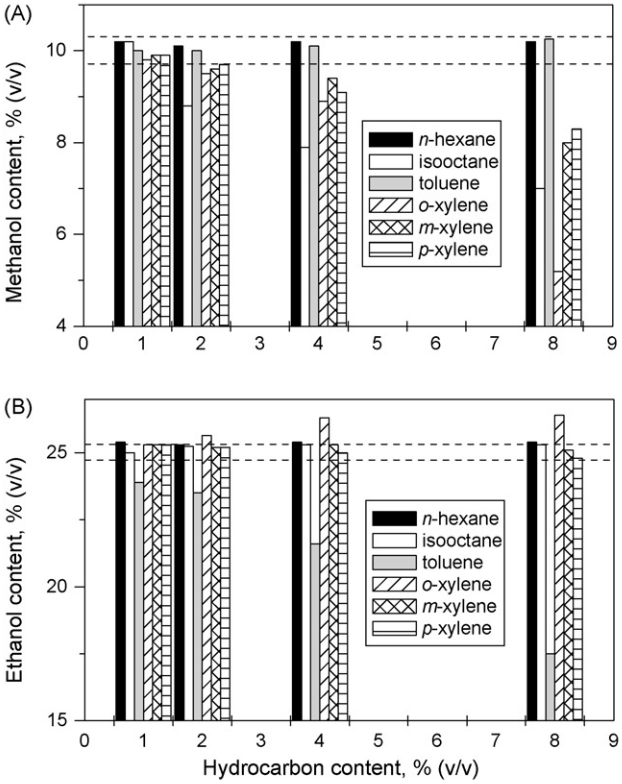

Fig. 2. Results obtained for determination of methanol (A) and ethanol (B) in gasoline samples whose composition was modified by addition of different hydrocarbons. The horizontal lines indicated in each figure were traced based on expected concentration values for methanol (10.0%, v/v) and ethanol (25.0%, v/v) and the root mean square error of prediction (RMSEP) from models (Table 2). The model was constructed using PLS-2 and the spectral range from 1105 to 1682 nm. Results represent averages of two determinations.

the alcohol content determination in gasoline, when NIR spectroscopy is used, is at least three times better than the standard method. The average repeatability expressed by the estimated standard deviation for the proposed method ($n = 4$) was 0.29% for methanol and 0.19% for ethanol, evaluated for gasoline samples containing ratios of 2.5:2.5; 2.5:20.0; 15.0:12.5; 25.0:25.0 and 30.0:2.5% (v/v) of methanol and ethanol, respectively. These results demonstrate that the method presents superior repeatability compared to the standard method, being capable to differentiate methanol and ethanol when the concentration ratio between these alcohols is higher than 10 times (30.0:2.5%, v/v methanol:ethanol).

3.2. *Effect of gasoline composition on the determination of alcohol*

Gasoline compositions may vary depending on the origin of the oil used in its production and on the processing characteristics of a given refinery. This fact can affect the determination of different species using NIR spectroscopy, if the total variability of the sample matrix is not considered in the construction of the calibration model. Thus, this work also evaluated the effect of gasoline composition on the determination of methanol and ethanol. Changes in the sample matrix were simulated by the addition of linear, branched and aromatic hydrocarbons, commonly found in some gasolines A, before preparing the solutions containing the alcohols. Hydrocarbons such as *n*-hexane, isooctane, toluene, *o*-xylene, *m*-xylene and *p*-xylene were added to gasoline in the concentration range from 1.0 to 8.0% (v/v), followed by the addition of appropriate volumes of methanol and ethanol in order to make their final concentrations equal to 10.0% (v/v) and to 25.0% (v/v), respectively. These samples had their contents of methanol and ethanol predicted by the PLS model constructed with the original gasoline composition, whose results are shown in Fig. 2. The interrupted horizontal lines in each figure indicate the interval of concentrations delimited by the value of the RMSEP obtained from the models shown in Table 2, around the expected reference values for the alcohol concentrations in the samples.

It is possible to observe in Fig. 2A that the addition of *n*-hexane and toluene in gasoline in the 1.0–8.0% (v/v) range does not affect the prediction of methanol contents in gasoline, as the results are inside of the accepted interval (RMSEP) of the proposed method. On the other hand, the presence of others hydrocarbons (isooctane, *o*-xylene, *m*-xylene and *p*-xylene) at concentrations levels higher than 2.0% (v/v) significantly affect the determination of methanol content, with prediction values lower than the expected values. For instance, the addition of *o*-xylene at 8.0% causes a relative error of −48% in prediction of methanol content.

For the determination of ethanol (Fig. 2B), it is observed that the presence of 8.0% (v/v) of toluene as well as *o*-xylene in the fuel causes relative errors of −30% and +6%, respectively. The addition of other hydrocarbons did not produce interferences in ethanol content prediction in gasoline, as the results are inside of the expected interval, considering the root mean square error of prediction (RMSEP) of the model.

These results indicate that the variation of gasoline composition significantly affects methanol and ethanol determination when multivariate calibration models are constructed from NIR spectra. This type of interference can be totally prevented if the sample set used in the construction of the calibration model represents the total variability of gasoline composition. However, the construction of a global model would be very difficult because it will requires the inclusion of samples from different regions according with the variation of the gasoline composition, which, by its time, is dependent on the crude oil source. Local models are easily constructed, because the gasoline composition variability can be accomplished with the use of relatively few samples. Furthermore, in cases in which it is not possible to

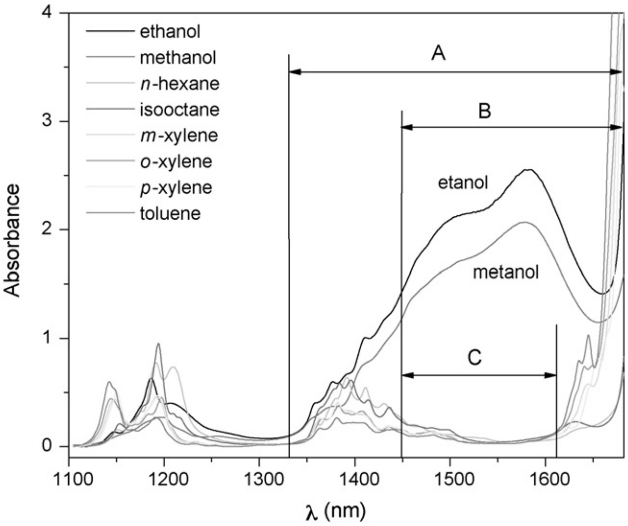

Fig. 3. Spectra of the hydrocarbons used for alteration of the gasoline matrix and of the alcohols studied. A–C are defined in the text.

prepare samples that represent matrix variations, the selection of variables or spectral ranges can lead to the construction of more robust models.

3.3. Selection of the spectral regions

Fig. 3 shows NIR spectra of methanol, ethanol and hydrocarbons used in the study of modification of the gasoline composition. It is observed that in the spectral range used for the calibration model construction there are some overlapping absorption bands, mainly those occurring between 1120 and 1270 nm, attributed to the 2nd overtone of C–H bond stretching. On the other hand, the range between 1400 and 1700 nm, related to first overtone of alcohol O–H bond (methanol and ethanol), presents lower overlap with the bands produced by the first overtone of combination bands (1350–1500 nm) due to C–H + C–H and C–H + C–C stretching. Thus, it is reasonable to suppose that calibration models made by using this range, or part of it, can provide more robust models, whose results are less dependent on the gasoline composition. In such a way, three spectral ranges were evaluated for determination of methanol and ethanol (indicated in Fig. 3): region “A” (1331–1682 nm), region “B” (1449–1682 nm) and region “C” (1449–1611 nm). The RMSEP values for methanol and ethanol determinations obtained for the external validation set by using the calibration models constructed using these three regions, are shown in Table 3.

For regions “A” (1331–1682 nm) and “B” (1449–1682 nm), the RMSEP values are similar those found when the wider spectral range is used for model construction (Table 2). For region “C” (1449–1611 nm) an increase in the RMSEP value is observed, indicating a decrease in the prediction capability of the regression model based on that spectral region. This is more evident for ethanol when PLS-2 is used. This result indicates that the use of only the region of first overtone of O–H bond makes the discrimination between methanol and ethanol, difficult since the region presenting absorption of the methyl ($-CH_3$) and methylene ($-CH_2-$) groups is not included in the calibration model.

Table 3
Results obtained for determination of methanol and ethanol in samples of the external validation set using the calibration models constructed PLS-1 and PLS-2 with the three regions shown in Fig. 3 after first derivative spectra (RMSEP, root mean square error of prediction)

Spectral range (nm)	RMSEP (%, v/v)			
	Methanol		Ethanol	
	PLS-1	PLS-2	PLS-1	PLS-2
A (1331–1682)	0.33	0.34	0.30	0.30
B (1449–1682)	0.32	0.32	0.28	0.28
C (1449–1611)	0.47	0.47	0.39	1.04

By using the constructed models for the spectral data from these three regions, the determination of methanol and ethanol in the same gasoline samples used for Fig. 2 construction was carried out. For the regions “A” and “B”, the results show that there is interference from isooctane and the three xylenes for the methanol determination and that toluene also begins to interfere when the calibration model using region “B” is employed. For ethanol determination, the interference of toluene and *o*-xylene continues being observed. On the other hand, the models constructed with region “C” show lower dependence on gasoline composition, as it can be seen through the data shown in Table 4. Considering that a relative error of 4% is acceptable for alcohol determination in gasoline, it can be concluded that only isooctane continues causing interference in methanol determination while for ethanol no interference from the studied hydrocarbons is observed.

A detailed analysis of region “C” (Fig. 3) shows that above 1611 nm there are absorptions referring to aromatic hydrocarbons (first overtone of C–H + C–H and C–H + C–C stretching), which is overlapped by absorptions of O–H stretching of alcohols. Thus, removing this spectral region for the construction of the calibration model minimizes the interference of aromatic hydrocarbons. In the region below 1449 nm, methyl (–CH3) and methylene (–CH2–) group absorptions coming from the different added hydrocarbons, are observed. Elimination of part of this region prevents interference of linear and aromatic hydrocarbons. However, if the lower limit selected for region “C” (1449–1611 nm) is increased to somewhat wavelengths, lager errors are observed due to the loss of information related to the methyl and methylene groups present in the alcohols. In the case of the isooctane interference, it was not possible to establish, in a definitive way, how much of its interference remains, even after carrying out the study of the different spectral regions. The most acceptable hypothesis is that isooctane has five methyl groups per molecule, which overlap with the absorption band from the only methyl group of methanol. On the other hand, ethanol has, besides the methyl group, a methylene group whose information must be used to differentiate ethanol and methanol, which would justify the reduced interference of isooctane in ethanol determination. The only way to deal with the interference of hydrocarbons such as isooctane is to ensure that the average composition

Table 4
Results obtained for determination of methanol and ethanol in gasoline samples whose matrix compositions were modified by the addition of different hydrocarbons, using the calibration model constructed in the spectral range from 1449 to 1611 nm

Hydrocarbons[a]	Methanol		Ethanol	
	Predicted (%, v/v)	Relative error[b] (%)	Predicted (%, v/v)	Relative error[b] (%)
n-Hexane	9.8	2.2	25.1	0.4
Isooctane	7.8	−21.7	25.9	3.6
Toluene	9.7	3.3	24.1	−3.6
m-Xilene	9.7	3.3	24.1	−3.6
o-Xilene	9.7	3.3	24.8	−0.8
p-Xilene	9.9	1.1	24.0	−4.0

[a] Hydrocarbons content equal to 8.0% (v/v).

[b] Calculated value in relation to predicted value for the sample without hydrocarbon addition (25.0%, v/v for ethanol and 10.0%, v/v for methanol). Results represent averages of two determinations.

Table 5
Results obtained by PLS-1 for ethanol determination in type C gasoline samples collected from gas stations

Sample	Standard method (% v/v)	1105–1682 nm		1449–1611 nm	
		Proposed method (%, v/v)	Relative error (%)	Proposed method (%, v/v)	Relative error (%)
1	26.0	25.2	−3.2	26.0	0.0
2	24.0	24.6	2.3	24.7	2.9
3	26.0	25.2	−3.3	25.4	−2.3
4	25.0	24.8	−0.8	25.5	2.0
5	26.0	25.3	−2.5	25.6	−1.5
6	25.0	25.4	1.6	25.9	3.6
7	25.0	25.5	1.9	26.0	4.0
8	25.0	25.2	0.6	25.6	2.4
9	25.0	25.4	1.5	25.8	3.2
10	25.0	25.5	2.0	25.9	3.6
11	61.0	61.3	0.5	63.9	4.8
12	25.0	22.4	−10.3	24.6	−1.6
13	25.0	25.4	1.6	25.8	3.2
14	26.0	26.5	2.0	26.4	1.5
15	25.0	24.6	−1.8	25.0	0.0

Calibration models were constructed using first derivative NIR spectra in the ranges 1105–1682 nm and 1449–1611 nm

of the gasoline does not change very much from batch-to-batch.

To validate the proposed method, the ethanol contents were determined in 15 commercial gasoline (type C) samples collected from gas stations in the Campinas region (SP, Brazil). Table 5 shows the results obtained with the PLS-1 model using all the spectral range and the PLS-1 model using only region "C" (1449–1611 nm). The results obtained were compared to the alcohol content determined by the standard method (ABNT-NBR 13992) [9]. Except for samples 11 and 12, all the results obtained are within the relative error range of ±4%, accepted for ethanol determination in gasoline, in agreement with the standards of the ANP (National petroleum Agency, Brazil). Principal Component Analysis (PCA) reveals that samples 11 and 12 show different spectral behaviors from the other samples. In the case of sample 11, this behavior is justified by its high ethanol content (61%, v/v), being, therefore, classified as an adulterated gasoline. It is also interesting to note that the relative error of 4.8% found for this sample demonstrates perhaps that the method can produce good results even when the alcohol content is higher than the upper limit of 30.0% (v/v) used in the PLS-1 calibration model. The confidence limit found for the prediction of this sample also demonstrates this fact. However, this result must be seen with caution as the majority of chemometric algorithms would give a very large confidence interval for this result.

In the case of sample 12, the results found using both models reveal that probably the composition of this sample is quite different from those used in calibration set and also from the other samples collected from the gas stations. This fact is justified on the basis of interference studies carried out, which demonstrate that only toluene causes negative errors on ethanol predictions when spectral region "C" is used for model construction. The results of ethanol prediction agree with the standard method.

4. Conclusions

The results obtained in this work show that NIR spectroscopy together with multivariate calibration (PLS-2) can be used for simultaneous determination of methanol and ethanol in gasoline. The main advantages are the non-destructive and non-polluting characteristics of the NIR method. Moreover, the method can determine methanol and ethanol in presence of each other, being appropriate for use in inspections and identification of adulterations made by the addition of methanol to gasoline. It is important to emphasize that the standard method does not have this capability. The selection of the spectral region to be employed in the construction of the calibration model minimizes interference from linear and aromatic hydrocarbons on the determination of both alcohols. In the case of branched hydrocarbons, it was observed that the selection does not eliminate the interference of these types of compounds in methanol determination. Therefore, it is necessary to employ samples that represent the variability of these compounds or ensure that the variability is within an acceptable range.

Acknowledgements

The authors thank CTPETRO/FINEP for financial support (Process no. 65.00.0181.00) and Dr. C.H. Collins for manuscript revision. H.L. Fernandes thanks PIBIC/CNPq for a fellowship.

References

[1] M. Korn, M.C.U. Araújo, L.S.G. Teixeira, F.S. de Oliveira, Fuel 83 (2004) 917.

[2] D.A. Azevedo, L.A. d'Avila, L.S.M. Wiedemann, Fuel 84 (2005) 467.

[3] R. Pozzi, F. Pinelli, P. Bocchini, G.C. Galletti, Anal. Chim. Acta 504 (2004) 313.

[4] Y. Rong, W. Tong, Environ. Forens. 6 (2006) 355.

[5] P.A.P. Pereira, J.B. Andrade, Quim. Nova 21 (1998) 744.

[6] Resolução do Conselho Interministerial do Açúcar e do Álcool (CIMA) no. 30 de 15 May 2003.

[7] A.D.S. Santos, M.L.M. Valle, R.G. Giannini, Economia e Energia, ano IV, no. 19, 2000.

[8] M. Abu-Zaid, O. Badran, J. Yamin, Energ. Fuel 18 (2004) 312.

[9] ABNT-NBR 13992: "Motor gasoline—determination of fuel anhydrous ethylic alcohol content", Associação Brasileira de Normas Técnicas, Rio de Janeiro, Brazil, 1997.

[10] C. Pasquini, J. Braz. Chem. Soc. 14 (2003) 198.

[11] G. Buttner, Proc. Control Qual. 9 (1997) 197.

[12] A. Espinosa, M. Sanchez, S. Osta, C. Boniface, J. Gil, A. Martens, B. Descales, D. Lambert, Oil Gas J. 92 (42) (1994) 49.

[13] W.T. Welch, M.L. Bain, S.M. Maggard, J.M. May, Oil Gas J. 92 (26) (1994) 48.

[14] B.R. Buchanan, D.E. Honigs, Appl. Spectrosc. 41 (1987) 1388.

[15] D.E. Honigs, T.B. Hirschfeld, G.M. Hieftje, Anal. Chem. 57 (1985) 443.

[16] N.M. Faber, Appl. Spectrosc. 53 (1999) 1011.

[17] G. Bohács, Z. Ovádi, A. Salgó, J. Near Infrared Spectrosc. 6 (1998) 341.

[18] J. Malinen, M. Kansakoski, R. Rikola, C.G. Eddison, Sens. Actuators B 51 (1998) 220.

[19] J.J. Kelly, J.B. Callis, Anal. Chem. 62 (1990) 1444.

[20] J.J. Kelly, C.H. Barlow, T.M. Jinguji, J.B. Callis, Anal. Chem. 61 (1989).

[21] C. Pasquini, S.H.F. Scafi, Anal. Chem. 75 (2003) 2270.

[22] S. Macho, M.S. Larrechi, Trends Anal. Chem. 21 (2002) 799.

[23] C. Han, M. Kim, Y.H. Lee, Comput. Chem. Eng. 24 (2000) 513.

[24] L.A. Sacorage, PhD Thesis, UNICAMP, Campinas, Brazil, 2004.

[25] R. Guchardi, P.A. da Costa Filho, R.J. Poppi, J.C. Pasquini, J. Near Infrared Spectrosc. 6 (1998) 333.

[26] M.C. Breitkreitz, I.M. Raimundo Jr., J.J.R. Rohwedder, C. Pasquini, H.A. Dantas Filho, G.E. José, M.C.U. Araújo, Analyst 128 (2003) 1204.

[27] J.C. Rubim, L.S. Mendes, F.C.C. Oliveira, P.A.Z. Suarez, Anal. Chim. Acta 493 (2003) 219.

Available online at www.sciencedirect.com
ScienceDirect
Talanta 75 (2008) 710–716
Talanta
www.elsevier.com/locate/talanta

Enantioselective determination of the organochlorine pesticide bromocyclen in spiked fish tissue using solid-phase microextraction coupled to gas chromatography with ECD and ICP–MS detection

Natalia Fidalgo-Used, Maria Montes-Bayón, Elisa Blanco-González, Alfredo Sanz-Medel*

Department of Physical and Analytical Chemistry, University of Oviedo, C/Julian Clavería 8, 33006 Oviedo, Spain

Received 2 July 2007; received in revised form 27 November 2007; accepted 7 December 2007
Available online 15 December 2007

Abstract

A method for enantioselective determination of bromocyclen enantiomers in fish tissue has been developed. The enantiomers were resolved by capillary gas chromatography (GC) using a commercial chiral column (CP-Chirasil-Dex CB) and a temperature program from 50 °C (held for 1 min), raised to 140 °C at 40 °C $\min^{-1}$ and then raised at 0.2 °C $\min^{-1}$ to 155 °C. This enantioselective gas chromatographic separation was combined with a clean-up/enrichment procedure based on solid-phase microextraction (SPME). Under SPME optimized conditions, precision, linearity range and detection limits of the developed SPME–enantioselective GC procedure were evaluated and compared using two different detection systems: a classical electron-capture detection (ECD) and an element specific detection using inductively coupled plasma mass spectrometry (ICP–MS). The SPME–GC–ECD method exhibited an excellent sensitivity, with detection limits of 0.2 ng L^{-1} for each enantiomer of bromocyclen. Although ICP–MS offered poorer detection limits (7 ng L^{-1} as Br, equivalent to 36 ng L^{-1} of each enantiomer) than conventional ECD detector, it proved to be clearly superior in terms of selectivity. The relative potential and performance of the two compared methods for real-life analysis has been illustrated by the determination of enantiomers of bromocyclen in spiked tissue extracts of trout.

Keywords: Enantioselective gas chromatographic separation; Chirasil-Dex; Solid-phase microextraction; Organochlorine pesticides; Bromocyclen; GC–ECD; GC–ICP–MS; Fish samples

1. Introduction

The significance of molecular chirality is today widely recognized in life sciences [1]. A lesser-known fact is that many pesticides also contain chiral structures and thus consist of enantiomers [2], even if, due to economic reasons, chiral pesticides are primarily used as racemates (50:50 mixtures of the two enantiomers) [3]. Enantiomers of the same compound have identical physico-chemical properties [4] and thus they appear as a single compound in non-enantioselective analytical methods. Enantioselective determinations are, however, needed because their biological behaviour can differ considerably [1,3,5–7]. In brief, when dealing with chiral pesticides, it is important to obtain accurate analytical information to understand their stereoselective biological processes, metabolic breakdown and elimination for a complete evaluation of their risks posed to environment and public health [8,9].

Bromocyclen (5-bromomethyl-1,2,3,4,7,7-hexachlorobicyclo[2,2,1]hept-2-ene, trade-name Bromodan®, Alugan®) is a brominated organochlorine compound belonging to the group of cyclodiene insecticides. Due to its low mammalian toxicity, bromocyclen has been widely used as an acaricide or insecticide against ectoparasites for the treatment of domestic animals in Europe [10,11]. Because of its highly persistent and lipophilic character it can be accumulated in fish and is more risky because it persists in the aquatic environment [10,11]. In fact, relatively high concentrations of this insecticide have been found in fish samples, surface water and waste water [10,11]. Up to now, neither information about production quantities of bromocyclen, nor their environmental fate and toxicological properties have been described in literature.

As several other persistent organochlorine pesticides, bromocyclen is chiral and applied as racemate. Studies dealing with the enantiomeric ratios of bromocyclen has presented evidence

---

* Corresponding author. Tel.: +34 98 5103474; fax: +34 98 5103125.
E-mail address: asm@correo.uniovi.es (A. Sanz-Medel).

0039-9140/$ – see front matter © 2007 Elsevier B.V. All rights reserved.
doi:10.1016/j.talanta.2007.12.006

that the initial 1:1 enantiomeric ratio of the racemate is altered in the muscle tissue of bream, indicating that the (+)-enantiomer was preferentially degraded or the (−)-enantiomer preferentially accumulated [10]. However, this result appears to be contradictory with the results from a previous investigation of rainbow trout that has led to the contrary assumption [11].

On the other hand, the enantioselective determination of chiral organochlorine pesticides in complex matrices (e.g. biota) is still a challenge. Besides the difficulties to find appropriate enantioselective chromatography columns, able to separate into enantiomers pairs each chiral congener, there is a higher risk of co-elution because of the presence in the sample of a great number of other organochlorine persistent pollutants. A few reports on the determination of individual bromocyclen enantiomers in fish samples have appeared in literature and the use of enantioselective capillary gas chromatography (CG), using a modified cyclodextrin stationary phase, and electron-capture detection (ECD) [10,11] are recommended. However, some potentially interfering organochlorine compounds such as PCBs may coelute with the bromocyclen enantiomers on the cyclodextrin column used [10] and interfere using ECD. This limitation has been mitigated by the use of extensive clean-up and fractionation steps before the GC separation [10]. However, an alternative approach to improve selectivity is the use of element-specific detection techniques (more selective than ECD).

Recently, we have reported that the use of GC hyphenated with inductively coupled plasma mass spectrometry (ICP–MS) detector shows a high potential for specific monitoring of heteroelements (e.g. ^{31}P, ^{34}S, ^{35}Cl, ^{79}Br) present in pesticides [12]. Moreover, we have also shown that the combination of solid-phase microextraction (SPME) with enantioselective GC and ICP–MS detection enables “chiral speciation”, that is, sensitive and selective determination of the enantiomers of organophosphorus pesticide ruelene in complex environmental samples [13].

Moreover, SPME is an extraction technique which can avoid the general drawbacks of other traditional methods used for sample preparation [14–16] and has been applied to the analysis of organochlorine pesticides mainly in aqueous samples [17]. Application of SPME to more complex samples such as biota is more difficult and such studies are scarce. However, as we have demonstrated previously [18] SPME can be also used as a simple clean-up/enrichment procedure for the analysis of organochlorine pesticides in fish tissue if they are extracted first with a suitable organic solvent via a conventional liquid–solid extraction procedure.

In the present study, a method of enantioselective determination of bromocyclen in fish tissue was developed taking advantage of the “chiral speciation” concept via ICP–MS [13]. The method is based on SPME combined with enantioselective GC using a commercial chiral column (CP-Chirasil-Dex CB) and ICP–MS. The performance of this approach is compared with that using more conventional ECD detection. Optimization of enantioselective separation and different SPME parameters, such as extraction mode, type of fibre, extraction time, extraction temperature, pH and ionic strength was carried out by GC–ECD. Later, the suitability of coupling the optimized SPME–enantioselective GC procedure to detect a specific halogen (^{79}Br, ^{81}Br, ^{35}Cl and ^{37}Cl) by ICP–MS has been investigated. Validation parameters such as linearity, precision and detection limits were determined and compared for the two proposed detectors. Finally, their comparative application to the determination of the two bromocyclen enantiomers in spiked fish tissue extracts have been accomplished successfully.

2. Experimental

2.1. Reagents, standards and samples

Bromocyclen ($C_8H_5BrCl_6$, MW: 393.75) was obtained from Riedel-de Haën (Seelze, Germany). This pesticide was only available as the racemate. A stock standard solution of bromocyclen at a concentration of 4×10^9 ng L^{-1} was prepared in *n*-hexane and stored at −20 °C. This solution was used for the preparation of standard solutions of bromocyclen in methanol. The more diluted working solutions were prepared in water from that methanol solution just before use. Acetone and *n*-hexane for pesticides residue analysis were supplied by Riedel de Haën (Seelze, Germany), methanol for ultratrace analysis and sodium chloride (99.5% purity) were purchased from Merck (Darmstadt, Germany). Anhydrous sodium sulphate (analytical-reagent grade) from Fluka (Buchs, Switzerland) was purified by overnight heating at 300 °C. Ultrapure water was obtained from a Milli-Q water purification system (Millipore, Bedford, MA, USA).

Helium (99.999%) was used as GC carrier gas and nitrogen (99.999%) was used as an additional plasma gas.

Brown trouts (*Salmo trutta*) of average weight 65 g (lipid content 2–6% and water content 75%) were fished using electrofishing equipment from a river (Pigüeña river, Asturias, Spain) located in an area without agricultural or industrial activities. The fish samples were wrapped in hexane-washed aluminium foil and stored at −20 °C until analysis.

2.2. Chromatographic equipment and experimental conditions

GC–ECD analysis was carried out with a HP-5890 Series II gas chromatograph equipped with an electron-capture detector (Hewlett-Packard, Avondale, PA, USA). Enantiomeric separation was investigated using a CP-Chirasil-Dex CB column (25 m × 0.25 mm i.d., Varian, Walnut Creek, CA); this column has a maximum temperature of 200–225 °C. Helium was used as carrier gas at a pressure of 10 p.s.i. The injector was equipped with thermogreen LB-2 pre-drilled septa of 11 mm from Supelco (Bellefonte, PA, USA) and an injection liner of 0.75 mm i.d. (Supelco) special for SPME. The injector was operated in a split/splitless mode, with a splitless injection time of 2 min. The temperature of the injector was maintained at 260 °C and the temperature of the detector was fixed at 300 °C. The oven temperature program was as follows: 50 °C for 1 min, raised to 140 °C at 40 °C min^{-1} and then raised at 0.2 °C min^{-1} to 155 °C.

GC–ICP–MS analysis was carried out using a GC, Agilent 6890 N (Agilent Technologies, Avondale, PA, USA) interfaced

Table 1
SPME–GC–ECD and SPME–GC–ICP–MS operating conditions

GC–ECD parameters		GC–ICP–MS parameters	
Gas chromatograph	HP-5890 Series II	Gas chromatograph	Agilent 6890 N
Detector	Electron-capture detector (ECD)	ICP–MS	Agilent 7500c
Column	CP-Chirasil-Dex CB (25 m × 0.25 × mm × 0.25 μm)	Column	CP-Chirasil-Dex CB (25 × m × 0.25 mm × 0.25 μm)
Carrier gas	Helium (10 psi)	Carrier gas	Helium (10 psi)
Injection	Splitless (2 min)	Injection	Splitless (2 min)
Column temperature	50 °C (1 min) 40 °C/min–140 °C 0.2 °C/min–155 °C	Column temperature	50 °C (1 min) 40 °C/min–140 °C 0.2 °C/min–155 °C
Detector temperature	300 °C	GC–ICP–MS interface	Agilent
Injector temperature	260 °C	Transfer line temperature	260 °C
		Integration time	0.1 s
		Measured isotopes	^{35}Cl, ^{37}Cl, ^{79}Br, ^{81}Br
		Carrier gas/Rf power	Ar, 0.75 L min^{-1}/950 W
		Optional gas	N_2 9%

SPME conditions	
SPME fibre	85 μm PA
Extraction time	45 min
Extraction temperature	80 °C
Desorption temperature	260 °C (5 min)

to an Agilent Model 7500c ICP–MS (Agilent Technologies, Tokyo, Japan) equipped with an octapole ion guide. Details on the interface can be found described elsewhere [19]. This instrument can be run with or without collision gas. The CP-Chirasil-Dex CB capillary column was used for GC enantiomeric separation with helium as the carrier gas, while all the GC–ECD and GC–ICP–MS systems operating conditions used are summarised in Table 1.

2.3. Soxhlet extraction procedure

A previously reported sample extraction procedure was used [18]. Fish muscle tissue (10 g wet weight) was ground with 4-fold excess of activated anhydrous sodium sulphate until a fine powder was obtained. This mixture was Soxhlet extracted with 300 mL of hexane/acetone (1:1, v/v) for 16 h. The extract was concentrated under vacuum rotatory evaporation to 100 mL. Aliquots of 0.5 mL of this extract were then taken for SPME–enantioselective GC analysis.

2.4. SPME equipment and experimental conditions

The SPME device used for manual extraction, a holder assembly and several replaceable fibres, were purchased from Supelco (Madrid, Spain). Two different fibre types were compared, polydimethylsiloxane (PDMS, 100 μm) and polyacrylate (PA, 85 μm). The fibres were conditioned before used, as recommended by the manufacturer, by heating at 260 °C for 1 h (PDMS) and heating at 300 °C for 2 h (PA) in the injection port of the gas chromatograph. A magnetic stirrer hotplate from Selecta (IKA-Werke) was used for stirring and heating the samples during extraction. 10 mL glass vials, closed with PTFE-coated silicone septa, for SPME were purchased from Supelco (Madrid, Spain).

Direct immersion (DI)-SPME was carried out as follows: 1 mL aliquots of the fish tissue organic extract from the Soxhlet were placed into a 10 mL Teflon-lined screw-capped vials and evaporated just to dryness under a gentle stream of nitrogen. The residue was redisolved in 10 mL of 5% (v/v) methanol in water. Then the vial was closed and placed in a water bath on top of the hot plate stirrer and the fibre was immersed into the solution and kept there for 45 min at ambient temperature (25 ± 1 °C). For headspace (HS)-SPME the residue (aliquots of 0.5 mL) was redisolved in 5 mL of 5% (v/v) methanol–water and the fibre was exposed to the solution headspace for 45 min at a temperature of 80 ± 1 °C.

During extraction, in both DI and HS modes, the solution was vigorously stirred at a constant speed with a new PTFE-coated small magnetic stir bar. After extraction, the fibre was thermally desorbed at 260 °C for 5 min into the glass liner of the chromatograph injection port.

Possible carryover was removed by keeping the fibre in the injector port for an additional period of time of 5 min with the injector in the split mode. Moreover, procedure blanks were also run periodically during the analysis to check possible fibre contaminations.

3. Results and discussion

3.1. Optimization of the enantioselective separation

The separation of bromocyclen enantiomers has been so far performed just using GC with a 25 m fused-silica capillary column coated with 50% heptakis-(2,3-di-O-methyl-6-O-t-

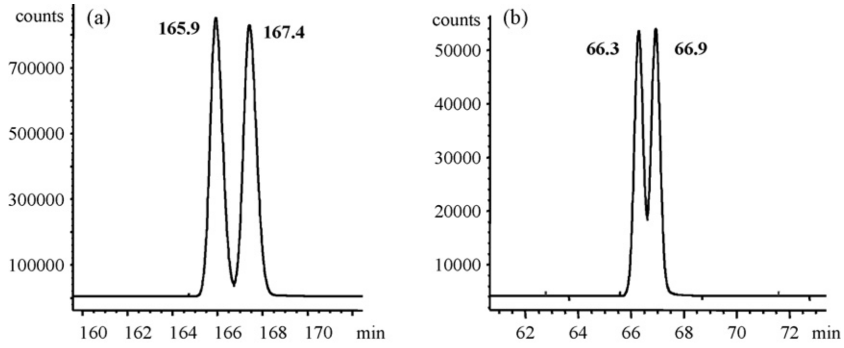

Fig. 1. Enantiomeric separation ob bromocyclen obtained by GC–ECD on a CP-Chirasil-Dex CB column of standard racemic solutions of: (a) 50×10^6 ng L^{-1} in hexane under the following conditions: 50 °C for 1 min, raised to 110 °C at 30 °C min^{-1} and then raised to 190 °C at 0.2 °C min^{-1}; (b) 1×10^6 ng L^{-1} in hexane under the following conditions: 50 °C for 1 min, raised to 140 °C (at 40 °C min^{-1}) and then raised to 155 °C at 0.2 °C min^{-1}.

butyldimethyl-silyl)-β-cyclodextrin and 50% OV-I70 (w/w) [10]. In this work, we investigated such separation on a commercially available GC column (CP-Chirasil-Dex CB column) containing a stationary phase of heptakis (2,3,6-tri-O-metil)-β-cyclodextrin directly bonded to dimethylpolysiloxane. Optimization of the separation conditions was carried out by GC–ECD under isothermal elution, at temperatures ranging from 120 to 190 °C. The enantioselective separation was also investigated under different temperature programs, such as 50 °C for 1 min and then raised to 190 °C at different rate from 0.2 to 40 °C min^{-1}. As can be seen in Fig. 1a, the enantiomers of bromocyclen could be baseline separated in about 170 min (resolution, $R_S = 1.29$ calculated as $R_S = (t_2 - t_1)/(w_{b1} + w_{b2}) \times 0.5$; t_1 and w_{b1} retention time and peak width at the base of the first eluted enantiomer, t_2 and w_{b2} retention time and peak width at the base of the second eluted enantiomer) in the CP-Chirasil-Dex CB column under the following conditions: 50 °C for 1 min, raised to 110 °C at 30 °C min^{-1} and then raised to 190 °C at 0.2 °C min^{-1}. Retention times longer than 90 min were considered too long from a practical point of view. Therefore, as a compromise between resolution ($R_S = 0.94$) and analysis time (70 min), we finally selected for further experiments: 50 °C for 1 min, raised to 140 °C (at 40 °C min^{-1}) and then raised to 155 °C at 0.2 °C min^{-1}. The chromatogram obtained under these conditions is shown in Fig. 1b.

It should be pointed out that the retention order of the individual separated enantiomers of bromocyclen could not be determined because unfortunately such individual enantiomers were not available.

3.2. Optimization of the solid-phase microextraction

The influence of different parameters affecting the SPME process was studied. This study was carried out by enantioselective GC–ECD analysis of fish tissue organic extracts (bromocyclen free) prepared as described in Section 2 and then spiked with a racemic solution of bromocyclen to obtain a final concentration in the SPME vial of 1000 ng L^{-1} of the pesticide racemate.

Firstly, both extraction modes HS-SPME and DI-SPME were examined and compared using PDMS (100 μm) and PA (85 μm) fibres at different temperatures (from 25 to 80 °C) and different extraction times (from 15 to 120 min). Fig. 2 shows that the extraction efficiencies (peak area) obtained under optimum conditions by HS-SPME were better than those obtained using DI-SPME (for both fibres under study). Fig. 2 also presents the comparison of extraction efficiencies for bromocyclen between PDMS and PA fibres. It can be seen that the PA fibre (85 μm) shows slightly better extraction efficiency than the PDMS (100 μm) with comparable relative standard deviations, in spite of the differences in the fibre diameter which determines fibre capacity. Thus, HS-SPME mode and the PA fibre coating were selected for all further experiments.

The effect of extraction time, from 15 to 120 min, on the amount of studied compound extracted by HS-SPME with the PA fibre was then investigated. The equilibrium conditions were reached at 45 min, a value selected for the bromocyclen extraction. The extraction temperature was also studied and an increase of the extraction efficiency (peak area) of bromocyclen was observed by increasing the extraction temperature from 25 to 80 °C. Therefore, HS-SPME work was carried out at an extraction temperature of 80 °C.

The analyte amount extracted by the fibre can be increased if its solubility in water is decreased, e.g. changing the pH and/or ionic strength. The effect of the pH (from 4 to 8) of the sample solution was studied using adequate HCl or NaOH solutions. Maximum extraction efficiency was obtained at pH values 6–7. As this value corresponds to

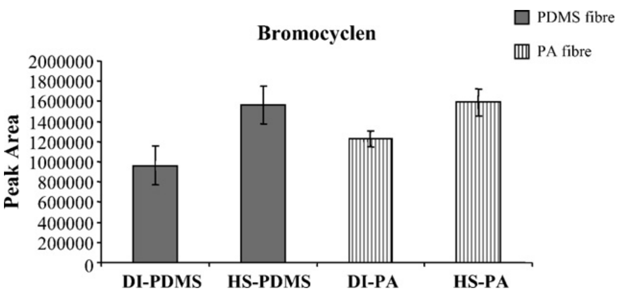

Fig. 2. Influence of the fibre coating and comparison between HS-SPME–GC–MS and DI-SPME–GC–MS. Conditions: extraction temperature, 80 °C; extraction time, 30 min; 100 μm PDMS and 85 μm PA fibres. Other experimental conditions in the text.

the sample diluted in water no pH final adjustment was adopted.

Also, sodium chloride at various concentrations (from 0 to 20%, w/v) was added to the sample to observe its possible effect on extraction efficiency. Results revealed that sodium chloride was no effective to improve the pesticide extraction efficiency.

The main difficulty in HS-SPME preconcentrations in lipid samples is a strong matrix effect that causes the decrease of SPME efficiency [18]. Indeed, the lipids of the sample having a high affinity with organic compounds, participate along with the analyte in the distribution equilibrium between the sample and the fibre coating. In order to investigate the influence of sample matrix (lipid content) on the extraction, aliquots of spiked fish tissue organic extracts (see Section 2.3), ranging from 0.5 to 2 mL, were submitted to the HS-SPME procedure and analysed by GC–ECD. In our experiments, the final concentration of bromocyclen in the vial was 1000 ng L^{-1} while the content in lipids ranged from 1 to 3 mg (this corresponds to about 0.5 mL aliquot of the fish tissue extract) to 6–10 mg (2 mL aliquot of the fish tissue extract). A dramatic decrease in the observed extraction efficiency was obtained with increasing lipid contents in the sample. A satisfactory recovery (>84%), determined as the observed peak area ratio of fish sample to ultrapure water sample, both spiked with the analyte at the same level, was obtained only for samples with low level lipid contents (1–3 mg).

Finally, optimum desorption conditions were determined by testing various temperatures and heating times. The time and temperature required to successfully desorbs bromocyclen from the PA fibre coating to the GC, with minimal carryover in a subsequent analysis (fibre blank), were established as 5 min at 260 °C.

3.3. Optimization of the GC–ICP–MS system

Bromine and chlorine, the two heteroelements present in the bromocyclen are elements difficult to ionise in an argon plasma because of their very high ionization potential. However, it has been reported previously that with the addition of N_2 to the central argon plasma channel a sensitive ICP–MS response for these elements can be obtained [19,20]. Therefore, the effect of the addition of nitrogen to the ICP on the signals intensities to noise ratios for bromocyclen, monitoring the two stable isotopes of Cl (^{35}Cl,^{37}Cl) and Br (^{79}Br, ^{81}Br) by ICP–MS, was investigated here. The results obtained have been plotted in Fig. 3. As can be seen the signal to noise ratios increased with the percentage of nitrogen relative to the argon carrier gas flow until about a10% level. Further increases of nitrogen resulted in a reduction of the signal to noise ratio for all isotopes monitorized. Therefore, a 9% of nitrogen was selected as the optional gas flow in all further experiments using ICP–MS.

Different parameters affecting the ionization of Br and Cl in the GC–ICP–MS system such as rf power and argon carrier gas flow were also studied. This study was carried out by injecting the same concentration of bromocyclen at different settings of these parameters and in presence of 9% nitrogen as optional gas. The results obtained are presented in Figs. 4 and 5, respectively. Fig. 4 shows that the best peak area of bromocyclen for both measured elements (Br and Cl) was obtained for relatively low rf powers plasma, while for the argon carrier gas flow rate the maximum peak area for bromocyclen was obtained at 0.7–0.8 L min^{-1} in both cases (Fig. 5). Therefore, best detection conditions turned out to be 9% nitrogen as optional gas, 950 W as rf power and 0.75 mL min^{-1}of argon carrier gas flow. It should be noted that the sensitivity obtained monitoring Cl is about ten times lower than that obtained monitoring Br, in spite of the fact that bromocyclen has six chloride atoms in their structure and there is only one bromide atom. The most abundant isotopes ^{35}Cl and ^{79}Br were selected for monitoring by ICP–MS in all further experiments.

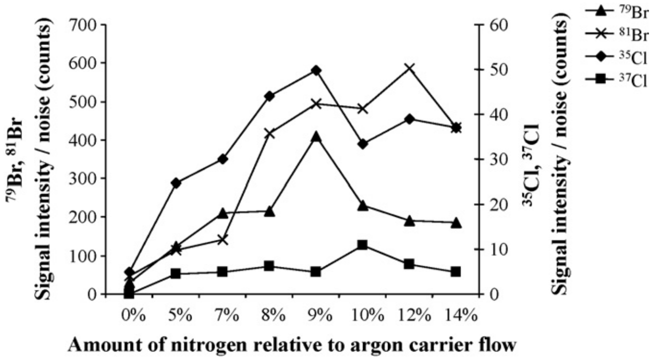

Fig. 3. Optimization of amount of nitrogen optional gas.

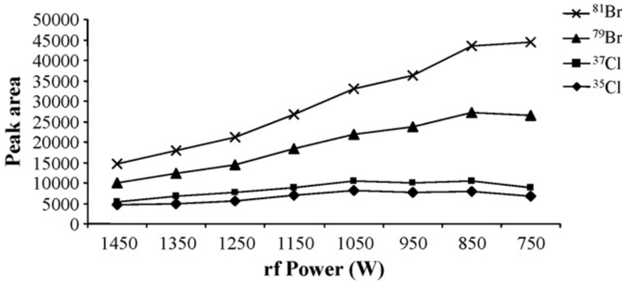

Fig. 4. Optimization of the rf power on the analytical signal (peak area) of bromocyclen monitoring ^{35}Cl, ^{37}Cl, ^{79}Br and ^{81}Br.

The effect of different extraction lens voltage settings was also evaluated and the best analytical signal (peak area), for both Cl and Br, was obtained under an extraction lens voltage setting of −190 V, which resulted in a more efficient ions extraction from the plasma into the mass analyser [20].

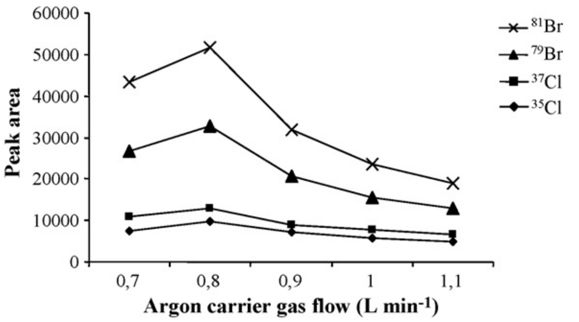

Fig. 5. Optimization of argon carrier gas flow on the analytical signal (peak area) of bromocyclen monitoring ^{35}Cl, ^{37}Cl, ^{79}Br and ^{81}Br.

Table 2
Sensitivity, repeatability and detection limit data for the enantiomers of bromocyclen

Compound[a]	SPME–GC–ECD			SPME–GC–ICP–MS (^{79}Br)		
	Sensitivity[b]	LOD (ng L^{-1})[c]	R.S.D. %[d]	Sensitivity[b]	LOD Compound/^{79}Br (ng L^{-1})[c]	R.S.D. %[e]
Bromocyclen 1	1149708	0.2	5.6	7586	36.5/7.4	8.4
Bromocyclen 2	1149636	0.2	5.8	7661	36.2/7.3	8.6

[a] Bromocyclen 1: first eluted enantiomer; bromocyclen 2: second eluted enantiomer.
[b] As slope of the calibration curve area per unit of concentration.
[c] LOD: detection limits calculated as IUPAC guidelines: three times the standard deviation of the background divided by the slope of the calibration curve.
[d] R.S.D.: relative standard deviation. Test concentration 1 ng mL^{-1} ($n = 3$).
[e] R.S.D.: relative standard deviation. Test concentration 1 ng mL^{-1} ($n = 3$).

3.4. Analytical performance characteristics

The comparative analytical performance of the developed SPME–GC–ECD and SPME–GC–ICP–MS methodologies was evaluated in terms of linearity range, precision and detection limits.

The linearity of the SPME–GC–ICP–MS method (monitoring ^{79}Br) was tested, using increasing concentrations of racemic bromocyclen in 5% (v/v) methanol in water, from the detection limit up to 70,000 ng L^{-1} (maximum concentration of the pesticide assayed). The calibration curves, using peak area versus concentration, showed a good linear behaviour in all the tested range for both enantiomers and correlation coefficients (R^2) of 0.9991 and 0.9995 (the less retained enantiomer) were observed. With the SPME–GC–ECD method the calibration plots were found to be linear at least up to 3000 ng L^{-1}, with correlation coefficients (R^2) of 0.9999 and 1, respectively.

The repeatability, in terms of percent relative standard deviation (% R.S.D.) of peak area, was determined by three replicate analysis of a racemic standard solution of bromocyclen at a concentration level of 1000 ng L^{-1} by both methods under scrutiny. As shown in Table 2, the observed relative standard deviation by SPME–GC–ICP–MS was slightly worse than that obtained by SPME–GC–ECD at such low level of pesticide concentration.

Table 2 also shows the observed detection limits (IUPAC criteria of three times the standard deviation of the background divided by the slope of the calibration curve) for both techniques under study. As expected, detection limits obtained by SPME–GC–ICP–MS (monitoring ^{79}Br) turned out to be much worse than those obtained by ECD detection. However, as Table 2 shows both techniques allow detection limits at the ng L^{-1} (ppt) level. Since bromocyclen in a 10 g of sample (fish muscle tissue) was dissolved in 100 mL of organic extract and aliquots of 0.5 mL were taken for the SPME–GC analysis, the limits of detection referred to the fish sample were of 0.02 ng g^{-1} for each enantiomer of bromocyclen by ECD detection and 3.6 ng g^{-1} (0.7 ng g^{-1} as Br) by ICP–MS detection.

Table 3
Recoveries of bromocyclen enantiomers in spiked fish samples using SPME–GC–ECD and SPME–GC–ICP–MS

Compound	SPME–GC–ECD[a] Recovery (%) (mean ± S.D.)	SPME–GC–ICP–MS (^{79}Br)[b] Recovery (%) (mean ± S.D.)
Bromocyclen 1	84 ± 0.5	88 ± 1
Bromocyclen 2	84 ± 2	89 ± 2

Bromocyclen 1: first eluted enantiomer; bromocyclen 2: second eluted enantiomer.
[a] Fish samples (spiked at 10 ng mL^{-1} level, $n = 3$).
[b] Fish samples (spiked at 10 ng mL^{-1} level, $n = 3$).

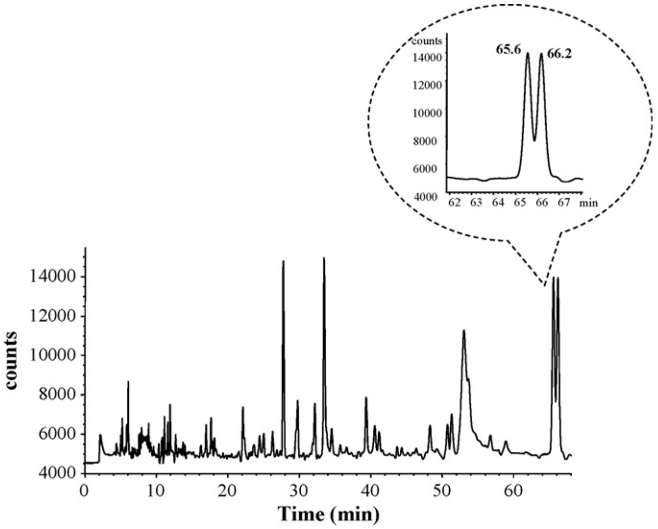

Fig. 6. Chromatograms of spiked fish tissue (final concentration in the SPME vial of 500 ng L^{-1}) obtained by SPME–GC–ECD. Experimental conditions in the text.

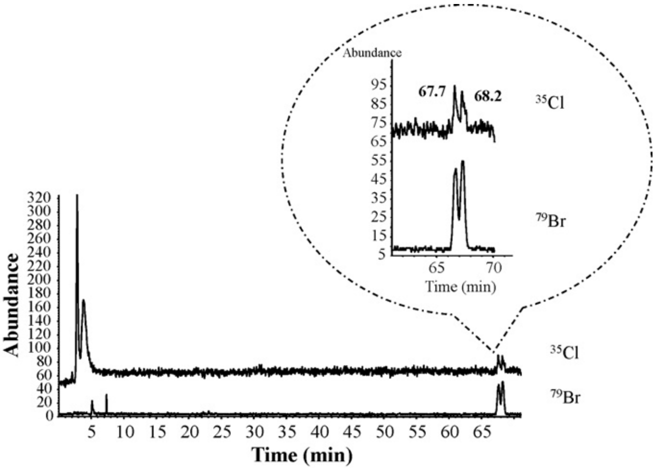

Fig. 7. Chromatograms of spiked fish tissue (final concentration in the SPME vial of 1000 ng L^{-1}) obtained by SPME–GC–ICP–MS (monitoring ^{35}Cl and ^{79}Br). Experimental conditions in the text.

3.5. Application to real samples

Finally, the suitability of the proposed SPME–GC–ICP–MS method for the determination of enantiomers of bromocyclen in real samples was investigated by analysing real fish tissue samples (brown trout). The levels of bromocyclen enantiomers in the samples were originally below the detection limits for both methods. Therefore, in order to evaluate the accuracy of the developed methods, the same fish tissue samples were spiked with the pesticide.

The recoveries were studied by spiking fish tissue organic extracts ($n=3$) with a standard mixture of racemic bromocyclen at a concentrations level of 10,000 ng L^{-1} and analysed by the two assayed methods. The results obtained were compared with those obtained by similar analysis of racemic standard solutions made up just in Milli-Q-water. The mean recoveries obtained for each enantiomer of bromocyclen in the fish tissue sample were higher than 84% by both methods and slightly better using ICP–MS detection (more selectivity) (see Table 3).

Typical SPME–GC–ECD and SPME–GC–ICP–MS cromatograms of one of the analysed “spiked fish tissue” are presented in Figs. 6 and 7, respectively. However, as can be seen in Fig. 6 the chromatographic profile obtained by SPME–GC–ECD is quite dirty with a lot of peaks, corresponding to unknown compounds present in the extract of the fish samples, which elute during the chromatographic run. As expected, when the detection is carried out by ICP–MS (monitoring both, Br and Cl) the chromatogram is much cleaner (see Fig. 7) due to the Br- and Cl-specificity of the detector. Thus, the high selectivity achievable by ICP–MS detection together with the adequate sensitivity obtained (low ng g^{-1} range) make the GC–ICP–MS coupling system an interesting alternative to GC–ECD in the analysis of samples with complex matrices.

4. Conclusions

HS-SPME has proved to be a very effective technique for the clean-up of racemic bromocyclen extracts from fish tissue samples, prior to enantioselective GC separation on a commercial cyclodextrin column (CP-Chirasil-Dex CB). The developed procedure is simple, rapid and allows sample manipulation to be substantially reduced as compared to more conventional sample preparation alternatives.

Furthermore, the successful development of a method for the chiral speciation [13] of bromocyclen based on the combination of such HS-SPME–enantioselective GC procedure with ICP–MS detection has been worked out and compared with a more conventional ECD detection.

The comparison of the two methods illustrates their relative advantages and drawbacks. Both methodologies show adequate analytical performance characteristics in terms of linearity range and precision with recoveries higher than 84% for both enantiomers of bromocyclen. The addition of nitrogen as optional gas to the plasma and the optimization of the different instrumental parameters such as plasma conditions and lens settings increased the analytical sensitivity of the SPME–GC–ICP–MS methodology and allowed to obtain detection limits in the ppt level (36 ng L^{-1} of the compound, 7 ng L^{-1} as Br and 88 ng L^{-1} as Cl). Such detection limits are clearly higher than those obtained by SPME–GC–ECD (0.2 ng L^{-1}), but halogen specific detection by ICP–MS proved to be superior to the ECD detection in terms of selectivity. This aspect may become critical for enantioselective analysis of complex samples of environmental interest where co-elution problems on the chiral GC column can very often take place [10]. In such cases resorting to ICP–MS detection could solve the problems.

Acknowledgments

The authors are grateful to the “Fundación para el fomento en Asturias de la Investigación Científica Aplicada y la Tecnología” (FICYT) for the grant to Natalia Fidalgo-Used and financial support from the Project BQU-2003-04671 from the Ministerio de Ciencia y Tecnología de España, Madrid.

References

[1] N.M. Maier, P. France, W. Lidner, J. Chromatogr. A 906 (2001) 3.
[2] W.P. Liu, J.Y. Gan, D. Schlenk, W.A. Jury, Proc. Natl. Acad. Sci. U.S.A. 120 (2005) 701.
[3] W.J.M. Hegeman, R.W.P.M. Laane, Rev. Environ. Contam. Toxicol. 173 (2002) 85.
[4] D.W. Armstrong, G.L. Reid, M.L. Hilton, C.-D. Chang, Environ. Pollut. 79 (1993) 51.
[5] D.L. Lewis, A.W. Garrison, K.E. Wommack, A. Whittemore, P. Steudler, J. Melillo, Nature 401 (1999) 898.
[6] H. Huhnerfuss, Chemosphere 40 (2000) 913.
[7] H.R. Buser, M.D. Muller, T. Poiger, M.E. Balmer, Environ. Sci. Technol. 36 (2002) 221.
[8] J.J. Ridai, T.F. Bidleman, B.R. Kerman, M.E. Fox, W.M.J. Strachan, Environ. Sci. Technol. 31 (1997) 1940.
[9] K. Wiberg, R.J. Letcher, C.D. Sandau, R.J. Norstrom, M. Tysklind, T.F. Bidleman, Environ. Sci. Technol. 34 (2000) 2668.
[10] B. Bethan, K. Bester, H. Hühnerfuss, G. Rimkus, Chemosphere 34 (1997) 2271.
[11] B. Pfaffenberger, H. Hühnerfuss, B. Gehrcke, I. Hardt, W.A. König, G. Rimkus, Chemosphere 29 (1994) 1385.
[12] N. Fidalgo-Used, M. Montes-Bayón, E. Blanco-González, A. Sanz-Medel, J. Anal. At. Spectrom. 20 (2005) 876.
[13] N. Fidalgo-Used, M. Montes-Bayón, E. Blanco-González, A. Sanz-Medel, J. Anal. At. Spectrom. 21 (2006) 876.
[14] C. Arthur, J. Pawliszyn, Anal. Chem. 62 (1990) 2145.
[15] H. Kataoka, H.L. Lord, J. Pawliszyn, J. Chromatogr. A 880 (2000) 35.
[16] G. Theodoridis, E.H.M. Koster, G.J. de Jong, J. Chromatogr. B 745 (2000) 49.
[17] J. Beltran, F.J. Lopez, F. Hernandez, J. Chromatogr. A 885 (2000) 389.
[18] N. Fidalgo-Used, G. Centineo, E. Blanco-González, A. Sanz-Medel, J. Chromatogr. A 1017 (2003) 35.
[19] A.P. Vonderheide, J. Meija, M. Montes-Bayón, J.A. Caruso, J. Anal. At. Spectrom. 18 (2003) 1097.
[20] D. Pröfrock, P. Leonhard, S. Wilburg, A. Prange, J. Anal. At. Spectrom. 19 (2004) 623.

Available online at www.sciencedirect.com
ScienceDirect
Talanta 75 (2008) 740–747
Talanta
www.elsevier.com/locate/talanta

Labeled magnetic nanoparticles assembly on polypyrrole film for biosensor applications

H. Ben Fredj[a], S. Helali[a], C. Esseghaier[a], L. Vonna[b,*], L. Vidal[b], A. Abdelghani[a]

[a] *Unité de Recherche de Physique des Semi-conducteurs et Capteurs, IPEST, La Marsa 2070, Tunis, Tunisia*
[b] *Institut de Chimie des Surfaces et Interfaces CNRS-UPR9069, 15 Rue Jean Starcky, 68057 Mulhouse Cedex, France*

Received 20 July 2007; received in revised form 1 December 2007; accepted 7 December 2007
Available online 3 January 2008

Abstract

In recent years, conducting polymers combined with metallic nanoparticles have been paid more attention due to their potential applications in microelectronics, microsystems, optical sensors and photoelectronic chemistry. The work presented in this paper describes the preparation and characterization of a nanocomposite composed by a thin polypyrrole (PPy) film covered with an assembly of magnetic nanoparticles (NPs). The magnetic particles were immobilized on PPy films under appropriate magnetic field in order to control their organization on the PPy film and finally to improve the sensitivity of the system in potential sensing applications. The electrical properties and morphology of the resulting PPy film and the PPy film/NPs composite were characterized with cyclic voltammetry, impedance spectroscopy (IS), scanning electron microscopy (SEM), atomic force microscopy (AFM) and infra-red spectroscopy (IR). By using streptavidin labeled magnetic particles it was possible to functionalize the NPs assembly with biotin-Fab fragment K47 antibody. The designed biosensor had been successfully applied in rapid, simple, and accurate measurements of atrazine concentrations, with a significantly low detection limit of 5 ng/ml.

Keywords: Polypyrrole; Magnetic beads; Impedance spectroscopy; Biosensor; Nanoparticles

---

1. Introduction

Polypyrrole (PPy) is a semiconducting polymer that has proven to be relatively highly conductive, easy to synthesize, and environmentally stable [1–3]. PPy can be prepared by plasma and vapor phase polymerization techniques. In applications like coating dielectric materials, the most suitable process is the in situ chemical polymerization, because it provides relatively high conductivity as well as suitable thickness and uniformity of the film [2]. Moreover, PPy have been paid more attention due to their potential application values in microelectronics, microsystems, optical sensors and photoelectronic chemistry [4–6]. Most of the optical, electrical and morphologic properties of the PPy depend on the synthesis procedure as well as on the dopant nature.

In many recent works, PPy films are found to be associated with metallic nanoparticles (NPs) [7]. The development of such nanocomposites is essentially motivated by their high analytical sensitivity in sensing applications [8]. Different properties emerging from the nanostructuration with NPs are at the origin of the increased sensing sensitivity. The NPs size and high surface area have first the ability to facilitate direct and fast electron transfer between the nanocomposite and the transducer. Second, when compared to homogeneous bulk matrices, the high surface area of the NPs assembly also leads to nanoporosity for signal amplifications and increased sensitivity toward surface adsorption or surface reactions [9–11]. Because of the same geometric properties the NPs assembly also allows minimum diffusion of the target molecule, and in the same time, miniaturization of the device. Finally it was shown that the selectivity of the sensor could be enhanced by tuning the molecular interactions between the NPs and linker molecules. The improvement of the sensing properties resulting from the nanostructuration is such that various routes were proposed in order to incorporate NPs either in the PPy film [12–16] or by synthesis of the metallic NPs directly on the PPy film [17–19].

In this work, PPy films were prepared by electropolymerization and covered in a second step by streptavidin labeled

---

* Corresponding author. Tel.: +33 3 89 60 87 18; fax: +33 3 89 60 87 99.
E-mail address: l.vonna@uha.fr (L. Vonna).

0039-9140/$ – see front matter © 2007 Elsevier B.V. All rights reserved.
doi:10.1016/j.talanta.2007.12.034

magnetic particles using a controlled magnetic field. This method allowed us to control the distribution and morphology of the NPs assembly on the PPy film for improved sensing applications. Electrical and morphological properties of both NPs covered and uncovered films, were assessed by using voltammetry, impedance spectroscopy (IS), scanning electron microscopy (SEM), atomic force microscopy (AFM) and infrared spectroscopy (IR). In order to test the performance of this nanocomposite electrode in biosensing applications, biotin-Fab fragment K47 was immobilized on the streptavidin labeled magnetic particles. This system was successfully used in detecting atrazine with a detection limit of 5 ng/ml.

2. Experimental

2.1. Chemicals and particles

Pyrrole monomer (98%) and lithium perchlorate ($LiClO_4$) was purchased from Sigma–Aldrich (France). Atrazine was purchased from Supelco, Bellefonte, Pennsylvania, USA. The antibody Fab 60 fragment K47 was obtained from Technische Universität München, Germany, and then labeled with biotin in the Institut National de la Recherche Agronomique (INRA), Paris, France. The buffer solution used for all experiments was phosphate buffered saline (PBS) containing 140 mM NaCl, 2.7 mM KCl, 0.1 mM Na_2HPO_4, 1.8 mM KH_2PO_4, pH 7 and the redox couple $Fe(CN)_6^{3-}$/$Fe(CN)_6^{4-}$ at a 5 mM concentration. All reagents were of analytical grade and ultrapure water (resistance 18.2 $M\Omega\,cm^{-1}$) produced by a MilliporeMilli-Q system was used. The magnetic particles coated with streptavidin are Fe_2O_3 particles characterized by a mean diameter of 200 nm and purchased from Ademtech SA, Pessac, France.

2.2. Gold electrodes cleaning

The gold electrodes were cleaned with organic solvents (acetone and ethanol) and with piranha solution (1:3 H_2O_2—concentrated H_2SO_4) for 1 min. After each treatment, the gold substrates were rinsed with ethanol and dried under nitrogen flow.

2.3. Electropolymerization

The PPy film was coated on a gold electrode using cyclic voltammetry. The gold electrode was bulked in an acetonitril solution (Bu_4NPF) containing pyrrole monomer (C_4H_5N 0.1 M) and lithium perchlorate ($LiClO_4$ 0.1 M). The potential sweep was used instead of a polymerization in potentiostatic mode in order to obtain a smoother film. The potential sweep was performed from −300 to 1100 mV with 25 mV/s scan rate for 6 cycles. Three-electrodes cells were used, a platinum as counter electrode, calomel reference electrode and gold substrate as working electrode.

2.4. Cyclic voltammetry

Cyclic voltammetry measurement was performed in a 5 mM solution of redox couple $Fe(CN)_6^{-4/-3}$ prepared in PBS buffer. Scanning potential was conducted between −600 and 600 mV with 100 mV/s scan rate. Cyclic voltammetry enabled the detection of PPy and magnetic beads film immobilized on gold surface.

2.5. Impedance spectroscopy

The impedance analysis was performed with the Voltalab 40 impedance analyser in the frequency range 0.05 Hz to 100 kHz, using a modulation voltage of 10 mV. A three-electrode system was employed with a saturated calomel electrode (SCE), an immunosensor working electrode (0.11 cm^2), and a platinum strip counter electrode (0.54 cm^2). The impedance measurements were performed in the presence of a 5 mM $K_3[Fe(CN)_6]$/$K_4[Fe(CN)_6]$ (1:1) mixture as redox probe in PBS.

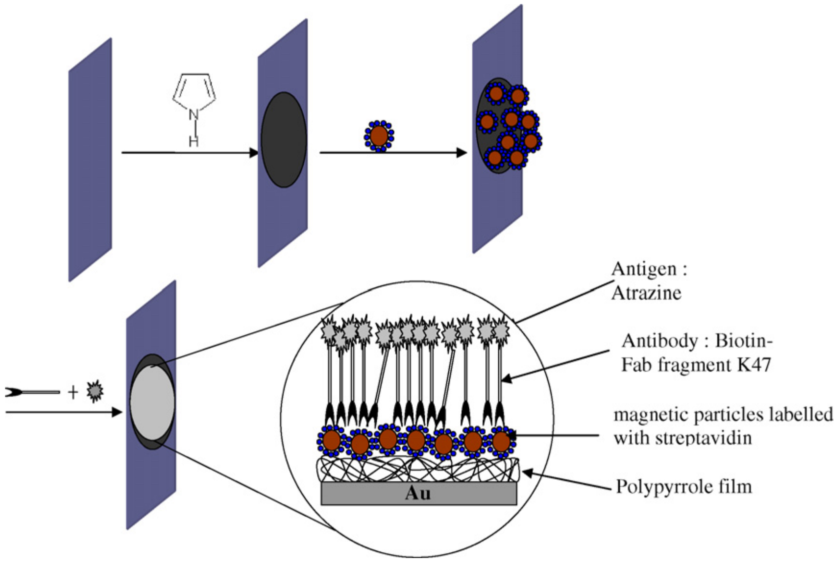

Fig. 1. A schematic diagram of the immunosensor showing the stepwise immunosensor fabrication process.

The measured spectra of the impedance was analysed in terms of electrical equivalent circuits model using a Zview modelling programme (Scribrer and associates, Charlottesville, VA). All electrochemical measurements were carried out at room temperature and in a faraday cage. More details on electrochemical impedance spectroscopy (EIS) can be found in Refs. [20–23].

2.6. Scanning electron microscopy

Electron micrographs of gold electrode functionalized with PPy, with and without the NPs assembly, were observed with a FEI QUANTA 400 model scanning electron microscope (SEM) working at an accelerating voltage of 30 keV. Since this electrode is a conducting material all observations were preformed without any prior gold sputtering.

2.7. Atomic force microscopy

Electrode surfaces were imaged with a D3000 AFM from Digital Instruments. All images were acquired in the tapping mode, processed by means of a plane fit and finally flattened in the first mode using a built-in software procedure. Because of the high roughness of the PPy electrode surface, the scan rate we applied was relatively low (0.1–0.5 Hz).

2.8. Fourier transformed infra-red spectroscopy

Burcker IFS66VIS spectrometer equipped with a middle infrared (MIR) source, a DTGS detector and a KBr separating mirror was used to obtain the FTIR spectra. Our method consisted on recording the spectrum of the cleaned gold substrate and then the gold substrate with PPy film. The spectrum of the cleaned electrode served as a reference. The ratio of the two spectra gave the spectrum of the PPy. The same method was used to confirm the deposition of the functionalized streptavidin labeled magnetic NPs.

3. Results and discussion

3.1. Cyclic voltammetry

Cyclic voltammetry is an electrochemical technique, which can be used to study the kinetics of oxido-reduction reaction on material, their insulating and conducting properties. The molecular structure of the biosensor developed in this work is shown in Fig. 1. Cyclic voltammograms of the gold electrode (Fig. 2a) shows a reversible phenomenon, which is the typical behaviour of gold surface with redox couple. The two peaks of the cathodic and anodic waves of redox probe have been obtained. After modification of the gold surface with PPy, the dc-current increases due to the conducting properties of the PPy film (Fig. 2b). After immobilization of the magnetic particles on the PPy film, the direct current decreases due to the insulating properties of the functionalized film (streptavidin) covering the particles (Fig. 2c). The same explanation applies for the decrease of the direct current after immobilization of the antibody (Fig. 2d) and after the BSA blocking step (Fig. 2e). To confirm all these results, impedance spectroscopy measurements were performed on those systems.

3.2. Impedance spectroscopy

EIS has been widely recognized as a powerful diagnostic tool for the investigation of the electrical behaviour of an electrochemical system in which various processes proceed at different rates [23–27,20]. The EIS can further give information on the impedance changes of the immunoelectrode surface

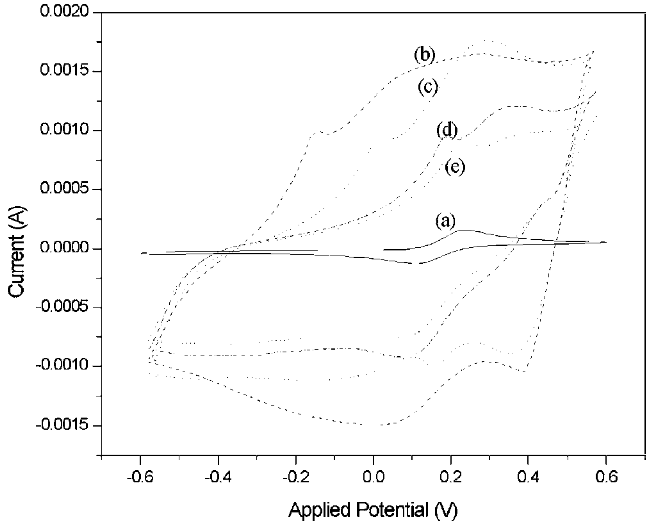

Fig. 2. Cyclic voltammograms (CVs) with 100 mV s^{-1} scan rate in a 5 mM Fe(CN)$^{-4/-3}$ solution (PBS, pH 7.0), after different steps of modification: (a) bare gold electrode, (b) PPy film modified gold electrode, (c) PPy covered with streptavidin labeled magnetic particles, (d) immobilization of the antibody biotin-Fab fragment K47 and (e) BSA blocking layer.

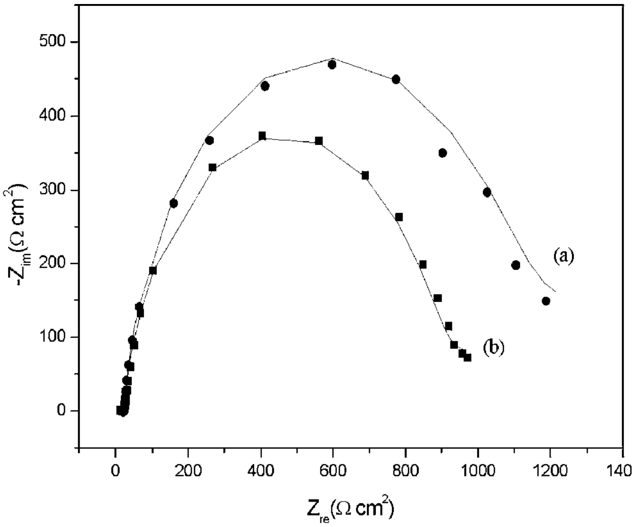

Fig. 3. Nyquist diagram (Z_{re} vs. Z_{im}) for the faradic impedance measurements corresponding to (a) bare Au-electrode and (b) PPy film functionalized Au-electrode. All measurements were performed in PBS (pH 7.0) + 5 mM Fe(CN)$_6{}^{-4/-3}$ solution. Amplitude of alternating voltage 10 mV. Solid curves show the computer fitting of the data using the equivalent circuits shown in Fig. 4.

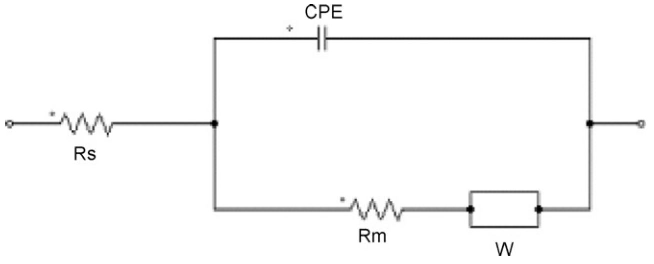

Fig. 4. Equivalent circuit used for impedance spectra.

in the modification process. The complex impedance can be presented as a combination of the real impedance (Z_{re}) and imaginary impedance (Z_{im}), Nyquist plot. Typical Nyquist plots for gold electrode and gold/PPy film from 50 mHz to 100 kHz at −1200 mV potential (versus calomel electrode), with 5 mM redox couple, are shown in Fig. 3. A more stable PPy film in liquid medium was obtained for an applied electrical potential of −1200 mV versus calomel electrode. Impedance spectra may be interpreted through equivalent circuits representing the different processes involved in the description of the system with discrete electric elements. We have used in the present work the Randles equivalent circuit modified by inclusion of distributed elements to take into account the finite spatial extension of the system under study [25,26,20]. This latter manifest in impedance spectra as 'depressed' semicircles, with their origin located below the real axis. The equivalent circuit used for the interpretation of the data is shown in Fig. 4, diffusion is represented by Warburg element. A CPE was thus used to represent the non-homogeneous nature of the electrode material, the electrode material and the distribution of relaxation time of the processes occurring within it, with impedance given by [25,26,20]:

$$Z = \left(\frac{1}{\sigma}\right)(j\omega)^{-\alpha}$$

where σ and α are positive constants.

A CPE describes a capacitor when $\alpha = 1$, in which case $\sigma = C$, and tends to a resistor as $\alpha \to 0$. The presence of a CPE with $0 < \alpha < 1$ depresses high frequency semicircles below the real axis. The semicircle diameter of EIS equals the electron transfer resistance, R_{m}. This resistance controls the electron transfer kinetics of the redox probe at the electrode interface. Curve a in Fig. 3 shows EIS of the bare gold electrode.

It can be seen that the bare gold electrode exhibits a semicircle giving the resistance equal to 1020 Ω cm^2. After the bare gold electrode was modified with PPy film, the EIS of the modified electrode shows a lower interfacial resistance equal at 849.7 Ω cm^2 (curve b in Fig. 3). The decrease in R_{m} resistance indicates an increase in the conductivity, which confirms the results obtained with cyclic voltammetry.

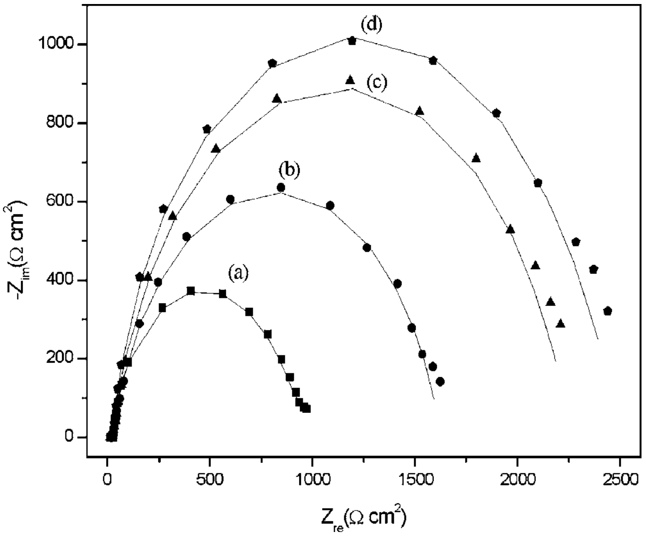

Fig. 5. Nyquist diagram for the faradic impedance measurements corresponding to (a) PPy film/Au-electrode, (b) streptavidin labeled magnetic particles/PPy film/Au-electrode, (c) biotin-Fab fragment K47 antibody/streptavidin labeled magnetic particles/PPy film/Au-electrode and (d) blocked layer with BSA/biotin-Fab fragment K47 antibody/streptavidin labeled magnetic particles/PPy film/Au-electrode. Solid curves show the computer fitting of the data using the equivalent circuits shown in Fig. 4. Symbols show the experimental data.

The PPy film was covered with magnetic particles labeled with streptavidin using a magnetic field (0.3 mT). Fig. 5 shows the impedance spectrum of a PPy film coated gold electrode (curve a) compared with streptavidin labeled magnetic particles surface (curve b), with an antibody-immobilized surface (curve c) and with BSA blocking layer (curve d). Note that all the spectra are almost similar, containing a distorted semicircle. The diameter of the semicircle provides an estimate of the film charge transfer resistance. Using the same equivalent circuit model described in Fig. 4, an excellent fitting between the simulation and experimental spectra was obtained. The values obtained for the different elements composed the equivalent circuit are shown in Table 1. The resistance of the studied interface increases after the immobilization of each step. This increase is due to the decrease of the conductivity due to the insulating properties of grafted layers. This confirms the results obtained with cyclic voltammetry.

Table 1
Fitting values of the equivalent circuit elements for PPy, magnetic layer, after binding of the antibody and blocking with BSA

	PPy film	Streptavidin labeled magnetic particles	Antibody: biotin-Fab fragment K47	Blocking layer: BSA
R_{s}(Ω cm^2)	24.26	24.23	22.95	24.36
R_{m} (Ω cm^2)	849.7	1593	2196	2377
σ (μF cm^{-2})	71.77	86.77	85.52	82.08
α	0.9	0.84	0.86	0.9
W (mΩ cm^2)	12.67	60	50	23

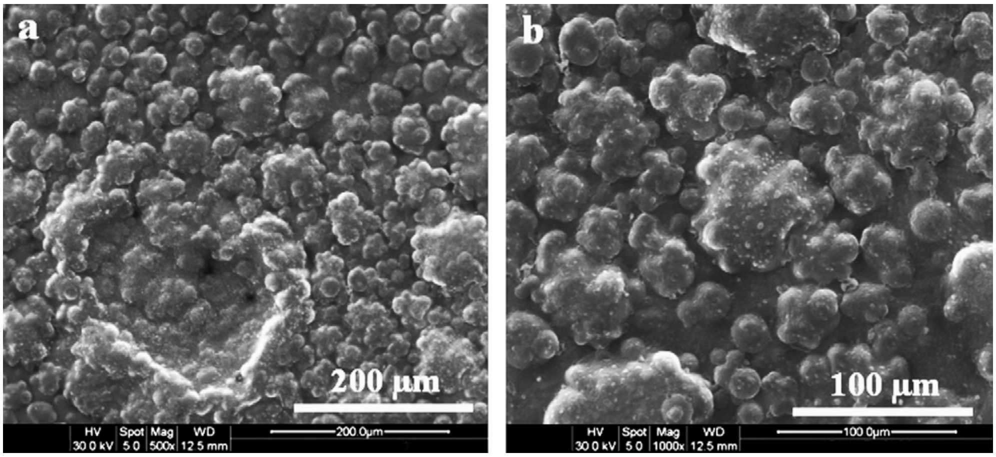

Fig. 6. SEM micrographs of the PPy film formed on gold electrode.

3.3. Scanning electron microscopy

Fig. 6 shows two SEM micrographs of a PPy film surface formed after 6 deposition cycles. These micrographs reveal the cauliflower morphology usually observed for electrochemically deposited PPy films which is attributed to the nodular fractal-type growth of these polymers [28,29]. SEM observations associated with optical microscopy observations showed that such a film grew uniformly over the whole surface of the electrode. After deposition of the NPs, the surface of the PPy film seems to be smoother and the cauliflower structure is less pronounced as shown in Fig. 7a and b. Moreover cracks are clearly observable in the NPs assembly probably due to constraints emerging during the drying step. The side view of the PPy film/NPs assembly composite shown in Fig. 7c and d were observed after breaking the sample in two parts. One can clearly see the thicknesses of both the PPy film and the NPs assembly which are, respectively around 2 and 4 μm. The morphology of the NPs assembly shown in this image fulfill the porosity and large surface area conditions for high sensitivity of the sensor. Wrinkling of the PPy film may come from the fracture of the sample.

3.4. Atomic force microscopy

The atomic force microscopy images of the PPy film shown in Fig. 8 confirm the SEM observations at the microscopic scale. The micrometric structure of the polymer is still characterized by a cauliflower morphology as expected for a fractal morphology [30]. However, the high roughness of this surface does not allow

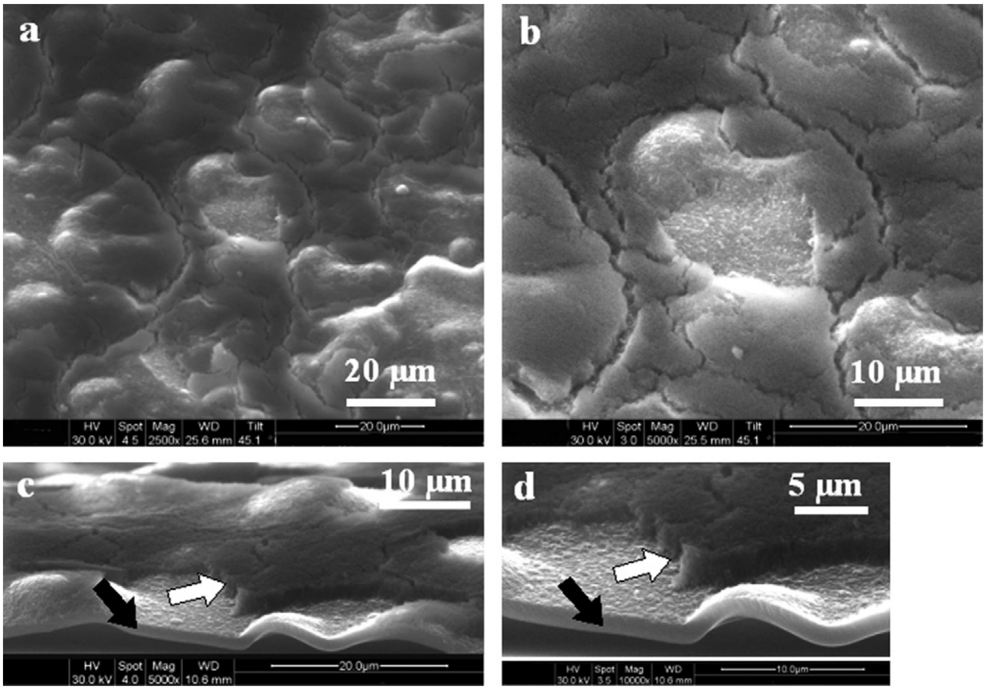

Fig. 7. SEM micrographs of the magnetic NPs assembly covering the PPy film. Top view (a) and (b), side view (c) and (d). The black arrow indicates the PPy film and the white arrow the NPs assembly.

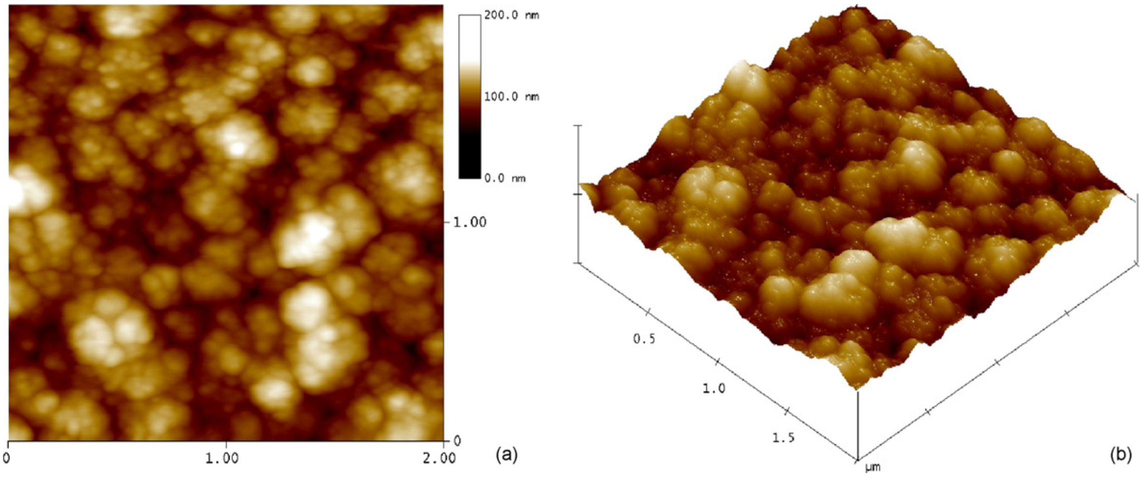

Fig. 8. Top (a) and 3D (b) AFM images of a PPy film showing the cauliflower structure of this polymer. *Z* range on the 3D view is 200 nm.

atomic force microscopy acquisitions on large area. The NPs assembly is clearly observable with atomic force microscopy as shown in Fig. 9. Cracks in the NPs assembly are again present at microscopic scale as under SEM at larger scale. Both SEM and AFM observations allow us to assess for the distribution of both the PPy and the NPs on the electrode, which should provide enhanced adsorption and sensitivity in sensing application.

3.5. *FTIR*

The infrared absorption spectra of PPy films without and with functionalized magnetic particles are shown in Fig. 10. The shown spectra is nearly same in the two cases, indicating that the structure of PPy film was not changed after particles immobilization. The broad band at 3440 cm^{-1} corresponds to the absorption of N–H stretching vibration mode. The absorption at 1635 and 1554 cm^{-1} assigned to the C=C and C–C ring stretching mode, respectively. The bands at 1365 and 1189 cm^{-1} are assigned to C–H and C–N stretching vibrations [31–34]. The peaks located at 907, 786 and 676 cm^{-1} should be assigned to C–H out-of-plane deformation, C–H out-of-plane ring deformation and C–C out-of-plane ring deformation, respectively [35,36]. No peak has been observed at 1700 for C=O stretching, which suggests that the pyrrole is not overoxidized. After the immobilization of streptavidin functionalized magnetic particles, the measured spectra shows an increase of the peak intensity below 1500 cm^{-1} and the presence of a band located at 2040 cm^{-1}. This band is attributed to one of the vibrations mode of streptavidin.

3.6. *Biosensor application*

Atrazine (2-chloro-4-ethytlamino-6-isopropylamine-1,3,5-triazine) is a worldwide and commonly used herbicide. Despite it is usually considered toxic only at high doses, it was shown recently that atrazine may interfere with metamorphosis and sex differentiation even at low and ecologically relevant doses [37]. The detection of this pollutant is of fundamental importance for environmental safety and human health. In this work biotinylated Fab fragment K47 was covalently bound to the particles through streptavidin/biotin linkage. This allows specific bounding of atrazine on the NPs and variation of the electrode impedance response. Atrazine–antibody interactions were mon-

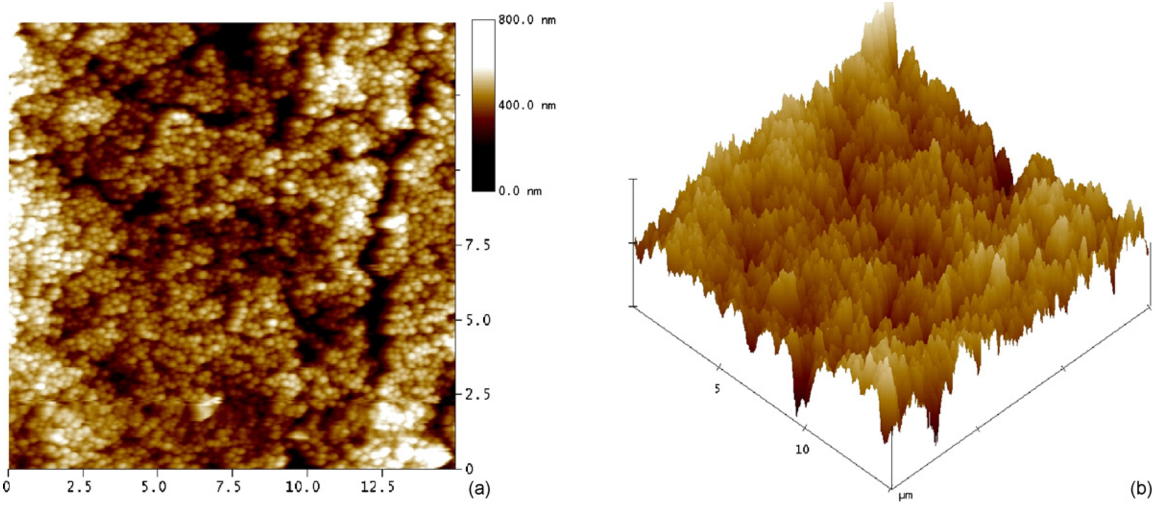

Fig. 9. Top (a) and 3D (b) AFM images of a PPy film (6 cycles) covered with an array of nanoparticles. *Z* range on the 3D view is 600 nm.

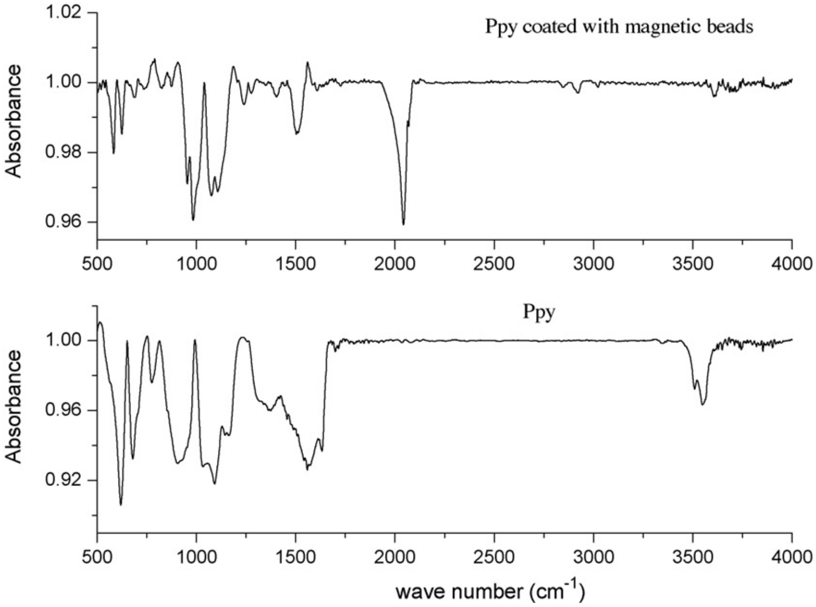

Fig. 10. FTIR spectra for pure PPy film and PPy/streptavidin labeled magnetic particles.

itored by impedance spectroscopy at −1200 mV. The impedance variation after atrazine injections in the range of 0–70 ng/ml are shown in Fig. 11. The semicircle diameter in the Nyquist plot is increasing with the atrazine concentration, implying that more amount of atrazine was linked to the interface.

The change of the charge transfer resistance ΔR is obtained by subtracting the resistance of the immobilized BSA layer from the resistance of the resultant immuno-complex. As for the control, ΔR is obtained by deducting the resistance of the PPy/BSA film from the resistance of the antibody–atrazine complex. Fig. 12 shows an increase in the charge transfer resistance ΔR with the increment of atrazine concentration in the range of 0–170 ng/ml. These results revealed that the presence of the PPy film under the NPs assembly increases over four orders of magnitude the sensitivity of the sensor as compared to only the NPs assembly, with an excellent detection limit of 5 ng/ml [38]. Whereas the response of the immunosensor to different concentrations of non-specific molecules (IgG mouse antigen) was clearly non-significant.

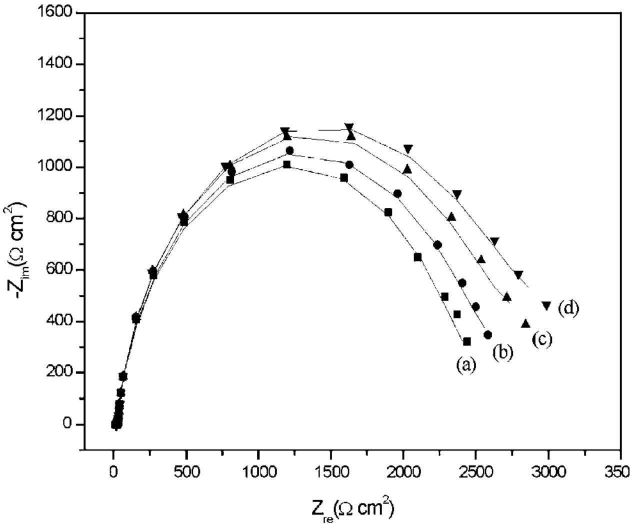

Fig. 11. Complex impedance plots of antigen–antibody/streptavidin labeled magnetic particles/PPy film/Au-electrode under various concentrations of antigen. The concentrations of antigen (ng/ml): (a) 0; (b) 5; (c) 10; (d) 70. Applied frequency from 0.5 Hz to 100 kHz.

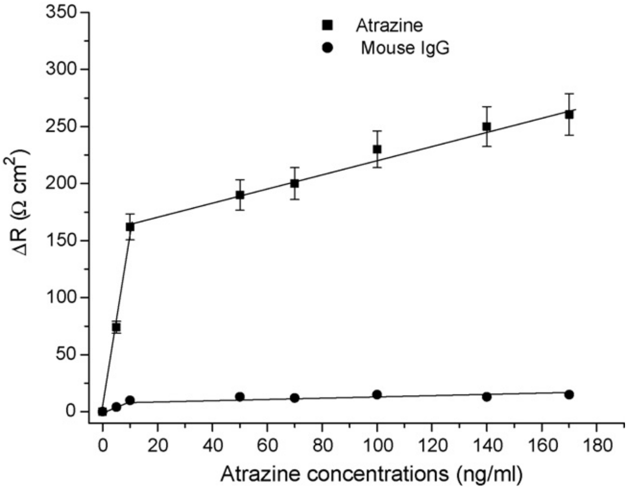

Fig. 12. Calibration plots for the immunosensor in PBS + 5 mM $Fe(CN)_6{}^{-4/-3}$ solution at pH 7.0 in the presence of different concentrations of atrazine and non-specific antigen.

4. Conclusion

In this work, we report the preparation and characterization of a nanocomposite PPy/NPs films for biosensor applications. An assembly of magnetic particles labeled with streptavidin was immobilized on the PPy film under appropriate magnetic field. In a second step, biotin-Fab fragment K47 antibody was coupled to the particles through streptavidin for atrazine detection.

The designed biosensor is characterized by high sensitivities and low detection limits (5 ng/ml atrazine or 2.3×10^{-8} M). This study demonstrates that the assembling of magnetic NPs under magnetic field on conductive polymer films (PPy for example), is a convenient way to construct easily and rapidly sensitive nanocomposites electrodes. The NPs assembly on the PPy film was shown to be uniform and stable enough to be used in biosensing applications, and suggests that the method developed in this work could be useful for the fabrication of other biological sensors.

Acknowledgments

The authors thank the Alexander Von Humboldt Foundation for material donation, Pr. N. Jaffrezic–Renault (UCB, Lyon1, France) and Hamidou Haidara (Institut de Chimie des Surfaces et Interfaces—CNRS, UPR9069, Mulhouse, France) for scientific support.

References

[1] L.-X. Wang, X.-G. Li, Y.-L. Yang, React. Funct. Polym. 47 (2001) 125.
[2] M. Ferenets, A. Harlin, Thin Solid Films 515 (2007) 5324.
[3] M.A. de la Plaza, M.C. Izquierdo, Eur. Polym. J. 42 (2006) 1446.
[4] W. Geng, N. Li, X. Li, R. Wang, J. Tu, T. Zhang, Sens. Actuator B 125 (2007) 114.
[5] M. Liu, Y. Zhang, M. Wang, C. Deng, Polymer 47 (2006) 3372.
[6] A. Hallik, A. Alumaa, J. Tamm, V. Sammelselg, M. Väärtnõu, A. Jänes, E. Lust, Synth. Met. 156 (2006) 488.
[7] R. Gangopadhyay, A. De, Chem. Mater. 12 (2000) 608.
[8] C.W. Welch, R.G. Compton, Anal. Bioanal. Chem. 384 (2006) 601.
[9] K.R. Brown, A.P. Fox, M.J. Natan, J. Am. Chem. Soc. 118 (1996) 1154.
[10] T.G. Drummond, M.G. Hill, J.K. Barton, Nat. Biotechnol. 21 (2003) 1192.
[11] A.N. Shipway, M. Lahav, L. Willner, Adv. Mater. 12 (2000) 993.
[12] J.L. Besombes, S. Cosnier, P. Labbe, Talanta 44 (1997) 2209.
[13] A.C. Arango, S.A. Carter, P.J. Brock, Appl. Phys. Lett. 74 (1999) 1698.
[14] P. Zhang, Z.H. Yang, D.J. Wang, S.H. Kan, X.D. Chai, J.Z. Liu, T.J. Li, Synth. Met. 84 (1997) 165.
[15] Y.C. Liu, H.T. Lee, S.J. Yang, Electrochim. Acta 51 (2006) 3441.
[16] A. Alqudami, S. Annapoorni, P. Sen, R.S. Rawat, Synth. Met. 157 (2007) 53.
[17] X.J. Zhou, A.J. Harmer, N.F. Heinig, K.T. Leung, Langmuir 20 (2004) 5109.
[18] Y. Li, G.Q. Shi, J. Phys. Chem. B 109 (2005) 23787.
[19] J. Li, X. Lin, Sens. Actuator B 124 (2007) 486.
[20] A. Abdelghani, S. Hleli, K. Cherif, Mater. Lett. 56 (2002) 1064.
[21] Y. Hou, S. Helali, A. Zhang, N. Jaffrezic-Renault, C. Martelet, J. Minic, T. Gorojankina, M.-A. Persuy, E. Pajot-Augy, R. Salesse, F. Bessueille, J. Samitier, A. Errachid, V. Akimov, L. Reggiani, C. Pennetta, E. Alfinito, Biosens. Bioelectron. 21 (2006) 1393.
[22] S. Hleli, A. Abdelghani, A. Tlili, Sensors 3 (2003) 472.
[23] S. Hleli, C. Martelet, A. Abdelghani, N. Burais, N. Jaffrezic-Renault, Sens. Actuator B 113 (2006) 711.
[24] J.R. MacDonald, Impedance Spectroscopy, Wiley, New York, 1987.
[25] H. Hillebrandt, A. Abdelghani, C. Abdelghani, E. Sackmann, Appl. Phys. A 73 (2001) 539.
[26] Wiegand, PhD thesis: Fundamental principles of the electric properties of supported lipid membranes investigated by advanced methods of impedance spectroscopy, 1999, Shaker verlag, Technishe Universität of München, Germany, ISBN 3-8265-7231-9.
[27] A. Tlili, A. Abdelghani, S. Hleli, M.A. Maaref, Sensors 4 (2004) 105.
[28] S. Paschen, M. Carrard, B. Senior, F. Chao, M. Costa, L. Zuppiroli, Acta Polym. 47 (1996) 511.
[29] R. Singh, A.K. Narula, R.P. Tandon, S.U.M. Rao, V.S. Panwar, A. Mansingh, S. Chandra, Synth. Met. 79 (1996) 1.
[30] T. Silk, Q. Hong, J. Tamm, R.G. Compton, Synth. Met. 93 (1998)59.
[31] J. Zhu, J.Z. Xu, J.T. He, Y.J. Wang, Q. Miao, H.Y. Chen, Anal. Lett. 36 (2003) 1547.
[32] Y.Q. Miao, J.G. Guan, Anal. Lett. 37 (2004) 1053.
[33] J. Li, H. Zhan, Y. Zhou, Electrochem. Commun. 5 (2003) 555.
[34] M. Bazzaoui, E.A. Bazzaoui, L. Martins, J.I. Martins, Synth. Met. 130 (2002) 73.
[35] P. Dutta, S.K. De, Synth. Met. 139 (2003) 201.
[36] M. Omastová, M. Trchová, J. Pionteck, J. Prokeš, J. Stejskal, Synth. Met. 143 (2004) 153.
[37] T.B. Hayes, A. Collins, M. Lee, M. Mendoza, N. Noriega, A.A. Stuart, A. Vonk, Proceedings of the National Academy of Sciences of the United States of America 99, 2002, p. 5476.
[38] S. Helali, C. Martelet, A. Abdelghani, N. Jaffrezic-Renault, Electrochim. Acta 51 (2006) 5182.

Available online at www.sciencedirect.com

ScienceDirect

Talanta 75 (2008) 792–796

Talanta

www.elsevier.com/locate/talanta

An inexpensive, portable and microcontrolled near infrared LED-photometer for screening analysis of gasoline

Edvaldo da Nóbrega Gaião, Sérgio Ricardo Bezerra dos Santos, Vagner Bezerra dos Santos, Elaine Cristina Lima do Nascimento, Renato Sousa Lima, Mário César Ugulino de Araújo*

Universidade Federal da Paraíba, CCEN, Departamento de Química, Caixa Postal 5093, 58051-970 João Pessoa, PB, Brazil

Received 4 September 2007; received in revised form 13 November 2007; accepted 8 December 2007
Available online 23 December 2007

Abstract

A microcontrolled, portable and inexpensive photometer is proposed. It uses a near infrared light emitting diode (NIR LED) as radiation source, a PbSe photoresistor as infrared detector and a programmable interrupt controller (PIC) microcontroller as control unit. The detector system presents a thermoresistor and a thermoelectric cooling to control the detector temperature and keep the noise at low levels. The microcontroller incorporated total autonomy on the proposed photometer. As its components are inexpensive and of easy acquisition, the proposed NIR LED-photometer is an economical alternative for chemical analyses in small routine, research and/or teaching laboratories. By being portable and microcontrolled, it also allows carrying out field chemical analyses. The instrument was successfully applied on the screening analysis to verify adulteration in gasoline samples.

Keywords: Near infrared; Light emitting diode; Photometer; Microcontroller; Screening analysis; Gasoline

---

1. Introduction

The light emitting diode (LED) [1] is a semiconductor device usually adapted on portable photometers (LED-photometers) as radiation source because it confers some advantages for optical instruments [1,2] as simplicity, easy operation, light stability and low power and cost.

LED-photometers are usually applied as dedicated instruments since ordinary LEDs emit only a fairly narrow band radiation with half maximum intensity of about 20–50 nm [1,2]. When spectrophotometers are constructed for general purpose, complex configurations to adapt a higher number of LEDs [3,4], interference filters [5,6] or grating monochromators [7] must be adapted to select the desired wavelengths. These are modifications that naturally increase the complexity and consequently the cost of the instrument.

Since the beginning, LEDs for analytical purposes are basically emitters of visible radiation [8] and most of the LED-photometers are applied on spectrometric determinations in flow injection analysis, area where they are widely used [9–15]. On the other hand, the sort of infrared (IR) LED emitters was limited [1,2] and so was its analytical applications. Advances in the IR LED construction enabled to develop good near infrared (NIR) LEDs [2] for analytical purposes. Also, chemometric techniques [16] allowed to apply NIR technology [17] to analyze very diverse materials [18–22].

Although the application of analytical procedures based on NIR methods have increased in recent years [23,24], NIR LED-photometers developed and commercialized based on screening philosophy were not elaborated. The screening analysis [25] is a qualitative procedure based on binary answers like positive/negative or yes/no useful to take timely decisions for identification of measurements or sample classification. In the screening analysis, for example, only the samples that surpass an established threshold, for example a cut-off concentration, are directed for a deeper analytical procedure. As advantages, fast analytical assays and minimization of cost are achieved.

In this work was constructed a portable and microcontrolled NIR LED-photometer (NLP) applied on the screening analysis of gasoline type C, a Brazilian blended gasoline having 25% (v/v) ethanol, aiming at to verify its conformity in regard to some of its principal adulterants (solvents and kerosene) in Brazil. The

---

* Corresponding author. Tel.: +55 83 216 7438; fax: +55 83 216 7437/7117.
E-mail address: laqa@quimica.ufpb.br (M.C.U. de Araújo).

0039-9140/$ – see front matter © 2007 Elsevier B.V. All rights reserved.
doi:10.1016/j.talanta.2007.12.014

NLP was developed to present total autonomy and all the advantageous characteristics of the LED-photometers. As detector was used a PbSe photoresistor equipped with a temperature sensor and refrigerated by a thermoelectric cooler. The detector system kept the noise at very low levels permitting to carry out very precise measurements. With the microcontroller unit was possible to control external devices, perform analytical data acquisition and display the results on a liquid crystal display (LCD).

2. Experimental

2.1. Sample, solvents and kerosenes

Thirty-five samples of pure gasoline, 10 of solvent and 10 of kerosene, all of different manufacturers were purchased, respectively, from gas stations and markets at João Pessoa and Bayeux cities, state of Paraiba, Brazil.

Twenty-five samples of gasoline were used as blank and 10 were used to prepare adulterated gasolines. Thus, solvent adulterated gasolines having a adulterant concentration of 2.0, 3.0, 3.5, 4.0, 4.5, 5.0, 5.5 and 6.0% (v/v) were prepared by spiking the respective volume of solvent into pure gasoline samples. Also, kerosene adulterated gasolines were prepared by adding the respective volume of kerosene into pure gasoline in order to obtain 2.0, 3.0, 3.5, 4.0, 4.5, 5.0, 5.5, 6.0 and 7.0% (v/v) of adulterant. For each adulteration level were prepared 10 samples.

2.2. NIR spectra

A FT-NIR/MIR spectrometer PerkinElmer, model GX, equipped with a quartz cell presenting an optical path length of 1.0 cm was used to register the NIR spectra of the gasoline samples. A spectral resolution of 4 cm^{-1} and 16 scans were used. The NIR region in the range 1000–1700 nm was adopted for this study. The absorbance values for wavelengths above 1700 nm, which are associated to the first overtone of OH and CH vibrational transitions, are very intense and lead to saturation of the detector.

2.3. The NLP

The observation of the NIR spectra (Fig. 1) allowed defining the spectral region around 1550 nm as the most adequate for identification of the gasoline adulteration. As showed in Fig. 1, clearly there exist very different response intensities between adulterants and pure gasolines which are not so expressive in other regions and that enable an accurate distinction between these materials. At 1550 nm, the absorbance intensities from gasoline samples are lower than that from solvent but higher than that from kerosene. Thus, it is expected an increasing of the absorbance intensities when solvent is added in the gasoline samples and a decreasing when the adulteration is carried out by kerosene.

Another advantage of this region is the broad absorption band presented by the analyzed samples that compensates the broad NIR LED emission band (±50 nm). Closer wavelengths as that ones around 1200, 1400 and 1650 nm could not produce a linear analytical signal due to the NIR LED bandwidth limitation.

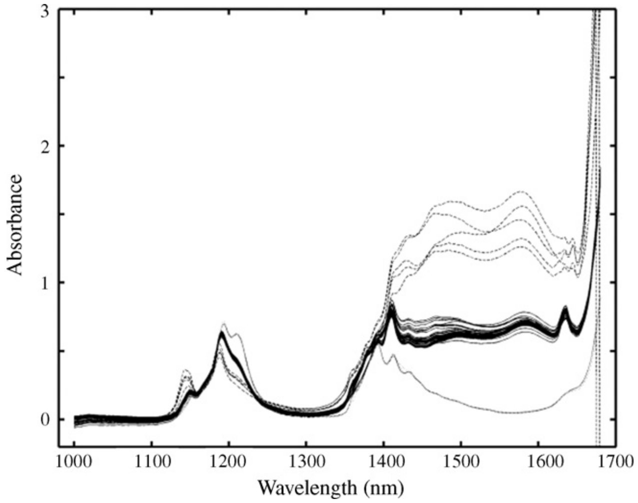

Fig. 1. NIR spectra of 10 samples of solvent (dashed line), 35 of gasoline (solid dark line) and 10 samples of kerosene (solid light line).

Therefore, a NIR LED (L1550-35k42, Epitex incorp.) with an InAsGaP substrate and 1550 nm emission wavelength was used as radiation source in the NLP.

For detection of the NIR LED radiation, a PbSe photoresistor (PR2-27-20-320, RMT Ltd.) with 2 mm sensitivity area and detection limit at 2700 nm was used. The detector package involves three devices: the PbSe photoresistor chip that generates the analytical signal under infrared radiation, a NTC thermistor for temperature control and a thermoelectric cooler for refrigeration of the photoresistor.

The NIR LED and detector were adapted 3 cm apart on two Perspex® fixed bars and a 2 cm quartz cell was fitted on a support between them. The support presents a central hole with 1 cm diameter which allows radiation to pass throughout the cell and to reach the detector.

Fig. 2 shows details of the components of the NLP. All the electronic components were adapted into a box of 20 cm × 15 cm × 10 cm and the optics is adapted into the cell compartment upon this box.

Fig. 3 shows the block diagram of the NLP. The instrument uses as control unit a PIC 16F877 microcontroller programmable with C language and driven by a stabilized power supply or by 9 V batteries. The microcontroller presents a 10-bit multichannel analog to digital converter (A/D), 8 k × 14 words of flash program memory, 256 × 8 bytes of EEPROM data memory, 368 × 8 bytes of RAM, three timers and three ports with eight channels (multiplexed pins) each, for general purpose, that can be configured for data acquisition. The microcontroller allows drastic reduction of the number of electronic components on the photometer and makes possible to introduce or alter functionalities in the instrument without any hardware modification.

The NIR LED control module pulses the NIR LED radiation at 50 Hz. The module turns the NIR LED on for readings of the analytical signals and off for determination of instrumental

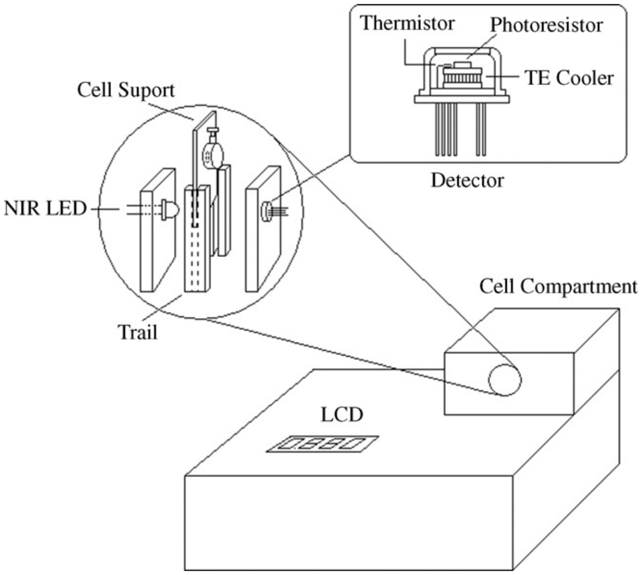

Fig. 2. Details of the NLP.

noise. These signals are detected, filtered and amplified in the detection module of the NLP. After being processed, both signals are transmitted to the A/D converter, selecting the respective channel, to generate digital analytical signals that are converted into absorbance data. After digitalization the absorbance data are sent by the microcontroller for the LCD module which uses a WH-1602A character type LCD with an eight bits data and a three bits control buses. In this work, the communication between microcontroller and LCD was always carried out with seven bits, four for data transmission and three for data control.

The temperature control module controls the detector temperature. Temperature signals furnished by a NTC thermistor with a temperature coefficient of −3.4%/deg (20 °C) located into the detector package, enables the microcontroller to change the electric current on the thermoelectric cooler to keep the operation temperature of the detector on a fixed value (5 °C).

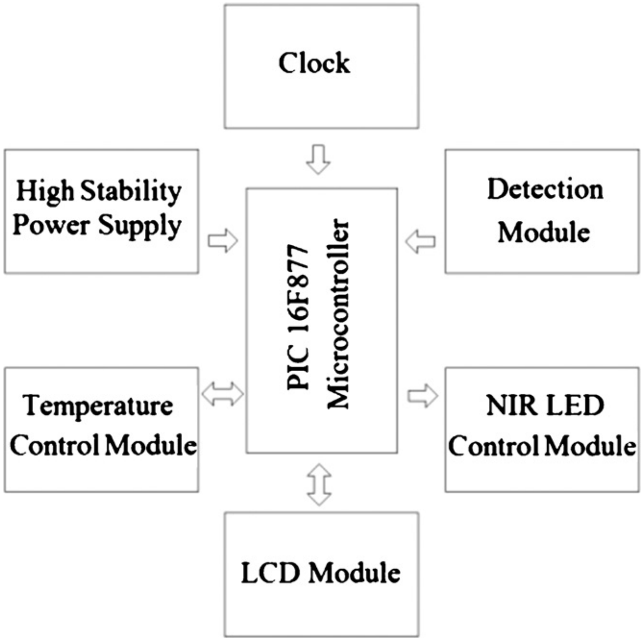

Fig. 3. Block diagram of the NLP.

A clock elaborated with a 4 MHz piezoelectric crystal is used for synchronization of all microcontroller internal functions.

2.4. Operation of the NLP

The measurements with the NLP are performed in a simple way. The quartz cell is filled with the sample and adjusted on the cell support. The cell compartment is closed and the transmittance appears automatically on the LCD screen. Transmittance measurements of pure and adulterated samples of C gasoline were carried out to define a reliability region that indicates the unconformity of the gasoline type C with the quality requirements.

2.5. Analytical procedure for the NLP calibration

Twenty-five samples of gasolines were used to register the blank signal (b) and its standard deviation (s) on the developed photometer which yielded the limits of detection, LD (blank plus three times its standard deviation, $LD = b \pm 3s$), and quantification, LQ (blank plus 10 times its standard deviation, $LQ = b \pm 10s$). In these measurements, 100% of transmittance (zero of absorbance) was determined when the cell was empty and the zero of transmittance was determined when the LED was off.

The reliability of the NLP analysis was verified by performance curves [25]. The parameter used to establish the cut-off adulterant concentration and the unreliability region was the limit of quantification considering samples of pure gasoline as blank. It is an appropriated parameter due to its narrower unreliability region in regard to the detection limit what means higher precision on the screening classification. A linear regression was carried out with the points around 50% of correct response in the performance curves to elaborate straight lines used to define the concentrations at which is possible to achieve a confidence level of 95% in the screening analysis.

3. Results and discussion

The NLP was applied on the analysis of 25 samples of pure gasolines (blank) in order to determinate the standard deviations of measurements. The mean and standard deviation for this sample set were 0.498 ± 0.003.

The adulterated gasolines (see Section 2.1) were prepared with solvent and kerosene whose spectral behaviors were closer to that from pure gasolines (Fig. 1) in such a way to difficult the adulteration detection. Fig. 4 shows the analytical curves for both adulterations. Each point on the plot is an average of 10 measurements from 10 samples. Based on the *s* value for the blank, it was found values of 1.2 and 1.4% for kerosene and solvent LDs, respectively. Samples representing the adulteration level of 1% (v/v) were not analyzed.

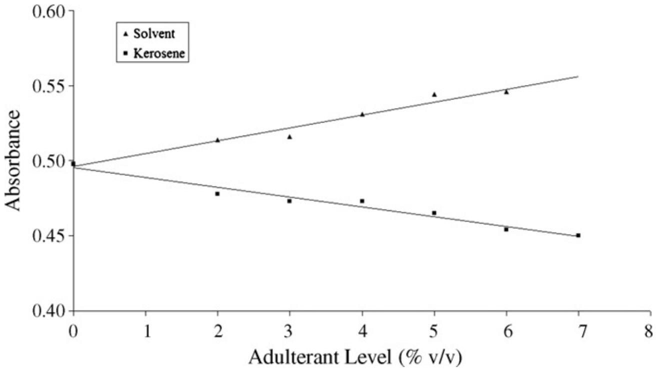

Fig. 4. Analytical curves obtained when pure and adulterated gasolines were analyzed by the NLP.

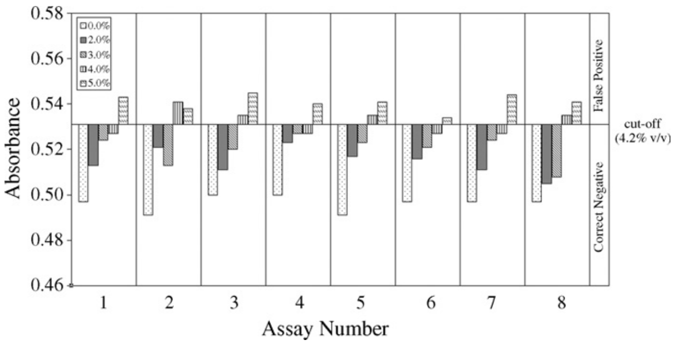

Fig. 6. Results for gasoline verification of no adulteration by solvent. A correct negative is a confirmation for no adulteration with a confidence level of 95%. Legend: concentration in percentage (v/v).

The analytical curves obtained for solvent and kerosene are given by the following equations:

$$A^{\text{solvent}} = 0.00850C + 0.495 \quad (r = 0.9815) \tag{1}$$

$$A^{\text{kerosene}} = -0.00650C + 0.496 \quad (r = 0.9890) \tag{2}$$

where A is the absorbance and C is the concentration of the adulterant.

The LQs for solvent and kerosene was found to be 4.2 and 4.8% (v/v), respectively. These values were used as cut-off concentrations to elaborate performance curves in order to determine an unreliability region related to the verification of gasoline adulteration by solvent or kerosene. In the construction of these curves a correct response is a positive response for adulteration and a correct negative response is positive response for no adulteration.

Fig. 5 shows the performance curves obtained when gasoline samples having different adulteration levels were analyzed by the NLP using LQ as cut-off concentration. The unreliability regions on these graphs were calculated by regression curves elaborated with the points around 50% of correct response for adulteration (Fig. 5). Thus, at 95% of confidence level, adulteration by solvent and kerosene can only be confirmed (correct positive) if their concentrations are at least 5.1% (v/v) (Fig. 5a) and 5.9% (v/v) (Fig. 5b), respectively. At this confidence level, is possible to find 5% of false negative responses. On the other hand, a confirmation for adulteration absence (correct negative) is established when the concentration levels are below 2.7 and 4.0% (v/v), for solvent and kerosene, at a confidence level of 95% (5% of false positive responses).

It is interesting to analyze that if false negative responses appear in a screening procedure elaborated using the correct positive region of the performance curves in Fig. 5, adulterated gasolines can be classified as good ones. Therefore, it is not a good criterion to analyze adulteration. On the other hand, if the procedure is elaborated to verify absence of adulteration using the correct negative region, false positive responses will direct the tested samples to a deeper analysis to confirm or not the initial suspicion. In spit of the confirmation for “no adulteration” can only be carried out for concentrations beyond 2.7 and 4.0% (v/v) for solvent and kerosene, respectively, these concentrations are better thresholds for verification of gasolines quality than the correct positive thresholds. Thus, the NLP was calibrated using the LQs of solvent and kerosene as cut-off concentrations and the correct negative region given by the performance curves of Fig. 5 to confirm “no adulteration” on the gasolines type C.

Fig. 6 shows the results obtained when the NLP was applied on the quality control of eight gasolines samples where solvent was spiked at the levels 0.0, 2.0, 3.0, 4.0 and 5.0% (v/v). The

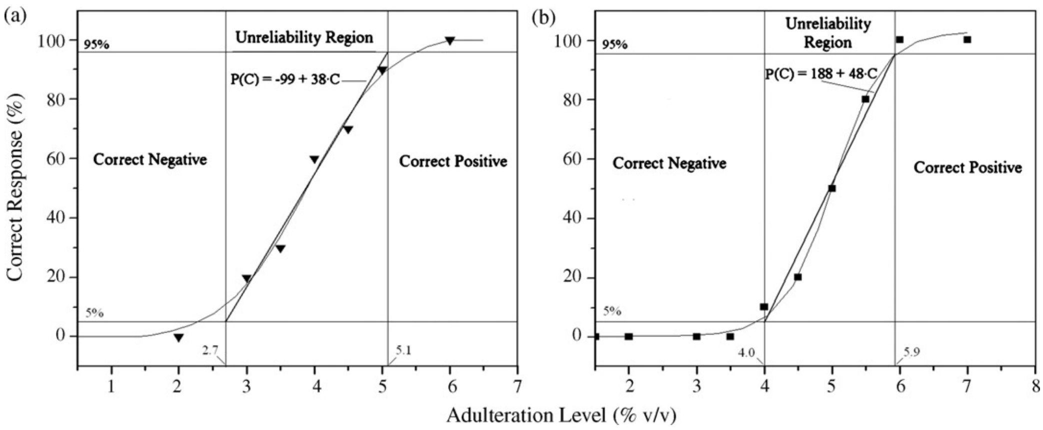

Fig. 5. Performance curves elaborated for evaluation of the unreliability region for the screening analysis of adulterants in gasoline: (a) adulteration by solvent and (b) adulteration by kerosene. Equations are the regression curves used to define thresholds for correct positive and negative response regions at 95% of confidence level.

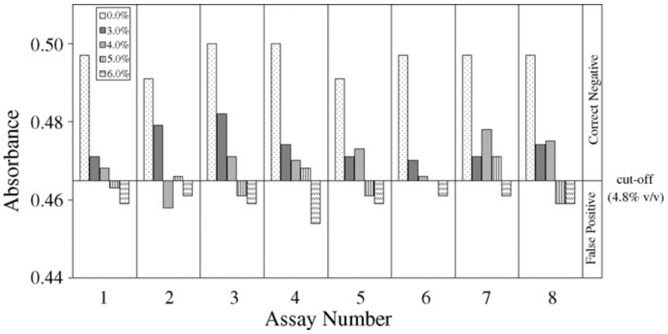

Fig. 7. Results for gasoline verification of no adulteration by kerosene. A correct negative is a confirmation for no adulteration with a confidence level of 95%. Legend: concentration in percentage (v/v).

cut-off was 4.2% (v/v). Thus, when the concentration level was at 3.0% (v/v) or below it, all samples were classified as not adulterated. A certain level of false positive responses at 3.0% (v/v) was expected but it did not appear on these assays. At the level of 4.0% (v/v), half of the adulterated samples was classified as not adulterated, generating 50% of false positive results, as expected. At 5.0% (v/v) of solvent, all analyzed samples were classified as adulterated.

Fig. 7 shows the results obtained by eight assays carried out using gasolines where the kerosene concentrations were at the levels 0.0, 3.0, 4.0, 5.0 and 6.0% (v/v). The cut-off was established at 4.8% (v/v). Samples containing kerosene at levels below 3.0% (v/v) were classified as not adulterated. At levels of 4.0 and 5.0% (v/v), 88 and 50% of the samples, respectively, were classified as not adulterated by the NLP. At 6.0% (v/v) all samples are classified as adulterated.

As it can be seen from the results, “no adulteration” responses for the gasoline screening analysis were obtained when the concentration of solvent and kerosene were below 3.0 and 5.0%, respectively. If the levels of adulteration surpass these limits, samples can be classified as adulterated and must be directed to a deeper analytical procedure.

It is important to consider the adulteration caused by addition of both solvent and kerosene. In this situation a determination of the adulteration could only be possible if the concentration of one of the adulterants was larger then the other. In cases at which the adulteration is caused by a close amount of both adulterants the NLP will fail on its screening analysis. A way to overcome this drawback is being studied.

4. Conclusion

A portable and microcontrolled NIR LED photometer was developed for screening analysis of gasoline type C aiming at to verify adulteration by solvent and kerosene. The NLP uses a NIR LED emitting at 1550 nm and a PbSe photoresistor as detector whose noise is kept at low levels by a control system based on thermistor and thermoelectric cooling. To calibrate it the analytical signal of pure and adulterated samples of gasoline type C were registered by the photometer and cut-off concentrations for solvent and kerosene were calculated as a threshold to classify the sample as adulterated or not. The correct negative region yielded by the performance curves related to the “no adulteration” response was used to calibrate the NLP for the screening analysis of the gasolines. At a confidence level of 95%, samples of solvent and kerosene were considered not adulterated when the levels of adulterant were below 3.0 and 5.0% (v/v), respectively. Thus, the NLP showed to be an economical and viable alternative for screening analysis of gasoline type C adulterated by solvent or kerosene.

Acknowledgments

The authors gratefully acknowledge the support by CNPq, Brazil (Proc. No.: 478961/2001–4) and FINEP (Proc. No.: 478961/2001–4) and CAPES and CNPq scholarship, respectively.

References

[1] P.K. Dasgupta, H.S. Bellamy, H. Liu, J.L. Lopes, E.L. Loree, K.J. Morris, K. Petersen, K.A. Mir, Talanta 40 (1993) 53.
[2] P.K. Dasgupta, I.Y. Eom, K.J. Morris, J. Li, Anal. Chim. Acta 500 (2003) 337.
[3] A.M. Tan, J.L. Huang, J.D. Geng, J.H. Xu, X.N. Zhao, J. Autom. Chem. 16 (1994) 71.
[4] M.K. Cantrell, J.D. Ingle, Anal. Chem. 75 (2003) 27.
[5] P.C. Hauser, T.W.T. Rupasinghe, N.E. Cates, Talanta 42 (1995) 605.
[6] J. Malinen, M. Känsäkoski, R. Rikola, C.G. Eddison, Sens. Actuators B 51 (1998) 220.
[7] H. Flaschka, C. McKeithan, R.M. Barnes, Anal. Lett. 6 (1973) 585.
[8] D. Betteridge, E.L. Dagless, B. Fields, N.F. Graves, Analyst 103 (1978) 897.
[9] D. Betteridge, Anal. Chem. 50 (1978) 832A.
[10] C. Pasquini, I.M. Raimundo Jr., Quim. Nova 7 (1984) 24.
[11] P.J. Worsfold, J.R. Clinch, Anal. Chim. Acta 197 (1987) 43.
[12] J. Huang, H. Liu, A. Tan, J. Xu, X. Zhao, Talanta 39 (1992) 589.
[13] H. Liu, P.K. Dasgupta, Anal. Chim. Acta 289 (1994) 347.
[14] E.N. Gaião, R.S. Honorato, S.R.B. Santos, M.C.U. Araújo, Analyst 124 (1999) 1727.
[15] M.C.U. Araujo, S.R.B. Santos, E.A. Silva, G. Veras, J.L.F.C. Lima, R.A.S. Lapa, Quim. Nova 20 (1997) 137.
[16] E.A. Pereira, A.A. Cardoso, P.K. Dasgupta, Quim. Nova 24 (2001) 443.
[17] F.R.P. Rocha, P.B. Martelli, B.F. Reis, J. Braz, Chem. Soc. 15 (2004) 38.
[18] M. Cocchi, C. Duarte, G. Foca, A. Marchetti, L. Tassi, A. Ulrici, Talanta 68 (2006) 1505.
[19] M. Blanco, J. Pagès, Anal. Chim. Acta 463 (2002) 295.
[20] E.L. Bergman, H. Brage, M. Josefson, O. Svensson, A. Sparén, J. Pharm. Biomed. Anal. 41 (2006) 89.
[21] F.S. Falla, C. Larini, G.A.C. Le Roux, F.H. Quina, L.F.L. Moro, C.A.O. Nascimento, J. Petrol. Sci. Eng. 51 (2006) 127.
[22] C.C. Felício, L.P. Brás, J.A. Lopes, L.L. Cabrita, J.C. Menezes, Chem. Intell. Lab. Syst. 78 (2005) 74.
[23] J.V. Stanfford, G.S. Weaving, J.C. Lowe, J. Agric. Eng. Res. 43 (1989) 45.
[24] J.V. Stanfford, C.R. Bull, G.S. Weaving, J. Agric. Eng. Res. 43 (1989) 57.
[25] C. Gonzalez, E. Prichard, S. Spinelli, J. Gille, E. Touraud, Trends Anal. Chem. 4 (2007) 315.

Available online at www.sciencedirect.com

ScienceDirect

Talanta 75 (2008) 748–752

Talanta

www.elsevier.com/locate/talanta

Optimization and validation of a capillary electrophoresis methodology for inorganic anions in atmospheric aerosol samples

Silvia Talaván García, Mª Isabel Acedo Valenzuela, Eduardo Pinilla Gil *

Departamento de Química Analítica, Facultad de Ciencias, Universidad de Extremadura, Avda. de Elvas, s/n, E-06071 Badajoz, Spain

Received 25 July 2007; received in revised form 5 December 2007; accepted 7 December 2007
Available online 23 December 2007

Abstract

Optimization and validation of a method for the determination of inorganic anions, such as chloride, nitrate, sulphate, fluoride and phosphate, in atmospheric particulate matter is described. Ultrasonic extraction followed by CE, using CTAB as EOF modifier, has been established for this separation using chromate as visualization reagent for the indirect UV/vis detection. Optimization of the experimental chemical conditions (pH, surfactant concentration, chromate concentration and acetonitrile concentration) and instrumental parameters (temperature, applied voltage and injection time) is described. Linear calibrations plots are obtained for the five ions, with detection limits in the high ng/mL range. A standard reference material, SRM 1648 Urban Particulate Matter, has been used to validate the proposed method. Satisfactory reproducibility and acceptable agreement to the matter atmospheric samples has been found (recoveries ranging from 86 to 96%). Application to real particulate matter atmospheric samples, collected on high volume samplers from the air quality surveillance network of Extremadura, southwest Spain, is shown.

Keywords: Capillary electrophoresis; Inorganic anions; Atmospheric aerosol; Aerosol standard reference material

1. Introduction

Airborne particulate matter (atmospheric aerosol) provides valuable chemical information in atmospheric research and atmospheric pollution surveillance systems. Major anions as nitrate, chloride, sulphate or phosphate are relevant parameters in aerosol samples, since they are connected with important phenomena like primary pollutant emissions and evolution to secondary substances, pollution source apportioning, or chemical composition of bulk and wet deposition (acidifying substances and eutrophication risk). These analytes are routinely assayed in the frame of air quality monitoring programs.

Many CE methods have been developed for inorganic anions determination in a wide range of environmental matrices. Two specific reviews about the subject have been recently published [1,2] and they are also considered in a recent review about pollutants analysis by CE [3]. Indirect UV/vis is the usual detection approach in inorganic anions CE applications, chromate is the most used probe [4]. Pyrometillic acid (PMA) has been also used for the same purposes, but comparative evaluation has shown lower sensitivity for the latter probe [5]. Moreover, many EOF modifiers form insoluble precipitates with PMA [4]. Selectivity control in CE for inorganic anions is afforded by several chemical and instrumental ways [6,7]. Organic solvents as methanol, acetonitrile, tetrahydrofuran and other, added to the separation buffer are used to modify retention times and elution order. At the same time, interaction of the analytes with the capillary wall is depressed, so narrower peaks are obtained. Buffer pH adjustment is also effective, especially for the anions derived from weak acids as phosphate or fluoride. The effect of cationic surfactant EOF modifiers on the separation selectivity of inorganic anions has been widely studied [7,8]. Tetradecyltrimethylammonium bromide (TTAB), tetradecyltrimethylammonium hydroxide, dodecyltrimethylammonium bromide, cetyltrimethylammonium bromide (CTAB), hexamethonium bromide or hydroxide, are common choices. Cationic polymers exhibit different separation selectivities to those of cationic surfactants. Capillary temperature, applied voltage and injection time are the relevant instrumental parameters used to adjust selectivity.

The most established methodology for inorganic anions determination in atmospheric samples is ion chromatography

---

* Corresponding author.
E-mail address: epinilla@unex.es (E.P. Gil).

0039-9140/$ – see front matter © 2007 Elsevier B.V. All rights reserved.
doi:10.1016/j.talanta.2007.12.010

with conductimetric detection [9]. Potential advantages of CE approaches in terms separation efficiency, equipment simplicity and operation price, miniaturization potential, less sample consumption and less waste generation have prompted some research work about CE methodologies for the same application. CE is also a useful independent technique for quality control purposes. Dabek-Zlotorzynska and Dlouhy [10] first proposed CE use for major ions in aerosol samples collected on PTFE filters. They compare different probes for UV/vis indirect detection with equivalent results. Ultrasonic extraction was used for solubilization of the ions before the electrophoretic separation. Detailed comparison studies of CE with IC and photometric methods in routine anions atmospheric monitoring on large sample sets have been performed by the same group [11,12]. A good agreement was found for ion levels above 1 mg L^{-1}. This was attributed to the poorer sensitivity of the CE method and possible calibration errors (larger intercept). Krivácsy et al. [13], determined inorganic anions and organic acids in real aerosol samples by CE with UV/vis indirect detection, using chromate as the visualization reagent and Anion BT as EOF modifier. Acceptable precision was found but no accuracy evaluation was afforded. The same method has been also applied for assaying atmospheric aerosols in Budapest during a comprehensive characterisation campaign [14]. Ions in aerosol and bulk/dry deposition from Hong Kong were monitored by Tam et al. [15] by CE with UV/vis indirect detection based on salicylic acid and EOF modification by dodecyltrimethylammonium hydroxide. A microchip capillary electrophoresis method for the analysis of nitrate and sulphate in ambient aerosols have been published by Liu et al. [16].

Atmospheric particulate matter standard reference materials have been only scarcely used for validation of chromatographic analytical methodologies for inorganic anions. Talebi and Abedi [17] used SRM 1648 Urban Particulate Matter for the validation of a IC method for F^-, Cl^-, $NO_3{}^-$ and $SO_4{}^{2-}$, based on ultrasonic extraction from quartz fiber filters and conductimetric detection. SRM 1648 is mostly used for validation of trace elements determination, but the certification document also contains analytical information about chemical composition of major ions including chlorine, sulphate and nitrate, that can be valuable for method evaluation [18]. No reference has been found about validation of CE analytical methodologies for inorganic anions in atmospheric samples by standard reference materials.

The aim of this research work is to optimize the chemical and instrumental conditions of a CE method for inorganic anions in atmospheric samples, and to demonstrate method performance by using SRM 1648 Urban Particulate Matter standard reference material and real aerosol samples collected from an air quality surveillance system.

2. Experimental

2.1. Instrumentation

A Hewlett-Packard Mod. 3D CE system was used for the analysis of the samples, using fused silica capillaries of 54.2 cm effective and 61 cm total length, 50 μm internal diameter. The ionic species were detected by indirect UV/vis detection with chromate probe. Detection and reference wavelengths were selected by exploring the UV spectrum of chromate in the selected buffer. Chloride, sulphate, fluoride and phosphate were assayed at 520 nm with 373 nm reference. Nitrate was assayed at 228 nm, with 373 nm reference. Capillary conditioning was conducted at the beginning of analytical sessions by ultrapure water (10 min), 0.1 M sodium hydroxide (10 min), ultrapure water (10 min) and separation buffer (20 min). Between runs, conditioning was conducted by ultrapure water (2 min), 0.1 M sodium hydroxide (2 min) and separation buffer (15 min). Analytical signals in the electropherograms were measured as corrected peak areas (CPA).

2.2. Reagents

Borate separation buffer was prepared on 3 mM H_3BO_3 (Merck), adding 100 mM $Na_2B_4O_7$ (Merck) for pH adjustment. Chromate probe concentrations were obtained by adding appropriate amounts of aqueous solutions prepared from Na_2CrO_4 (Merck). EOF modifier concentration was adjusted by adding the surfactant CTAB (Panreac, Spain) aqueous solutions prepared by weight. Acetonitrile (Merck, HPLC Grade) was used as organic modifier. Anion calibration standards were prepared from sodium or potassium salts. All reagents used were of analytical grade. Ultrapure water was obtained from a Milli-Q system (Millipore).

2.3. Standard reference material and real samples: pretreatment

SRM 1648 Urban Particulate Matter standard reference material (NIST) was used for method validation. Certified values are restricted to constituent and trace elements, but the material certificate also lists complementary concentration values including chlorine, nitrate and sulphate (Certificate, 1998). The material was dried for 8 h at 105 °C before use. 100 mg samples were accurately weighted, then extracted with water in an ultrasonic bath for 30 min and taken to a total volume of 50 mL. Real aerosol samples from monitoring stations belonging to the air quality surveillance system of Extremadura, Spain, were collected on 15 cm quartz membrane filters by a Digitel DAH80 high volume samplers (30 m^3/h), with an automatic daily sample protocol. Half filters were extracted with water in an ultrasonic bath and repeatedly washed to a total volume of 50 mL. All sample solutions were filtered before injection through a 0.45 μm nylon membrane (Millipore).

3. Results and discussion

3.1. Separation buffer chemical composition

Buffer pH, CTAB and chromate concentration and acetonitrile percentage were changed for optimization of the chemical composition of the mobile phase.

Table 1
Calibration data and analytical figures of merit

	Chloride	Nitrate	Sulphate	Fluoride	Phosphate
Migration time (min)	2.55	2.72	2.70	3.33	3.67
R.S.D. migration time (%)[a]	1.1	1.4	3.1	2.0	2.3
Corrected peak area	11.34	6.02	6.77	21.22	10.62
R.S.D. peak areas (%)[a]	2.3	2.0	1.9	3.5	2.7
Intercept, S.D.	0.123, 0.057	0.335, 0.054	0.022, 0.050	0.012, 0.093	0.017, 0.072
Slope, S.D.	0.3627, 0.0042	0.2953, 0.0039	0.2258, 0.0032	0.6629, 0.0068	0.3244, 0.0052
Regression coefficient	0.9986	0.9989	0.9992	0.9994	0.9984
Detection limit (ng mL^{-1})	470	550	340	420	660

[a] Relative standard deviations calculated from 9 injections of a mixed anion standard (30 mg L^{-1}).

pH changes from 8 to 9 generate mobility shifting in the weak acid anions fluoride and phosphate.

30×10^{-6} M to 200×10^{-6} M CTAB concentrations were used to check the effect of the surfactant EOF modifier in migration times. Interaction of anionic species with positive charge surfactant micelles has been previously reported [19]. However, we have observed no significant change in migration times for the inorganic anions in the CTAB concentration range studied in this work. Chromate concentration change from 3×10^{-3} M to 40×10^{-3} M caused significant changes in migration times. Nitrate and sulphate were only resolved above 20×10^{-3} M chromate. Buffer turbidity was observed above 40×10^{-3} M. Acetonitrile was used as buffer organic modifier in the range 0.01–0.5%, causing a progressive decreasing of retention times and peak widths. Optimized parameters for the composition of the separation buffer were pH 8.5, 32×10^{-6} M CTAB, 30×10^{-3} M chromate and 0.1% acetonitrile.

3.2. Instrumental parameters

Capillary temperature, applied voltage and hydrodynamic injection time were varied to obtain the optimum values. Increasing temperature from 20 to 30 °C caused higher ion mobility and slightly higher peak areas, but also and undesirable increasing of electric current. 25 °C was selected as optimum temperature of capillary and sample vials. Maximum applied voltage in the Ohm's law domain was found to be −25 kV. Corrected peak areas were linearly dependent with injection time in the range 5–25 s. Peak symmetry and signals resolution were lost for higher injection times. 20 s was selected as the optimum value.

3.3. Calibration and analytical figures: validation by standard reference material

Optimal chemical and instrumental conditions were applied for precision estimation at the 30 mg L^{-1} concentration level (Fig. 1). The analytical run for chloride, nitrate, sulphate, fluoride and phosphate is resolved in around 4 min. Acceptable values of R.S.D. were found for retention times and corrected peak areas (Table 1).

Calibration lines were constructed for the selected inorganic anions in the range 0.5–30 mg L^{-1}. Analytical figures of merit are shown in Table 1. Detection limits in the ng mL^{-1} range were obtained for the analysed anions according with Long and Winefordner [20]. The analytical useful range of the proposed method is sufficient for atmospheric aerosol monitoring purposes.

The accuracy of the proposed method was validated by use of the certified reference material SRM 1648 Urban Particulate Matter. A sample electropherogram is presented in Fig. 2. Acceptable agreement with the reference values provided (chloride, nitrate and sulphate) was found (Table 2).

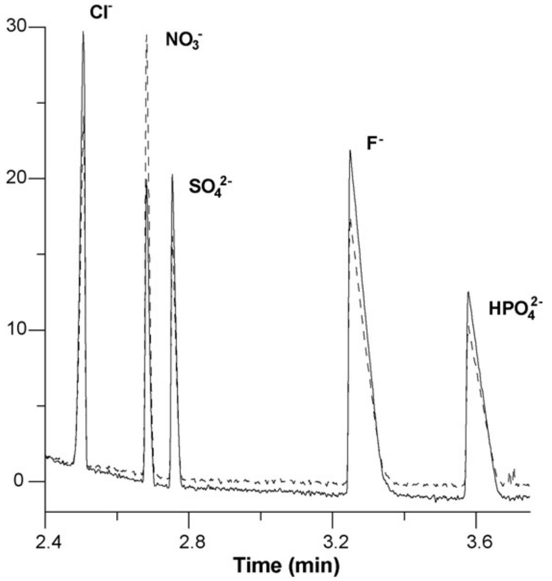

Fig. 1. Electropherogram of a standard containing 30 mg L^{-1} of each anion. Solid line: 520 nm with 373 nm reference. Dashed line: 228 nm with 373 nm reference. See the text for optimized chemical and instrumental conditions.

Table 2
Method validation with SRM 1648 "Urban Particulate Matter"

Anion	Reference value	Measured value	Standard deviation[a]	Recovery
Chloride	0.45	0.42	0.01	93.2
Nitrate	1.07	0.92	0.05	86.0
Sulphate	15.42	14.83	1.30	96.2

All values in % (w/w).

[a] Standard deviation calculated from six samples.

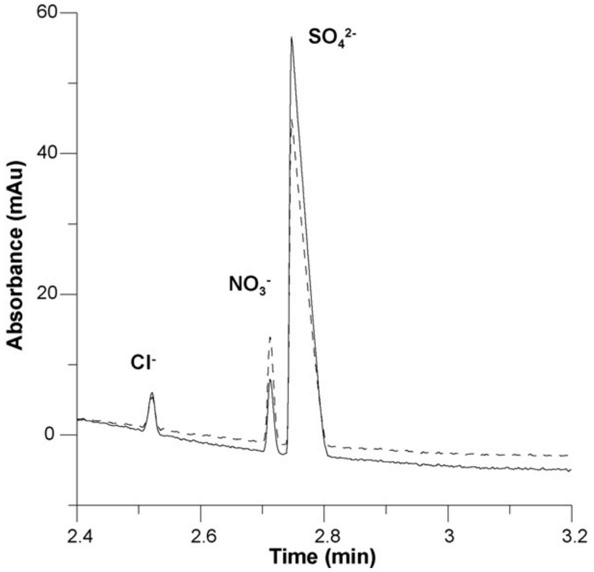

Fig. 2. Electropherogram of the extracted solution from a reference material SRM 1648 Urban Particulate Matter sample. Solid line: 520 nm with 373 nm reference. Dashed line: 228 nm with 373 nm reference. See the text for optimized chemical and instrumental conditions.

3.4. Real aerosol samples

The inorganic anions were quantified in real aerosol samples by the proposed method. A set of samples from different suburban locations within Extremadura, Spain, were processed by the proposed method. Well-defined electropherograms were obtained, as shown in Fig. 3. Analysis results are shown in Table 3.

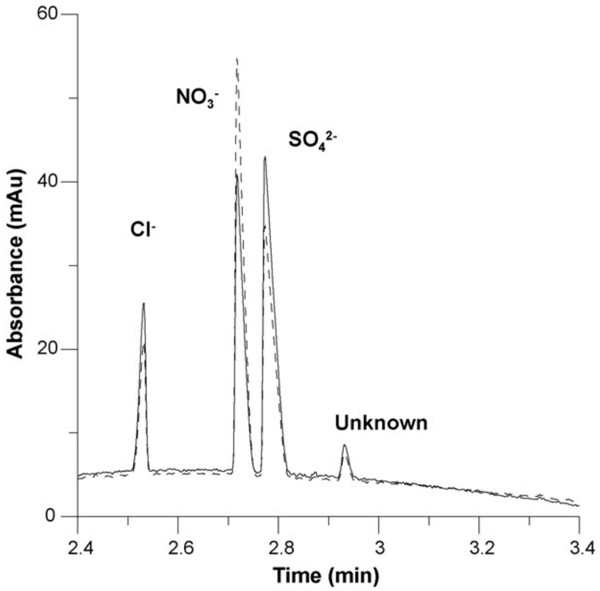

Fig. 3. Electropherogram of the extracted solution from a real aerosol sample. Solid line: 520 nm with 373 nm reference. Dashed line: 228 nm with 373 nm reference. See the text for optimized chemical and instrumental conditions.

Table 3
Analysis of aerosol samples from suburban locations of Extremadura, Spain

Anion	Mean ($\mu g\,m^{-3}$)	Minimum ($\mu g\,m^{-3}$)	Maximum ($\mu g\,m^{-3}$)
Chloride	0.34	0.12	0.85
Nitrate	6.72	2.16	13.40
Sulphate	2.55	0.81	4.00

4. Conclusions

The proposed capillary electrophoresis method has been proven useful as a valid alternative for the routine determination of the inorganic anions chloride, nitrate, sulphate, fluoride and phosphate in atmospheric samples. Acceptable detection limits for the application were found, in the high ng/mL range. The method was successfully applied to particulate matter reference material (SRM 1648 Urban Particulate Matter) and real aerosol samples from an air quality surveillance system. Advantages of the proposed CE method respect to the more established IC methodologies for the same application can be obtained in terms of equipment simplicity and operation price, miniaturization potential, less sample consumption and less waste generation. It is also a useful independent technique for quality control purposes.

Acknowledgements

We are grateful to the Consejería de Medio Ambiente, Junta de Extremadura, Spain, for financial support (partly provided by FEDER European funds) and for providing the aerosol samples from the air quality monitoring network of Extremadura, Spain.

References

[1] D. Kaniansky, M. Masár, J. Marák, R. Bodor, J. Chromatogr. A 834 (1999) 133.
[2] B. Paul, M. King, Electrophoresis 24 (2003) 1892.
[3] E. Dabek-Zlotorzynska, H. Chen, L. Ding, Electrophoresis 24 (2003) 4128.
[4] P. Doble, P.R. Haddad, J. Chromatogr. A 834 (1999) 189.
[5] M.M. Rhemrev Boom, J. Chromatogr. A 680 (1994) 675.
[6] W. Buchberger, P.R. Haddad, J. Chromatogr. 608 (1992) 59.
[7] A.H. Harakuwea, P.R. Haddad, J. Chromatogr. A 834 (1999) 213.
[8] M.T. Galceran, L. Puignou, M. Diez, J. Chromatogr. A 732 (1996) 167.
[9] P.R. Haddad, P.E. Jackson, Ion Chromatography: Principles and Applications (Journal of Chromatography Library, vol. 46), Elsevier, Amsterdam, 1990.
[10] E. Dabek-Zlotorzynska, J.F. Dlouhy, J. Chromatogr. A 671 (1994) 389.
[11] E. Dabek-Zlotorzynska, J.F. Dlouhy, N. Houle, M. Piechowski, S. Ritchie, J. Chromatogr. A 706 (1995) 469.
[12] E. Dabek-Zlotorzynska, M. Piechowski, F. Liu, S. Kennedy, J.F. Dlouhy, J. Chromatogr. A 770 (1997) 349.
[13] Z. Krivácsy, A. Molnar, E. Tarjány, A. Gelencsér, G. Kiss, J. Hlavay, J. Chromatogr. A 781 (1997) 223.
[14] I. Salma, W. Maenhaut, E. Zemplén-Papp, G. Záray, Atmos. Environ. 35 (2001) 4367.

[15] W. Tam, P.A. Tanner, P.T.R. Law, K. Bächmann, S. Pötzsch, Anal. Chim. Acta 427 (2001) 259.

[16] Y. Liu, D.A. MacDonald, X.Y. Yu, S.V. Hering, J.L. Collett, C.S. Henry, Analyst 131 (2007) 1226.

[17] S.M. Talebi, M. Abedi, J. Chromatogr. A 1094 (2005) 118.

[18] Certificate of Analysis, Standard Reference Material (SRM) 1648, Urban Particulate Matter, National Institute of Standards and Technology, Gaithersburg, MD, April 28, 1998.

[19] S.A. Steiner, D.M. Watson, J.S. Fritz, J. Chromatogr. A 1085 (2005) 170.

[20] G.L. Long, J.D. Winefordner, Anal. Chem. 55 (1983) 713.

Available online at www.sciencedirect.com

ScienceDirect

Talanta 75 (2008) 851–855

Talanta

www.elsevier.com/locate/talanta

Short communication

Potentiometric measurement of ascorbate by using a solvent polymeric membrane electrode

Huimin Guo[a,b], Tanji Yin[a], Qingmei Su[a], Wei Qin[a,*]

[a] *Laboratory of Environmental Chemistry, Yantai Institute of Coastal Zone Research for Sustainable Development, Chinese Academy of Sciences, P.O. Box 1488, Yantai 264003, PR China*

[b] *Department of Chemistry, School of Chemical Engineering, Dalian University of Technology, Dalian 116024, PR China*

Received 4 September 2007; received in revised form 12 December 2007; accepted 14 December 2007

Available online 26 December 2007

Abstract

A novel potentiometric method for the determination of ascorbate is described in this communication. It is based on ascorbate oxidation with permanganate which is continuously released from the inner reference solution of a ligand-free tridodecylmethylammonium chloride (TDMAC)-based polymeric membrane ion selective electrode (ISE). The ISE potential determined by the activity of permanganate ions released at the sample–membrane phase boundary is increased with the consumption of permanganate. The proposed membrane electrode is useful for continuous and reversible detection of ascorbate at concentrations in 0.1 M NaCl ranging from 1.0×10^{-6} to 1.0×10^{-3} M with a detection limit of 2.2×10^{-7} M.

Keywords: Potentiometry; Ion selective electrodes; Ion fluxes; Polymeric membranes; Ascorbate; Irreversible chemistries

1. Introduction

In recent years, many efforts were made in understanding the principles that dictate the lower detection limits of solvent polymeric membrane-based ion selective electrodes (ISEs) [1–4]. It has been realized that a transmembrane concentration gradient of primary ions will occur whenever the compositions of the sample and the inner solution are not the same [3]. Either fluxes of primary ions from the inner aqueous solution towards the sample solution or fluxes in the opposite direction may perturb the primary ion concentrations at the sample–membrane phase boundary and hence deteriorate the lower detection limit of ISEs [3,4]. Numerous strategies have been developed to fabricate ISE membranes that suffer much less from ion flux effects for large improvement of lower detection limits [5–7]. However, ion fluxes across the ISE membrane have been found also analytically useful, and most of current applications are based on the ion fluxes of primary ions in the direction of inner solution. Such examples include polyion sensors [8,9], pulstrodes [10], steptrodes [11], ion-channel biosenors [12,13], electrodes sensitive to total ion concentrations [14] and ISE indicators for complexometric titrations [15].

Here, we introduce a novel detection system that makes use of outward ion fluxes through ISE membrane, i.e. the fluxes in the direction of sample solution, to provide controlled-release reagent for measuring reductants. It is well known that one significant limitation of reagent-based chemical sensors is the use of inherently irreversible recognition reactions such as most redox reagent systems [16] and immunochemical reactions [17]. To solve this problem, continuously sensing reservoir sensors have been developed for reagent renewal, and polymer matrix is commonly used to incorporate the reagent which can be released slowly upon contact with aqueous solution. However, most of such polymeric delivery systems are used for optical sensors [18–21]. The conventional membrane ISEs have been found to show the fluxes of primary ions from the inner aqueous solution towards the sample solution, which may provide an alternative way for controlled release of analytical reagents. But, so far, ISEs based on such outward ion fluxes are rather rare, only an anion electrode based on precipitate equilibrium at the sample–membrane phase boundary with the released silver ions from the sensing membrane was reported [22]. In this paper, the outward ion fluxes of ISE membrane are first used for irreversible sensing chemistries. It will be shown that the ISE membrane not

---

[*] Corresponding author. Tel.: +86 535 6910580; fax: +86 535 6910566.
E-mail address: wqin@yic.ac.cn (W. Qin).

doi:10.1016/j.talanta.2007.12.023

only can serve as a polymer matrix for reagent release as used in the polymeric delivery systems for optical sensors, but also can work as a transducer for sensitive potentiometric detection in irreversible redox systems.

2. Experimental

2.1. Reagents

Tridodecylmethylammonium chloride (TDMAC), 2-nitrophenyl octyl ether (*o*-NPOE), bis(2-ethylhexyl) sebacate (DOS), and high molecular weight poly(vinyl chloride) (PVC) were purchased from Fluka AG (Buchs, Switzerland). All chemicals and reagents were of Selectophore or analytical reagent grade. Aqueous solutions were prepared with freshly deionized water (18.2 MΩ cm specific resistance) obtained with a Pall Cascada laboratory water system.

2.2. Membranes and electrode preparation

The ionophore-free permanganate selective membranes contained 10 wt% lipophilic anion exchanger TDMAC, 65 wt% plasticizer *o*-NPOE and 25 wt% PVC. Membranes of ∼130 (65) μm thickness were obtained by casting a solution of ∼240 (160) mg of the membrane components dissolved in 2.5 mL of tetrahydrofuran (THF) into a glass ring of 36 mm diameter fixed on a glass plate and letting the solvent evaporate overnight. Membrane thicknesses were visually measured with a CX31-32C02 Olympus microscope (Tokyo, Japan).

For each ISE, a disk of 7 mm diameter was punched from the membranes and glued to a plasticized PVC tube (i.d. 6 mm, o.d. 9 mm) with a THF/PVC slurry. Experimental selectivity coefficients for permanganate selective TDMAC-based membrane electrodes were measured by using 0.01 M NaCl as the internal filling and conditioning medium. For ascorbate detection, a 0.08 M potassium permanganate solution containing 0.02 M NaCl was added to each electrode as the inner filling solution, while 0.1 M NaCl was used as the conditioning solution. Before measurements, the electrodes were conditioned overnight for selectivity coefficient measurements and 3 days for ascorbate detection, respectively.

2.3. EMF measurements

All measurements of EMF were performed at 25 °C using a CHI-660 workstation (Shanghai, China) with a saturated calomel electrode (SCE) as reference electrode in the galvanic cell: SCE//sample solution/ISE membrane/inner filling solution/AgCl/Ag. For selectivity coefficient measurements, all the EMF values were corrected for the liquid-junction potential according to the Henderson equation and activity coefficients were calculated by the Debye–Hückel approximation. For reductant determination, the sample solutions were prepared with 0.1 M NaCl and adjusted with NaOH and HCl to pH 7.0 measured by a PXSJ-216 pH meter (Shanghai, China). In this case, most of the reductants exist in the anionic forms and can be completely dissolved in the whole concentration range for interference study.

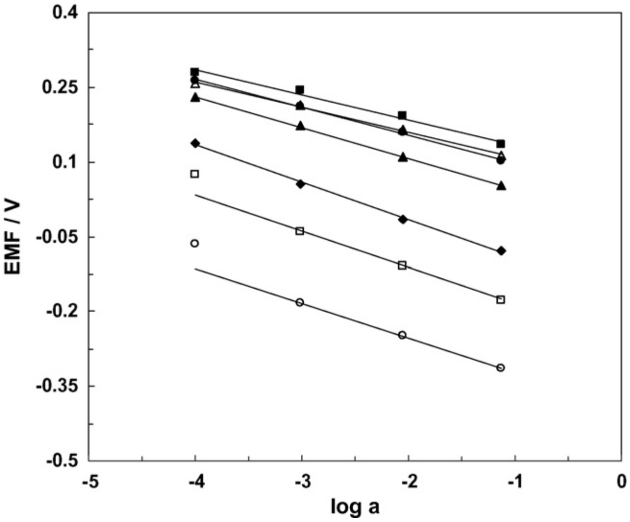

Fig. 1. EMF responses obtained according to Bakker's method toward the anions: (◯) permanganate, (□) thiocyanate, (♦) nitrate, (▲) chloride, (●) ascorbate, (△) hydrogen carbonate and (■) acetate. Membrane A as shown in Table 2.

2.4. Diffusion measurement of permanganate anion through ionophore-free TDMAC-based polymeric membrane

A 7-mm diameter disk was cut from the parent membrane and glued to a PVC tube (i.d. 6 mm, o.d. 9 mm). This tube was connected with a pipette tip containing 1.0 mL of 0.08 M potassium permanganate solution with 0.02 M NaCl, and immersed into 5.0 mL of deionized water in a glass vial. With continual stirring of the water solution in the glass vial, the amount of permanganate released per day in the recipient solution was assayed by an AA-7001 flame/graphite stove atom absorption spectrophotometer (Beijing East & West Analytical Instruments, China).

3. Results and discussion

Potassium permanganate, $KMnO_4$, is a commonly used chemical oxidizing agent and has been widely used for titrations of reductants by irreversible redox reactions. Interestingly, permanganate was found very lipophilic and showed a high anion response compared to other tested anions such as thiocyanate, nitrate, chloride, ascorbate, hydrogen carbonate and acetate when using a ligand-free ISE membrane based on anion exchanger TDMAC. The selectivity of such TDMAC-based polymeric membrane electrodes was characterized by using Bakker's method to eliminate the influence of the inherent sensitivity limit on the response toward discriminated ions [23]. The results are shown in Fig. 1. The apparent super-Nernstian response which occurs at a relatively high concentration of 10^{-4} M for permanganate and thiocyanate is induced by the high concentration of ion-exchanger in the membrane [24]. The

Table 1
Potentiometric selectivity coefficients for a permanganate-selective membrane electrode[a]

Ion J	$\log K^{\mathrm{pot}}_{\mathrm{MnO_4J}}$ [b]	Ion J	$\log K^{\mathrm{pot}}_{\mathrm{MnO_4J}}$ [b]
SCN^-	−2.36 ± 0.05	$AscH^-$ [c]	−6.86 ± 0.17
$NO_3{}^-$	−3.97 ± 0.03	$HCO_3{}^-$	−7.07 ± 0.17
Cl^-	−6.08 ± 0.10	OAc^- [d]	−7.50 ± 0.08

[a] Membrane A as shown in Table 2.

[b] Mean value obtained from three corresponding pairs of concentrations of permanganate and the respective interfering anion in the measuring range of 10^{-1} to 10^{-3} M ± standard deviation.

[c] Ascorbate anion.

[d] Acetate anion.

logarithmic Nikolskii coefficients for permanganate ($K^{\mathrm{pot}}_{\mathrm{MnO_4J}}$) over other anions are summarized in Table 1. The high discrimination against these anions allows the permanganate membrane ISE to be used in the presence of physiological saline medium (e.g. 0.1 M NaCl). Fig. 1 also illustrates that TDMAC-based membrane ISE shows much less response toward ascorbate with a low logarithmic selectivity coefficient of −6.86. This indicates that it is impossible to directly measure low concentrations of ascorbate in the presence of interfering anions by using the conventional ion-exchanger-based ISE.

The constant release of primary ions under zero-current conditions from inner solution into sample solution which dictates the detection limit of the potentiometric sensor at low sample concentrations has been extensively studied in recent years [3]. In the case of the present permanganate selective membrane electrode, the release of permanganate may be accompanied by a simultaneous release of the ion-exchanger TDMAC [25], which shows less lipophilicity compared with other tetraalkylammonium salts [24]. The diffusion of permanganate ions across the polymeric membrane was monitored by atom absorption spectroscopy in the recipient solution as a function of time. The results are shown in Fig. 2. It can be seen that a constant release of permanganate ions could be available after conditioning the electrode for 3 days.

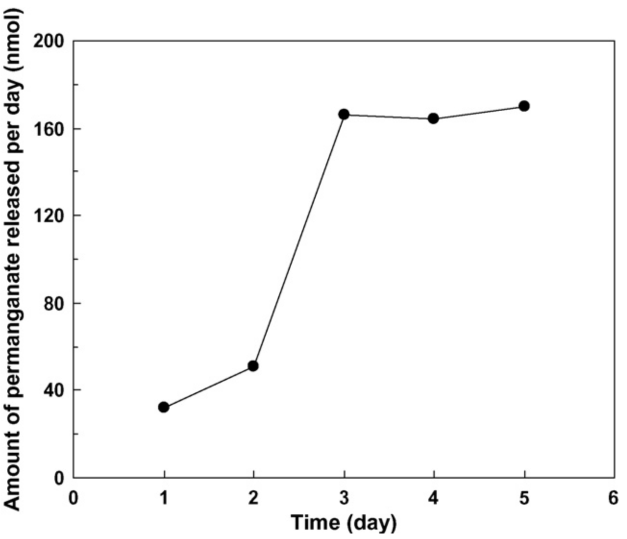

Fig. 2. Dependence of the amount of permanganate ions released per day in the receiving phase as a function of time. The average of five measurements. Membrane C as shown in Table 2.

In the absence of reductant, the flux of permanganate ions released from the inner solution into the membrane surface layer equals to the flux diffusing further into the sample bulk, thus generating a stead-state process with a constant concentration of permanganate ions released at the sample–membrane phase boundary [21]. The potential response of the electrode is determined by the activity of those permanganate ions, assuming the influence of the background anion activities is negligible:

$$E_{\mathrm{min}} = E^0 - \frac{RT}{F}\ln \alpha_{\mathrm{MnO_4}^-} \tag{1}$$

When a reductant is added into the sample solution, an efficient redox reaction occurs and the permanganate activity at the phase boundary is decreased, thus increasing the measured potential. A steady-state response can be obtained when the difference between the fluxes into and out of the membrane surface layer of permanganate ions equals to the consumption rate of permanganate ions in the redox reaction with the reductant. Such consumption rate depends not only on the concentration of reductant in sample solution but also on the reducing power of the tested reductant (see below). The maximum potential will reach if all the permanganate ions at the interface are consumed by the reductant, and the sample activity of the interfering anion governs the sensor response:

$$E_{\mathrm{max}} = E^0 - \frac{RT}{F}\ln\left(K^{\mathrm{pot}}_{\mathrm{MnO_4J}}(\alpha_{\mathrm{J}^{z-}})^{\frac{1}{z_{\mathrm{J}}}}\right) \tag{2}$$

The total potential change can be expressed as:

$$\Delta E_{\mathrm{total}} = \frac{RT}{F}\ln\left(\frac{\alpha_{\mathrm{MnO_4}^-}}{K^{\mathrm{pot}}_{\mathrm{MnO_4J}}(\alpha_{\mathrm{J}^{z-}})^{\frac{1}{z_{\mathrm{J}}}}}\right) \tag{3}$$

Apparently, higher potential response for reductants will be obtained with higher activities of permanganate ions released at the sample–membrane interface, with higher selectivities over the sample interfering anions, and with lower interfering ion activities. In our experiments, 0.1 M NaCl was used as the sample medium. Fig. 3 illustrates a typical response curve of the ISE showing changes in EMF with successive addition of ascorbate. It can be seen that a total voltage change of ca. 160 mV could be obtained using 0.08 M potassium permanganate with 0.02 M NaCl as inner filling solution of the permanganate selective membrane electrode. The released permanganate activity at the sample–membrane phase boundary was 2.7×10^{-5} M, measured by calibrating with a series of permanganate solutions at higher concentrations of 10^{-3}, 10^{-2}, and 10^{-1} M [26]. Factors influencing the potential response such as membrane compositions and thicknesses were studied. The results are summarized in Table 2. It was found that higher EMF values could be induced by higher concentrations of ion-exchangers, thinner membranes and higher contents of polar plasticizers, all of which could promote the ion fluxes from the inner filling solution into the sample solution and therefore cause higher permanganate activities at the sample–membrane interface. These results are con-

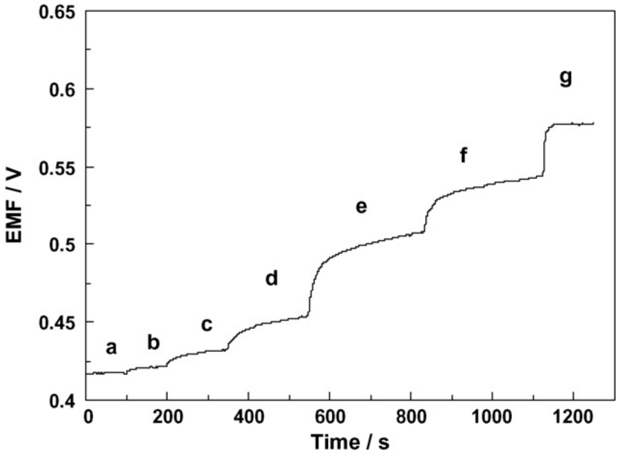

Fig. 3. Time history of ISE response to successive additions of ascorbate: (a) 0 (the blank), (b) 1.0×10^{-6} M, (c) 5.0×10^{-6} M, (d) 1.0×10^{-5} M, (e) 5.0×10^{-5} M, (f) 1.0×10^{-4} M, and (g) 1.0×10^{-3} M. Membrane C as shown in Table 2.

sistent with those for ion fluxes of primary ions in the direction of inner solution which result in a super-Nernstian response [4].

Reversibility of the sensor was evaluated by measuring the alternating responses to ascorbate at a high concentration (1.0×10^{-3} M) and a low concentration (3.0×10^{-6} M). The results are shown in Fig. 4. It can be seen that the signal changes are fully reversible in both cases. For the high concentration measurement, the time to achieve 95% of the full-scale response is very fast (0.5 min), whereas recovery to 95% of the initial value takes ca. 30 min. In contrast, response toward low concentrations of ascorbate is a bit longer (1.5 min), but the recovery time is considerably shorter (2 min). It should be noted that the response time for medium concentrations of ascorbate ranging from 5.0×10^{-5} to 1.0×10^{-4} M is much longer (ca. 4 min) as compared to those for high and low concentrations (Fig. 3). This is probably due to the fact that the permanganate ions released at the sample–membrane interface may be largely consumed by the efficient reduction with ascorbate at medium concentrations so that chloride ions in the sample solution are able to partially ion exchange with the permanganate ions in the interfacial layer of the membrane phase, which renders the response processes longer. Indeed, faster potential response was observed when no NaCl was added in the sample solution (data not shown). A recent paper shows that using thin supported liquid membranes can establish steady-state concentration profiles across ion-selective membranes rapidly [27], which might significantly reduce both the response time and recovery time for the present sensor.

Table 2
Total potentiometric response for ascorbate in the presence of 0.1 M NaCl obtained by using TDMAC-based PVC membrane ion selective electrodes with various membrane compositions and thicknesses

Membrane	ΔE_{total}[a] (mV)	TDMAC (wt%)	Plasticizer (wt%)	PVC (wt%)	Thickness[a] (μm)
A	60 ± 6	5	63(NPOE)	32	107 ± 4
B	84 ± 8	10	65(NPOE)	25	131 ± 7
C	164 ± 11	10	65(NPOE)	25	65 ± 3
D	58 ± 7	10	65(DOS)	25	63 ± 3
E	9 ± 3	10	40(NPOE)	50	73 ± 3

[a] Average value of three determinations ± standard deviation.

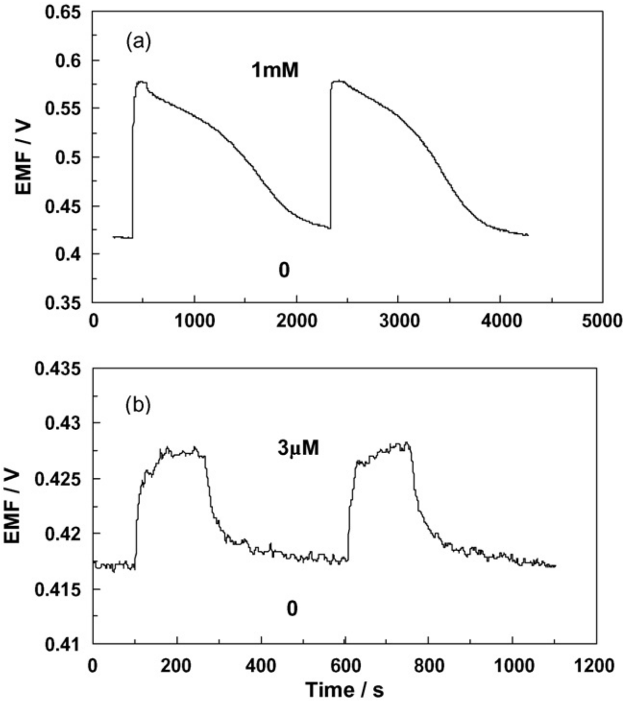

Fig. 4. Recycle response profiles for the blank and ascorbate solutions: (a) 1.0×10^{-3} and (b) 3.0×10^{-6} M. Membrane C as shown in Table 2.

Typical calibration curves for ascorbate and for other reductants including dopamine, urate, sulfite and oxalate are shown in Fig. 5. As indicated in the figure, the present membrane electrode is useful for measuring ascorbate in the presence of 0.1 M NaCl at concentrations ranging from 1.0×10^{-6} to 1.0×10^{-3} M with a relative standard deviation of less than 5 % for 1.0×10^{-5} M ($n = 5$). The detection limit is 2.2×10^{-7} M which gives a signal equal to the blank signal plus three times the

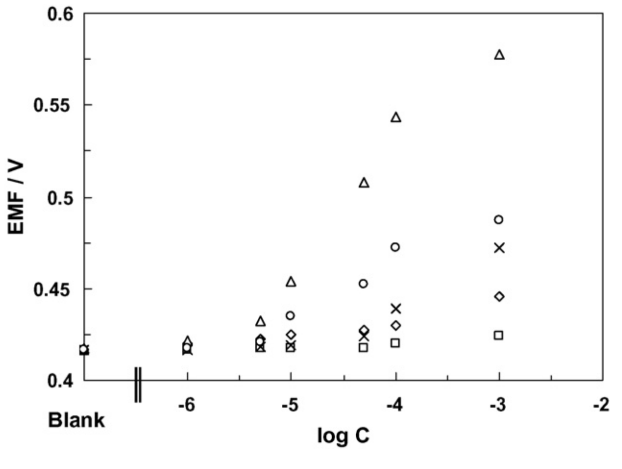

Fig. 5. ISE response curves for reductants: (△) ascorbate, (◯) dopamine, (×) urate, (◊) sulfite, and (□) oxalate. The average of five measurements. Membrane C as shown in Table 2.

Table 3
Results of ascorbate in vegetables and pharmaceutical preparations

Sample	Proposed sensor (mg/g)[a]	Iodiometry (mg/g)[a]
Tomato	0.117 ± 0.005	0.122 ± 0.002
Mung bean sprouts	0.092 ± 0.004	0.095 ± 0.002
Vitamin C tablet[b]	950 ± 5	952 ± 5
Multi-vitamin tablet[c]	35 ± 1	36 ± 1

[a] Average value of five determinations ± standard deviation.
[b] Jiangsu Jiangshan Pharmaceutical Factory, China.
[c] Jiangxi Jurentang Pharmaceutical Industries Co., China.

standard deviation of the blank measurement ($n = 11$). No significant changes were observed in the response characteristics of the polymeric membrane electrode after one week. At neutral pH, permanganate ions released at the membrane–sample interface are converted to manganese dioxide by the redox reaction with reductants. However, the formation of manganese dioxide could not poison the electrode membrane surface, which is due to the fact that manganese dioxide produced is in relatively small amounts and can be dissolved in the sample solution. Negligible response was observed up to 10^{-5} M for urate, sulfite and oxalate, while dopamine showed nearly 50% of the potential changes as compared with those for ascorbate. The order of decreasing potential response for these reductants is ascorbate > dopamine > urate > sulfite > oxalate, which corresponds directly to the order of reducing powers. Compared with other electrochemical sensors [28,29], the proposed polymeric membrane electrode offers potential advantages of simplicity, rapidity and high sensitivity for ascorbate determination.

Finally, the present sensor was applied to the determination of ascorbate in vegetables and pharmaceutical preparations. The samples were treated for analysis as described before [30]. Potentionmetric measurement was done for each sample and the concentration of ascorbate was quantified according to the calibration curve of the proposed electrode. The results are listed in Table 3 which agree well with those obtained by iodimetric analysis [31].

4. Conclusion

In summary, using permanganate–ascorbate redox system as a prototype, we have shown that the outward ion fluxes of ISE membrane can be used as a reagent controlled-release approach for irreversible sensing chemistries with submicromolar lower detection limits. The ISE membrane not only serves as a polymer matrix for reagent release as used in the polymeric delivery systems for optical sensors, but also works as a transducer for sensitive potentiometric detection. This combination makes the ISE membrane very attractive for sensor miniaturization. Further studies on the mechanism of this new detection principle and its application to other irreversible sensing chemistries are in progress in our laboratory.

Acknowledgements

This work was financially supported by the Chinese Academy of Sciences (KZCX2-YW-410) and the Department of Science and Technology of Shandong Province (2006GG2205033).

References

[1] T. Sokalski, A. Ceresa, T. Zwickl, E. Pretsch, J. Am. Chem. Soc. 119 (1997) 11347.
[2] E. Bakker, E. Pretsch, Anal. Chem. 74 (2002) 420A.
[3] T. Sokalski, T. Zwickl, E. Bakker, E. Pretsch, Anal. Chem. 71 (1999) 1204.
[4] T. Sokalski, A. Ceresa, M. Fibbioli, T. Zwickl, E. Bakker, E. Pretsch, Anal. Chem. 71 (1999) 1210.
[5] E. Bakker, E. Pretsch, Trends Anal. Chem. 24 (2005) 199.
[6] Z. Szigeti, T. Vigassy, E. Bakker, E. Pretsch, Electroanalysis 18 (2006) 1254.
[7] E. Pretsch, Trends Anal. Chem. 26 (2007) 46.
[8] M.E. Meyerhoff, B. Fu, E. Bakker, J.H. Yun, V.C. Yang, Anal. Chem. 68 (1996) 168A.
[9] A. Shvarev, E. Bakker, J. Am. Chem. Soc. 125 (2003) 11192.
[10] S. Makarychev-Mikhailov, A. Shvarev, E. Bakker, J. Am. Chem. Soc. 126 (2004) 10548.
[11] T. Vigassy, W.E. Morf, M. Badertscher, A. Ceresa, N.F. de Rooij, E. Pretsch, Sens. Actuators B 76 (2001) 477.
[12] P. Reichmuth, H. Sigrist, M. Badertscher, W.E. Morf, N.F. de Rooij, E. Pretsch, Bioconjug. Chem. 13 (2002) 90.
[13] R.E. Gyurcsányi, T. Vigassy, E. Pretsch, Chem. Commun. 20 (2003) 2560.
[14] A. Ceresa, E. Prestch, E. Bakker, Anal. Chem. 72 (2000) 2050.
[15] S. Peper, A. Ceresa, E. Bakker, E. Prestch, Anal. Chem. 73 (2001) 3768.
[16] H. Gunsasingham, C.H. Tan, J.K.L. Seow, Anal. Chem. 62 (1990) 755.
[17] S.M. Barnard, D.R. Walt, Science 251 (1991) 927.
[18] S.F. Luo, D.R. Walt, Anal. Chem. 61 (1989) 174.
[19] P.E. Michel, S.M. Gautier-Sauvigné, L.J. Blum, Talanta 47 (1998) 169.
[20] J.W. Choi, I.H. Lim, H.H. Kim, J.H. Min, W.H. Lee, Biosens. Bioelectron. 16 (2001) 141.
[21] W. Qin, S.O. Obare, C.J. Murphy, S.M. Angel, Anal. Chem. 74 (2002) 4757.
[22] E. Bakker, Sens. Actuators B 35-36 (1996) 20.
[23] E. Bakker, J. Electrochem. Soc. 143 (1996) L83.
[24] A. Malon, A. Radu, W. Qin, Y. Qin, A. Ceresa, M. Maj-Zurawska, E. Bakker, E. Pretsch, Anal. Chem. 75 (2003) 3865.
[25] S. Mathison, E. Bakker, Anal. Chem. 70 (1998) 303.
[26] A. Ceresa, E. Bakker, B. Hattendorf, D. Günther, E. Pretsch, Anal. Chem. 73 (2001) 343.
[27] K. Tompa, K. Birbaum, A. Malon, T. Vigassy, E. Bakker, E. Pretsch, Anal. Chem. 77 (2005) 7801.
[28] J.Y. Heras, A.F.F. Giacobone, F. Battaglini, Talanta 71 (2007) 1684.
[29] A. Salimi, H. MamKhezri, R. Hallaj, Talanta 70 (2006) 823.
[30] Z.J. Zhang, W. Qin, Talanta 43 (1996) 119.
[31] M.Z. Barakat, S.K. Shehab, N. Darnish, A. El-Zoheivy, Anal. Biochem. 53 (1973) 245.

Available online at www.sciencedirect.com

ScienceDirect

Talanta 75 (2008) 824–831

Talanta

www.elsevier.com/locate/talanta

Determination of 3-MCPD by GC-MS/MS with PTV-LV injector used for a survey of Spanish foodstuffs

Nuria León [a], Vicent Yusà [a], Olga Pardo [a], Agustín Pastor [b,*]

[a] *Public Health Laboratory of Valencia, Conselleria de Sanitat, Camí de la Marjal, s/n 46470 Albal, Valencia, Spain*
[b] *Analytical Chemistry Department, University of Valencia, Dr. Moliner 50, 46100 Burjassot, Valencia, Spain*

Received 19 July 2007; received in revised form 12 December 2007; accepted 18 December 2007
Available online 28 December 2007

Abstract

3-Monochloropropane-1,2-diol (3-MCPD) is the most common chemical contaminant of the group of chloropropanols. It can occur in foods and food ingredients at low levels as a result of processing, migration from packaging materials during storage and domestic cooking.

A sensitive method for determination of 3-MCPD in foodstuffs using programmable temperature vaporization (PTV) with large-volume injection (LVI) gas chromatography (GC) with tandem mass spectrometry detection (MS/MS) has been developed and optimized. The optimization of the injection and detection parameters was carried out using statistical experimental design. A Plackett–Burman design was used to estimate the influence of resonance excitation voltage (REV), isolation time (IT), excitation time (ET), ion source temperature (IST), and electron energy (EE) on the analytical response in the ion trap mass spectrometer (ITMS). Only REV was found to have a statically significant effect. On the other hand, a central composite design was used to optimize the settings of injection temperature (T_{inlet}), vaporization temperature (T_{vap}), vaporization time (t_{vap}) and flow (Flow). The optimized method has an instrumental limit of detection (signal-to-noise ratio 3:1) of 0.044 ng mL^{-1}. From Valencian, Spain, supermarkets 94 samples of foods were surveyed for 3-MCPD. Using the optimized method levels higher than the limit established for soy sauce by the European Union were found in some samples. The estimated daily intake of 3-MCPD throughout the investigated foodstuffs for adults and children was found about 0.005 and 0.01%, respectively, of the established provisional tolerable daily intake.

Keywords: Large-volume injection (LVI); Programmable temperature vaporization (PTV); 3-Monochloropropane-1,2-diol; GC-MS/MS; Experimental design; Optimization

1. Introduction

3-Monochloropropane-1,2-diol (3-MCPD) is the most common chemical contaminant of the group of chloropropanols. 3-MCPD can occur in food from: migration from polyamdeamine-epichlorohydrin (PAE) resin treated food contact materials, thermal processing (from chloride and glycerol or glycero-lipids), smoking processes, use of acid-HVPs (without controls) or enzyme (lipase) catalysed hydrolysis of 3-MCPD esters. The European Community (EC) limit on 3-MCPD in acid-hydrolysed vegetable proteins and soy sauce is 0.02 mg Kg^{-1} in dried weight [1]. Also the Joint FAO/WHO Expert Committee on Food Additives (JECFA) has established the provisional maximum tolerable daily intake (PMTDI) at the level of 2 mg Kg^{-1} bw day^{-1} under safety factor of 500 [2].

Different levels of this contaminant have been reported in sauces and in many other foods and food ingredients [3–13] and some heat processed foods and fermented sausages such as salami have been found to contain low levels of this chloropropanol [14–17].

Studies have shown that 3-MCPD is carcinogenic in animals [18](SCF 2001) and, the EC advised that levels should be the minimum level detectable by the most sensitive and reliable method available [2]. In view of that any related enforcement is being focused on the detection of the lowest concentration for this compound.

There are several methods available for the determination of 3-MCPD such as capillary electrophoresis coupled to electrochemical detection [19–21] and gas chromatography (GC) with electron-capture detection (ECD) [22], electrolytic conductivity detection (ELCD) [23] and mass spectrometry detection (MSD)

---

* Corresponding author.
E-mail address: Agustin.Pastor@uv.es (A. Pastor).

0039-9140/$ – see front matter © 2007 Elsevier B.V. All rights reserved.
doi:10.1016/j.talanta.2007.12.028

[3,5,6,8–13,24–28]. The ECD and ELCD are not widely used and MSD is used extensively. The most common technique is GC coupled with mass spectrometry employing different derivatization agents. Tandem mass spectrometry (MS/MS) analysis by ion trap mass spectrometry became a competitive technique for the determination of different contaminants but only one paper describes the detection of 3-MCPD using this detection mode [25].

The limit of detection ranges between 0.005 and 0.05 $\mu g\,g^{-1}$ for GC-MS with splitless injection.

Several studies have been reported in which large volume injection (LVI) methods were used for the GC determination of trace pollutants [29]. The LVI technique enables significant improvement of sensitivity of the analytical methods. Instead of conventional splitless volumes of 1–3 μL, with LVI volumes between 30 and 100 μL can be used.

The aim of this study was to develop a sensitive method using programmable temperature vaporization (PTV) with LVI gas chromatography (GC) with tandem mass spectrometry detection (MS/MS). The sensitivity of the method was improved through the optimization of PTV-LV injection and MS–MS detection using statistical design of experiments (DOE). The method was then used in the monitoring program of the Regional Valencia Government (Spain) and the levels of 3-MCPD in several foodstuffs are reported in this paper.

The optimization of the PTV injection system requires studying a multitude of parameters and can be very tedious by the approach of changing-one-factor-at-a-time (COST). In addition, this approach does not give information on interactions between factors, so it can miss the optimal settings when interactions exist [30]. Statistically designed experiments such as Plackett–Burman designs and central composite designs can help to optimize these kind of analytic parameters much more efficiently and in less experimental runs than the COST approach [31–34].

2. Experimental

2.1. Standards and reagents

All reagents were of analytical grade unless otherwise stated grade Hexane, diethyl ether, ethyl acetate, 2,2,4-trimethylpentane and Extrelut™ were supplied by Merck (Darmstadt, Germany) and ultrapure water was obtained from a Milli-Q filter system (Millipore, Bedford, MA, USA). The heptafluorobutyrylimidazole was from Sigma–Aldrich (Steinheim, Germany). Sodium chloride and anhydrous sodium sulphate were from Scharlau (Barcelona, Spain). Due to the risks for the health the managing of solvents must be very careful, specially with diethyl ether.

3-MCPD (≥97%) and 2,2-dichloro-1,3-propanediol (1,3-DCPD) were purchased from Sigma–Aldrich and 3-MCPD-d5 was obtained from Isotec, Inc., Ohio.

Individual stock solutions of 3-MCPD and 3-MCPD-d5 containing 1000 $\mu g\,mL^{-1}$, intermediate and working solutions containing 0.04–100 μg mL approximately were prepared in ethyl acetate. For optimization experiments a 4.41 $ng\,mL^{-1}$ derivatizated standard solution of 3-MCPD was injected into the gas chromatograph-mass spectrometer. Certified Reference Materials were from the Central Science Laboratory, UK.

The statistical package MINITAB, Release 14 (MINITAB, Birmingham, UK) was used to analyze and to optimize the factor settings from the experimental design that affect the PTV-LV injection.

3. Instrumentation

The GC-MS/MS system consists on a Finnigan ion trap mass spectrometer Polaris Q (Austin, TX, USA) connected with a Thermoquest Trace GC 2000 (Whatmam, MA, USA) gas chromatograph equipped with a Combi Pal Autosampler from CTC Analytics AG (Zwingen, Zwitzerland). The capillary column was a SGE-BPX5 (30 m × 0.25 mm, 0.25 μm) connected to a BEST PTV injector and a PTV-LV 2.75 × 2TRC from Thermo Finnigan (Milano, Italy).

3.1. Sample preparation

Different matrices such as bread, miscellaneous cereals, beer, fermented sausages, hydrolysed vegetable proteins (HPV) and soy sauce, were analyzed. The sample preparation procedure used in this work was based on that previously reported by the AOAC Official Method 2001 [19], Determination of 3-chloro-1,2-propanediol in foods and food ingredients.

In short, samples were homogenized and an analytical aliquot was weighed, 8 g of beer, 8 g of soy sauce and soups, 20 g of processed sausages and 10 g for cookies, bread and breakfast cereals were taken and processed following the AOAC method. The sub-samples were analyzed. After adding 3-chloro-1,2-propanediol-d5 (3-MCPD-d5) as internal standard samples were extracted into 5M sodium chloride solution. The extracts were mixed with Extrelut® and introduced into chromatographic columns. In the first step, the column was washed with 80 mL of a mixture of hexane and diethyl ether (90:10). 3-MCPD was then eluted with 250 mL diethyl ether. The extracts were concentred and dissolved in 10 mL of diethyl ether. A portion of 1 mL was dried and dissolved in 0.9 mL 2,2,4-trimethylpentane. Then, 100 μL of heptafluorobutyrylimidazole (HFBI) was added to give the corresponding 3-MCPD di-esters. The final extracts were then introduced into the GC-tandem mass spectrometry (MS–MS) using a PTV-LV injector prior to determination by gas chromatography ion trap mass spectrometer GC-MS–MS.

For validation experiments, spiked samples were used. Aliquots of 8 g for soy sauce and 10 g for breakfast cereals were spiked with 3-MCPD, a fixed amount of 3-MCPD-d5 standard solution, and then processed. Three levels of this contaminant were validated in breakfast cereals and soy sauce.

3.2. Gas chromatography-tandem mass spectrometry

The GC temperature program was from 50 °C, hold 1 min and rate 2 $°C\,min^{-1}$ to 90 °C. The PTV conditions were: injection volume, 70 μL; injection temperature, 70 °C; transfer and vaporization ramp, 14 $°C\,s^{-1}$; vaporization temperature, 40 °C;

transfer temperature 130 °C; cleaning temperature, 250 °C; split flow, 55 mL min^{-1}; and vaporizing, transfer and cleaning times of 0.10, 1.50, and 3.00 min, respectively. The MS conditions were as follows: ions source temperature (IST), 250 °C, ionization mode EI at 70 eV, transfer line temperature, 280 °C, He, 1 mL min^{-1} constant flow, 70 μL were injected with PTV and MS–MS mode.

The confirmation criteria were according to the European Decision 2002/657/CE [35]: (1) the two product ions intensity must be, at least, three times greater than the base noise of the MS detector, (2) relative abundance between ions in the sample should be the same as in the standard, with the acceptable deviations described in this legislation (3) and the ratio between the chromatographic retention time of the analyze and those of the internal standard must correspond to the one of the calibration solutions, with a tolerance of ±0.5%. The calibration curves were established using isotopic dilution methodology.

3.3. *Quality control and quality assurance*

The quality control and quality assurance measures in the monitoring program of 3-MCPD represents more than 30% of the whole analytical effort. Each batch of samples included a procedural blank, an in house reference material spiked at 5.5 μg kg^{-1} and a quality control reference material provided by Central Science Laboratory (CSL). Through these quality control procedures we have checked that the recoveries and precision achieved in the validation process for soy sauce and breakfast cereals can be used for the other matrices.

During this study, the laboratory participated in some Laboratory Proficiency testing FAPAS® (series 2616–2621) provided by CSL with satisfactory *z*-scores. The Laboratory works under the quality assurance system established by ISO/IEC/EN 17025, and has been accredited by ENAC, the accreditation body of Spain.

4. Results and discussion

4.1. *MS/MS settings optimization*

In order to maximize the signal of the 3-MCPD the optimization of different parameters is necessary. The concentration of the 3-MCPD standard solution used for this work was 0.0441 ng mL^{-1}.

The most abundant ion from the full scan spectra of the chloropropanol, *m/z* 253 was selected as precursor ion and it was then isolated in the ion trap and fragmented by collision-induced dissociation (CID). The two most abundant product ions were selected, *m/z* 225 and *m/z* 169. The ion ratio for the different matrices was similar. In all the cases the *m/z* 225 was 100% of relatively intensity. The *m/z* 169 presented an ion ratio of 59 ± 18 (standard deviation) for level 1 (5.5 ng g^{-1} for soy sauce and 4.4 ng g^{-1} for breakfast cereals), 66 ± 21 for level 2 (68.9 ng g^{-1} for soy sauce and 55.1 ng g^{-1} for breakfast cereals) and 67 ± 18 for level 3 (275.4 ng g^{-1} for soy sauce and 220.3 ng g^{-1} for breakfast cereals). The spectrum was obtained with the default operating parameters from the GC-MS/MS system.

Table 1
Experimental conditions and analytical response of Placket–Burman design used for optimization of detector settings for 3-MCPD

Run	REV	ET	IT	IST	EE	Response *m/z* 225
8	2.00	5.0	34	150	35	375,452
10	2.00	50.0	4	250	35	1,093,285
14	0.10	50.0	34	150	75	29
15	2.00	5.0	34	250	35	505,698
9	2.00	50.0	4	250	75	292,879
5	2.00	50.0	34	150	75	212,022
2	1.05	27.5	19	200	55	3,667,210
4	1.05	27.5	19	200	55	3,636,251
12	1.05	27.5	19	200	55	3,404,996
11	0.10	50.0	34	250	35	18,012
7	0.1	5.0	34	250	75	49
1	0.10	5.0	4	250	75	5,602
13	2.00	5.0	4	150	75	612
3	0.10	50.0	4	150	35	30,796
6	0.1	5.0	4	150	35	82,89

Considering the literature [36,37] and previous experimentation, five factors were selected that could potentially affect the analytical response of the MS/MS system: resonance excitation voltage (REV), isolation time (IT), excitation time (ET), ion source temperature (IST) and electron energy (EE). The relative influence of these factors on the analytical response was studied with a Plackett–Burman [30]. This screening design, allows to find the parameters that have the largest influence with a reduced number of experiments. Although Plackett–Burman designs for studying 5 factors may require as few as 8 runs, we used 12 runs plus a triplicate centre point in order to have generous degrees of freedom for testing the statistical significance of the estimated effects The 15 runs with the different values of the factors examined and the response of the ion *m/z* 225 are shown at the Table 1. Table 2 shows the estimated effects of the five factors and their statistical significance at 95% confidence level ($\alpha < 0.05$). Only the effect of REV on the response of the 3-MCPD is statistically significant.

The following step was to find the best value for REV. Different resonance excitation voltages were studied at the following fixed values of the other parameters: IT 4 ms (negative effect), ET 50 ms (positive effect), IST 250 °C (positive effect) and EE

Table 2
Estimated effects[a] and *P*-value (between parenthesis) of the five factors of the Placket–Burman design used in the ion source settings optimization on the analytes responses (taken as arbitrary units)

	REV	ET	IT	IST	EE
3-MCPD	4029 (0.011)	1252 (0.332)	−534 (0.671)	2147 (0.115)	2534 (0.070)

[a] Coded units, $\alpha = 0.05$; REV, resonance excitation voltage (V); IT, isolation time (ms); ET, excitation time (ms); IST, ion source temperature (°C); EE, electron energy (eV).

Table 3
Experimental conditions of the CCD design used for optimization of PTV settings for 3-MCPD

Run order	T_{inlet} (°C)	T_{vap} (°C)	t_{vap}(min)	Flow (mL min^{-1})	Response *m/z* 225
1	43.75	61.25	1.525	32.5	118,079
2	61.25	103.75	1.525	77.5	3,557
3	43.75	103.75	1.525	32.5	18,950
4	43.75	103.75	1.525	77.5	5,609
5	61.25	61.25	0.575	32.5	196,023
6	43.75	61.25	0.575	32.5	232,479
7	61.25	103.75	1.525	32.5	20,221
8	61.25	103.75	0.575	32.5	30,030
9	52.50	82.50	1.050	100.0	3,559
10	35.00	82.50	1.050	55.0	9,883
11	52.50	82.50	1.050	55.0	9,945
12	52.50	82.50	1.050	55.0	9,501
13	52.50	82.50	2.000	55.0	9,518
14	52.50	82.50	1.050	55.0	10,179
15	52.50	82.50	1.050	55.0	10,506
16	43.75	61.25	0.575	77.5	35,146
17	43.75	103.75	0.575	32.5	23,439
18	52.50	40.00	1.050	55.0	9,495
19	43.75	61.25	1.525	77.5	5,441
20	61.25	103.75	0.575	77.5	6,028
21	52.50	82.50	1.050	55.0	9,844
22	52.50	82.50	1.050	10.0	194,708
23	43.75	103.75	0.575	77.5	5,044
24	61.25	61.25	1.525	77.5	3,726
25	52.50	125.00	1.050	55.0	11,827
26	61.25	61.25	0.575	77.5	45,075
27	52.50	82.50	1.050	55.0	8,183
28	70.00	82.50	1.050	55.0	9,685
29	61.25	61.25	1.525	32.5	11,4725
30	52.50	82.50	1.050	55.0	8,029
31	52.50	82.50	0.100	55.0	68,202

75 V (positive effect). The results are shown in Fig. 1. The REV that provided the best response was 0.5 V.

4.2. Optimization of PTV injection

After optimization of the MS/MS settings, the PTV injection was optimized. Since in samples 3-MCPD is present at low levels, we tried to increase the response of the analytical system by introducing a large volume of the final extract into the GC-MS/MS.

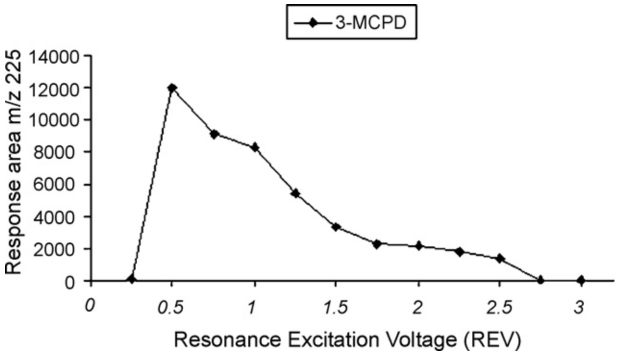

Fig. 1. Effect of the resonance excitation voltage (REV) on the peak area response of *m/z* 225.

Three modes of large-volume introduction into a PTV injector are possible: (1) at once, (2) speed controlled injection and (3) multiple injection. We used the at once mode at 100 μL s^{-1} because optimization procedure was simpler than the others. The concentration of the 3-MCPD derivatizated standard solution used for the injection was 4.41 ng mL^{-1}.

Four factors were selected for optimization: injection temperature (T_{inlet}), vaporization temperature (T_{vap}), vaporization time (t_{evap}) and flow of the evaporation step (Flow). In all the experiments we fixed the transfer temperature at 280 °C, 2 min in splitless mode and 300 °C for the cleaning temperature during 5 min with the split valve open (300 mL min^{-1}). A central composite design (Table 3) was used. This design consisted on a full factorial 2^4 design (16 hypercube points), 8 axial points and 7 central points. The 31 runs were randomized to provide protection against the effect of hidden variables.

The analytical responses obtained were fitted into a linear equation that included second-order (curvature) and interaction terms. The equation model for the analytical response (Y) for the ion *m/z* 225 was as follows:

$$\begin{aligned} Y = {} & b_0 + b_1x_1 + b_2x_2 + b_3x_3 + b_4x_4 + b_{11}x_1^2 \\ & + b_{22}x_2^2 + b_{33}x_3^2 + b_{44}x_4^2 + b_{12}x_1x_2 + b_{13}x_1x_3 \\ & + b_{14}x_1x_4 + b_{23}x_2x_3 + b_{24}x_2x_4 + b_{34}x_3x_4 \end{aligned}$$

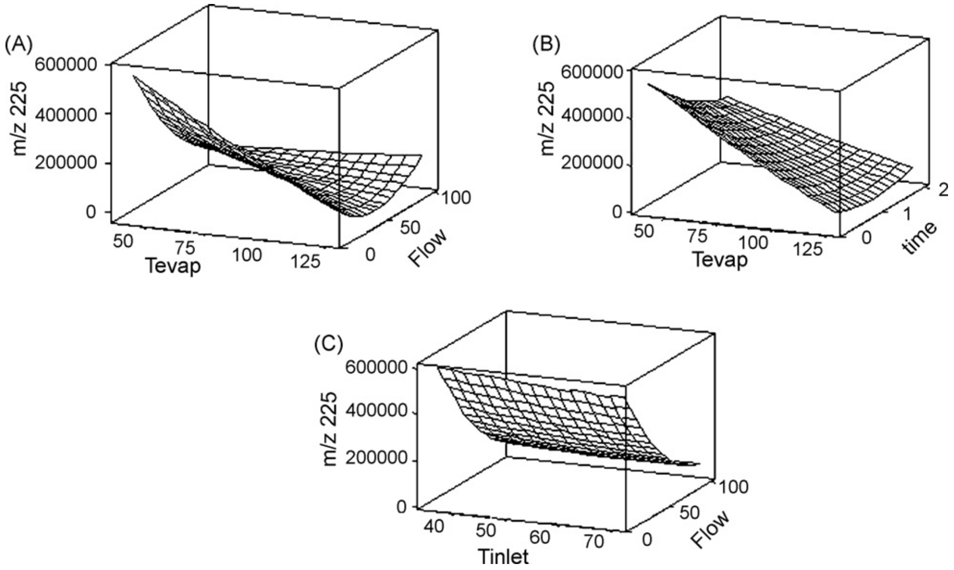

Fig. 2. Response surfaces obtained for 3-MCPD; fixed conditions (A) $T_{\rm inlet}$: 70 °C, time: 0.1 min; (B) $T_{\rm inlet}$:70 °C, flow:10 mL min^{-1}; (C) $T_{\rm evap}$:40 °C, time: 0.1 min.

where b_0 is the average response factor; x_1, x_2, x_3, x_4 are the $T_{\rm inlet}$, $T_{\rm vap}$, $t_{\rm evap}$ and Flow factor, respectively; b_1, b_2, b_3 and b_4 are the coefficients for the main effect (1 for the $T_{\rm inlet}$, 2 for the $T_{\rm vap}$, 3 for the $t_{\rm evap}$ and 4 is for the Flow factor; b_{11}, b_{22}, b_{33} and b_{44} are the coefficients for the quadratic effect; b_{12}, b_{13}, b_{14}, b_{23}, b_{24} and b_{34} are the coefficients for the two-factor interaction. The coefficients of the significant factors ($\alpha < 0.05$) obtained by central composite design were 9455.3 for b_0, −26,381 for b_2, −16,680.2 for b_3, −42,775.8 for b_4, 24,813.5 for b_{44}, 1569.3 for b_{23} and 31,219.8 for b_{24}.

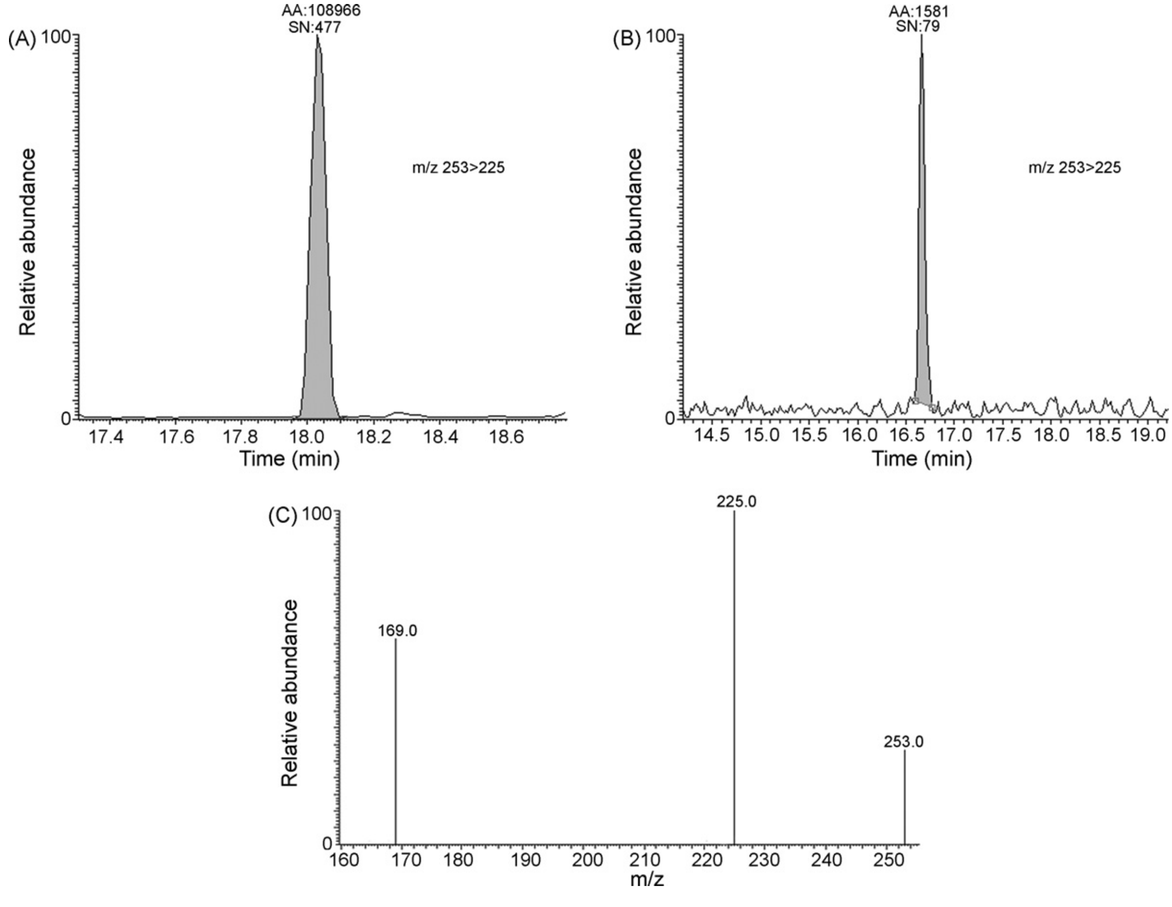

Fig. 3. MS/MS chromatograms of spiked soy sauce at 5.51 ng g^{-1} for the product ion *m/z* 225 in (A) PTV-LV mode; (B) Splitless mode; (C) MS/MS spectrum of spiked soy sauce at 5.51 ng g^{-1} for the PTV-LV injection.

Table 4
Recovery and reproducibility (RSD) of the proposed method

	Level 1[a]		Level 2[b]		Level 3[c]	
	Recovery (%)	RSD (%)	Recovery (%)	RSD (%)	Recovery (%)	RSD (%)
Soy sauce	95	12	98	9	100	9
Breakfast cereals	105	9	99	7	97	5

Validation schedule: 3 days, 7, 7 and 8 replicates each day, $n = 20$.

[a] Level 1: 5.5 ng g^{-1} for soy sauce and 4.4 ng g^{-1} for breakfast cereals.

[b] Level 2: 68.9 ng g^{-1} for soy sauce and 55.1 ng g^{-1} for breakfast cereals.

[c] Level 3: 275.4 ng g^{-1} for soy sauce and 220.3 ng g^{-1} for breakfast cereals.

Fig. 2 shows the three-dimensional response surface for two factors at a constant value of the other two factors.

The factors settings that maximize the peak area of the compound were selected using the "response optimiser" found in MINITAB. The optimized factor settings were T_{inlet}: 70 °C, T_{vap}: 40 °C, t_{vap}: 0.1 min and Flow: 10 mL min^{-1} and provided a composite desirability of 1.

In the final extract, 70 μL of the sample were introduced into the liner at 70 °C when the split valve is open. Then, the PTV was ramped to 40 °C at 14 °C s^{-1}, for 0.10 min to eliminate the solvent through the split valve at 10 mL min^{-1}. In the following step, the transfer phase, the split valve was closed and the temperature increased to 130 °C at 14 °C s^{-1} in splitless mode for 1.50 min. And for the cleaning step the liner was keep at 250 °C during 3 min with a flow of 250 mL min^{-1}.

With the optimized detector and PTV parameters, we have proved that the analyte,1,3-DCPD (with the selected ions *m/z* 225 and *m/z* 169) can be detected separately from 3-MCPD. However this analyte is not included in the EC regulation, it has not been validated and not included in the monitoring program.

The linear relationship of absolute peak area versus injected volume was studied by injecting different volumes (10, 20, 30, 40, 50, 60 and 70 μL of a 0.00441 μg mL^{-1} standard solution) using the optimized values. The result shows than the coefficient of determination (R^2) was higher than 0.98 for the 3-MCPD.

Finally, the instrumental limit of detection (i-LOD) for the PTV-LV was 0.044 ng mL^{-1}. This value was calculated as the lowest concentration of 3-MCPD that provides a signal to noise value higher than 3 for every monitored ion (*m/z*). The i-LOD obtained with the splitless mode injection (2 μL) in the same MS conditions was 0.001 μg mL^{-1}. Hence, it can be seen that large-volume injection increases the sensitivity. Fig. 3 presents the GC-MS/MS chromatograms of a spiked soy sauce sample (5.5 ng g^{-1}) for the product ion m/z 225 in splitless injection versus PTV-LV injection and MS/MS spectrum for the PTV injection. Also the chromatogram of m/z 225 and the corresponding spectrum at the limit of detection (0.055 ng g^{-1}) was show on Fig. 4.

4.3. Validation process

Analyte fortification was carried out by applying a known concentration of 3-MCPD to a known quantity of blank (matrix without analyte). Following fortification, spiked samples were allowed to equilibrate overnight at room temperature prior to extraction. *m/z* 253 was the parent ion, *m/z* 225 and *m/z* 169 were monitored as product ions. For quantification *m/z* 225 was used.

Linearity of the analytical method described was studied using calibration curves with six concentration levels including blank level: 0.0, 4.4, 8.8, 55.1, 110.2 and 220.3 ng mL^{-1}.

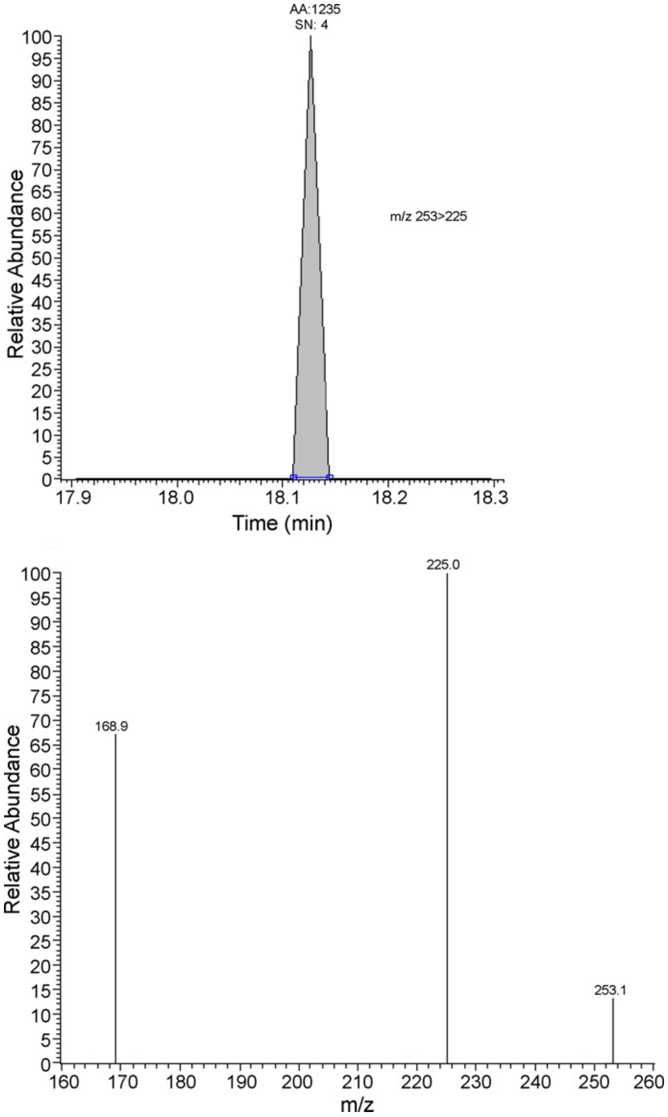

Fig. 4. MS/MS chromatogram and spectrum of a spiked soy sauce at the limit of detection 0.0551 ng g^{-1}.

Table 5
Summary of 3-MCPD levels (μg g^{-1}) in food samples from the Spanish market

Sample	Number of samples	Median (μg g^{-1})	Range (μg g^{-1})
Bread and breakfast cereals	30	0.068	<0.00022–0.143
Processed sausages	24	0.027	<0.00011–0.94
Beer	5	<0.00028	<0.00028
Soups	5	0.0105	<0.00028–0.098
Cookies	5	0.103	<0.00022–0.103
Soy sauce	5	0.00028	<0.00028–0.020

The lower value of the range were calculated assuming than when 3-MCPD was below the established limit, the concentration was equal to one-half the respective limit of quantitation.

Table 6
Estimation of the daily intake for adults and children of 3-MCPD based on the median concentrations found in the study

	Occurrence (median μg g^{-1})	Consumption		Daily intake		% PMTDI[a]	
		Average adult[b] (g/day person)	Average children[c] (g/day person)	Adult (μg/person day)	Children (μg/person day)	Adult	Children
Bread and breakfast cereals	0.068	88.64	85.20	6.02	5.79	0.004	0.009
Processed sausages	0.027	11.78	14.85	0.32	0.40	0.00002	0.0006
Beer[d]	0.00028	33.87	0.07	9.5×10^{-3}	1.96×10^{-5}	0.0000007	0.00000003
Soups	0.0105	0.00018	0.41	1.89×10^{-6}	4.30×10^{-3}	0.000000001	0.000006
Cookies	0.103	13.21	20.68	1.36	2.13	0.001	0.003
Total						0.005	0.01

[a] PMTDI of 3-MCPD = 2 mg Kg^{-1} bw day^{-1}.

[b] Average adult weight: 70 kg.

[c] Average children weight: 34 kg.

[d] For calculations, when an element was under the limit of quantification, the value was assumed to be one-half the respective limits.

The linear model was statistically validated taking into account that residual values were randomly distributed about the regression line, the p-value of the F-test statistic was <0.05, and the coefficient of determination (R^2) was better than 0.999 [38].

Recovery and reproducibility (between-day) were studied in spiked soy sauce and breakfast cereals samples at three levels of concentration and the blank level in three different days ($n \geq 20$ for each level). Table 4 shows the values of these parameters. The method limit of detection (signal to noise ≥3) for the different commodities was set at 0.055 ng g^{-1} .The limit of quantitation, based on compliance with the confirmatory criteria, was set at 5.5 ng g^{-1} for soy sauce and 4.4 ng g^{-1} for breakfast cereals.

4.4. Occurrence and daily intake of 3-MCPD

The optimized method was used in the 3-MCPD monitoring program of the Regional Valencia Government. During 2005–2007, 94 food samples were analyzed, including soy sauce, bread, breakfast cereals, beer, cookies, soups and processed sausages. The median concentration of 3-MCPD, and the maximum and minimum levels (range) in each group of samples are summarized in Table 5. The results are presented in this form because the 3-MCPD content is not normally distributed.

Of all samples examined, 23 of them contained levels greater than 0.02 mg kg^{-1}, the limit established by the European Union for soy sauce and HVPs [2]. The highest value was 0.94 mg kg^{-1}, founded in a sample of processed sausage. All of the beer samples analyzed showed levels of 3-MCPD lower than the quantitation limit.

The levels of 3-MCPD found in this study for bread and breakfast cereals and processed sausages are similar to those reported by other authors [3,4,12,24]. On the other hand, the levels found in soups are greater than these reported by the aforementioned authors.

The main route of exposure to 3-MCPD is through the diet. Consequently, information about dietary intake in necessary in order to evaluating the potential health risk for the individual. The assessment of potential health hazards for consumers may be obtained by calculating the daily intake of this compound deriving from the consumption of different foodstuffs and comparing the PMTDI set by JEFCA. It should be said that the purpose here is not to evaluate the total diet exposure but rather to study the intake of 3-MCPD.

The daily intake of 3-MCPD was calculated by multiplying the respective average concentration (median) by weight of foodstuffs consumed by an average individual from Spain per day. Table 6 shows the daily intake of 3-MCPD based on the concentrations founded in this study, calculated taking into account the total consumption of the foodstuffs studied [39]. As we can see the daily intake for adults and children are 0.005 and 0.01%, respectively, of the level reported from JEFCA (2 mg kg^{-1}).

5. Conclusions

The results obtained indicate that the determination of 3-MCPD using PTV with LVI gas chromatography (GC) with tandem mass spectrometry detection (MS/MS) provides a method limit of detection of 0.055 ng g^{-1}. This LOD is more sensitive than those provided by other GC-MS methods.

This paper shows that the experimental design is a rapid and useful tool to optimize this kind of analytic parameters. Of the studied factors of MS settings only the REV had a significant effect on the response. The optimization of MS/MS parameters and PTV-LV injection settings evidence a sensitive method suitable for the identification and quantification of 3-MCPD at background levels. The method is available for the wide range of matrices studied like soy sauce, cereals, bread, acid hydrolysed vegetable proteins and sausages. For these reasons, this procedure can be used in foodstuffs for the national monitoring programs to evaluate low levels of this contaminant in the framework of the European Legislation.

The results of the monitoring study do not show evidence of risk by means of intake of 3-MCPD for the average adult and children consumers. However, some samples of soy sauce have concentrations of 3-MCPD higher that the limit established for the European Commission.

Acknowledgement

The author's wish to thank Dr. Joan Ferré (Rovira i Virgili University) for his collaboration in the experimental design development.

References

[1] EC, Commission Regulation No. 1881/2006, Off. J. Eur. Commun. L364 (2006) 5.

[2] Joint FAO/WHO Expert Committee on Food Additives (JECFA), http://www.who.int/ipcs/food/jefca/en.

[3] C.G. Hamlet, S.M. Jayaratne, W. Matthews, Food Addit. Contam. 19 (2002) 15.

[4] C.G. Hamlet, P.A. Sadd, C. Crews, J. Velísek, D.E. Baxter, Food Addit. Contam. 19 (2002) 619.

[5] D.C. Meierhans, S. Bruehlmann, J. Meili, C. Taeschler, J. Chromatogr. A 802 (1998) 325.

[6] C.A. van Bergen, P.D. Colier, D.D.O. Cromie, R.A. Lucas, H.D. Preston, D.J. Sissons, J. Chromatogr. 589 (1992) 109.

[7] K.O. Wong, Y.H. Cheong, H.L. Seah, Food Control 17 (2006) 408.

[8] C. Crews, P. Hough, P. Brereton, D. Harvey, R. Macarthur, W. Matthews, Food Addit. Contam. 19 (2002) 22.

[9] C. Retho, F. Blanchard, Food Addit. Contam. 22 (2005) 1189.

[10] F.M. Dayrit, M.R. Ninonuevo, Food Addit. Contam. 21 (2004) 204.

[11] P.J. Nyman, G.W. Diachenko, G.A. Perfetti, Food Addit. Contam. 20 (2003) 903.

[12] P.J. Nyman, G.W. Diachenko, G.A. Perfetti, Food Addit. Contam. 20 (2003) 909.

[13] S. Abu-El-Haj, M.J. Bogusz, Z. Hassan, M. Al Tufail, Food Control 18 (2007) 81.

[14] G. Sunhara, I. Perrin, M. Marchenissi, Report No. RE-SR93003, Nestec Ltd. Research and development, Stwitzerland, 1993.

[15] B.S. Lynch, D.W. Bryant, G.J. Hook, E.R. Nestman, I.C. Munro, Int. Toxicol. 17 (1998) 47.

[16] P. Olsen, Chloropropanols in JECFA, in: Procceedings of the 41st Meeting of WHO Food Additives Series, World Health Organization, Genenva, 1993, p. 267.

[17] J. Schlatter, A.J. Baars, M. DiNovi, S. Lawrie, R. Lorentzen, WHO Food. Addit. Ser. (2002) 401.

[18] Scientific Committee for Food 2001, Opinion of the Scientific Committee on Food on 3-monochloropropane-1,2-diol (3-MCPD). Available at: http://www.europa.eu.int/comm/food/fs/sc/scf/out91_en.pdf.

[19] T.Y. Xie, N. Li, Y.J. Tang, J.Y. Mo, Chinese J. Chromatogr. 21 (2003) 513.

[20] X. Xing, Y. Cao, L. Wang, J. Chromatogr. A 1072 (2005) 267.

[21] X. Xing, Y. Cao, Food Control 18 (2007) 167.

[22] R.L. Pesselman, M.J. Feit, J. Chromatogr. A 439 (1988) 448.

[23] G. Spyres, J. Chromatogr. 638 (1993) 71.

[24] P. Brereton, J. Kelly, C. Crews, S. Honour, R. Wood, J. AOAC Int. 84 (2001) 455.

[25] C.G. Hamlet, Food Addit. Contam. 15 (1998) 451.

[26] W. Chung, K. Hui, S. Cheng, J. Chromatogr. A 952 (2002) 185.

[27] M.K.P. Leung, B.K.W. Chiu, M.H.W. Lam, Anal. Chim. Acta 491 (2003) 15.

[28] M.J. Huang, G.B. Jiang, B. He, J.F. Liu, Q.X. Zhou, W.S. Fu, Y.N. Wu, Anal. Sci. 21 (2005) 1343.

[29] V. Yusà, G. Quintàs, O. Pardo, A. Pastor, M. de la Guardia, Talanta 69 (2006) 807.

[30] D.L. Masart, B.G.M. Vandeginste, C.M.C. Buydens, S. de Jong, P.J. Lewi, J. Smeyers-Vrbeke, Handbook of Chemometrics and Qualimetrics, Part A, Elsevier Science B.V., Amsterdam, 1997.

[31] V. Flotron, J. Houessou, A. Bosio, C. Delteil, A. Bermond, V. Camel, J. Chromatogr. A 999 (2003) 175.

[32] C. Peña-Farfal, A. Moreda-Piñero, A. Bermejo-Barrera, H. Pinochet-Cancino, I. De Gregori-Hernandez, Talanta 64 (2004) 671.

[33] O. Pardo, V. Yusà, N. León, A. Pastor, J. Chromatogr. A 1107 (2006) 70.

[34] C. Van Poucke, F. Dumoulin, C. Van Peteghem, Anal. Chim. Acta. 529 (2006) 211.

[35] EU, Commission of the European Communities 2002/657/EC, Off. J. Eur. Commun. L221 (2002) 8.

[36] V. Yusà, O. Pardo, A. Pastor, M. de la Guardia, Anal. Chim. Acta 557 (2006) 304.

[37] C. Naert, S. de Saeger, C. Van Petenghem, Rapid Commun. Mass Spectrom. 18 (2004) 2317.

[38] Eurachem Guide, The Fitness for Purpose of Analytical Methods: a Laboratory Guide to Method Validation and Related Topics, LGC, Teddington, Middlesex, UK, 1998 (available at: http://www.eurachem.org).

[39] AESA (Agencia Española de Seguridad Alimentaria), Modelo de dieta española para la determinación de la exposición del consumidor a sustancias químicas, Madrid, Ministerio de Sanidad y Consumo, 2006 (available from: http://www.aessa.msc.es/aesa).

Available online at www.sciencedirect.com

ScienceDirect

Talanta 75 (2008) 677–683

Talanta

www.elsevier.com/locate/talanta

Cationic double-chained surfactant as pseudostationary phase in micellar electrokinetic capillary chromatography for drug separations

Yanqing Li, Qian Liu, Shouzhuo Yao*

College of Chemistry and Chemical Engineering, Hunan University, Changsha 410082, China

Received 11 August 2007; received in revised form 3 December 2007; accepted 3 December 2007
Available online 1 February 2008

Abstract

The cationic double-chained surfactant didodecyldimethylammonium bromide (DDAB) was used as pseudostationary phase (PSP) in micellar electrokinetic capillary chromatography (MEKC). Its performance on the three kinds of drugs, i.e., basic, acidic, and neutral drugs, was systematically investigated. Nicotine, cotinine, caffeine, lidocaine, and procaine were selected as the model basic drugs. Good baseline separation and high efficiency were obtained under the optimal separation condition that consisted of 50 mM phosphate (pH 4.0) and 0.08 mM DDAB. Three basic phenylenediamine isomers can also be well separated with DDAB in buffer. In addition, DDAB can form cationic bilayer on the capillary wall, thus the wall adsorption of basic analytes was greatly suppressed. Compared with commonly used CTAB, the separation of basic drugs was significantly improved with a much lower amount of DDAB present in the buffer. The DDAB-involved MEKC also showed superiority to CTAB upon the separation of acidic drugs, amoxicillin and ampicillin. In the case of neutral compounds, a good separation of resorcinol, 1-naphthol and 2-naphthol was achieved with 0.1 mM DDAB and 30% (v/v) acetonitrile (ACN) present in buffer. Hence, it was concluded that the double-chained cationic surfactant DDAB can be a good substitute for traditional single-chained surfactant CTAB in MEKC.

Keywords: Didodecyldimethylammonium bromide; Double-chained surfactant; Micellar electrokinetic capillary chromatography; Pseudostationary phase

1. Introduction

Micellar electrokinetic capillary chromatography (MEKC) is an important analytical technique with high separation efficiency, short analysis time, and low reagent consumption [1–4]. It has been used in a large number of applications, such as pharmaceutical, environmental, forensic, and general product analysis [4]. It takes advantage of the feature of liquid chromatography (LC) which utilizes the partition equilibrium of compounds between two different phases. Although MEKC was first developed for the separation of neutral compounds, it has been soon applied to separate ionic analytes. Now MEKC is widely considered as an important separation mode of CE.

The separation mechanism of MEKC is based on the difference in electrophoretic mobility and distribution between the aqueous phase and the pseudostationary phase (PSP). A number of PSPs for MEKC were developed, including surfactants, polymers, and their mixtures. In particular, the cationic surfactants not only form micellar pseudostationary phase to facilitate the separation, but also reverse the orientation of electroosmotic flow (EOF) [5,6]. Cationic surfactants adsorb on the capillary wall through the electrostatic attraction between the positively charged head group ions and the negatively charged silanol groups. A bilayer of cationic surfactant thus forms on the capillary wall with a positive charge facing the bulk solution in the capillary and then the EOF is reversed [7]. Compared with the anionic surfactants, cationic surfactants have complementary characters because of the different type of charge [8–10]. The complementary selectivity of cationic surfactants results in the viable separation of the compounds which have low affinity with anionic surfactant. In the cationic surfactant systems, larger EOF can be obtained at the low pH values than that in the anionic surfactant systems. Also, the cationic surfactants can be more appropriate to separate mixtures of compounds differing in their hydrogen-bond acidity than the anionic surfactants [11].

Recently, the double-chained surfactant didodecyldimethylammonium bromide (DDAB) was used as a semipermanent

---

* Corresponding author. Fax: +86 731 8821848.
E-mail address: szyao@hnu.cn (S. Yao).

0039-9140/$ – see front matter © 2008 Published by Elsevier B.V.
doi:10.1016/j.talanta.2007.12.001

coating for the control of EOF and wall adsorption of basic proteins [12–14]. It was found that the aggregation properties were quite different between single- and double-chained surfactants in solution [12]. Due to the increased tail group cross-section area, DDAB aggregates to form bilayer structure or vesicle in solution [15], while the single-chained surfactant cetyltrimethylammonium bromide (CTAB) forms spheric micelles. The critical vesicle concentration (CVC) of DDAB in water (0.035 mM [16]) is almost 30-fold lower than the critical micelle concentration (CMC) of CTAB. The very low CVC of DDAB makes it rather favorable to form stable wall coatings in CE. Furthermore, it was reported that the CVC of DDAB is lower in phosphate buffer than in pure water (0.010, 0.0037 and 0.0018 mM in 8.7, 22.1 and 44.2 mM phosphate buffer (pH 3), respectively [13]). As known, vesicles are bilayers or multilayer aggregates, which are usually bigger in size than the micelles. Vesicles have high surface charge density and high electrophoretic mobility, thus can provide wide migration window and potential for the separation of compounds with similar hydrophobicity [17]. Fuguet et al. found that dihexadecyldimethylammonium bromide (DHAB) has different properties to, but comparable selectivity as the single-chained cationic surfactants with different chain lengths [18]. As the resolving capability of MEKC directly depends on solute partition coefficient into the PSPs, and the double-chained surfactant vesicle can provide more hydrophobic space for the hydrophobic interaction that is the most important contributor to retention [19], we think the special aggregate structure of double-chained surfactant vesicle may bring some benefits to MEKC. In this work, we investigated the feasibility of using a more common double-chained surfactant, DDAB, as PSP in MEKC, and carried out a more systematical study on the performance of DDAB-enhanced MEKC on the three different types of drugs, i.e., basic, acidic, and neutral drugs. The aim of this work is to evaluate a new candidate for PSP in MEKC of drugs. Herein, the surfactant-based electrokinetic capillary chromatography is called MEKC for short in the following text, despite that the PSP is micelle or vesicle.

2. Experimental

2.1. Instrumentation

CE was performed on a Beckman P/ACE MDQ CE system (Beckman Instrument, Fullerton, CA, USA) equipped with a PDA detector, which was controlled by 32 Karat software (Beckman Instruments). A fused-silica capillary (Yongnian Photoconductive Fiber Factory, Hebei, China) of 40 cm (30 cm to detector) ×50 μm i.d. was used for separation. The virgin capillary was conditioned by rinsing in the following sequence: methanol (MeOH) for 5 min, water for 2 min, 1 M HCl for 5 min, water for 2 min, 0.1 M NaOH for 10 min, water for 2 min, and finally buffer for 5 min. All the rinses were made under 138 kPa unless otherwise noted. The samples were injected under a pressure of 3.45 kPa for 3 s. The separation voltage was ±15 kV. The capillary was thermostated at 25 °C.

2.2. Chemicals

DDAB was purchased from Sigma (St. Louis, MO, USA). Cotinine, caffeine, lidocaine, and procaine were bought from Alfa Aesar (UT, USA). Nicotine was from Merck (Darmstadt, Germany). *m*-Phenylenediamine, *o*-phenylenediamine, and *p*-phenylenediamine were bought from Guangfu (Tianjin, China). Ampicillin and amoxicillin were purchased from Amresco (OH, USA). Resorcinol, 1-naphthol and 2-naphthol were bought from Damao (Tianjin, China). A 0.1% (v/v) aqueous solution of *N,N*-dimethylformamide (DMF) was used as neutral EOF marker. Dodecanophenone was used as a tracer for the migration time test of the micelle (t_{mc}). The sample solutions were directly prepared in water. The samples of the neutral compounds were prepared in ACN/water mixed solution (v/v, 3:7). DDAB solution (1 mM) was prepared in water and diluted to desired concentrations by running buffer. Phosphate, acetate and borate buffer were prepared with their sodium salts or acids and then adjusted to the desired pH with NaOH. Double-distilled water was used throughout. All reagents were of analytical grade.

2.3. EOF and efficiency measurement

Before each run, the capillary was rinsed with MeOH for 10 min, 1 M HCl for 10 min, 1 M NaOH for 10 min, and finally buffer for 5 min for the different buffer systems, while simply with buffer for 2 min for the same buffer systems. The rinses of MeOH, HCl and NaOH were made under high pressure of 207 kPa. A 0.1% (v/v) DMF aqueous solution was injected at 3.45 kPa for 3 s and then ran under a constant voltage of ±15 kV. The EOF (μ_{eof}) and the effective mobility (μ_{eff}) were calculated using the following formulas:

$$\mu_{\mathrm{eof}} = \frac{L_{\mathrm{d}} L_{\mathrm{t}}}{t_{\mathrm{eof}} V} \tag{1}$$

$$\mu_{\mathrm{eff}} = \frac{L_{\mathrm{d}} L_{\mathrm{t}}}{V} \left(\frac{1}{t_{\mathrm{m}}} - \frac{1}{t_{\mathrm{eof}}} \right) \tag{2}$$

where L_{t} and L_{d} are the total length of the capillary and the capillary length to the detector, t_{eof} and t_{m} are the migration time of the EOF marker and the analyte, respectively, and V is the applied voltage. The separation efficiency and resolution were calculated by 32 Karat software based on the following formulas:

$$N = 5.54 \left(\frac{t_{\mathrm{m}}}{W_{1/2}} \right)^2 \tag{3}$$

$$R = 1.18 \frac{t_2 - t_1}{W_{1/2} + W_{\mathrm{P}1/2}} \tag{4}$$

where N is the theoretical plates number, t_{m} is the migration time, R is the resolution between the peak of interest (peak 2) and the peak preceding it (peak 1), t_1 is the migration time of peak 1, t_2 is the migration time of peak 2, $W_{1/2}$ is the width of the component peak at 50% peak height and $W\mathrm{p}_{1/2}$ is the width of the previous component peak at 50% peak height. The migration

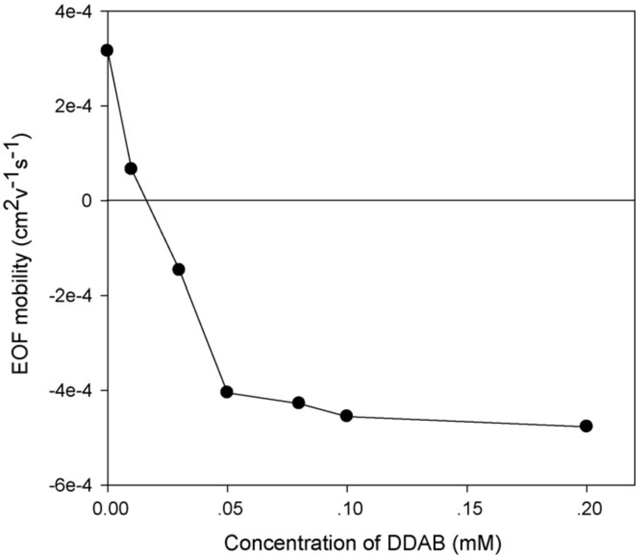

Fig. 1. Effect of DDAB concentration on EOF. Buffer, 50 mM phosphate (pH 5.0), 0–0.2 mM DDAB. EOF marker, 0.1% (v/v) DMF. Capillary, uncoated fused silica of 40 cm total length (30 cm to detector) ×50 μm i.d. Applied voltage, ±15 kV. Detection, 210 nm. Cartridge temperature, 25 °C. Injection, 3.45 kPa for 3 s.

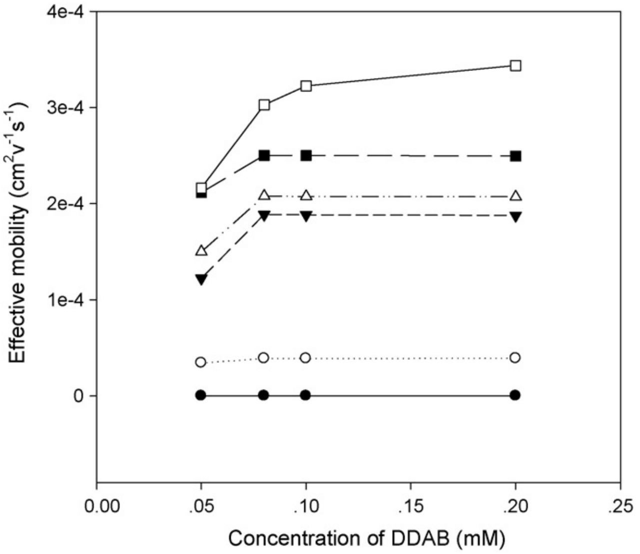

Fig. 2. Effect of DDAB concentration on the effective mobilities of basic drugs and DDAB vesicles. Samples: (●) caffeine, (○) cotinine, (▼) lidocaine, (△) procaine, (■) nicotine, and (□) DDAB vesicles. Sample concentration, 1 mM. Buffer, 30 mM phosphate (pH 5.0), 0.05–0.2 mM DDAB. Applied voltage, −15 kV. Other conditions as in Fig. 1.

window is defined as the difference between the migration time of micelles and EOF (t_{mc}/t_{eof}).

3. Results and discussion

3.1. Characterization of DDAB-mediated EOF

DDAB interacts with the negatively charged silica capillary wall, and reverses the EOF direction, thus the samples were injected from the cathode end of the capillary and the detector was placed at the anode end. The positive EOF is denoted as from anode to cathode. Fig. 1 shows the influence of DDAB concentration on the EOF in the range of 0–0.2 mM in 50 mM phosphate buffer (pH 5.0). Even if 0.03 mM DDAB was added in the buffer, EOF was still strongly reversed. With the increase of the DDAB concentration, the magnitude of reversed EOF at first increased rapidly. At DDAB concentration above 0.1 mM, however, the EOF changed rather insignificantly. This process of EOF reversal induced by DDAB is similar to CTAB [20].

The pH value of the buffer plays an important role in the EOF variations. The ionic strength of the buffer was maintained constant at 50 mM to investigate the pH effect. It was found that with pH increasing from 3.0 to 6.0, the EOF magnitude significantly decreased from -5.4×10^{-4} to -2.6×10^{-4} $cm^2\,V^{-1}\,s^{-1}$. The result may be explained as follows: at low pH, i.e., pH 3.0, even 0.1 mM DDAB is sufficiently high to saturate the capillary wall and to cause a highly reversed EOF even if the silica is partly ionized. With pH increasing, the further dissociation of the silanol groups increases the negative charges on the capillary wall [7]. Thus the EOF decreases gradually. At pH above 6.0, the EOF changed slightly, because the amount of Si–O$^-$ on the underlying silica surface changed little (the pK_a of the surface silanols = 5.3). From the above discussion, acidic pH condition may be favorable for a rapid separation.

3.2. Study on separation of basic drugs

3.2.1. Effect of DDAB concentration

We first studied the performance of MEKC using DDAB as PSP in the basic drugs separation. Nicotine, cotinine, caffeine, lidocaine and procaine were selected as model basic drugs. The DDAB concentration effect was first studied ranging from 0.05 to 0.2 mM in 30 mM phosphate (pH 5.0). Here, we aimed to show the effect of the interactions between the analytes and DDAB vesicles on the separation, thus the effective mobilities (μ_{eff}) of the analytes and DDAB vesicles were determined. The μ_{eff} of the DDAB vesicles was determined based on the migration of dodecanophenone [19]. As shown in Fig. 2, the μ_{eff} of DDAB vesicles increases from 2.2×10^{-4} to 3.4×10^{-4} $cm^2\,V^{-1}\,s^{-1}$ within the DDAB concentration 0.05–0.2 mM probably due to the variation of the vesicle size. The μ_{eff} of lidocaine, procaine and nicotine also significantly increases with DDAB ranging from 0.05 to 0.08 mM, definitely indicating that these three analytes have a strong partitioning into the vesicles, thus co-migrate with the DDAB vesicles. However, when DDAB is above 0.08 mM, the μ_{eff} of lidocaine, procaine and nicotine change little, suggesting that their interactions with the DDAB vesicles are saturated. For the other two analytes, caffeine and cotinine, almost no change in μ_{eff} was observed with the increase of DDAB concentration, suggesting that their interactions with the DDAB vesicles are weak. Conclusively, although electrostatic repulsion may exist between the basic analytes and the DDAB vesicles, strong partitioning was still observed for some analytes. Therefore, DDAB PSP is still available for the separation of basic drugs. The DDAB concentration should be optimized to gain the strongest inter-

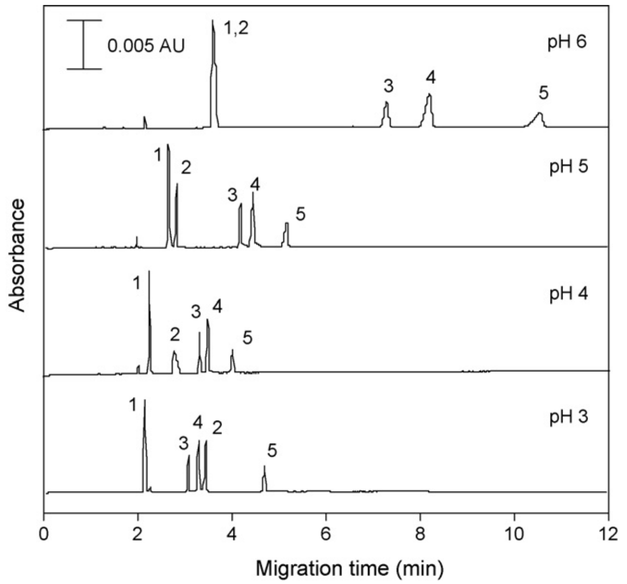

Fig. 3. pH effect on separation of basic drugs. Identification of peaks: (1) caffeine, (2) cotinine, (3) lidocaine, (4) procaine, and (5) nicotine. Buffer, 30 mM phosphate (pH 3.0–6.0), 0.08 mM DDAB. Other conditions as in Fig. 2.

action between the PSP and the analytes. Thus, the 0.08 mM DDAB was adopted in the following studies to obtain a rapid and good separation. In addition, we found that the DDAB concentration affects little on the detection signal and peak shape.

3.2.2. *Effect of buffer pH*

Buffer pH as a governing factor in separation influences the EOF of the DDAB-coated capillary and the mobility of analyte. For charged compounds, altering the buffer pH value may affect the dissociation of the compounds, and then impact on both the electrophoretic motilities and the interaction between analytes and PSPs [21]. To study the effect of buffer pH, experiments were performed with pH ranging from 3.0 to 6.0 (Fig. 3). At low pH (<5.0), the caffeine, cotinine, lidocaine, procaine and nicotine can be baseline separated. At pH 6.0, it appears that cotinine and caffeine co-migrate due to their partly deprotonation and lack of significant interaction with the DDAB aggregates. The optimal resolutions of the tested drugs with short migration times are obtained under pH 4.0, thus pH 4.0 is used in the further studies. Furthermore, we note that cotinine (pK_a 4.27 [22]) migrates faster than lidocaine and procaine at pH 4.0–6.0, while lags behind them at pH 3.0 because of the change of their charges under different pH conditions.

3.2.3. *Effect of buffer concentration*

Generally, high buffer concentration results in high separation efficiency and well-shaped peaks. However, it also causes high Joule heat and long analysis time. Herein, the buffer concentrations in the range of 5–100 mM were tested. For lidocaine, cotinine, procaine, and caffeine, the good peak shapes and the high resolutions are obtained when buffer concentration is above 50 mM. While for nicotine, the efficiency decreases markedly when buffer concentration increases from 50 to 100 mM due to the increased Joule heat. Therefore, to compromise among good separation efficiency, short migration time and good resolution, 50 mM was chosen as the proper phosphate buffer concentration. Other buffer systems were also investigated. Changing the buffer to acetate or citrate, however, resulted in worse resolution and peak shape than that in the phosphate buffer. Thus the phosphate buffer was throughout used.

Based on the above-mentioned studies, the optimal MEKC conditions were 50 mM phosphate (pH 4.0) with 0.08 mM DDAB. The separation under the above optimal conditions is illustrated in Fig. 4C. The basic drugs are baseline separated and have good peak shapes. Without DDAB present in buffer (Fig. 4A), caffeine cannot be detected within 20 min, which is thought to be enough long for a routine analysis, and the peaks of cotinine and procaine overlap. Also, the peaks show band-broadening, indicating that the analytes adsorb on the capillary wall to some extent. Thus, DDAB as PSP shows much better performance for the separation of these drugs, e.g., the resolution for cotinine and procaine is greatly improved from $R = 1.45$ (Fig. 4A) to $R = 15.6$ (Fig. 4C).

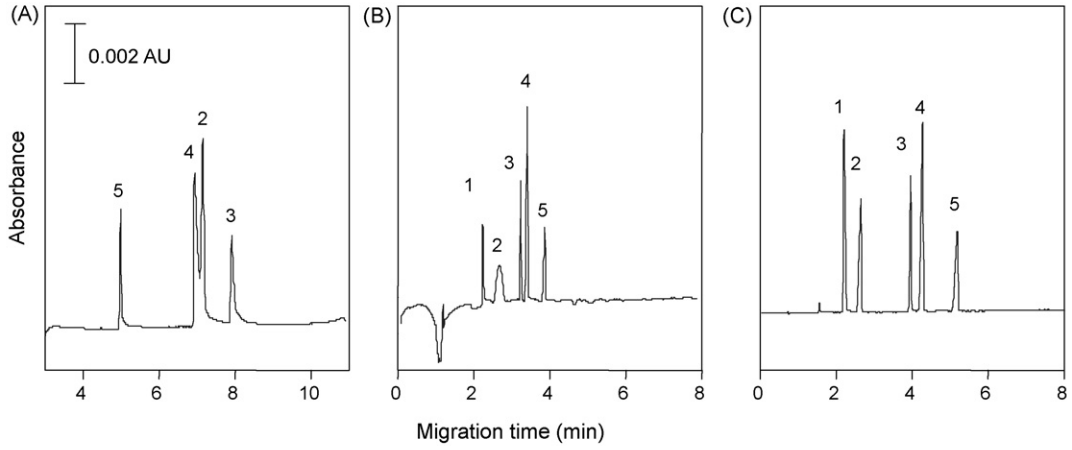

Fig. 4. Separation of basic drugs. With no additive (A), 2 mM CTAB (B), and 0.08 mM DDAB (C) as additive. Buffer, 50 mM phosphate (pH 4.0). Applied voltage, +15 kV for (A), −15 kV for (B) and (C). Other conditions and peak identification as in Fig. 3.

3.2.4. Comparison of DDAB with CTAB

The performance of the cationic double-chained surfactant was compared with the commonly used single-chained CTAB. To get a rather reasonable comparison of the performance of CTAB with DDAB systems, they were tested at the concentration of the same times of CMC or CVC, i.e., 0.08 mM for DDAB and 2 mM for CTAB, respectively (ca. twice the respective CVC or CMC). For CTAB, as shown in Fig. 4B, the analytes can be baseline separated. However, the migration window with the CTAB ($t_{mc}/t_{eof} = 1.83$) is narrower than that with the DDAB ($t_{mc}/t_{eof} = 2.51$) (Fig. 4C). Due to the bilayer structure, the DDAB vesicles have a higher charge density than that of the typical micelles. Hence, they have greater electrophoretic mobility in the opposite direction of EOF, which results in a wider migration window [21]. The wider migration window and the stronger partitioning of the analytes into the PSP yield better resolution for the analytes, e.g., the resolution $R_{2,3}$, $R_{3,4}$, and $R_{4,5}$ are remarkedly increased from 3.22, 2.19, 2.10 for CTAB to 15.11, 3.80, 7.67 for DDAB, respectively (here, $R_{i,j}$ represents the resolution between peak i and peak j). In addition, the separation efficiencies of the basic drugs with DDAB are higher than that with CTAB because the DDAB can suppress the wall adsorption of basic analytes more effectively [12]. Especially for cotinine, N are greatly enhanced from 1300 with CTAB to 13 300 with DDAB. Therefore, the double-chained DDAB provides a better performance than the single-chained CTAB when used as PSP in MEKC, with stronger resolving capability, better peak shape, and less consumption of surfactant.

3.2.5. Isomer separation

We also investigated the separation of three basic phenylenediamine isomers, *m*-phenylenediamine, *o*-phenylenediamine and *p*-phenylenediamine, which are thought to be hardly separated in CE [23]. When DDAB concentration increases from 0.04 to 0.1 mM, its effect on separation was not remarkable. With pH value increasing from 3.0 to 5.0, the migration times decreased and the peak signals were enhanced. Therefore, the best conditions were 30 mM acetate buffer (pH 5.0) with 0.04 mM DDAB (Fig. 5B). For comparison, the experiments were also carried out with 1 mM CTAB. As shown in Fig. 5A, worse peak shape and longer migration time than that of DDAB were observed.

From the above discussions, it can be concluded that DDAB vesicle can provide a more powerful resolving capability in MEKC as PSP for the separation of basic drugs due to its special vesicle structure in aqueous solution. Moreover, adding cationic surfactant in buffer suppresses the adsorption of basic drugs on capillary wall, which often causes peak tailing and bad efficiency in CE. DDAB, which has double hydrophobic chains, can form much more stable coating than CTAB. That allows stronger reversed EOF and higher efficiency.

3.3. Study on separation of acidic drugs

We then investigated the potential of MEKC for the analysis of acidic drugs. Since the acidic analytes can strongly interact with DDAB vesicles via electrostatic attraction, it is expected to obtain a good separation performance in DDAB-facilitated MEKC of acidic drugs. Amoxicillin and ampicillin were tested as the model compounds. The influence of DDAB concentration, buffer pH, and buffer ionic strength were studied. With DDAB concentration increasing, the migration times decrease slightly, and the efficiency is enhanced slightly. For further studies, 0.05 mM (ca. 1.4 times CVC) DDAB was used. At pH < 8.0, amoxicillin and ampicillin did not give satisfactory baseline separation. At pH higher than 9.3, they were well separated, but the analysis time became longer. Thus pH 9.3 is selected. The buffer concentration was investigated within 30–150 mM, and the best resolution was obtained at 100 mM. For higher concentration (150 mM), Joule heat results in bad peak shapes and low efficiency. Hence, the optimal buffer was 100 mM borate, pH 9.3, with 0.05 mM DDAB (Fig. 6C). Compared with the results of adding the same concentration of CTAB in the buffer (Fig. 6B), MEKC with DDAB shows much better separation, that is, the N of amoxicillin and ampicillin are significantly enhanced from 24 100 and 24 800–652 000 and 74 000, respectively; and the R is improved from 3.9 to 4.2. Elevating the CTAB concentration to 1.3 mM, i.e., 1.4 times its CMC, surprisingly, causes serious peak band-broadening (Fig. 6A). Since the acidic drugs do not strongly interact with the silanols on the capillary wall, we think that such separation efficiency enhancement with DDAB should be benefited from the unique aggregate properties of DDAB vesicle.

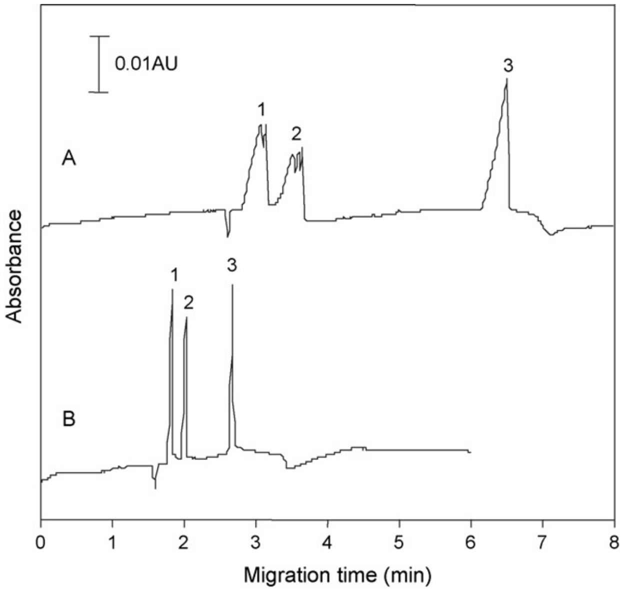

Fig. 5. Separation of phenylenediamine isomers. Identification of peaks: (1) *m*-phenylenediamine, (2) *o*-phenylenediamine, and (3) *p*-phenylenediamine. Sample concentration, 1 mM. Buffer, 30 mM acetate (pH 5.0) with 1 mM CTAB (A) and 0.04 mM DDAB (B). Applied voltage, −15 kV. Other conditions as in Fig. 1.

3.4. Study on separation of neutral compounds

MEKC has been acknowledged as a powerful tool for separation of neutral analytes since its emergence. Thus, we also conducted the experiments with some neutral compounds,

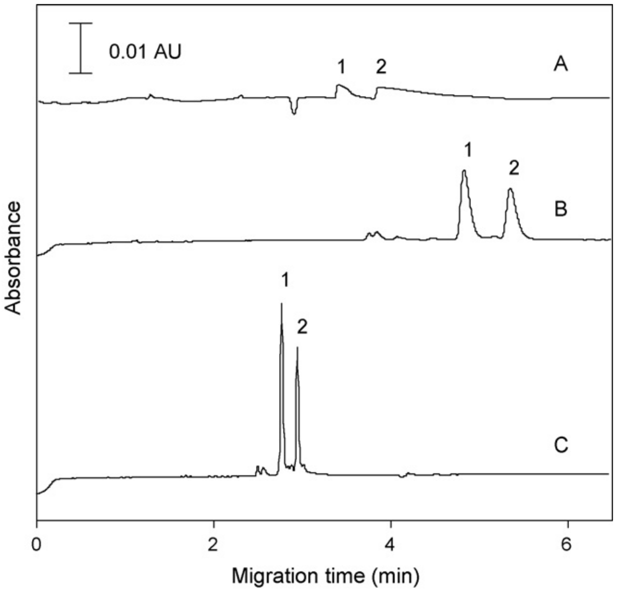

Fig. 6. Separation of penicillins. Identification of peaks: (1) amoxicillin and (2) ampicillin. Sample concentration, 1 mM. Buffer, 100 mM borate (pH 9.3) with 1.3 mM CTAB (A), 0.05 mM CTAB (B) and 0.05 mM DDAB (C). Applied voltage, −15 kV. Other conditions as in Fig. 1.

including resorcinol, 1-naphthol and 2-naphthol. In the buffer consisted of 30 mM phosphate, 0.1 mM DDAB, and 30% (v/v) acetonitrile (ACN) at pH 6.7, these neutral analytes were well separated (Fig. 7B). Furthermore, we found that the addition of some organic solvent into the buffer was critical for the analysis of neutral compounds. Without adding ACN in buffer, the two naphthols are hard to baseline separate even at high concentration of DDAB. The reason may be that these neutral analytes are rather hydrophobic that they unspecifically interact with DDAB vesicles, resulting in low selectivity. Organic modifier can influence the distribution of the analytes between the PSP and the aqueous phase [24]. ACN can change the solubility of the hydrophobic analytes and thus mediate the partitioning of the analytes into vesicles. On the other hand, organic modifier added in the separation buffer can change the migration window ($t_{\mathrm{mc}}/t_{\mathrm{eof}}$ ratio) [10]. In this study, the t_{eof} increases with the ACN concentration due to the variation of the dielectric constant-to-viscosity ratio (ε/η) of the solvent [25]. Meanwhile, the t_{mc} increases more rapidly with the ACN concentration than t_{eof} (data not shown), so the migration window becomes wider. In the case of CTAB, however, the baseline separation of naphthols cannot be obtained even 30% ACN was added into the buffer (Fig. 7A). The migration window with CTAB is smaller than that with DDAB, e.g., with 30% ACN, the $t_{\mathrm{mc}}/t_{\mathrm{eof}}$ values are 2.93 for CTAB and 4.12 for DDAB. In summary, the double-chained cationic surfactant is more powerful than the single-chained cationic surfactant in the MEKC of neutral compounds.

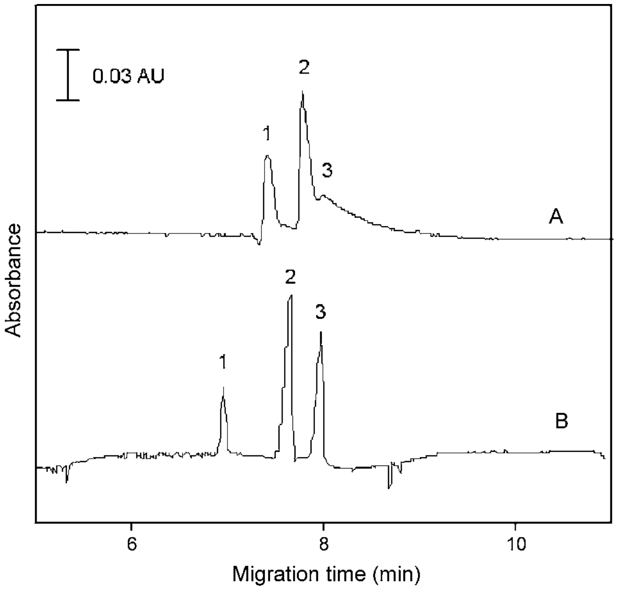

Fig. 7. Separation of the neutral drugs. Peaks: (1) resorcinol, (2) 1-naphthol, and (3) 2-naphthol. Sample concentration, 1 mM. Buffer, 30 mM (pH 6.7) phosphate with 2.6 mM CTAB (A) and 0.1 mM DDAB (B). Applied voltage, −15 kV. Other conditions as in Fig. 1.

4. Conclusions

The low CVC and unique vesicle structure of DDAB makes it rather attracting as PSP in MEKC. Good separations of basic and acid drugs are achieved with low concentration of DDAB present in buffer within 5 min under the optimal conditions. It was also able to get satisfactory separation of neutral drugs when some organic solvent is added into the buffer. This work definitely showed that DDAB provide a better performance than conventional CTAB with regard to analysis time, separation efficiency, migration widow, and consumption amount of surfactant in MEKC. Therefore, we believe that the double-chained cationic surfactant is a promising PSP in MEKC.

Acknowledgement

This work was financially supported by the National Natural Science Foundation of China (Nos. 20335020 & 20575019).

References

[1] S. Terabe, K. Otsuka, K. Ichikawa, A. Tsuchiya, T. Ando, Anal. Chem. 56 (1984) 111.
[2] M. Molina, M. Silva, Electrophoresis 23 (2002) 3907.
[3] S. Terabe, Anal. Chem. 77 (2004) 240A.
[4] T.J. Pappas, M. Gayton-Ely, L.A. Holland, Electrophoresis 26 (2005) 719.
[5] J.P. Quirino, S. Terabe, Electrophoresis 21 (2000) 355.
[6] C.A. Lucy, R.S. Underhill, Anal. Chem. 68 (1996) 300.
[7] Q. Liu, Y. Li, F. Tang, L. Ding, S. Yao, Electrophoresis 28 (2007) 2275.
[8] M.G. Khaledi, J. Chromatogr. A 780 (1997) 3.
[9] S.K. Poole, C.F. Poole, Analyst 122 (1997) 267.
[10] M.J. Hihorst, A.F. Derksen, M. Steringa, G.W. Somsen, G.J. de Jong, Electrophoresis 22 (2001) 1337.
[11] E. Fuguet, C. Ràfols, E. Bosch, M.H. Abraham, M. Rosés, J. Chromatogr. A 942 (2002) 237.
[12] J.E. Melanson, N.E. Baryla, C.A. Lucy, Anal. Chem. 72 (2000) 4110.
[13] M.M. Yassine, C.A. Lucy, Anal. Chem. 76 (2004) 2983.
[14] M.M. Yassine, C.A. Lucy, Anal. Chem. 77 (2005) 620.
[15] J. Israelachvili, D. Mitchell, B.E. Ninham, J. Chem. Soc., Faraday Trans. 72 (1976) 1525.

[16] T.F. Svitova, Y.P. Smirnova, S.A. Pisarev, N.A. Berezina, Colloids Surf. A 98 (1995) 107.
[17] A. Mohanty, J. Dey, J. Chromatogr. A. 1128 (2006) 259.
[18] E. Fuguet, C. Ràfols, E. Bosch, M.H. Abraham, M. Rosés, Electrophoresis 27 (2006) 1900.
[19] A.A. Agbodjan, M.G. Khaledi, J. Chromatogr. A 1004 (2003) 145.
[20] A.G. Diress, C.A. Lucy, J. Chromatogr. A 1027 (2004) 185.
[21] A. Mohanty, J. Dey, J. Chromatogr. A 1070 (2005) 185.
[22] O.A. Ghosheh, L.P. Duoskin, D.K. Miller, P.A. Crooks, Drug Metab. Dispos. 29 (2001) 645.
[23] A. Hilmi, J.H.T. Luong, A.-L. Nguyen, Chemosphere 36 (1998) 3137.
[24] S. Gong, F. Liu, W. Li, F. Gao, C. Gao, Y. Liao, H. Liu, J. Chromatogr. A 1121 (2006) 274.
[25] M. Jansson, J. Roeraade, Chromatographia 40 (1995) 163.

Available online at www.sciencedirect.com
ScienceDirect
Talanta 75 (2008) 770–774
Talanta
www.elsevier.com/locate/talanta

FRET-based aptamer probe for rapid angiogenin detection

Wei Li, Xiaohai Yang, Kemin Wang*, Weihong Tan, Huimin Li, Changbei Ma

Engineering Center for Biomedicine, State Key Laboratory of Chemo/Biosensing and Chemometrics, College of Chemistry and Chemical Engineering, Key Laboratory for Bio-Nanotechnology and Molecular Engineering of Hunan Province, Hunan University, Changsha 410082, PR China

Received 28 September 2007; received in revised form 4 December 2007; accepted 7 December 2007
Available online 23 December 2007

Abstract

A sensitive method for rapid angiogenin (Ang) detection based on fluorescence resonance energy transfer (FRET) has been described. A dual-labeled probe based on high affinity aptamer for Ang was constructed. As donor and acceptor, 6-carboxyfluorescein (FAM) and 6-carboxy-tetramethylrhodamine (TMR) were labeled at 5′- and 3′-termini of the aptamer probe, respectively. The dual-labeled probe showed obvious fluorescence changes due to the specific binding between aptamer and Ang. By monitoring the fluorescence intensity of donor and acceptor, quantitative Ang detection could be achieved. This assay is highly specific and sensitive, with a detection limit of 2.0×10^{-10} mol L^{-1} and a linear range of 5.0×10^{-10} to 4.0×10^{-8} mol L^{-1} Ang. Ang in serum samples of health and lung cancer were also detected.

Keywords: Aptamer; Angiogenin; Fluorescence resonance energy transfer; Dual-labeled probe

1. Introduction

There have been recent advances in the *in vitro* selection of nucleic acid aptamers for their specific binding to target molecules, as well as in the exploitation of their bioanalytical and biotechnological applications [1]. By using the systematic evolution of ligands by exponential enrichment (SELEX) process, aptamers can be isolated for recognizing virtually any class of molecules [2–5] and even whole cells [6,7]. Compared with antibodies, aptamers not only have similar high affinity and selectivity for proteins, but also have several clear advantages over antibodies, including simple production, easy storage, great reproducibility and easy modification [8].

The key in the development of aptamer-based analytical methods and sensors is to transduce aptamer recognition events to detectable signals [9–13]. Fluorescent techniques offer excellent choices for signal transduction because of their nondestructive and highly sensitive characteristic [14–16]. For example, single-fluorophore-labeled aptamers can be used to report ligand–aptamer binding by monitoring the changes of fluorescence intensity or anisotropy resulting from the changes of the microenvironment or rotational motion of the fluorophore [17,18]. Taking advantage of the ligand induced conformational changes of aptamers, dual-fluorophore-labeled aptamers have been developed to give target-dependent fluorescence changes through fluorescence resonance energy transfer (FRET) [19,20]. Usually, FRET-based analytical method has higher sensitivity and more simplicity in detection of ligand–receptor binding, since merely the fluorescence changes of the acceptor were observed [21].

Angiogenin (Ang), one of the most potent angiogenic factors, a 14.4-kDa polypeptide, is a homologue of bovine pancreatic ribonuclease A (RNaseA) with a ribonucleolytic activity of four to six orders of magnitude less than that of RNaseA. It is related with the growth and metastasis of numerous tumors [22,23]. Serum concentration of Ang is commonly detected with antibody-based enzyme-linked immunosorbant assay (ELISA) [24]. AL6, a 45 nt DNA aptamers of Ang, was generated by *in vitro* selection process [5]. Instead of antibody, a single-fluorophore-modified derivative of this aptamer has been used to detect Ang in sera based on fluorescence anisotropy [18].

In this paper, we developed a FRET-based aptamer probe for rapid and quantitative Ang detection. The donor and acceptor were attached to the two ends of the aptamer oligonucleotide to construct FRET-based probe. Sensitive fluorescence signal changes were observed upon addition of Ang. Compared with

---

[*] Corresponding author. State Key Laboratory of Chemo/Biosensing and Chemometrics, Hunan University, Changsha 410082, PR China.
Tel.: +86 731 8821566; fax: +86 731 8821566.
E-mail address: kmwang@hnu.cn (K. Wang).

0039-9140/$ – see front matter © 2007 Elsevier B.V. All rights reserved.
doi:10.1016/j.talanta.2007.12.012

Table 1
List of the DNA sequences used in the experiments

Designation	Sequence
Dual-labeled probe	5′-FAM-CGG ACG AAT GCT TTG ATG TTG TGC TGG ATC CAG CGT TCA TTC TCA-TMR-3′
Single-labeled aptamer	5′-FAM-CGG ACG AAT GCT TTG ATG TTG TGC TGG ATC CAG CGT TCA TTC TCA-3′
Random labeled DNA	5′-FAM-TTG ATG TTG TGC TGC GAA TGC TGA TCC AGC GTT CAT TCG GAC-TMR-3′

previous fluorescence anisotropy method, lower detection limit and broader linear range were achieved using FRET-based aptamer probe.

2. Experimental

2.1. Materials

A single-fluorophore-labeled and a dual-fluorophore-labeled probe based on the 45 nt DNA aptamer of Ang, and a random dual-labeled DNA oligonucleotide were synthesized by Dalian Takara Bio Inc. (Dalian, China). All DNA oligonucleotides were purified by reverse phase high-performance liquid chromatography.

Sequences of the oligonucleotides were listed in Table 1. 6-Carboxyfluorescein (FAM, $\lambda_{ex/em}$ = 493/520 nm) and 6-carboxy -tetramethylrhodamine (TMR, $\lambda_{ex/em}$ = 558/577 nm) were conjugated to the termini of the oligonucleotide strand as donor and acceptor.

Recombinant human Ang was purchased from R&D Systems (Minneapolis, MN). The protein was dissolved in 2.0×10^{-3} mol L^{-1} phosphate buffer (pH 7.2) without further purification. Other proteins such as human serum albumin (HSA), immunoglobulin G (IgG), bovine serum albumin (BSA), thrombin (Thr), actin and RNaseA were obtained from Sigma. All proteins were left on ice when not used to minimize any denaturation. All other chemicals were of research or analytical purity and used without further purification. Purified water obtained through a Nanopure Infinity ultrapure water system (Barnstead/Thermolyne Corp., Dubuque, IA) with an electrical resistance larger than 18.2 MΩ was used in all experiments.

2.2. Measurements and methods

All fluorescence measurements were performed on a Fluorolog-Tau-3 spectrofluorometer (Jobin Yvon Inc., NY) equipped with a thermostat that had a temperature control accuracy of 0.1 °C. The excitation wavelength was set at 493 nm. Slits for both the excitation and the emission were set at 5 nm. The sample cell was a 150 μL quartz cuvette.

For fluorescence measurements, the fluorescence spectra from 510 to 700 nm were scanned (λ_{ex} = 493 nm). The fluorescence intensity of acceptor fluorophore (FI_{577}) and donor fluorophore (FI_{520}) were recorded, and the fluorescence intensity ratios ($Fr = FI_{577}/FI_{520}$) were used to evaluate the change of FRET efficiency. A single-labeled aptamer and a random dual-labeled DNA oligonucleotide were used as control probes when all other experimental conditions were the same as those for the dual-labeled aptamer probe.

Titration curves were obtained by titrating dual-labeled probe with Ang. To examine the specificity of the aptamer probe, several other proteins were used, including HSA, BSA, Actin, RNaseA, Thr and IgG.

2.3. Ang detection of pratical samples

Pretreatment of samples: serum samples (healthy and malignant lung tumor patients) and HSA solution (40 g/L, dissolved in 0.9% NaCl) were loaded into a centrifugal filter device (Amicon Ultra-15, MWCO = 30,000, Millipore), and subjected to centrifugation (7500 × *g*, 40 min). HSA centrifugation ultrafiltrate and seum centrifugation ultrafiltrate were used for the following measurements.

Standard curve: Ang solutions with different concentration were prepared by adding various amount of Ang and 10 μL HSA ultrafiltrate into 140 μL 10 mM Tris–HCl (pH 7.4, 0.5 mM EDTA). Fluorescence detection was performed after adding HSA centrifugation ultrafiltrate and Ang solutions with different concentration, respectively. The standard curve was traced by Ang concentration and Fr value.

Detection of Ang in serum samples: 10 μL serum ultrafiltrate and known amount of Ang were added into 140 μL 10 mM Tris–HCl (pH 7.4, 0.5 mM EDTA) and fluorescence assays were performed.

3. Results and discussion

3.1. Design of FRET-based aptamer probe

A dual-labeled probe was designed based on a 45 nt DNA aptamer designed as AL6-B [5]. FAM and TMR were conjugated to the terminis of the DNA strand as fluorophore donor and fluorophore acceptor. The aptamer exists at equilibrium between a non-structured random coil and a secondary structure similar to stem-loop. Formation of a correct secondary structure is critical for interaction with Ang [5]. Addition of Ang shifts the equilibrium in favor of the secondary stem-loop structure, which draws the fluorophore donor (F1) and fluorescence acceptor (F2) closer (Fig. 1), leading to the enhanced FRET efficiency.

As shown in Fig. 2, the aptamer probe experienced a significant fluorescence signal change when binding with Ang. With the adding of twofold amount of Ang, the fluorescence intensity of acceptor fluorophore (FI_{577}) increased while that of the donor fluorophore (FI_{520}) decreased. The distinct difference of the fluorescence intensity ratio ($Fr = FI_{577}/FI_{520}$) could be observed from the aptamer probe before and after Ang adding. The reaction was quick and the signals become stable within 1 min. As reported, the utilization of the fluorescence ratio should pro-

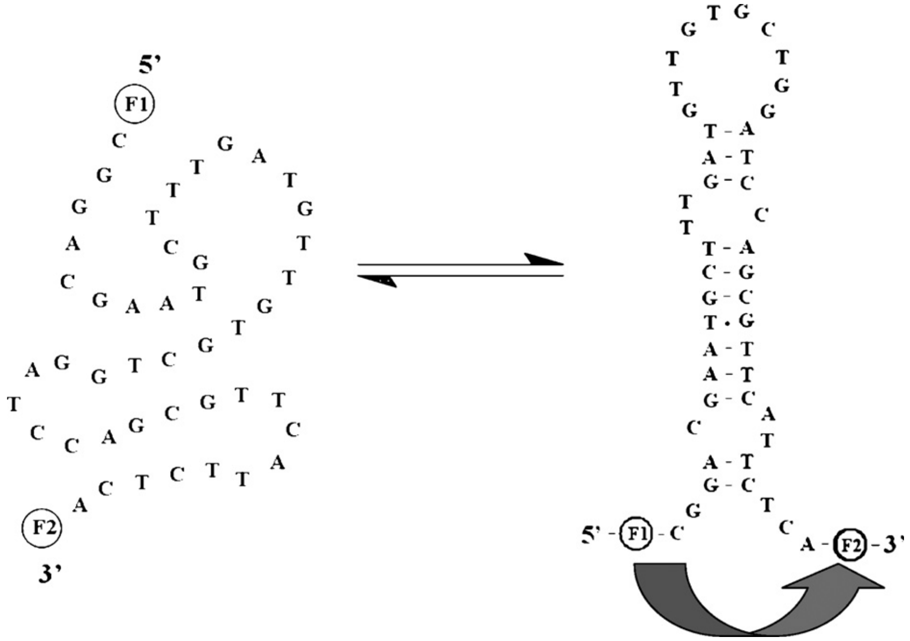

Fig. 1. Cartoon illumination of FRET-based aptamer probe for binding with the target protein, Ang. (Left) Random coil structure and (right) predicted secondary structure.

vide several significant advantages over fluorescence detection of donor or acceptor only, such as higher fluorescence detection sensitivity, wider application in ratiomatric image *in vivo* [25].

To demonstrate that the fluorescence signal change was induced by the specific Ang–aptamer binding, two control probes were used. One is a random oligonucleotide, also labeled with FAM and TMR at the strand ends; another is a single-labeled aptamer probe, without acceptor fluorophore. For the two control probes, the fluorescence intensity did not change significantly with the addition of Ang. Therefore, it is Ang–aptamer binding that induces the conformational change of dual-labeled probe, then the donor fluorophore and the acceptor fluorophore are brought closer to each other and energy transfer occurred.

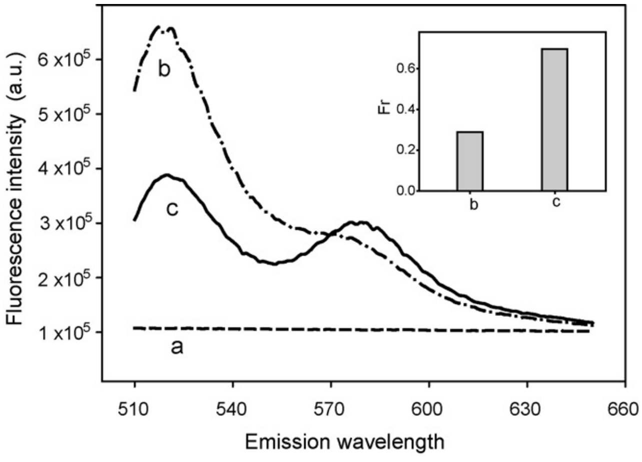

Fig. 2. Fluorescence spectra of FRET-based aptamer probe before and after Ang adding. (a) Buffer: 1.0×10^{-2} mol L^{-1} Tris–HCl (pH 7.4) + 1.0×10^{-2} mol L^{-1} NaCl; (b) buffer + 2.0×10^{-8} mol L^{-1} aptamer probe; (c) buffer + 2.0×10^{-8} mol L^{-1} aptamer probe + 4.0×10^{-8} mol L^{-1} Ang. (Inset) Fr value (fluorescence ratio, $Fr = FI_{577}/FI_{520}$). $\lambda_{ex} = 493$ nm.

3.2. Effect of ion strength on FRET-based aptamer probe

In order to study the effect of ion strength on FRET-based aptamer probe, a series of titration experiments with sequential adding of cations were performed.

Both Na^+ and Mg^{2+} caused an obvious fluorescence intensity decrease of the donor fluorophore and the acceptor fluorophore, as shown in Figs. 3 and 4. This phenomenon, with a simultaneous fluorescence decrease of donor and acceptor, referred to as contact quenching [26], is quite different from FRET. In fluorescence analysis with dual-labeled probe, contact quenching and FRET effect are coexisted and both induced changes of fluorescence ratio ($Fr = FI_{acceptor}/FI_{donor}$). As shown in Fig. 3, with increasing of [Na^+], Fr value experienced a gradual increase.

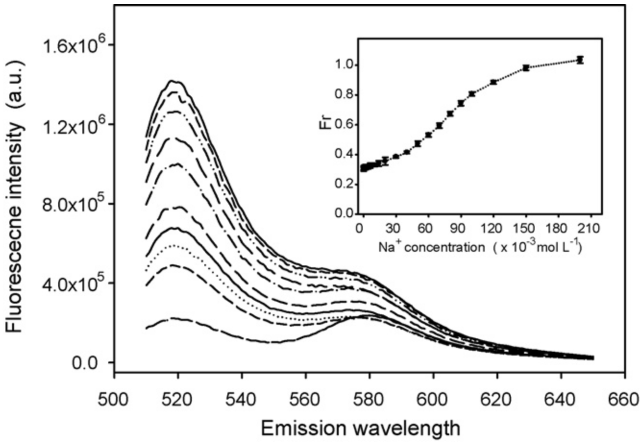

Fig. 3. Effects of Na^+ concentration on the FRET assay. Conditions were as follows: 1.0×10^{-2} mol L^{-1} Tris–HCl, pH 7.4, 2.0×10^{-8} mol L^{-1} aptamer probe, from top to bottom: 20 nM probe, 0.05, 0.1, 0.5, 1, 2, 5, 10, 20, 50, 200 mM Na^+; (inset) Fr value (fluorescence ratio, $Fr = FI_{577}/FI_{520}$), $\lambda_{ex} = 493$ nm.

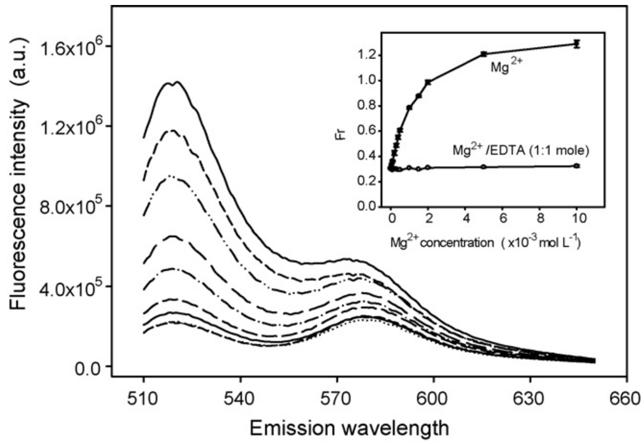

Fig. 4. Effects of Mg^{2+} concentration on the FRET assay. Conditions were as follows: 1.0×10^{-5} mol L^{-1} Tris–HCl, pH 7.4, 2.0×10^{-8} mol L^{-1} aptamer probe, from top to bottom: 20 nM probe, 0.01, 0.05, 0.1, 0.2, 0.5, 1.0, 5.0, 10.0 mM Mg^{2+}; (inset) Fr value (fluorescence ratio, Fr = FI_{577}/FI_{520}), $\lambda_{ex} = 493$ nm.

For [Na^+] within 0–10 mM range, a slight shift of Fr value was observed.

Mg^{2+} caused a correspondingly intensive contact quenching (Fig. 4). In order to decrease the influence of the Mg^{2+}, chelating reagent EDTA was used. As shown in Fig. 4, no obvious Fr value was observed with the mixture of Mg^{2+} and EDTA (molar ratio 1:1). Moreover, presence of EDTA did not affect Ang–aptamer binding and FRET-based Ang detection (data shown in supplementary information). Consequently, to enhance the FRET effect induced by Ang–aptamer binding and reduce the contact quenching caused by Mg^{2+}, the following detection buffer were chosen in all experiments (unless specified otherwise): 1.0×10^{-2} mol L^{-1} Tris–HCl (pH 7.4), 1.0×10^{-2} mol L^{-1} NaCl.

3.3. Detection of Ang using FRET-based probe

Titration experiments were performed with sequential adding of Ang into the FRET-based aptamer probe solution. For every concentration of Ang, the fluorescence intensities of donor fluorophore (FI_{520}) and acceptor fluorophore (FI_{577}) were measured. Upon addition of Ang, the fluorescence intensity at 520 nm decreased; whereas that at 577 nm increased. Fig. 5 gives fluorescence ratio (Fr = FI_{577}/FI_{520}) changes as a function of Ang concentration. As shown in the inset, with the Ang concentration ranged from 5.0×10^{-10} to 4.0×10^{-8} mol L^{-1}, a linear correlation ($R^2 = 0.9963$) between Fr value and Ang concentration was achieved. The detection limit of Ang was 2.0×10^{-10} mol L^{-1} (S/N = 3).

The value of the equilibrium constant and the stoichiometry of the complex from the FRET signals shown in Fig. 5 were also determined according to the following equation:

$$\mathrm{Fr} - \mathrm{Fr}_{\min} = (\mathrm{Fr}_{\max} - \mathrm{Fr}_{\min}) \left\{ \frac{c}{2nD_t} - \sqrt{\left(\frac{c}{2nD_t}\right)^2 - \left(\frac{P_t}{nD_t}\right)} \right\}$$

where D_t is the concentration of dual-labeled aptamer probe, P_t is the concentration of the titrant protein, Fr is measured fluorescence ratio (Fr = FI_{577}/FI_{520}), $\mathrm{Fr}_{\min}$ is the Fr value without titrant, $\mathrm{Fr}_{\max}$ is treated as a fitting parameter because the amount of protein added was rarely enough to attain saturation, *n* is the number of binding sites on aptamers, Kd is the microscopic dissociation constant for the binding of Ang to a DNA binding site, and $c = \mathrm{Kd} + n \times D_t + P_t$). The equilibrium constant of 1.5 nM and the stoichiometry of 1.3 were similar to that of the former results concluded from detection using fluorescence anisotropy with single-labeled aptamer probe [18].

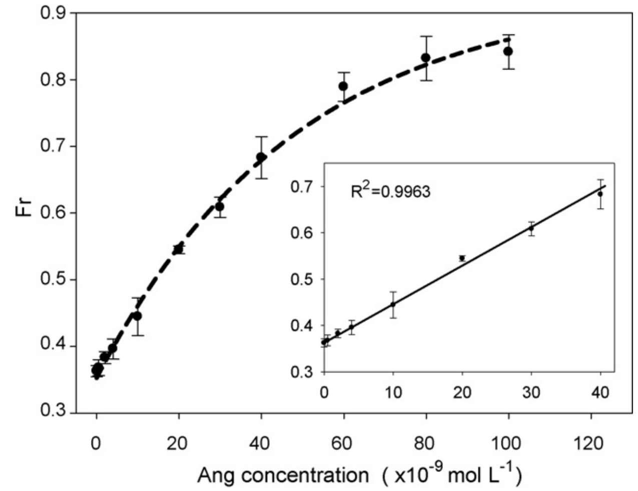

Fig. 5. Detection of Ang with the FRET-based aptamer probe. Conditions were as follows: 1.0×10^{-2} mol L^{-1} Tris–HCl, pH 7.4, 1.0×10^{-2} mol L^{-1} NaCl, 2.0×10^{-8} mol L^{-1} aptamer probe, $\lambda_{ex} = 493$ nm. Fr = FI577/FI520. Inset: the linear range of FRET assay.

3.4. Demonstration of specificity of FRET-based probe

An excellent probe is required to selectively respond only to its target, free from interferences with other components. Since Ang is an angiogenic protein excreted by cells with certain amount in plasma, we tested the probe's specificity with

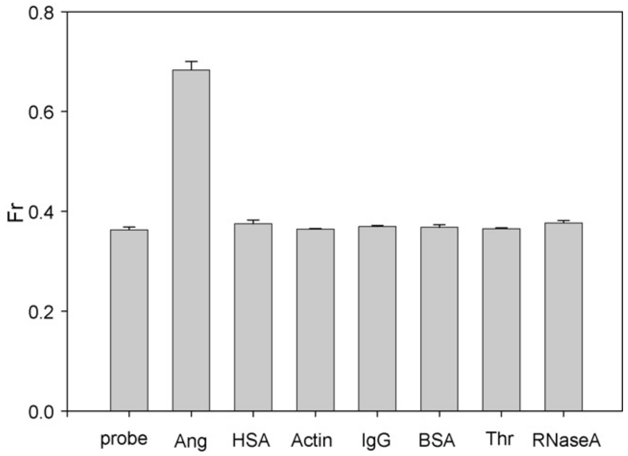

Fig. 6. Binding specificity of the FRET-based aptamer probe. Different proteins were compared to Ang in their capability to change the Fr value of the FRET-based probe. The concentrations of aptamer probe, Ang and control proteins were 2.0×10^{-8}, 4.0×10^{-8} and 2.0×10^{-7} mol L^{-1}, respectively. Conditions were as follows: 1.0×10^{-2} mol L^{-1} Tris–HCl, pH 7.4, 1.0×10^{-2} mol L^{-1} NaCl.

Table 2
Detection of Ang in serum

	Fr_{serum}	C_{serum} (nM)	ΔC (nM)	Fr_{ang}	$\Delta C'$ (nM)	Recovery rate (%)
1	0.3426	2.5	5.0	0.3484	4.8	96
2	0.3425	2.5	5.0	0.3484	4.9	99
3	0.3440	4.6	5.0	0.3505	4.8	96
4	0.3441	4.7	5.0	0.3507	4.9	99
5	0.3445	5.5	5.0	0.3517	5.0	100
6	0.3444	5.4	5.0	0.3514	4.8	96

Fr_{serum}: Fr value of aptamer with serum ultrafiltrate; C_{serum} (nM): Ang concentration of serum ultrafiltrate checked according to standard curve; ΔC (nM): known Ang concentration added to serum ultrafiltrate; Fr_{ang}: Fr value of aptamer with increased 5 nM Ang to serum ultrafiltrate; $\Delta C'$ (nM): increased Ang concentration checked according to standard curve; recovery rate: $\Delta C'_{ang}/\Delta C_{ang}$.

some plasma proteins, such as HSA, IgG, BSA, actin, Thr and RNaseA. The result in Fig. 6 shows that only Ang brought obvious Fr value ($Fr = FI_{577}/FI_{520}$) change to FRET-based aptamer probe, while 20-fold excess of all other proteins did not cause apparent changes. This is due to the high affinity and high specificity of the aptamer toward its target protein.

3.5. *Detection of Ang in a practical sample*

For analyses of practical samples, the interference and fluorescence quenching by some serum samples should be taken into account. In this paper, the advance process of centrifugation with a centrifugal filter device was performed to remove HSA and other abundant protein in serum. Two serum samples of healthy persons and four serum samples of lung cancer patients were measured and the Ang concentrations were checked on the standard curve. Table 2 gives fluorescence ratio ($Fr = FI_{577}/FI_{520}$) changes as a function of Ang concentration. Ang in sera of healthy persons (samples 1 and 2), lung cancer patients (samples 3 and 4) and invasive lung cancer patients (samples 5 and 6) caused different Fr value change (Fr_{serum}). Also, added Ang displayed a corresponding change of Fr value (Fr_{ang}). Compared with the known concentration of added Ang (ΔC_{ang}), the rate of recovery showed a satisfactory result.

4. Conclusions

A dual-labeled aptamer probe based on FRET was constructed. The probe offered an effective signal transduction method for rapid Ang recognition and quantitative monitoring. The method was highly specific and sensitive. Under the optimal detection conditions, a linear range within 5.0×10^{-10} to 4.0×10^{-8} mol L^{-1} and a detection limit of 2.0×10^{-10} mol L^{-1} were obtained. The detection limit should meet the requirement of clinical tests for Ang.

Acknowledgements

This work was supported in part by the National Key Basic Research Program of China (2002CB513110), Key Project of Natural Science Foundation of China (90606003), Major International (Regional) Joint Research Program of Natural Science Foundation of China (20620120107), Natural Science Foundation of China (20475015), Key Project of International Technologies Collaboration Program of China (2003DF000039), and China National Key Projects (2005EP090026).

Appendix A. Supplementary data

Supplementary data associated with this article can be found, in the online version, at doi:10.1016/j.talanta.2007.12.012.

References

[1] D.H.J. Bunka, P.G. Stockley, Nature 4 (2006) 588.
[2] C. Tuerk, L. Gold, Science 249 (1990) 505.
[3] S. Jhaveri, M. Rajendran, A.D. Ellington, Nat. Biotechnol. 18 (2000) 1293.
[4] A. Vater, F. Jarosch, K. Buchner, S. Klussmann, Nucleic Acids Res. 31 (2003) e130.
[5] V. Nobile, N. Russo, G. Hu, J. Riordan, Biochemistry 37 (1998) 6857.
[6] D. Shangguan, Y. Li, Z. Tang, Z. Cao, H. Chen, P. Mallikaratchy, K. Sefah, C. Yang, W. Tan, Proc. Natl. Acad. Sci. U.S.A. 103 (2006) 11838.
[7] D. Shangguan, Z. Cao, Y. Li, W. Tan, Clin. Chem. 53 (2007) 1153.
[8] S. Jayasena, Clin. Chem. 45 (1999) 1628.
[9] R. Nutiu, Y. Li, Angew. Chem. Int. Ed. 44 (2005) 1061.
[10] E. Katilius, Z. Katiliene, N.W. Woodbury, Anal. Chem. 78 (2006) 6484.
[11] R. Nutiu, Y. Li, Chem. Eur. J. 10 (2004) 1868.
[12] C. Yang, S. Jockusch, M. Vicens, N. Turro, W. Tan, Proc. Natl. Acad. Sci. U.S.A. 102 (2005) 17278.
[13] N. Rupcich, R. Nutiu, Y. Li, J.D. Brennan, Angew. Chem. Int. Ed. 45 (2006) 3295.
[14] B.R. White, J.A. Holcombe, Talanta 71 (2007) 2015.
[15] F. He, Y. Tang, S. Wang, Y. Li, D. Zhu, J. Am. Chem. Soc. 127 (2005) 12343.
[16] N. Rupcich, W. Chiuman, R. Nutiu, S. Mei, K.K. Flora, Y. Li, J.D. Brennan, J. Am. Chem. Soc. 128 (2006) 780.
[17] X. Fang, Z. Cao, T. Beck, W. Tan, Anal. Chem. 73 (2001) 5752.
[18] W. Li, K. Wang, W. Tan, C. Ma, X. Yang, Analyst 132 (2007) 107.
[19] J. Wang, T. Li, X. Guo, Z. Lu, Nucleic Acids Res. 33 (2005) e23.
[20] H. Ueyama, M. Takagi, S. Takenaka, J. Am. Chem. Soc. 124 (2002) 14286.
[21] Q. Ma, X. Su, X. Wang, Y. Wan, C. Wang, B. Yang, Q. Jin, Talanta 67 (2005) 1029.
[22] J.W. Harper, E.A. Fox, R. Shapiro, B.L. Vallee, Biochemistry 29 (1990) 7297.
[23] N. Yoshioka, L. Wang, K. Kishimoto, T. Tsuji, G. Hu, Proc. Natl. Acad. Sci. U.S.A. 103 (2006) 14519.
[24] T.M. Katona, B.L. Neubauer, P.W. Iversen, S. Zhang, L.A. Baldridge, L. Cheng, Clin. Cancer Res. 11 (2005) 8358.
[25] P. Zhang, T. Beck, W. Tan, Angew. Chem. Int. Ed. 40 (2001) 402.
[26] S.A.E. Marras, F.R. Kramer, S. Tyagi, Nucleic Acids Res. 30 (2002) e122.

Available online at www.sciencedirect.com

ScienceDirect

Talanta 75 (2008) 797–803

Talanta

www.elsevier.com/locate/talanta

Liposome-mediated enhancement of the sensitivity in immunoassay based on surface-enhanced Raman scattering at gold nanosphere array substrate

Xiangjiang Liu, Shuangyan Huan*, Yali Bu, Guoli Shen, Ruqin Yu*

State Key Laboratory of Chemo/Biosensing & Chemometrics, College of Chemistry & Chemical Engineering,
Hunan University, Changsha, Hunan Province 410082, China

Received 7 July 2007; received in revised form 11 December 2007; accepted 11 December 2007
Available online 26 December 2007

Abstract

A novel immunoassay based on surface-enhanced Raman scattering (SERS) has been developed. The method exploits the SERS-derived signal from reporter molecules (crystal violet, CV) encapsulated in antibody-modified liposome particles. The antigen is firstly captured by the primary antibody immobilized in microwell plates and then sandwiched by secondary antibody-modified liposome. The CV molecules are released from the liposome and transferred to specially designed substrate of gold nanosphere arrays with sub-10-nm gaps. The concentration of the antigen is indirectly read out by the SERS intensity of the CVs. The substrate used could substantially improve the sensitivity and reproducibility of SERS measurement. The SERS intensity responses are linearly correlated to logarithm of antigen concentration in the range of 1.0×10^{-8} to 1.0×10^{-4} g mL^{-1} with a detection limit of 8 ng mL^{-1}. To our knowledge, this is the first report describing liposome-mediated enhancement of the sensitivity in immunoassay based on surface-enhanced Raman scattering. Experimental results show that the proposed method illustrates a potential prospect of applications in immunoassay.

Keywords: Immunoassay; Surface-enhanced Raman scattering (SERS); Liposome

1. Introduction

Surface-enhanced Raman scattering (SERS) holds vast potential as a highly sensitive and selective tool for the identification of biological or chemical analytes. Its narrow, well-resolved bands allow simultaneous detection of multiple analytes, and the low intensity of SERS signal of water simplifies investigation of biological samples [1]. A series detection methods based on SERS have been developed for biological species. The sandwich-type immunoassay based on SERS is one example. It involves the immobilization of capture antibodies on a surface for capturing the analyte antigens from solution and indirect measurement of SERS signal from Raman tags which labeled the secondary antibodies. The pioneering work was reported by Cotton's group in 1989 [2] for the human thyroid stimulating hormone (TSH). A roughened silver electrode and resonance dye, *p*-dimethylaminoazobenzene (DAB) were used to obtain SERS signal in proportion to TSH antigen concentration. Sufficiently low detection limit was hardly attainable due to relatively large distance between the resonance dye and the roughened silver substrate separated by the bimolecular layers as the SERS signal used to decrease sharply with this distance.

Ozaki's group [3] proposed enzyme labeled immunoassay employing SERS signals of an enzyme reaction product azoaniline. Owing to the direct absorption of azoaniline on silver colloids, a low detection limit (10^{-15} M mL^{-1}) was realized though the measurement range was relatively narrow (0.158–2.5 ng mL^{-1}). Porter and co-workers [4] showed that gold nanoparticles immobilized with 4-mercaptobenzoic acid and antibodies could be used for immunoassay readout. Natan's group [5] synthesized "SiO$_2$-coated, analyte-tagged" nanoparticles for use in multiplexed bioassays. Besides the problem

---

* Corresponding authors. Tel.: +86 731 8821916; fax: +86-731-8822577.
E-mail addresses: shuangyanhuan@yahoo.com.cn (S. Huan), rqyu@hnu.cn (R. Yu).

0039-9140/$ – see front matter © 2007 Elsevier B.V. All rights reserved.
doi:10.1016/j.talanta.2007.12.017

associated with detection limit and range, another common problem faced in sandwich-type immunoassay is the reproducibility of the SERS signal which depends usually on very careful control of experimental conditions.

In this paper, we tried to use an alternative Raman probe, the secondary antibody-modified liposome encapsulating crystal violet to obtain a SERS signal amplification effect. The immunoassay is conducted by following the typical procedure for sandwich-type immunoreactions in microwell plates. As shown in Scheme 1, the antibody specific to a model analyte human IgG (hIgG) is immobilized on the wells of microwell by physical adsorption. The human IgG analyte is firstly captured by the primary antibody on the plate and then sandwiched by the secondary antibody-modified by CV-encapsulating liposome. The addition of ethanol followed by sonication will break the liposomes and release the encapsulating CV molecules. Then transfer a droplet of the solution to a specially designed gold nanosphere arrays with controlled sub-10-nm gaps, followed by final CV SERS signal readout. The last step is designed for solving the above mentioned problems associated with sensitivity and reproducibility. The recent nanoparticle array studied [6–8] show that the precise control of gaps in the sub-10 nm regime, known as "hot spots", is crucial for fabrication of substrate with uniformly high SERS activity for collective surface plasmons existing inside the gaps [9]. According the discovery of Halas's research group [10], we managed to prepare a convenient and cost-effective substrate–gold nanosphere arrays with sub-10 nm gaps to obtain high, stable and reproducible SERS signal, which enables trace-level quantitative analysis of CVs released.

To our knowledge, this is the first report describing liposome-mediated enhancement of the sensitivity in immunoassay based on SERS as combined with the used of specially designed substrate. Experimental results show that the proposed method illustrates some useful ways to improve the analytical performance of SERS-based immunoassay.

2. Experimental section

2.1. Materials and apparatus

Phosphocholine, phosphoethanolamine, cholesterol and glutaraldehyde were purchased from Sinopharm Chemical Reagent (Shanghai, China). Goat anti-hIgG antibody and hIgG (affinity purification), bovine serum albumin (BSA) and glycine were supplied by Beijing DingGuo Biotechnology Company (Beijing, China). $HAuCl_4\cdot 3H_2O$, NH_2OH, trisodium citrate, cetyltrimethylamonium bromide (CTAB) and other chemicals were all of analytical grade and used as received.

The size distribution of liposomes was measured by Malvern Zetasizer 3000 HS (Malvern Instruments, Worcs, UK) and the SEM images were obtained with a JSM-5600LV SEM (JEOL Ltd., Japan, acceleration voltage 20 K).

For Raman measurements, a Confocal Raman System Laboram 010 (Jobin Yvon Inc., USA) based on an integral Olympus BX40 microscope was used. Calibration was done referring to the 520.6 cm^{-1} line of silicon. A 632.8 nm laser source (5 mW) was used for excitation and the slit and pinhole were set at 100 μm and 1000 μm, respectively. The spectrometer grating was 1800 lines mm^{-1}. An automatic motorized translator XY stage was utilized to perform Raman mapping.

2.2. Preparation of CV-encapsulating liposomes

Liposome was prepared by the standard sonication procedure as described elsewhere [11] with slight modifications.

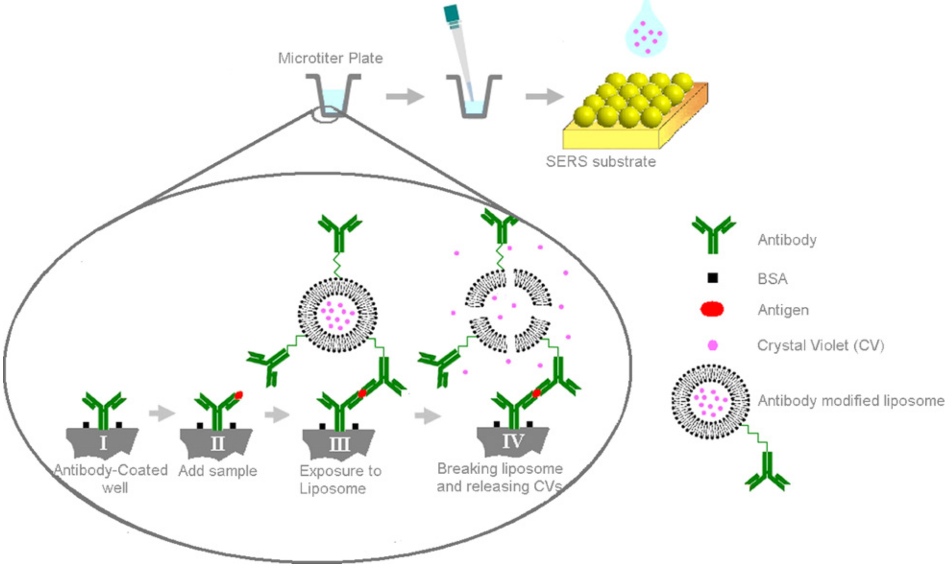

Scheme 1. Schematic diagram of the immunoassay based on SERS. (I) Coat the microwell plate with antibody. Wash away unbound antibody and block free active sites with BSA; (II) add antigen sample to the microwell; (III) add secondary antibody-modified liposome encapsulating crystal violet to make a "sandwich"; wash away unbound antibody; (VI) breaking the liposome to release CVs; (V) then the CV molecules are transferred to a specially designed gold nanosphere arrays with controlled sub-10-nm gaps, followed by final CV SERS signal readout.

A mixture containing 75 mg phosphocholine, 35 mg phosphoethanolamine and 40 mg cholesterol were dissolved in 2 mL chloroform/methanol solution (6:1, v/v), and then dried to a thin film using a rotary evaporator at 45 °C. Afterwards, the film was hydrated in 5 mL of phosphate buffer (pH 7.4) containing 0.5 mM CV at 75 °C for 30 min and then vigorously sonicated for 10 min. The CV-encapsulating liposomes (about 3 mg lipid mL^{-1}) were thus prepared for use. The average size and the distribution of the liposomes were measured by Malvern Zetasizer 3000 HS.

2.3. *Coupling of antibody to the CV-encapsulating liposomes*

The goat anti-hIgG antibody was immobilized on the surface of the CV-encapsulating liposomes via glutaraldehyde coupling by following procedure [12]: 1 mL of liposome was added into 0.6 mL of 2.5% glutaraldehyde solution in drops with gently stirring for 1 h at 4 °C. Excess glutaraldehyde solution was removed by dialysis overnight in phosphate buffer (pH 7.4) at 4 °C. Then, 0.2 mL of 1 mg mL^{-1} goat anti-hIgG antibody solution was added at 4 °C under gently stirring. One hour later, 0.2 mL of 3 M glycine–NaOH (pH 7.2) was added to block excess aldehyde groups on the liposome surface and incubated for 6 h at 4 °C. The unpacked CV molecules were separated form liposome solution by dialysis overnight. Then the CV-encapsulating, antibody-modified liposome solution (1.5 mg lipid mL^{-1}) was stored at 4 °C until use.

2.4. *Preparation of gold nanosphere array substrate for SERS detection*

Gold seeds colloids (maximum at 518 nm, UV–visible absorption spectra) was acquired by quickly mixing 5 mL of 38.8 mM sodium citrate and 1.7 mL of 1% $HAuCl_4$ with 50 mL of boiling water solution under vigorous stirring, as described by Natan's group [13]. Then the mixture was kept on boiling for 15 min before it cooled down to room temperature and stored at 4 °C until use. By changing the volume of seeds added, gold colloid (∼10^{10} particles mL^{-1}) with different diameters was generated in the solution, which contained 1 mL of 1% $HAuCl_4$, 4.2 mL of 40 mM NH_2OH and 190 mL H_2O at room temperature.

The specially designed SERS substrates were prepared according to Wang et al. [10]: gold nanoparticles were functionalized with CTAB with a droplet dried on indium-doped tin oxide (ITO) glass under ambient conditions. In brief, 50 mL of gold colloid solution was mixed with 50 mL of 40 mM CTAB aqueous solution for 1 h. Hence, the CTAB-capped nanoparticles were centrifuged and redispersed twice in H_2O to get rid of the excess CATB in the solution and adjusted to a concentration of approximately 10^{12} particles mL^{-1}. The SERS substrates were obtained by depositing a droplet of CTAB-capped gold particles solution onto the surface of the conductive side of ITO glass slide, and allowing it dry undisturbed under ambient conditions.

2.5. *Immunoassay protocol*

The immunoassay was conducted by following typical procedure: 100 μL of 0.25 mg mL^{-1} goat anti-human IgG solution in 0.05 M $NaHCO_3$–Na_2CO_3 (pH 9.6) buffer was added into each microwell followed by overnight incubation at 4 °C. In this way, the goat anti-human IgG antibodies were immobilize on the wells of microwell through physical adsorption. After removing the solution from each well, the wells were washed by 0.01 M PBS (pH 7.4) six times and then 200 μL of 10 mg mL^{-1}. BSA was introduced in each to block active sites. Then 100 μL of human IgG antigen analyte was added and incubated for 1 h at 37 °C. Afterwards, 100 μL of the CV-encapsulating antibody-modified liposome solution was added followed by 2 h incubation at room temperature. The secondary antibodies conjugate with the immobilized antigen analyte to form a sandwich of antibody–antigen–antibody/liposome bound to the microwell. After the wells were rinsed by PBS, 100 μL ethanol was added followed by sonication for 1 min, and then a droplet of the solution was transferred and dried on the SERS substrate to record the SERS spectra of CV.

3. Results and discussion

3.1. *Choosing proper SERS substrate*

Preparation of SERS substrate is always the core procedure in the surface-enhanced Raman scattering experiments. An ideally SERS substrate should generate significantly large enhancement factor and, what's more, it should generate equal enhancement factor in different areas on its surface. Besides, it must be easy to prepare. Under some circumstances, the preparation of a usable substrate could be proved to be a formidable task.

In the following experiments, highly ordered gold spherical nanoparticle SERS substrates were prepared and used. The gold colloids of different diameters were synthesized by seed-mediated growth approach. The average size of gold nanoparticle used in this experiment is about 47 nm (300 particles analyzed, R.S.D.% is about 12.9%). The size distribution is shown in Fig. 1. Using CTAB as a capping surfactant, positively charged bilayers could be formed on gold nanoparticles, providing repulsive interaction between the nanoparticles to prevent random disordered aggregation during solvent evaporation. This led to the formation of close-packed NP arrays. A highly ordered gold spherical array with sub-10 nm gaps was prepared and the SEM image was shown in Fig. 2. Such a structure created uniform densities of well-defined "hot spot" at the junctions between neighboring NPs exploitable for large SERS enhancements. The as-fabricated substrates displayed quite stable SERS enhancements. There was almost no observable activity loss after stored under ambient conditions for about 30 days [10].

The SERS responses of CV of different concentrations were acquired by dropping a few microlitres of CV solution onto the substrate as shown in Fig. 3. One can see that the SERS signal intensity on the close-packed Au–NP arrays was strong. In addition, a good linear response was obtained, that make it

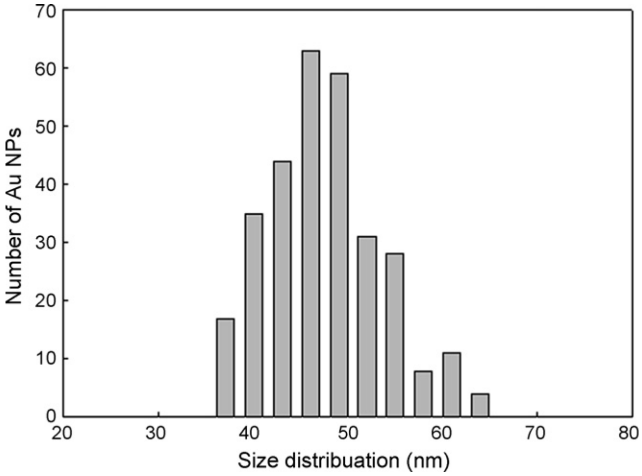

Fig. 1. The size distribution of Au–NPs. The average size of Au–NPs is about 47 nm, R.S.D.% is 12.9%.

possible to conduct CV-encapsulating liposome-tagged SERS detection. Then, this close-packed Au–NP arrays substrate was chosen for the following experiment.

The reproducibility of the SERS substrates is also important. Fig. 4 shows the Raman mapping spectra (25 points) collected in a 120 μm × 120 μm area of CV solution of same concentrations on three different substrates, prepared in the same batch. The band at 1619 cm^{-1} and 1578 cm^{-1}, can be assigned to out-of-plane ring stretch. The board band, which appears at 1381 cm^{-1} and 1360 cm^{-1} in Fig. 4, consists of the unresolved in-plane C–H bending mode and symmetrical N–C-ring-C–C stretching mode. And the band at about 1169 cm^{-1} can be assigned to the in-plane aromatic C–H bending modes. The average SERS intensities at 1169 cm^{-1} are 1890.7 c s^{-1}, 1928.7 c s^{-1} and 1901.4 c s^{-1}, respectively. And average SERS intensities at 1619 cm^{-1} are 3409.5 c s^{-1}, 3482.7 c s^{-1} and 3462.8 c s^{-1}, respectively. The substrate exhibits quite uniform SERS activity. The R.S.D.% of 1169 cm^{-1} bands (1.02%) is smaller than 1619 cm^{-1} bands (1.09%). In this work, the peak intensity of Raman band at

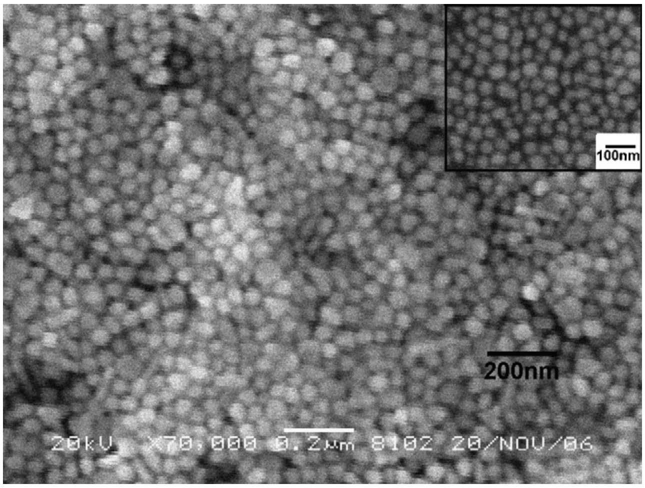

Fig. 2. A SEM image showing the surface of the CTAB–AuNP close-packed SERS substrate.

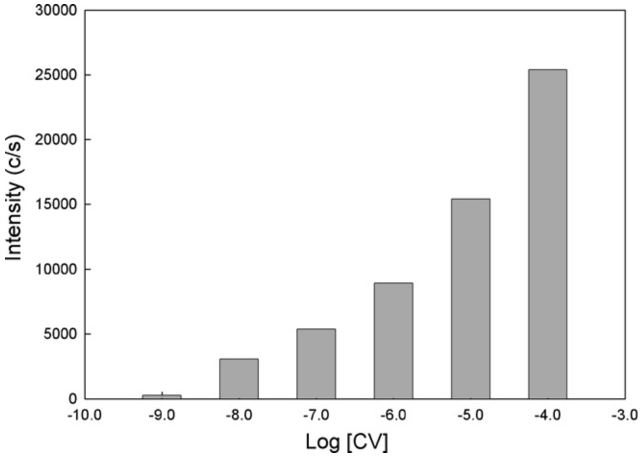

Fig. 3. Peak intensity of the Raman band at 1169 cm^{-1}, recorded for pure CV solutions on CTAB–AuNP close-packed SERS substrate.

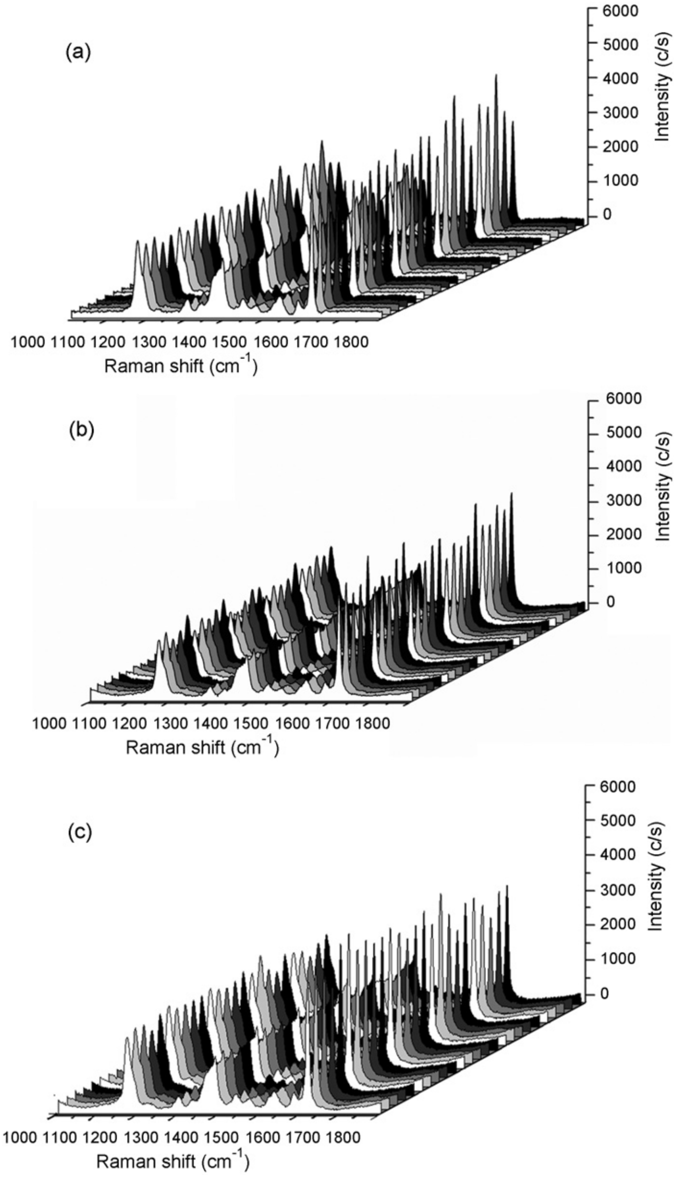

Fig. 4. SERS mapping spectra of 5 μL of CV of the same concentrations deposited on three SERS substrates (a, b and c) prepared in the same batch, which were collected at 25 points in an area of 120 μm × 120 μm.

1169 cm^{-1} is selected as a characteristic peak to quantify hIgG in immunoassay.

3.2. Optimization the concentration of CV-encapsulating liposome

Liposome is widely used as drug delivery vehicle in controlled release. Fluorescent dye-encapsulating liposomes have also been used for many years to study the liposome–cell interactions. Liposome is a perfect artificial vehicle for active molecules delivery in bioanalysis. In this study, the SERS active water soluble CVs are used as signal reporter molecules. Before coupling with the secondary antibodies for immunoassay, they are encapsulated in liposomes. The average size of the CV-encapsulating liposomes measured by Zeta sizer is about 45 nm (analysis by number).

The liposome preparation contain phosphoethanolamine component, which can provide free amino groups essentially on the surface of the liposomes. In the experiment, 1 mL of liposome solution (3 mg lipid mL^{-1}) is added very slowly into 0.6 mL of glutaraldehyde solution (2.5%). In this way, the glutaraldehyde in the solution is comparative excessive to the liposomes. This protocol helps to keep concentration of unreacted liposome at low level, thus the distance between them is large. So, it is unlikely that a large number of liposomes are connected together. After removal of the excess glutaraldehyde and unpacked CV molecules by dialysis, insufficient amount of anti-hIgG is added (compared to the total amount of amino groups on liposomes). And then excess glycine is added to block the residual aldehyde groups on the liposome surface by this protocol, maybe there are some liposomes be connected by glutaraldehyde, but the quantity might be very small. The unpacked CV molecules are dialyzed from the system and the concentration of the final stock solution is estimated to be 1.5 mg lipid mL^{-1}.

The CV-encapsulating liposomes are easy producing and can be stable in solution for a period of time with no significant changes in size or structure. So, it is feasible to use CV-encapsulating liposomes as labels to modify antibodies and give amplified signals when coupling with highly sensitive SERS technique.

In the experiment, an excessive amount of liposomes presented in the detection system will result in comparatively high background SERS response. On the contrary, if there is insufficient amount in the system, the intensity of the SERS signal will be comparatively weak and will lead to a high detection limit. It is considered that, the molecules encapsulated in liposome will leak very slowly [14]. Those leaking CV molecules can adsorb onto the antibodies or antigens, and are difficult to be washed away. In order to find a suitably concentration of CV-encapsulating liposomes for detection, different concentrations (1.5, 0.15, 0.075, 0.03, 0.015 mg lipid mL^{-1}) of CV-encapsulating liposome solutions are used in the test, which are prepared by diluting the liposome stock solution (1.5 mg lipid mL^{-1}). The concentration of antigen fixed at 1.0×10^{-4} g mL^{-1}, and BSA (1.0×10^{-4} g mL^{-1}) are used as a control group. And the relationship of liposome's concentration between the final SERS response are shown in Fig. 5. Since group C (0.075 mg lipid mL^{-1}) in Fig. 5 exhibits a relative higher signal to noise ratio than other four groups, the final 0.075 mg lipid mL^{-1} is chosen as the final concentration of liposome solution used in assay.

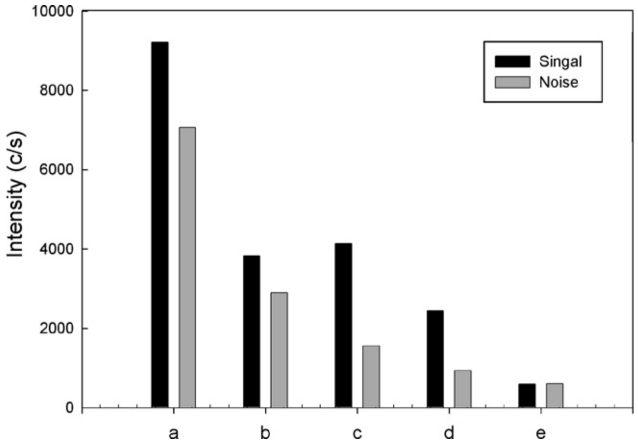

Fig. 5. The comparison of finial SERS intensity (at 1169 cm^{-1}) responses to hIgG (10^{-4} g mL^{-1}, black bars) and BSA (gray bars) with different concentrations of liposome solution: (a) 1.5 mg lipid mL^{-1}; (b) 0.15 mg lipid mL^{-1}; (c) 0.075 mg lipid mL^{-1}; (d) 0.03 mg lipid mL^{-1}; (e) 0.015 mg lipid mL^{-1}.

What influence the stability of the liposomes with respect to dye leaking are the lipid composition, the molecular dye structure and charge, and temperature. Preparing the dye-encapsulating liposome of long-term stability still deserves further research.

3.3. Quantification of human IgG analyte

In our experiment, the capture antibodies are firstly immobilized in well by physical adsorption. This procedure is widely used in immunoassays, which is a very simple and efficient way compared to covalent immobilization method. Hence, the antigen (if exists) in the sample can be captured by antibodies and then sandwiched by secondary antibody/liposome. After washing procedure, the excessive liposomes will be removed. The CV molecules are released from the liposomes by sonicating in the presence of alcohol for a minute. A droplet of this solution was transferred and dried on the above mentioned gold nanosphere array SERS substrate. The concentrations of the antigens are indirectly read out by the SERS intensity of the CV transferred. Since one liposome can encapsulate thousands of CV molecules, the release of encapsulated CVs allows amplification of the signals. The concentration of CVs is detected by highly sensitive SERS technique, which allows a second signal amplification. So, great enhancement could be obtained both by the SERS enhancement and the signal magnification of the encapsulated CVs in the liposomes.

The proposed technique is subsequently used to detect human IgG ranging from 1.0×10^{-4} g mL^{-1} to 1.0×10^{-10} g mL^{-1}. Intensities of the characteristic Raman band at 1169 cm^{-1} are used to quantify the concentrations of IgG in samples (Fig. 6),

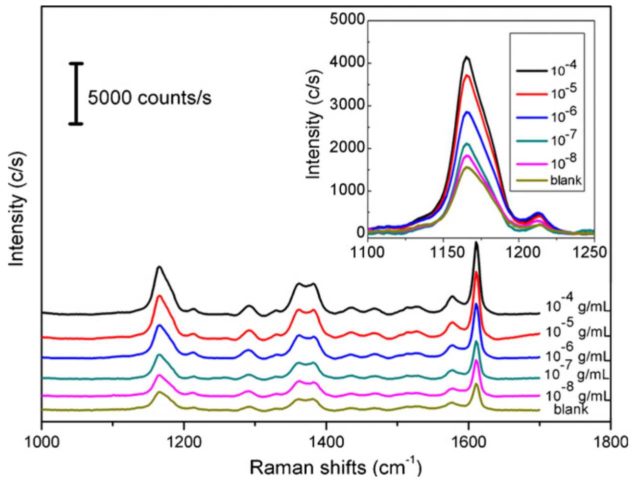

Fig. 6. SERS spectra of CV corresponding to varying hIgG concentrations. Each data line represents an average of 25 measurements collected in an area of 40 μm × 40 μm.

and a linear relationship is observed as shown in Fig. 7. Note that each data point in Fig. 7 represents an average of 25 measurements in an area of 40 μm × 40 μm. Compared with conventional SERS arrays which just relied on only a few points, this method based on SERS mapping shows better reproducibility and reliability. The linear relationship holds for the logarithm over 4 orders of magnitude concentrations of IgG (from 1.0×10^{-8} to 1.0×10^{-4} g mL^{-1}). Its correlation coefficient is 0.9766 and the detection limit is about 8 ng mL^{-1}.

Compared with conventional SERS-based immunoassay, this CV-encapsulating liposomes-based methodology offers several advantages. Firstly, the problems of high fluorescence background interference associated with conventional SERS-based immunoassay has been circumvented in our studies. The sandwich like immune complex is bound to the wall of the microwell plate and the biomolecules in the reaction system do not influence the final SERS detection. Secondly, the CV-encapsulating liposomes for labeling are easy production and modification. The gold nanosphere arrays substrates also possess the merits of easy preparation, highly sensitive, good reproducibility, considerable uniformity and good stability. Thirdly, due to the unique amplification of the encapsulated CVs in the liposomes and a second SERS enhancement, linear response covers 4 orders of magnitude (from 1.0×10^{-8} to 1.0×10^{-4} g mL^{-1}) is obtained, which is much more attractive than the conventional immunoassay based on SERS. Additionally, this method could be readily expanded for measurement of a large number of other antigens or antibodies. All these advantages suggest that, the liposome-mediated enhancement of the sensitivity based on SERS at gold NP array substrate reported here offers a new direction for immunoassay based on SERS. Further effort will focus on the improvement of the stability of liposomes and SERS substrates, such as decrease the leaking of encapsulated molecules, enhance the sensitivity and uniformity of the SERS response, improve the stability of the substrates against washing treatment. In this way, a lower detection limit might be expected.

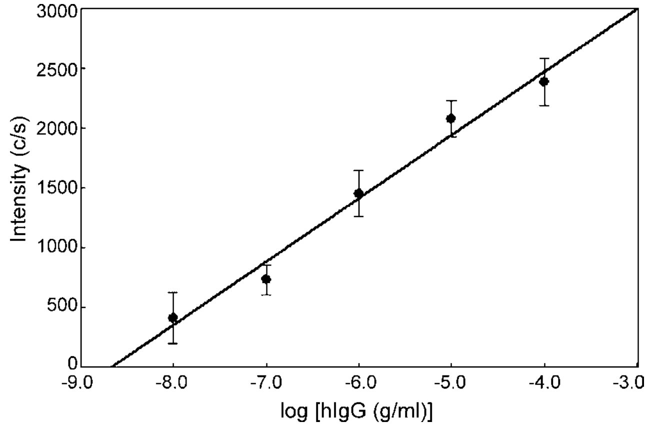

Fig. 7. Immunoassay by measuring peak intensities of the SERS band at 1169 cm^{-1}.

4. Conclusions

A novel SERS-based sandwich-type immunoassay method has been fabricated to detect human IgG. It involves the immobilization of capture antibodies on the surface of microwell plate, the use of the immobilized antibodies to capture antigens from solution, and the indirect measurement of SERS signal of CVs that encapsulated by antibody-modified liposome. The use of substrate of gold nanosphere arrays with sub-10-nm gaps for CV SERS signal recording substantially improved the sensitivity and reproducibility as compared to conventional Ag-colloid substrates. Linear response has been obtained for the logarithm of concentration from 1.0×10^{-8} to 1.0×10^{-4} g mL^{-1} with a detection limit of 8 ng mL^{-1}. The method holds potential applications in detection of various antigens or other clinically important entities.

Acknowledgments

The work was financially supported by National Natural Science Foundation of China (Grant Nos. 20605007, 20675028, 20435010, 20475014, 20505008).

References

[1] C.L. Haynes, A.D. McFarland, R.P. Van Duyne, Anal. Chem. 77 (2005) 338A.
[2] T.E. Rohr, T. Cotton, N. Fan, P.J. Tarcha, Anal. Biochem. 182 (1989) 388.
[3] X. Dou, T. Takama, Y. Yamaguchi, H. Yamamoto, Y. Ozaki, Anal. Chem. 69 (1997) 1492.
[4] J. Ni, R.J. Lipert, G.B. Dawson, M.D. Porter, Anal. Chem. 71 (1999) 4903.
[5] S.P. Mulvaney, M.D. Musick, C.D. Keating, M.J. Natan, Langmuir 19 (2003) 4784.
[6] L. Gunnarsson, E.J. Bjerneld, H. Xu, S. Petronis, B. Kasemo, M. Käll, Appl. Phys. Lett. 78 (2001) 802.
[7] A. Wei, B. Kim, B. Sadtler, S.L. Tripp, Chem. Phys. Chem. 2 (2001) 743.
[8] Y. Lu, G.L. Liu, J. Kim, Y.X. Mejia, L.P. Lee, Nano Lett. 5 (2005) 119.

[9] H.H. Wang, C.Y. Liu, S.B. Wu, N.W. Liu, C.Y. Peng, T.H. Chan, C.F. Hsu, J.K. Wang, Y.L. Wang, Adv. Mater. 18 (2006) 491.
[10] H. Wang, C.S. Levin, N.J. Halas, J. Am. Chem. Soc. 127 (2005) 14992.
[11] H. Chen, J.H. Jiang, Y.F. Li, T. Deng, G.L. Shen, R.Q. Yu, Biosens. Bioelectron. 22 (2007) 993.
[12] Y. Nakano, M. Mori, S. Nishinohara, Y. Takita, S. Naito, H. Kato, M. Taneichi, K. Komuro, T. Uchida, Bioconjugate Chem. 12 (2001) 391.
[13] K.R. Brown, D.G. Walter, M.J. Natan, Chem. Mater. 12 (2000) 306.
[14] K.P. McNamara, Z. Rosenzweig, Anal. Chem. 70 (1998) 4853.

Available online at www.sciencedirect.com

ScienceDirect

Talanta 75 (2008) 753–759

Talanta

www.elsevier.com/locate/talanta

Comparison of stir bar sorptive extraction and solid-phase microextraction to determine halophenols and haloanisoles by gas chromatography–ion trap tandem mass spectrometry

Luana Maggi[a], Amaya Zalacain[b], Valeria Mazzoleni[a], Gonzalo L. Alonso[b], M. Rosario Salinas[b,*]

[a] *Istituto di Enologia e Ingegneria agro-alimentare, Università Católica del Sacro Cuore, 29100 Piacenza, Italy*
[b] *Cátedra de Química Agrícola, E.T.S.I. Agrónomos, Universidad Castilla-La Mancha, Campus Universitario, 02071 Albacete, Spain*

Received 6 August 2007; received in revised form 27 November 2007; accepted 7 December 2007
Available online 23 December 2007

Abstract

Solid-phase microextraction by immersion (IS-SPME) and headspace mode (HS-SPME), together with stir bar sorptive extraction (SBSE), have been assayed in combination with gas chromatography–ion trap tandem mass spectrometry (MS/MS) for analysing 2,4,6-trichlorophenol, 2,3,4,6-tetrachlorophenol, 2,4,6-tribromophenol, 2,4,6-trichloroanisole, 2,3,4,6-tetrachloroanisole and 2,4,6-tribromoanisole in different liquid matrices. Once, the optimization of MS/MS fragmentation analysis was carried out, sample enrichment was performed using the three mentioned extraction methods, and comparison through the determination of linearity, and LOD and LOQs were carried out. SBSE and IS-SPME methods described enabled us to determine the target compounds at ng/l levels, concentrations lower than their olfactory threshold, which is not the case of HS-SPME. SBSE showed a higher concentration capability than both SPME techniques, especially when compared to the HS-SPME mode. Thus, SBSE should be the definitive technique to analyse halophenols and haloanisoles in aqueous matrices. SBSE has been also applied to nine aqueous matrices as different as tap water, wines or commercial lemon juice extract.

Keywords: Aqueous matrices; Haloanisoles; Halophenols; IS-SPME; HS-SPME; SBSE; GC–MS/MS

1. Introduction

Taste and odours associate to earthy-musty descriptors in liquid aqueous matrices cause numerous consumer complaints, and determining their origin and causes is one of the priority objectives of companies which package drinking water, wine or fruit juice companies, among others. The compounds responsible for this off-flavour are haloanisoles and their respective precursors, the halophenols, which are transformed by microbial-induced methoxylation [1–3]. Halophenols are toxic, in particular 2,4,6-trichlorophenol (TCP) is recognized as an environmental pollutant which presents toxicity risks when surpassing 5 μg/l in water, which may be generated while chlorinate process of drinking water [4,5]. No toxicological studies have been carried out yet at the concentrations measured in other matrices, such as wines or fruit juices. Haloanisoles are characterized by their low olfactory thresholds, as 2,4,6-trichloroanisole (TCA) shows olfactory threshold levels in wines from 5 to 10 ng/l [6–8] and between 30 pg/l and 50 ng/l in water [9]. Other haloanisoles such as the 2,3,4,6-tetrachloroanisole (TeCA) and pentachloroanisole (PCA) also contributed to taint but to a lesser extent as they have higher olfactory thresholds [10–15]. More recently, another anisole, the 2,4,6-tribromoanisole (TBA), has been identified as responsible of this off-flavour when insufficient amounts of TCA were detected in wines [7], while in water it has been identified with olfactory thresholds ranging from 20 pg/l [16] to 30 pg/l [9]. For fruit juice, up to now no sensorial studies have been carried out to determine the odour threshold values of these compounds that can affect the organoleptic characters of products, although the problem is present in fruit juice companies.

There is an increasing interest in analytical methods with sufficient sensitivity and reproducibility to determine halophenols

---

[*] Corresponding author. Tel.: +34 967 599310; fax: +34 967 599238.
E-mail address: Rosario.Salinas@uclm.es (M.R. Salinas).

0039-9140/$ – see front matter © 2007 Elsevier B.V. All rights reserved.
doi:10.1016/j.talanta.2007.12.013

and haloanisoles in liquid matrices. The gas chromatography technique coupled to several detectors such as atomic emission detector [17], mass spectrometer detector [10,18,19], or coupled to an electron capture detector (ECD) [9,19–22], is the most used technique to analyse the mentioned compounds in different matrices. However, compounds having a low concentration within the liquid aqueous matrices make a prior extraction and concentration step necessary [11,12,23]. Modern trends in analytical chemistry lean towards the simplification and miniaturization of sample preparation, and the minimization of the organic solvent used, such as solid-phase microextraction (SPME) and stir bar sorptive extraction (SBSE). SPME is generally performed by leaving the fiber in the sample headspace (HS-SPME) [18,21,24–26]. Another SPME extraction possibility could be by fiber immersion into the liquid matrix, but to date there are only few references on this technique concerning water [27,28]. This lack is probably due to the interferences between the target analytes and high molecular weight compounds and other substances present in wine or fruit juice. The most recent extraction and concentration technique is the SBSE (Twister, Gerstel GmbH) which has been successfully applied to the analysis of halophenols and haloanisoles in water and wines [30–33]. The analyte enrichment is done in both techniques by portioning between the PDMS polymer and the aqueous phase according to their distribution constant [34]. SPME and SBSE have been compared for the analysis of different compounds such as organophosphorous insecticides in honey [35], pesticides in orange [36], volatiles in malt [37], and wines [38], or in Arabica roasted coffee [39]. All the studies reached the same conclusions, the SBSE concentration capability was better than those presented by SPME because of the higher PDMS phase ratio coating. Thus, the main aim of this study was the comparison between SBSE and SPME, used in the immersion and headspace mode, in order to evaluate the most rapid, suitable and efficient extraction technique for the analysis of 2,4,6-trichlorophenol, 2,3,4,6-tetrachlorophenol, 2,4,6-tribromophenol, 2,4,6-trichloroanisole, 2,3,4,6-tetrachloroanisole, 2,4,6-tribromoanisole in liquid aqueous matrices. Considering the complexity of wine and fruit juice matrices, a gas chromatographic method based on ion trap tandem mass spectrometry has been optimized to determine such target compounds by reducing the effects of both background and potential interferences on the accuracy of the quantification. The MS/MS parameters and collision-induced dissociation amplitude have been determined and optimized for the greatest yield of daughter ions. Calibration curves for each analyte were created for a wide range of concentration levels.

2. Experimental

2.1. Chemicals and reagents

(a) Standards: 2,4,6-trichlorophenol (TCP), 2,3,4,6-tetrachlorophenol (TeCP), 2,4,6-tribromophenol (TBP), 2,4,6-trichloroanisole (TCA), 2,3,4,6-tetrachloroanisole (TeCA), 2,4,6-tribromoanisole (TBA) and γ-hexalactone (internal standard) were acquired from Sigma–Aldrich (Madrid, Spain) and pentachloroanisole (PCA) from LGC Promochem (Molsheim, France).

Exact masses of the chemical standards were dissolved in absolute ethanol.

(b) Solvents: ethanol absolute (analytical reagent grade) was obtained from Merck (Darmstadt, Germany), while water was purified through a Milli-Q System (Millipore, Bedford, MA, USA).

Spiked solutions were prepared by adding all target compounds together with the internal standard into a hydroalcoholic solution (12%, v/v) to which 5 g/l L(+)-tartaric acid were added. Solution pH was adjusted to 3.6 with 1 M sodium hydroxide (Panreac, Barcelona, Spain).

2.2. Sampling collection

(a) Three tap water samples corresponding to the different sources of the water distribution system in Albacete (Spain).
(b) Five different commercial Spanish wines were selected: a white wine from Ribera de Guadiana Origin Designation; a rosé wine from Navarra Origin Designation; two aged red wines from Ribera del Duero Origin Designation (wines 1 and 2) and another red wine from La Mancha Origin Designation (wine 3).
(c) A commercial lemon juice extract.

All samples were analysed by triplicate with the proposed SBSE method followed by GC–MS/MS.

2.3. Extraction procedures

For all extraction techniques, the volume of samples was 5 ml, containing 25 μl water solution of γ-hexalactone (IS) at 1% (v/v). The extraction conditions common for all techniques were set as follows.

2.3.1. SBSE (stir bar sorptive extraction)

A polymethylsiloxane coated stir bar (0.5 mm film thickness, 10 mm length, Twister, Gerstel GmbH, Mülheim and der Ruhr, Germany) was introduced in the spiked solution. The samples were stirred at 700 rpm at room temperature for 60 min. The stir bar was then removed from the sample, rinsed with distilled water and dried with a cellulose tissue, and later transferred into a thermal desorption tube for GC/MS analysis.

2.3.2. SPME (solid-phase microextraction)

A polymethylsiloxane fiber (PDMS 100 μm, for Varian autosampler Red, Supelco, Bellefonte, USA) was conditioned in the injector of the gas chromatograph according to the instructions provided by the supplier ($T = 250\,^{\circ}\mathrm{C}$ for 30 min), and then the vial was tightly capped with a PTFE-face silicone septum (Supelco, Bellefonte, USA) and placed into the sample tray of the CombiPaL (Varian, Palo Alto, CA, U.S.A.).

2.3.2.1. IS-SPME (immersion solid-phase microextraction). SPME was carried out by immersing the fiber into the liquid matrices with the following extraction conditions: 700 rpm at room temperature for 60 min.

2.3.2.2. HS-SPME (headspace solid-phase microextraction). HS-SPME was carried out by exposing the fiber to the headspace over the sample that was heated at 35 °C with shaking at 700 rpm for 60 min.

2.4. Instrumentation

2.4.1. SBSE desorption unit

Thermal desorption of the stainless steel tubes, which contained the stir bars, was carried out using a thermal desorption system PerkinElmer Turbo Matrix ATM (Norwalk, CT, U.S.A.). The thermal desorption conditions were as follows: oven temperature, 280 °C; desorption time, 5 min; cold trap temperature, −30 °C; He inlet flow 45 ml/min. The desorption unit was coupled to a gas chromatograph.

2.4.2. Solid-phase microextraction desorption

The SPME fibers were fixed in the CombiPal autosampler for analysis and then the fiber was inserted into the GC port for desorption time of 5 min at 280 °C. Once the analysis was finished, the fiber was automatically cleaned by heating it at 200 °C for 5 min and N_2 was passed through to eliminate any possible contamination.

2.4.3. GC–MS equipment

The gas chromatograph (Varian CP-3800, Palo Alto, CA, U.S.A.) was equipped with a Saturn 2200 ion trap mass spectrometry and an CombiPal autosampler provided with a fused silica capillary column factor four (30 m × 0.25 mm i.d.; 0.25 μm film thickness VF-5MS; Varian, Palo Alto, CA, U.S.A.). The chromatographic program was set at 70 °C (held for 2 min), raised to 150 °C at 20 °C/min (held for 2 min) and to 300 °C at 10 °C/min maintained for 5 min; injector temperature, 280 °C; transfer line at 250 °C; detector temperature 300 °C; He carrier gas flow 1.0 ml/min.

2.4.3.1. Ion preparation and analysis. The capability of ion trap technology for manipulating the ion population after ion creation but prior to ion analysis is very advantageous, especially when there is a need to quantify very low levels of compounds with a high level of interference, as is the case with wine, water or juice matrices. In this case, the scan function has to be optimized by studying the ion parameters which allow for control of the ions that are ejected, those that are retained and for those that will undergo collision-induced dissociation (CID). This preparation determines how the scan function is constructed and what custom waveforms are created to complete the analysis [40]. For each analyte has been optimized the scan functions, which were used on the pre-selected retention time windows called “segment” defined by the retention time of the target compounds (Table 1). Due to very close the retention time values co-elution of TBP, TBA and PCA at the chosen GC parameters, a multiple reaction monitoring (MRM) mode had been used to quantify these analytes. MRM mode uses different precursor ion masses

Table 1
Optimized parameters for identification of halophenols and haloanisoles by gas chromatography–ion trap tandem mass spectrometry

Compound	t_R (min)	Segment start–end (min)	Low–high mass (m/z)	Compound ion[a] (m/z)	Ion selected[b] (m/z)	Excitation storage level (m/z)	Excitation amplitude (V)	Ion preparation
IS	4.2	2.00–6.00	60–120	85	85.0	48.0	0.20	MS/MS
TCA	6.78	6.00–7.20	100–230	195, 210, 212	212.0	48.0	0.20	MS/MS
TeCA	9.80	7.20–10.20	110–270	203, 231, 246	246.0	48.0	0.20	MS/MS
TCP	10.30	10.20–10.60	110–290	160, 196, 198	198.0	48.0	0.20	MS/MS
TeCP	10.90	10.60–11.50	100–250	166, 232	232.0	48.0	0.20	MS/MS
TBA	12.08	11.50–13.30	100–360	329, 344, 346	346.0	120.0	0.10	MRM
TBP	12.70	11.50–13.30	100–360	332	332.0	120.0	0.10	MRM
PCA	13.90	13.30–13.90	100–300	237, 265, 280	280.0	120.0	0.10	MRM

IS: γ-hexalactone; TCA: 2,4,6-trichloroanisole; TeCA: 2,3,4,6-tetrachloroanisole; PCA: pentachloroanisole; TCP: 2,4,6-trichlorophenol; TeCP: 2,3,4,6-tetrachlorophenol; TBA: 2,4,6-tribromoanisole; TBP: 2,4,6-tribromophenol; MS/MS: mass/mass; MRM: multiple reaction monitoring.

[a] Ions used for compounds identification.

[b] Ion selected for compounds quantification.

Table 2
Analytical parameters using the SBSE GC–MS/MS technique

SBSE	TCA	TeCA	PCA	TCP	TeCP	TBA	TBP
Concentration range (ng/l)	0.4–500	1.0–500	0.4–500	0.4–500	0.4–500	0.4–500	0.4–500
Intercept	110.10	307.30	74.80	17.10	32.80	277.50	31.00
Slope	19072.00	657.30	2468.70	346.10	282.60	1229.90	9212.50
Linearity curve (r^2)	1.00	1.00	0.99	0.99	0.98	0.99	1.00
LOD (ng/l)	0.03	0.71	0.05	0.06	0.27	0.23	0.01
LOQ (ng/l)	0.10	1.27	0.08	0.10	0.61	0.23	0.01
Reproducibility (%)	17.90	12.64	6.30	2.22	6.02	0.39	1.87
Repeatability (%R.S.D.)	13.34	7.30	3.64	1.28	3.50	0.23	1.08

TCA: 2,4,6-trichloroanisole; TeCA: 2,3,4,6-tetrachloroanisole; PCA: pentachloroanisole; TCP: 2,4,6-trichlorophenol; TeCP: 2,3,4,6-tetrachlorophenol; TBA: 2,4,6-tribromoanisole; TBP: 2,4,6-tribromophenol.

and different dissociation parameters throughout all stages of the MS/MS analysis.

In addition to the common MS parameters used for the target compounds, each segment was associated with an ion preparation mode (IPM), which defined the MS/MS parameters and *m*/*z* scan range. The MS/MS conditions used for all analytes were as follows: solvent delay: 2 min; peak threshold: 0; background mass: 40 *m*/*z*; RF dump value: 650 *m*/*z*; filament current: 80 μA; target TIC: 5000; ionization time: 25 ms; prescan ionization time: 1500 μs; scan time: 0.50 s/scan; multiplier offset: ±200 V. Moreover the precursor ions were isolated using a 3 *m/z* window and subjected to further collision-induced dissociation.

2.5. *Analytical method validation*

For linearity study, calibration curves were constructed by spiking five different analyte concentrations into the solutions. For SBSE, each level of concentration was analysed twice with two different stir bars, thus totaling four replicates. Also for IS-SPME and HS-SPME, four replicates for each level of concentration were carried out. In Tables 2–4, we have reported the analytical parameters corresponding to SBSE, IS-SPME and HS-SPME, respectively, using GC/MS/MS analysis.

The detection and quantification limits (LOD and LOQ, respectively) were calculated with the data generated in the linearity studies. LOD was defined as $(a+3S_a)/b$ and LOQ as $(a+10S_a)/b$, with "a" being the origin ordinate, "S_a" the origin ordinate variance and "b" the slope. The limit of quantification was taken to be validated within-batch relative standard deviation, according to Catice's methodology [41]. The standard deviation for each compound (square root of the arithmetic mean of the variances) was calculated to obtain the repeatability (%R.S.D.). The standard deviation of the four values for each compound (measurements on two different days) multiplied by the square root of 3 was taken as the reproducibility value [41].

3. Results and discussion

3.1. *Optimization of MS/MS fragmentation analysis for halophenols and haloanisoles*

Target compounds detection will be carried out by desorbing the different extraction devices (SPME vs. SBSE) followed by GC/MS/MS analysis. The MS/MS analysis consist in three steps, the first one is electronic impact (EI), the second step is the isolation of the precursor ion which takes out the matrix (selectivity), and finally the third step is MS/MS fragmentation (sensibility) with full scan of the product ions. Due to the differences in chemical structure of the halophenols and haloanisoles, the selection of the ion for quantification is very important in their MS/MS analysis (Table 1) which was based on the relative abundance of the main fragments, as well as the intensity of the product ions in the mass spectrum of each compound quantified.

The optimization of MS/MS conditions for the dissociation of the selected precursor ions was carried out using the automated method development (AMD) option built into the Varian Saturn GC software. AMD uses up to 10 different CID (collision-induced dissociation) voltages between the ranges that we select, in our case we used a resonant waveform and the voltage was between 0 and 0.9 V for the same precursor ion. The optimized

Table 3
Analytical parameters using the IS-SPME GC–MS/MS technique

SPME	TCA	TeCA	PCA	TCP	TeCP	TBA	TBP
Concentration range (μg/l)	0.5–40	0.5–40	0.5–40	0.5–40	0.5–40	0.5–40	0.5–40
Intercept	186.30	586.60	1850.90	2.90	2.80	959.90	3.40
Slope	439.30	1345.80	2780.90	9.80	11.30	1831.50	16.00
Linearity curve (r^2)	0.97	0.98	0.99	0.99	0.98	1.00	0.99
LOD (ng/l)	0.46	0.66	0.88	0.30	0.25	0.52	0.22
LOQ (ng/l)	0.56	1.14	1.39	0.32	0.25	0.53	0.22
Reproducibility (%)	4.17	17.51	24.61	0.30	0.01	0.78	0.03
Repeatability (%R.S.D.)	2.41	10.11	14.21	0.17	0.01	0.46	0.13

TCA: 2,4,6-trichloroanisole; TeCA: 2,3,4,6-tetrachloroanisole; PCA: pentachloroanisole; TCP: 2,4,6-trichlorophenol; TeCP: 2,3,4,6-tetrachlorophenol; TBA: 2,4,6-tribromoanisole; TBP: 2,4,6-tribromophenol.

Table 4
Analytical parameters using the HS-SPME GC–MS/MS technique

HS-SPME	TCA	TeCA	PCA	TCP	TeCP	TBA	TBP
Concentration range (μg/l)	0.25–10	0.25–10	0.25–10	0.25–10	0.25–10	0.25–10	0.25–10
Intercept	1010.30	2108.60	2262.10	7897.00	6645.00	8332.70	102.30
Slope	405.40	739.60	382.70	52.38	74.01	2738.90	33.20
Linearity curve (r^2)	1.00	1.00	0.99	1.00	1.00	1.00	1.00
LOD (ng/l)	87.40	107.40	243.10	0.35	0.17	221.90	7.60
LOQ (ng/l)	285.50	351.20	796.40	0.80	0.36	732.70	18.00
Reproducibility (%)	18.36	18.18	18.53	1.03	0.86	7.74	1.23
Repeatability (%R.S.D.)	10.6	10.5	10.7	0.60	0.50	4.47	0.71

TCA: 2,4,6-trichloroanisole; TeCA: 2,3,4,6-tetrachloroanisole; PCA: pentachloroanisole; TCP: 2,4,6-trichlorophenol; TeCP: 2,3,4,6-tetrachlorophenol; TBA: 2,4,6-tribromoanisole; TBP: 2,4,6-tribromophenol.

energies and CIDs required for the dissociation of each target compound are shown in Table 1.

3.2. Optimization of the analytical procedures

Once the optimization of collision-induced dissociation parameters for the target analytes and the MS/MS method was fixed, the different extraction techniques were assayed.

3.2.1. Sorbent selection

Polymeric sorbent coating as different as polydimethylsiloxane (PDMS), divinylbenzene (DVD), polyacrylate (PA), carboxen (CAR) have been tested for the analysis of chloroanisoles and chlorophenols by SPME liquid matrices [21,29,42,43]. The type of fiber was found to be a fundamental parameter together with the exposure time in order to optimize the recovery and reproducibility of the analytical method. The most appropriate fibers were found to be PDMS (100 μm), followed by PA (85 μm) [18,42–44]. In the case of SBSE, the stir bar is only available coated with PDMS, which provided excellent sensitivity and method repeatability when analysing these target compounds in wine [33] or water matrices [30,31]. Hence, for the present study the enrichment step will be performance only on polydimethylsiloxane coating, although the extraction theory indicates that PA will be more appropriate for halophenols when a derivation reaction was also carried out [43].

3.2.2. Extraction methods comparison

Due to the economic losses attributed to earthy-musty off-flavour, researchers are asked to give a definitive method for the analysis of these compounds. There are several bibliography papers showing the effectiveness of extraction methods such as HS-SPME or SBSE. Nothing is found for IS-SPME nor has comparison between them been carried out to establish a definitive method when analysing drinking water, wine, fruit juice or other liquid aqueous matrices. The fundamental aspects of SBSE for liquid sampling are similar to principles of IS-SPME, because both techniques are based on sorptive extraction. Thus, both extraction conditions in terms of time (1 h), temperature (RT) and agitation mode (700 rpm) will be the same, as it was already described by other authors [31–33,44]. Headspace sampling by SPME has been successfully studied for the target compounds, and higher extraction temperatures were required for volatile adsorption, i.e. 35 °C [10,21,42].

Tables 2–4 show the results obtained, respectively, with SBSE, SPME immersion and headspace mode followed by GC/MS/MS detection. In all cases, a good linearity was obtained for each analyte and LOQs were calculated according to the European Union Guidelines as the lowest concentration that provides repeatabilities under 20%. The SBSE has been seen to offer much lower LOD and LOQ than both SPME techniques, thus overcoming one of its main limitations, namely, the low concentration capability due to the low volume of polymeric coating. In SPME the maximum volume of PDMS coated onto the fiber is 0.6 μl (100 μm fiber), whereas, the stir bar used about 24 μl, which theoretically means an increment of 40-fold.

TCA, the most studied compound related to taint, showed LOD and LOQs lower than its olfactory threshold (in wine: 4–10 ng/l [45]; water: 30 pg/l to 50 ng/l [9]) when SBSE and IS-SPME mode were tested, although $\mathrm{LOD_{SBSE}}$ was 15 times lower than $\mathrm{LOD_{IS\text{-}SPME}}$. Surprisingly, when comparing both SPME methods, headspace extraction has always been preferred by the different authors to direct extraction in order to prevent the direct contact of the fiber with the complex matrix and related matrix effects. Nevertheless, this is not the case here, as IS-SPME was 188.4 times more sensitive than HS-SPME, higher temperatures will only improve HS-SPME results when derivatization reaction takes place [43]. But this situation has not been

Table 5
LOD differences observed between the three extraction methods: SBSE, IS-SPME and HS-SPME GC–MS/MS

LOD	TCA	TeCA	PCA	TCP	TeCP	TBA	TBP
SBSE vs. IS-SPME	13.65	0.93	19.20	4.72	0.95	2.32	54.00
SBSE vs. HS-SPME	2570.59	151.05	5284.78	5.40	0.64	981.86	1900.00
HS-SPME vs. IS-SPME	188.36	161.75	275.31	1.15	0.69	423.47	35.18

TCA: 2,4,6-trichloroanisole; TeCA: 2,3,4,6-tetrachloroanisole; PCA: pentachloroanisole; TCP: 2,4,6-trichlorophenol; TeCP: 2,3,4,6-tetrachlorophenol; TBA: 2,4,6-tribromoanisole; TBP: 2,4,6-tribromophenol.

Table 6
SBSE GC–MS/MS analysis of different liquid matrices (tap water, fruit juice and wines)

Matrix	TCA (ng/l)	TeCA (ng/l)	PCA (ng/l)	TCP (ng/l)	TeCP (ng/l)	TBA (ng/l)	TBP (ng/l)
Water 1	6.83	n.d.	n.d.	8.27	Traces	n.d.	n.d.
Water 2	6.27	313.35	n.d.	n.d.	n.d.	n.d.	n.d.
Water 3	9.13	9.15	n.d.	n.d.	109.21	n.d.	n.d.
Lemon juice	291.94	Traces	Traces	321.64	n.d.	n.d.	n.d.
White wine	n.d.	n.d.	n.d.	n.d.	n.d.	n.d.	n.d.
Rosé wine	n.d.	n.d.	n.d.	n.d.	n.d.	n.d.	n.d.
Red wine aged in wood 1	n.d.	n.d.	n.d.	n.d.	n.d.	n.d.	n.d.
Red wine aged in wood 2	n.d.	n.d.	n.d.	56.81	n.d.	n.d.	n.d.
Red wine aged in wood 3	n.d	n.d.	n.d.	99.67	n.d.	n.d.	n.d.

n.d.: not detected; traces < LOD.

forced so as to maintain similar extraction conditions for the three techniques assayed. If IS-SPME and HS-SPME methods are compared with SBSE, a LOD increment of 13.6 and 2570.5 times were observed, respectively (Table 5).

For SBSE and IS-SPME, similar results were observed with the other anisole compounds (TeCA, PCA and TBA) but not for HS-SPME. LOD and LOQ values were lower than their respective olfactory threshold for TeCA 25 ng/l in wine [6] and 4 ng/l in water [14,15] and for TBA 7.9 ng/l in wine [7], respectively. As expected, SBSE extraction has also been observed to be more sensitive than SPME ones, especially with regard to PCA (Table 5).

Chlorophenols are less volatile than their respective chloroanisole family, and this fact is reflected in the results (Tables 2–4). No significant differences have been observed for TCP between both SPME modes (Tables 3 and 4), but not expected were the LOD values for TeCP as HS-SPME gave better results than with IS-SPME. The detection limit of TBP by SPME immersion was 35 times more sensitive than by HS-SPME. It is important to mention the efficiency of the SBSE method as compared to HS-SPME, 1900 times more (Table 5).

3.3. Application of SBSE to different liquid matrices

The best extraction method proposed, the SBSE, has been applied to nine different liquid aqueous samples and the results are shown in Table 6. The water samples have been analysed due to the fact that consumers in Albacete, although a new purification plant based on nanofiltration has been installed recently. Consumers were right as the samples revealed that TCA has been identified in all samples at concentration levels close to its olfactory threshold (7 ng/l). Two of the samples also contain TeCA and TeCP. The well-studied environmental pollutant, TCP, was only found in one tap water sample, with concentration levels far from the toxicity risks established at 5 μg/l.

The analysis of these haloanisoles and halophenols are more important in the oenological industry due to the defect known as “cork taint”. Between 1% and 5% of bottled wine is cork-tainted, but its consequences can be quite damaging to a winery’s reputation, since consumers will think twice before buying another bottle. TCA is detected in at least 80% of cork taint cases [46] and may be found together with other anisoles such as TeCA and PCA. All wine samples analysed were free of anisoles, but special importance should be given to the presence of TCP in two of the red wine samples, which can be transformed into TCA by fungal methylation [1,47].

Recently, another liquid sample, fruit juice, been affected by this taint problem. Juice-producing companies explain that these compounds may be found in their extracts through the use of halophenols as pesticides, or the cleaning products used such as hypochlorite-based disinfectants, among other reasons. The sample of lemon juice analysed shows an enormous contamination with TCA and TCP, and traces of TeCA and PCA.

In conclusion, stir bar sorptive extraction, SBSE, coupled to GC with tandem mass spectrometry-ion trap mode for the analysis of halophenols and haloanisoles showed better sensitivity than SPME (IS-SPME and HS-SPME), especially if it is compared to the headspace mode. The SBSE and IS-SPME methods described enabled us to determine such compounds in liquid aqueous matrices at ng/l levels. The selectivity increment between SBSE and SPME is not the 40-fold reported by the supplier, as greater differences are observed for the haloanisole family when SBSE and HS-SPME are compared. However, SPME presents some advantages with respect to SBSE, which can hardly be deduced from the data presented, as the halophenol limits could be further increased when using different types of commercially available fibers. Up to now, stir bars offer a limited capability for enrichment of polar compounds since they are only available with PDMS coating and are also much more difficult to obtain commercially than fibers.

Acknowledgements

We wish to thank the Ministerio de Ciencia y Tecnología for financial support given to project AGL2004-04609. Thanks also go to Jorge Hurtado de Mendoza (Sailab, S.L.) for his technical assistance with the MS/MS analysis and to Kathy Walsh for proofreading the English manuscript.

References

[1] M.L. Álvarez-Rodríguez, L. López-Ocaña, J.M. López-Coronado, E. Rodríguez, M.J. Martínez, G. Larriba, J.-J.R. Coque, Appl. Environ. Microbiol. 68 (2002) 5860.

[2] A.S. Allard, M. Remberger, A.H. Neilson, Appl. Environ. Microbiol. 53 (1987) 839.

[3] C. Silva Pereira, J.J. Figueiredo Marques, M.V. San Romao, Crit. Rev. Microbiol. 26 (2000) 147.
[4] ATSDR, Agency for Toxic Substances and Disease Registry, U.S. Department of Health and Human Services, Atlanta, GA, USA, 1999.
[5] IRIS, Integrated Risk Information System, U.S. Environmental Protection Agency, Washington, DC, 1998.
[6] J.M. Amon, J.M. Vandepeer, R.F. Simpson, N.Z. Aust, Wine Ind. J. 4 (1989) 62.
[7] P. Chatonnet, S. Bonnet, S. Boutou, M.D. Labadie, J. Agric. Food Chem. 52 (2004) 1255.
[8] V. Mazzoleni, L. Maggi, Food Res. Int. 40 (2007) 694.
[9] A. Diaz, C. Fabrellas, F. Ventura, J. Agric. Food Chem. 53 (2005) 383.
[10] S. Jönsson, T. Usitalo, B. Van Bavel, I.B. Gustafsson, G. Lindström, J. Chromatogr. A 1111 (2006) 71.
[11] A. Peña-Neira, B. Fernández de Simón, M.C. García-Vallejo, T. Hernández, E. Cadahía, J.A. Suárez, Eur. Food Res. Technol. 211 (2000) 257.
[12] G.J. Soleas, J. Yan, T. Seaver, D.M. Goldberg, J. Agric. Food Chem. 50 (2002) 1032.
[13] H. Tanner, C. Zanner, G. Würdig, Z. Schweiz, Obst Weinbau 117 (1981) 752.
[14] R.F. Curtis, D.G. Land, N.M. Griffiths, M. Gee, D. Robinson, J.L. Peel, C. Demis, J.M. Gee, Nature 235 (1972) 223.
[15] N.M. Griffith, Chem. Senses Flavor 1 (1974) 187.
[16] F.B. Whitfield, T.H.L. Nguyen, C.R. Tindale, J. Sci. Food Agric. 55 (1991) 19.
[17] I. Rodríguez, M.I. Turnes, M.C. Mejuto, R. Cela, J. Chromatogr. A 721 (1996) 297.
[18] T.J. Evans, C.E. Butzke, S.E. Ebeler, J. Chromatogr. A 786 (1997) 293.
[19] A. Martínez-Uruñuela, J.M. González-Sáiz, C. Pizarro, J. Chromatogr. A 1056 (2004) 49.
[20] R. Alzaga, L. Ortiz, F. Sanchez-Baeza, M.P. Marco, J.M. Bayona, J. Agric. Food Chem. 51 (2003) 3509.
[21] M. Riu, M. Mestres, O. Busto, J. Guash, J. Chromatogr. A 977 (2002) 1.
[22] M. Riu, M. Mestres, O. Busto, J. Guash, J. Chromatogr. A 1107 (2006) 240.
[23] S. Rocha, I. Delgadillo, A.J. Ferrer Correia, J. Agric. Food Chem. 44 (1996) 865.
[24] O. Ezquerro, M.T. Tena, J. Chromatogr. A 1068 (2005) 201.
[25] M. Portillo, N. Prohibas, V. Salvadó, B.M. Simonet, J. Chromatogr. A 1103 (2006) 29.
[26] B. Zierler, B. Siegmund, W. Pfannhauser, Anal. Chim. Acta 520 (2004) 3.
[27] N. Guerra Simoes, V. Vale Cardoso, E. Ferreira, M.J. Benoliel, C.M.M. Almeida, Chemosphere 68 (2007) 501.
[28] Supelco applications, Bulletin 923 (1998) 1.
[29] A. Diaz, F. Ventura, M.T. Galceran, Anal. Bioanal. Chem. 386 (2006) 293.
[30] D. Benanou, F. Acobas, M.R. de Roubin, F. David, P. Sandra, Anal. Bioanal. Chem. 376 (2004) 69.
[31] M. Kawaguchi, Y. Ishii, N. Sakui, N. Okanouchi, R. Ito, K. Saito, H. Nakazawa, Anal. Chim. Acta 533 (2005) 57.
[32] N. Ochiai, K. Sasamoto, M. Takino, S. Yamashita, S. Daishima, A. Heiden, A. Hoffman, Analyst 126 (2001) 1652.
[33] A. Zalacain, G.L. Alonso, C. Lorenzo, M. Iñiguez, M.R. Salinas, J. Chromatogr. A 1033 (2004) 173.
[34] E. Baltussen, P. Sandra, F. David, C.A. Cramers, J. Microcolumn Sep. 11 (1999) 737.
[35] C. Blasco, M. Fernández, Y. Picó, G. Font, J. Chromatogr. A 1030 (2004) 77.
[36] C. Blasco, G. Font, Y. Picó, J. Chromatogr. A 970 (2002) 201.
[37] J.C.R. Demyttenaere, J.I. Sanchez, R. Verhé, P. Sandra, N. De Kimpe, J. Chromatogr. A 985 (2003) 221.
[38] R.F. Alves, A.M.D. Nascimento, J.M.F. Nogueira, Anal. Chim. Acta 546 (2005) 11.
[39] C. Bicchi, C. Iori, P. Rubiolo, P. Sandra, J. Agric. Food Chem. 50 (2002) 449.
[40] S.S. Verenitch, C.J. Lowe, A. Mazumber, J. Chromatogr. A 1116 (2006) 193.
[41] Catice, Centro de Asistencia Técnica e Inspección del Comercio Exterior, Ministerio de Economía y Hacienda, 2003.
[42] E. Lizarraga, A. Irigoyen, V. Belsue, E. González-Peñas, J. Chromatogr. A 1052 (2004) 145.
[43] C. Pizarro, N. Pérez del Notario, J.M. González-Sáiz, J. Chromatogr. A 1143 (2007) 26.
[44] International Standards Organisation, Cork Stoppers-Determination of Releasable 2,4,6-Trichloroanisol (TCA), ISO 20752, ISO, Geneva, Switzerland, 2007.
[45] M.A. Sefton, R.F. Simpson, J. Aust, Grape Wine Res. 11 (2005) 226.
[46] C.E. Butzke, T.J. Evans, S.E. Ebeler, ACS Symp. Ser. 714 (1999) 208.
[47] L. Maggi, V. Mazzoleni, M.D. Fumi, M.R. Salinas, Food Addit. Contam., doi:10/1080/02652030701522991.

Available online at www.sciencedirect.com

ScienceDirect

Talanta 75 (2008) 613–623

Talanta

www.elsevier.com/locate/talanta

Review

Energy scavenging for long-term deployable wireless sensor networks

Cian Ó Mathúna*, Terence O'Donnell, Rafael V. Martinez-Catala, James Rohan, Brendan O'Flynn

Tyndall National Institute, Lee Maltings, Prospect Row, Cork, Ireland[1]

Received 5 April 2007; received in revised form 30 November 2007; accepted 8 December 2007

Abstract

The coming decade will see the rapid emergence of low cost, intelligent, wireless sensors and their widespread deployment throughout our environment. While wearable systems will operate over communications ranges of less than a meter, building management systems will operate with inter-node communications ranges of the order of meters to tens of meters and remote environmental monitoring systems will require communications systems and associated energy systems that will allow reliable operation over kilometers. Autonomous power should allow wireless sensor nodes to operate in a "deploy and forget" mode. The use of rechargeable battery technology is problematic due to battery lifetime issues related to node power budget, battery self-discharge, number of recharge cycles and long-term environmental impact. Duty cycling of wireless sensor nodes with long "SLEEP" times minimises energy usage. A case study of a multi-sensor, wireless, building management system operating using the Zigbee protocol demonstrates that, even with a 1 min cycle time for an 864 ms "ACTIVE" mode, the sensor module is already in SLEEP mode for almost 99% of the time. For a 20-min cycle time, the energy utilisation in SLEEP mode exceeds the ACTIVE mode energy by almost a factor of three and thus dominates the module energy utilisation thereby providing the ultimate limit to the power system lifetime. Energy harvesting techniques can deliver energy densities of 7.5 mW/cm^2 from outdoor solar, 100 μW/cm^2 from indoor lighting, 100 μW/cm^3 from vibrational energy and 60 μW/cm^2 from thermal energy typically found in a building environment. A truly autonomous, "deploy and forget" battery-less system can be achieved by scaling the energy harvesting system to provide all the system energy needs. In the building management case study discussed, for duty cycles of less than 0.07% (i.e. in ACTIVE mode for 0.864 s every 20 min), energy harvester device dimensions of approximately 2 cm on a side would be sufficient to supply the complete wireless sensor node energy. Key research challenges to be addressed to deliver future, remote, wireless, chemo-biosensing systems include the development of low cost, low-power sensors, miniaturised fluidic transport systems, anti-bio-fouling sensor surfaces, sensor calibration, reliable and robust system packaging, as well as associated energy delivery systems and energy budget management.

Keywords: Wireless sensors; Energy harvesting/scavenging; Energy budget; Building management systems; Remote environmental monitoring

---

Contents

---

* Corresponding author. Tel.: +353 21 4904350; fax: +353 21 4270271.
E-mail address: cian.omathuna@tyndall.ie (C.Ó. Mathúna).

[1] www.tyndall.ie.

0039-9140/$ – see front matter © 2008 Published by Elsevier B.V.
doi:10.1016/j.talanta.2007.12.021

1. Introduction

The coming decade will see the rapid emergence of low cost, intelligent, wireless sensors and their widespread deployment throughout our environment. This sensor-rich world, referred to as "Ambient Intelligence" or "Smart Environments", will be based on smart electronic systems or wireless sensor network technologies. It will have millions of sensors embedded throughout our environment and it will dramatically improve the quality of peoples' lives in terms of our environment, health and well being, security, comfort, education and entertainment.

Chemo-biosensing, using wireless sensor systems, is being investigated across a broad range of applications including environmental monitoring of the external environment (i.e. remote environmental monitoring of the quality of air, water and ground soil including precision agriculture) [1–3], the built environment (building energy management and occupant comfort, safety and security) [4], automotive (i.e. for safe and efficient motoring), aeronautical/aerospace (i.e. for safety and security) [5] and in both wearable (i.e. physiological monitoring and fitness) [6] and in vivo (i.e. smart pills, catheters and implants) applications.

A typical wireless sensor module consists of a number of functional blocks which include sensors, data acquisition, microcontroller for control and signal processing, an RF transceiver for wireless communications and a power source. In some cases, where local signal processing is required, a digital signal processing (DSP) chip or field programmable gate array (FPGA) may also be used. Most existing systems contain a power source which consists of a standard primary battery or a rechargeable battery. In the case of wireless chemo-biosensing systems, extra operational and functional issues arise due to the need for many sensor types to be in direct contact with the fluid being monitored, introducing issues of fluidic transport, sensor fouling, drift and calibration.

Remote monitoring applications require reliable and extended lifetime deployments of potentially a very large number of wireless sensor nodes. As electronic hardware becomes cheaper and smaller, more of these applications are likely to appear, particularly as these miniaturised nodes offer the opportunity for the electronics to be embedded unobtrusively into everyday objects. A key issue for these wireless node designs is that they achieve high degrees of power-efficiency for autonomous, maintenance-free operation, where it is likely that nodes will require deployment for periods of years since the cost of battery replacement will be prohibitive and impractical. This can effectively be described as a "deploy and forget" scenario.

At first glance, batteries appear to offer the optimum source of energy for wireless sensor systems with commercial battery technologies offering significant energy capacities in relatively small form-factors. The principle trend in battery technology is towards higher energy densities, which has obvious advantages for portable equipment where increasing time between charges and miniaturisation of system size are important drivers. However, energy density is not necessarily the critical factor for the choice of battery technology for a wireless sensor node in a "deploy and forget" application. In such a case, battery characteristics such as lifetime, self-discharge rate and, if charging from a renewable energy source such as solar, the number of allowable charge cycles, are perhaps more important than energy density or capacity.

For example, self-discharge rates for batteries vary from, 30% per month for nickel metal hydride (Ni-MH) to 2–3% per month for lithium batteries. Therefore, for a typical wireless sensor node with low-energy consumption and long duty-cycle operation, the self-discharge rate of the battery could exceed the discharge due to the system consumption. For rechargeable batteries, the battery lifetime, measured in charge cycles, varies from approximately 500 cycles for NiCd, Ni-MH, and Li-ion to approximately 300 for Li polymer. Thus, for example, if battery recharging from a solar cell is used, and a charge cycle is completed in a day, the lifetime may be limited to 500 days or less than 18 months. Furthermore, another issue that is not well characterised is the impact on battery lifetime of temperature variations and other environmental conditions in the end-use application, which can significantly undermine the long-term reliability of the battery technology. Considering these factors it may be seen that, in a "deploy and forget" scenario, regardless of whether some form of battery recharging can be implemented, the battery performance and reliability is still likely to limit the lifetime of the wireless sensor node.

This "deploy and forget" nature of wireless sensor systems effectively results in the energy available to the system being constrained by the initial energy capacity of the battery and the unpredictable lifetime performance of the battery. This has driven the development of approaches to maximise wireless sensor system lifetime through minimising energy usage by employing ultra-low power sensors, electronics and wireless communications and through the use of duty cycling based on long sleep times (i.e. the wireless system remains in a low power SLEEP mode for greater than 99% of the time). Thus the sensor node components will be active only for the time required to perform the operations of sensor sampling, data processing and wireless data transmission or communication. In this duty-cycle mode of operation, it is appropriate to refer to energy utilisation in joules and not power consumption in watts as we are concerned with the lifetime of the power system delivering energy (i.e. the product of the component operating mode power and the time the component spends in that mode) and the energy utilisation, or energy budget, of the various components of the wireless system.

Given the above limitations of battery technology and the resulting potential incompatibilities of conventional batteries with wireless sensor systems, significant research is ongoing to deliver power from the environment using energy scavenging or harvesting techniques such as vibration/motion, thermal gradients and solar energy which can deliver energy directly to the wireless sensor load or to a storage element such as a rechargeable battery or capacitor.

This paper addresses some of the key issues relating to the delivery of autonomous power for wireless sensor systems. Section 2 initially provides a summary review of research and development into wireless sensor nodes and then presents a summary review of the major energy scavenging techniques and the levels of available energy which can be harvested from the environment. In Section 3, we present a case study for a wireless sensor deployment in a building management application in order to illustrate the energy budget requirements of a typical wireless node operating using the Zigbee protocol. We then discuss the potential lifetime of the wireless sensor system by undertaking a comparison of a battery-driven scenario with systems supported by a range of energy-harvesting techniques. In Section 4, a case study is presented of the energy requirements for a wireless sensor module in a remote environmental monitoring scenario. Finally, in Section 5, we look to the future and consider the opportunities and challenges for remote wireless, chemo-biosensing systems.

2. State-of-the-art

2.1. Wireless sensor modules

Wireless sensor nodes (typically called motes) have recently become available commercially from a number of start-up companies, mainly US-based. These include Crossbow [7], Moteiv [8], Dust [9], Phidgets [10], Meshnetics [11], Sensicast [12], AccSense [13], Millennial Net [14] and Ember [15]. These first generation products have been used in developmental test beds, however, the demonstrated deployments have typically low numbers of nodes and do not address real-world issues of scalability, network robustness and quality of service [16].

A number of research groups are developing motes to address specific research challenges in sensor networks such as algorithm testing, power management, antenna miniaturisation and wireless range improvements. Increasingly, the motes are also being designed for specific applications, including environmental monitoring, building energy monitoring, e-health and animal tracking. Active research groups include Tyndall National Institute [17], (see Fig. 1) Fraunhofer-IZM [18], IMEC [19], Harvard [20], Imperial College London [21], the Centre for Embedded Networked Sensing at UCLA [22], UC Berkeley [23], Lancaster University [24], ETH Zurich [25], MIT [26], Sandia National Laboratories [27], Yale [28], EPFL [29] and companies such as Intel [30] and Philips [31].

Advanced mote research into miniaturised and robust hardware configurations and 3D packaging of motes, using stacked PCBs or silicon, is being carried out at Tyndall National Institute [17], Fraunhofer-IZM [18] and IMEC [19].

2.2. Harvesting of energy from the environment

In order to provide an autonomous source of energy for the wireless sensor system, one can consider extracting energy from the environment in order to augment the battery energy storage or indeed replace it. A comprehensive review of the many possible sources of energy which could potentially be harnessed is given in [32,33]. Among the more feasible, for which promising results have already been achieved, is the extraction of power from solar energy, from thermal gradients and from vibrations and movement. In the review which follows, the energy harvesting techniques are not exhaustively reviewed as such detailed reviews are available elsewhere. The objective of this review is to determine typical values for the energy levels which can be harvested from the various techniques, so that these values can be used in Section 3 to assess the feasibility of using energy harvesting to power a typical wireless sensor node.

2.2.1. Solar power

The use of ambient light to generate power is well established, with solar-powered calculators and wristwatches being popular for several decades. The power available from solar cells varies widely depending on the illumination level (e.g. indoors or outdoors) and on the solar cell technology. The efficiencies of various solar cell technologies at different illumination levels have been reported in [53]. For a typical outdoor illumination level of 500 W/m^2 (bright, sunny day in Ireland), efficiencies vary from approximately 15% (for polycrystalline silicon and gallium indium phosphide) to 2–5% for amorphous silicon cells. For typical indoor illumination levels of 10 W/m^2, efficiencies vary from approximately 10% for crystalline silicon and gallium indium phosphide, to approximately 2% for amorphous silicon. Therefore, in order to assess the feasibility of solar energy harvesting for powering wireless sensor nodes, we will assume a typical power density of 75 μW/mm^2 for outdoor solar cell operation and a typical power density of 1 μW/mm^2 for indoor operation.

2.2.2. Thermal energy harvesting

Harvesting of energy from heat sources (such as the human body) can be achieved by the conversion of thermal gradients to electrical energy using the Seebeck effect. Many such large-scale devices exist, for example, for the generation of electricity from hot exhausts on vehicles. At a smaller scale, the main interest has been in the generation of power from body heat, as a means to power wearable devices. For example, Seiko have produced a wristwatch powered by body heat [54]. Reported results for power densities achieved from micro-fabricated devices are 0.14 μW/mm^2 for a 700 mm^2 device [55], 0.37 μW/mm^2 for a 68 mm^2 device [56] and 0.60 μW/mm^2 for a 1.12 mm^2 device [56]. All these results relate to a temperature gradient/difference of 5 K, which is typically achievable for wearable applications. Higher temperature differences may be achievable in other environments, e.g. heaters in a building, and in that case the assumed

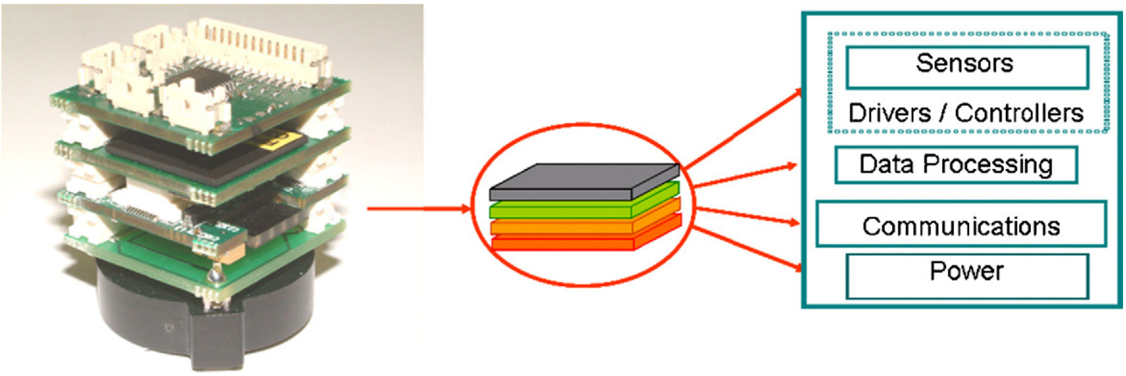

Fig. 1. Photograph and schematic of Tyndall 25 mm wireless sensor module.

power density can in principle be scaled by the square of the temperature difference [57,58].

2.2.3. *Energy from vibration and movement*

Ambient vibrations are present in many environments, such as automotive, buildings, structures (bridges, railways), industrial machines, household appliances, etc. The energy present in the vibrations can be extracted using a suitable mechanical-to-electrical energy converter or generator. Generators proposed to-date use electromagnetic, electrostatic or piezoelectric principles.

The majority of electromagnetic generators make use of Faraday's law of electromagnetic induction. The energy in the environmental vibration is used to make a magnetic mass move relative to a coil, thus inducing a voltage and causing a current to flow in the attached electrical load. Piezoelectric generators make use of the piezoelectric properties of some materials which develop a voltage when stressed. The vibration is used to stress the piezoelectric element, thus developing a voltage which can be extracted as electrical energy. Electrostatic generators generally make use of the vibrational energy to pull apart the plates of a charged capacitor, against the force of electrostatic attraction, thus converting the vibrational energy to energy stored in the capacitor's electric field.

Detailed reviews of recent work in the area of vibrational energy harvesting have been conducted elsewhere [34,35], and the reader is referred to these works for a thorough discussion of the different types of generator which have been developed. Here we restrict ourselves in summarising the important results from the work to-date.

From the theory of the resonant vibrational generator, where a spring mounted mass, m, is made to vibrate at its mechanical resonant frequency, the maximum power generated, P, can be expressed as;

$$P = \frac{\omega^3 m Y^2}{4\xi} \tag{1}$$

where ω is the angular frequency of vibration and is assumed equal to the mechanical resonant frequency of the system, m is the moving mass, Y is the amplitude of the vibrating source, and ξ is the damping ratio which consists of useful damping due to the extraction of electrical power and parasitic damping due to mechanical damping in the structure. Making use of the fact that, for a sinusoidal source vibration, the amplitude of the acceleration, a, can be written as $\omega^2 Y$, then the above equation can also be re-written as

$$P = \frac{ma^2}{4\xi\omega} \tag{2}$$

This highlights the fact that the generated power is proportional to the moving mass and the square of the acceleration. The graph in Fig. 2(a) summarises the levels of power generation which

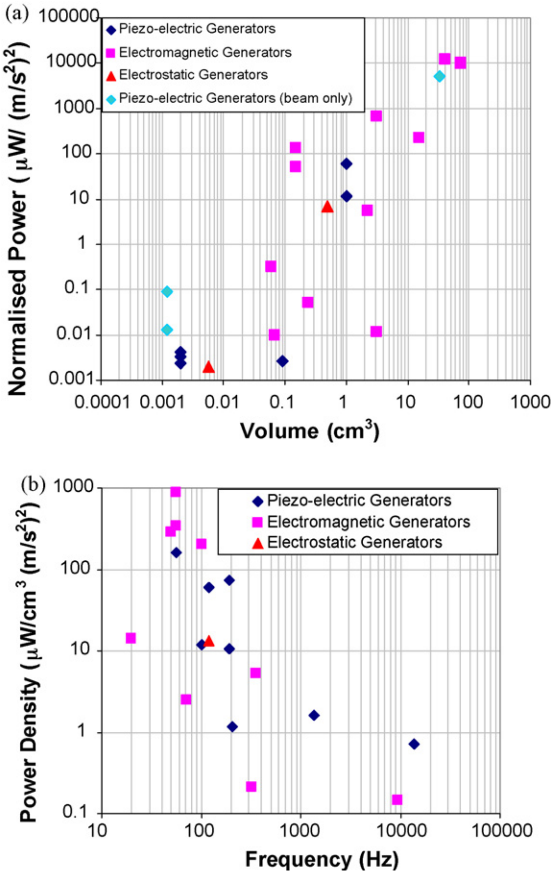

Fig. 2. (a) Power density of reported vibrational generators normalised to $(1\ \mathrm{m/s^2})^2$; (b) power density of reported vibrational generators vs. the frequency of operation. Note the decrease in power density with frequency.

have been reported in the literatures todate [36–48]. Note that the results from the various different generation techniques can only be validly compared if the reported generated power is normalised by the square of the input acceleration. Therefore, the graphs in Fig. 2(a) and (b) plot the reported power generated, normalised to an acceleration of 1 m/s^2.

We can see from the graph that generated power levels generally increase with device volume, indicating that power levels are directly proportional to the volume of the device. In large devices of approximately 100 cm^3 volume, power levels of 10 mW have been achieved (normalised to 1 m/s^2 acceleration) and for small devices with a volume of less than 0.01 cm^3, power levels are less than 10 nW (again normalised to 1 m/s^2 acceleration). Such smaller devices could be batch fabricated using micro-fabrication techniques, and this is a desirable goal from the point of view of cost reduction.

However, it is also worth noting that very few of the reported devices have been fully micro-fabricated.

In general, micro-fabrication is more suitable for electrostatic devices and piezoelectric devices than for electromagnetic devices as it can be shown that the scaling laws dictate that micro-fabricated electromagnetic devices are difficult to operate at optimum conditions [49].

The devices for which the results are summarised in Fig. 2(a) have mostly been designed to operate at a very specific frequency. Although Eq. (1) indicates that the power generated is proportional to the cube of the frequency, this does not account for the fact that, in practical situations, displacements are much smaller at higher frequencies. Thus a more practical analysis is suggested by Fig. 2(b) which indicates that for a fixed acceleration level, the generated power is inversely related to frequency. In fact this is borne out by an analysis of the results reported to date, which show a decrease in generated power with frequency as shown in Fig. 2(b).

It should also be noted that the majority of the piezoelectric and electromagnetic generators reported to-date are resonant devices, i.e. the natural resonant frequency of the generator is matched to the vibration frequency, so that the displacement of the generator mass can be maximised. At resonance, the displacement of the mass is limited only by the damping, which is composed of useful and parasitic damping. This leads to the situation where maximum energy can be extracted where the parasitic damping is a minimum. However, such a device with very low parasitic damping will have a very narrow frequency band and very sharp resonance. In practice, this means that if the resonant frequency of the generator should shift or the frequency of the vibration change, then the generated power decreases drastically. In practice, a generator which has a more broadband response would be of greater practical use. However, there are, to-date, very few reports of such devices in the literature.

To the best of the authors' knowledge, the highest, normalised power density which has been achieved, is approximately 880 μW/cm^3, reported in [48]. This device, shown in Fig. 3, had a volume of 150 mm^3 and achieved a power level of 45 μW, for a 0.6-m/s^2 acceleration at 50 Hz.

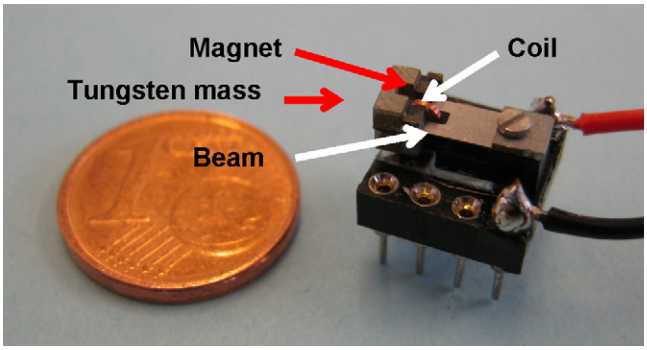

Fig. 3. An electromagnetic-based vibration generator which has delivered approximately 880 μW/cm^3, the highest energy density reported for a vibrational energy harvesting device [48]. This device, with a volume of 150 mm^3, achieved a power level of 45 μW, for a 0.6-m/s^2 acceleration at 50 Hz.

Optimistically, and considering that improvements are possible, a power density of 1 mW/cm^3 at 1 m/s^2 may be achievable for vibration-based generators. Taking into account the fact that real world generators will probably require a more broadband operation than the majority of devices reported todate, and that this broadband response is achieved at the expense of power density, a more conservative estimate of the achievable power density might be 0.1 mW/cm^3 at 1 m/s^2. Considering this, a quick assessment of the feasibility of vibrational energy harvesting for any particular application can be made if the vibration acceleration levels, and the allowable size of the final solution, are known. Some applications such as powering of tyre pressure sensors are entirely feasible based on this, as the acceleration levels present in such an application can be very high (tens of grams). Applications with very low acceleration levels, for example industrial machine monitoring (0.6 m/s^2) are feasible if the volume of the device can be sufficiently large, e.g. >1000 mm^3 in order to supply several hundred μW. The key challenges to be addressed are widening of the bandwidth of the device and a greater understanding of the parasitic damping issues so that the overall power densities can be improved.

2.2.4. Power from human movement

Although not directly relevant to remote sensing, we include a short review of human-powered energy harvesting systems which have relevance to on-the-body environmental monitoring in the form of wearable physiological monitoring systems. Compared to vibrations, human movements are generally characterised by large amplitude and high acceleration levels but very low frequency or, more generally, non-periodic. For example, acceleration levels of up to 100 m/s^2 at frequencies of 2 Hz have been measured for positions on the foot while jogging. The extraction of energy from human movement is far from new. Perhaps the most successful examples of such energy extraction are the self-powered watches of which the Seiko Kinetic and the ETA Autoquartz [32] are the best modern examples. Apart from these wristwatches, the most researched area is the extraction of energy from walking. For example, it has been calculated that up to 7 W of power is available per foot for the average human walking. Several examples of generators which convert walking motion have been reported. These range from approaches which use shoe-mounted, conventional rotary generators [50] and linear generators [51], hydraulics coupled to piezoelectrics [52]

Table 1
Typical data for various energy harvesting techniques that can be used for remote wireless environmental sensing

	Conditions	Power density	Area or volume	Energy/day
Vibration	1 m/s^2	100 μW/cm^3	1 cm^3	8.64 J
Solar	Outdoors	7500 μW/cm^2	1 cm^2	324 J (assuming light is available for 50% of the time)
Solar	Indoors	100 μW/cm^2	1 cm^2	4.32 J (assuming light is available for 50% of the time)
Thermal	$\Delta T = 5\,^\circ$C	60 μW/cm^2	1 cm^2	2.59 J (assuming heat is available for 50% of the time)

and electroactive polymers [32] and piezoelectric sole inserts [50]. The highest power actually achieved to date from any of these approaches has been in the range of 0.2–0.8 W, so that there is still significant room for improvement.

We conclude this review by summarising, in Table 1, the typical power density levels which are achievable from the various energy harvesting techniques that can be used for remote wireless environmental sensing. These power densities are used to calculate energy levels available over the course of a single day assuming, in the case of solar and thermal energy, that the light or heat source is only available 50% of the time. In the later sections, these values are used to illustrate the potential impact that energy harvesting techniques can have on wireless sensor node lifetimes.

3. Wireless sensor deployment case study in building management

In order to illustrate the energy requirements for wireless sensor systems, we present, in case study form, the analysis of a wireless sensor operation using the Zigbee protocol in a wireless building management application [59]. The Zigbee standard is a low-power, wireless communications standard defined by Zigbee alliance. The intended applications of Zigbee are home and building management, industrial controls, and general sensing applications. In this case study, since there is lots of possibilities of network topologies and networking management strategies, we limit ourselves to estimate the energy consumption for the Zigbee end device to sample data from different commercial-off-the-shelf (COTS) sensors and transmit the data back to the base station.

The Zigbee platform employed is based around the Zigbee compliant EM2024 transceiver and the low power, 8-bit, Atmega128L microcontroller. In this case, the sensor node is required to sense five different parameters: temperature, light level, humidity, vibration levels and barometric pressure. Thus a complete cycle for the sensor node involves sampling from the five sensors, processing the data and transmitting the sampled data. Table 2 details the specifications of the sensors used. In particular, the energy per sensor sample shows that the temperature sensor has the lowest energy utilisation while the light and temperature sensors require the shortest sampling time of 0.2 ms.

Table 2
Sensor specifications for wireless module in building management system

Sensor	Voltage (V)	Current (mA)	Power (mW)	Sampling time (s)	Energy/sample (μJ)
Temperature	3.3	0.008	0.026	0.0002	0.00528
Light	3.3	0.03	0.099	0.0002	0.0198
Humidity	3.3	0.3	0.99	0.8	792
Vibration	3.3	0.6	1.98	0.02	39.6
Barometric Pressure	5.0	7.0	35.0	0.02	0.7

The key sources of energy utilisation to be considered in defining the wireless sensor module energy budget are as follows:

- *Sensor sampling*: This includes the wake-up/stabilisation time associated with the sensor and the data acquisition time. At all other times, the sensors are completely off and consume no power.
- *Processor*: The microcontroller controls the wireless module operation and undertakes any required processing of the sensor data. When not processing data or controlling the system operation, the processor is in a low power SLEEP mode.
- *Transceiver*: The RF transceiver enables the wireless module to communicate and transmit the processed sensor data. Again, when not transmitting or receiving, the transceiver is in a low power SLEEP mode.

Table 3 provides detailed data of the calculated energy utilisation for the wireless sensor in both ACTIVE and SLEEP mode. The wireless system undertakes a full operation of sampling, processing and transmission in 864 ms. It is interesting to note that, although the transceiver has by far the largest power consumption, in this application, and contrary to the general opinion, some of the sensors dissipate significantly more energy than the transceiver. In particular the humidity sensor requires a long sampling time, during which time the processor is also active, thus giving rise to energy usage which is 60 times higher than the transceiver energy utilisation. This issue of power-hungry sensors is going to present a major R&D challenge in the wireless, chemo-biosensor space.

Note that in Table 3, even in SLEEP mode, the module is dissipating 54 μW of power due to the stand-by power of the transceiver and the microcontroller. Table 4 presents data for a range of cycle times from 1 s to 24 h in order to illustrate the impact of the duty cycle-driven operation. Here the duty cycle is defined as $t_{\text{on}}/t_{\text{cycle}}$, where t_{on} is the time for which the system is active (sampling, processing and transmitting or receiving data), and t_{cycle} is the time between measurements. It is clear from the table that, even with a 1-min cycle time for an 864 ms ACTIVE time, the sensor module is already in SLEEP mode for almost 99% of the time. It is also clear that for a 20 min cycle time, the energy utilisation in SLEEP mode exceeds the ACTIVE

Table 3
Detailed data for the calculated energy budget for the wireless sensor system in operation and sleep mode

Operation mode	Time (s)	Sensors power (mW)	Processor power (mW)	Transceiver power (mW)	Total power (mW)	Total energy (mJ)
Transmitting	0.003908	0.000	19.965	63.162	83.127	0.325
Receiving	0.000452	0.000	19.965	71.511	91.476	0.041
Processing	0.02	0.000	19.965	0.018	19.983	0.400
Sampling 1 (temperature)	0.0002	0.029	21.054	0.018	21.101	0.004
Sampling 2 (light)	0.0002	0.109	21.054	0.018	21.181	0.004
Sampling 3 (humidity)	0.8	1.089	21.054	0.018	22.161	17.729
Sampling 4 (vibration)	0.02	2.178	21.054	0.018	23.250	0.465
Sampling 5 (pressure)	0.02	38.500	21.054	0.018	59.572	1.191
Total active	0.86476					20.160
Sleep		0	0.0363	0.018	0.054	

mode energy by almost a factor of three and thus dominates the module energy utilisation, thereby providing the ultimate limit to the power system lifetime. Table 4 also shows the dramatic reduction in total energy utilisation over the period of 1 day, as the module cycle time is extended from 1 s to 24 h.

This energy must be supplied to the system and, in the most common case, is simply stored in a battery. Clearly therefore, the lifetime of the sensor node depends on the storage capacity of the battery and the total energy consumption of the system. However, if the energy harvesting techniques discussed above are used to augment the battery power, then the energy storage requirement is reduced by the amount of energy harvested from the environment. An estimate of the energy harvesting capabilities of various techniques has been given in Table 1 above. For reference, Table 5 provides the energy capacity of typical commercially available battery form factors.

In Fig. 4, the impact of the various energy harvesting techniques on the stored energy requirements, E_s, is presented by plotting the system energy, E_{sys}, minus the harvested energy, E_h, i.e. $E_s = E_{sys}–E_h$, for a 24-h period, as a function of the on-duty cycle for the sensor node. For the sake of comparison, we have arbitrarily chosen the size of the energy-harvesting device to be 1 cm^2 for the solar and thermal scavenger and 1 cm^3 for the vibration harvester. With no energy harvesting, the energy storage requirement varies from a constant sleep energy of approximately 5 J for duty cycles less than 0.02% to a maximum of 1746 J for a duty cycle of approximately 86%. Considering the energy available from harvesting techniques in Table 1, the sleep energy of the system could be provided by the outdoor solar and vibration harvesting techniques. For these energy-harvesting techniques, there is, in principle, a maximum duty cycle, below which all of the system energy could be provided by the energy-harvesting system. For outdoor solar, this maximum duty cycle is approximately 20%, and for vibration harvesting it is approximately 0.4%. At duty cycles less than these, the system could essentially be battery-less. At duty cycles greater than these, the various energy harvesting techniques can only provide part of the system energy and therefore energy storage, in the form of a battery, is required with the battery lifetime implications discussed above.

To have a truly autonomous, battery-less system one could consider scaling the energy harvester so as to provide all of the system energy needs. In such a case, energy storage would still be required in order to supply the system peak power requirements, however this could be provided by a capacitor, the lifetime of which, in terms of charge cycles is orders of magnitude greater than a typical battery. In order to consider realistic scaling of the thermal and vibration harvesting devices, it would be vital that specific information relating to the available temperature difference and vibration acceleration levels be known. We assume that, in a building management application, temperature differences of 5 °C would be available by placing the thermal energy-harvesting device on a heater. In a building situation, vibrations are present in air-conditioning units, windows, floors and most equipment which use electric machines (e.g. pumps and motors). Roundy et al. [37] measured vibrations in HVAC

Table 4
Energy budget for a range of wireless sensor system cycle times from 1 s to 24 h

Sleep time	Sleep time (s)	Duty cycle on-time (%)	Duty cycle off-time (%)	Energy in sleep mode (mJ)	Energy in operation mode (mJ)	Total energy per cycle (mJ)	Total energy/day (J)
1 s	1	90.48	9.52	0.05	21.53	21.59	1864.95
2 s	2	45.24	54.76	0.11	21.53	21.64	934.83
30 s	30	3.02	96.98	1.63	21.53	23.16	66.71
1 min	60	1.51	98.49	3.27	21.53	24.80	35.71
2 min	120	0.75	99.25	6.53	21.53	28.06	20.21
20 min	1,200	0.08	99.92	65.34	21.53	86.87	6.25
1 h	3,600	0.025	99.975	196.02	21.53	217.55	5.22
12 h	43,200	0.002	99.998	2352.24	21.53	2373.77	4.75
24 h	86,400	0.0010	99.9990	4704.48	21.53	4726.01	4.73

Table 5
Energy capacities of typical battery form-factors

Battery type	Voltage (V)	Capacity (mA h)	Energy (J)
12 V Car battery	12	32,000	1,382,400
AA 1.5 V × 2	3	2,900	31,320
Mobile/cell phone	3.7	900	11,988
Coin cell CR2450	3	600	6,480
Coin cell CR2032	3	250	2,700
Coin cell LR44	3	105	1,134
Li polymer film	3	25	270

Move to later in text to show energy capacity of batteries.

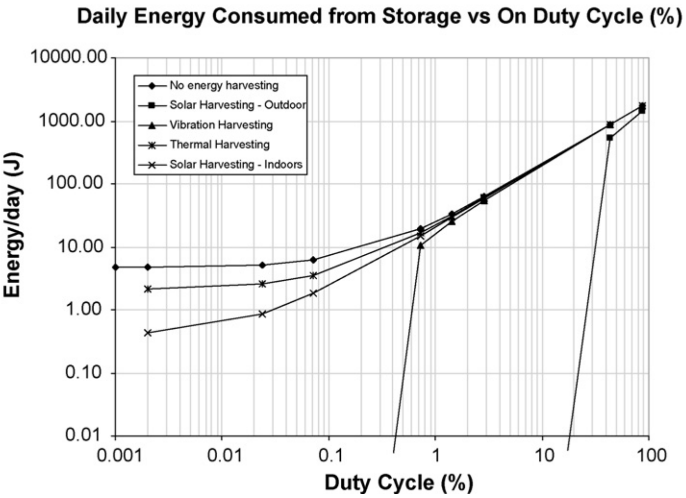

Fig. 4. Daily energy consumed by wireless sensor node in Zigbee application within building management system. Graph also includes the contribution that can be made to the wireless sensor system energy budget by the various energy harvesting approaches under consideration. Note that the size of the energy harvesting devices used in the analysis are 1 cm^2 for the solar and thermal scavenger and 1 cm^3 for the vibration harvester.

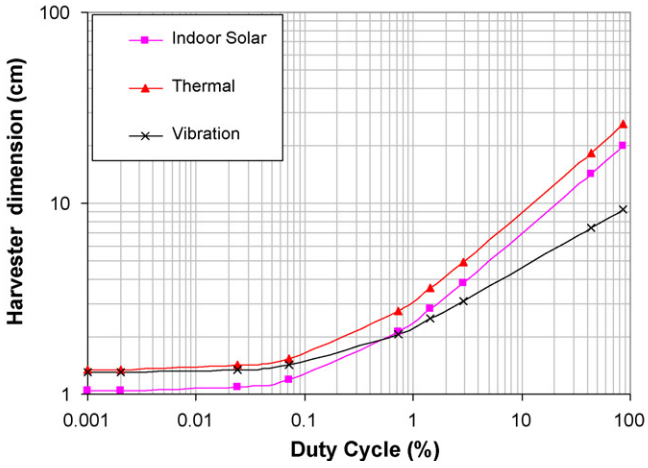

Fig. 5. For the building management case study under discussion, this graph plots the dimension of energy harvester required to supply the sensor node daily energy needs as a function of sensor node duty cycle. A temperature difference of 5° is assumed for the thermal harvester and vibrations of 0.5 m/s^2 are assumed for the vibration harvester.

vents in the range of 0.2–1.5 m/s^2 at 60 Hz and in office windows in the range of 0.7 m/s^2 at 100 Hz. Torah et al. designed their generator to operate from vibrations in an air compressor unit, which they found to be in the range of 0.5 m/s^2 at 50 Hz. We can therefore assume that vibration with acceleration levels of 0.5 m/s^2 are available in a building environment.

In the graph in Fig. 5, the dimension of the energy harvester required to supply the system energy is plotted against sensor node duty cycle. The dimension is taken as the square root of the required area for the thermal and solar energy harvesters, and the cube root of the required volume for the vibration harvester. The plot indicates that for low duty cycles of less than 0.07% (a reading every 20 min), an energy harvester device with linear dimensions of approximately 2 cm on a side would be sufficient to supply the energy. For high duty cycles, dimensions of up to 25 cm for thermal, 20 cm for indoor solar and 10 cm for vibration are required.

4. Wireless sensor deployment case study in remote environmental monitoring

The promise of wireless sensor systems is that they can deliver remote environmental monitoring technology whereby autonomous wireless sensor modules can be deployed in large numbers for long periods of time; of the order of years. This requirement is not in line with the utilisation of batteries as the principle energy source as it precludes the possibility of regularly replacing batteries. Even if one could afford the manpower resource to replace batteries, this would assume that one could reliably and quickly locate all the wireless devices. This is the driver for identifying suitable, truly autonomous sources of power for wireless sensors – that is to facilitate the long term, large-scale deployment of millions of sensors which do not need replenishing of the energy source during the lifetime of the monitoring programme – that is “deploy and forget”.

Table 6 presents data for a prototype remote environmental monitoring system which is being investigated for assessment of wireless sensors to address the EU Water Framework Directive. The directive requires that, by 2015, all European bodies of water will be required to achieve pre-defined quality levels [60]. From Table 6, the power requirements and sampling time for the developmental sensors result in over 8.5 J of energy per measurement cycle. This figure contrasts with the very low figure, in Table 3, of 20.16 mJ for a full operation cycle of sensor sampling, data processing and data transmission in the building management case study.

Table 7 provides a first-order estimate of the anticipated energy budget associated with a fully operational remote environmental monitoring unit. A system operating cycle of once in every 20 min is assumed. As well as the energy budget for the sensor measurement cycle, the table includes estimates for the other system functions with significant energy usage. These include data processing (assumed as 10% of sensor measurement energy budget), long-range data transmission, liquid pumping required for fluid transport and control during sensing, sensor calibration and cleaning operations. For data transmission, a long-range transceiver, operating at 433 MHz, is assumed which

Table 6
Sensor specifications for a prototype, remote, wireless, water-quality, monitoring system

Sensing parameter	Voltage (V)	Current (mA)	Power (mW)	Warm-up time (s)	Energy per sample (mJ)
Temperature	10	12	120	5	600
pH	10	17.5	175	3	525
Conductivity	12	12.8	153.6	3	460.8
Dissolved oxygen	10	27.5	275	10	2750
Turbidity	10	43	430	10	4300
Water level	10	12	120	0.01	1.2

will transmit data over a distance of 6 km, line of sight, while dissipating 100 mW over a time interval of 1 s (worst case), thereby dissipating 100 mJ per operation cycle. For the fluid transport system, a worst case estimation is also assumed, that the system requires a 240 mW pump (i.e. 20 mA at 12 V) operating for 5 min after every measurement cycle for sensor cleaning and calibration purposes, thereby requiring 72 J of energy per measurement. One also needs to take into account the "SLEEP" mode energy usage of the system. An estimate for this figure is taken from the building management case study which was less than 6 J per day for measurement cycles over 20 min. From Table 7, it can be seen that the fluid transport system energy budget is almost an order of magnitude higher than the sum of the next highest energy figures, that is the sensor measurements and the sleep mode energy. It is also noteworthy that the energy used in the data processing and data transmission operations are negligible in comparison.

Currently, this first prototype system is housed in a 125 l water tight, plastic container, mainly to accommodate the fluidic system associated with the sensor measurement, cleaning and calibration. A car battery is used as the power source which has a capacity of approximately 32 A h equivalent to 1.38 MJ of energy. Furthermore, the lifetime of a car battery is typically 4 years in a harsh automotive environment, giving the option of a relatively long term, large capacity, energy storage unit.

To deliver a "deploy and forget" solution, the battery would also require an energy source for daily recharging. If we assume an outdoor solar cell providing the energy to the system, at a harvesting level of 324 J/(day cm^2) (as presented in Table 1 for 12 h of light on a cloudy, overcast day), the daily energy budget for the system of 6296.4 J could be delivered by a solar cell panel of approximately 20 cm^2 in area. Therefore, even assuming significantly lower daylight hours, standard, commercial, solar panels, available in low cost, robust formats, can more than adequately supply the energy requirements for the proposed remote environmental monitoring system. These solar panels come in water-proof, corrosion-proof solar cell arrays with adjustable mounting stands, UV-proof polycarbonate plastic case and built-in blocking diode to prevent discharge at night.

Table 7
Estimated energy budget for remote environmental monitoring system

Operation	Energy per operation cycle (J)	Energy per day (J)
Sensor measurement	8.5	612
Data processing	0.85	61.2
Data transmission	0.1	7.2
Fluidic transport, sensor calibration, system cleaning	72	5184
Sleep Mode	6	432
Total system energy budget	87.45	6296.4

5. Conclusions and future perspectives

Wireless sensor systems are emerging as a key technology for future remote environmental monitoring in both our built and external environments. A case study presented for a multi-sensor, building management system, operating using the Zigbee protocol shows that, even with a 1-min cycle time for an 864 ms ACTIVE time, the sensor module is already in SLEEP mode for almost 99% of the time. It is also clear that, for a 20-min cycle time, the energy utilisation in SLEEP mode exceeds the ACTIVE mode energy by almost a factor of three and thus dominates the module energy utilisation thereby providing the ultimate limit to the lifetime of the energy source.

A key issue for these wireless node designs is that they must achieve high degrees of power-efficiency for truly autonomous, maintenance-free operation, where it is likely that nodes will require deployment for periods of years and the cost of battery replacement will be prohibitive and impractical. From a review of energy harvesting technologies, including outdoor and indoor solar energy and energy from thermal gradients and vibrations, there is, in principle, a maximum duty cycle of operation for a wireless sensor node, below which all of the system energy could be provided by the energy harvesting system in conjunction with a rechargeable battery to store energy for peak power requirements and for periods when the energy harvester is not operating (i.e. at night for solar cells). Alternatively, a capacitor could be utilized to store the energy, the lifetime of which, in terms of charge cycles, is orders of magnitude greater than a typical battery.

Clearly, large-scale deployment of bulky, remote water quality monitoring systems will not be economically viable, even with the predicted volumes required on a European-wide, or even a global scale. Therefore, a key issue for the future emergence of a viable market in this area will be the development of miniaturised systems which will ultimately be enabled by "lab-on-a-chip" technologies. In this case, microelectronics and microsystems will be required to deliver robust, miniaturised, low power and low-cost chemo-biosensors and associated microfluidic/micropumping systems which can be interfaced to the already miniaturised electronics. Reliable sensors will require anti-fouling coatings on sensor surfaces and, most likely, utilising non-contact measurement protocols. The microfluidic transport systems will be required to be low power, ideally zero power, with high reliability over the full lifetime of the system. These "lab-on-a-chip" systems also raise the challenge of providing adequate supply of reagents to enable proper cleaning and calibration over the entire lifetime of the system. Again, ideally, a sensor system that does not require cleaning or calibration would solve many of these challenges. These miniaturised systems can also be expected to deliver significant reductions in system energy budgets and therefore the size of the required power supply system (i.e. the energy harvester and the energy storage element), thereby dramatically increasing the lifetime of the system in the field. Further study is required to evaluate the long-term performance and reliability of conventional rechargeable battery technologies. The remote and large scale nature of future environmental deployments may restrict their application due to their inherent lifetime characteristics of self-discharge, number of charge cycles, impact of environmental conditions and potential environmental impact of the batteries.

As a closing remark, serious consideration should be given to the ultimate water-based chemo-biosensor, the fish. Fish, and shell-fish, have been used to monitor water quality for centuries. The interfacing of electronics to a mussel "biosensor" has been demonstrated in a water quality monitoring system using electrodes to monitor impedance changes in the shell fish [61,62] and deserves further attention in the context of future large scale, autonomous environmental monitoring.

Acknowledgements

The authors wish to acknowledge the Irish Martine Institute and Ireland's Environmental Protection Agency for funding for the Smart Coast project (Grant-aid Agreement No. AT/04/01/06) under the Marine RTDI Measure, Productive Sector Operational Programme, National Development Plan 2000–2006.

References

[1] C.M. McGraw, S.E. Stitzel, J. Cleary, C. Slater, D. Diamond, Talanta 71 (3) (2007) 1180–1185.
[2] Ho.B. Glasgow, J.M. Burkholder, R.E. Reed, A.J. Lewitus, J.E. Kleinman, J. Exp. Mar. Biol. Ecol. 300 (1/2) (2004) 409–448.
[3] H. Auernhammer, Comput. Electron. Agric. 30 (1–3) (2001) 31–43.
[4] W. Vandenberghe, B. Latre, F. De Greve, P. De Mil, S.V. den Berghe, K. Lamont, I. Moerman, M. Mertens, J. Avonts, C. Blondia, G. Impens, A System Architecture for Wireless Building Automation, IST Mobile & Wireless Communication Summit, Myconos, Greece, 2006.
[5] Strategic Research Agenda of European Technology Platform on Smart Systems Integration, version 2, February 28, 2007.
[6] K. Baert, B. Gyselinckx, T. Torfs, V. Leonov, F. Yazicioglu, S. Brebels, S. Donnay, J. Vanfleteren, E. Beyne, C. Van Hoof, Microelectron. J. 37 (12) (2006) 1563–1568.
[7] www.xbow.com/.
[8] www.moteiv.com/.
[9] www.dust-inc.com/.
[10] www.phidgets.com/.
[11] www.meshnetics.com/.
[12] www.sensicast.com/wireless_sensors.php.
[13] www.accsense.com/.
[14] www.millennial.net/products/meshscape.asp.
[15] www.ember.com/products_index.html.
[16] www.onworld.com.
[17] J. Barton, et al., Sensor Actuat. A 132 (2006) 362–369.
[18] M. Niedermayer, et al., Proceedings of the Fifth International Conference on Information Processing in Sensor Networks, IPSN 2006, 2006, pp. 391–398.
[19] S. Stoukatch, et al., Proceedings of the ECTC 2006, Sheraton San Diego, San Diego, California, May 30–June 2, 2006, pp. 404–408.
[20] K. Lorincz, et al., IEEE Perv. Comput. 3 (4) (2004) 16–23.
[21] B. Lo, et al., Proceedings of the Perspective in Pervasive Computing Conference, October, 2005, pp. 23–28.
[22] D. Mclntire, et al., Proceedings of the Fifth International Conference on Information Processing in Sensor Networks (IPSN 2006), April 19–21, 2006, pp. 449–457.
[23] J. Polastren, et al., Proceedings of the Fourth International Symposium on Information Processing in Sensor Networks (IPSN 2005), 2005, pp. 370–375.
[24] H. Gellersen, et al., IEEE Perv. Comput. 3 (3) (2004) 74–82.
[25] J. Beutel, et al., Proceedings of the First European Workshop on Sensor Networks (EWSN 2004), 2004, pp. 323–338.
[26] E.M. Tapia, et al., Proceedings of the Extended Abstracts Ubicomp 2004: Ubiquitous Computing, 2004.
[27] N. Edmonds, et al., Proceedings of the Fourth International Symposium on Information Processing in Sensor Networks, IPSN 2005, 2005, pp. 393–397.
[28] D. Lymberopoulos, et al., Proceedings of the Fourth International Symposium on Information Processing in Sensor Networks, IPSN 2005, 2005, pp. 449–454.
[29] H. Dubois-Ferriere, et al., Proceedings of the Fifth International Conference on Information Processing in Sensor Networks, IPSN 2006, 2006, pp. 358–365.
[30] L. Nachman, et al., Proceedings of the Fourth International Symposium on Information Processing in Sensor Networks, IPSN 2005, 2005, pp. 437–442.
[31] M. Ouwerkerk, F. Pasveer, N. Engin, in: Proceedings of the International Workshop on Wearable and Implantable Body Sensor Networks (BSN'06).
[32] J. Paradiso, T. Starner, IEEE Perv. Comput. 4 (1, January–March) (2005).
[33] T. Starner, J. Paradiso, in: C. Piguet (Ed.), Low Power Electronics Design, CRC Press, 2004 (Chapter 45).
[34] S. Beeby, J. Tudor, N.M. White, Meas. Sci. Technol. 17 (2006) R175–R195.
[35] N.G. Stephen, J. Sound Vib. 293 (2006) 209–425.
[36] PMG Perpetuum, http://perpetuum.co.uk/products.htm.
[37] S. Roundy, P.K. Wright, J. Rabaey, Comput. Commun. 26 (2003) 1131–1144.
[38] S. Roundy, P.K. Wright, Smart Mater. Struct. 13 (2004) 1131–1142.
[39] Y. K. Hong, K. S. Moon, M. Levy, Single crystal piezoelectric transducers to harvest vibration energy, Procedure SPIE 2005.
[40] B. Cavallier, P. Berthelot, H. Nouira, E. Foltete, L. Hirsinger, S. Ballandras, Energy harvesting using vibrating structures excited by shock, Ultrasonic symposium 2005, IEEE.
[41] Y.B. Jeon, R. Sood, J.-h. Jeong, S.-G. Kim, Sensors Actuat. A: Phys. 122 (1) (2005) 16–22.
[42] E. Lefeuvre, A. Badel, C. Richard, L. Petit, D. Guyomar, Sensor Actuat. A: Phys. 126 (2 14 February) (2006) 405–416.
[43] E.P. James, M.J. Tudor, S.P. Beeby, N.R. Harris, P. Glynne-Jones, J.N. Ross, N.M. White, Sensor Actuat. A 110 (2004).
[44] M. El-hami, P. Glynne-Jones, N.M. White, M. Hill, S. Beeby, E. James, A.D. Brown, J.N. Ross, Sensor Actuat. A: Phys. 92 (1–3) (2001) 335–342.
[45] P. Glynne-Jones, M.J. Tudor, S.P. Beeby, N.M. white, Sensor Actuat. A 110 (2004).

[46] S.P. Beeby, M.J. Tudor, R.N. Torah, E. Koukharenko, S. Roberts, T. O'Donnell, S. Roy, Macro and microscale electromagnetic kinetic energy harvesting generators, DTIP, 2006.
[47] C.L. Steve, Yuen, M.H. Johnny, Lee, J. Wen, Li, H.W. Philip, Leong, An AA-sized Micropower generator and its Application to a Wireless Sensor System, IEEE Pervasive Computing 6 (1) (2006) 64–72.
[48] R.N. Torah1, S.P. Beeby1, M.J. Tudor1, T. O'Donnell, S. Roy, Proceedings of the Sixth International Workshop on Micro and Nanotechnology for Power Generation and Energy Conversion Applications, PowerMEMS, November 29–December 1, Berkley, CA, 2006.
[49] T. O'Donnell, C. Saha, S. Beeby, J. Tudor, Microsys. Technol., January, 2007.
[50] N.S. Shenck, J.A. Paradiso, IEEE Micro 21 (3) (2001) 30–42.
[51] M. Duffy, D. Carroll, IEEE Power Electronic Specialists conference, Aachen, Germany, 2004.
[52] J.F. Antaki t, et al., ASAIO J. 41 (3) (1995) M5888–M6595.
[53] J.F. Randall, Designing Indoor Solar Products: Photovoltaic Technologies for AES, John Wiley & Sons, 2005 (Chapter 5).
[54] Seiko Instruments Inc., http://www.sii.co.jp/info/eg/thermic_main.html.
[55] V. Leonov, P. Fiorini, S. Sedky, T. Torfs, C. Van Hoof, Thermoelectric MEMS generators as a power supply for a body area network, Tranducers '05, Seoul, Korea, June 5–9, 2005.
[56] Thermo Life Energy Corp. http://www.poweredbythermolife.com/.
[57] H. Bottner, et al., J. Microelectromech. Syst. 13 (3) (2004) 414–420.
[58] G.J. Snyder, J.R. Lim, C.K. Huang, J.P. Fleurial, Nat. Mater. 2 (2003) 528–531.
[59] www.zigbee.org
[60] www.wfdireland.ie
[61] M.C. Lucas, Sci. Total Environ. 251/252 (2000) 223–232.
[62] T. Damien, C. Pierre, C. Aurélie, D. Gilles, M. Jean-Charles, Environ. Toxicol. Chem. 22 (4) (2003) 914–920.

Available online at www.sciencedirect.com
ScienceDirect
Talanta 75 (2008) 624–628
Talanta
www.elsevier.com/locate/talanta

Position-independent chemical quantitation with passive 13.56-MHz radio frequency identification (RFID) sensors

Radislav A. Potyrailo*, Henri Mouquin, William G. Morris

Materials Analysis and Chemical Sciences, General Electric Global Research Center, Niskayuna, NY, United States

Received 23 February 2007; accepted 13 June 2007
Available online 28 June 2007

Abstract

Recently, we have demonstrated an attractive approach to adapt conventional radio frequency identification (RFID) tags for multianalyte chemical sensing. These RFID sensors could be very attractive as ubiquitous distributed remote sensor networks. However, critical to the wide acceptance of the demonstrated RFID sensors is the analyte-quantitation ability of these sensors in presence of possible repositioning errors between the RFID sensor and its pickup coil. In this study, we evaluate the capability for such position-independent analyte quantification using multivariate analysis tools. By measuring simultaneously several parameters of the complex impedance from such an RFID sensor and applying multivariate statistical analysis methods, we were able to compensate for the repositioning effects such as baseline signal offset and magnitude of sensor response to an analyte.

Keywords: Radio frequency identification (RFID) tag; RFID sensor; Ubiquitous distributed sensor network; Chemical sensing; Complex impedance; Multivariate statistical analysis

1. Introduction

Proximity sensors operating on the principles of inductive coupling have been under development since the 1950s when “endo-radiosonde” sensors of 2–6 mm in diameter were reported [1] that consisted of a passive LC resonant circuit, the resonant frequency of which was predictably affected by an ambient environment and was measured with an external pickup coil. More recently, a variety of other similar passive LC resonant circuit-based sensors have been demonstrated [2–5].

Radio frequency identification (RFID) tags are widely employed for automatic identification of animals, tagging of garments, labels, and combinatorial chemistry reaction products, and detection of unauthorized opening of containers [6–8]. For these and many other applications, the attractiveness of conventional passive RFID tags come from their low cost of being less than $1 [9,10]. For sensing applications such as temperature, pressure, and some others, RFID tags required a specific redesign of portions of their electronic circuitry [11,12]. Furthermore, those RFID sensors also required a battery [6], that eliminated their attractiveness as passive sensors.

Recently, we have demonstrated an approach for multianalyte chemical identification and quantitation using a single conventional passive RFID tag [13–15]. These RFID sensors are very attractive as ubiquitous distributed remote sensor networks. Unlike other approaches of using RFID sensors, where a special tag should be designed at a much higher cost, we utilized a conventional RFID tag and coated it with chemically sensitive films to form a chemical sensor (see Fig. 1). Upon a careful selection of the sensing film and measurement conditions, we were able to achieve part-per-billion vapor detection limits in air. In such RFID chemical sensor, both the digital tag ID and the complex impedance of the resonant circuit of the RFID antenna are measured. The measured digital ID provides information about the sensor and the object onto which the sensor is attached, while measured complex impedance provides multivariate response for chemical determinations.

However, critical to the wide acceptance of the demonstrated RFID sensors is the analyte-quantitation ability of these sensors in presence of possible repositioning errors between the RFID sensor and its pickup coil. In this study, we evaluate the capability for such position-independent analyte quantification using

---

* Corresponding author.
E-mail address: Potyrailo@crd.ge.com (R.A. Potyrailo).

0039-9140/$ – see front matter © 2007 Elsevier B.V. All rights reserved.
doi:10.1016/j.talanta.2007.06.023

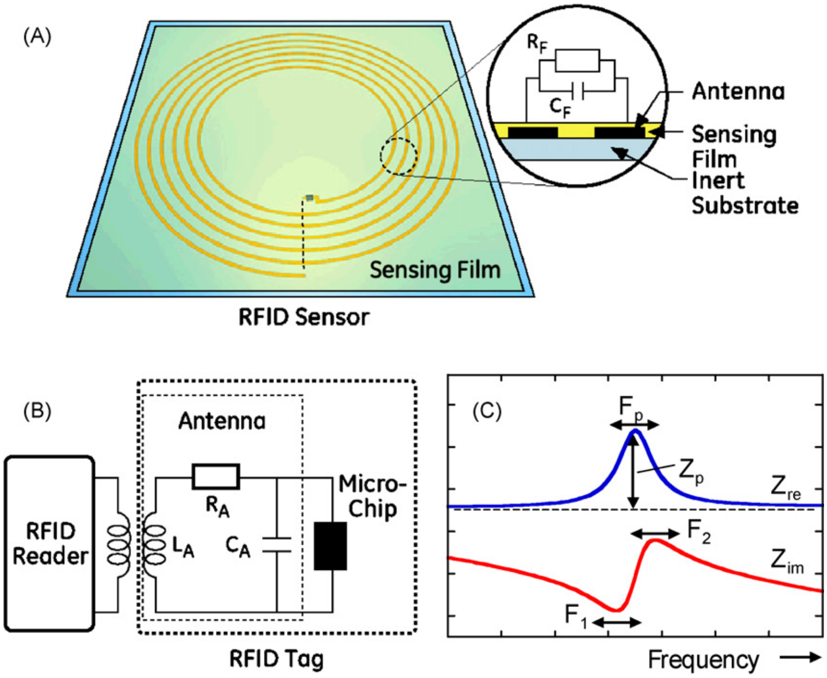

Fig. 1. Strategy for the application of conventional passive RFID tags for chemical sensing. (A) Adaptation of a conventional RFID tag for chemical sensing by deposition of a sensing film onto the resonant circuit of the RFID antenna. Inset, analyte-induced changes in the film material affect film resistance (R_F) and capacitance (C_F) between the antenna turns, (B) schematic of digital ID reading from the RFID tag and the equivalent circuit of the antenna of the RFID tag, and (C) measured parameters from a single RFID sensor for multiparameter chemical detection and quantitation. Arrows indicate changes of respective measured parameters.

multivariate analysis tools. By measuring simultaneously several parameters of the complex impedance from such an RFID sensor and applying multivariate statistical analysis methods, we were able to compensate for the repositioning effects.

2. Experimental

2.1. RFID sensor

To perform analyte-quantitation measurements, an RFID sensor was made by applying a chemically sensing polymeric film onto a 13.56-MHz RFID tag (Texas Instruments, model RI-I03-112A-03, antenna size 22.5 mm × 38 mm). The sensing film was a composite poly(vinyl acetate)/carbon black polymer film responsive to relative humidity in air. To form an RFID sensor, the film was applied onto the RFID tag by a draw-coating process [16]. For each position of the sensor, two replicate exposures to humid air were performed. Humid air was generated by bubbling dry air through water at room temperature. Thus, during each step, the sensor environment was switched twice from dry air to 45% relative humidity (RH) air as measured with a reference humidity meter.

2.2. Test setup

For evaluations of repositioning effects, we assembled a test system as shown in Fig. 2. It contained an RFID sensor positioned in a low dead volume gas flow cell. A pickup coil was made from several turns of a copper wire with a form factor matching the RFID sensor and was positioned outside the flow cell on a *X*–*Z* translation stage. The relative position of the RFID sensor and the pickup coil was changed in a controlled fashion. Fig. 3 illustrates the different tested positions of the RFID sensor in the *X*- and *Z*-direction with respect to the pickup antenna coil. The studied repositioning conditions-included 5-mm step changes in *Z*-direction (0, 5, 10, 15, 20 mm and back to 0 mm) and 5-mm step changes in *X*-direction (0, 5, 10, 15, 20, 15, 10, 5, 0 mm).

Digital ID readings from the memory micro-chip of the RFID tag were performed with an RFID reader (Model M-1, SkyeTek, Westminster, CO) operated under a computer control using LabVIEW. RFID sensor measurements were performed with a network analyzer (Model 8751A, Hewlett Packard, Palo Alto, CA) under a computer control using LabVIEW. The network analyzer was used to scan the frequencies over the range of interest and to collect the complex impedance response from

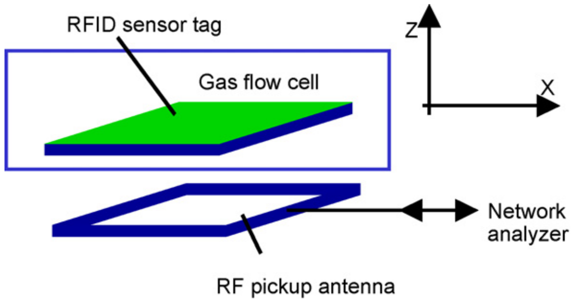

Fig. 2. Schematic of a test system for the evaluation of the analyte-quantitation ability of RFID sensors in presence of repositioning errors between the RFID sensor and a pickup coil.

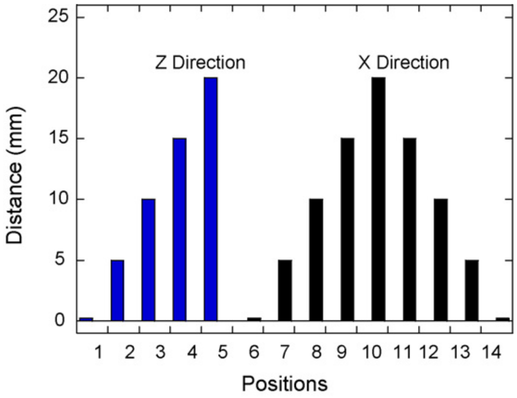

Fig. 3. Different tested positions of the RFID sensor in the *X*- and *Z*-direction with respect to the pickup antenna.

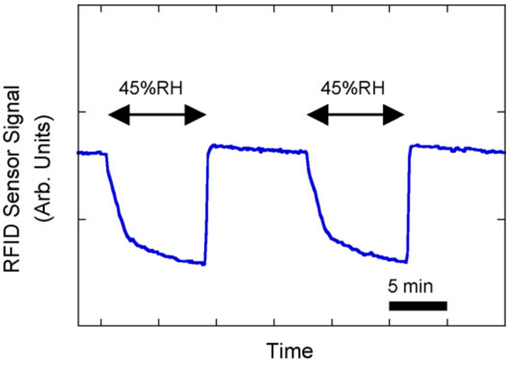

Fig. 4. Example of replicate ($n = 2$) responses of the RFID sensor to 45% RH and dry air for a (0, 0) position of the sensor.

the RFID sensor. The collected complex impedance data was analyzed using KaleidaGraph (Synergy Software, Reading, PA) and PLS_Toolbox (Eigenvector Research, Inc., Manson, WA) operated with Matlab (The Mathworks, Inc., Natick, MA).

3. Results and discussion

3.1. Sensor film response at a fixed position

As a model system for studies of repositioning effects, we selected detection of humidity because of the ease in the implementation of a humidity sensor with a stable, reproducible response. Polymeric films that use a poly(vinyl acetate) as a pure polymer or formulated with carbon black or carbon nanotubes are well known as materials for sensing of polar vapors [17–23].

In polymeric sensors based on electrical energy transduction, polymer swelling induces the conductivity or capacitance change in composite polymeric formulations. Typically, these composite polymeric formulations are comprised of nonconductive polymers and conductive additives such as carbon particles, carbon nanotubes, metal nanoclusters, etc. [20,24–31]. The function of this type of sensors can be explained with the classical percolation theory [32,33], which assumes the polymer matrix to be a perfect insulator and the conductivity change of the polymer composite from a perfect insulator to a conductor.

An example of replicate ($n = 2$) responses of the RFID sensor to 45% RH and dry air for a (0, 0) position (X, Z) of the sensor is presented in Fig. 4. Upon sensor repositioning, we were interested in three aspects of position-induced sensor response effects: (1) sensor signal shift upon exposure to dry carrier gas (baseline signal offset), (2) sensor signal change from the baseline signal upon exposure to 45% RH (analyte response), and (3) changes in sensor noise.

3.2. Measurements of multiple responses from RFID sensor

For position-independent analysis with RFID sensors, multiple parameters from the measured real and imaginary portions of the complex impedance were calculated (see Fig. 1C). These parameters include frequency of the maximum of the real part of the complex impedance (F_p), magnitude of the real part of the complex impedance (Z_p), resonant frequency of the imaginary part of the complex impedance (F_1), and antiresonant frequency of the imaginary part of the complex impedance (F_2). Because F_1 and F_2 are related to different components of the equivalent circuit, in general, F_1 and F_2 are not expected to be correlated [34]. In the past, evaluation of the resonant and antiresonant frequencies was done for determination of behavior of the resonators for electronic filter applications [35]. In this work, we use F_1 and F_2 as inputs for the multivariate analysis of chemical sensor response. Of course, more parameters can be measured and calculated from the complex impedance. However, we have found that the use of individual parameters F_p, Z_p, F_1, and F_2 was sufficient for multivariate analysis [15].

Results of the measured response of the RFID sensor to the changes in RH at different distances from the pickup

Table 1
Position-induced affects of RFID sensor response

	Z-effects	*X*-effects
F_1 shift	Sensor baseline increase Sensitivity to analyte decrease	Sensor baseline slightly increases Sensitivity to analyte does not significantly change
F_2 shift	Sensor baseline decrease Sensitivity to analyte increase	The sensor baseline does not significantly change Sensitivity to analyte does not significantly change
F_p shift	Sensor baseline increase Sensitivity to analyte does not significantly change	Sensor baseline slightly changes Sensitivity to analyte does not significantly change
Z_p shift	Sensor baseline decrease Sensitivity to analyte decrease	Sensor baseline slightly decreases Sensitivity to analyte does not significantly change

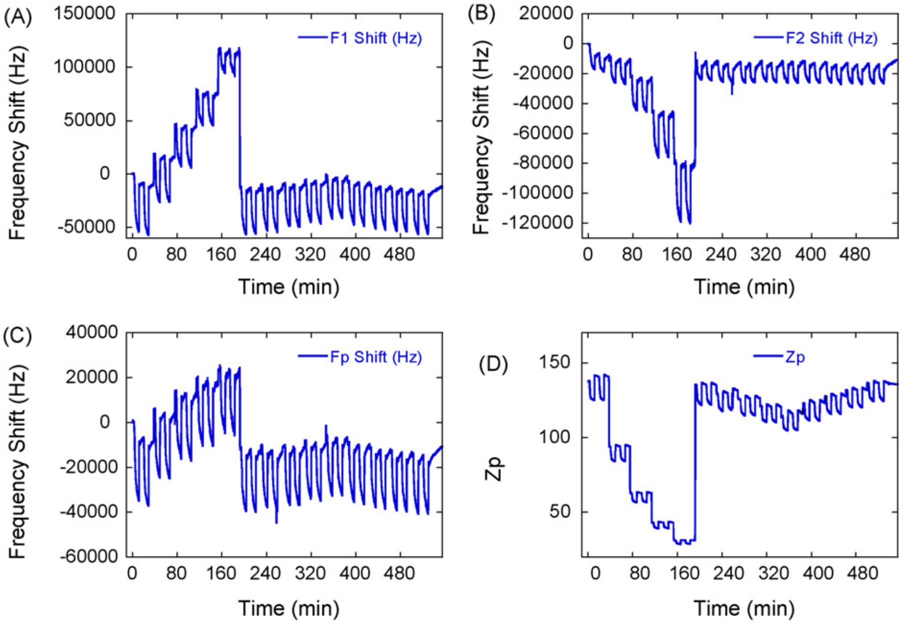

Fig. 5. Measurements of RFID sensor responses upon variation of *X* and *Z* positions: (A) F_1 frequency shift of the maximum of the imaginary part of the complex impedance, (B) F_2 frequency shift of the minimum of the imaginary part of the complex impedance, (C) F_p frequency shift of the maximum of the real part of the complex impedance, and (D) Z_p the magnitude of the real part of the complex impedance.

antenna coil are summarized in Fig. 5A–D. Unfortunately, as shown in Fig. 5A–D, none of the individual measured parameters provided a position-independent analyte-quantitation. The position-induced affects are summarized in Table 1 as the changes in the baseline sensor signal upon exposure to dry carrier gas and changes in analyte response magnitude upon exposure to 45% RH. It was also observed that the sensor noise did not noticeably change under these testing conditions.

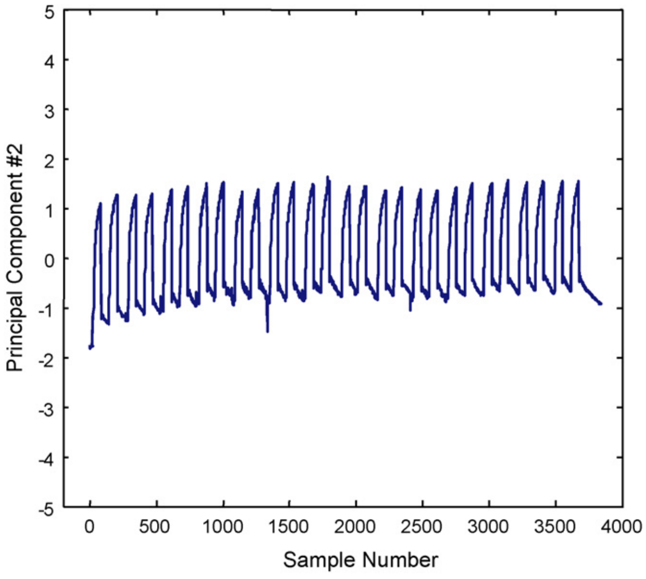

Fig. 6. Results of principal components analysis of measured F_1, F_2, F_p, and Z_p parameters for determination of position-independent analyte quantification.

3.3. *Multivariate analysis of repositioning effects*

To correct for the sensitivity of the sensor response to the position of the pickup coil, we performed a principal components analysis (PCA) of measured parameters [36]. The goal was to identify a possibility of rejecting the repositioning effects in the multivariate domain. PCA is a multivariate data analysis tool that projects the data set onto a subspace of lower dimensionality with removed collinearity. PCA achieves this objective by explaining the variance of the data matrix in terms of the weighted sums of the original variables with no significant loss of information. These weighted sums of the original variables are called principal components (PCs). Upon applying the PCA, the data matrix is expressed as a linear combination of orthogonal vectors along the directions of the principal components.

Results of the multivariate analysis of response of the RFID sensor to the changes in RH at different distances from the pickup antenna are summarized in Fig. 6. Thus, using multivariate analysis of RFID sensor response, we were able to preserve position stability of the baseline sensor signal upon exposure to dry carrier gas and the magnitude of the sensor signal change upon exposure to 45% RH.

4. Summary

In conclusion, we demonstrated that a conventional passive 13.56-MHz RFID tag is easily adapted for chemical sensing by coating the RFID tag with chemically sensitive films to form a chemical sensor. Repositioning of the resulting RFID sensor and its pickup coil affects the quantitative analyte response of the RFID sensor when the sensor complex impedance is measured and is related to changes in analyte concentration. By measuring simultaneously several parameters of the complex impedance from such an RFID sensor and applying multivariate statistical analysis methods, we were able to compensate for the repositioning effects such as baseline signal offset and magnitude of sensor response to an analyte.

Acknowledgement

This work has been supported from General Electric's fundamental research funds.

References

[1] R.S. Mackay, B. Jaconson, Nature 179 (1957) 1239–1240.
[2] C.C. Collins, IEEE Trans. Bio. Med. Eng. 14 (1967) 74–83.
[3] K.G. Ong, C.A. Grimes, C.L. Robbins, R.S. Singh, Sens. Actuator A 93 (2001) 33–43.
[4] M.C. Hofmann, F. Kensy, J. Buechs, W. Mokwa, U. Schnakenberg, J. Biosci. Bioeng. 100 (2005) 172–177.
[5] M. Lei, A. Baldi, E. Nuxoll, R.A. Siegel, B. Ziaie, Diabetes Technol. Ther. 8 (2006) 112–122.
[6] K. Finkenzeller, RFID Handbook. Fundamentals and Applications in Contactless Smart Cards and Identification, 2nd ed., Wiley, Hoboken, NJ, 2003.
[7] N. Wang, N. Zhang, M. Wang, Comput. Electron. Agric. 50 (2006) 1–14.
[8] K.C. Nicolaou, X.-Y. Xiao, Z. Parandoosh, A. Senyei, M.P. Nova, Angew. Chem. Int. Ed. 34 (1995) 2289–2291.
[9] F. Bachner, Presented at Organic RFID Conference, San Diego, CA, October 19–21, 2005.
[10] D. Lawrence, Presented at Organic RFID Conference, San Diego, CA, October 19–21, 2005.
[11] R. Artmann, Comput. Electron. Agric. 24 (1999) 5–26.
[12] R. Want, Computer 84–86 (April) (2004).
[13] R.A. Potyrailo, W.G. Morris, Proceedings of the 2006 International Symposium Spectral Science Research, U.S. Army Edgewood Chemical and Biological Center, Bar Harbor, MA, USA, May 29–June 2, 2006, pp. 264–265.
[14] R.A. Potyrailo, W.G. Morris, Abstracts of Papers American Chemical Society 232nd National Meeting & Exposition, San Francisco, CA, September 10–14, 2006, ANYL-300.
[15] R.A. Potyrailo, W.G. Morris, Anal. Chem. 79 (2007) 45–51.
[16] D.S. Ballantine Jr., R.M. White, S.J. Martin, A.J. Ricco, G.C. Frye, E.T. Zellers, H. Wohltjen, Acoustic Wave Sensors: Theory, Design, and Physico-Chemical Applications, Academic Press, San Diego, CA, 1997.
[17] P. Liu, Eur. Polym. J. 41 (2005) 2693–2703.
[18] N. Grossiord, J. Loos, O. Regev, C.E. Koning, Chem. Mater. 18 (2006) 1089–1099.
[19] C.S. Choi, B.J. Park, H.J. Choi, Diamond Relat. Mater. 16 (2007) 1170–1173.
[20] M.C. Lonergan, E.J. Severin, B.J. Doleman, S.A. Beaber, R.H. Grubbs, N.S. Lewis, Chem. Mater. 8 (1996) 2298–2312.
[21] E.J. Severin, B.J. Doleman, N.S. Lewis, Anal. Chem. 72 (2000) 658–668.
[22] T.P. Vaid, M.C. Burl, N.S. Lewis, Anal. Chem. 73 (2001) 321–331.
[23] T.L. Porter, M.P. Eastman, D.L. Pace, M. Bradley, Sens. Actuator A 88 (2001) 47–51.
[24] S. Srivastava, R. Tchoudakov, M. Narkis, Polym. Eng. Sci. 40 (2000) 1522–1528.
[25] A.J. Matzger, C.E. Lawrence, R.H. Grubbs, N.S. Lewis, J. Comb. Chem. 2 (2000) 301–304.
[26] J.F. Feller, I. Linossier, G. Levesque, Polym. Adv. Technol. 13 (2002) 714–724.
[27] K. Arshak, E. Moore, L. Cavanagh, J. Harris, B. McConigly, C. Cunniffe, G. Lyons, S. Clifford, Composites A: Appl. Sci. Manufact. 36 (2005) 487–491.
[28] M. Penco, L. Sartore, F. Bignotti, S.D. Sciucca, V. Ferrari, P. Crescini, S. D'Antone, J. Appl. Polym. Sci. 91 (2004) 1816–1821.
[29] J. Wang, M. Musameh, Anal. Chem. 75 (2003) 2075–2079.
[30] B. Zhang, R.W. Fu, M.Q. Zhang, X.M. Dong, P.L. Lan, J.S. Qiu, Sens. Actuator B 109 (2005) 323–328.
[31] S. Hrapovic, Y. Liu, K.B. Male, J.H.T. Luong, Anal. Chem. 76 (2004) 1083–1088.
[32] F. Lux, J. Mater. Sci. 28 (1993) 285–301.
[33] L. Flandin, J.Y. Cavaillé, G. Bidan, Y. Brechet, Polym. Compos. 21 (2000) 165–174.
[34] L.J. Giacoletto (Ed.), Electronics Designers' Handbook, 2nd ed., McGraw-Hill, New York, NY, 1977.
[35] B.A. Buchine, W.L. Hughes, F.L. Degertekin, Z.L. Wang, Nano Lett. 6 (2006) 1155–1159.
[36] P.C. Jurs, G.A. Bakken, H.E. McClelland, Chem. Rev. 100 (2000) 2649–2678.

Available online at www.sciencedirect.com

ScienceDirect

Talanta 75 (2008) 841–845

Talanta

www.elsevier.com/locate/talanta

Short communication

The simultaneous determination of chloride, nitrate and sulphate by isotachophoresis using bromide as a leading ion

Jeff E. Prest*, Peter R. Fielden

School of Chemical Engineering and Analytical Science, The University of Manchester, PO Box 88, Manchester M60 1QD, UK

Received 27 July 2007; received in revised form 27 November 2007; accepted 7 December 2007
Available online 23 December 2007

Abstract

A new method has been devised to allow the determination of small inorganic anions using isotachophoresis. This method makes use of indium(III) as a counter ion to manipulate the effective mobilities of inorganic anion species by means of complexation reactions. This new procedure successfully allowed the simultaneous determination of nitrate, chloride and sulphate to be realised on a capillary scale instrument and in a chip-based separation device. The electrolyte system developed to allow the separation to be achieved employed a 10 mM bromide-based leading electrolyte containing 1.25 mM indium(III) at pH 3.15 and a terminating electrolyte of cyanoacetic acid.

Keywords: Isotachophoresis; Inorganic anions; Chloride; Nitrate; Sulphate

1. Introduction

Isotachophoresis is a powerful analytical technique that has proven to be highly suited to the analysis of small ionic species [1,2]. The technique offers a number of features such as the ability to preconcentrate dilute samples and the capacity to handle a wide variety of concentrations, which can be of benefit when performing practical analytical measurements. However, to perform an isotachophoretic separation it is necessary to use a discontinuous electrolyte system comprising of a leading electrolyte and a terminating electrolyte. The leading electrolyte must contain an ion with a higher mobility than the sample species and the terminating electrolyte an ion with a lower mobility than the sample species. The latter requirement can usually be realised easily but the former can cause problems if there is a requirement to analyse ions which exhibit a high electrophoretic mobility.

The ability to analyse nitrate, chloride and sulphate simultaneously is of great importance to many applications particularly those involving the analysis of waters. However, such a separation is difficult to realise using isotachophoresis because all three of these anions possess high electrophoretic mobilities. The most problematic of the species to analyse is chloride because in most practical situations this ion has a higher effective mobility than nitrate or sulphate. Indeed, in most electrolyte systems developed for anionic separations using isotachophoresis, chloride is employed as the leading ion. Previously several methods have been proposed for allowing the simultaneous determination of nitrate, chloride and sulphate to be made using isotachophoresis. The most successful of these saw the use of dithionate as a leading electrolyte, which has a higher mobility than chloride, together with magnesium as a complexing agent to retard the effective mobility of sulphate behind that of nitrate [3]. However, whilst this method works well and has been subsequently used for chip-based separations [4] it requires the use of dithionic acid, a substance which is difficult to source. Only the sodium salt of dithionate is commonly available so that an ion exchange process is needed to obtain the acid. Other solutions to the problem have seen the use of hydroxide as a leading ion together with calcium as a complexing agent [5] and simply using chloride as the leading ion with 1,3-bis-[tris(hydroxymethyl)methylamino]propane as a complexing agent [6]. Problems with these approaches are that the former is an unbuffered system and thus likely to suffer irreproducibility problems [7] and the latter only allows quantification of chloride via an indirect method based on the change in length of the leading ion zone.

This paper describes the findings of a preliminary study into the development of a new method to enable the simultaneous

---

* Corresponding author. Tel.: +44 161 3068900; fax: +44 161 3064896.
E-mail address: j.prest@manchester.ac.uk (J.E. Prest).

0039-9140/$ – see front matter © 2007 Elsevier B.V. All rights reserved.
doi:10.1016/j.talanta.2007.12.011

determination of nitrate, chloride and sulphate to be made using isotachophoresis. Through the employment of indium(III) as a complexing counter ion it was possible to identify a set of conditions where the required separation could be achieved using bromide as a leading ion.

2. Experimental

2.1. Instrumentation

Separations were performed using either an ItaChrom EA202M electrophoretic analyser (JH-Analytik, Aalen, Germany) or using a miniaturised poly(methyl methacrylate) (PMMA) separation device fabricated in-house. The ItaChrom instrument was fitted with two columns: a 100 mm long, 0.8 mm internal diameter (ID) fluorinated ethylene–propylene copolymer preseparation column and a 140 mm long, 0.3 mm ID silica analytical column. Both columns were fitted with contactless conductivity detectors. The analytical column also contains an on-column UV detector. Control of the analyser and data processing was carried out on a personal computer using ITPPro32 software version 1.0 (Kas Comp, Bratislava, Slovakia). In this study the separations were carried out using only the preseparation column. To perform runs, samples were injected using the internal 30 μl sample loop and then analysed using a two step control program. In this program the first step involved applying a current of 400 μA for 260 s. Detection was undertaken in the second step, during which a lower current of 200 μA was applied.

The miniaturised separation device comprised a PMMA chip with an integrated on-column conductivity detector, full details of which have been previously described [8]. Briefly, the device contained two channels; a 200 μm wide, 300 μm deep separation channel with an effective length of 44 mm and a 57 mm long injection channel with a width of 300 μm and depth of 300 μm. This arrangement results in the system having an injection volume of 5.1 μl. A schematic diagram of the layout of the chip is shown in Fig. 1. Control of the separations, data capture and data analysis was done using LabVIEW software (National Instruments, Austin, TX, USA). Sample injection was made using a gravity feed hydrodynamic system. Separations were performed by applying a current of 40 μA for 260 s and then reducing this current to 20 μA. Detection was undertaken whilst the lower current was applied.

2.2. Chemicals

The electrolyte system developed incorporates a leading electrolyte composed of hydrobromic acid (48% analytical grade, Riedel-de Haën, Gillingham, Dorset, UK) and indium bromide (99.99%, Alfa Aesar, Heysham, Lancashire, UK). The terminating electrolyte was 20 mM cyanoacetic acid (99%, Aldrich, Gillingham, Dorset, UK). To suppress electro-osmotic flow 1 g l^{-1} of hydroxyethyl cellulose (HEC) (molecular weight ca. 250000, Aldrich) was added to the leading electrolyte. The pH of the leading electrolyte was adjusted using glycylglycine (99+%, Acros, Loughborough, UK). Chloride samples were prepared using an ion standard solution (1000 mg l^{-1}, BDH, Poole, UK). Nitrite and sulphate samples were prepared using sodium salts (>99%, Aldrich). Iodide (99.5%, BDH) and nitrate (99+%, Aldrich) samples were produce using potassium salts. All samples were prepared using >18 MΩ water (Elga Maxima Ultra Pure, Vivendi Water Systems, High Wycombe, UK).

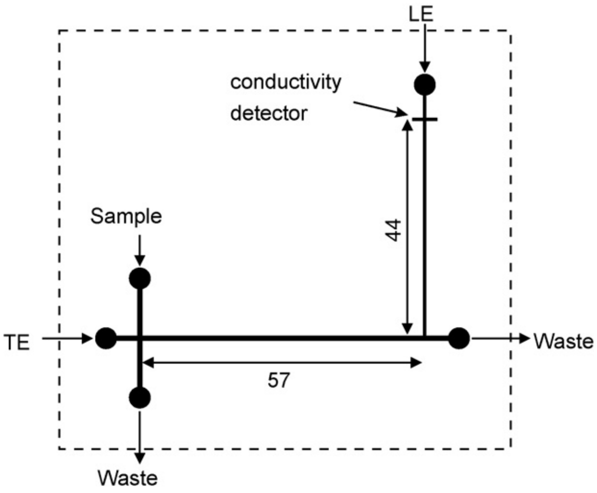

Fig. 1. Schematic diagram of the channel network in a miniaturised PMMA separation device. LE = leading electrolyte and TE = terminating electrolyte. Dimensions shown are in mm.

3. Results and discussion

Previously the authors had discovered that by using indium(III) as a complexing agent, the halide ions, chloride, bromide and iodide could be readily separated using an electrolyte system based on using nitrate as the leading ion [9]. This group of ions is notoriously difficult to separate using isotachophoresis so this represented a useful finding. Unfortunately, the use of nitrate as the leading ion meant that the method was not suitable for the analysis of this species. However, despite this it was believed that the complexation that occurs between various anions and indium(III) might offer a potential means of enabling a separation of nitrate, chloride and sulphate to be achieved. The reasoning behind this belief was the fact that indium(III) forms complexes of different stabilities with a range of inorganic anions. This feature can be seen in the size of the stability constants ($\log K_1$) of the indium(III) complexes formed which are 0.18, 2.01 and 2.41 with nitrate, bromide and chloride, respectively [10] and 3.04 with sulphate [11].

From the different stability constants of the indium(III)–anion complexes it was thought that it may be possible to find a set of conditions under which bromide could be employed as a leading ion to allow the separation of nitrate, chloride and sulphate to be achieved. Such an idea was thought possible because bromide possess a somewhat higher absolute mobility of $-80.9 \times 10^{-9}\,\mathrm{m^2\,V^{-1}\,s^{-1}}$ than that of nitrate which is $-74.0 \times 10^{-9}\,\mathrm{m^2\,V^{-1}\,s^{-1}}$ [12]. Thus, in the absence of any complexation, bromide will be faster than nitrate and the two species can be readily separated. If indium(III) is added to the leading electrolyte the effective mobilities of these two ions will change due to complexation and eventually the migration order is reversed. Chloride has an absolute mobility of $-79.1 \times 10^{-9}\ \mathrm{m^2\,V^{-1}\,s^{-1}}$ [12], a value similar to that of bromide. Thus, without complexation, bromide and chloride cannot be separated. However, as chloride complexes with indium(III) more strongly than bromide the effective mobility of the two species changes so that such a separation can be readily achieved. Sulphate has a higher absolute mobility than bromide of $-82.9\ 10^{-9}\ \mathrm{m^2\,V^{-1}\,s^{-1}}$ [12]. However, as this species is divalent, even in the absence of any complexation, it exhibits a lower effective mobility than bromide due to ionic strength effects. The addition of indium(III) to the leading electrolyte would be expected to slow this down to a greater extent than the other species of interest due to forming stronger complexes.

To see whether the required separation could be achieved in practice a series of experiments were carried out using a range of leading electrolytes containing 10 mM bromide at pH 3.0 as the leading ion. The terminating ion used was cyanoacetate. This species was selected for this purpose as compared to more commonly employed terminating ions in isotachophoresis, such as acetate, it has a reasonably high effective mobility under the conditions used due to having a pK_a of 2.45 [12]. Using a higher mobility terminating ion lowers the voltages arising during the separations, thus reducing the possibility of adverse heating effects such as bubble formation occurring and will also reduce the range between the leading and terminating steps. This latter effect was thought likely to assist in the identification of the small steps expected from the analysis of the high mobility inorganic anions of prime interest in this study. To the leading ion were added varying concentrations of indium(III) of between 0 and 1.5 mM. With each of the different electrolyte systems, separations were performed with single component samples of nitrate, chloride and sulphate. The resulting relative step heights (RSH) of the different species were recorded. In this work the RSH was calculated as the height of the sample step divided by the height of the step for the terminating ion. The results obtained are shown in Fig. 2. From the RSHs observed it can be seen that the use of bromide as a leading ion allowed sulphate to be determined under all conditions. When indium(III) concentrations of 0.25 mM and above were used it was possible to separate chloride from bromide whereas nitrate could be seen with indium concentrations of 1.25 mM and below. The results indicated that chloride and nitrate were likely to co-migrate with indium(III) concentrations of between 0.5 and 1.0 mM. Therefore, the two potential systems which seemed likely to allow the for the analysis of nitrate, chloride and sulphate were those with leading electrolytes containing either 0.25 mM indium(III) or 1.25 mM indium(III) as a complexing agent.

The system that was selected as being most useful for further investigation was that containing 1.25 mM indium(III), as it gave the biggest difference in RSHs between the three species of interest. Thus, further experiments were carried out using such a system. For these further experiments the pH of the system was raised to pH 3.15. This change was made as it was thought it may allow the method to also be used for the determination of nitrite. At pH 3.0 nitrite possess too low an effective mobility to migrate isotachophoretically ahead of the cyanoacetate terminating ion.

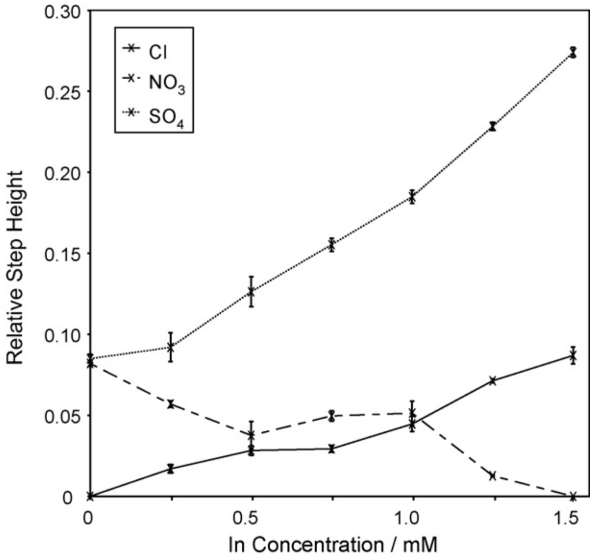

Fig. 2. Effect of indium concentration on the relative step heights observed for chloride, nitrate and sulphate. The leading electrolyte is at pH 3.0, the leading ion is 10 mM bromide and the terminating electrolyte is 20 mM cyanoacetate. Error bars represent ±S.D. ($n = 3$).

When separations were attempted using the leading electrolyte at pH 3.15 it did prove possible to achieve a simultaneous separation of nitrate, chloride and sulphate. An example of such a separation can be seen in Fig. 3. From this result it can be seen that the three sample species could be well resolved from one

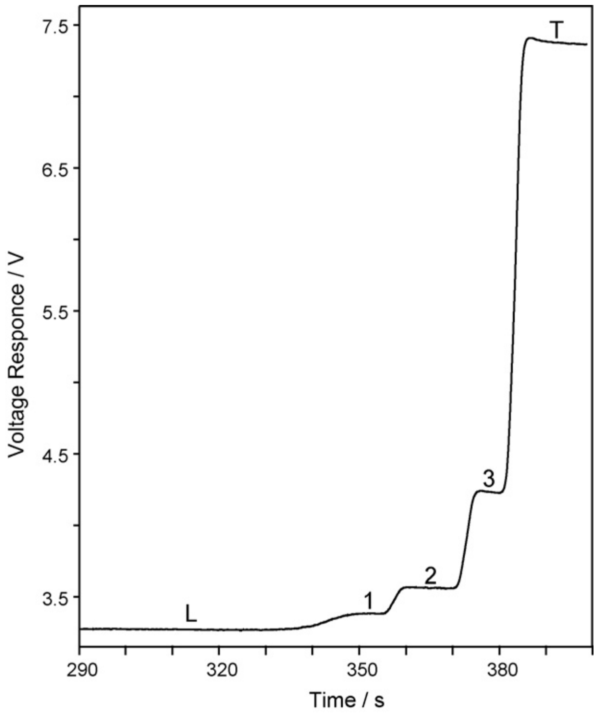

Fig. 3. Isotachopherogram of a separation of a sample containing 20 mg $\mathrm{l^{-1}}$ chloride, nitrate and sulphate performed on an ItaChrom EA202 electrophoretic analyser. Leading electrolyte 6.25 mM HBr, 1.25 mM $\mathrm{InBr_3}$, 1 g $\mathrm{l^{-1}}$ HEC, pH 3.15 (glycylglycine). Terminating electrolyte 20 mM cyanoacetic acid. 1 = nitrate; 2 = chloride; 3 = sulphate; L = leading ion; T = terminating ion.

Table 1
Relative step heights (RSH) observed for nitrate, chloride and sulphate when using a an electrolyte system comprising a leading electrolyte of 6.25 mM HBr, 1.25 mM $InBr_3$, 1 g l^{-1} HEC at pH 3.15 (glycylglycine) and a terminating electrolyte of 20 mM cyanoacetic acid

	RSH ± S.D.	
	Capillary scale	Chip
NO_3^-	0.025 ± 0.005	0.043 ± 0.017
Cl^-	0.065 ± 0.006	0.125 ± 0.011
SO_4^{2-}	0.227 ± 0.007	0.418 ± 0.013

Standard deviations (S.D.s) were calculated over 12 runs.

Table 2
Details of the parameters of the calibration lines produced using the ItaChrom instrument

	a ± S.D. (s)	b ± S.D. (s l mg^{-1})	r	n	Concentration range (mg l^{-1})
Cl^-	1.68 ± 0.39	0.647 ± 0.014	0.996	7	2.5–60
NO_3^-	1.42 ± 0.53	0.628 ± 0.024	0.994	7	2.5–60
$SO4^{2-}$	0.25 ± 0.16	0.460 ± 0.007	0.996	7	2.5–60

a = intercept; b = slope; n = number of data points (three replications performed at each); r = correlation coefficient; S.D. = standard deviation.

another. The observed RSHs for nitrate, chloride and sulphate together with associated standard deviations (S.D.s) are shown in Table 1. The results show that similar levels of reproducibility were noted in the step heights for all three species. When attempts were made to analyse nitrite with the system this also proved possible. Nitrite was found to produce a higher step than the other species with a RSH ± S.D. of 0.663 ± 0.005 (n = 4).

A possible problem with other methods that have been proposed for allowing the simultaneous determination of nitrate, chloride and sulphate using isotachophoresis is that they are susceptible to interference from bromide and iodide. This is because bromide and iodide have very similar mobilities and chemical properties to chloride and thus tend to co-migrate with this ion. With the method developed in this study, bromide is used as the leading ion so the presence of this species in any samples will not cause any interference. Iodide forms weaker indium(III) complexes than either chloride or bromide ($\log K_1 = 1.64$ [10]) so was not expected to cause any problems either. This expectation was confirmed when experiments were made with samples containing iodide. The results obtained with such separations showed no visible steps and extended leading ion zones indicating that the species was co-migrating with the leading ion.

To test the potential of the method and to see whether reproducible separations could be achieved a series of seven mixtures were analysed. The mixtures, which were analysed in three repeat determinations, contained equal concentrations of nitrate, chloride and sulphate. With these various mixtures, reproducible separations were observed. The average relative standard deviations for the zone lengths observed in these mixtures were 4.8% for nitrate, 5.2% for sulphate and 5.4% for chloride. The results from these analyses were used to produce a series of calibration curves. The findings of these experiments showed that the method behaved in a linear manner over the 2.5–60 mg l^{-1} concentration range used, with correlation coefficients of 0.996, 0.994 and 0.996 being achieved for chloride, nitrate and sulphate, respectively. Full details of the calibration curves, produced using weighted linear regression, can be found in Table 2.

Whilst the aim of this work was primarily to investigate the potential of the method for enabling the separation of the three species to be achieved, the results used to produce the calibration curves could be used to estimate limits of detection (LOD) for the three species. Calculation of a LOD in isotachophoresis is not a straightforward procedure due to the stepwise form of the output. This is because in isotachophoresis a blank usually does not produce a step, unless there is background contamination present. Thus, no meaningful standard deviation in the blank result can be obtained. Therefore, it is not possible to calculate a LOD on the basis of such a result. In this work LODs were taken as being the intercept, which is an estimate of the blank, plus three times the standard deviation of this parameter. Using this procedure the LODs were found to be 1.0 mg l^{-1} for sulphate, 1.8 mg l^{-1} for chloride and 2.5 mg l^{-1} for nitrate. These values represent a reasonable performance, being similar to those previously achieved with a similar type of instrument [13], and are adequate for many applications as these anions are often present in significant concentration. However, these limits could be significantly reduced, albeit with increased analysis times, if separations were carried out using the analytical column of the instrument. Under such conditions LODs of the order of 10–100 μg l^{-1} could be possible making the method applicable to trace analysis [1].

To further test the applicability of the new method, work was done to see whether separations could be achieved using a different type of separation device. Therefore, attempts were made to employ the developed electrolyte system in analyses using a miniaturised PMMA chip device. These attempts proved successful and separations of nitrate, chloride and sulphate were achieved on such a device. Details of the RSHs and associated S.D.s observed on the miniaturised device are shown in Table 1. In a similar result to that seen on the capillary scale instrument, the reproducibility of the heights noted on the chip device were similar for all three species. However, the reproducibility was lower in the results from the miniaturised system. In the miniaturised separations it was found that all species exhibited higher steps than were seen in the capillary scale separations as can be seen from a comparison of the two sets of results shown in Table 1. This difference was thought to arise from differences in the behaviour of the conductivity detectors in the two devices. Examples of chip-based separations are shown in Fig. 4. One example is of a separation of a model sample of 20 mg l^{-1} of chloride, nitrate and sulphate whereas the other is of Silver Spring a commercially available mineral water. It can be seen that isotachopherograms for both samples are similar. This result is in agreement with the stated composition of mineral water which was that it contained 20 mg l^{-1} sulphate, 21 mg l^{-1} nitrate, 26 mg l^{-1} chloride and 292 mg l^{-1} carbonate.

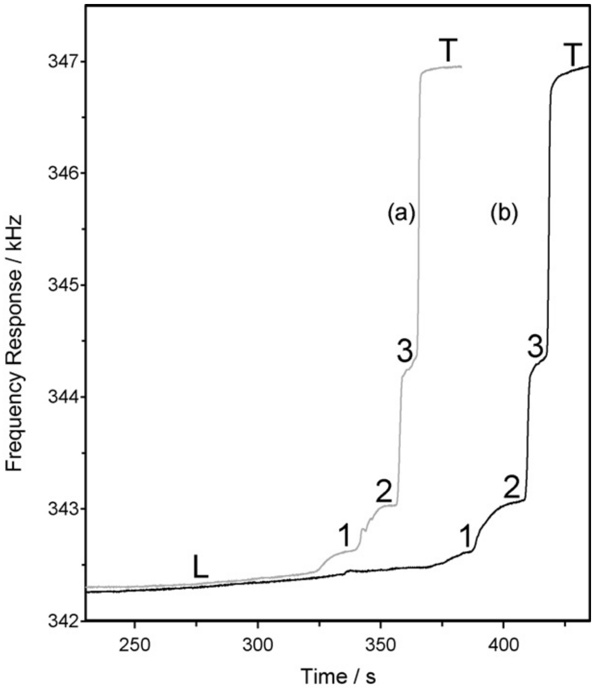

Fig. 4. Isotachopherograms of separations performed on a PMMA chip. (a) Sample containing 20 mg l^{-1} chloride, nitrate and sulphate and (b) mineral water. Leading electrolyte 6.25 mM HBr, 1.25 mM $InBr_3$, 1 g l^{-1} HEC, pH 3.15 (glycylglycine). Terminating electrolyte 20 mM cyanoacetic acid. 1 = nitrate; 2 = chloride; 3 = sulphate; L = leading ion; T = terminating ion.

4. Conclusions

The simultaneous determination of nitrate, chloride and sulphate using isotachophoresis is hard to accomplish. A preliminary study has thus been carried out into the feasibility of using bromide as a leading ion to allow such a separation to be achieved. It was found that it was possible to achieve such separations by incorporating a concentration of 1.25 mM indium(III) as a complexing agent in the leading electrolyte. This complexing agent interacts with the different anions to a different degree meaning that the species separate out in the order nitrate followed by chloride followed by sulphate. The devised method is seen as offering a relatively simple means, using readily available chemicals, of being able to allow what is regarded as a difficult analysis when using isotachophoresis to be achieved. The developed method uses a leading electrolyte at pH 3.15 meaning that it can also be used for nitrite determination.

Acknowledgements

The authors would like to thank the United Kingdom Home Office for funding this research programme and the Forensic Explosives Laboratory, of the Defence Science and Technology Laboratory, Fort Halstead, for their support.

References

[1] T. Meissner, F. Eisenbeiss, B. Jastorff, Fresen. J. Anal. Chem. 361 (1998) 459.

[2] V. Madajová, E. Turcelová, D. Kaniansky, J. Chromatogr. 589 (1992) 329.

[3] T. Meissner, F. Eisenbeiss, B. Jastorff, J. Chromatogr. A 838 (1999) 81.

[4] R. Bodor, V. Madajová, D. Kaniansky, M. Masár, M. Jöhnck, B. Stanislawski, J. Chromatogr. A 916 (2001) 155.

[5] J. Vacík, I. Muselasová, J. Chromatogr. 320 (1985) 199.

[6] I. Zelenský, V. Zelenská, D. Kaniansky, P. Havaši, V. Lednárová, J. Chromatogr. 294 (1984) 317.

[7] L. Křivánková, F. Foret, P. Gebauer, P. Boček, J. Chromatogr. 390 (1987) 3.

[8] J.E. Prest, S.J. Baldock, P.R. Fielden, N.J. Goddard, B.J. Treves Brown, Anal. Bioanal. Chem. 376 (2003) 78.

[9] J.E. Prest, S.J. Baldock, P.R. Fielden, N.J. Goddard, B.J. Treves Brown, Analyst 130 (2005) 1375.

[10] D.G. Tuck, Pure Appl. Chem. 55 (1983) 1477.

[11] E. Högfeldt (Ed.), Stability Constants of Metal–Ion Complexes. Part A. Inorganic Ligands, Pergamon, Oxford, 1982.

[12] D.R. Lide (Ed.), CRC Handbook of Chemistry and Physics, Chemical Rubber Publishing Co., Boca Raton, 1993.

[13] P. Kosobucki, B. Buszewski, J. Liquid Chromatogr. Relat. Technol. 29 (2006) 1951.

Available online at www.sciencedirect.com

ScienceDirect

Talanta 75 (2008) 684–690

Talanta

www.elsevier.com/locate/talanta

Homogenous electrogenerated chemiluminescence immunoassay for human immunoglobulin G using *N*-(aminobutyl)-*N*-ethylisoluminol as luminescence label at gold nanoparticles modified paraffin-impregnated graphite electrode

Honglan Qi, Yi Zhang, Yage Peng, Chengxiao Zhang [*]

Key Laboratory of Analytical Chemistry for Life Science of Shaanxi Province, School of Chemistry and Materials Science,
Shaanxi Normal University, Xi'an 710062, PR China

Received 22 August 2007; received in revised form 3 December 2007; accepted 3 December 2007
Available online 8 December 2007

Abstract

A homogeneous electrogenerated chemiluminescence (ECL) immunoassay for human immunoglobulin G (hIgG) has been developed using a *N*-(aminobutyl)-*N*-ethylisoluminol (ABEI) as luminescence label at gold nanoparticles modified paraffin-impregnated graphite electrode (PIGE). ECL emission was electrochemically generated from the ABEI-labeled anti-hIgG antibody and markedly increased in the presence of hIgG antigen due to forming a more rigid structure of the ABEI moiety. The concentration of hIgG antigen was determined by the increase of ECL intensity at a gold nanoparticles modified PIGE. It was found that the ECL intensity of ABEI in presence of hydrogen peroxide was dramatically enhanced at gold nanoparticles modified PIGE in neutral aqueous solution and the detection limit of ABEI was 2×10^{-14} mol/L (S/N = 3). The integral ECL intensity was linearly related to the concentration of hIgG antigen from 3.0×10^{-11} to 1.0×10^{-9} g/mL with a detection limit of 1×10^{-11} g/mL (S/N = 3). The relative standard deviation was 3.1% at 1.0×10^{-10} g/mL ($n = 11$). This work demonstrates that the enhancement of the sensitivity of ECL and ECL immunoassay at a nanoparticles modified electrode is a promising strategy.

Keywords: Electrogenerated chemiluminescence; Immunoassay; Human immunoglobulin; *N*-(aminobutyl)-*N*-ethylisoluminol; Gold nanoparticles

1. Introduction

The immunoassay is an analytical methodology that has been widely employed in clinical, pharmaceutical, and biochemical fields due to its high specificity [1]. Immunoassays are usually divided into two formats, i.e., heterogeneous and homogeneous ones. In the homogeneous immunoassays, the method involves no separation steps. The commonly used heterogeneous assay such as enzyme-linked immunosorbent assay and sandwich immunochemiluminometric assay, are normally conducted on microtiter plates and required several incubation and washing steps or centrifugation steps [2]. Homogeneous immunoassay has received much attention due to its simplicity, automation and high throughput. The development of a rapid, sensitive and non-separation immunoassay has been a long-standing goal since the beginning of immunoassay technology. Chemiluminescence immunoassay is promising as an alternative method of radioimmunoassay because of its high sensitivity, and safety. However, most of the chemiluminescence-based methods required the bound form/free form separation process and prolonged incubation for effective chemical amplification.

Electrogenerated chemiluminescence immunoassay (ECLIA), which combines electrogenerated chemiluminescence (ECL) and immunoassay, has received much attention because not only ECL reaction can be controlled and manipulated by alteration to the applied potential but also a wide range of different formats can be readily developed in homogeneous immunoassay [3–6]. Most of the homogeneous ECLIA established are based on the signal changes deriving from steric hindrance, conformational change and change in the diffusion coefficient induced by immunoreactions. In most of the homogeneous ECLIA methods reported, the concentration

---

[*] Corresponding author. Tel.: +86 29 85307567; fax: +86 29 85307567.
E-mail address: cxzhang@snnu.edu.cn (C. Zhang).

0039-9140/$ – see front matter © 2007 Elsevier B.V. All rights reserved.
doi:10.1016/j.talanta.2007.12.002

of antigen or antibody is related with the decrease of ECL intensity while the immunoreaction takes place between antigen and its antibody [2,7–9]. However, the homogeneous ECLIA based on the decrease of ECL intensity normally suffered from a high ECL background and a limited linear response range.

Some efforts have been devoted to improve the sensitivity of ECL and homogeneous ECLIA including employment of new or multiple labels [8,9] and exploration of new electrode materials [10–14]. Cui and coworkers reported that a high sensitivity of ECL detection luminol could be obtained at a gold nanoparticles self-assembled electrode [10–12] or a silver nanoparticles self-assembled electrode [13]. However, the reported ECL system has not been applied to immunoassay. Wang and coworkers [14] developed an ECL method for the determination of biological substances including bovine serum albumin (BSA) and immunoglobulin G (IgG) using a 4-(dimethylamino) butyric acid (DMBA) as a label at a gold nanoparticles modified gold electrode and a 10- and 6-fold sensitivity enhancement was obtained. However, the sensitivity of 1–80 μg/mL for BSA and 5–100 μg/mL for IgG was only obtained. Our group reported some homogeneous ECLIA work based on the multiple labels using protein as a carrier. However, the reported system was based on a decrease of ECL signal [8,9].

N-(4-ainobutyl)-*N*-ethylisoluminol (ABEI), a derivative of luminol, has been used as a favorable ECL marker for immunoassay [15] and DNA hybridization detection [16,17] since there is no significant reduction in luminescence activity when ABEI is labeled to biological substances. Arai et al. [15] reported a sensitive immunoassay of hIgG using ABEI-labeled anti-hIgG, based on the increase of ECL intensity while the binding of hIgG to the ABEI-labeled anti-hIgG resulted in a more rigid structure of the ABEI moiety and increased luminescence intensity. We found that the ECL intensity of ABEI at a gold nanoparticles modified paraffin-impregnated graphite electrode (PIGE) was greatly enhanced. In this work, a homogeneous ECL immunoassay for hIgG was developed using ABEI-labeled anti-hIgG antibody at a gold nanoparticles modified PIGE. The ECL behavior of ABEI was investigated at a gold nanoparticles modified PIGE in neutral aqueous solution and the performance of the resulting homogeneous immunoassay was studied. To our best knowledge, ECL of ABEI and ECLIA using ABEI as an ECL label at a gold nanoparticles modified electrode have not been reported.

2. Experimental

2.1. Chemicals and apparatus

N-(aminobutyl)-*N*-ethylisoluminol (ABEI), hIgG, anti-hIgG monoclonal antibody (rabbit), Sephadex G-25 and $HAuCl_4 \cdot 4H_2O$ (99% w/w) were purchased from Sigma (USA). Bovine serum albumin (BSA, Mt: 67000) was obtained from Huamei Co. Ltd (China).

A 1.8×10^{-2} mol/L stock solution of ABEI was prepared by dissolving 50 mg ABEI in 10.00 mL of 0.10 mol/L hydrogen chloride solution. Working solutions of ABEI were prepared by diluting the stock solution with 0.10 mol/L phosphate buffer solution (PBS, pH 7.40). All other reagents were of analytical grade, and redistilled water was used throughout.

The experimental set-up for ECL measurement consisted of a MEC-12B Electrochemical Analyzer (Jiangsu Electroanalytical Instrument Co., Jiangsu, China), an Ultra-Weak Chemiluminescence Analyzer (photomultiplier operated at −900 V) controlled by a personal computer with the BPCL program (Institute of Biophysics, Chinese Academy of Science, Beijing, China). The electrode system was a three-electrode system, including a bulk gold electrode ($\phi = 3$ mm), a paraffin-impregnated graphite electrode (PIGE, $\phi = 6$ mm) or a gold nanoparticles modified PIGE working electrode, a platinum counter electrode and a salt bridge connected with an Ag/AgCl (Sat. KCl) reference electrode. All potentials were referred to this reference electrode. Scanning electronic microscopy (SEM) pictures were obtained with a Philips-FEI Quanta 200 Microscope.

2.2. Preparation of ABEI-labeled anti-hIgG antibody

ABEI-labeled anti-hIgG antibody was prepared according to references [15,18]. Ten milligrams of *N*-hydroxy succinimide was dissolved in 1.00 mL of dimethylsulfoxide. 8.0 mg of anti-hIgG antibody was dissolved in 1.00 mL of 0.10 mol/L PBS (pH 7.40). 100 μL of 0.018 mol/L ABEI (pH 7.40) adjusted by 0.10 mol/L $NaHCO_3$ (pH 9.00) was slowly mixed with the above-mentioned solution and incubated in dark for 6 h under stirring. The resulting mixture was loaded onto a Sephadex G-25 column ($d = 1$ cm, $h = 20$ cm) and a 0.085 mol/L PBS (pH 7.40) was used to elute ABEI-labeled anti-hIgG antibody, free ABEI and hIgG with a flow rate of 0.50 mL/min. The elutant collected between 32 and 35 min was used as ABEI-labeled anti-hIgG antibody solution for the ECLIA.

2.3. Preparation of gold nanoparticles modified paraffin-impregnated graphite electrode

Gold nanoparticles were prepared by the reduction of $HAuCl_4$ (1.0×10^{-2}%, w/v) with trisodium citrate (1%, w/v) according to reference [19] and stored at 4 °C. The resulting gold nanoparticles were characterized by transmission electron microscopy (TEM, Hitachi H-800, Japan) and UV–vis spectrometry (UV–vis spectrophotometer, TU-1900, Beijing Puxi, China).

The paraffin-impregnated graphite electrode was prepared by putting a graphite rod ($\phi = 6$ mm out-diameter) just into a suitable diameter Teflon tube and sealing the surface of graphite rod and the gap between the graphite rod and the tube using melted paraffin, allowed to stay under infrared light for 1 h. Then it was polished at an abrasive paper and then rinsed with water. 210 μL of gold nanoparticles suspension prepared was carefully dropped on the surface of a electrode pretreated, and then dried at 45 °C to form gold nanoparticle modified PIGE. Before used, the gold nanoparticle modified PIGE was rinsed with water to remove the other reagents brought in the immobilized process on the surface.

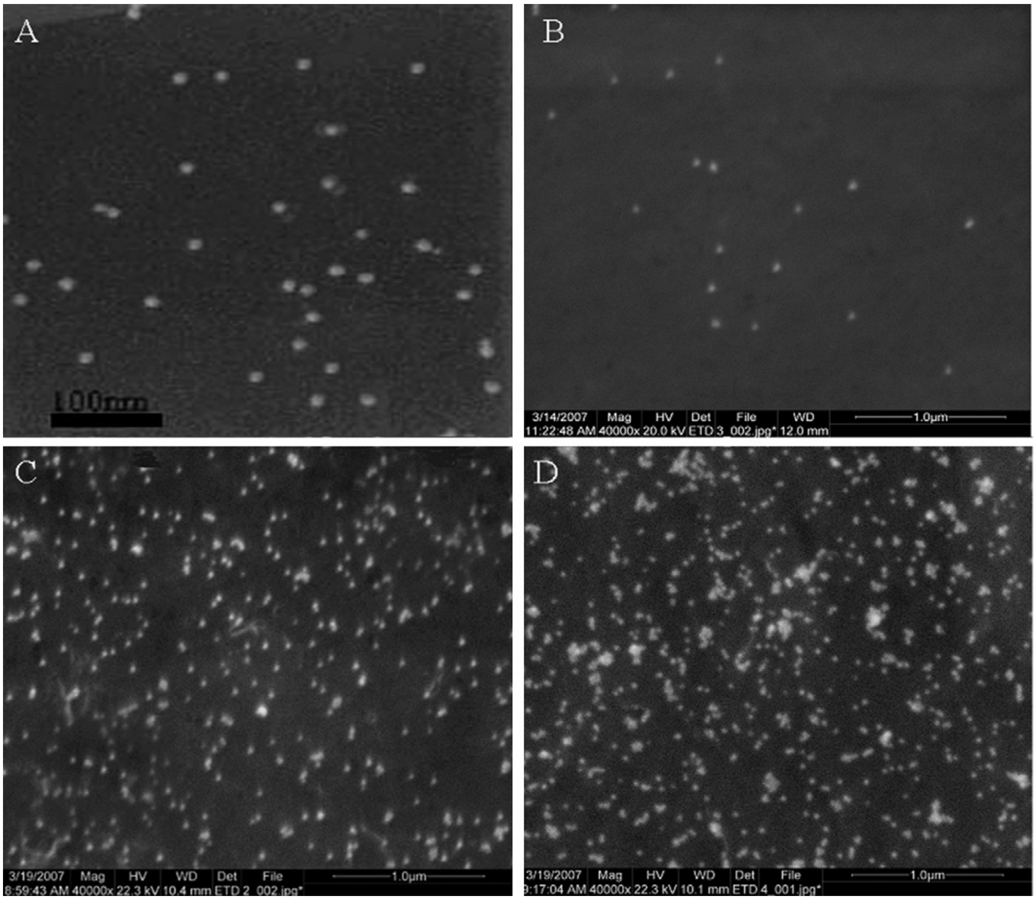

Fig. 1. TEM of gold nanoparticle (A) and SEM images (B-D) of PIGE modified with gold nanoparticles. (B) 100 μL of gold nanoparticles; (C) 210 μL of gold nanoparticles; (D) 250 μL of gold nanoparticles.

2.4. *ECL homogeneous immunoassay*

A series of 0.50 mL of 0.10 mol/L PBS (pH 7.40) containing different concentrations of hIgG antigen analyte from 1.0×10^{-11} to 1.0×10^{-9} g/mL were prepared. Each of them was mixed with 2 μL of a fixed concentration of the ABEI-labeled anti-hIgG (10^{-6} g/mL) antibody solution and incubated at 37 °C for 1 h. After dilution with 0.50 mL of 0.10 mol/L PBS (pH 7.40) containing 2.0 mmol/L H_2O_2, the ECL detection was performed at a constant potential of +0.80 V. The concentration of hIgG antigen was quantified by the integral ECL intensity for 40 s after the potential was applied.

3. Results and discussion

3.1. *Quantification of ABEI*

3.1.1. *Characteristics of gold nanoparticles modified PIGE*

Fig. 1A shows a TEM of gold nanoparticles prepared, demonstrating that the gold nanoparticles prepared is well separated and their mean size in diameter was about 8–10 nm. Fig. 1B–D show the SEM images of PIGE modified with gold nanoparticles when the different volumes of the gold nanoparticles suspension prepared were used. From Fig. 1B–D, it can be seen that the surface density of gold nanoparticles modified on the PIGE surface significantly increases and mean size of gold nanoparticles modified on the surface of PIGE slightly increases from Fig. 1B–D. The aggregation of gold nanoparticles on the surface of PIGE was observed as the volume of the gold nanoparticles suspension was 250 μL. This indicates that the used volume of the gold nanoparticles suspension can affect the surface density and mean size of gold nanoparticles modified on the surface of PIGE and gold nanoparticles on the surface of PIGE slightly grow up in the process of the solvent vaporization.

3.1.2. *ECL behavior of ABEI*

Although ECL behavior of ABEI at conventional electrodes including glassy carbon electrode [16], carbon fiber electrode [15], platinum electrode [17] and gold electrode [20] was investigated, the study on ECL behavior of ABEI at a gold nanoparticles modified PIGE were not reported. Therefore, we investigated ECL behavior of ABEI at a gold nanoparticles modified PIGE in this work.

ECL emission-applied potential profiles of ABEI in the presence of H_2O_2 at a bare PIGE and at a gold nanoparticles modified PIGE are shown in Fig. 2. From Fig. 2, it can be seen that on the positive scan an ECL emission starts increase from 0.46 V at a bare PIGE (line, a) and 0.40 V at a gold nanoparticles modified PIGE (line, b), and peak of ABEI appeared at +0.88 V at a bare PIGE (line, a) and at +0.82 V at a gold nanoparti-

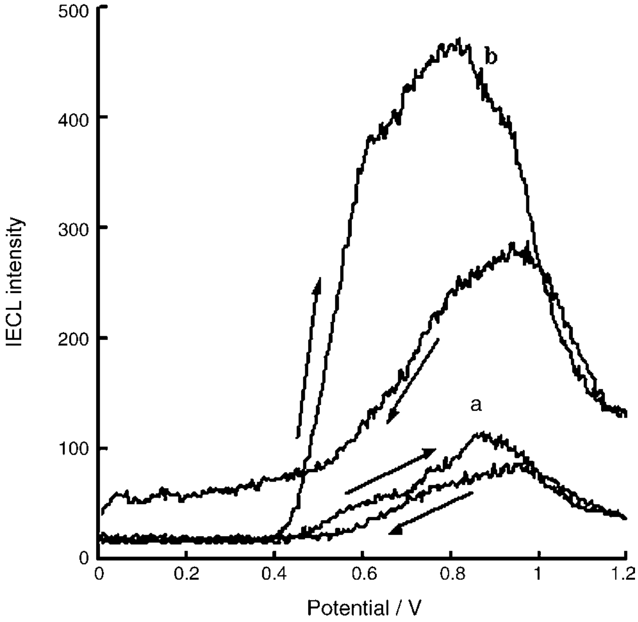

Fig. 2. ECL emission-applied potential profiles of ABEI at a bare PIGE (line a) and at a gold nanoparticles modified PIGE (line b). 0.10 mol/L PBS containing 1.0×10^{-11} mol/L ABEI and 5.0×10^{-4} mol/L H_2O_2, scan rate, 10 mV/s.

cles modified PIGE (line, b), respectively. The negative shift on the start potentials of ECL emission and the peak potentials is 0.06V. This indicates that the gold nanoparticles on the surface of PIGE can catalyze the ECL process. Furthermore, the five-fold enhancement of the ECL emission of ABEI was obtained at a gold nanoparticles modified PIGE, compared with that at a bare PIGE. In order to understand the sort of catalysis of gold nanoparticles as a reason for the observed enhancement of the ECL emission, the electrochemical behaviors of ABEI at a bulk gold electrode, at bare PIGE and at a gold nanoparticles modified PIGE were investigated by cyclic voltammetry. The results are shown in Fig. 3. From Fig. 3, it can be seen that on the positive scan, the oxidation peak current at about +0.50 V increases and start oxidation potential negatively shift in sequence from a bulk gold electrode to a bare PIGE and then to at a gold nanoparticles modified PIGE. This indicates that gold nanoparticles on the surface of the modified PIGE can catalyze an electrochemically oxidizing process of ABEI.

3.1.3. *Optimization for ECL determination of ABEI*

In order to obtain a highly sensitive ECL method for the determination of ABEI at gold nanoparticles modified PIGE in neutral aqueous solution, the test conditions including applied potential, the amount of gold nanoparticles, pH and concentration of hydrogen peroxide were optimized.

3.1.3.1. Applied potential. The dependence of the integral ECL intensity on the applied potential was examined and the results showed that the integral ECL intensity increased when an applied potential was stepped from +0.45 to +0.85 V and reached the maximum at +0.85 V. However, the reproducibility of ECL intensity at the potential of +0.85 V was poorer than that of at the potential of +0.80 V due to the oxidation of gold nanoparticles. Therefore, a constant potential of +0.80 V was selected in subsequent experiment.

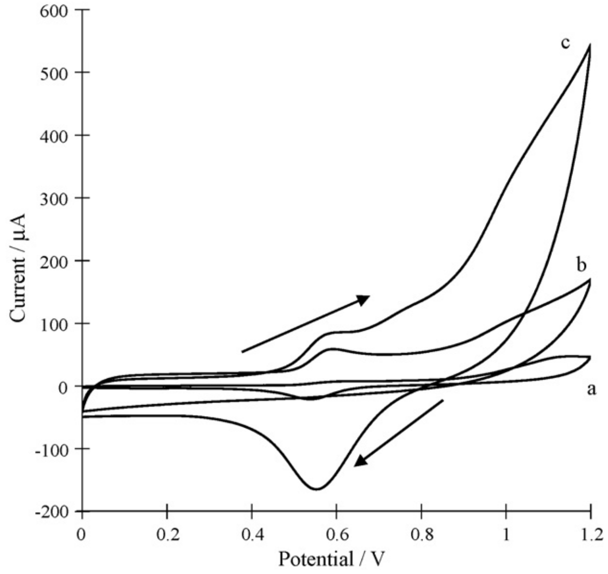

Fig. 3. CV of ABEI at a bulk gold electrode (line a), at a bare PIGE (line b) and at a gold nanoparticles modified PIGE (line c) in 0.10 mol/L PBS containing 1.8×10^{-4} mol/L ABEI, scan rate, 10 mV/s.

3.1.3.2. Size and amount of gold nanoparticles. As expected, the ECL intensity of ABEI was strongly dependent on size and amount of gold nanoparticles on PIGE surface. The dependence of the ECL intensity of ABEI on the different sizes of gold nanoparticles including 8–10 nm, 16–18 nm and 25–30 nm was examined. The results showed that the nanoparticles modified electrode fabricated with 8–10-nm gold nanoparticles exhibits the largest ECL response to ABEI than that of the other sizes. This was attributed to the fact that a higher catalytic activity and the very high surface to volume ratio of gold nanoparticles occur on the smaller gold nanoparticle [21]. It should be noted that the Au nanoparticles with particle size smaller than 10 nm was not checked because they were not obtained by using the reference method [19]. Therefore, 8–10 nm gold nanoparticles (gold atoms by atomic absorption spectrum, 2.45×10^{-4} mol/L) are chosen in the following experiments.

Fig. 4 shows the effect of volume of gold nanoparticles (8–10 nm) modified onto PIGE surface from 10 to 300 μL, on the ECL intensity of ABEI. From Fig. 4, it can be seen that the integral ECL intensity increases with the increase of the volume of gold nanoparticles from 10 to 210 μL. The integral ECL intensity reached the maximum at 210 μL and decreased while the volume was higher than 210 μL. This is corresponding to the fact that the gold nanoparticles on graphite electrode surface aggregates (as shown in Fig. 1D). Therefore, 210 μL of gold nanoparticles prepared was chosen in further experiments in order to obtain a high sensitivity.

3.1.3.3. pH. The dependence of the integral ECL intensity on pH was examined and the results showed that the integral ECL

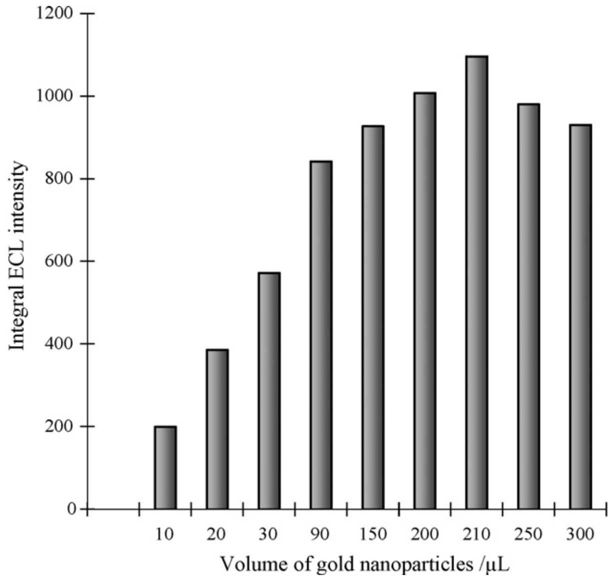

Fig. 4. Effect of the amount of gold nanoparticles on PIGE surface on the integral ECL intensity. 0.10 mol/L PBS containing 1.0×10^{-12} mol/L ABEI and 5.0×10^{-4} mol/L H_2O_2, applied potential, 0.80 V.

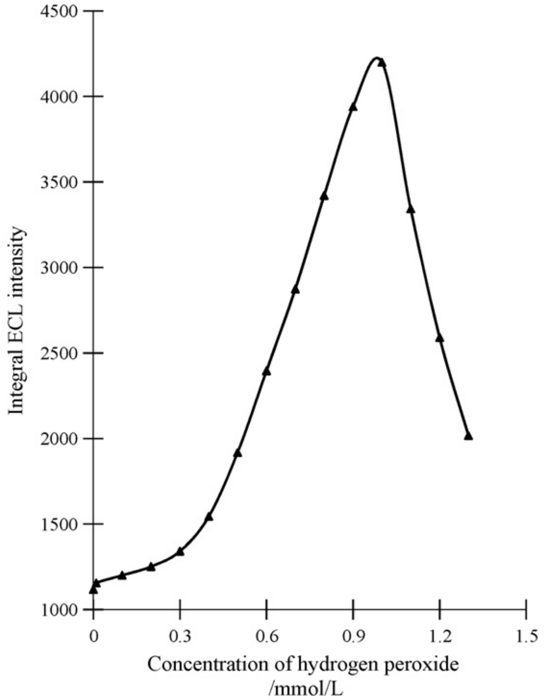

Fig. 5. Dependence of the integral ECL intensity on the concentration of hydrogen peroxide. 0.10 mol/L PBS (pH 7.40) containing 1.0×10^{-10} mol/L ABEI, applied potential, 0.80 V.

intensity was very low in acid solution. The integral ECL intensity increased from pH 7.00 to 11.00 and reached a maximum at pH 11.00. This is similar with the chemiluminescence behavior of ABEI [22]. The integral ECL intensity decreased when pH was higher than 11.00. This is maybe attributed to the fact that hydrogen peroxide was decomposed. Additionally, it was found that the reproducibility of ECL intensity in a neutral solution was obtained by repetitive measurements at a gold nanoparticles modified electrode electrodes. Therefore, on consideration of bioanalytical application, subsequent experiment was conducted in medium of pH 7.40.

3.1.3.4. Concentration of hydrogen peroxide. Fig. 5 shows the dependence of the integral ECL intensity on the concentration of hydrogen peroxide. From Fig. 5, it can be seen that the integral ECL intensity increased with an increase of the concentration of hydrogen peroxide from 0.010 to 1.0 mmol/L due to the increase of co-oxidizing function of hydrogen peroxide. And the integral ECL intensity reached maximum at 1.0 mmol/L. The blank ECL intensity was much high (data not shown) when the concentration of hydrogen peroxide was higher than 1.0 mmol/L. Therefore, 1.0 mmol/L hydrogen peroxide was chosen in this work.

3.1.4. Linear range, detection limit and precision for ABEI

Under the optimized conditions, the integral ECL intensity has a good linear relationship with the logarithm of the concentration of ABEI from 3.0×10^{-14} to 1.0×10^{-10} mol/L. The relationship between the logarithm of the concentration of ABEI and integral ECL intensity (I) is given as $I = 1241 \lg C + 767$ ($R^2 = 0.9999$, unit of C is 10^{-14} mol/L). The detection limit of ABEI was 2×10^{-14} mol/L (S/N = 3), which was much lower than that at carbon fiber electrode (1.2 fmol/μL) [15]. The relative standard deviation for 1.0×10^{-10} mol/L ABEI was 1.9% in 11 successive detections. A satisfactory sensitivity of the proposed method is, therefore, feasible. The stability of a gold nanoparticle modified PIGE was estimated by discontinuously determining the ECL response to ABEI every day in 0.10 mol/L PBS containing 1.0×10^{-10} mol/L ABEI and 1.0 mmol/L hydrogen peroxide using a gold nanoparticle modified PIGE stored in water at 4 °C. The result showed that the decrease of the ECL intensity was less than 5% within 10 days. This indicates that the detachment of the gold nanoparticles is negligible within 10 days.

3.2. Evaluation of ABEI-labeled anti-hIgG antibody

ABEI-labeled anti-hIgG antibody synthesized according to the process described in Section 2.2 was characterized by UV–vis spectrophotometry. UV–vis spectrum of ABEI-labeled anti-hIgG antibody in 0.10 mol/L PBS (pH 7.40) was shown in Fig. 6. From Fig. 6, it can be seen that characteristic absorption peaks of ABEI-labeled anti-hIgG antibody appeared at 328 nm and 276 nm (Fig. 6a), respectively, corresponding to the characteristic peak of ABEI at 328 nm and 288 nm (Fig. 6b) and the characteristic peak of anti-hIgG antibody at 276 nm (Fig. 6c). This suggests that ABEI is labeled to anti-hIgG antibody. The concentration of the ABEI-labeled anti-hIgG antibody solution was calculated according to the values of UV absorption of anti-hIgG antibody at 276 nm and the molar ratio of ABEI and anti-hIgG antibody was estimated by the value of UV absorption of protein at 276 nm ($\varepsilon = 1.28 \times 10^5$ L mol^{-1} cm^{-1}) and ABEI at 325 nm($\varepsilon = 5.38 \times 10^3$ L mol^{-1} cm^{-1}), respectively. The label ratio obtained was 24 ABEI per hIgG in the ABEI-labeled anti-hIgG antibody.

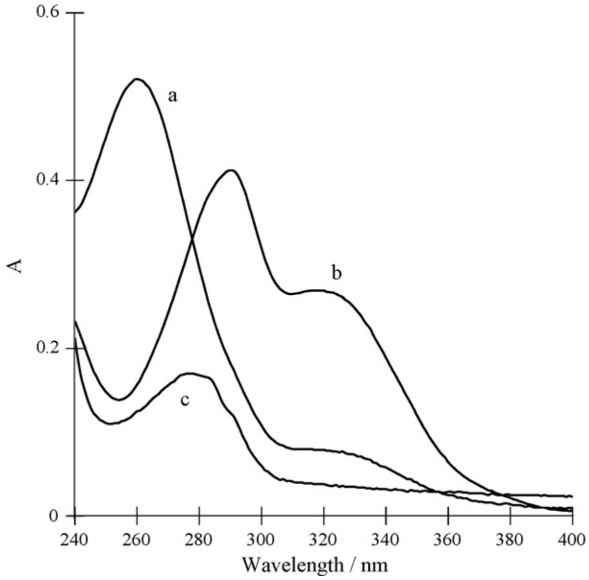

Fig. 6. UV–vis spectra of ABEI-labeled anti-hIgG antibody (a), ABEI (b) and anti-hIgG antibody (c) in 0.10 mol/L PBS (pH 7.40).

ECL behavior of the ABEI-labeled anti-hIgG antibody at a gold nanoparticles modified PIGE in 0.10 mol/L PBS (pH 7.40) was investigated using linear potential scan technique with a scan rate of 20 mV/s. The results showed that ECL peak of ABEI-labeled anti-hIgG antibody appeared at +0.84 V at a gold nanoparticles modified PIGE, which were very close to ECL peak of ABEI at +0.82 V. This also indicates that ABEI is labeled to anti-hIgG antibody and ECL behavior of the ABEI-labeled anti-hIgG antibody is similar with that of ABEI. Therefore, the optimized ECL measurement condition for ABEI was also applied to quantify the concentration of the ABEI-labeled anti-hIgG antibody.

Fig. 7 shows the ECL profiles of ABEI-labeled anti-hIgG antibody in the absence and presence of hIgG antigen at a bulk gold electrode and at a gold nanoparticles modified PIGE. Comparing the peak height of line a with line c, the ECL intensity increase from 59, which is a background of ECL intensity generated from ABEI-labeled anti-hIgG antibody, to 151 at a bulk gold electrode. Comparing the peak height of line b with line d, the ECL intensity increase from 101 to 458 at a gold nanoparticles modified PIGE. Those results indicate that hIgG antigen can enhance the ECL intensity of ABEI-labeled anti-hIgG antibody and the sensitivity for hIgG antigen at a gold nanoparticles modified PIGE is a higher than that a bulk gold electrode. Therefore, a gold nanoparticles modified PIGE was employed in the following immunoassay for hIgG.

ECL characteristics of ABEI-labeled anti-hIgG antibody in the presence of BSA and thrombin were also tested. The results showed that the ECL intensity of ABEI-labeled anti-hIgG antibody (ECL peak intensity is 101) was about the same as that in the presence of 2.0×10^{-9} g/mL BSA (ECL peak intensity is 109) and 5.0×10^{-8} g/mL thrombin (ECL peak intensity is 128), indicating that the non-specific proteins did not influence the ECL intensity because no binding with ABEI-labeled anti-hIgG antibody occurred. This suggests that ABEI-labeled anti-hIgG antibody can be used as an ECL probe for the detection of hIgG antigen.

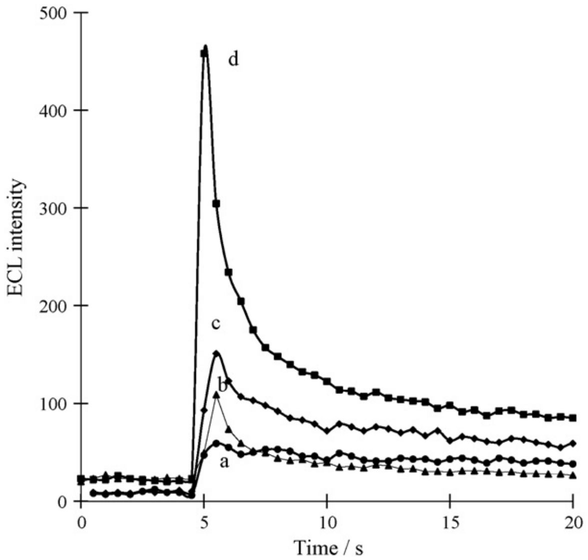

Fig. 7. ECL profiles of the ABEI-labeled anti-hIgG antibody in 0.10 mol/L PBS (pH 7.4) containing 1.0×10^{-3} mol/L H_2O_2 at a bulk gold electrode (a and c) and at a gold nanoparticles modified PIGE (b and d) in the absence (a and b)/presence(c and d) of 1.0×10^{-9} g/mL hIgG. ABEI-labeled anti-hIgG antibody, 1.0×10^{-9} g/mL, applied potential, 0.80 V.

3.3. Homogeneous ECL immunoassay for hIgG antigen

In order to obtain the higher sensitivity of the designed immunoassay, the concentration of ABEI-labeled anti-hIgG antibody was optimized when a fixed concentration of 1.0×10^{-9} g/mL hIgG antigen was used. The results showed that the integral ECL intensity increased with an increase of the concentration of ABEI-labeled anti-hIgG antibody from 3.0×10^{-10} to 1.0×10^{-9} g/mL, and achieved maximum at 1.0×10^{-9} g/mL. Further increasing the concentration of ABEI-labeled anti-hIgG antibody, the ECL intensity gradually decreased due to the increase of background ECL of ABEI-labeled anti-hIgG antibody used. Therefore, 1.0×10^{-9} g/mL ABEI-labeled anti-hIgG antibody was chosen in following experiment.

The quantitative behavior of the designed ECL immunoassay for hIgG antigen was assessed according to the protocol described in Section 2.4. The calibration curve for hIgG antigen is shown in Fig. 8. From Fig. 8, it can be seen that the integral ECL intensity had a linear relationship with the concentration of hIgG antigen in the range from 3.0×10^{-11} to 1.0×10^{-9} g/mL. The regression equation was $I = 842 + 114.8\,C$ (unit of C is 10^{-11} g/mL) and the correlation coefficient was 0.9939. This indicates that the homogenous ECL immunoassay designed is feasible. The detection limit was 1×10^{-11} g/mL hIgG antigen (S/N = 3). It should be noted that the detection limit of hIgG antigen in this work is higher than that reported by Arai et al. [15]. This is maybe attributed to low activity of both antigen and antibody used and low label ratio of ABEI per hIgG antibody in this work.

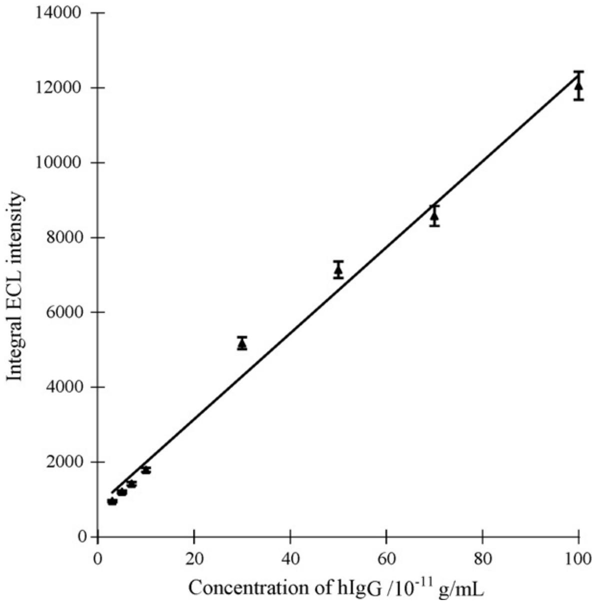

Fig. 8. The relationship between integral ECL intensity and the concentration of hIgG antigen at gold nanoparticles modified PIGE. 0.10 mol/L PBS containing 1.0×10^{-3} mol/L H_2O_2 and 1.0×10^{-9} g/mL ABEI-labeled anti-hIgG antibody. Applied potential, 0.80 V.

The reproducibility of one gold nanoparticle modified PIGE to assay IgG was examined in 0.10 mol/L PBS containing 1.0×10^{-9} g/mL hIgG and 1.0×10^{-9} g/mL ABEI-labeled anti-hIgG antibody and 1.0 mmol/L hydrogen peroxide. The relative standard deviation was 1.9% in 11 successive detections. This suggests that the fouling of proteins to gold nanoparticle modified PIGE was not significant.

4. Conclusion

A homogeneous ECL immunoassay for hIgG antigen at gold nanoparticles modified PIGE using ABEI-labeled anti-hIgG antibody has been developed. The proposed ECL method for the determination of ABEI is very simple and greatly sensitive. The homogeneous ECL immunoassay for hIgG antigen is easily performed with a high sensitivity. This work demonstrates that the homogeneous ECL immunoassay at nanoparticles modified electrode is a promising approach to improving the sensitivity of ECL label and ECL immunoassay. It is expected that gold nanoparticles modified electrode and ABEI as an ECL label for design ECL immunoassay based on a signal increase could be applied in the analysis of other biological molecules.

Acknowledgement

Financial support from the National Science Foundation of China (No. 20375025, 90607016) is gratefully acknowledged.

References

[1] S.B. Zhang, Z.S. Wu, M.M. Guo, G.L. Shen, R.Q. Yu, Talanta 71 (2007) 1530–1535.
[2] T. Suzawa, Y. Ikariyama, M. Aizawa, Anal. Chem. 66 (1994) 3889–3894.
[3] H. Yu, J.W. Raymonda, T.M. McMahon, A.A. Campagnari, Biosens. Bioelectron. 14 (2000) 829–840.
[4] G.F. Blackburn, H.P. Shah, J.H. Kenten, J. Leland, R.A. Kamin, J. Link, J. Peterman, M.J. Powell, A. Shah, D.B. Talley, S.K. Tyagi, E. Wilkens, T. Wu, R.J. Massey, Clin. Chem. 37 (1991) 1534–1539.
[5] H. Yang, J.K. Leland, D. Yost, R.J. Massey, Bio/Technology 12 (1994) 193–194.
[6] M.M. Richter, Chem. Rev. 104 (2004) 3003–3006.
[7] C.X. Zhang, H.H. Zhang, M.L. Feng, Anal. Lett. 36 (2003) 1103–1114.
[8] H.L. Qi, C.X. Zhang, Anal. Chim. Acta 501 (2004) 31–35.
[9] C.X. Zhang, H.L. Qi, M.N. Zhang, Luminescence 22 (2007) 53–59.
[10] H. Cui, Y. Xu, Z.F. Zhang, Anal. Chem. 76 (2004) 4002–4010.
[11] Y.P. Dong, H. Cui, C.M. Wang, J. Phys. Chem. B 110 (2006) 18408–18414.
[12] Y.P. Dong, H. Cui, Y. Xu, Langmuir 23 (2007) 523–529.
[13] C.M. Wang, H. Cui, Luminescence 22 (2007) 35–45.
[14] X.B. Yin, B. Qi, X.P. Sun, X.R. Yang, E.K. Wang, Anal. Chem. 77 (2005) 3525–3530.
[15] K. Arai, K. Takahashi, F. Kusu, Anal. Chem. 71 (1999) 2237–2240.
[16] M.L. Calvo-Munoza, A. Dupont-Filliardb, M. Billonb, S. Guillerezb, G. Bidanb, C. Marquettec, L. Blum, Bioelectrochemistry 66 (2005) 139–143.
[17] M.L. Yang, C.L. Liu, K.J. Qian, P.G. He, Y.Z. Fang, Analyst 127 (2002) 1267–1271.
[18] M. Pazzagli, J.B. Kim, G. Messeri, G. Martinazzo, F. Kohen, F. Franceschetti, G. Moneti, R. Salerno, A. Tommasi, M. Serio, Clin. Chim. Acta 115 (1981) 277–286.
[19] G. Frens, Nat. Phys. Sci. 241 (1973) 20–22.
[20] O.M. Steijger, D.A. Kamminga, A. Brummelhuis, H. Lingeman, J. Chromatogr. A 799 (1998) 57–66.
[21] A.N. Shipway, I. Willner, Chem. Commun. 20 (2001) 2035–2045.
[22] M. Pazzagli, J.B. Kim, G. Messeri, G. Martinazz, F. Kohen, F. Franceschetti, G. Moneti, R. Salerno, A. Tommasi, M. Serio, Clin. Chim. Acta 115 (1981) 277–286.

Available online at www.sciencedirect.com

ScienceDirect

Talanta 75 (2008) 760–764

Talanta

www.elsevier.com/locate/talanta

A highly sensitive and selective chemosensor for cyanide

Jiaqiang Ren, Weihong Zhu, He Tian *

Key Laboratory for Advanced Materials & Institute of Fine Chemicals, East China University of Science & Technology, Shanghai 200237, PR China

Received 21 August 2007; received in revised form 4 December 2007; accepted 7 December 2007
Available online 26 December 2007

Abstract

A highly sensitive and selective cyanide chemosensor based on fused indoline and benzooxazine fragment was reported with fast response. The detection of cyanide was performed via the nucleophilic attack of cyanide anion on the oxazine. ^{1}H NMR and MS studies confirmed the cleavage of C–O bond of oxazine and binding of cyanide to the spiro center of oxazine. The specific reaction results in high selectivity for cyanide ion. Addition of cyanide anion to the oxazine in MeCN/H_2O solution results in a loss in absorbance at 343 nm and an increase in new absorbance at 411 nm, thus resulting in obvious color changes. Cyanide can be detected down to 1 μM levels in a fast response of less than 30 s with no interference of other anionic species. The cyanide detection method should have potential application in a variety of settings requiring rapid and accurate analysis of cyanide anion for drinking and fresh water.

Keywords: Cyanide anion; Oxazine; Chemosensor; Chemical reaction

1. Introduction

Cyanide is extremely toxic, and even relatively small amounts of this species are lethal to humans. As known, its toxicity results from its propensity to bind the iron in cytochrome *c* oxidase, interfering with electron transport and resulting in hypoxia [1]. Nevertheless, a large amount of cyanides are extensively utilized in industries such as mining, metallurgy, photographic processing, and the production of nitriles, nylon and acrylic plastics, which raises a number of environmental concerns, particularly in terms of its retention in leech circuits, recovery and potential for contamination. The Environmental Protection Agency (EPA) has set the maximum contaminant level (MCL) for cyanide at 0.2 mg/L to regulate the safe level for drinking water systems [2]. Up to date, a variety of analytical methods concerning cyanide anion have been developed including chemiluminescence sensors [3,4], spectroscopic and spectrofluorometric methods [5,6], electrochemical sensors [7,8], biosensors [9,10] and a flow injection analysis [11,12]. However, the current detection of cyanide involves certain inherent disadvantages. For instances, Shan et al. [9] reported an extremely sensitive detection limit (0.1 nM) for cyanide based on amperometric biosensor. Although its response time is about 7 s, the pretreatment time of cyanide by enzyme incubation was as long as 10 min. Also, Legako et al. [13] reported a cyanide sensor derived from the porphyrin system by spectroscopic methods with a short response time of 6 s, but the change of absorbance wavelength maxima from 418 to 421 nm is too small, not obvious by naked detection. Moreover, the interferences with anions, such as F^-, SCN^-, S^{2-}, I^-, $SO_3{}^{2-}$, $NO_2{}^-$ and $NO_3{}^-$ [5,6,12,14,15], are always complicated in cyanide detection. Even the interfering effect of S^{2-} has to be overcome by using standard lead precipitation techniques. Therefore, there is an urgent need and issue to develop fast, accurate detections of cyanide in a variety of settings.

Recently, a particularly attractive alternative is the utilization of chemodosimeters as analytes through a specific chemical reaction (usually irreversible) between guest molecules and target species, leading to the formation of a fluorescent or colored product, in which an accumulative effect is directly related to the analyte concentration [10,16,17]. In this way, our group has developed the first selective fluorescent chemodosimeter for mercury ion based upon the reactivity of intramolecular cyclic guanylation by thiourea derivatives toward Hg(II) ion [18]. Thus, high selectivity toward the analyte is a welcome feature of chemodosimeters, which is also preferable for the

---

* Corresponding author at: Key Laboratory for Advanced Materials & Institute of Fine Chemicals, East China University of Science & Technology, Meilong Road 130, Shanghai 200237, PR China. Fax: +86 21 64252288.

E-mail address: tianhe@ecust.edu.cn (H. Tian).

0039-9140/$ – see front matter © 2007 Elsevier B.V. All rights reserved.
doi:10.1016/j.talanta.2007.12.024

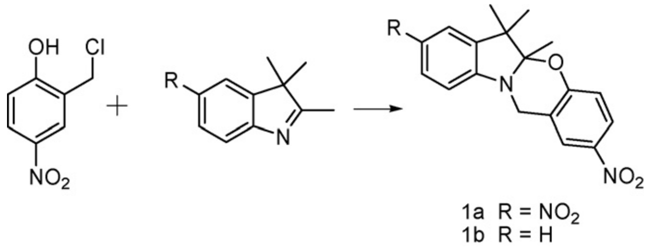

Scheme 1. Synthesis of oxazine 1a and 1b.

detection of CN^- ion. Raymo's group [19,20] designed a chromogenic oxazine for cyanide detection, in which the interference is just free of halide anions and a longer response time of about 1 min. As a further advance, here we report chemosensors 1a and 1b derived from the fused indoline and benzooxazine fragments (Scheme 1) for selective detection of cyanide anion. The design is based on the specific ring-open reaction of oxazine derivatives with cyanide. When titrated with cyanide, the C–O bond of oxazine becomes cleaved by the cyanide anion attack on the spiro center via nucleophilic addition, which causes drastic changes in color, easily detected by the naked eyes. This specific reaction results in a highly selective and fast response detection for cyanide ion.

2. Experimental

2.1. Apparatus

^1H NMR spectra were measured on a Brucker AM 400 spectrometer. Mass spectra (MS) were carried out on a MA1212 instrument using standard conditions (EI, 70 eV). UV/vis spectra were done on a Varian Cary 500 spectrophotometer with 1 cm quartz cell at 25 °C.

2.2. Reagents

All chemicals were of analytical grade and used as received with the exception of MeCN, which was distilled over CaH_2. Water was doubly distilled in quartz apparatus. The standard cyanide solution was prepared as 0.1 mol/L of sodium cyanide stock solution unless noted otherwise, and stored in the dark. All anionic solutions used in controlling testing were prepared by dilution from their stock solutions of sodium salts.

2.3. Synthesis

5-Nitro-2,3,3′-trimethyl-3*H*-indole and 2-nitro-5a,6,6-trimethyl-5a,6-dihydro-12*H*-indolo[2,1-*b*][1,3]benzooxazine (1b) were synthesized according to literatures [19,21]. 2,8-Dinitro-5a,6,6-trimethyl-5a,6-dihydro-12*H*-indolo[2,1-*b*][1,3]benzooxazine (1a) was synthesized, mostly based on the established method [19], via the cyclization of indoline derivatives and 2-chloromethyl-4-nitrophenol.

2,8-Dinitro-5a,6,6-trimethyl-5a,6-dihydro-12H-indolo [2,1-b][1,3]benzooxazine (1a). A mixture of 5-nitro-2,3,3′-trimethyl-3*H*-indole (102 mg, 0.5 mmol) and 2-chloromethyl-4-nitrophenol (94 mg, 0.5 mmol) in MeCN (15 mL) was heated and refluxed for 48 h. After cooled down to ambient temperature, the solvent was evaporated under reduced pressure. The residue was dissolved in CH_2Cl_2 (10 mL), and washed with aqueous KOH (0.2 M, 5 mL) and H_2O (10 mL). The organic phase was concentrated, and the residue was purified by column chromatography eluted with ethyl acetate/petroleum ether (1:10) to afford the oxazine 1a (76 mg) as yellow solid, yield 43%, m.p. 197–199 °C. ^1H NMR (400 MHz, $CDCl_3$, ppm): δ 8.09–8.11 (m, 2H, Ar–H), 8.00–8.04 (m, 2H, Ar–H), 6.81 (d, 1H, $J = 9.1$ Hz, Ar–H), 6.60 (d, 1H, $J = 8.7$ Hz, Ar–H), 4.72 (s, 2H, $-CH_2$), 1.61 (s, 3H, $-CH_3$), 1.27 (s, 6H, $-CH_3$); ^{13}C NMR (400 MHz, $CDCl_3$, ppm): δ 16.36, 18.73, 25.88, 40.42, 47.71, 102.26, 107.32, 118.15, 118.56, 118.79, 123.14, 124.45, 125.64, 138.97, 141.76, 152.26, 158.11; EI-MS (70 eV): $m/z = 355.1$ $[M]^+$, 338.1 $[M-17]^+$, 204.1 $[M-151]^+$, 189.1 $[M-166]^+$.

2.4. Analytical procedure

In $MeCN/H_2O$ solution, oxazine 1a of 0.1 mM was transferred into the spectrophotometer quartz cell (1.0 cm light path length). The sodium cyanide stock solution of 0.1 mol/L was diluted to 1.0×10^{-4} and 1.0×10^{-3} mol/L with deionized water, respectively. The absorbance was measured from 200 to 600 nm, against a blank MeCN solution. Different cyanide solutions (0, 2, 4, 6, 8, 10, 12, 14, 16, 18, 20 μL, of 1.0×10^{-4} M, and 4, 8, 12, 16, 20 μL, of 1.0×10^{-3} M) were added, and the added volume during titration was negligible (at the most 0.02 mL) as compared with the initial volume of the oxazine (2 mL), the mixtures were shaken and the absorption spectra were measured from 200 to 600 nm. Calibration curves were constructed by plotting the absorbance change at each wavelength against the cyanide concentration to give linear relationships. A calibration plot of cyanide concentration against the most sensitive absorption at 411 nm was used for all subsequent measurements of cyanide test and interference test solutions. The spectrophotometric measurements were measured in a mixture of MeCN and H_2O (19:1, v/v, 298 K) with a buffer solution of Na_2HPO_4/NaH_2PO_4 (7.5 mM, pH 7.6).

3. Results and discussion

3.1. Mechanism

In $MeCN/H_2O$ solution, the absorption spectrum of 1a shows a band centered at 343 nm. When titrated with NaCN solution buffered with sodium phosphate solution (pH 7.6), a new absorption band at 411 nm was observed (Fig. 1), which might be attributed to the cleavage of the [C–O] bond of oxazine 1a in the presence of cyanide anion (Fig. 2) [22–24]. As a matter of fact, the nucleophilic cyanide anion can specifically attack at the spiro carbon, resulting in the opening of the [1,3] oxazine ring to form the opened form of 2a (Fig. 2) [19,20]. Mass spectra and ^1H NMR studies give strong proofs consistent with the above analysis. The mass spectrum shows a peak at m/z 383.2, corresponding to the formation of 2a ($[M+2]^+$). Moreover, ^1H

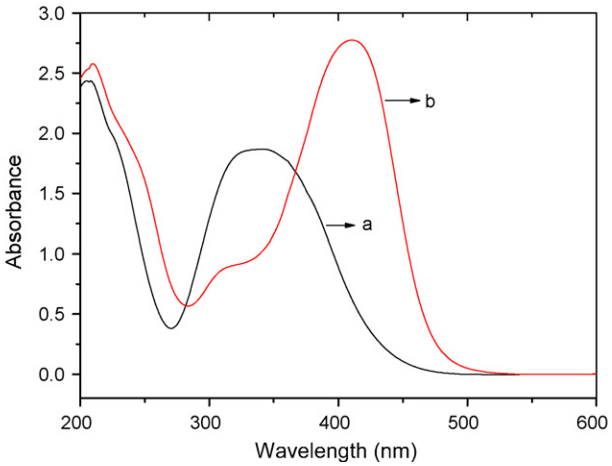

Fig. 1. Absorption spectra of oxazine 1a (0.1 mM, 298 K) in a mixture of MeCN–H_2O (19:1, v/v) without NaCN (curve a) and with NaCN (1 mM, curve b) buffered with sodium phosphate solution (7.5 mM, pH 7.6).

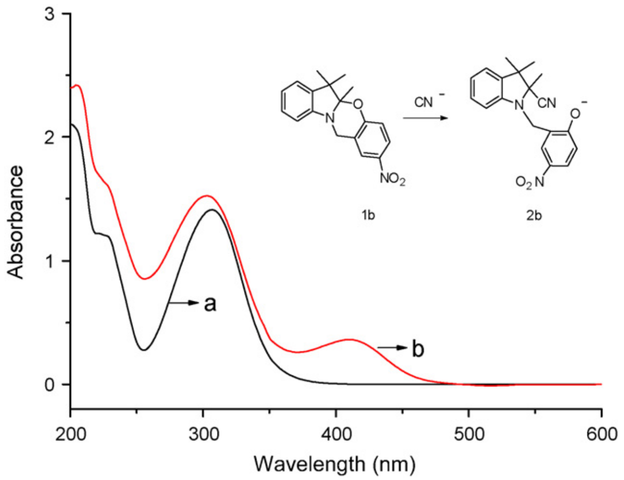

Fig. 3. Absorption spectra of oxazine 1b (0.1 mM, 298 K) in a mixture of MeCN–H_2O (19:1, v/v) without NaCN (curve a) and with NaCN (1 mM, curve b) buffered with sodium phosphate solution (7.5 mM, pH 7.6).

NMR spectrum of 1a changes dramatically after the addition of NaCN. The chiral center at the junction of two heterocycles in oxazine unit imposed two distinct environments on the adjacent pairs of methylene protons (H_g and H_h), and the ^1H NMR spectra of 1a showed an AB system for H_g and H_h. As a result, the characteristic AB system associated with the diastereotopic pair of methylene protons H_g and H_h was disappeared, and exhibited a single signal after the interconversation from 1a to 2a. The largest change (−0.42 ppm for H_f) in chemical shifts was observed for the proton in the ortho position relative to the phenolate oxygen atom. Other aromatic protons also shifted to the upfield to some extent.

Similarly, the absorption spectrum of oxazine 1b shows a band centered at 307 nm before addition of NaCN, and a new absorption peak at 410 nm was observed when adding NaCN solution buffered with sodium phosphate (Fig. 3). With respect to compound 1b, the electron-withdrawing nitro group substituted at the indole segment of oxazine 1a resulted in a red shift before the addition of NaCN and slightly red shift after the addition.

3.2. *Fast response*

As known, chemosensors always have a problem of long response time. In our previous report for Hg chemosensor, the intramolecular cyclic guanylation reaction is irreversible and produces a time-dependent dosimetric response that is controlled by the reaction kinetics [18]. In that case, it takes a response time of about 10 min to achieve completion with the changes in the emissive intensity. Unexpectedly, chemosensor 1a responses very fast (Fig. 4). When titrated with sodium cyanide, a new band appeared very rapidly at 411 nm within 30 s, and remains quite stable from 30 s to 30 min. As a consequence, the interconversion from 1a to 2a is an immediate response, thus providing a new real-time method for cyanide detection.

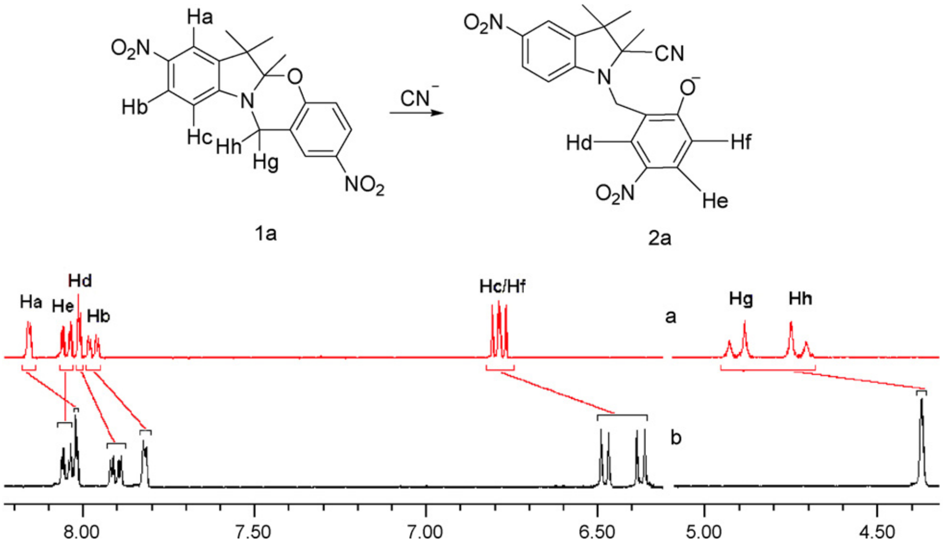

Fig. 2. Partial ^1H NMR spectra (400 MHz, $CD_3CN/D_2O = 9:1$) of 1a without NaCN (a) and with NaCN (b).

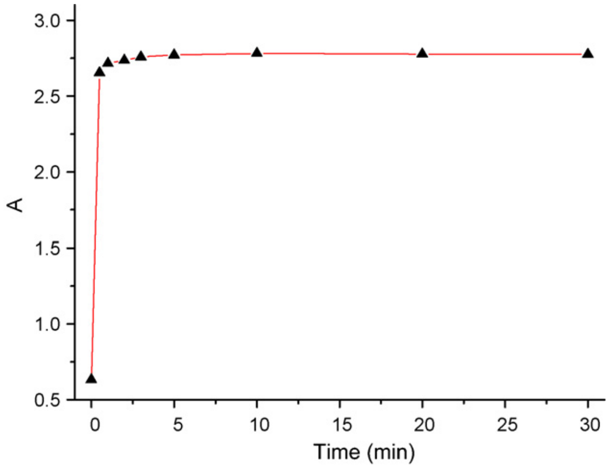

Fig. 4. Absorbance changes at 411 nm for oxazine 1a (0.1 mM, 298 K) in a mixture of MeCN–H_2O (19:1, v/v) with a buffer solution of Na_2HPO_4/NaH_2PO_4 (7.5 mM, pH 7.6) after addition of NaCN (1 mM).

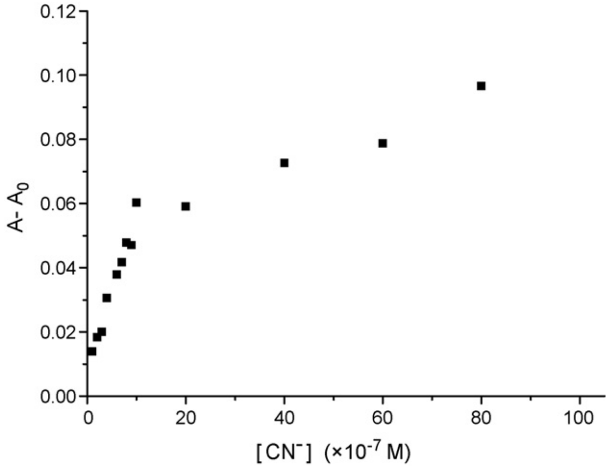

Fig. 6. Absorbance changes at 411 nm for oxazine 1a (0.1 mM, 298 K) in a mixture of MeCN–H_2O (19:1, v/v) with a buffer solution of Na_2HPO_4/NaH_2PO_4 (7.5 mM, pH 7.6) in the presence of different concentration of CN^-. Note: A_0 is the absorbance at wavelength 411 nm without CN^-.

3.3. Anionic interferences

The colorimetric detection of cyanide in water is generally complicated by the interference with some anions. Fig. 5 illustrated the spectroscopic response of 1a when titrated with a variety of anions in aqueous solution (including F^-, Cl^-, Br^-, I^-, CH_3COO^-, $ClCH_2COO^-$, IO_4^-, $C_2O_4^{2-}$, HCO_3^-, HSO_3^-, HSO_4^-, NO_2^-, NO_3^- SCN^- SO_3^{2-}, SO_4^{2-} and $S_2O_3^{2-}$), which indicated that the oxazine chemosensor is essentially unaffected by the presence of these common anions, even at relatively high concentration levels (1 mM). Notably, the characteristic absorption peak at 411 nm for the oxazine chemosensor can only be observed in the presence of cyanide, virtually insensitive to other anions. In fact, the addition of NaCN to oxazine 1a solution resulted in the cleavage of the [C–O] bond of oxazine and the appearance of the indolium cation, then part of the positive charge was enriched to spiro carbon atom. Furthermore, the cyanide anion is a particularly stronger nucleophile than others. Clearly, chemosensor 1a exhibits high selectivity for cyanide anion in that they are based upon the specific reactivity of cyanide anion toward oxazine.

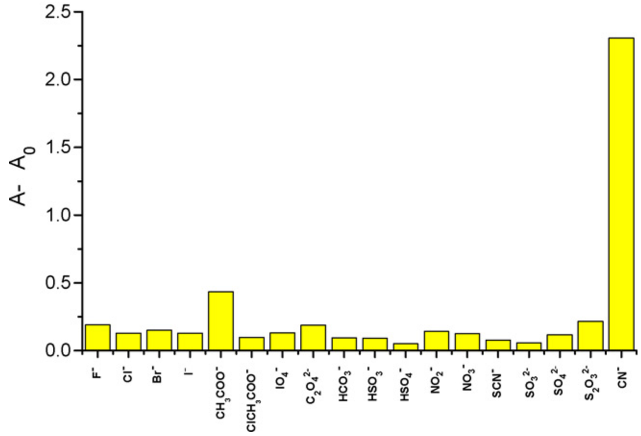

Fig. 5. Absorbance changes at 411 nm for oxazine 1a (0.1 mM, 298 K) in a mixture of MeCN–H_2O (19:1, v/v) with a buffer solution of Na_2HPO_4/NaH_2PO_4 (7.5 mM, pH 7.6) in the presence of CN^- or other common anions (1 mM). Note: A_0 is the absorbance at wavelength 411 nm without CN^-.

3.4. Detection limits

As mentioned above, the C–O bond of oxazine at the spiro center can specifically be cleaved via the nucleophilic cyanide anion attack, resulting in obvious color changes with a fast response. Thus for oxazine 1a, a highly sensitive colorimeter based on absorbance changes at 411 nm can be proposed as cyanide chemosensor. As shown in Fig. 6, the chemosensor exhibits fast response for cyanide anion with a linear working range from 10^{-6} to 10^{-5} M. Thus the micromolar concentrations of cyanide are sufficient to impose a detectable change on the absorbance, the low detection limit is 1.0×10^{-6} M and meets the U.S. EPA water quality criterion of sensitivity below 0.2 mg/L.

3.5. Applications

In order to assess the utility of the proposed method, it was applied successfully to the quantitative determination of cyanide anion in tap and drinking water samples (drinking water from commence). The water samples were found to be free from cyanide and so the samples were prepared by adding known amounts of cyanide to samples. Recovery studies were carried out to check the accuracy of the proposed method on different samples of water (drinking and tap water). All applications were performed using 2 mL of sample volume, and after addition of cyanide with the concentration of 5.0×10^{-6} mol/L, which was within the linear calibration range, the samples were injected in triplicate. The average contents of cyanide anion were found to be 5.07×10^{-6} and 4.77×10^{-6} mol/L for tap water and drinking water, respectively. Then, the recovery percentages performed well with relative standard deviations lower than 2% and 5% for tap water and drinking water, respectively. The results show that this method is suitable for determination of cyanide concentrations in such samples.

4. Conclusion

A highly sensitive and selective chemosensor based upon oxazine derivatives for cyanide have been synthesized and studied. The C–O bond of the oxazine at the spiro center cleaves when titrated with nucleophilic cyanide anions, resulting in obvious changes in color. It shows a very fast response within 30 s and can be detected by the naked eyes, providing a new, real-time method for cyanide detection. The detection limit for the sensor is 1.0×10^{-6} M, fully meeting the U.S. EPA water quality criterion of sensitivity. Notably, the characteristic absorption peak for the oxazine chemosensor can only be observed in the presence of cyanide, virtually insensitive to other anions. The results clearly demonstrate that a highly selective detection system for an analyte can be developed on the basis of a specific chemical reaction, at this time, via the nucleophilic reaction of oxazine toward cyanide. The cyanide detection method should have potential application in a variety of settings requiring rapid and accurate analysis of cyanide anion for drinking and fresh water.

Acknowledgements

This work was supported by NSFC/China, National Basic Research 973 Program (2006CB806200), Education Committee of Shanghai and Scientific Committee of Shanghai. W.H.Z. thanks the Program for New Century Excellent Talents in University (NCET-06-0418) and Shanghai Shuguang Project (07SG34).

References

[1] Y.G. Timofeyenko, J.J. Rosentreter, S. Mayo, Anal. Chem. 79 (2007) 251.
[2] http://www.epa.gov/safewater/contaminants/index.html.
[3] P. Anzenbacher, D.S. Tyson, K. Jursíková, F.N. Castellano, J. Am. Chem. Soc. 124 (2002) 6232.
[4] W.J. Jin, M.T. Fernández-Argüelles, J.M. Costa-Fernández, R. Pereiro, A. Sanz-Medel, Chem. Commun. (2005) 883.
[5] E. Palomares, M.V. Martínez-Díaz, T. Torres, E. Coronado, Adv. Funct. Mater. 16 (2006) 1166.
[6] A. Afkhami, N. Sarlak, A.R. Zarei, Talanta 71 (2007) 893.
[7] A.E. Lindsay, D. O'Hare, Anal. Chim. Acta 558 (2006) 158.
[8] W. Liu, J.G. Jiang, G.Y. Shi, Y. He, Y. Liu, L.T. Jin, Chin. J. Chem. 25 (2007) 203.
[9] D. Shan, C. Mousty, S. Cosnier, Anal. Chem. 76 (2004) 178.
[10] K.K.W. Mak, H. Yanase, R. Renneberg, Biosens. Bioelectron. 20 (2005) 2581.
[11] A. Ipatov, M. Ivanov, S. Makarychev-Mikhailov, V. Kolodnikov, A. Legin, Y. Vlasov, Talanta 58 (2002) 1071.
[12] A.R. Surleva, V.D. Nikolova, M.T. Neshkova, Anal. Chim. Acta 583 (2007) 174.
[13] J.A. Legako, B.J. White, H.J. Harmon, Sens. Actuator B 91 (2003) 128.
[14] Y. Chung, H. Lee, K.H. Ahn, J. Org. Chem. 71 (2006) 9470.
[15] A. Afkhami, N. Sarlak, Sens. Actuator B 122 (2007) 437.
[16] G. Zhang, D. Zhang, S. Yin, X. Yang, Z. Shuai, D. Zhu, Chem. Commun. (2005) 2161.
[17] J.S. Wu, I.C. Hwang, K.S. Kim, J.S. Kim, Org. Lett. 9 (2007) 907.
[18] B. Liu, H. Tian, Chem. Commun. (2005) 3156.
[19] M. Tomasulo, F.M. Raymo, Org. Lett. 7 (2005) 4633.
[20] M. Tomasulo, S. Sortino, A.J.P. White, F.M. Raymo, J. Org. Chem. 71 (2006) 744.
[21] S. Murphy, X. Yang, G.B. Schuster, J. Org. Chem. 60 (1995) 2411.
[22] M. Tomasulo, S. Sortino, A.J.P. White, F.M. Raymo, J. Org. Chem. 70 (2005) 8180.
[23] M. Tomasulo, S. Sortino, F.M. Raymo, Org. Lett. 7 (2005) 1109.
[24] M. Tomasulo, I. Yildiz, F.M. Raymo, J. Phys. Chem. B 110 (2006) 3853.

Available online at www.sciencedirect.com
ScienceDirect
Talanta 75 (2008) 811–816
Talanta
www.elsevier.com/locate/talanta

Non-chromatographic speciation of toxic arsenic in vegetables by hydride generation-atomic fluorescence spectrometry after ultrasound-assisted extraction

Mariela N. Matos Reyes [a], M. Luisa Cervera [b,*], Reinaldo C. Campos [a], Miguel de la Guardia [b]

[a] Department of Chemistry, Pontifícia Universidade Católica do Rio de Janeiro, Rua Marquês de São Vicente 225, 22453-900 Rio de Janeiro, RJ, Brazil
[b] Department of Analytical Chemistry, University of Valencia, 50 Dr. Moliner Street, 46100 Burjassot, Valencia, Spain

Received 12 April 2007; received in revised form 17 December 2007; accepted 17 December 2007
Available online 26 December 2007

Abstract

A non-chromatographic, sensitive and simple analytical method has been developed for the determination of toxic arsenic species in vegetable samples by hydride generation-atomic fluorescence spectrometry (HG-AFS). As(III), As(V), dimethylarsinic acid (DMA) and monomethylarsonic acid (MMA) were determined by hydride generation-atomic fluorescence spectrometry using a series of proportional equations. The method is based on a single extraction of the arsenic species considered from vegetables through sonication at room temperature with H_3PO_4 1 mol L^{-1} in the presence of 0.1% (w/v) Triton XT-114 and washing of the solid phase with 0.1% (w/v) EDTA, followed by direct measurement of the corresponding hydrides in four different experimental conditions. The limit of detection of the method was 3.1 ng g^{-1} for As(III), 3.0 ng g^{-1} for As(V), 1.5 ng g^{-1} for DMA and 1.9 ng g^{-1} for MMA, in all cases expressed in terms of sample dry weight. Recovery studies provided percentages greater than 91% for all considered species in spiked samples of chards and aubergines. Total toxic As found in the aforementioned samples was at the level of 90 ng g^{-1}; As(III) is followed by As(V), DMA and MMA which are the main species of As in chards being As(V) the main As compound in aubergines.

Keywords: HG-AFS; Inorganic and toxic arsenic; Non-chromatographic arsenic speciation; Ultrasound-assisted extraction; Vegetables

1. Introduction

Arsenic is a toxic element to humans and it has been classified by the International Agency for Research on Cancer (IARC) as a carcinogen to humans [1].

Arsenic is naturally found at low levels in air, soil, water and organisms. However, natural or anthropogenic sources have produced very high levels of arsenic in certain regions around the world [2,3]. As a result of several epidemiological studies carried out in endemic arsenic areas, drinking water is now considered the main source of inorganic arsenic for humans [3,4]. Foods are also considered an important part of the arsenic intake as shown for seafood [5,6], fish [7–9] and cereals [10,11].

There are only few reports of arsenic content in vegetables grown in non-polluted soils [12–14] due to the lack of sufficient sensitivity of the available analytical tools. Helgesen and Larsen [12] compare the arsenic species present in carrots grown in mixtures of arsenic-contaminated and uncontaminated soil, while Heitkemper and co-workers studied the arsenic species in carrots [13], and in purée infant food products [14]. However, most of studies were carried out in terrestrial plants grown on arsenic contaminated substrates [12,15–18].

Arsenic speciation in solid samples constitutes a challenge since the arsenic species must be first extracted from the matrix. Mild but efficient extraction conditions are required to ensure complete removal of arsenic compounds to be determined from the matrix without modifying the identity and concentration of individual species. In the literature a variety of methods have been applied for the extraction of arsenic from plants and vegetables, including microwave-assisted extraction with 0.3 mol L^{-1} orthophosphoric acid [15], ethanol–water mixture (1 + 1) [16] or methanol–water (1 + 9) [12], accelerated solvent extraction (ASE) with water [13], enzymatic attack with α-amylase followed by acetonitrile–water (40 + 60) extraction

---

* Corresponding author. Fax: +34 96 3544838.
E-mail address: M.Luisa.Cervera@uv.es (M.L. Cervera).

0039-9140/$ – see front matter © 2008 Elsevier B.V. All rights reserved.
doi:10.1016/j.talanta.2007.12.018

under sonication [19], extraction with 2 mol L^{-1} trifluoroacetic acid at 100 °C during 6 h [14], and water extraction by mechanical shaking [18].

On the other hand ultrasound-assisted extraction has become popular as a way for a fast solubilization of total extractive arsenic [20] and for the elemental analysis of different materials [21].

Speciation of arsenic usually involves several steps such as derivatization, separation and detection. Several analytical techniques have been applied involving separation by liquid chromatography (LC) and detection by inductively coupled plasma-mass spectrometry (ICP-MS) [12–14,18,19], hydride generation-atomic fluorescence spectrometry (HG-AFS) [15,16] or graphite furnace atomic absorption spectrometry (GF-AAS) [17].

Non-chromatographic methods of elemental speciation may offer cheaper, simpler, faster and more sensitive procedures than chromatographic ones. Based on our previous studies in this field [9,22,23] the present work proposes a simple analytical method that enables the speciation of arsenic by means ultrasound assisted extraction and quantification of As(III), As(V), DMA and MMA by HG-AFS.

2. Experimental

2.1. Instrumentation

A PS Analytical Millennium Excalibur (Kent, UK) atomic fluorescence spectrometer was employed for arsenic detection. The system was equipped with an arsenic boosted discharge hollow cathode lamp from Photron (Victoria, Australia), a specific filter, a solar blind detector and a Perma Pure dryer.

Table 1 summarizes the experimental conditions employed for the determination of As species in vegetable samples by AFS.

Table 1
Experimental conditions for the non-chromatographic determination of total and arsenic species in vegetables by HG-AFS

Parameter	Total As	Speciation
Wavelength (nm)	197.3	
Primary current (mA)	27.5	
Boost current (mA)	35	
Delay time (s)	10	
Analysis time (s)	30	
Memory time (s)	30	
HCl (mol L^{-1})	3.5	2 (A), 4 (B), 3.5 (C and D)
$NaBH_4$% (w/v)	0.7	1.4 (A and B), 1.2 (C and D)
Ar flow rate (mL min^{-1})	330	
Air flow rate (L min^{-1})	2.5	
Carrier flow rate (mL min^{-1})	9	
$NaBH_4$ flow rate (mL min^{-1})	4.5	

A–D correspond to special conditions for the determination of As fluorescence in different sub-samples of a sonicated vegetable in order to obtain four independent equations with four unknowns for the estimation of As(III), As(V), MMA and DMA. Conditions A–C means the use of different HCl and $NaBH_4$ concentrations in the analysis of the extracts and D also includes a previous reduction with KI and ascorbic acid of the extract.

An ultrasound water bath (Selecta, Barcelona, Spain) operating at 50 W power and 50 Hz frequency was employed for sample sonication.

Other equipments used were a Cryodos lyophilizer Telstar (Barcelona, Spain), a PL 5125 sand bath Raypa Scharlau (Barcelona, Spain) and a K1253 muffle furnace equipped with a Eurotherm Control 902 control program Heraeus (Madrid, Spain).

2.2. Reagents, solutions and samples

All reagents used were of analytical grade and all solutions were prepared in nanopure water, with a minimum resistivity of 18.0 MΩ cm, obtained from a Milli-Q Millipore system (Bedford, MA, USA).

The 1000 mg L^{-1} As(V) standard solution was supplied by Merck (Darmstadt, Germany). An As(III) stock solution of 1000 mg L^{-1} was prepared by dissolving As_2O_3 Riedel de Häen (Hannover, Germany) in 20% (w/v) KOH solution from Panreac (Barcelona, Spain), neutralizing with 20% (v/v) H_2SO_4 and diluting with 1% (v/v) H_2SO_4. The 1000 mg L^{-1} dimethylarsinic acid (DMA) stock solution was prepared from its sodium salt $(CH_3)_2AsO(ONa)\cdot 3H_2O$ Fluka (Buchs, Switzerland). The 1000 mg L^{-1} monomethylarsonic acid (MMA) stock solution was prepared from $CH_3AsO(ONa)_2\cdot 6H_2O$ Carlo Erba (Milano, Italy). The 1031 mg L^{-1} arsenobetaine standard solution ($(CH_3)_3As^+CH_2COO^-$) was obtained from the Community Bureau of Reference (BCR-626).

The 10 mg L^{-1} diluted stock solutions of As(III), As(V), MMA, DMA and arsenobetaine were prepared monthly and stored in a refrigerator at 4 °C to preserve the chemical species.

For the ultrasound-assisted extraction 37% HCl Merck, 65% HNO_3 J.T. Baker (Deventer, Holland), concentrated acetic acid (>99.5%) Fluka, 85% H_3PO_4 Analar BDH Chemicals (Poole, UK), methanol 99.98% Sharlau, trifluoroacetic acid Merck and trichloroacetic acid Probus (Barcelona, Spain) were used.

A 0.1% (w/v) solution of the disodium salt of ethylenediaminotetraacetic acid Panreac, a surfactant agent Triton XT-114 Feinbiochimica (Heidelberg, Germany) and Antifoam A from Fluka were also employed for the extraction and measurement of As species.

A 50% (w/v) KI reducing solution from Merck and a 10% (w/v) ascorbic acid from Scharlau were employed to reduce As(V) and MMA after extraction of As species.

Sodium tetrahydroborate from Fluka dissolved in 0.1 mol L^{-1} NaOH, was used to generate the corresponding As hydrides, previously to the AFS measurements. This solution was prepared daily and filtered before use.

Argon C-45 (purity > 99.995%) was employed as carrier gas and synthetic air was used to dry the formed hydride. Both were supplied by Carburos Metálicos (Barcelona, Spain).

2.3. Reference material and samples

The certified reference material NIST 1573 Tomato leaves was obtained from the National Institute of Standards and Technology. Vegetable samples were purchased at the local market of Valencia (Spain).

2.4. General procedures

2.4.1. Sample preparation

Chards and aubergines were cut into pieces with a knife and frozen at −20 °C. Afterwards, they were freeze-dried for a minimum of 48 h at a chamber pressure of 0.05 mbar. The dried samples were crumbled and pulverized with a mill. The resulting fine powder was stored in a dessicator until analysis.

2.4.2. Dry ashing mineralization for total arsenic determination in vegetable samples

Lyophilized samples (1 g ± 0.1 mg) were treated with 2.5 mL of ashing aid suspension of 20% (w/v) $Mg(NO_3)_2 \cdot 6H_2O$ and 2% (w/v) MgO and 5 mL of nitric acid 50% (v/v). The mixture was evaporated to dryness in a sand bath and mineralized in a muffle furnace at 450 °C with a gradual increase in temperature [24]. The white ashes were wetted with 1 mL of water and dissolved with 9 mL of 10% (v/v) HCl; 3 mL of this solution were transferred to a 50 mL polyethylene tube as well as 8.75 mL of concentrated HCl and 600 μL of the reducing solution 50% (w/v) KI and 10% (w/v) ascorbic acid. The volume was made up to 30 mL with ultrapure water. Total arsenic was determined in this solution by HG-AFS using the experimental conditions shown in Table 1.

2.4.3. Ultrasound-assisted extraction of toxic arsenic from vegetables

Portions of 1 g (±0.0001) powdered samples were weighed into 50 mL polyethylene tubes and 10 mL of the extractant containing 0.1% (v/v) Triton XT-114 were added to each tube and the obtained slurries were sonicated for 10 min. The extracts were separated by centrifugation at 3500 rpm for 10 min. The remaining solids were washed with 10 mL of 0.1% (w/v) EDTA and they were centrifuged again for additional 10 min. In the case of trifluoroacetic acid and trichloroacetic acid slurries were heated to 90 °C during 6 h and centrifuged [14]. The final medium was fitted to the corresponding HCl concentration. One sub-sample was prepared in a medium containing 1% (w/v) KI and 0.2% (w/v) ascorbic acid and the obtained solution was let to react for 30 min before measurement in the experimental conditions shown in Table 1. In fact for each extract, fluorescence measurements were made without an additional treatment with 2 mol L^{-1} HCl and 1.4% (w/v) $NaBH_4$ (condition A), with 4 mol L^{-1} HCl and 1.4% (w/v) $NaBH_4$ (condition B), with 3.5 mol L^{-1} HCl and 1.2% (w/v) $NaBH_4$ (condition C) and after reduction with 3.5 mol L^{-1} HCl and 1.2% (w/v) $NaBH_4$ (condition D).

3. Results and discussion

3.1. Selection of the extraction conditions for toxic arsenic determination

A preliminary study was made to evaluate the best extraction of inorganic As from lyophilized vegetables. Several extractants; such as 6 mol L^{-1} HCl, 1 mol L^{-1} HNO_3, 1 mol L^{-1} H_3PO_4, 1 mol L^{-1} acetic acid, aqua regia, 2 mol L^{-1} trifluoroacetic acid, 2 mol L^{-1} trichloroacetic acid and the mixture methanol:water (1:1) were evaluated.

In previous studies it was employed aqua regia for dairy products [22] and diluted nitric acid for seafoods treatment [9]. Hydrochloric acid has not oxidant behavior and in addition it forms trichloride and pentachloride from As(III) and As(V). The acetic acid and phosphoric acid were recently proposed as extractants in pressurized extraction systems and trifluoroacetic acid has been employed for rice and infant food products analysis. Table 2 shows the obtained results in the present study for the different extractants evaluated for chard and aubergine samples treatment.

Results for arsenic determination in aubergines show that the best extractants are HCl, H_3PO_4 and the mixture methanol:water. They give an extraction percentage of 100% as compared with data found for total As after dry ashing. The aqua regia extracts 86% of total As while HNO_3 only 80%. By the way, with HCl and H_3PO_4 the concentration of As(V) obtained is greater than that of As(III) (results not shown), but with the mixture methanol:water the distribution of these species is completely inverse, thus indicating some problems that could arise from interconversion of species during the extraction step.

In the case of chards, any extractant give contents close to the total arsenic determined after sample dry ashing (131 ± 4 ng g^{-1}), thus, the extraction yield for methanol:water was 75%, 70% for H_3PO_4 and 65% for HCl. The rest of extractants give extraction yields below 50%. It could be explained by the presence of additional As species than those considered or by an inefficient extraction of As(III), As(V), MMA or DMA.

On the other hand it has been found that As(III) and As(V) are the main species in chards and aubergines as it has been also reported for carrots, cabbage, potatoes and shallots [15].

In the present study H_3PO_4 1 mol L^{-1} was selected as the best extractant for the determination of toxic As in the studied vegetables

Table 2
Study of the extractant agents for the arsenic determination in chards and aubergines

Extractant	Chards	Aubergines
	Arsenic extracted (ng g^{-1})	Arsenic extracted (ng g^{-1})
6 mol L^{-1} HCl	85 ± 3	81 ± 4
1 mol L^{-1} HNO_3	75 ± 8	67 ± 3
1 mol L^{-1} acetic acid	61 ± 2	73 ± 3
1 mol L^{-1} H_3PO_4	92 ± 2	80 ± 3
Methanol:H_2O 1:1	98 ± 1	87 ± 1
Aqua regia	81 ± 1	52 ± 3
2 mol L^{-1} trifluoroacetic acid	83 ± 3	92 ± 2
2 mol L^{-1} trichloroacetic acid	61 ± 1	68 ± 1

Note: samples of 1 g were shaken at room temperature with 10 mL of the different extractants assayed for 10 min, and heated at 90 °C for 6 h in the case trifluoroacetic acid and trichloroacetic acid. Data of total As obtained after dry-ashing of samples were 131 ± 4 ng g^{-1} for chards and 84 ± 3 ng g^{-1} for aubergines.

3.2. Strategy for the speciation analysis of As(III), As(V), MMA and DMA

In a previous study [9] it was observed that As(V) can react with $NaBH_4$ with a lower reaction kinetic than As(III). So, the signal produced by the pentavalent species, depend on the hydride generation conditions and it represents around 50–70% of that produced by the trivalent species [22]. The same was observed for DMA and MMA [9]. HG-AFS measurements of standards and samples were made at four different experimental conditions which allows us to establish a set of four independent proportional equations for the measurement of each sample, being the fluorescence intensity obtained in each case proportional to the concentration of As(III), As(V), DMA and MMA as

$$I_{(A)} = 281.0[\mathrm{As(III)}] + 264.9[\mathrm{As(V)}] + 120.4[\mathrm{DMA}] + 87.3[\mathrm{MMA}]$$

$$I_{(B)} = 319.7[\mathrm{As(III)}] + 269.5[\mathrm{As(V)}] + 69.8[\mathrm{DMA}] + 67.4[\mathrm{MMA}]$$

$$I_{(C)} = 430.4[\mathrm{As(III)}] + 306.6[\mathrm{As(V)}] + 75.7[\mathrm{DMA}] + 84.1[\mathrm{MMA}]$$

$$I_{(D)} = 478.5[\mathrm{As(III)}] + 431.4[\mathrm{As(V)}] + 106.4[\mathrm{DMA}] + 151.3[\mathrm{MMA}]$$

The conditions chosen (A–D) are summarized in Table 1. Condition A represents a maximum signal for MMA and DMA, while in condition C the maximum sensitivity is achieved for As(III) and As(V). Condition B represents an intermediate behavior for all species and finally, in condition D a mixture of KI/ascorbic acid was added before HG-AFS measurement in order to reduce As(V) and MMA.

This strategy was applied to chard and aubergine samples for the determination of As(III), As(V), DMA and MMA. Tables 3 and 4 show the concentration data obtained of each species in vegetables.

From data found on the natural content of the toxic species of arsenic in vegetables it can be concluded that the main species are As(III) and As(V) and at a minor level DMA (1.14–4.27 ng g^{-1}) and MMA (1.19–3.72 ng g^{-1}). In aubergines the principal specie is As(V) and in chards As(III). It must be also noticed the excellent repeatability found between data corresponding to different sub-samples of unspiked chards and aubergines. The total toxic arsenic found correspond to 95 and 97% of total As determined after dry ashing of chards and aubergines, respectively, data which are in good agreement with the results reported for freeze-dried apples with percentages between 73 and 91% [19], for freeze-dried infant products (sweet potatoes, carrots, green beans and peaches) where DMA and MMA were lower of the method detection limit (10 ng g^{-1}) [14] and for carrots where no methylated arsenic species were found [12].

3.3. Recovery experiments

100 ng g^{-1} of each one of the considered species were added to chard and aubergine samples and results summarized in Table 4 shows that recoveries are approximately around 100% for all the species considered in aubergines. In chards, As(III) and As(V) were recovered at 100% level and methylated species at 92% level (see Table 3).

Table 3
Determination of toxic arsenic species in a chard sample by HG-AFS and recovery percentages

Samples	As(III) (ng g^{-1})	As(V) (ng g^{-1})	DMA (ng g^{-1})	MMA (ng g^{-1})	Sum of species (ng g^{-1})	Recovery (%)
AC1	89.2	14.7	4.3	3.5	111.7	
AC2	90.6	15.3	4.1	3.7	113.8	
AC3	90.1	14.2	4.1	3.5	111.9	
AC4 + As(III)[a]	184.4	13.9	4.0	3.5	205.9	97.8 ± 0.8
AC5 + As(III)[a]	185.6	13.4	4.1	3.9	206.9	
AC6 + As(III)[a]	187.5	13.0	4.1	4.0	208.6	
AC7 + As(V)[b]	90.5	113.5	3.8	3.8	211.6	99.0 ± 0.4
AC8 + As(V)[b]	90.0	113.2	3.9	3.7	210.9	
AC9 + As(V)[b]	89.7	114.0	4.0	3.8	211.6	
AC10 + DMA[c]	90.1	14.6	103.9	3.9	212.5	92.80 ± 0.15
AC11 + DMA[c]	88.8	13.6	104.0	3.9	210.5	
AC12 + DMA[c]	89.1	14.1	104.2	3.9	211.5	
AC13 + MMA[d]	90.6	14.1	4.0	104.0	212.7	90.71 ± 0.10
AC14 + MMA[d]	89.8	13.1	4.0	103.8	210.7	
AC15 + MMA[d]	90.7	13.5	4.0	103.9	212.2	

Note: 1 g sample was shaken for 10 min at room temperature with 10 mL of 1 mol L^{-1} H_3PO_4 in the presence of 0.1% (w/v) Triton XT-114 and the remaining solid phase washed with 0.1% (w/v) EDTA. AC1–AC3 correspond to different sub-samples of unspiked chards.

[a] AC4–AC6 correspond to different sub-samples spiked with addition of 100 ng g^{-1} of As(III).

[b] AC7–AC9 correspond to different sub-samples spiked with addition of 100 ng g^{-1} of As(V).

[c] AC10–AC12 correspond to different sub-samples spiked with addition of 108 ng g^{-1} of DMA.

[d] AC13–AC15 correspond to different sub-samples spiked with addition of 111 ng g^{-1} of MMA.

Table 4
Determination of toxic arsenic species in aubergine sample by HG-AFS and recovery percentages

Samples	As(III) (ng g^{-1})	As(V) (ng g^{-1})	DMA (ng g^{-1})	MMA (ng g^{-1})	Sum of species (ng g^{-1})	Recovery (%)
B1	20.7	61.2	1.1	1.2	84.3	
B2	20.6	61.0	1.2	1.2	84.1	
B3	20.9	61.9	1.2	1.2	85.2	
B4 + As(III)[a]	120.2	61.3	1.2	1.2	183.9	100.0 ± 0.6
B5 + As(III)[a]	120.5	61.2	1.2	1.2	184.1	
B6 + As(III)[a]	121.7	60.4	1.2	1.2	184.6	
B7 + As(V)[b]	20.8	160.2	1.2	1.2	183.3	99.53 ± 0.14
B8 + As(V)[b]	21.0	160.5	1.2	1.2	183.9	
B9 + As(V)[b]	21.0	161.1	1.2	1.2	184.5	
B10 + DMA[c]	20.3	59.6	109.4	1.2	190.5	100.0 ± 0.3
B11 + DMA[c]	20.8	59.5	109.1	1.2	190.5	
B12 + DMA[c]	19.7	60.0	108.9	1.2	189.7	
B13 + MMA[d]	20.4	59.9	1.1	111.5	193.0	99.7 ± 0.3
B14 + MMA[d]	20.7	60.6	1.1	112.2	194.6	
B15 + MMA[d]	19.6	60.2	1.2	112.0	192.9	

Note: extraction was made in the same conditions indicated in Table 3. B1–B3 correspond to different sub-samples of unspiked aubergines.

[a] B4–B6 correspond to different sub-samples spiked with addition of 100 ng g^{-1} of As(III).

[b] B7–B9 correspond to different sub-samples spiked with addition of 100 ng g^{-1} of As(V).

[c] B10–B12 correspond to different sub-samples spiked with addition of 108 ng g^{-1} of DMA.

[d] B13–B15 correspond to different sub-samples spiked with addition of 111 ng g^{-1} of MMA.

3.4. *Interference of arsenobetaine*

To guarantee the absence of degradation of non-hydride reactive As compounds during sample extraction and HG-AFS measurement, 100 ng g^{-1} of arsenobetaine were added to the samples (aubergines and chards) before the extraction procedure. Total toxic As results found were 90 ± 3 and 92.0 ± 1.8 ng g^{-1} for chards samples unspiked and spiked, respectively; and 85.1 ± 1.1 and 87.0 ± 2.6 ng g^{-1} for aubergine samples. So, it can be concluded that the difference between the concentration of total arsenic in chards and the content found after the extraction process and the application of the system of four equations could be due to the presence of organo-arsenical species that do not generate hydride in the proposed conditions.

By the way, samples of aubergines and chards were analyzed for the determination of inorganic arsenic using an extraction with hydrochloric acid and chloroform and a back-extraction to the aqueous phase [24]. The concentration of inorganic arsenic found in aubergine samples was 83.5 ± 1.1 and for chards 126 ± 3 ng g^{-1} which are of the same order than those obtained by the proposed methodology. In short it can be concluded that the extraction efficiencies obtained by the recommended procedure are of the same order than those reported in the literature for vegetables and terrestrial plants: 75–111% for carrots [13], 79–117% for freeze-dried apples [19], 70–102% for various vegetables [15] and 72–92% for rice straw [16].

3.5. *Speciation of As in a reference material*

There are previous studies on inorganic As in CRM material but there is no data concerning to arsenic speciation in vegetable reference materials. In the present work it was determined the concentration of As(III), As(V), DMA and MMA in a certified reference material NIST 1573 (tomato leaves) and results obtained (see Table 5) evidence that the sum of the considered species compares well with the total As certified value. So, indicating the absence of non-hydride reactive As and the accuracy of the proposed procedure.

3.6. *Limit of detection of the method*

Limit of detection values were calculated by dividing three times the standard deviation of the fluorescence signal of 10 reagent blanks by the slope of the calibration line, in the best experimental conditions, for each arsenic species. The limit of detection was also established for samples taking into account the sample mass and dilution factor involved in the proposed methodology. The lowest LOD corresponds to DMA (1.5 ng g^{-1}); As(III) and As(V) have a similar LOD of 3.1 ng g^{-1}

Table 5
Non-chromatographic arsenic speciation analysis of a certified reference material NIST 1573 (tomato leaves)

Sample	As(III) (ng g^{-1})	As(V) (ng g^{-1})	DMA (ng g^{-1})	MMA (ng g^{-1})	Sum of species (ng g^{-1})	Extraction efficiency (%)[a]
T1	83.5	44.2	117.2	6.0	250.9	95 ± 2
T2	87.1	46.8	121.8	6.0	261.8	
T3	86.7	45.6	118.7	6.5	257.4	

[a] Extraction efficiency in relation to the certified value (0.27 ± 0.02 $\mu g\, g^{-1}$).

and 3.0 ng g^{-1}, respectively, whereas MMA gives 1.9 ng g^{-1}. As compared with previous published papers these LOD values are of the same order than those found by high-performance liquid chromatography with ICP-MS detection (between 0.6 and 1.2 μg kg^{-1} [19], 5–10 ng g^{-1} [14], 6–12 ng g^{-1} [13]), and with HF-AFS detection (5–8 μg kg^{-1} [15]).

4. Conclusions

It has been demonstrated that sonication of freeze-dried vegetable samples with 1 mol L^{-1} H_3PO_4, at room temperature, is an efficient toxic arsenic extraction procedure that does not modify the original arsenic species. The non-chromatographic strategy developed for the further determination of As(III), As(V), DMA and MMA by HG-AFS offers a simple and fast alternative procedure for the speciation analysis of toxic forms of As in the studied samples which requires 30 min extraction and 30 min additional time for reduction of the extracts before the determination of As fluorescence in four different experimental conditions. On the other hand it must be taken into consideration that several samples could be treated simultaneously with the subsequent improvement of sample throughput.

Good recoveries were observed for all studied arsenic species as well as comparable results with an alternative extraction procedure with chloroform and hydrochloric acid.

Taking arsenobetaine as model species for non-toxic and non-hydride reactive forms, it can be concluded that no degradation of complex arsenic forms occurs during the procedure. Although no adequate certified reference material is available for the present work, 95% extraction yields as well as coherent speciation results were obtained in the speciation analysis of a vegetable reference material certified for total arsenic.

Vegetable samples analyzed present total arsenic contents below the maximum limit permitted by the Spanish Legislation [25] but values found for inorganic arsenic (the more toxic species) were close to the levels of total arsenic.

On comparing the proposed methodology with the classical chromatographic approach it must be accepted that chromatography offers a way for direct observation and quantification of the different species of As present in an appropriate extract in spite of the indirect estimation made in this study. However, chromatography also requires a previous extraction of As species from solid samples and a careful control of extract pH and involves the use of additional instrumentation and extra costs.

Acknowledgements

The authors gratefully acknowledge the support of the Programme Alβan, the European Union Programme of High Level Scholarships for Latin America, scholarship no. E05D049710BR and the financial support of the University of Valencia Project UV-AE-20070213.

References

[1] T. Tsuda, A. Babazono, T. Ogawa, H. Hamad, Y. Mino, H. Aoyama, N. Kuramatani, T. Nagira, M. Harada, S. Inomata, Appl. Organomet. Chem. 6 (1992) 309.

[2] D. Chakraborti, M.M. Rahman, K. Paul, U.K. Chowdhury, M.K. Sengupta, D. Lodh, C.R. Chanda, K.C. Saha, S.C. Mukherjee, Talanta 58 (2002) 3.

[3] A.H. Smith, M. Goycolea, R. Haque, M.L. Biggs, Am. J. Epidemiol. 147 (1998) 660.

[4] M. Tondel, M. Rahman, A. Magnuson, I.A. Chowdhury, M.H. Faruquee, Sk.A. Ahamad, Environ. Health Perspect. 107 (1999) 727.

[5] W. Li, C. Wei, C. Zhang, M. Van Hulle, R. Cornelis, X. Zhang, Food Chem. Toxicol. 41 (2003) 1103.

[6] R. Heinrich-Ramm, S. Mindt-Prüfert, D. Szadkowski, J. Chromatogr. B 778 (2002) 263.

[7] J. Entwisle, R. Hearn, Spectrochim. Acta B 61 (2006) 438.

[8] I. Serafimovski, I.B. Karadjova, T. Stafilov, D.L. Tsalev, Microchem. J. 83 (2006) 5.

[9] P. Cava-Montesinos, K. Nilles, M.L. Cervera, M. de la Guardia, Talanta 66 (2005) 895.

[10] E. Sanz, R. Muñoz-Olivas, C. Cámara, Anal. Chim. Acta 535 (2005) 227.

[11] D.T. Heitkemper, N.P. Vela, K.R. Stewart, S. Craig, J. Anal. At. Spectrom. 16 (2001) 299.

[12] H. Helgesen, E.H. Larsen, Analyst 123 (1998) 791.

[13] N.P. Vela, D.T. Heitkemper, K.R. Stewart, Analyst 126 (2001) 1011.

[14] N.P. Vela, D.T. Heitkemper, J. AOAC Int. 87 (2004) 244.

[15] Y. Bohari, G. Lobos, H. Pinochet, F. Pannier, A. Astruc, M. Potin-Gautier, J. Environ. Monit. 4 (2002) 596.

[16] C. Yuan, G. Jiang, B. He, J. Anal. At. Spectrom. 20 (2005) 103.

[17] R.A. Pyles, E.A. Woolson, J. Agric. Food Chem. 30 (1982) 866.

[18] S. Londesborough, J. Mattusch, R. Wennrich, Fresenius J. Anal. Chem. 363 (1999) 577.

[19] J.A. Caruso, D.T. Heitkemper, C. B'Hymer, Analyst 126 (2001) 136.

[20] K. Ashley, R.N. Andrews, L. Cavazos, M. Demage, J. Anal. At. Spectrom. 16 (2001) 1147.

[21] J.L. Capelo, I. Lavilla, C. Bendicho, Anal. Chem. 73 (2001) 3732.

[22] P. Cava-Montesinos, A. de la Guardia, C. Teutsch, M.L. Cervera, M. de la Guardia, Anal. Chim. Acta 493 (2003) 195.

[23] P. Cava-Montesinos, A. Domínguez-Vidal, M.L. Cervera, A. Pastor, M. de la Guardia, Talanta 66 (2005) 895.

[24] O. Muñoz, O.P. Díaz, I. Leyton, N. Núñez, V. Devesa, M.A. Súñer, D. Velez, R. Montoro, J. Agric. Food Chem. 50 (2002) 642.

[25] Food Legislation Surveys No. 6, Metallic contaminants in food—a survey of international prescribed limits, 3rd ed., Leatherhead FOOD RA, UK, 1993.

Available online at www.sciencedirect.com
ScienceDirect
Talanta 75 (2008) 846–850
Talanta
www.elsevier.com/locate/talanta

Short communication

Rapid determination of chloramphenicol residues in milk powder by liquid chromatography–elektrospray ionization tandem mass spectrometry

L. Rodziewicz*, I. Zawadzka

Department of Hygiene Veterinary, ul. Zwycięstwa 26a, 15-959 Bialystok, Poland

Received 2 August 2007; received in revised form 3 December 2007; accepted 7 December 2007
Available online 26 December 2007

Abstract

A simple and rapid liquid chromatography tandem mass spectrometry (LC–ESI–MS–MS) confirmation method for the analysis chloramphenicol (CAP) in milk powder has been developed. Samples were extracted by using liquid–iquid extraction steps with ethyl acetate. Lipids were removed using hexsan. LC separation was achieved by using a Phenomenex Luna C-18 column and acetonitryle–water as a mobile phase. The mass spectrometer was operated in multiple reaction monitoring mode (MRM) with negative electro-spray interface (ESI–). The four transitions were monitored m/z 321 → 257, 321 → 194, 321 → 152, 326 → 157 (IS) and for quantification, the transition m/z 321 → 152 was chosen. Validation of the method was done according to criteria of Decision Commission No 2002/657 EC. Validation includes the determination of specification, linearity, precision (within- and between-day), accuracy, decision limit (CCα) and detection capability (CCβ). Samples were fortified at CAP levels 0.30, 0.45 and 0.60 μg/kg with CAP-5d as internal standard. The precision within-day (RSD%) was lower than 12% and accuracy (RE%) ranged from −9.8 to −3.7%. The precision between-day (RSD%) was less than 15%. The limit of decision (CCα) and detection capability (CCβ) for milk powder 0.09 and 0.11 μg/kg. Value CCα and CCβ were calculated for the 321 → 152 ion transition. This method has been successfully used for routine analysis.

Keywords: Milk powder; Chloramphenicol; Residue; LC–MS/MS

1. Introduction

Chloramphenicol (CAP) is a broad-spectrum antibiotic previously used in veterinary medicine. CAP has been included in Annex IV Regulation 2377/90/EEC [1], which prohibits the use of certain chemicals in food producing animals in EU and USA. CAP has displayed significant toxicological effects on humans e.g. aplastic anemia and hypersensitivity. The EU has set up MRPL (minimum required performance level) at 0.3 μg/kg for CAP in milk [2]. The Commission Decision 2002/657/EC [3] necessitates control of CAP residues in milk and milk products.

Methods for the determination of CAP in liquid milk rapid enzyme linking immunosorbent assay (ELISA) and mass spectrometric in combination with gas chromatography or liquid chromatography are currently used. ELISA method is suitable for screening purposes whereas mass spectrometric methods are utilized for confirmation. The European inter-laboratory study for screening of CAP in raw milk by ELISA test kits, shows a total false positive rate of 16.7% and a total false negative rate of 2.2% [4]. GC–MS methods can provide definitive qualitative and quantitative results but require a derivatization step of polar non-volatile analytes, such as CAP [5]. The combination of LC–ESI–MS–MS offers a rapid, simplified, specific and sensitive alternative to GC–MS methods, without derivatization [6–9].

Very few methods LC–MS–MS have been published on analysis residues of CAP in milk powder [4]. LC–ESI–MS–MS method for quantitative and determination of residues of CAP in milk powder includes three basic step. First step liquid-liquid extraction of CAP uses organic solvent. The second step removes lipids and the third one includes purification on a solid-phase extraction (SPE) using different sorbents.

This paper describes the development of rapid method for determination of the CAP residues in milk powder. The procedure involves single extraction of sample with ethyl

---

* Corresponding author.
E-mail address: rodziewicz@wiw.bianet.com.pl (L. Rodziewicz).

0039-9140/$ – see front matter © 2008 Elsevier B.V. All rights reserved.
doi:10.1016/j.talanta.2007.12.022

acetate followed by removal of lipids by hexane. No additional clean-up (SPE) of the sample solution was performed. Extracted CAP was determined by LC–ESI–MS–MS equipped with two position valve cut-off. The method was validated according to the decision 2002/657//EC.

2. Experimental

2.1. Reagents

Analytical standard chlorampenicol from Sigma–Aldrich, deuterated chloramphenicol-d5 (100 μg/ml in acetonitryle) was used as internal standard from Cambridge Isotope Laboratories (FSD-117-100, 98%), ethyl acetate, hexane LC grade, acetonitrile LC–MS grade and anhydrous sodium sulphate were from Baker. The water used was purified by a Milli-Q water purification system from Millipore.

2.2. Standard solution

A CAP standard stock solution of 1 mg/ml was prepared by dissolving 100 mg CAP in 100 ml of acetonitrile and this solution was diluted 50 times in acetonitrile obtaining intermediate standard solution of 20 μg/ml. A CAP working solution of 50 ng/ml was made by diluting stock solution with acetonitrile. Internal standard of CAP-d5 was prepared by dissolving the ampoule with 100 μg/ml in acetonitrile, which was adequately diluted till a working solution of 3 μg/ml. The stock standard solution kept at −20 °C was stable for 1 year. The working solutions stored at 4 °C was stable for 3 months.

2.3. Samples

The blank control samples of milk powder were collected by the Poland Veterinary Public Health at inspection points. The samples of milk powder were stored at +4°C until analysis.

2.4. Sample preparation

5 g milk powder was fortified by internal standard 0.3 μg/kg. Milk powder was dissolved in 25 ml water and the mixture was placed in water bath at 40 °C and mixed for about 10 min until a homogeneous sample was obtain. 3 g of homogeneous sample was weighed into a 25 ml centrifuge tube with 3 g sodium sulfate and 6 ml ethyl acetate was added. The mixture was vortexed for 2 min and centrifuged at 3500 rpm for 15 min at 4 °C. 4 ml of extract (ethyl acetate) was transferred to 10 ml tubes and evaporated to dryness under a stream of nitrogen using a heating block at 45 °C. The dry residue was redissolved in 1 ml acetonitrile and 2× 1 ml hexane was added. The sample was mixed and hexane phase was discarded. Samples were evoporated to dryness under a stream of nitrogen using a heating block at 45 °C. The dry reasidue milk powder was redissolved in 0.4 ml of mobile phase acetonitryl:water (50:50, v/v) and was filtered through a 0.45 μm cellulose filter. Twenty μl was injected into LC–MS/MS.

Table 1
MRM transitions reactions monitored for CAP and internal standard CAP-d5

Compound	Transition reaction (*m*/*z*)	CE (eV)
CAP	321 → 152	18
	321 → 194	14
	321 → 257	14
CAP-d5 (IS)	326 → 157	23

2.5. Calibration curves

The calibration curves at five concentration levels were prepared by spiking milk powder with CAP at the following concentrations: 0.0 (blank sample), 0.3, 0.45, 0.6 and 0.9 μg/kg. A fixed amount of internal standard CAP-d5 was added to all samples. Calibration curves were obtained relating ratio CAP area (*m*/*z* 152)/CAP-d5 area (*m*/*z* 157) with CAP concentration in μg/kg. Peak area ratios of the analyte to internal standard were computed using Analyst 1.4 software from Applied Biosystems.

2.6. LC–ESI–MS–MS

LC analyses were performed on a Luna C18 column (150 mm × 2 mm i.d., 5 μm) (Phenomenex, Torrance, USA) using an Agilent 1100 series liquid chromatograph, equipped with a binary pump and an autosampler. The column was thermostated at 40 °C. The mobile phase was water (A) and acetonitryle (80:20; v/v). The linear gradient program was: 0.0–0.1 min 80% A; 0.1–7.0 min 0.0% A; 7.0–7.3 min 80% A; 7.3–20 min 80% A. Flow rate was set at 300 (l/min and the injection volume was 20 μl.

MS analyses were performed on an API 3000 triple stage quadrupole mass spectrometer (Applied Biosystems, Foster City, CA) equipped with a turbo-ionspray interface and two position microelectric valve. The LC flow was directed into the MS detector between 5 and 9 min using a valve cut-off (Valco Instument Co.Inc. Huston TX, USA). The source block temperature was set at 400 °C and the electrospray capilare voltage was at −3500 V. The dwell time for each transition reaction was set 200 ms, the declustering potential was set −91 V and the entrance potential −10 V. Resolution was set for Q1 and Q2 at unit. Nitrogen was used as collision gas. MS detection was performed in negative mode using Multiple Reaction Monitoring (MRM). The collision energy was optimized for each of the forth MRM transitions reactions monitored throughout the LC run. The MRM transitions and their collision energies (CE) are shown in Table 1.

3. Results and discussion

According to Commission Decision 2002/657/EC for the confirmation of banned substances a minimum of four identification points were required. The four identification points were obtained using LC–MS/MS with one precursor and two product ions. The presented research method detected three product ions. Thus the performance criteria for confirmation was fulfilled.

The method was based on the validation according to the criteria of the decision 2002/657/EC. According to these criteria, validation includes the determination of specification, linearity, repeatability, within-laboratory reproducibility, accuracy, decision limit (CCα) and detection capability (CCβ).

Specificity of the method was checked by the preparation and analysis of different 20 blank and spiked samples at 0.3 μg/kg in order to investigate possible interference retention time. No interference was observed around the CAP retention time either in milk powder in the samples. The retention time for CAP and CAP-d5 were 6.8 min. The signal-to-noise ratio for each diagnostic ion was >3:1. Typical chromatograms blank samples and spiked samples milk powder are shown in Fig. 1, respectively.

Response linearity was evaluated by calibration curves. The calibration curves were prepared by using samples spiked milk powder in the 0.0–0.9 μg/kg and were repeated on three different days. The calibration curves were linear. The mean linear correlation coefficient (*r*) was higher than 0.998 with a weighting factor of 1/*x*. and mean slope 3.05.

Precision within-day and accuracy were calculated from the analysis of blank spiked samples of milk powder at three levels 0.30, 0.45 and 0.60 μg/kg. The samples were analyzed by the same instrument and the same operator. Six replicates were obtained for each concentration.

The precision (within- and between-day), were determined by calculating the relative standard deviation (RSD%). The accuracy (relative error RE%) was calculated by the agreement between the measured and the nominal concentrations of the spiked samples. Results of precision within-day and accuracy are presented in Table 2.

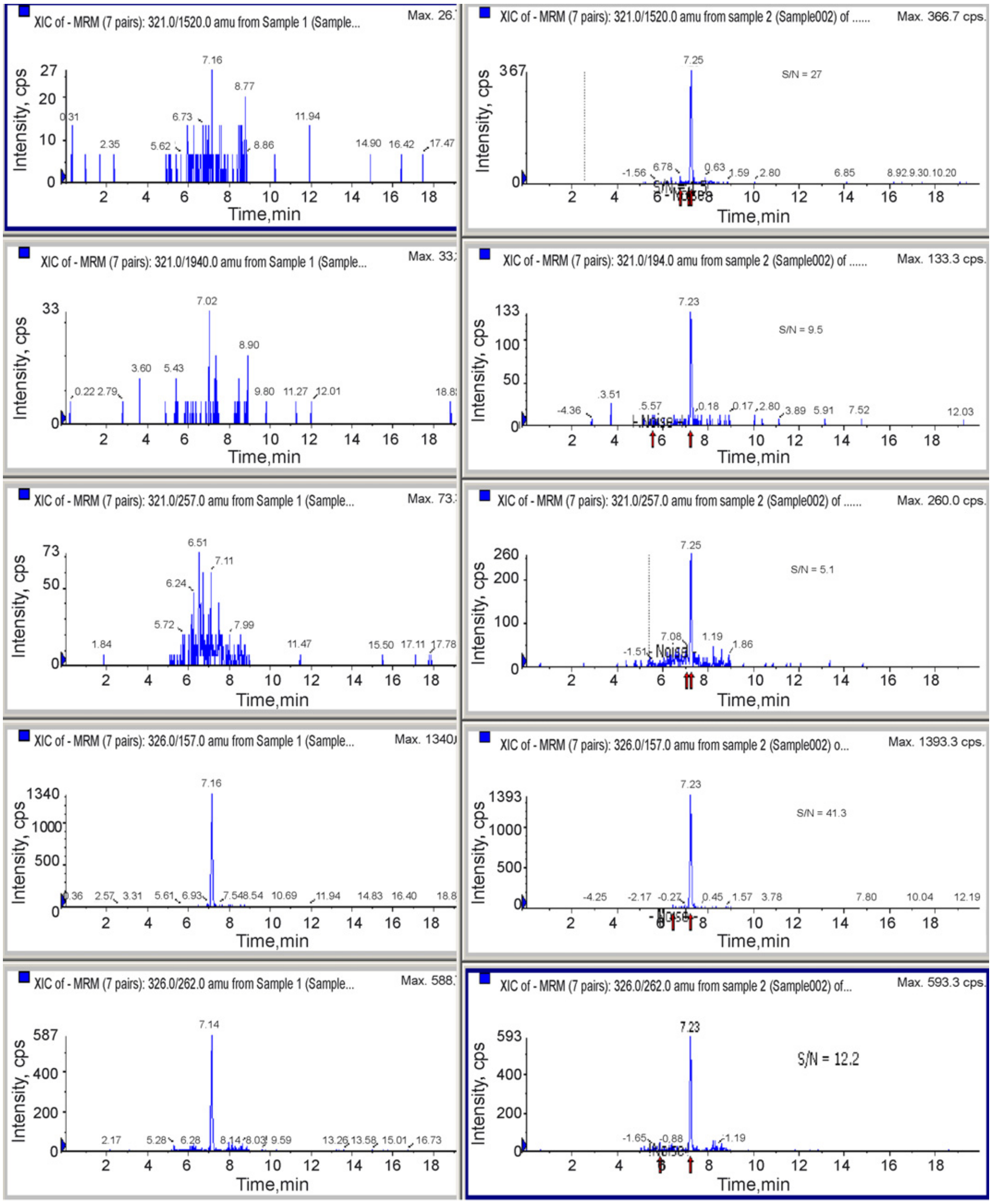

Fig. 1. MRM chromatograms of blank milk powder and milk powder spiked at 0.1 μg/kg.

Table 2
Precision (within-day) and accuracy in spiked milk powder ($n = 6$)

Level of spiking (μg/kg)	0.30	0.45	0.60
Average (μg/kg)	0.289	0.413	0.541
Precision (RSD%)	10.8	7.8	11.8
Accuracy (RF%)	−3.7	−8.2	−9.8

Precision between-day was calculated in spiked samples at concentration of 0.3 μg/kg. They were analyzed on three different days (3 ×6), with the same instrument and the different operators. RSD of the means contraction was 14.8%. According to decision 2002/657/EC coefficient of variation from method not expect the value calculated by the Horwitz. The coefficient of variation should be as low as possible in the cases.

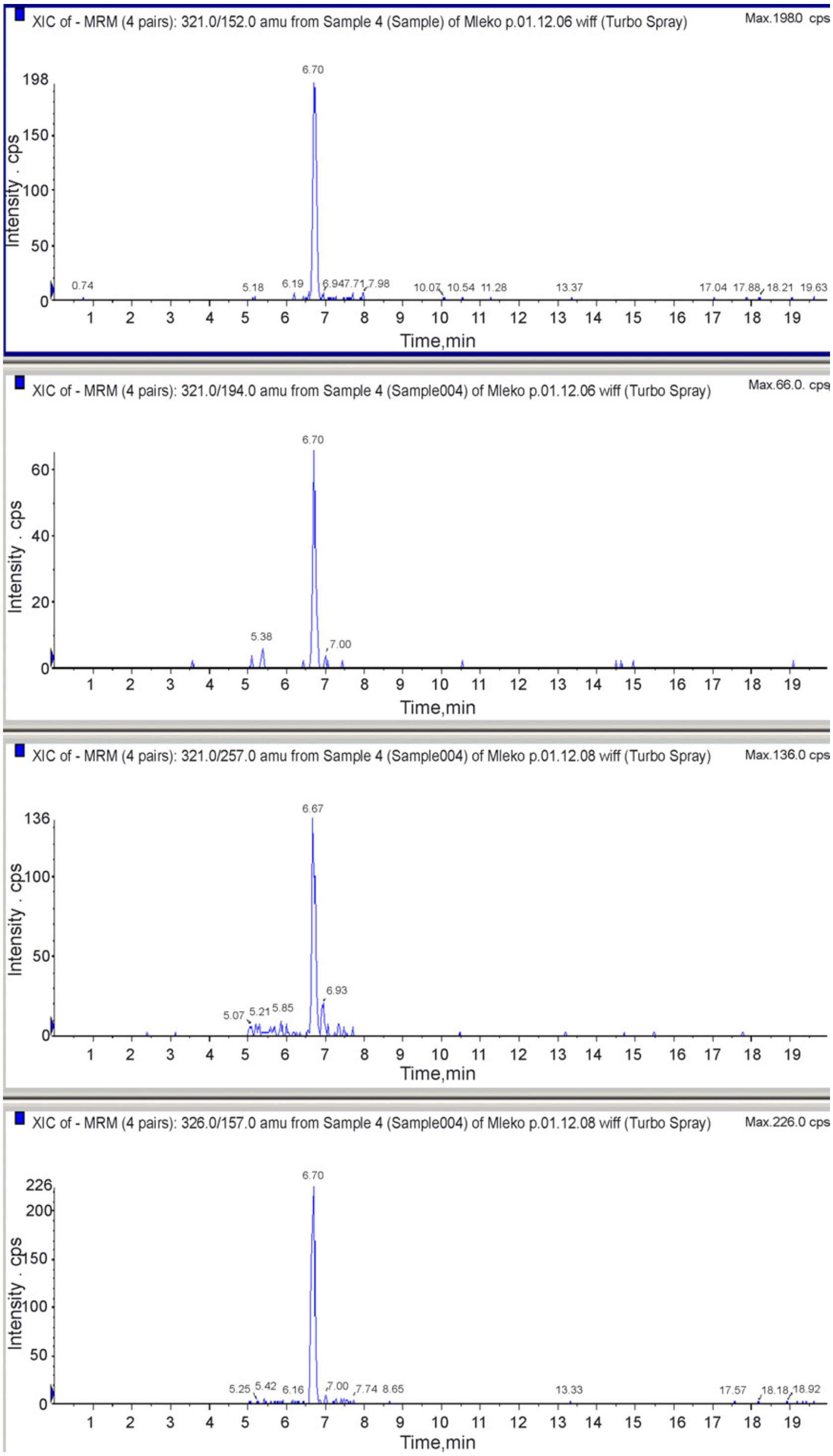

Fig. 2. MRM chromatograms of milk powder containing CAP 0.48 μg/kg.

The values CCα and CCβ were determined by the matrix calibration curve procedure according to ISO 11843. These limits were determined using six curves obtained at four levels 0.00, 0.15, 0.30 and 0.45 μg/kg. CCα and CCβ were calculated for the 321 → 152 ion transition. The value CCα and CCβ were 0.08 and 0.10 μg/kg.

The proposed analytical method was tested incurred milk powder. CAP was considered as positive identified in milk powder when the retention time of the analyte should correspond to the standard analyte from the spiked sample, with a tolerance of ±2.5% and the peak area ratios of the various transitions reactions have been according to the tolerances given in decision 2002/657/EC. The peak area ratio *m*/*z* 152–257 and *m*/*z* 152–194 for standard samples and with their tolerances 0.72 ± 20% and 0.40 ± 25%, respectively. Fig. 2 show chromatogram incurred milk powder sample. Average contraction of CAP ($n = 6$) was 0.48 μg/kg with RSD 9.3%.

4. Conclusion

This presented LC–MS/MS method is fast compared to the other presented methods. The sample preparation is simple and has good precision and recoveries. The CCα and CCβ for milk and milk powder are below the MRPL of 0.3 μg/kg. The validation results are in accordance with the performance method of the European Commission Decision 2002/657/EC. The method was used for routine analysis of CAP in samples milk powder.

References

[1] European Council Regulation (EEC) No. 2377/90/EC 26 of June 1990 laying down a community procedure for the establishment of maximum residue limit of veterinary medicinal products in foodstuff of animal orgin, Off. Eur. Commun. L224 (1990).

[2] Commission Decision of 13 March 2003 amending Decision 2002/657/EC as regards the seating of minimum required performance limits (MRPLs) for certain residues in food animal origin (2003/18/EC), Off. Eur. Commun. L71 (2003) 17.

[3] Commission Decision of 12 August 2002 implementing Council Directive 96/23/EC concerning the performance of analytical methods and the interpretation of results, Off. Eur. Commun. 2002/657/EC, L221 (2002) 8.

[4] P.A. Guy, D. Royer, P. Mottier, E. Gremaud, A. Perisset, R.H. Stadler, J. Chromatogr. A 1054 (2004) 365.

[5] T. Sniegocki, A. Posyniak, J. Zmudzki, Bull. Vet. Inst. Pulavy 50 (2006) 353.

[6] R.S. Nicolich, E. Weneck-Barroso, M.A. Sipoli Marques, Anal. Chim. Acta 565 (2006) 97.

[7] H.T. Ronnig, K. Einarsen, T.N. Asp, J. Chromatogr. A 118 (2006) 226.

[8] L. Penney, A. Smith, B. Coates, A. Wijewickreme, J. AOCA Int. 88 (2005) 645.

[9] J.F. Huang, H.J. Zhang, Y.Q. Feng, J. Agric. Food Chem. 13 (2006) 9279.

Available online at www.sciencedirect.com
ScienceDirect
Talanta 75 (2008) 725–733
Talanta
www.elsevier.com/locate/talanta

Development and validation of a method for active drug identification and content determination of ranitidine in pharmaceutical products using near-infrared reflectance spectroscopy: A parametric release approach

Sílvia S. Rosa[a,b,*], Pedro A. Barata[a], José M. Martins[a], José C. Menezes[b]

[a] *Laboratórios Atral SA, Rua da Estação 42, Vala do Carregado, P 2600 726 Castanheira do Ribatejo, Portugal*
[b] *Centre for Biological and Chemical Engineering, IST, Technical University of Lisbon, Av. Rovisco Pais, P 1049 001, Lisbon, Portugal*

Received 13 July 2007; received in revised form 4 December 2007; accepted 7 December 2007
Available online 23 December 2007

Abstract

In this paper we describe the strategy used in the development and validation of a near-infrared diffuse reflectance spectroscopy method for identification and quantification of ranitidine in pharmaceutical products (granulates, cores and coated tablets) at-line, with a fiber optic probe. This method was developed in a pharmaceutical industry for routine application, to replace reference methods and was submitted and approved to the National Medicine Regulatory Agency (Infarmed). We consider that this is the first step of a broader parametric release approach to pharmaceutical products.

Keywords: Near-infrared spectroscopy; Fiber optic probe; Multivariate analysis; Ranitidine; Pharmaceutical products; Validation; Parametric release

1. Introduction

Near-infrared (NIR) is the region of the electromagnetic spectrum that extends from about 780 to 2500 nm (or 12,800 to 4000 cm^{-1}). Although it was discovered 200 years ago, it was only in the past 30 years that its analytical potential has been exploited. Near-infrared spectroscopy (NIRS) has become widely used for a range of analyses in various industries [1].

The usefulness of this technique is mainly attributed to: (1) its capability for non-destructive analyses, no need of sample preparation or reagents consumption; (2) its speed, economy and (3) accuracy and precision, among others [2].

Pharmaceutical applications of the NIR appeared in the late 1960s, with the majority appearing in the last two decades [3]. Nowadays, NIR has found increased use in the pharmaceutical industry. The most common application of NIR in the pharmaceutical industry is the identification of raw materials [4,5], but in the last decade it has proved its usefulness in other applications: (1) the quantification of active drug compounds in several pharmaceutical products (granulates, powders, tablets) with different analytical principles (i.e., reflectance and transmittance) [6–9], (2) the determination of moisture content [10], (3) for blend homogeneity [11–13], hardness [14], film coating experiences [15,16], evaluation of particle size distribution [17,18], studies with polymorphic and crystalline forms [19,20]. Mention to near-infrared spectroscopy in the pharmacopeias is a proof of acceptance of NIR methods based on pharmaceutical applications [21,22]. The development of a method for identification and quantification of active compounds in pharmaceutical products has been described in previous papers. However different products and different realities could mean different approaches.

There are several guidelines that must be taken into account during the development and validation of a NIR method [23,26,27]. These guidelines are not mandatory, but in order to develop a method that will be approvable by regulatory agencies, it is important to follow the instructions and recommendations therein.

The use of NIRS for quantitative purposes should involve a suitability test as first step, to find out if it is possible to develop a calibration that allows the quantification of a specific parameter in the type of available samples. The next step is calibration development, which is done with a set of

---

* Corresponding author at: Centre for Biological and Chemical Engineering, IST, Technical University of Lisbon, Av. Rovisco Pais, P 1049 001, Lisbon, Portugal, Tel.: +351 916010086.
E-mail address: silviarosa@ist.utl.pt (S.S. Rosa).

0039-9140/$ – see front matter © 2007 Elsevier B.V. All rights reserved.
doi:10.1016/j.talanta.2007.12.008

spectra from samples with known concentrations (performed by the reference method), with a range wider than the product specifications range—at least 80–120% of the concentrations. The samples should originate from different batches in order to cover nominal variations, including physical properties, moisture content, etc. [6,26]. Considering that a manufacturing process is well established and give origin to homogeneous samples with concentrations around the specified range, then it is necessary to prepare samples outside that range to widen its calibration purposes. Those samples could be production samples with out-of-specification results or laboratory samples, which could be prepared for instance by adding excipients or active compounds to production samples. However, lab-engineered samples may sometimes introduce greater than nominal variances in the samples properties and later on lead to considerable errors on production samples prediction [6].

Once a calibration is developed and favorable predictions are expected, they must be validated to be accepted for routine use. For external validation an independent set of samples is needed. The external validation set may include only production samples that are similar to those that are intended to be analysed, but they could also include samples with a wide concentration range like laboratory made samples, since they do not exceed the extremes of the calibration range [7,26]. There are several validation parameters that must be determined in order to be consistent with the recommendations of International Conference of Harmonisation (ICH) and other guidelines: accuracy, precision (repeatability and intermediate precision), specificity, linearity and range of application [23–26].

The aim of this study is the development of an NIR method that allows the identification and simultaneous quantification of an active compound (ranitidine) in granulates for compression, cores (intermediate products) and coated tablets (final product), at-line, with a diffuse reflectance fiber optic probe, for routine application in a pharmaceutical company, and to establish a relationship between that method and the parametric release concept.

Parametric release could be used as an alternative to routine release analysis of some specific parameters. According to the European Organization for Quality (EOQ), parametric release is: “A system release that gives assurance that the product is of the intended quality based on the information collected during the manufacturing process and on compliance with specific GMP requirements related to parametric release” [28–30]. So, parametric release is based on evidence of successful validation of the manufacturing process and review of the documentation on process monitoring carried out during manufacturing to provide the desired assurance of the quality of the product [28]. It is recognized that a comprehensive set of in-process tests and controls may provide greater assurance that the finished product is more likely to meet specifications than simple finished product testing [30]. Parametric release could be established by means of process analytical test methods, such as spectroscopy techniques like near-infrared spectroscopy (NIRS) used in combination with multivariate analysis [29]. The concepts of parametric release and PAT (process analytical technologies) are related, since the introduction of a PAT approach is a mean to obtain parametric release. PAT is a system that intends to analyze and control manufacturing processes through timely measurements, with the goal of enhancing process understanding and final product quality assurance [31].

In this work we try to demonstrate that monitoring the content of an active substance by NIR during the manufacturing process (granulates and cores) and in the final step (coated tablets) could replace the end-product testing by reference method, with the assurance that the final product meets the specification criteria.

2. Experimental

2.1. NIR apparatus and software

Spectra were recorded on a Bruker Optics® spectrophotometer, model MPA, equipped with a Bruker Optics® reflectance diffuse fiber optic probe. The calibration development and cross-validation were performed in the QUANT package of OPUS software, version 4.2, from Bruker Optics®, and the computation of statistics and figures of merit for calibration validation was done in Excel, version 2003, from Microsoft®.

2.2. Calibration samples

The samples used in calibration development were production and laboratory made samples. Production samples from 59 batches used were coated tablets with a theoretical unitary weight of 650 mg and with 300 mg of ranitidine. Thirty laboratory samples were prepared from granulates, and variable amounts of the excipients mixture and of ranitidine were added, in order to create an extended range (78.0–114.0%) of ranitidine content for calibration development. These laboratory samples were thoroughly mixed in a vortex and by hand before recording NIR spectra. The standard deviation between replicates is very low, which proves sample homogeneity.

2.3. Validation samples

The validation set of samples also combines production and laboratory made samples. 124 production samples and 6 laboratory samples were used to predict the error of the developed NIR method.

2.4. Recording of NIR data

Prior to the acquisition of the spectra, the tablet coating was removed, and only then and for the two sample types analysed were subject to grinding in a mortar to produce a fine powder. This procedure allows the use of the same calibration for samples from different manufacturing steps, with different physical properties like granulates and tablets, but with similar spectra as shown in Fig. 1. Samples have a minimum weight of 2000 mg. Six spectra were recorded for each sample, along the wavenumber range of 4000–12,000 cm^{-1}, from an average of 32 scans and with an 8 cm^{-1} resolution. Spectra were obtained inserting directly the diffuse reflectance probe into the powder. As a hand-held probe this operation needs specially attention in order to be

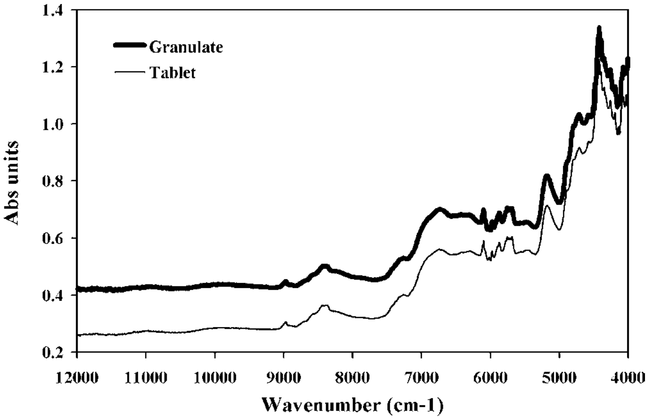

Fig. 1. NIR spectra for granulates and ranitidine tablets.

sure that the probe is immovable during the spectra acquisition. In between samples the probe was cleaned with water humidified paper.

2.5. Reference method

The reference method used for the determination of the active compound (ranitidine) was the HPLC assay recommended by the USP27 for ranitidine tablets [32]. The HPLC method was performed in an agilent series 1100 HPLC system. Two determinations were made for each sample, and the average was used as the reference value method for each sample.

2.6. Calibration development

Several partial least squares (PLS) calibration models were developed in order to obtain a suitable calibration. Calibrations were performed with the QUANT package in the OPUS 4.2 Bruker optics® software.

During the analytical development of the calibration several PLS models are tested. The number of PLS vectors used is defined in the QUANT package as calibration model "rank". The first PLS vector shows the correlations between the component values and the spectral intensities of the calibration spectra [33]. This kind of regression has the advantage that the PLS factors are arranged in the correct sequence, according to their relevance to predict the parameter values [33].

The statistics necessary to calibration development are automatically given by the software [33].

The residual (Res) is the difference between the true and the fitted value. Thus the sum of squared errors (SSE) is the quadratic summation of these values for all samples (i):

$$\text{SSE} = \sum [\text{Res}_i]^2 \tag{1}$$

Root mean square error of estimation (RMSEE) is calculated from this sum, with M being the number of standards and R the rank:

$$\text{RMSE} = \sqrt{\frac{1}{M - R - 1}\text{SSE}} \tag{2}$$

The determination coefficient (R^2) gives the percentage of variance present in the true component values (y_i), which is reproduced in the regression. R^2 approaches 100% as the fitted concentration values (y_m) approach the true values:

$$R^2 = \left(1 - \frac{\text{SSE}}{\sum (y_i - y_m)^2}\right) \times 100 \tag{3}$$

All calibrations were performed with leave-one-out cross-validation, as a preliminary calibration test. This type of test consists in performing a calibration, leaving one sample out and predicting that sample with the calibration developed. The algorithm performs this stepwise until all samples have been left out and calculated by the calibration model. The software gives the root mean square error of cross-validation (RMSECV) that can be taken as the first criterion to decide about the predicting power of the method. In order to avoid calibration overfitting and underestimation of the true prediction error, which is often the result of a leave-one-out cross-validation, an external validation were performed, in a large data set of production samples. By doing that we have obtained a calibration that is accurate and robust outside the calibration set.

$$\text{RMSECV} = \sqrt{\frac{1}{M}\sum_{i=1}^{M} (\text{Differ}_i)^2} \tag{4}$$

With Differ being the difference between the true value, measured by the reference method and the predicted NIR value [33].

Spectral regions related to the sample chemistry were investigated during calibration development to find out which of them was more correlated to ranitidine content. Also all outliers spectra were eliminated at this stage. During calibration development the standard error of laboratory (SEL) was determined according to the recommendations of EMEA's NIR guidance [26]. SEL is the error of the reference method, or an indication of its precision, and it was calculated for all the samples analysed in duplicate by the reference method. Then the standard error of prediction (SEP) was determined for each calibration model (Eq. (6)), and only for the external validation set of samples. The SEP and the SEL should be comparable values, and SEP should not be larger than 1.4 × SEL. The formulas below were used for SEL and SEP determinations [26]:

$$\text{SEL} = \sqrt{\frac{\sum_{i=1}^{m} (x_1 - x_2)^2}{m}} \tag{5}$$

m = number of samples; $x_1 - x_2$ = absolute value of the difference between values measured at different laboratory conditions:

$$\text{SEP} = \sqrt{\frac{\sum_{i=1}^{n} (y_i - Y_i)^2}{n}} \tag{6}$$

n = number of samples; Y = NIRS predicted value; y = reference method value.

Even though NIR guidelines [24–26] recommends a calibration range between 80.0 and 120.0% of the target concentration, we have used a range between 78.0 and 114.0%, which was sufficient to develop an appropriate and reliable method for the determination of ranitidine content, as proved by the validation results described below. The concentration range used is sufficient because the production samples which we intend to analyze by NIR are very homogeneous from batch to batch, and its ranitidine content most be in the range 95.0–105.0%. A range up to 114.0% is therefore sufficient to detect out-of-specifications samples.

The choice of the best model was made taken into account all these parameters. Once the method was chosen, it was validated by determination of the validation parameters recommended by the guidelines: specificity, accuracy, precision, intermediate precision, linearity, range and robustness [23,24,26].

3. Results and discussion

3.1. Quantitative analysis

Twelve PLS calibration models were developed. Six different pre-processing techniques were tested and for each one, two spectral ranges (SR) were evaluated: (1) 4381 ^{1}–9106 cm^{-1} (SR1) and (2) 4258.2–4948.6; 5523.3–6314.0; 8169.2–9175.9 cm^{-1} (SR2). For each calibration model the R^2 and the RMSEE were obtained, allowing a first evaluation of the predictive ability of the model. Then the SEP (Eq. (6)) was calculated for the external validation set of samples, and the best model was chosen. Table 1 gives the statistical figures of merit for each of the different models tested.

The chosen calibration model was the one with the lowest SEP value. This model uses multiplicative scatter correction (MSC) with mean centering as a pre-processing technique. MSC performs a linear transformation of each spectrum so that it best matches the average spectrum of the whole set, and is often used for diffuse reflection spectra [33]. As said in Section 2, 89 samples were used, comprising 59 production samples and 30 laboratory made samples that covers a ranitidine content range from 78 to about 114%. Fig. 2 represents the calibration model, with NIR predicted values versus reference method values.

Table 1
Results for the PLS calibration models developed in one and three spectral ranges

Pre-processing	SP	SR	PLS factors	R^2	RMSSE	SEP
MSC		3	4	96.83	1.180	1.485
		1	4	96.55	1.230	1.598
VN		3	4	96.81	1.180	1.527
		1	4	96.54	1.230	1.599
MMN		3	4	94.39	1.570	1.654
		1	4	96.78	1.190	1.604
First	9	3	4	95.96	1.330	1.768
Der + VN		1	4	95.79	1.360	1.787
First	9	3	4	96.42	1.250	1.697
Der + MSC		1	4	95.79	1.360	1.772
Second	9	3	4	90.32	2.060	2.824
Der		1	4	91.90	1.880	2.696

SP, smoothing points; SR, spectral ranges used; MMN, min-max normalization; VN, vector normalization; MSC, multiplicative scatter correction.

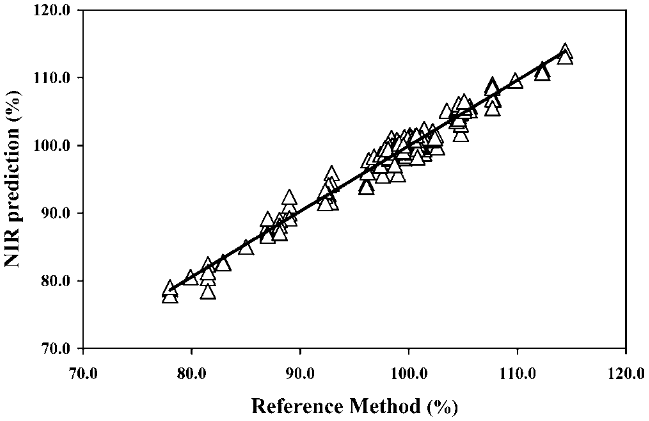

Fig. 2. NIR prediction values vs. reference method determinations.

The model uses four PLS vectors or components in the characterization of sample spectra. Fig. 3 represents the scores for the first and second principal component, showing that there is no significant differences between tablet powdered samples and laboratory samples, since they are in the same cluster. However, laboratory samples have a noticeable highest variance among PC 1 score values. This happens probably do to the extended ranitidine content range that these samples represent, and because the first PLS vector usually correlates with the spectral intensities of the calibration spectra. This can be seen in Fig. 4, were it is possible to see that the differences in PC 1 scores values are related with the ranitidine content of the samples. Tablet powdered samples forms a more compact cluster because they are within the specifications range of 95.0–105%.

3.2. Validation of the quantitative method

Since that there is not a standard procedure for validating a quantitative NIR method, the present method was validated by determining several parameters usually recommended by different guidelines: specificity, accuracy, precision or repeatability, intermediate precision, linearity, range and robustness [23,24,26].

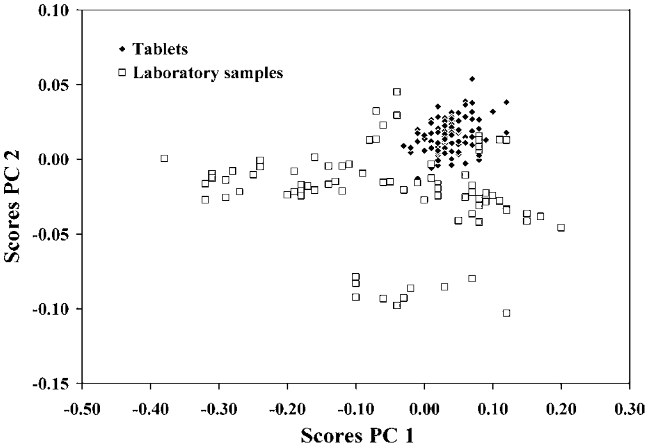

Fig. 3. PC scores plot from NIR spectra of tablets and laboratory made samples.

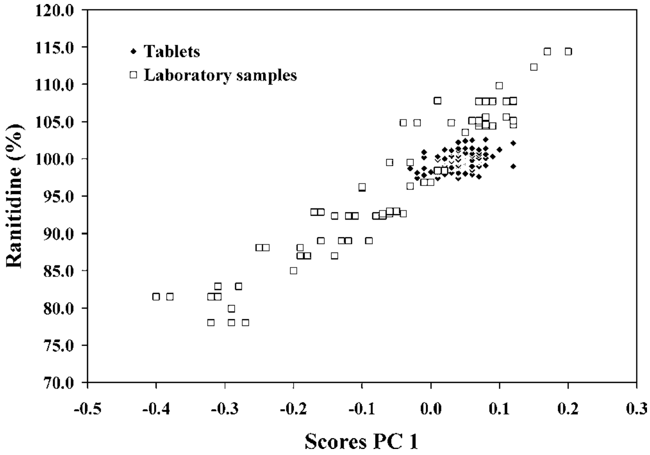

Fig. 4. Sample scores from first principal component vs. ranitidine content.

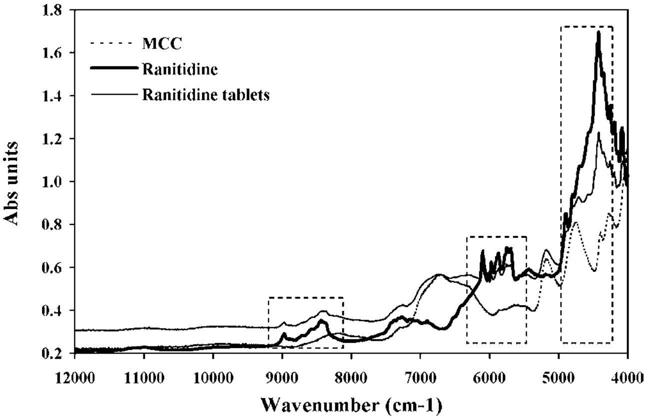

Fig. 6. NIR spectra of ranitidine tablets and its major components. The dashed line marks the wavenumber regions used in the calibration, which contain ranitidine bands.

3.2.1. *Specificity*

Specificity of a method is its capability to assess unequivocally the analyte in the presence of other components, like impurities, degradation products or matrix components. Some regulatory authorities prefer the term selectivity, reserving specificity for those procedures that are completely selective.

For NIR assays, like in this case, we consider that the specificity test must provide an exact result, which allows an accurate statement on the content or potency of the analyte in a specific sample—ranitidine content in granulates and powdered tablets.

Method selectivity could be proved in first step after the study of proportions and spectral analysis of the major components present in our ranitidine tablets formula. The tablets contain around 50% of ranitidine chloridrate and around 40% of microcrystalline cellulose (MCC). Fig. 5 represents the spectra of these two components, and the spectrum of ranitidine tablets.

It is possible to observe that the spectrum of ranitidine tablets results from the high proportion of these two components. The wavenumber regions used in the calibration were compared with the known bands of ranitidine, and to those of the excipients, to prove that only bands of ranitidine were used in the calibration model. The spectral regions used are marked in Fig. 6. Besides that the loadings first factor used in the model, to check if they are using the spectroscopic information of ranitidine, are depicted in Fig. 7.

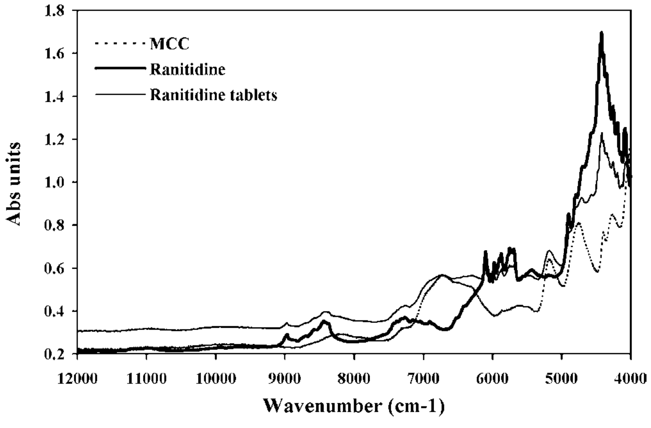

Fig. 5. NIR spectra of ranitidine tablets and its major components.

As to the specificity test of NIR quantitative methods, the approach used in this work considers the method's selectivity to measure ranitidine in a specific matrix—ranitidine tablets. So the method should be selective to ranitidine and specific to a unique matrix.

To prove the specificity of the method to granulates and powdered tablets, the concept of Mahalanobis distance was used. The Mahalanobis distance is a measure of the similarity between the analyzed spectrum and the calibration spectra. This distance is calculated for each calibration spectrum during the PLS calculation, and reported as safety threshold for each method. Spectra of unknown samples can be analyzed with a high level of confidence if the result for their Mahalanobis distance is within this threshold [33].

The prediction of ranitidine content by the method was made in three spectra of several different samples: ranitidine chloridrate, MCC, granulates and powdered samples of ranitidine tablets. Results are in Table 2.

Table 2 shows that all raw-material spectra analyzed have a Mahalanobis distance much higher than the threshold defined

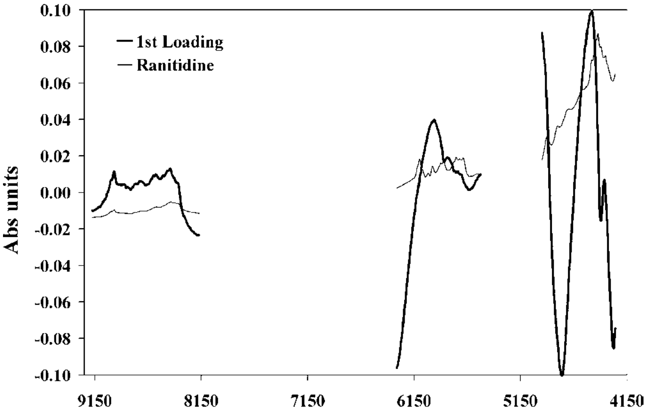

Fig. 7. First loading factor used in the model, and NIR spectra of ranitidine in the same spectral region.

Table 2
NIR predictions to study method specificity for granulates and ranitidine tablets

Product	NIR predictions	Spectrum Mahalanobis distance	Mahalanobis distance threshold	Outlier
Ranitide chloridrate	156.2	0.960	0.042	Yes
	157.0	1.000		
	155.1	1.000		
MCC	2448.7	7100		
	−3417.1	9200		
	10,589	110,000		
Granulates	100.1	0.004		No
	98.5	0.014		
	97.8	0.006		
Tablets	100.4	0.003		
	98.5	0.003		
	99.2	0.010		

by the method (0.042). These spectra are considered outliers because they are poorly represented by the calibration PLS vectors. On the other hand, all the tablets spectra have a Mahalanobis distance below the method threshold, showing that the method is specific to these pharmaceutical products.

3.2.2. *Accuracy*

The accuracy of an analytical method is the closeness of test results obtained by that method to the true values. The accuracy of an analytical method should be established across its range [23].

To establish the accuracy of the NIR method developed a paired *t*-test was performed between the NIR and reference method. This *t*-test allows to check if the results between the methods were significantly different. Three determinations for each one of three samples were performed by NIR method and by reference method. These three samples correspond to three different levels of concentration, within the methods range (see Table 3).

Before the paired *t*-test, a variance analysis test was made, to verify if there are significant differences between the values of the two methods, for each one of the samples. This test was the *F*-test, performed in excel, through the data analysis tool, selecting the *F*-test two sample for variance. Since, all samples presents statistically similar variances, the paired *t*-test was performed, through the data analysis tool, selecting the *t*-test two-sample assuming equal variances.

Table 3
Results for method accuracy test

Determination	Sample 1		Sample 2		Sample 3	
	NIR	Ref.	NIR	Ref.	NIR	Ref.
1	88.20	91.50	99.28	100.40	104.15	105.30
2	90.19	89.50	101.93	98.80	104.98	104.20
3	89.89	90.00	101.03	98.00	105.4	104.40
$\bar{x}$	89.43	90.33	100.75	99.07	104.84	104.63
S^2	1.15	1.08	1.81	1.49	0.40	0.34
R.S.D.	1.20	1.15	1.34	1.23	0.61	0.56

$\bar{x}$, average; S^2, variance; R.S.D., relative standard deviation; NIR, NIR method values; Ref., reference method values.

The acceptance criteria is defined by the formula: $|t_{\mathrm{exp}}| \leq t_{\mathrm{tab}}$, and the results, for a t_{tab} value of 2.78 for $P = 0.05$ and two degrees of freedom are represented in Table 4.

Because $|t_{\mathrm{exp}}| \leq t_{\mathrm{tab}}$, for all the samples, the results in Table 4 show that the accuracy of NIR method is comparable to reference method.

3.2.3. *Precision*

The precision of an analytical method is the degree of agreement among individual test results when the method is applied repeatedly to multiple samplings of a homogeneous sample [23].

Precision was measured as the degree of reproducibility or of repeatability of an analytical method, under normal operating conditions, and measured also as the intermediate precision, that refers to within-laboratory variation measurements made in different days by different analysts or in different equipment in the same laboratory.

3.2.3.1. Repeatability. Repeatability was determined by measuring the ranitidine content in granulates of a single batch, six times by the same analyst in the same day in the same equipment. Table 5 shows the results obtained, and as can be seen, the relative standard deviation (R.S.D.) obtained for the NIR method (1.26) was less than the obtained for the reference method (1.92), although with comparable average values for both methods.

Likewise before, the variance analysis *F*-test was made, to verify if there are significantly differences between the values of the two methods. This test was performed once more in excel, through the data analysis tool, selecting the *F*-test two sample for variance. The result obtained was $F = 2.29$, for an F_{tab} of 5.05. Since $F \leq F_{\mathrm{tab}}$ both methods have statistically similar variances.

3.2.3.2. Intermediate precision. Intermediate precision was determined by measuring the ranitidine content, six times, in

Table 4
Results for the paired *t*-test

	Sample 1	Sample 2	Sample 3
t_{exp}	1.05	1.60	0.42
t_{tab}		**2.78**	

Table 5
Results for method repeatability test

Determination	NIR	Ref.
1	99.3	100.4
2	101.9	98.8
3	99.3	98.0
4	99.8	97.2
5	101.0	102.0
6	98.6	97.3
$\bar{x}$	100.0	99.0
S^2	1.58	3.62
R.S.D.	1.26	1.92

$\bar{x}$, average; S^2, variance; R.S.D., relative standard deviation; NIR, NIR method values; Ref., reference method values.

the same sample, but in two different days, by two different analysts using the same equipment. Results obtained are shown in Table 6.

The dispersion degree calculated for the NIR method is lower, for both analysts, than the calculated for the reference method, which proves once more the precision of the NIR calibration developed.

A two-way analysis of variance (ANOVA) test was performed to study the variability between the methods for two different days, and for two different analysts in the same equipment. No systematic source of error was found.

3.2.4. Linearity and range

The linearity of an analytical method is its ability to elicit test results that are directly, or by a well-defined mathematical transformation, proportional to the concentration of analyte in samples within a given range. The range of an analytical method is the interval between the upper and lower levels of analyte that have been demonstrated to be determined with a suitable level of precision, accuracy, and linearity using the method as written [23].

To evaluate the linearity of the NIR method developed, a regression line between the NIR and reference method has been computed, in the range where the NIR calibration was developed. In practice, the ranitidine content was measured in triplicate, on seven different samples of powdered tablets, with different concentrations. Results for each sample are shown in Table 7 and Fig. 8.

Table 6
Results for method intermediate precision test

Determination	Analyst 1		Analyst 2	
	NIR	Ref.	NIR	Ref.
1	99.3	100.4	101.2	100
2	101.9	98.8	100.3	97.7
3	99.3	98.0	101.1	100.5
4	99.8	97.2	102.4	100.4
5	101.0	102.0	103.4	98.1
6	98.6	97.3	101.2	98.7
$\bar{x}$	100.0	99.0	101.6	99.2
S^2	1.58	3.62	1.21	1.49
R.S.D.	1.26	1.92	1.08	1.23

$\bar{x}$, average; S^2, variance; R.S.D., relative standard variation; NIR, NIR method values; Ref., reference method values.

Table 7
Average results for samples used in linearity test

Sample	NIR	Ref.
1	79.5	78.3
2	89.4	90.3
3	100.7	99.1
4	104.8	104.6
5	116.2	115.3
6	100.0	99.0
7	101.6	99.2

NIR, NIR method values; Ref., reference method values.

A linear regression test was performed between the two methods, and the agreement of results was evaluated by Eq. (7).

$$y = bx + a \tag{7}$$

Being (y) the NIR predicted value, (x) the obtained reference value, (a) the intercept and (b) the slope values.

The regression equation is $y = 0.9875\,x + 0.3447$, with a coefficient (R^2) of 0.9921.

To be considered linear:

1. The confidence interval associated to the intercept (CI_a): $a \pm \mathrm{S}_a t$, must contain the zero value;
2. The confidence interval associated to the slope (CI_b): $b \pm \mathrm{S}_b t$, must contain the number one;

S_a is the standard deviation of the intercept, S_b the standard deviation of the slope and t the tabled value according to the desirable confidence degree and $N-2$ degrees of freedom (N is the number of sample determinations).

This test was performed in excel, through the data analysis tool, selecting the regression test. Results obtained are:

$$CI_a = [-9.758; 10.448] \quad a \text{ associated error is } 10.10$$
$$CI_b = [0.886; 1.089] \quad b \text{ associated error is } 0.10$$

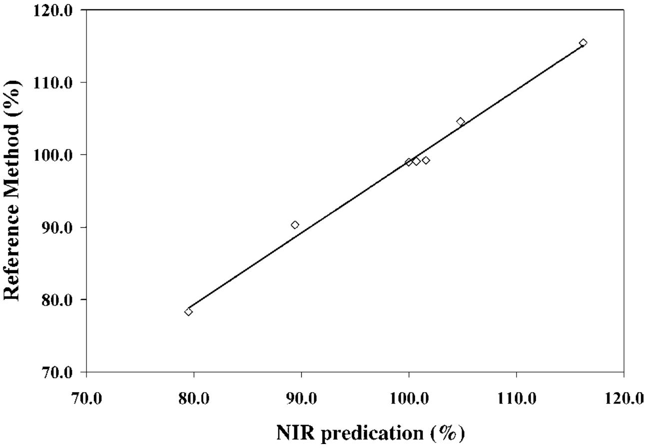

Fig. 8. Regression line between NIR predictions and reference method measurements.

And the regression equation becomes:

$$y = (0.98 \pm 0.10)x + (0.34 \pm 1010) \quad (8)$$

The developed NIR method is therefore linear as compared to the reference method, within the concentration range of the calibration developed.

3.2.5. Robustness

The robustness of an analytical method is a measure of its capacity to remain unaffected by small but deliberate variations in method parameters and provides an indication of its reliability during normal use [23].

The method development has been done along the manufacturing of 59 batches, which introduced many natural sample variability and robustness to the method. Besides that, the different kinds of samples included in the method developed (granulates, cores and tablets) have differences, even minor differences, like different particle sizes, they also provide robustness to the method.

The major factor that may affect the method robustness is those inherent to the equipment. To pass over that, all operational conditions are checked daily through an operational performance test, and the environmental conditions controlled and maintained stable.

The robustness of the method has been ascertained by comparing the results of the two methods over a period of time. The external validation described next was performed on 130 different manufacturing batches over a year period. Besides that after the acceptance of the proposed NIR method, 31 production samples, from 21 different batches has been analyzed, with an average value of 0.81% relative to the reference value.

The results show that the method is thus quite robust comparatively to the reference method.

3.2.6. External validation

The external validation was performed to obtain information on the predictive ability of the generated calibration model. It is a fundamental step to prove the accuracy and precision of the method along time in daily laboratory routine, computing the standard error of prediction (SEP). As acceptance criteria $\mathrm{SEP_{NIR}} \leq 1.4 \times \mathrm{SEL}$, where SEL is standard error of laboratory (Eqs. (5) and (6)).

The obtained SEL value is 1.10, calculated from 74 calibration samples, which determines the maximum SEP value of 1.54.

The whole external validation set includes 687 spectra, acquired from 130 different manufacturing batches of ranitidine tablets, which includes granulates for compression, cores and powdered tablets.

The value determined for SEP was 1.49, which proves once more the adequacy of the proposed NIR method.

3.3. Identification

For identification tests, selectivity ensures the identity of the analyte [23]. Going back to the validation parameter selectivity, it had been proved that the method is selective to ranitidine, and specific to the this ranitidine tablets, granulates and cores, respectively, so the identification of ranitidine is implicit, since the selectivity implicates the identity of the analyte.

Taking into account this principle, every time that a sample is analyzed, and if it is not an outlier, it is a sample from the same kind of those that composes the model, which means that the ranitidine spectral ranges used in the NIR method developed are present in the sample analysed. The ranitidine content is measured and simultaneously identified.

4. Conclusions

The NIR method developed allows the identification and simultaneous quantification of ranitidine in granulates for compression, cores (intermediate products) and coated tablets (final product).

Method selectivity has been proved, so ranitidine identification is performed every time that a measurement is done, since the selectivity ensures the identity of the analyte. The method is accurate, precise and linear in the concentration range studied, so it is equivalent to the reference method, and could replace it in routine analysis, as shown by the small SEP value obtained in the NIR calibration external validation.

Ranitidine content is monitored and controlled during the manufacturing process, which allows to check if the product meets the specification criteria and also to assure its final quality. This could be considered a PAT application, as multiple quality attributes of different nature are included in the NIR evaluation and can be seen as the first step to establish a parametric release system, since it allows the real-time measurement, monitoring and control of critical quality parameters as it is the API content in a solid dosage form.

Acknowledgments

The authors wish to thanks to Laboratórios Atral S.A., for supporting this works and for permission to publish the above results. S.R. gratefully acknowledges financial support from the Portuguese Foundation for Science and Technology (research grant no. SFRH/BDE/15,521/2004).

References

[1] R.D. Jee, in: A.C. Moffat, M.D. Osselton, B. Widdop (Eds.), Clarkeї̌s Analysis of Drugs and Poisons, vol. 1, 3rd ed., Pharmaceutical Press, London, 2004, pp. 346–357.
[2] L. Bokobza, in: H.W. Siesler, Y. Ozaki, S. Kawata, H.M. Heise (Eds.), Near-Infrared Spectroscopy: Principles, Instruments, Applications, Wiley–VCH, Weinheim, Germany, 2002, p. 11.
[3] E.W. Ciurczak, J.K. Drennen III (Eds.), Pharmaceutical and Medical Applications of Near-Infrared Spectroscopy, Marcel Dekker, Inc., New York, 2002, p. 73.
[4] K. Krämer, S. Ebel, Anal. Chim. Acta 420 (2000) 155–161.
[5] M.S. Kemper, L.M. Luchetta, J. Near-Infrared Spectrosc. 11 (2003) 155–174.
[6] M. Blanco, J. Coelho, H. Iturriaga, S. Maspoch, C. De la Pezuela, Anal. Chim. Acta 333 (1996) 147–156.

[7] M. Blanco, A. Eustaquio, J.M. González, D. Serrano, J. Pharm. Biom. Anal. 22 (2000) 139–148.

[8] R.P. Cogdill, C.A. Anderson, M. Delgado, R. Chisholm, R. Bolton, T. Herkert, A.M. Afnán, J.K. Drennen III, AAPS Pharm. Sci. Tech. 6 (2) (2005) E273–E283 (Article 38) (http://www.aapspharmscitech.org).

[9] C.P. Meza, M.A. Santos, R.J. Romañach, AAPS Pharm. Sci. Technol. 7 (1) (2006) E1–E9 (Article 29).

[10] G.X. Zhou, Z. Ge, J. Dorwart, B. Izzo, J. Kukura, G. Bicker, J. Wyvratt, J. Pharm. Sci. 92 (2003) 1058–1065.

[11] S. Sonja Sekulic, H.W. Ward II, D.R. Brannegan, E.D. Stanley, C.L. Evans, S.T. Sciavolino, P.A. Hailey, P.K. Aldridge, Anal. Chem. 68 (1996) 509–513.

[12] A.S. El-Hagrasy, H.R. Morris, F. D'Amico, R.A. Lodder, J.K. Drennen III, J. Pharm. Sci. 90 (2001) 1298–1307.

[13] A.S. El-Hagrasy, M. Delgado-Lopez, J.K. Drennen III, J. Pharm. Sci. 95 (2006) 407–421.

[14] M. Otsuka, I. Yamane, J. Pharm. Sci. 95 (2006) 1425–1433.

[15] M. Andersson, M. Josefson, F.W. Langkilde, K.-G. Wahlund, J. Pharm. Biomed. Anal. 20 (1999) 27–37.

[16] J.D. Kirsch, J. Drennen, J. Pharm. Biomed. Anal. 13 (1995) 1273–1281.

[17] P. Frake, I. Gill, C.N. Luscombe, D.R. Rudd, J. Waterhouse, U.A. Jayasooriya, Analyst 123 (1998) 2043–2046.

[18] A.J. O'Neil, R.D. Jee, A.C. Moffat, Analyst 128 (2003) 1326–1330.

[19] M. Blanco, A. Villar, J. Pharm. Sci. 92 (2003) 823–830.

[20] J.J. Seyer, P.E. Luner, M.S. Kemper, J. Pharm. Sci. 89 (2000) 1305–1316.

[21] Near-infrared spectrometry, European Pharmacopoeia, 5th edn., vol. 1, 2005, pp. 59–63, Chapter 2.2.40.

[22] Near-infrared Spectrophotometry, United States Pharmacopoeia USP29NF24, The United States Pharmacopeial Convention, Rockville, 2006, pp. 2979–2983, Chapter 1119.

[23] Validation of compendial methods, United States Pharmacopoeia USP29NF24, The United States Pharmacopeial Convention, Rockville, 2006, pp. 3050–3053, Chapter 1225.

[24] ICH Harmonised Tripartide guideline, Q2 (R1), Validation of Analytical Procedures: Text and Methodology, FDA, November 2005, (http://www.ich.org/LOB/media/MEDIA417.pdf).

[25] PASG Guidelines for the development and Validation of Near-Infrared (NIR) Spectroscopy methods, PASG NIR Subgroup, October 2001, pp. 1–41 (http://www.pasg.org.uk/NIRmay01.pdf).

[26] Note for guidance on the use of Near-infrared spectroscopy by the pharmaceutical industry and the data requirements for new submissions and variations, The European Agency for the Evaluation of Medicinal Products, CPMP/QWP/3309/01, EMEA/CVMP/961/01, February 2003, London, pp. 1–14 (http://www.emea.eu.int/pdfs/human/qwp/330901en.pdf).

[27] Concept paper on revision of the note for guidance on the use of Near-infrared spectroscopy by the pharmaceutical industry and the data requirements for new submissions and variations, The European Agency for the Evaluation of Medicinal Products, EMEA/CHMP/CVMP/QWP/173698/2006, London, June 2006, pp. 1–4 (http://www.emea.eu.int/pdfs/human/qwp/17369806en.pdf).

[28] Note for guidance on Parametric Release, The European Agency for the Evaluation of Medicinal Products, CPMP/QWP/3015/99, London, March 2001, pp. 1–5 (http://www.emea.eu.int/pdfs/human/qwp/301599en.pdf).

[29] Guideline on Parametric Release, Draft, The European Agency for the Evaluation of Medicinal Products, EMEA/CVMP/QWP/339588/2005-CONSULTATION, London, March 2006, pp. 1–7 (http://www.emea.eu.int/pdfs/vet/qwp/3395880en.pdf).

[30] Parametric release, final version of Annex 17 to the EU guide to good manufacturing practice (GMP), Working Party on Control of Medicine and Inspections, European Commission, Brussels, July 2001, pp. 1–5 (http://www.ec.europa.eu/enterprise/pharmaceuticals/eudralex/vol-4/pdfs-en/v4an17.pdf).

[31] PAT—a framework for innovative pharmaceutical development, manufacturing, and quality assurance guidance for industry. US Food and Drug Administration, Rockville, September 2004 (http://www.fda.gov/cder/guidance/6419fnl.pdf).

[32] Ranitidine Tablets. United States Pharmacopoeia USP27NF22, The United States Pharmacopeial Convention, Rockville, 2004, pp. 1627.

[33] OPUS, Optic Users Software Manual, Version 4.2, Bruker Optics GmbH, Germany, 2002.

Available online at www.sciencedirect.com
ScienceDirect
Talanta 75 (2008) 671–676
Talanta
www.elsevier.com/locate/talanta

An improved HPLC method for rapid quantitation of diazepam and its major metabolites in human plasma

Mohammad-Reza Rouini [*], Yalda H. Ardakani,
Kambiz A. Moghaddam, F. Solatani

Biopharmaceutics and Pharmacokinetic Division, Department of Pharmaceutics, Faculty of Pharmacy, Medical Sciences,
University of Tehran, 14155-6451 Tehran, Iran

Received 23 September 2007; received in revised form 28 November 2007; accepted 29 November 2007

Abstract

A rapid and specific HPLC method was developed and validated for simultaneous determination of diazepam and its main active metabolites, desmethyldiazepam, oxazepam and temazepam in human plasma. Plasma samples were extracted using toluene. HPLC system included a Chromolith^{TM} Performance RP-18e 100 mm × 4.6 mm column, using 10 mM phosphate buffer (pH 2.5)–methanol–acetonitrile (63:10:27, v/v) as mobile phase running at 2 mL min^{-1}. UV detector ($\lambda = 230$ nm) was used. The calibration curves were linear in the concentration range of 2–800 ng mL^{-1} for diazepam and 2–200 ng mL^{-1} for the three metabolites ($r^2 > 0.99$). The lower limit of quantification was 2 ng mL^{-1} for all analytes. Within and between-day precisions in the measurement of QC samples were in the range of 1.8–18.0% for all analytes. The developed procedure was used to assess the pharmacokinetics of diazepam and its main metabolites following single dose administration of 10 mg diazepam orally to healthy subjects.

Keywords: Diazepam; Metabolite; Plasma; Monolithic; Pharmacokinetics

1. Introduction

Diazepam (7-chloro-1, 3-dihydro-1-methyl-5-phenyl-2H-1, 4-benzodiazepin-2-one) is a benzodiazepine (BZD) generally used as hypnotic, anxiolytic and muscle relaxant. Diazepam (DZ) is also routinely prescribed as the standard first-line treatment for acute convulsions and prolonged status epilepticus [1]. It is metabolized by liver cytochrome P450s to three major active metabolites; *N*-desmethyldiazepam or nordiazepam (NDZ), oxazepam (OX) and temazepam (TZ), which are conjugated and excreted mainly as glucuoronide in urine. Fig. 1 [2].

Diazepam is important in treatment of a variety of disorders and is also subject to abuse and for that reason identification of diazepam in human biological fluids is very important for forensic and clinical toxicology as well as pharmacokinetic studies.

Several methods for the analysis of BZDs have been reported. A number of chromatographic methods, such as thin-layer chromatography (TLC) [3], gas chromatography [4–6] and gas chromatographic–mass spectrometry (GC–MS) [7,8] have been used in the analysis of diazepam and other 1,4-benzodiazopines. Several high-performance liquid chromatographic (HPLC) methods have also been reported for the determination of diazepam and other BZDs [9–13].

Since the three main metabolites of diazepam are active *in vivo*, their determination is imperative for pharmacokinetic studies. While numerous selective and sensitive methods have been developed for assay of diazepam, so far only a few HPLC methods have been reported for the simultaneous determination of the parent compound and its three active metabolites in serum or plasma [14–18]. However, all of these methods have limitations such as long run times and/or inadequate sensitivity. Long run time in most of HPLC methods may be a result of limited flow rate applied to routine HPLC columns. This may be resolved using recently developed monolithic HPLC columns such as Chromolith^{TM}. These types of columns have a biporous structure which results in higher porosity compared to usual

---

[*] Corresponding author. Tel.: +98 21 66959056; fax: +98 21 66461178.
E-mail address: rouini@tums.ac.ir (M.-R. Rouini).

0039-9140/$ – see front matter © 2007 Elsevier B.V. All rights reserved.
doi:10.1016/j.talanta.2007.11.060

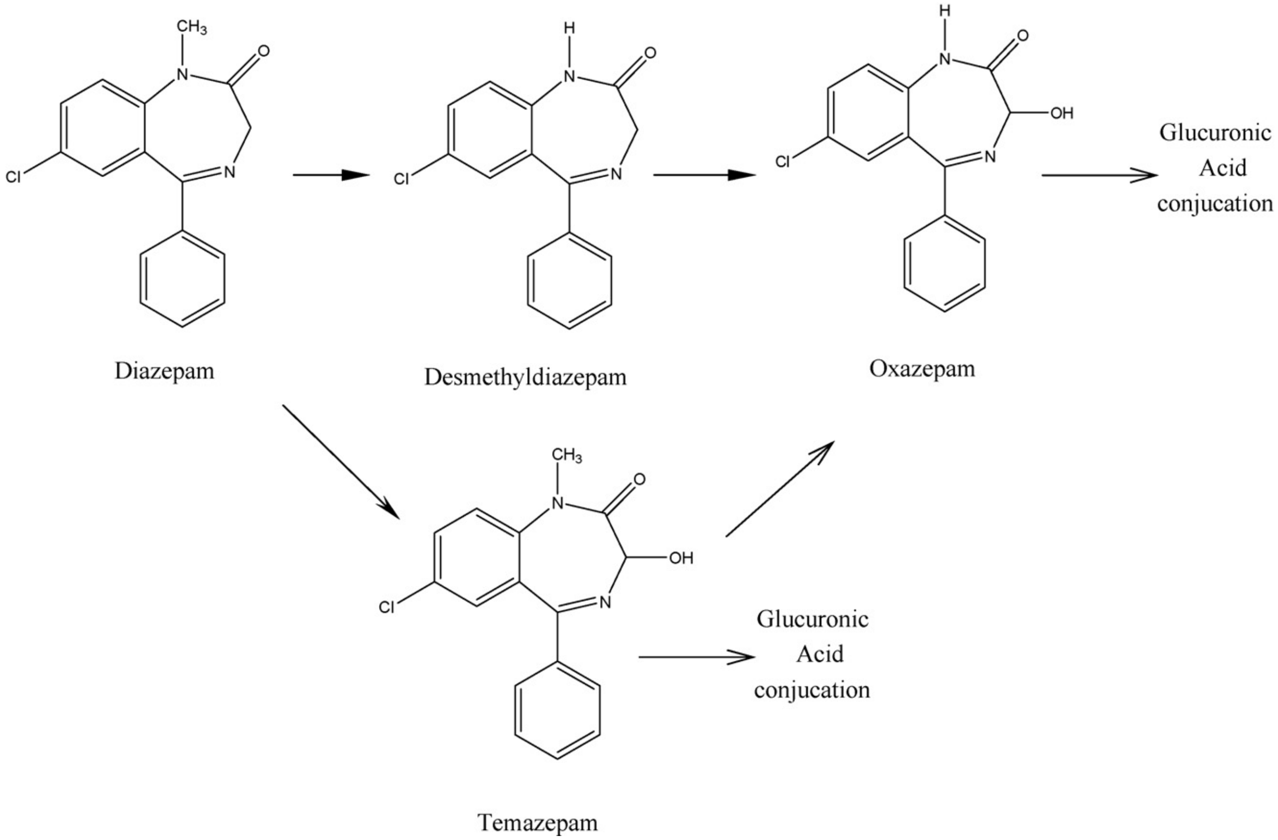

Fig. 1. Metabolic pathway of diazepam and chemical structure of its metabolites.

columns [13]. Therefore, they could be used with high flow rates without significant loss of performance or other limitations due to increased pressure. These columns therefore achieve faster separation compared to conventional columns. Shorter runs will usually result in better sensitivity. Hence, we decided to develop an HPLC method using a Chromolith™ column for quantitative determination of diazepam and its main metabolites. The objective of this study was to reduce the duration of analysis, while maintaining the resolution and sensitivity required for the detection of these compounds in their therapeutic range.

2. Experimental

2.1. Chemicals and reagents

Temazepam and *N*-desmethyldiazepam were purchased from Cerilliant (Austin TX). Standard diazepam, oxazepam and alperazolam used as internal standard (IS) were kindly supplied by Dr. Abidi Pharmaceutical Co. (Tehran, Iran). Acetonitrile and methanol were HPLC-grade and phosphoric acid (85%) was analytical grade (Merck, Germany).

2.2. Apparatus and chromatographic condition

Low-pressure HPLC pump (K-1001) was connected to a UV detector (K-2600) set at 230 nm (Knauer, Berlin Germany). A Reodyne model 7725i injector with a 100 μL loop was used. The data were acquired and processed by a ChromGate chromatography software (Knauer, Berlin, Germany).

A Chromolith™ Performance RP-18e 100 mm × 4.6 mm column preceded by a Chromolith™ Guard Cartridge RP-18e 5 mm × 4.6 mm (Merck, Darmstadt, Germany) was used for analysis. Mobile phase consisted of 10 mmol $\mathrm{L^{-1}}$ phosphate buffer (pH 2.5)–methanol–acetonitrile (63:10:27, v/v) which was run through the column at flow rate of 2 $\mathrm{mL\,min^{-1}}$.

2.3. Sample preparation

2.3.1. Standard solutions

Diazepam, oxazepam and alprazolam with concentrations of 1 $\mathrm{mg\,mL^{-1}}$ were prepared separately in methanol. Intermediate pooled stock standard of all compounds of 10 $\mathrm{\mu g\,mL^{-1}}$ were prepared using mobile phase as solvent. The solutions of all compounds were stored at 4 °C.

2.3.2. Preparation of calibration standards

Diazepam, desmethyldiazepam, oxazepam, and temazepam (10 $\mathrm{\mu g\,mL^{-1}}$) standards were prepared using human drug-free plasma obtained from healthy subjects as diluents. The calibration curve was performed with standards of the final concentrations of 2–800 $\mathrm{ng\,mL^{-1}}$ for diazepam and 2–200 $\mathrm{ng\,mL^{-1}}$ for its metabolites in human plasma.

2.3.3. Extraction procedure

The treatment of plasma samples was carried out by liquid–liquid extraction (LLE). To 0.5 mL of plasma was added 50 μL alprazolam as internal standard (1 $\mu g\,mL^{-1}$) in a 2 mL Eppendorf polypropylene tube and then extracted with 1.5 mL of toluene. After vertical agitation (5 min) and centrifugation (10,000 rpm, 2 min), the upper organic layer was transferred into a conical tube and evaporated under a gentle stream of air. The dried extract was reconstituted in 150 μL of the mobile phase and 100 μL of aliquot was injected onto the HPLC column.

2.4. Method development and optimization

A number of parameters in composition of mobile phase were examined to determine the one(s) that give the best separation.

The pH of mobile phase was studied between 2 and 5.5 as the safe pH range for the Chromolith^{TM} columns was from 2 to 7.5.

Starting from a mixture of phosphate buffer (10 $mmol\,L^{-1}$)–acetonitrile (30:70), the percentage of acetonitrile in mobile phase was varied from 27 to 32 in combination with 10 $mmol\,L^{-1}$ phosphate buffer. Using the best combination of acetonitrile–phosphate buffer as determined above, the addition of methanol was further examined to improve resolution of peaks. The effect of buffer concentration was also evaluated between 10 and 50 $m\,mol\,L^{-1}$.

2.5. Subjects

The study was approved by the ethics committee of Tehran University of Medical Sciences. Four healthy male subjects were enrolled in the study and written informed consent was obtained from them. The subjects weighed between 65 and 78 (73 ± 3.5) kg and aged 24–38 (26 ± 5) years.

3. Result and discussion

3.1. Optimization of chromatographic conditions

3.1.1. Effect of pH

The effect of pH on retention times of analytes was studied in the range of 2–5.5 (Fig. 2). As it is shown in Fig. 2, pH did not exert a significant change on retention times of OX, TZ and ALP. On the other hand, DZ and NDZ were highly affected by pH change. Moving from pH of 2–5.5, the retention times of NDZ and DZ increased from 1.5 and 3 min to 8.5 and 14.5 min, respectively. The optimum separation was achieved at pH of 2.5.

3.1.2. Percent acetonitrile in mobile phase

The plot of retention time versus percent of acetonitrile is shown in Fig. 3. As it was expected, an increase in acetonitrile portion from 25 to 32%, shortened the overall run time from 12 to about 5 min and reduced the resolution between all analytes. The order of peaks in 27–37% acetonitrile mobile phase changed from NDZ, DZ, OX, ALP and TZ to NDZ, OX, ALP, DZ and TZ. The resolution between matrix peaks and NDZ was acceptable in the presence of 27% acetonitrile, while there was not suitable resolution between oxazepam, alprazolam and diazepam.

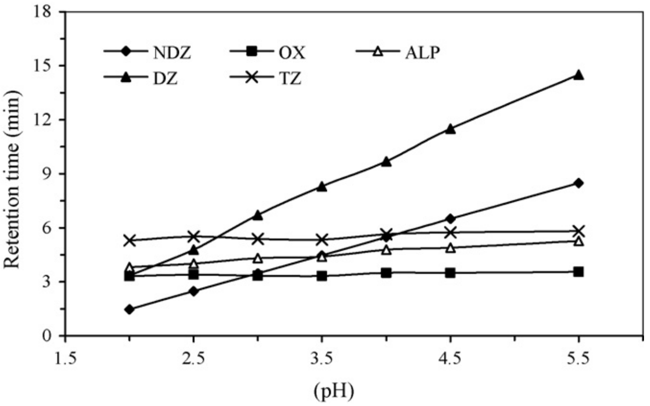

Fig. 2. Effect of pH on retention time of all analytes. Mobile phase: a mixture of 10 $mmol\,L^{-1}$ phosphate buffer–acetonitrile (70:30). DZ, diazepam; NDZ, desmethyldiazepam; OX, oxazepzm; TZ, temazepam; ALP, alprazolam.

3.1.3. Percent methanol in mobile phase

An increase in methanol portion from 5 to 11% in mobile phase, slightly increased the retention time of first analyte (NDZ), decreased the retention time of last analyte (TZ) and reduced the overall run time and finally better resolution was observed between oxazepam, alprazolam and diazepam. As a result, 10% methanol composition was chosen for optimal resolution (Fig. 4).

3.1.4. Buffer concentration

As it could be observed in Fig. 5, there was no difference in retention time of each analyte in various phosphate buffer concentrations.

3.2. Validation of the method

Method validation results are listed in Table 1.

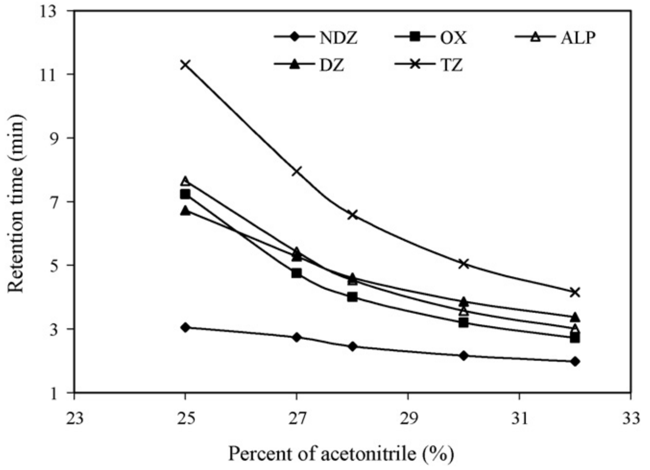

Fig. 3. Effect of percent of acetonitrile on retention times of all analytes. Mobile phase: a mixture of 10 $mmol\,L^{-1}$ phosphate buffer (adjusted to pH 2.5)–acetonitrile. DZ, diazepam; NDZ, desmethyldiazepam; OX, oxazepzm; TZ, temazepam; ALP, alprazolam.

Table 1
Between and within-day precision, accuracy, and recovery for determination of diazepam, desmethyldiazepam, oxazepzm, and temazepam ($n = 5$)

	Concentration (ng mL^{-1})	Between-day variability		Within-day variability		Recovery	
		RSD (%)	Accuracy (%)	RSD (%)	Accuracy (%)	(%)	RSD (%)
Diazepam	10	6.9	98.8	7.6	104.2	100.2	10.6
	25	1.8	102.5	12.2	101.2	98.6	8.2
	50	3.1	99.7	8.9	103.0	96.7	6.3
	100	3.4	102.5	4.7	102.6	96.8	5.4
N-Desmethyl diazepam	10	15.5	91.0	13.2	89.9	95.4	12.3
	25	11.3	104.7	12.7	95.5	96.7	10.2
	50	6.2	100.9	13.6	94.1	94.3	9.7
	100	2.4	100.0	4.1	101.8	90.4	6.7
Oxazepzm	10	16.9	100.9	7.5	81.6	60.5	10.5
	25	6.3	110.2	8.7	108.3	62.4	14.3
	50	11.7	102.4	9.4	114.5	52.6	12.6
	100	2.9	96.8	7.7	97.3	63.7	8.9
Temazepam	10	10.7	97.6	11.1	84.7	98.6	10.5
	25	15.5	106.6	10.4	103.3	99.6	9.8
	50	9.7	99.4	10.5	92.6	95.3	7.8
	100	18.0	106.7	5.2	115.1	95.6	6.3

3.2.1. *Recovery*

Average recovery of each compound was determined by comparing chromatographic peak area obtained after injection of the processed QC samples with those achieved by direct injection of the same amount of drug in mobile phase at different concentrations ($n = 5$). The recoveries ranged from 90.4–100.2% for NDZ, DZ and TZ to 52.6–63.7% for OX. (Table 1).

3.2.2. *Accuracy and precision*

Accuracy, between-day and within-day precisions of the method were determined for each compound according to FDA guidance for bioanalytical method validation [19]. Accuracy was assessed by analyzing known concentration samples (QC samples) and comparing the measured values to the true values. Five replicate spiked plasma samples were assayed between-day and within-day at four different concentrations (10, 25, 50 and 100 ng mL^{-1}) for each analyte. The concentrations were calculated using calibration curves. Accuracy at four concentration levels ranged from 81.6 to 115.1% for all analytes. Within- and between-day precisions were 5.2–13.6% and 1.8–18.0%, respectively (Table 1).

3.2.3. *Limit of quantification (LOQ)*

The limit of quantification (LOQ) was defined as the lowest analyte concentration, which can be determined with an accuracy and precision of less than 20% [19]. LOQs were 2 ng mL^{-1} for diazepam and its metabolites. The LOQ values for the four analytes of interest are reported in Table 2.

3.2.4. *Linearity*

Eleven point calibration curves for diazepam and its metabolites on separate days were linear over the concentration range of 2–800 ng mL^{-1} for diazepam and 2–200 ng mL^{-1} for the three metabolites. The equations for means ($n = 3$) of the three stan-

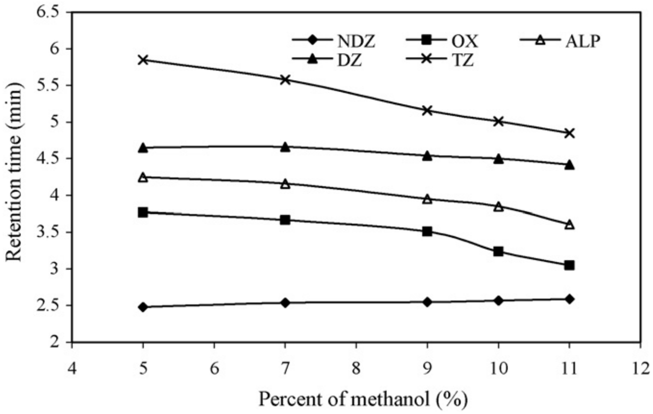

Fig. 4. Effect of percent of methanol on retention times of all analytes. Mobile phase: a mixture of 10 mmol L^{-1} phosphate buffer (adjusted to pH 2.5)–acetonitrile–methanol. DZ, diazepam; NDZ, desmethyldiazepam; OX, oxazepzm; TZ, temazepam; ALP, alprazolam.

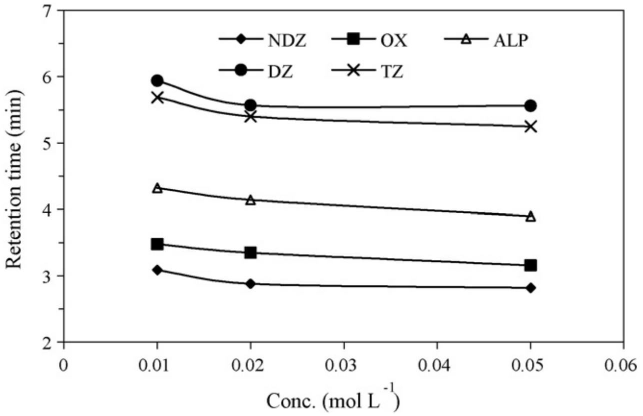

Fig. 5. Effect of buffer concentration on retention times of analytes. Mobile phase: a mixture of phosphate buffer (adjusted to pH 2.5)–acetonitrile–methanol (63:27:10). DZ, diazepam; NDZ, desmethyldiazepam; OX, oxazepzm; TZ, temazepam; ALP, alprazolam.

Table 2
Limit of quantitation (LOQ) for diazepam, desmethyldiazepam, oxazepzm, and temazepam ($n = 5$)

	LOQ (ng mL^{-1})	Between-day RSD (%)	Accuracy (%)
Diazepam	2	5.9	81.2
N-Desmethyldiazepam	2	11.1	82.0
Oxazepzm	2	14.1	111.0
Temazepam	2	7.5	88.5

dard curves were: diazepam, $y = 0.0104x - 0.0074$; desmethyldiazepam, $y = 0.0142x + 0.0187$; oxazepzm $y = 0.0061x + 0.0037$ and temazepam, $y = 0.0131x + 0.0043$ ($r^2 = 0.9995$). The RSD% values (slopes, intercepts) were (1.7, 5.2), (7.4, 1.3), (5.9, 9.7) and (11.3, 8.2) for diazepam, desmethyldiazepam, oxazepzm and temazepam, respectively. The intercepts for all above calibration curves were not significantly different from zero.

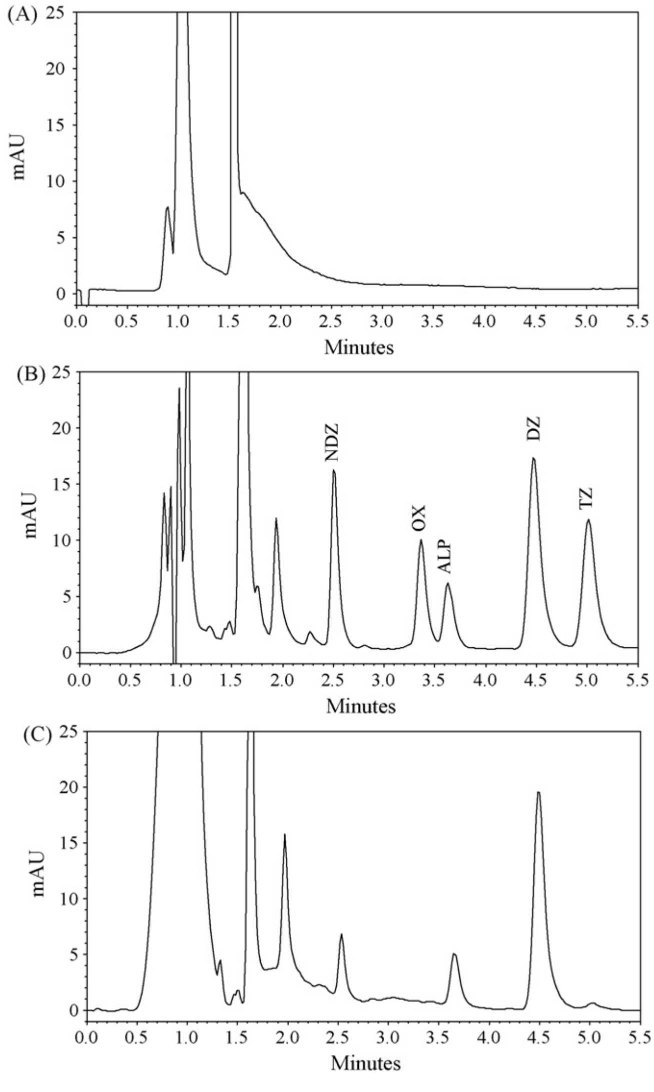

Fig. 6. Chromatograms of (A) blank human plasma, (B) plasma spiked with 100 ng mL^{-1} of diazepam (DZ), desmethyldiazepam (NDZ), oxazepam (OX), temazepam (TZ) and alprazolam (IS), (C) plasma of the same person 2.5 h after oral administration of 10 mg diazepam (diazepam 155 ng mL^{-1}, desmethyldiazepam 45 ng mL^{-1}, and temazepam 20 ng mL^{-1}.

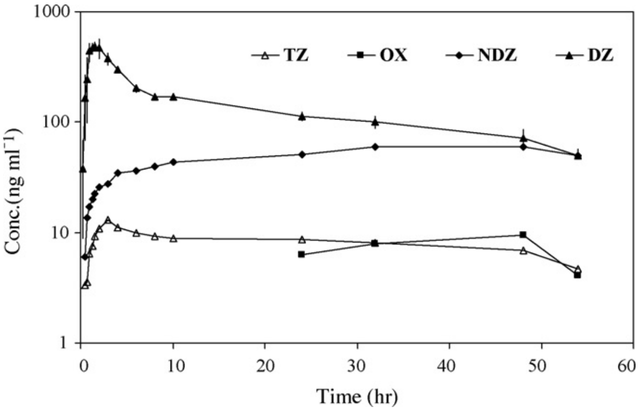

Fig. 7. Mean concentration–time profile of diazepam and its metabolites after administration of 10 mg oral dose of diazepam to four volunteers. DZ, diazepam; NDZ, desmethyldiazepam; OX, oxazepzm; TZ, temazepam; ALP, alprazolam.

3.2.5. Selectivity and chromatography

The separation achieved using the experimental conditions of the present assay for diazepam and its main metabolites are presented in Fig. 6. Selectivity was indicated by absence of any endogenous interference at retention times of peaks of interest as evaluated by chromatograms of blank human plasma (control) and plasma spiked with four compounds. Retention times for NDZ, OX, ALP, DZ and TZ were 2.5, 3.3, 3.6, 4.5 and 5.0 min, respectively.

3.3. Application of the method

To demonstrate the clinical applicability of the assay, we successfully used the method to quantitative diazepam and its metabolites in plasma samples obtained from volunteers who were orally administered single dose diazepam tablets (10 mg) (Dr. Abidi Pharmaceutical Co., Iran).

Peripheral venous blood samples (5 mL) were taken from each volunteer by an indwelling catheter at predetermined intervals (0, 0.25, 0.5, 0.75, 1.0, 1.25, 1.5, 2.0, 3.0, 4.0, 6.0, 8.0, 10.0, 24.0, 32.0, 48.0 and 54.0 h after administration). Blood samples were collected in heparinized tubes. Plasma samples were separated after 20 min centrifugation (Labufuge, HC 121 Heraeus, Christ GMBH, Germany) and were stored at −20 °C until analysis. Plasma samples were analysed by the above-mentioned method. $C_{\max}$ values of diazepam, desmethyldiazepam, oxazepzm and temazepam were 510.8 ± 73, 63.0 ± 23.2, 10.3 ± 3.8 and 13.0 ± 0.7 ng mL^{-1}, respectively. The corresponding $T_{\max}$ values for those analytes were determined to be 1.5 ± 0.4, 40 ± 9.2, 48.0 and 3.0 ± 0.1 h, respectively. Plot of diazepam, desmethyldiazepam, oxazepzm and temazepam mean plasma concentrations as function of time following oral dosing is shown in Fig. 7.

4. Conclusion

The aim of this study was to develop a selective method for determination of diazepam and its metabolites in human plasma. A rapid, selective, reproducible and easy to perform method was designed. The principal advantages of this method were found to be; use of a simple liquid–liquid extraction as part of the chromatographic procedure, shorter run time and better sensitivity (lower LOQ) in comparison with previously published routines. The lower LOQ obtained in this study is very important in pharmacokinetic studies, as the plasma concentrations of oxazepam and temazepam ($\sim$10 ng mL^{-1}) after a single 10 mg oral dose of diazepam are much lower than the LOQ of previously published methods [14–18].

In conclusion, the method presented herein may be fully recommended for pharmacokinetic studies as well as therapeutic drug monitoring.

Acknowledgements

This work was fully supported by a grant from Medical Sciences/University of Tehran. The authors wish to thank Mrs Lida Hakemi for her assistance. Kind contribution to this study by Dr S. Jalilfar from Dr Abidi Pharmaceutical Co. is highly appreciated. The authors also wish to thank Dr Ahmad Mirfazaelian for his help in the revision of the manuscript.

References

[1] J. Crawley, S. Smith, F. Kirkham, P. Muthinji, C. Waruiru, K. Marsh, QJM 89 (1996) 591.
[2] B.R. Ogutu, C.R. Newton, J. Crawley, S.N. Muchohi, G.O. Otieno, G. Edwards, K. Marsh, G.O. Kokwaro, Br. J. Clin. Pharmacol. 53 (2002) 49.
[3] P.J. van der Merwe, J.M. Steyn, J. Chromatogr. 148 (1978) 549.
[4] H. Gjerde, E. Dahlin, A.S. Christophersen, J. Pharm. Biomed. Anal. 10 (1992) 317.
[5] L.E. Fisher, S. Perch, M.F. Bonfiglio, S.M. Geers, J. Chromatogr. B Biomed. Appl. 665 (1995) 217.
[6] R. Herraez-Hernandez, A.J. Louter, N.C. Van de Merbel, U.A. Brinkman, J. Pharm. Biomed. Anal. 14 (1996) 1077.
[7] K.M. Hold, D.J. Crouch, D.E. Rolloin, D.G. Wilkins, D.V. Canfield, R.A. Maes, J. Mass Spectrom. 31 (1996) 1033.
[8] D. Borrey, E. Meyer, W. Lambert, S. Van Calenbergh, C. Van Peteghem, A.P. De Leenheer, J. Chromatogr. A 910 (2001) 105.
[9] El. Mahjoub, C. Staub, J. Pharm. Biomed. Anal. 23 (2000) 447.
[10] Bolner, F. Tagliaro, A. Lomeo, J. Chromatogr. B 750 (2001) 177.
[11] El. Mahjoub, C. Staub, Forensic Sci. Int. 123 (2001) 17.
[12] M. Wilhelm, H.J. Battista, D. Obendorf, J. Anal. Toxicol. 25 (2001) 250.
[13] Bugey, C. Staub, J. Pharm. Biomed. Anal. 35 (2004) 555.
[14] S. Cotler, C.V. Puglisi, J.H. Gustafson, J. Chromatogr. 222 (1981) 95.
[15] P.M. Klockowski, G. Levy, J. Chromatogr. 422 (1987) 334.
[16] C.E. Lau, S. Dolan, M. Tang, J. Chromatogr. 416 (1987) 212.
[17] R.M. Azzam, L.J. Notarianni, H.M. Ali, J. Chromatogr. B Biomed. Sci. Appl. 708 (1998) 304.
[18] Z. Liu, J. Short, A. Rose, S. Ren, N. Contel, S. Grossman, S. Unger, J. Pharm. Biomed. Anal. 26 (2001) 321.
[19] Guidance for Industry, Bioanalytical Method Validation, US Department of Health and Human Services Food and Drug Administration, Center for Drug Evaluation and Research (CDER), Rockville, USA, 2001.

Available online at www.sciencedirect.com

ScienceDirect

Talanta 75 (2008) 651–657

Talanta

www.elsevier.com/locate/talanta

Modeling and prediction (correction) of partition coefficients of bile acids and their derivatives by multivariate regression methods

Costel Sârbu[a,*], Cristina Onişor[a], Mihalj Posa[b], Slavko Kevresan[c], Ksenija Kuhajda[d]

[a] *Babeş-Bolyai University, Faculty of Chemistry and Chemical Engineering, Arany Janos 11, 400028 Cluj-Napoca, Romania*
[b] *University of Novi Sad, Department of Pharmacy, Faculty of Medicine, Hajduk Vejkova 3, 21000 Novi Sad, Serbia*
[c] *University of Novi Sad, Faculty of Agriculture, Trg D. Obradovica 3, 21000 Novi Sad, Serbia*
[d] *University of Novi Sad, Faculty of Sciences, Institute of Chemistry, Trg D. Obradovica 3, 21000 Novi Sad, Serbia*

Received 2 June 2007; received in revised form 2 November 2007; accepted 8 November 2007

Abstract

Different multiple regression methods including forward stepwise multiple linear regression (MLR), principal component regression (PCR) and partial least squares (PLS) have been applied to the modeling of partition coefficient (lipophilicity) of bile acids and their derivatives by means of 16 different descriptors obtained by using Alchemy package software and retention index R_{Mo} as an experimental estimation of lipophilicity. Retention indices for bile acids and their derivatives were determined by reversed phase high-performance thin layer chromatography on RP-18W bounded stationary phase with methanol–water in different volume proportions as mobile phase. The results achieved concerning the prediction of Log P are highly significant and consistent with the molecular structure of the compounds investigated. The sum of absolute values of the charges on each atom of the molecule, in electrons (SQ), the sum of absolute values of the charges on the nitrogens and oxygens in the molecule, in electrons ($\mathrm{SQ_{NO}}$), specific polarizability of a molecule (SP), the third-order connectivity index ($^3\chi$) and molecular lipophilicity, seem to be dominant in the partition mechanism. In addition, regression models developed have allowed a correct estimation of the partition coefficients of cholic acid (Log $P_{\mathrm{HA}} = 2.93$; Log $P_{\mathrm{A}}^{-} = 2.02$) as compared with reported experimental values (Log $P_{\mathrm{HA}} = 2.02$; Log $P_{\mathrm{A}}^{-} = 1.1$).

Keywords: Modeling; Bile acids; Partition coefficient; Lipophilicity; Multiple regression method; QSPR

---

1. Introduction

Lipophilicity is the key parameter used in quantitative structure-activity relationships (QSAR), quantitative structure-property relationships (QSPR) or quantitative structure-retention relationships (QSRR) studies, for modeling the biological and physicochemical properties of large classes of chemical compounds [1–10]. In many cases, this molecular parameter strongly correlates with the biological activity of chemicals, as well as with other important physicochemical properties [11–15]. Studies on the relationship between chromatographic retention and structure (QSRR) are helpful not only for the estimation of lipophilicity, but also to better understand the biochemical and biophysical processes. For this reason, the chromatographic method is a favorite tool having significant advantages in comparison with other physicochemical methods because it is fast and relatively simple, only small amounts of compounds are needed, compounds should not be very pure because they are purified during the chromatographic process, the process is dynamic and can be easily modeled [16–18].

The logarithm of partition coefficient between *n*-octanol and water (Log P) is the most widely used parameter in chemistry, pharmaceutical chemistry, environmental toxicology and many other practical fields and can give accurate predictions of activity in complex biological system such as membranes or soils. As a direct consequence from the magnitude of the Log P of a compound, one can infer its behavior through the cell membrane and other related events [1–3].

The interest concerning the role and exact mechanism of action of bile acids and their conjugates in living organisms has increased considerably in recent decades. Bile acids play a critical role in a multitude of biological processes such as digestion, secretion and the regulation of cholesterol metabolism: they are

---

[*] Corresponding author at: Babeş-Bolyai University, Faculty of Chemistry and Chemical Engineering, Department of Analytical Chemistry, Arany Janos 11, 400028 Cluj-Napoca, Romania. Tel.: +40 264 593833/77; fax: +40 264 590818.
E-mail address: costelsrb@yahoo.co.uk (C. Sârbu).

0039-9140/$ – see front matter © 2008 Published by Elsevier B.V.
doi:10.1016/j.talanta.2007.11.061

significant in the elimination of excess cholesterol and form as end products of cholesterol metabolism. Bile acids are natural detergents that aid in the solubilization and absorption of fats, fatty acids and lipid soluble vitamins. All bile acids and their conjugates form bile salts that are important in the formation of mixed micelles that enhance diffusion through the unstirred layer of the small intestine [19–21]. At this moment the reported experimental data concerning the partition coefficients of bile acids and their derivatives are incomplete and some of them appeared questionable. A carefully examination and the graphing representation of available data have been showing a quite difference between partition coefficients of cholic acid and the values corresponding to its congeners (Table 2, bolded values).

In this study, different multiple regression methods including forward stepwise multiple linear regression (MLR), principal component regression (PCR) and partial least squares (PLS) [22–29] have been applied to the modeling of partition coefficient (lipophilicity) of bile acids and their derivatives by means of 16 different descriptors obtained using Alchemy package software and retention index R_{Mo}. Valuable multiple regression models have been developed using the experimental data reported in the literature. Different validation procedures including linear regression of original and predicted data and also the graphing representation of partition coefficients corresponding for both the protonated (Log P_{HA}) and ionized (Log P_{A}^{-}) forms of bile acids and their derivatives confirm the high quality of models and their predictive capability. The powerful predictive ability of the models allowed the estimation of unknown partition coefficients for some bile acids and new derivatives and a correct prediction of partition coefficients for cholic acid.

2. Experimental part

The chromatographic behavior of bile acids and their derivatives presented in Table 1 was studied on RP-18W bounded stationary phases. Solutions (0.1 mg mL^{-1}) of each compound were prepared in methanol and 3 μL were spotted to origin the plate by hand. Chromatography was performed in a normal developing chamber at room temperature (∼20 °C), the developing distance being 8 cm. Methanol was used as the organic modifier of the mobile phase in the concentration range 50–75% (v/v) in steps of 5%, as the studied compounds differed significantly in their retention.

After being developed, the dried plates were sprayed with manganese chloride and heated to 100–120 °C for 10–15 min. Colored zones appeared on a colorless background and fluorescent blue-orange under UV lamp (λ = 365 nm).

The R_{M} values of each compound were obtained using the well-known equation:

$$R_{\mathrm{M}} = \log\left(\frac{1}{R_{\mathrm{F}}} - 1\right) \qquad (1)$$

The linear correlation between R_{M} values and the concentration of the organic modifier in the mobile phase were calculated separately for each compound by using of the chromatographic equation:

$$R_{\mathrm{M}} = R_{\mathrm{Mo}} + bC \qquad (2)$$

where C is the concentration of methanol in the mobile phase. R_{Mo} and b values (related to the molecular lipophilicity) and the correlation coefficients for Eq. (2) are shown in Table 2. As usual, a high correlation between the two regression parameters, the intercept R_{Mo} and the slope b in TLC Eq. (2) was observed ($r = 0.9822$). Also, in Table 2 are presented the experimental data of the partition coefficients corresponding for both the protonated (Log P_{HA}) and ionized (Log P_{A}^{-}) forms of bile acids and their derivatives, most reported in the literature [18,19,21].

Table 1
Abbreviations of the bile acids and their derivatives studied in this paper

Nr. Crit.	Compound	Abbreviation	Position and orientation of hydroxyl and oxo-groups
1	Lithocholic acid	LC	3α
2	Deoxycholic acid	DC	3α,12α
3	Chenodeoxycholic acid	CDC	3α,7α
4	Cholic acid	C	3α,7α,12α
5	Ursodeoxycholic acid	UDC	3α,7β
6	Hyocholic acid	HC	3α,6α,7α
7	Hyodeoxycholic acid	HDC	3α,6α
8	Glycochenodeoxycholic acid sodium salt	GCDC	Glyco-conjugate of CDC
9	Taurodeoxycholic acid sodium salt	TDC	Tauro-conjugate of DC
10	Glycocholic acid sodium salt	GC	Glyco-conjugate of C
11	Glycodeoxycholic acid sodium salt	GDC	Glyco-conjugate of DC
11	Taurolithocholic acid sodium salt	TLC	Tauro-conjugate of LC
13	Taurochenodeoxycholic acid sodium salt	TCDC	Tauro-conjugate of CDC
14	Glycolithocholic acid	GLC	Glyco-conjugate of LC
15	Taurocholic acid sodium salt	TC	Tauro-conjugate of C
16	3α,7α-Dihydroxy-12-oxo-5β-cholic acid	12-Oxo C	3α,7α,12-Oxo
17	3α,12α-Dihydroxy-7-oxo-5β-cholic acid	7-Oxo C	3α,12α,7-Oxo
18	3α-Hydroxy-7, 12-dioxo-5β-cholic acid	7,12-Dioxo C	3α,7,12-Oxo
19	7α-Hydroxy-3,12-dioxo-5β-cholic acid	3,12-Dioxo C	7α,3,12-Oxo
20	3,7,12-Trioxo-5β-cholic acid	3,7,12-Trioxo C	3,7,12-Oxo

Table 2
TLC regression data and experimental partition coefficients of bile acids and their derivatives studied in this paper

Compound	R_{Mo}	b	R	Log P_{HA}	Log P_A^-
1	3.51	−4.71	0.9987		
2	4.78	−6.01	0.9922	3.50	2.65
3	5.01	−6.29	0.9959	3.28	2.25
4	3.84	−4.99	0.9938	**2.02**	**1.10**
5	3.65	−4.73	0.9972	3.00	2.20
6	3.66	−4.77	0.9957	2.80	1.84
7	3.88	−4.98	0.9968	3.08	2.28
8	2.87	−3.96	0.9918	2.12	0.45
9	2.30	−3.54	0.9765		
10	2.30	−3.45	0.9778	1.65	−0.40
11	2.90	−4.05	0.9760	2.25	0.80
12	2.12	−3.13	0.9182		
13	2.27	−3.59	0.9671		
14	3.39	−4.55	0.9956		
15	2.29	−3.99	0.9798		
16	3.11	−4.51	0.9977		
17	2.99	−4.35	0.9972		
18	3.71	−4.99	0.9943		
19	3.80	−5.09	0.9911		
20	2.54	−3.58	0.9926		

3. Molecular descriptors

The molecular descriptors calculated with SciQSAR option of the molecular modeling computer programs ALCHEMY 2000 [30] were the following: the partition coefficient (Log P), the first-order ($^1\chi$) and the third-order ($^3\chi$) connectivity index, the zero-order ($^0\chi^v$) and the first-order ($^1\chi^v$) valence connectivity index, the third-order shape index for molecule ($^3K_\alpha$), the Wiener (W) index based on the graph of the molecule, volume (V), molar mass (M), dipole moment (DM), molecular polarizability (MP), specific molar polarizability (SP), the largest positive charge over the atoms in a molecule, in electrons (Q_+), the largest negative charge over the atoms in a molecule, in electrons (Q_-), the sum of absolute values of the charges on each atom of the molecule, in electrons (SQ) and the sum of absolute values of the charges on the nitrogens and oxygens in the molecule, in electrons (SQ_{NO}). The potential energy of each molecule is minimized (geometry optimization) by the standard technique of the molecular mechanics method. The obtained values are presented in Table 3.

4. Results and discussion

By reducing the number of features from 18 original descriptors (including also the retention indices R_{Mo} and b) to three principal components (latent variables) [31], the information preserved is enough to permit a primary examination and evaluation of the similarities and differences between descriptors on one hand, and bile acids and their derivatives on the other. The contribution of the first component represents 76.36% of the total variance and the second component 10.99%; a two component model accounts for 87.35% of the total variance. The first three components reproduce almost 95% of the total variance and the first five even 99.13%, and the eigenvalues become negligible after the fifth component.

All the statements above are well supported by the 2D- and 3D-representations of the scores and loadings. The projection of the 3D-representation of loadings (Fig. 1) gives a more complete pattern for descriptors and retention indices: it is clear, for example, that the majority of the descriptors considered in this study form two well defined clusters: the first one includes $^1\chi$, $^0\chi^v$, $^1\chi^v$, $^3K_\alpha$, W, V, Q_+, and the second one encompasses DM, b, $^3\chi$, SQ and SQ_{NO}; Log P, R_{Mo}, and Q_- appear more or less as outliers.

The scatter plot of scores on the plane described by PC1 and PC2 (Fig. 2) shows interesting results. Four linear clusters appear to be well defined and in a good agreement to the structure of

Table 3
The descriptors computed for bile acids and their derivatives

Compound	$^1\chi$	$^0\chi^v$	$^1\chi^v$	Log P	V	W	$^3\chi$	M	SP	DM	MP	Q_+	$^3K_\alpha$	SQ	SQ_{NO}	Q_-
1	12.75	17.62	11.65	6.04	385.14	1772	10.89	376.58	0.1118	3.00	43.08	0.244	3.21	3.76	1.02	−0.392
2	13.17	17.94	11.75	4.22	392.88	1901	11.47	392.58	0.1113	2.50	43.72	0.244	3.22	4.33	1.41	−0.392
3	13.16	17.94	11.74	4.25	391.96	1910	11.25	392.58	0.1115	2.14	43.72	0.244	3.31	4.33	1.41	−0.392
4	13.58	18.26	11.84	3.58	400.31	2045	11.83	408.58	0.1108	1.48	44.35	0.244	3.31	4.89	1.81	−0.392
5	13.16	17.94	11.74	4.26	392.32	1910	11.25	392.58	0.1114	2.18	43.72	0.244	3.31	4.33	1.41	−0.392
6	13.59	18.26	11.85	3.55	400.11	2060	11.89	408.58	0.1108	1.92	44.35	0.244	3.31	4.99	1.80	−0.392
7	13.16	17.94	11.74	3.99	392.52	1919	11.25	392.58	0.1114	3.46	43.72	0.244	3.31	4.33	1.41	−0.391
8	15.06	20.05	12.90	3.05	440.09	3011	12.40	449.64	0.1109	2.70	48.82	0.273	4.36	5.70	2.10	−0.424
9	15.86	21.90	15.05	3.27	468.44	3681	13.01	499.72	0.1129	5.49	52.87	0.294	5.02	5.65	2.07	−0.424
10	15.48	20.37	13.01	2.74	447.49	3187	12.98	465.64	0.1105	3.52	49.46	0.273	4.33	6.27	2.49	−0.424
11	15.07	20.05	12.92	2.94	440.55	2994	12.62	449.64	0.1108	4.34	48.82	0.273	4.24	5.70	2.10	−0.424
12	15.44	21.58	14.95	4.18	460.25	3486	12.43	483.72	0.1135	5.48	52.24	0.294	5.07	5.08	1.68	−0.424
13	15.85	21.90	15.04	3.24	467.48	3702	12.79	499.72	0.1131	5.27	52.87	0.294	5.16	5.65	2.07	−0.424
14	14.65	19.74	12.81	4.12	432.47	2824	12.04	433.64	0.1114	3.54	48.18	0.273	4.27	5.14	1.71	−0.424
15	16.27	22.21	15.14	3.13	475.80	3903	13.37	515.72	0.1125	5.27	53.51	0.294	5.10	6.21	2.46	−0.424
16	13.58	18.14	11.70	3.42	393.27	2045	11.83	406.57	0.1114	4.12	43.80	0.244	3.23	4.69	1.78	−0.392
17	13.58	18.14	11.69	3.47	393.39	2045	11.83	406.57	0.1114	2.78	43.80	0.244	3.23	4.70	1.78	−0.392
18	13.58	18.02	11.54	3.37	388.01	2045	11.83	404.55	0.1115	5.30	43.25	0.244	3.15	4.50	1.75	−0.392
19	13.58	18.02	11.54	3.36	386.76	2045	11.83	404.55	0.1118	4.92	43.25	0.244	3.15	4.49	1.75	−0.392
20	13.58	17.91	11.38	3.60	381.08	2045	11.83	402.54	0.1120	6.42	42.70	0.244	3.06	4.30	1.72	−0.362

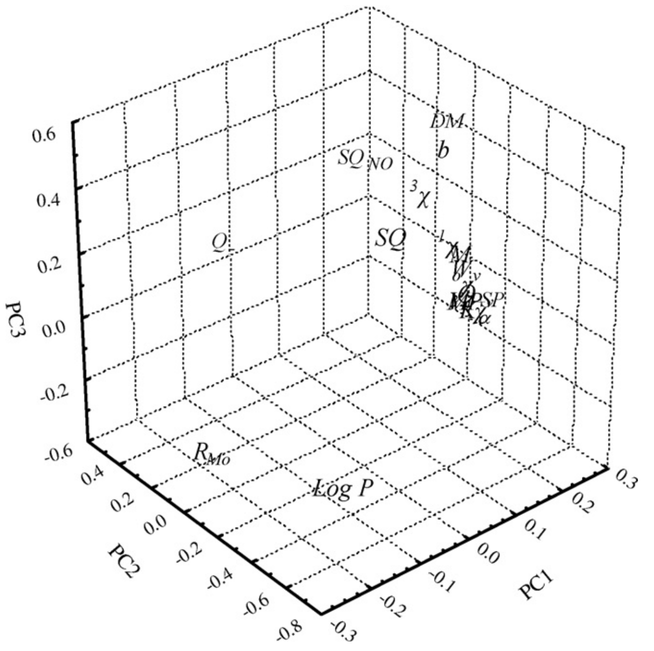

Fig. 1. PC1, PC2 and PC3 loading plot of the autoscaled all descriptors in Table 3 and retention indices.

compounds: one of them corresponds to the tauro-conjugates (right) the others include the group of glyco-conjugates (in the middle) and oxo-derivatives and bile acids, respectively (left). We have also to point out some very close pairs of compounds, including for instance cholic acid (C) and hyocholic acid (HC).

On the other hand, we have to remark the relative high difference between the partition coefficients of cholic acid and, for example, hyocholic acid, the closest congener. The questionable values of cholic acid are well supported by graphing Log P_{HA} versus Log P_{A}^{-}; where cholic acid appears clearly as an outlier (Fig. 3).

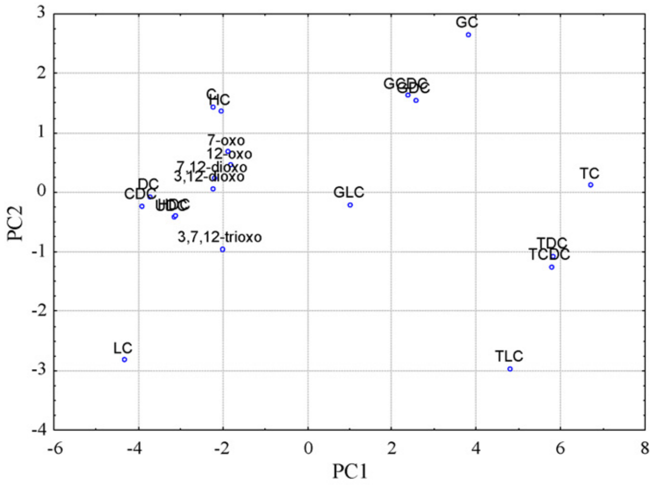

Fig. 2. PC1, PC2 score plot of the autoscaled all descriptors in Table 3 and retention indices.

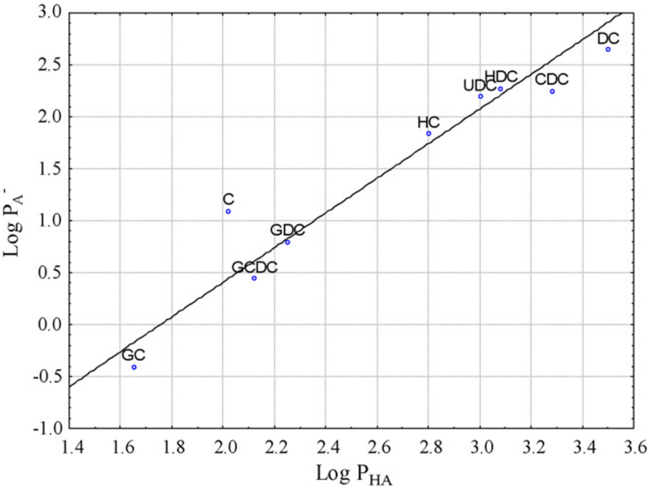

Fig. 3. Scatterplot of experimental partition coefficients of bile acids and their derivatives (Log P_{A}^{-} vs. Log P_{HA}).

In order to describe the relationship between Log P values of protonated (Log P_{HA}) and ionized (Log P_{A}^{-}) bile acids and their derivatives and the calculated structural parameters, including retention indice R_{Mo}, a multivariate regression analysis was performed. By applying forward stepwise regression analysis, high-quality regression equations were obtained in both cases: including the experimental values for cholic acid in the model (Eqs. (1) and (2)) and without these values in the model (Eqs. (3) and (4)).

$$\mathrm{Log}\ P_{\mathrm{HA}} = -6.89 - 3.70\mathrm{SQ}_{\mathrm{ON}} + 0.93\chi^{3},\quad n = 9,\quad R^{2} = 0.8902,\quad F = 24,\quad s = 0.245 \tag{1}$$

$$\begin{aligned}\mathrm{Log}\ P_{\mathrm{A}}^{-} &= 129.24 - 11.79\mathrm{SQ}_{\mathrm{ON}} + 2.45\chi^{3} - 0.23V \\ &\quad + 4.61\mathrm{SQ} + 0.07W - 715.87\mathrm{SP} + 0.03R_{\mathrm{Mo}}, \\ &\quad n = 9,\quad R^{2} = 0.9999,\quad F = 1,540,000, \\ &\quad s = 0.0009\end{aligned} \tag{2}$$

$$\mathrm{Log}\ P_{\mathrm{HA}} = -2.49 - 1.38\mathrm{SQ} + 0.95\chi^{3} + 0.22R_{\mathrm{Mo}},\quad n = 8,\quad R^{2} = 0.9947,\quad F = 251,\quad s = 0.061 \tag{3}$$

$$\begin{aligned}\mathrm{Log}\ P_{\mathrm{A}}^{-} &= 13.69 - 0.09M + 0.25V - 0.008W \\ &\quad + 0.14R_{\mathrm{Mo}} - 514.24\mathrm{SP} - 0.12\,\mathrm{Log}\ P, \\ &\quad n = 8,\quad R^{2} = 0.9999,\quad F = 3331,\quad s = 0.020\end{aligned} \tag{4}$$

where n is the number of compounds in the prediction model, R^{2} the determination coefficient, F the F-test value, and s is the standard error of estimates. The F and corresponding p values of all the equations are highly significant having high determination coefficients and small s values, with special remark in both cases of Log P_{A}^{-}.

The results suggest also that the most significant descriptors are SP and SQ, i.e. the electronic parameter and the shape ($^{3}\chi$,

Table 4
The estimated values of Log P_{HA} and Log P_A^- for bile acids and their derivatives by MLR, PCR and PLS

Compound	Abbreviation	Experimental values		Estimated by MLR		Estimated by PCR		Estimated by PLS	
		Log P_{HA}	Log P_A^-	Log P_{HA}	Log P_A^-	Log P_{HA}	Log P_A^-	Log P_{HA}	Log P_A^-
2	DC	3.50	2.65	3.48	2.65	3.50	2.69	3.50	2.69
3	CDC	3.28	2.25	3.32	2.45	3.28	2.22	3.28	2.22
5	UDC	3.00	2.20	3.03	2.20	3.00	2.16	3.00	2.16
6	HC	2.80	1.84	2.73	1.85	2.80	1.82	2.80	1.82
7	HDC	3.08	2.28	3.08	2.28	3.08	2.33	3.08	2.33
8	GCDC	2.12	0.45	2.06	0.47	2.12	0.49	2.12	0.49
10	GC	1.65	−0.40	1.70	−0.41	1.65	−0.38	1.65	−0.37
11	GDC	2.25	0.80	2.27	0.79	2.26	0.74	2.26	0.73
12	TLC			2.77	−2.99	0.49	−3.27	0.51	−3.13
13	TCDC			2.37	−4.04	0.10	−3.89	0.12	−3.74
14	GLC			2.61	1.24	2.61	0.99	2.61	0.98
15	TC			2.15	−4.72	0.02	−4.26	0.04	−4.14
16	12-Oxo C			2.96	0.10	2.27	1.01	2.28	1.05
17	7-Oxo C			2.93	0.15	2.29	1.08	2.29	1.12
18	7,12-Dioxo C			3.35	−0.99	2.43	1.14	2.43	1.18
19	3,12-Dioxo C			3.39	−1.45	2.14	0.53	2.15	0.60
20	3,7,12-Trioxo C			3.37	−2.99	1.42	−0.53	1.43	−0.45
1	LC			3.43	2.57	3.42	2.43	3.42	2.39
9	TDC			2.59	−3.54	0.38	−3.41	0.39	−3.27
4	C	2.02	1.10	2.84	2.06	2.93	2.01	2.93	2.00

Table 5
Values of root mean square (RMS)

Training data	Including cholic data		Without cholic data	
	PCR	PLS	PCR	PLS
Log P_{HA}	0.270	0.262	0.011	0.011
Log P_A^-	0.302	0.296	0.114	0.120

V, *W*) of the molecules. The chromatographic retention index R_{Mo} and the calculated Log *P* have also a significant contribution.

The prediction values for cholic acid were much higher in both cases (in the first case Log $P_{HA} = 2.43$ and Log $P_A^- = 1.1$, and in the second case Log $P_{HA} = 2.84$ and Log $P_A^- = 2.06$, respectively). All the predicted values by MLR are presented in Table 4.

For PCR and PLS methods, the original 16 descriptors and retention index R_{Mo} were used for the selection of the optimum number of factors using the cross-validation procedure. The prediction error was calculated as a root mean square (RMS) error according to [32]. The results of RMS were minimized in the case of the first two factors for both PCR and PLS, when the experimental values of cholic acid were included in the training set, and six factors for both PCR and PLS without the experimental values of cholic acid in the model as it is shown in Table 5. The prediction values for cholic acid were much higher in both cases: the values predicted by PCR were Log $P_{HA} = 2.93$ and Log $P_A^- = 2.01$ and in the case of PLS, Log $P_{HA} = 2.93$ and Log $P_A^- = 2.00$, respectively. All the predicted values by PCR and PLS without cholic acid in the model are also presented in Table 4.

In order to compare the MLR, PCR and PLS predictive models, linear regression was applied considering the experimental and the predicted values of both partition coefficients. Good

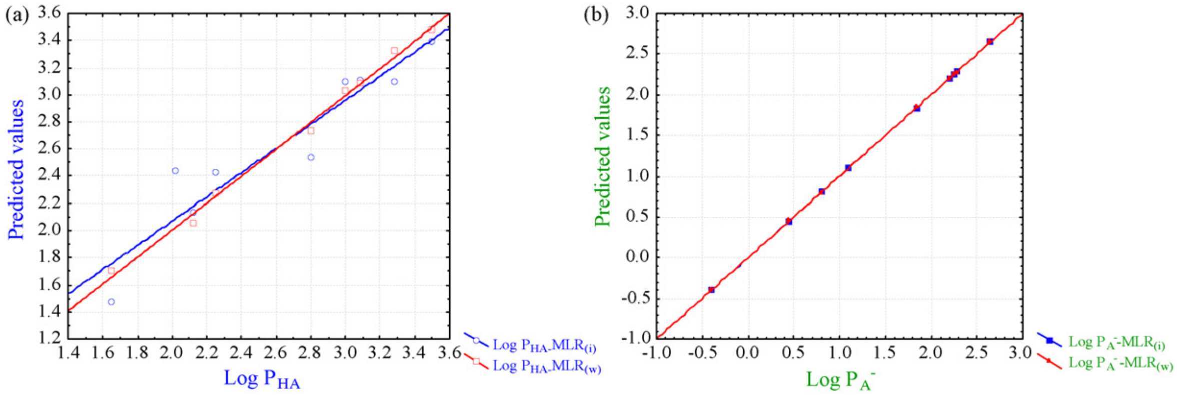

Fig. 4. Linear regression between predicted and experimental values of partition coefficients of bile acids and their derivatives obtained by using MLR including cholic acid values (i) and without cholic acid values (w) in the model: (a) Log P_{HA}; (b) Log P_A^-.

Table 6
Statistical parameters to evaluate linear relation between observed and predicted partition coefficients considering all three multiple regression methods (MLR, PCR and PLS)

Statistical parameter	Including experimental values of cholic acid in the training data						Without the experimental values of cholic acid in training data					
	MLR		PCR		PLS		MLR		PCR		PLS	
	Log P_{HA}	Log P_{A}^{-}	Log P_{HA}	Log P_{A}^{-}	Log P_{HA}	Log P_{A}^{-}	Log P_{HA}	Log P_{A}^{-}	Log P_{HA}	Log P_{A}^{-}	Log P_{HA}	Log P_{A}^{-}
R^2	0.8902	0.9999	0.8665	0.9351	0.8747	0.9377	0.9947	0.9983	0.9999	0.9983	0.9999	0.9983
F	57	75×10^6	45	101	49	105	1129	3481	16×10^4	3481	15×10^4	3472
p	0.0001	0.0000	0.0003	0.0000	0.0002	0.0000	0.0000	0.0000	0.0000	0.0000	0.0000	0.0000
s	0.214	0.0003	0.233	0.271	0.227	0.265	0.050	0.049	0.004	0.049	0.004	0.049
a_0	0.289	0.000	0.352	0.095	0.330	0.091	0.014	0.000	0.000	0.002	0.000	0.003
a_1	0.890	1.000	0.867	0.935	0.875	0.938	0.995	1.000	1.000	0.998	1.000	0.998

correlations between the observed and the predicted partition coefficients of the three methods were found when experimental cholic acid values were eliminated from the model as it is easy to observe in Table 6 and Figs. 4 and 5. In all cases, the intercept a_0 is statistically zero (t-test) and the slope a_1 is not statistically different from 1 (t-test). As a direct consequence, one can conclude that all straight lines are parallel and pass through the origin. In addition, high F values and very small s values were obtained in all cases with a special remark in the case of PCR and PLS, which appear to be the most effective for the estimation of partition coefficients of bile acids and their derivatives. The estimated values of partition coefficients of cholic acid using PCR and PLS seem to be more reliable and consistent with the chemical structure and other findings obtained in this study. This statement is very well supported and illustrated in Figs. 6 and 7 where it is easy to observe that cholic acid joins its congeners. The strong linear correlation obtained between experimental values of Log P_{HA} and Log P_{A}^{-} is very similar when estimated values of other compounds by PCR and PLS were considered.

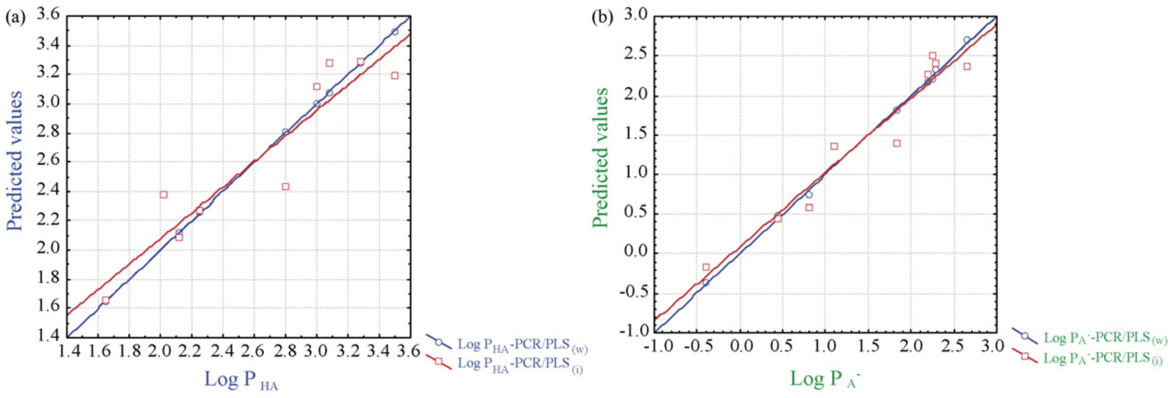

Fig. 5. Linear regression between predicted and experimental values of partition coefficients of bile acids and their derivatives obtained by using PCR and PLS including cholic acid values (i) and without cholic acid values (w) in the model: (a) Log P_{HA}; (b) Log P_{A}^{-}.

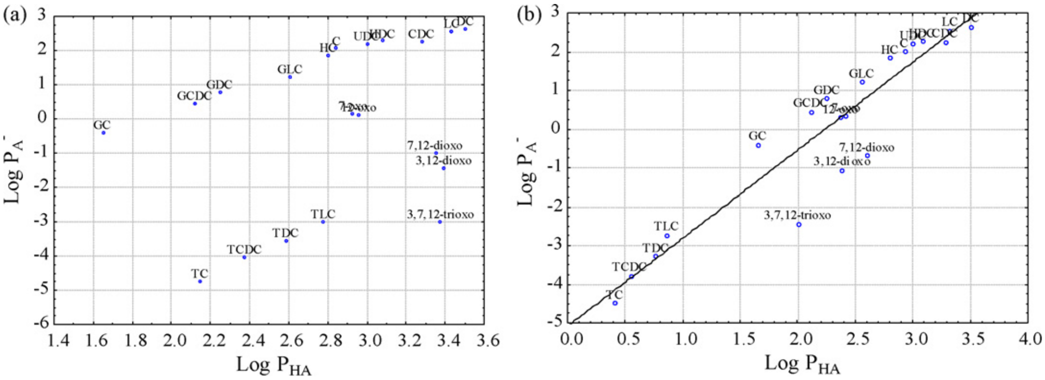

Fig. 6. Scatterplot of all partition coefficients of bile acids and their derivatives (Log P_{A}^{-} vs. Log P_{HA}): (a) experimental and estimated by MLR and (b) experimental and estimated by PCR and PLS.

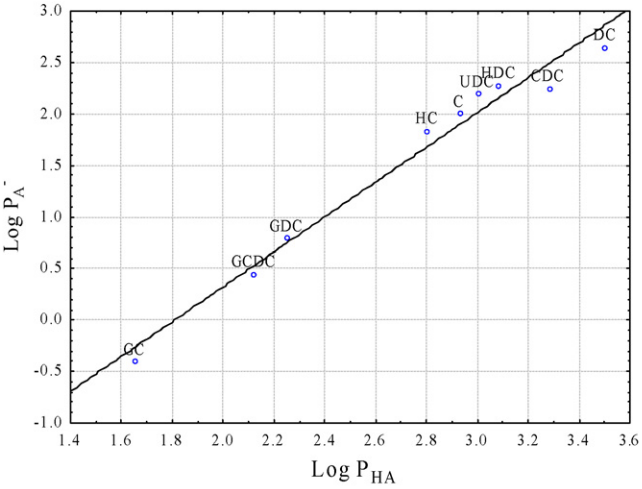

Fig. 7. Scatterplot of experimental partition coefficients of bile acids and their derivatives (Log P_A^- vs. Log P_{HA}) including the corrected values of cholic acid (Log $P_{HA} = 2.93$ and Log $P_A^- = 2.01$).

5. Conclusions

The correlation obtained between partitions coefficients and structure descriptors for bile acids and their derivatives is highly significant, therefore they can be used to predict the values of other members of the series. By comparing the multivariate regression methods used in this study, PCR and PLS appeared to be the most effective in predicting partition coefficients for the studied compounds. The high predictive ability of both QSPR models enabled the correction of cholic acid partition coefficients. The results suggested also that the most significant descriptors are specific molar polarizability and the sum of absolute values of the charges on each atom of the molecule, i.e. the electronic parameter and the shape (molecular volume, the third-order connectivity index and the Wiener index) of the molecule. The chromatographic retention index and the calculated Log *P* had also a significant contribution.

References

[1] C. Hansch, A. Leo, Exploring QSAR: Fundamentals and Applications in Chemistry and Biology, ACS, Washington, DC, 1995.
[2] M. Karelson, Molecular Descriptors in QSAR/QSPR, Wiley & Sons Inc., New York, 2000.
[3] R. Todeschini, V. Consonni, Handbook of Molecular Descriptors, Weinheim, Wiley–VCH, 2000.
[4] R. Kaliszan, Anal. Chem. 64 (1992) 619A–631A.
[5] S. Agatonovic-Kustrin, I.G. Tucker, M. Zecevic, L.J. Zivanovic, Anal. Chim. Acta 418 (2000) 181–195.
[6] D.J. Livingstone, J. Chem. Inf. Comput. Sci. 40 (2000) 195–209.
[7] T. Hou, X. Xu, Chemometr. Intell. Lab. Syst. 56 (2001) 123–132.
[8] R.M. McDowell, J. Jaworska, SAR QSAR Environ. Res. 13 (2002) 111–125.
[9] M. Nendza, M. Muller, Quant. Struct. Act. Rel. 19 (2000) 581–598.
[10] M. Daszykowski, I. Stanimirova, B. Walczak, F. Daeyaert, M.R. De Jonge, J. Heeres, L.M.H. Koymansc, P.J. Lewi, H.M. Vinkers, P.A. Janssen, D.L. Massart, Talanta 68 (2005) 54–60.
[11] M.P. Freitas, J.A. Martins, Talanta 67 (2005) 182–186.
[12] J. Dai, L. Jin, S. Yao, L. Wang, Chemosphere 42 (2001) 899–907.
[13] K.M. Biswas, D.R. DeVido, J.G. Dorsey, J. Chromatogr. A 1000 (2003) 637–655.
[14] B. Ren, Chemometr. Intell. Lab. Syst. 66 (2003) 29–39.
[15] K. Valko, J. Chromatogr. A 1037 (2004) 299–310.
[16] M.H. Abraham, A. Ibrahim, A.M. Zissimos, J. Chromatogr. A 1037 (2004) 29–47.
[17] A. Berthod, S. Carda-Broch, J. Chromatogr. A 1037 (2004) 3–14.
[18] A. Pyka, M. Miszczyk, Chromatographia 61 (2005) 37–42.
[19] A. Roda, A. Minutello, M.A. Angelotti, A. Fini, J. Lipid. Res. 31 (1990) 1433–1443.
[20] A.A. Powell, J.M. Larue, A.K. Batta, J.D. Martinez, Biochem. J. 356 (2001) 481–486.
[21] C. Sârbu, K. Kuhajda, S. Kevresan, J. Chromatogr. A 917 (2001) 361–366.
[22] H. Martens, T. Naes, Multivariate Calibration, Wiley, Chichester, 1989.
[23] Y. Zhou, L. Xu, Y. Wu, B. Liu, Chemometr. Intell. Lab. Syst. 45 (1999) 95–100.
[24] S. Wold, M. Sjostrom, L. Eriksson, Chemometr. Intell. Lab. Syst. 58 (2001) 109–130.
[25] K. Tang, T. Li, Anal. Chim. Acta 476 (2003) 85–92.
[26] E. Furusjo, A. Svenson, M. Rahmberg, M. Andersson, Chemosphere 63 (2006) 99–108.
[27] M.T.D. Cronin, T.W. Schultz, J. Mol. Struct. (THEOCHEM) 622 (2003) 39–51.
[28] A. Tropsha, P. Gramatica, V.J. Gombar, Quant. Struct. Act. Rel. 22 (2003) 69–77.
[29] C. Sârbu, B. Tiperciuc, J. Planar Chromatogr. 19 (2006) 342–347.
[30] http://www.tripos.com.
[31] http://www.statsoft.com.
[32] R.G. Brereton, Chemometrics: Data Analysis for the Laboratory and Chemical Plant, John Wiley & Sons Ltd., Chichester, 2003.

Available online at www.sciencedirect.com
ScienceDirect
Talanta 75 (2008) 658–665
Talanta
www.elsevier.com/locate/talanta

Liquid-phase microextration combined with liquid chromatography–electrospray tandem mass spectrometry for detecting diuretics in urine

Tzu-Feng Tsai [a,b], Maw-Rong Lee [a,*]

[a] *Department of Chemistry, National Chung Hsing University, Taichung 40227, Taiwan*
[b] *Department of Cosmetic Science, Providence University, Taichung 43301, Taiwan*

Received 1 September 2007; received in revised form 25 November 2007; accepted 26 November 2007
Available online 8 January 2008

Abstract

Trace amounts of diuretics were determined in human urine by hollow fiber liquid-phase microextraction (LPME) combined with liquid chromatography–electrospray ionization–tandem mass spectrometry (LC–ESI–MS/MS) in this study. Chromatography was performed on a C_8 reversed-phase column. A 25 μL *n*-octanol was used to extract analytes in urine. Extraction was optimized using a pH 2 solution spiked with 0.15 g/mL NaCl for 40 min at 40 °C with 1010 rpm stirring. The limits of detection of diuretics in urine were 0.3–6.8 ng/mL, and linearity range was 1–1000 ng/mL. Recoveries of spiked 50 ng/mL diuretics were 97.7–102.5%. The intra-day precision and inter-day precision were 3–18% and 4–21%, respectively. The diuretics concentration profiles in patient urine were also determined. The results of this study reveal the adequacy of LPME–LC–MS/MS method for analyzing diuretics in urine and quantification limits exceed World Anti-Doping Agency requirements.

Keywords: Liquid-phase microextraction; Diuretics; Liquid chromatography–mass spectrometry; Urine

1. Introduction

As therapeutic agents used to eliminate tissular liquids or enhance renal excretion of salt and water, diuretics are often used for treating congestive heart failure, hypertension, liver, kidney disease and lung disease [1,2]. Their effectiveness in water removal has led to misuse of diuretics by athletes attempting to reduce body weight. Diuretics have also been used to avoid detection of doping agents by diluting urine to reduce their concentration. Diuretics may also imbalance the thermoregulatory system, causing exhaustion, irregular heartbeat and ultimately heart failure or death [3]. Therefore, the Medical Commission of the International Olympic Committee (IOC) included diuretics as a banned substance since 1986 [4].

Diuretics drugs are available in several classes varying structures and physicochemical properties. The pK_a value of diuretics is 2.8–9.5 and log P (octanol–water partition coefficient) value is −0.071 to 3.376 [5–7]. Effective methods of identification diuretics are vital for clinical research and doping control. Pharmacokinetic studies of urine samples after a single dose have shown that most diuretics are essential unchanged when excreted. Hence, procedures for screening diuretics in urine can be designed to detect the suspected parent compound. Many techniques have been developed for determining diuretics in human urine. High-performance liquid chromatography (HPLC), capillary electrophoretic (CE) or micellar electrokinetic capillary chromatography (MEKC) with UV or photodiode arrays detection (DAD) [8–14] were used widely. However, these methods suffer from significant interferences in urine samples matrix and offer limited qualitative information. Gas chromatography–mass spectrometry (GC–MS) can confirm the structure of diuretic compounds [15–18]. However, diuretics cannot be analyzed by GC without derivatization procedures for most substances containing polar functional groups. Generally, methylation or silylation derivatization procedures are time-consuming and unsuitable for some diuretics. For detecting polar substances and identifying analytes from complicate urine, liquid chromatography–mass spectrometry/mass spectrometry (LC–MS/MS) [19–21] has been proved to be sensitive, rapid and without doing any derivatization.

Sample extraction clean-up from sample matrix and concentrate trace amounts of analyte are essential aspects of analysis.

---

* Corresponding author. Tel.: +886 4 2285 1716; fax.: +886 4 2286 2547.
E-mail address: mrlee@dragon.nchu.edu.tw (M.-R. Lee).

0039-9140/$ – see front matter © 2007 Elsevier B.V. All rights reserved.
doi:10.1016/j.talanta.2007.11.058

Liquid–liquid extraction (LLE) [9–15,20] and solid-phase extraction (SPE) [18,19,21] are the most common methods of preconcentration and clean-up. Solvents used for LLE and SPE normally require evaporation to concentrate and reconstitution of the sample for subsequent LC analysis. These steps are tedious and time-consuming and may cause loss of analytes. However, the major drawback in both techniques is the large amount of organic solvent consumed.

Hollow fiber liquid-phase micrextraction (LPME), a fast, simple, inexpensive, less solvent sample preparation and disposal method has been devised to extract analytes from water and biologic fluids [22–38]. This method employs a membrane as an interface between the sample solution (donor) and the organic solvent (acceptor), which avoids mixing of the two phases and other problems encountered in classical liquid–liquid extraction. The advantages of LPME are single step enrichment/clean-up, very low organic solvent consumption and low cost.

In this study, a hollow fiber LPME method was used to extract trace diuretics in urine samples. The analytes were analyzed by LC–MS with selected reaction monitoring (SRM) mode. The optimized parameters affecting LPME extraction efficiency including extraction temperature, extraction time, pH value of sample solution and ion strength were evaluated. Detection limits, linear ranges and precision of the technique as well as the feasibility of applying the proposed method in patient urine were studied.

2. Experimental

2.1. Chemicals and reagents

An HPLC-grade of acetonitrile was obtained from TEDIA Company (Fairfield, OH, USA), and methanol was purchased from Merck Company (Darmstadt, Germany). Analytical grade formic acid, ammonium formate, acetic acid, ammonium acetate and glycerine were also obtained from Merck. Sodium hydroxide (99%), *n*-octanol, toluene, cyclohexane and sodium chloride (99.8%) were purchased from Riedel-deHäen Company (Seelze, Germany). Hydrochloric acid (36.5%) was from Fisher Scientific Company (Fair Lawn, NJ, USA). Diuretics analyzed in this study, bumetanide (BUM), chlorothiazide (CT), clopamide (CA), ethacrynic acide (EAA), hydrochlorothiazide (HCT), hydroflumethiazide (HFT), probenecid (PRO) and trichlormethiazide (TCT), were purchased from Sigma–Aldrich Company (St. Louis, MO, USA). The structures of diuretics are shown in Fig. 1.

A stock solution of diuretics at 1.0 mg/mL was prepared by dissolving the solid bulk drug in methanol and stored at −30 °C. This solution was further diluted with methanol to yield the appropriate working solutions. The eight point calibration curves were prepared by serial dilution of stock solution with blank urine at the concentration of 1–1000 ng/mL. Pooled drug-free human urine samples as blank urine were obtained from six healthy volunteers, stored at −30 °C and thawed at room temperature before use. For optimum LPME study, urine samples were prepared by spiking with standard diuretics solution. The real urine samples collected from diuretics dosed patient were kept frozen at −30 °C until further treatment. The laboratory purified water (>18 MΩ) was obtained from a SG-Ultra Clear water purification system (SG Water Company, Germany).

2.2. Hollow fiber LPME device

The LPME device illustrated in Fig. 2 was used to preconcentrate the analyte from urine. The experimental apparatus employed an 8 cm Accurel Q 3/2 polypropylene tubular membrane (Membrana, Wuppertal, Germany) with 200 μm wall thickness, 0.2 μm pore size and 600 μm internal diameter. The fiber was washed with acetone in ultrasonic bath for 30 min to remove contaminants then dried in an oven at 50 °C before

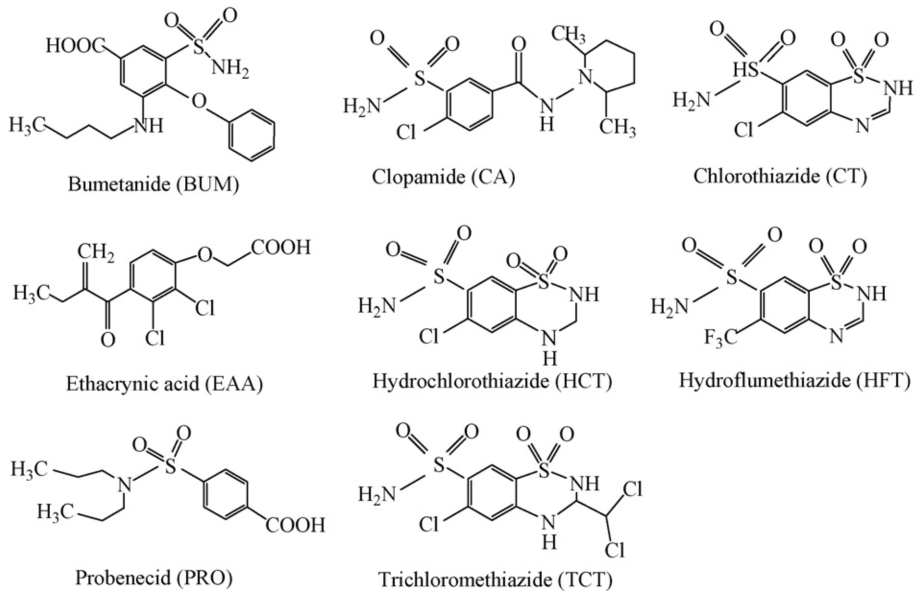

Bumetanide (BUM)
Clopamide (CA)
Chlorothiazide (CT)
Ethacrynic acid (EAA)
Hydrochlorothiazide (HCT)
Hydroflumethiazide (HFT)
Probenecid (PRO)
Trichloromethiazide (TCT)

Fig. 1. The structures of diuretics.

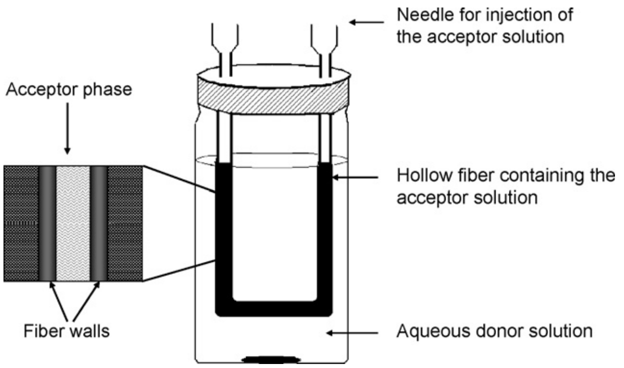

Fig. 2. Schematic diagram hollow fiber-protected liquid-phase microextraction device.

use. For each extraction, a new piece of fiber with the U-shape configuration was employed to avoid possibility of carryover.

Both a 7.5 mL urine solution and a 10 mm × 4 mm stir bar were placed in a 8 mL sample vial (diameter: 1.5 cm, height: 5.5 cm) with a screw top/silicone septum. The LPME device consisted of two 0.7 mm o.d. 24 Gauge intravenous catheter syringes (guiding needles) inserted through a silicon septum and connected with a section of polypropylene hollow fiber. Prior to extraction, the hollow fiber pores were dipped in organic solvent for 10 s to immobilize solvent in the pores. The excess solvent was then removed by ultrasonication in a water bath for 15 s. A 50 μL syringe was used to fill the hollow fiber with 25 μL of *n*-octanol as extraction solvent (acceptor solution). The assembly was then placed into the sample vial and with a magnetic stirrer at approximately 630 rpm for 40 min under room temperature. After extraction, the fiber was removed from the guiding needles, and the acceptor solution was retracted into the 10 μL Hamilton gas-tight syringe, (Hamilton, Bonaduz, Bonaduz, Switzerland) model 701 SN, with a beveled needle tip (length: 5.1 cm, o.d.: 0.071 cm, i.d.: 0.015 cm) from one end of the fiber. A 5 μL portion of the extractant was injected into the LC–MS/MS system.

2.3. LC–MS/MS analysis

A Varian 1200L triple-quadrupole LC–MS (Varian, Walnut Creek, CA, USA) coupled to the Dynamax ProStar 210 liquid chromatograph system was used. The analytes were separated on a Waters XTerra C_8 (15 cm × 2.1 mm, 3.0 μm) LC column (Waters Corp., Milford, MA, USA) preceded by an in-line pre-column filter of 3 mm frit (Supelco, Bellefonte, PA, USA). The mobile phase was filtered using a filter (0.22 μm) and degassed by using vacuum followed by sonication. The gradient separation of LC was proceed. A pH 2.76 of mixture solution of 0.05 mM ammonium formate containing 0.1% formic acid (A) and acetonitrile (B) was used as mobile phase at a flow-rate of 0.2 mL/min. The initial composition was 35% B for 1.0 min, then increased to 65% for 6 min, then decreased to 35% for 5 min until equilibrium. The volume of injection loop was 5 μL, and all the column effluent was directed into the mass spectrometer.

The selected reaction monitoring (SRM) mode of MS/MS was used for quantization. The data acquisition software Varian MS workstation, Version 6.2, was used for instrument control, data acquisition and data handling. Analysis was performed in both positive ionization and negative ionization modes. Voltages across the capillary, lens and the quadrupoles were tuned by an automated procedure to maximize the signal for analyzed ions. The parameters for the ionization efficiency were optimized by evaluating sensitivity using flow injection analysis (FIA) with the mobile phase at 0.2 mL/min. The instrumental parameters were optimized to maximize signal intensity of the deprotonated molecule ion $[M-H]^-$ or pseudomolecular ion $[M+H]^+$ by injecting 5 μL standard solution (1.0 μg/mL) through a sample loop. The MS/MS was performed based on collision-induced dissociation (CID) of specific precursor ion and the generation of the characteristic fragment ions. The Q1 was scanned a range of *m*/*z* 50–500 for precursor ion optimization. In all deprotoned molecule ions of analytes observed were more stable, abundant and less fragmented during negative scan. Both Q1 and Q3 quadrupoles were set at unit resolution. During SRM analysis mode, mass peak width was 1.0 mass unit at half height for both Q1 and Q3, scan time was 1 s. The spray conditions of API interface were: housing temperature 65 °C; nebulizing gas pressure 35 psi; drying gas temperature 250 °C; drying gas pressure 20 psi. Argon was used as the collisional gas at pressure of 2.0 mTorr.

2.4. Method validation

The method was validated for linearity, limit of detection (LOD), limit of quantification (LOQ), precision (RSD), accuracy and recovery. Urine calibration standards were a set of spiked diuretics in drug-free urine at concentrations of 1, 5, 10, 50, 100, 250, 500 and 1000 ng/mL. Three replicate analyses were performed for each concentration to evaluate linearity. The peak areas were used for quantification through the calibration curves of diuretics. The LOD and LOQ were determined as the ratio of 3 times and 10 times standard deviation at the lowest concentration of linear range divided to the slope of linear equation, respectively. Precision of the assay was determined by generating intra- and inter-day variability data from a 50 ng/mL sample. The analytical accuracy of purposed method was determined by analyzing spiked diuretics in urine samples at a concentration of 50 ng/mL five times and expressed as the ratio of mean measured concentration to spiked concentration. The analytical recovery was determined by analyzing triplicate of spiked diuretics in urine sample at concentration of 50 ng/mL. To verify specificity, blank samples were prepared with drug-free urine samples from five different donors.

3. Results and discussion

3.1. Mass spectrometry of diuretics

Both positive and negative ionization mode of ESI were used to evaluate the most sensitive ionization mode for the diuretics. The concentration of 1 μg/mL diuretics was used in this study with FIA. The pseudomolecular ion, $[M+H]^+$, of all diuretics was obtained in positive ionization mode as the base ion. In the negative ionization mode, the peak of the deprotonated molecule

Table 1
Precursor ion and product ion used in SRM of LPME–LC–MS/MS for detection diuretics

Analytes	Abb.	Precursor ion (*m/z*)	Product ion (*m/z*)
Chlorothiazide $C_7H_6ClN_3O_4S_2$	CT	294 $[M-H]^-$	214 $[M-H\text{-}SO_2NH_2]^-$
Hydrochlorothiazide $C_7H_8ClN_3O_4S_2$	HCT	296 $[M-H]^-$	205 $[M-H\text{-}SO_2CNH]^-$
Hydroflumethiazide $C_8H_8F_3N_3O_4S_2$	HFT	330 $[M-H]^-$	239 $[M-H\text{-}SO_2CNH]^-$
Clopamide $C_{14}H_{20}ClN_3O_3S$	CA	344 $[M-H]^-$	189 $[M\text{-}C_8N_2OH_{15}]^-$
Trichlormethiazide $C_8H_8Cl_3N_3O_4S_2$	TCT	378 $[M-H]^-$	306 $[M-H\text{-}2HCl]^-$
Bumetanide $C_{17}H_{20}N_2O_5S$	BUM	365 $[M+H]^+$	240 $[M+H\text{-}CO_2SO_2NH_2]^+$
Probenecid $C_{13}H_{19}NO_4S$	PRO	284 $[M-H]^-$	240 $[M-H\text{-}CO_2]^-$
Ethacrynic acid $C_{13}H_{12}Cl_2O_4$	EAA	301 $[M-H]^-$	243 $[M-H\text{-}CO_2\text{-}CH_2]^-$

ions, $[M-H]^-$ of all diuretics as the base ion and less fragment ions were observed. The structures of thiazide-base diuretics BUM, CA, CTA, HCT, HFT and TCT are a benzene ring and a sulfamonyl residue ortho-located to an electronegative substitute such as a chlorine atom (Fig. 1). In preliminary experiments for all thiazide-base diuretics except bumetanide indicated that the signal of $[M-H]^-$ was more sensitive than that of $[M+H]^+$. According to the paper described thiazides as acidic character, the use of negative ion electrospray ionization proved to be reasonable [39,40]. Therefore, the positive ionization mode was not considered further for using to analyze diuretics except for bumetanide.

In MS/MS experiments, ESI interface was used in conjunction with the FIA for optimization of the MS/MS parameters. The product ion mass spectrum of deprotoned molecule ion was obtained in the scan range of *m/z* 50–500. For all thiazide diuretics, the characteristic fragment ion $[M\text{-}SO_2NH_2]^-$ was observed in the product ion spectra. For CT, the ion $[M\text{-}SO_2NH_2]^-$, *m/z* 214 is the base peak. Therefore, in this assay, the mass transition pattern, *m/z* 294 → 214 was selected to monitor CT in negative ionization SRM analysis (Table 1). For other diuretics, the base peak ions were shown in Table 1. In negative ionization mode, the mobile phase of ACN exited the same mass transition *m/z* 363 → 319 as bumetanide. The pseudomolecular ion of bumetanide, $[M+H]^+$ *m/z* 365 was chosen as precursor ion, and the product ion, *m/z* 240, $[M+H\text{-}CO_2SO_2NH_2]^+$ was used for monitored in positive mode to avoid the interference from mobile phase. Therefore, in this assay both positive and negative ionization modes were used simultaneously to detect the diuretics in urine.

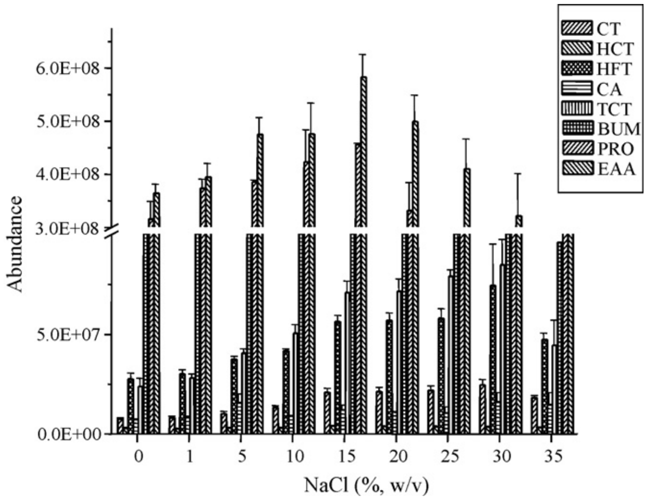

Fig. 3. Effect of salt concentration on the extraction efficiency of 50 ng/mL diuretics in urine produced by using LPME–LC–MS/MS.

3.2. The hollow-fiber LPME method

In order to increase the sensitivity, the optimum LPME conditions for the determination of diuretics were required to evaluate the various parameters that affect the LPME extraction procedure. Extraction efficiency of the membrane may be affected by extraction solvent, extraction temperature, extraction time, solution pH, ionic strength of aqueous phase, hollow fiber length and stir rate. It is very important to optimize these parameters for enhance extraction efficiency and then to improve detection.

For LPME, polypropylene membrane has proven effectively for increasing concentration and reducing matrix interference from urine [31,34,35]. The polypropylene fiber was selected in this study. The solvent used in LPME should have low water solubility and high solubility for analytes. Three organic solvents *n*-octanol, toluene and cyclohexane were used to evaluate the extraction efficiency of 50 ng/mL diuretics in urine at room temperature for 30 min. The experimental results indicated that the highest extraction efficiency was obtained with *n*-octanol. Therefore, *n*-octanol was chosen as extraction solvent in this study.

The pH value of sample solution influences both the dissociation equilibrium and the solubility of organic acid or base

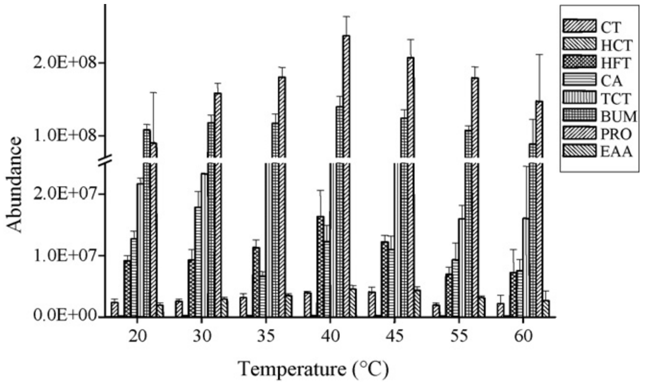

Fig. 4. Effect of extraction temperature on the extraction efficiency of 50 ng/mL diuretics in urine produced by using LPME–LC–MS/MS.

analytes. For diuretics, BUM, EAA and PRO are highly acidic and the other five compounds are less acidic. A sample pH range from 1 to 10 was used to evaluate the extraction efficiency of 50 ng/mL diuretics in urine at 20 °C for 30 min. The results indicated that lower pH value improved extraction efficiency of the target analytes. Hence, the pH of solution was adjusted to 2.

Salt-out effect was often used to improve extraction efficiency of analytes in LPME as in SPME [41]. Ionic strength increases in the sample solution will decrease the solubility of target analytes in water solution for salt-out effect. The NaCl is a conversional salt used to change the ionic strength in solution. The salt effect study was evaluated at salt concentrations from 0 to 0.35 g/mL. As Fig. 3 shows, extraction efficiency increased as NaCl concentration increased and reached a maximum at 0.15 g/mL and then decreased at higher NaCl concentrations. The decay in high concentration of NaCl was possible due to electrostatic interaction between polar analytes and NaCl ions in solution [41,42]. Hence, 0.15 g/mL NaCl was added in the further experiments.

Table 2
Estimated limits of detection and linear range for diuretics by LPME–LC–MS/MS

Compound	Linear range (ng/mL)	Correction coefficient (r^2)	LOD[a] (ng/mL)	LOQ[b] (ng/mL)	Enrichment factor[c]	Extraction efficiency (%)
CT	5–1000	0.9994	1.7	5.5	0.8	0.2
HCT	10–1000	0.9986	6.7	22.3	1.7	0.5
HFT	2–1000	0.9938	1.1	3.7	3.8	1.0
CA	2–1000	0.9995	0.3	0.9	95.2	25.4
TCT	2–1000	0.9989	0.4	1.4	11.3	3.0
BUM	10–500	0.9997	3.6	12	20.1	5.4
PRO	1–1000	0.9969	0.6	2.1	32.6	8.7
EAA	5–1000	0.9962	2.8	9.4	144.8	38.6

[a] LOD, limit of detection, determined as 3S.D./slope, standard deviation of the lowest concentration of calibration curve divided by the slope ($n = 3$).

[b] LOQ, limit of quantification, determined as 10S.D./slope, standard deviation of the lowest concentration of calibration curve divided by the slope ($n = 3$).

[c] Urine was spiked at 50 ng/mL.

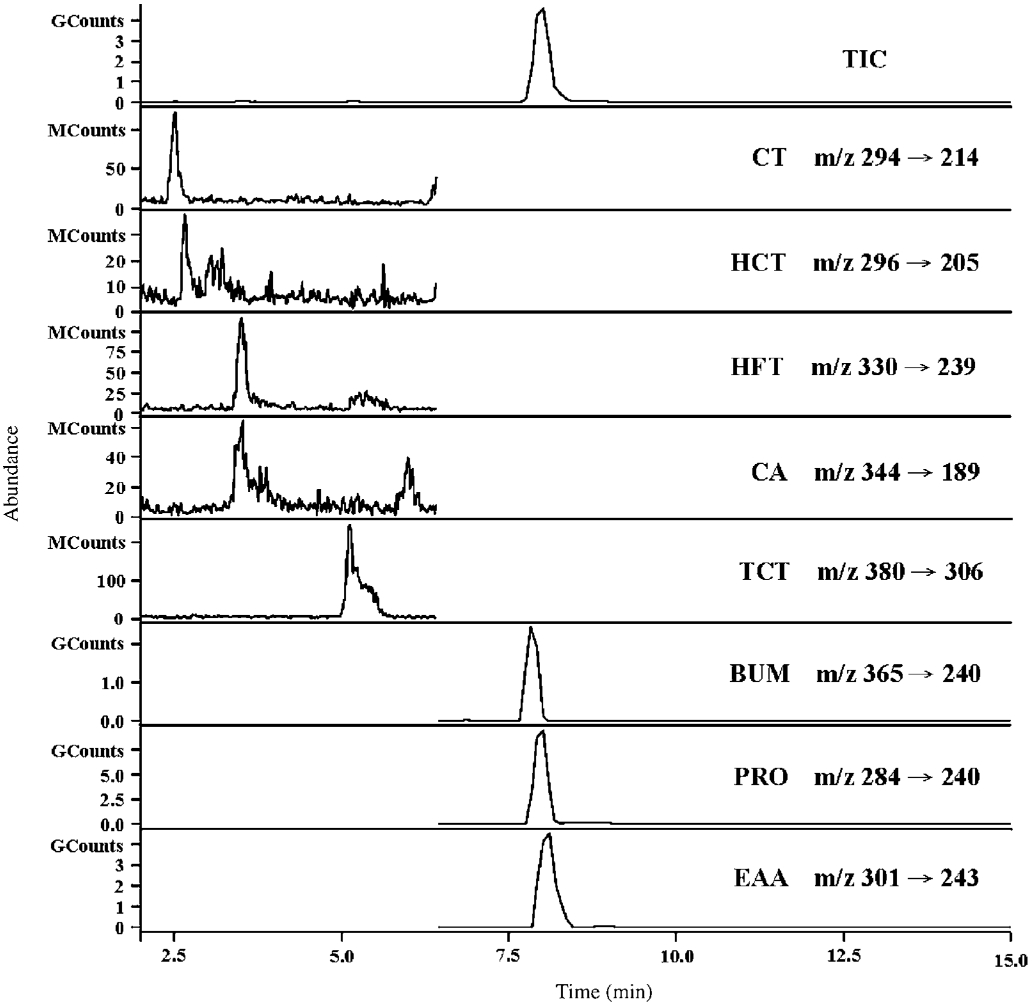

Fig. 5. Mass ion chromatograms of 50 ng/mL diuretics in urine produced by LPME–LC–MS/MS.

Matrix interference is often an important problem in biological samples during trace analysis [28,31,42–44]. To evaluate the influence of matrix, the MS signal intensities of 50 ng/mL standard diuretic solutions diluted with artificial urine and ultrapure water were tested. Almost the same intensities of diuretics were obtained no matter what matrices used. It was shown that LPME can improve the sample clean-up to remove urine components and thereby decreasing the amount of matrix injected onto the column.

Agitating stir bar can increase the mass transfer coefficient from the sample matrix to extraction phase. To trace the effect of stirring, eight stir rates (0–1200 rpm) were used to evaluate extraction efficiency of 50 ng/mL diuretics in urine at 40 °C for 40 min. The high stirring speed increased extraction efficiency but also produced instability of the organic solvent in hollow fiber and the air bubbles would affected the precision and reproducibility of the extraction process. Therefore, a stirring speed of 1010 rpm was used for subsequent experiments.

3.2.1. Extraction temperature and time

The LPME method employs a partition equilibrium process in target analytes between extraction phase (accept solution) and sample matrix (donor solution) [30]. Extraction temperature and time affect partition equilibrium. The higher extraction temperature normally has a positive effect on extraction yield by increases both solubility and diffusion of analytes into extraction phase. However, heating might also cause swelling in fibers and does not favor organic solvent immobilization in membrane pore. Extraction temperature was studied at a room temperature to 60 °C. The experimental results in Fig. 4 show that extraction efficiency was maximum at 40 °C. In optimization extraction time investigated, a spiked 50 ng/mL urine solution was used within 20–50 min at 40 °C. The experimental results showed that the peak areas of diuretics were reached maximum at extraction for 40 min. When extraction time exceeded 40 min, the peak areas of analytes slowly decreased. Thus, 40 °C extraction temperature and 40 min extraction time were selected for the following experiments.

3.2.2. Acceptor phase volume

The ratio between the volume of the donor phase (V_0) and the acceptor phase (V_{org}) governs the extraction efficiency (EE) and enrichment factor (EF) of analytes in the acceptor phase,

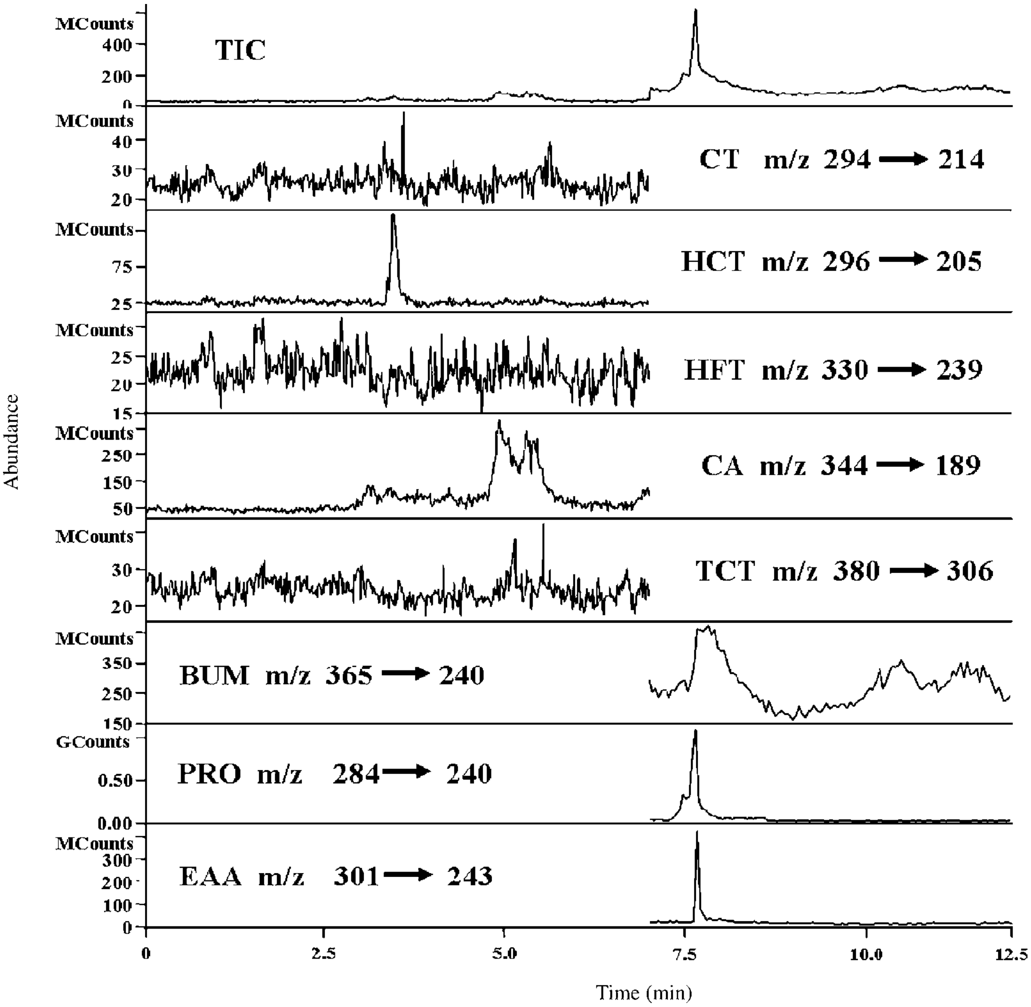

Fig. 6. Total ion chromatogram and mass ion chromatograms of dosed patient urine sample produced by LPME–LC–MS/MS.

according to the expression:

$$EE = \left(\frac{n_{org}}{n_0}\right) 100\% = \left(\frac{V_{org}}{V_0}\right)\left(\frac{C_{org}}{C_0}\right) 100\%$$

and

$$EF = \frac{C_{org}}{C_0}$$

where n_{org}, V_{org} and C_{org} are the mass, the volume and the concentration of analyte extracted in the organic solvent, respectively, and n_0, V_0 and C_0 are the mass, the volume and the concentration of analytes present in the original sample, respectively [18]. To optimize acceptor-to-donor phase volume ratio, the donor phase volume (V_0) is kept constant, and the volume of organic solvent (V_{org}) is changed from 15–36 μL by adjusting the length of the hollow fiber at 5, 6, 8, 10 and 12 cm. The experimental results showed the peak areas of the analytes were maximum at a 6.0 cm of hollow fiber with an acceptor phase volume of 20 μL. The parameters of optimum condition of LPME were list in Table 2.

3.3. Assay validation

Calibration curves for eight diuretics were established for the concentration range from 1 to 1000 ng/mL. The linear range, precision, limit of detection (LOD), and limit of quantification (LOQ) of this method were evaluated under the optimum condition as shown in Table 2. The linearity of the proposed method was with correlation coefficients (r^2) being greater than 0.9938. The LOD and LOQ were 0.3–6.7 ng/mL and 0.9–22.3 ng/mL, respectively. The LOD of eight diuretics were found in low ng/mL level and lower than the minimum required performance limits (MRPL) of the World Anti-Doping Agency (WADA). The mass ion chromatograms of 50 ng/mL diuretics in urine analyzed by LPME-LC-MS/MS were shown in Fig. 5.

The recovery and precision of this method expressed with % by analyzing 50 ng/mL diuretics spiked urine samples. The recovery of diuretics was 97.7–102.5%. The intra-day and inter-day relative standard deviations (R.S.D.s, $n = 6$) were 3–18 and 4–21%, respectively. LPME is a non-exhaustive extraction procedure as solid-phase microextraction, the extraction efficiency is defined as the ratio of the amount of analyte in acceptor phase to donor phase and dependant on the distribution coefficient of the compound. As shown in Table 2, the extraction efficiency of diuretics from spiked urine was 0.2–38.7%, the high enrichment factor could be obtained. For EAA, the high enrichment factor was reached 144.8-fold.

3.4. Application

The diuretics dosed patient urine was analyzed by the LC–ESI–MS/MS method described. The LPME was operated at the optimum conditions studied. Representative SRM chromatograms of urine sample collected from the patient first urine after post-administration were shown in Fig. 6. The total ion chromatogram (TIC) and extracted ion chromatogram of urine sample obtained from a hypertension patient was shown in Fig. 6. The concentrations of diuretics detected were HCT, 24.9 μg/mL; BUM, 0.046 μg/mL; PRO, 0.011 μg/mL; EAA, 0.008 μg/mL.

4. Conclusion

This study evaluated the coupling of LPME with LC–ESI-MS/MS to determine the trace amount of diuretics in urine samples. A 6 cm Q 3/2 hollow fiber was used to extract trace diuretics from urine. The optimized procedure was revealed satisfactory intra-day and inter-day precision with R.S.D. of 3–18% and 4–21%, respectively. The limit of detection was 0.3–6.7 ng/mL and limit of quantification was 0.9–22.3 ng/mL. In addition, the feasibility of applying the methods to determine diuretics in real samples was also examined by analyzing urine samples from diuretics dose patient. The concentrations of diuretics detected were ranged from 0.008 μg/mL (EAA) to 24.9 μg/mL (HCT). The LPME method represents a valuable advance in sample preparation and offers numerous advantages, including procedural simplicity, low cost and organic solvent less used.

Acknowledgment

The authors would like to thank the National Science Council of the Republic of China for financially supporting this research under Contract No. NSC94-2113-M-005-001.

References

[1] A.S. Mehanna, M. Dowling, J. Pharm. Biom. Anal. 19 (1999) 967.

[2] R. Faris, M. Flather, H. Purcell, M. Henein, P. Pool-Wilson, A. Coats, Int. J. Cardiol. 82 (2002) 149.

[3] L.M. Antes, P.C. Fernandez, Disease-a-Month 44 (1998) 254.

[4] Olympic Movement Anti-Doping Code, Prohibited Class of Substances and Prohibited Methods, IOC, Lausanne, 2001, Appendix A.

[5] http://redpoll.pharmacy.ualberta.ca/drugbank.

[6] The Merck Index, Merck & Co., Inc., tenth ed., 1983.

[7] A. Berthod, Anal. Chem. 71 (1999) 879.

[8] R. Ventura, J. Segura, J. Chromatogr. B 687 (1996) 127.

[9] M.R. Taylor, P. Teale, J. Chromatogr. A 768 (1997) 89.

[10] A. Rosado-Maria, A.I. Gasco-Lopez, A. Santos-Montes, R. Izquierdo-Hornillos, J. Chromatogr. B 748 (2000) 415.

[11] D.L. Hertzog, J.F. McCafferty, X. Fang, R.J. Tyrrell, R.A. Reed, J. Pharm. Biomed. Anal. 30 (2002) 747.

[12] M.L. Luis, S. Corujedo, D. Blanco, J.M.G. Graga, A.I. Jiménez, J.J. Arias, Talanta 57 (2002) 223.

[13] M.J. Ruiz-Angel, J.R. Torres-Lapasió, M.C. Garcia-Alvarez-Coque, J. Chromatogr. A 1022 (2004) 51.

[14] J.A.M. Pulgarin, A.A. Molina, G.P.O. Nieto, Anal. Chim. Acta 518 (2004) 37.

[15] D. Carreras, C. Imaz, R. Navajas, M.A. Garcia, C. Rodriguez, A.F. Rodriguez, R. Corres, J. Chromatogr. A 683 (1994) 195.

[16] J. Segura, R. Ventura, C. Jurado, J. Chromatogr. B 713 (1998) 61.

[17] R.K. Műller, J. Grosse, D. Thieme, R. Lang, J. Teske, H. Trauer, J. Chromatogr. A 843 (1999) 275.

[18] L. Amendola, C. Colamonici, M. Mazzarino, F. Botré, Anal. Chim. Acta 475 (2003) 125.

[19] D. Thieme, J. Grosse, R. Lang, R.K. Mueller, A. Wahl, J. Chromatogr. B 757 (2001) 49.

[20] Y. Qin, X.B. Wang, C. Wang, M. Zhao, M.T. Wu, Y.X. Xu, S.Q. Peng, J. Chromatogr. B 794 (2003) 193.

[21] C. Goebel, G.J. Trout, R. Kazlauskas, Anal. Chim. Acta 502 (2004) 65.

[22] L. Zhao, H.K. Lee, Anal. Chem. 74 (2002) 2486.
[23] G. Shen, H.K. Lee, Anal. Chem. 74 (2002) 648.
[24] L. Hou, G. Shen, H.K. Lee, J. Chromatogr. A 985 (2003) 107.
[25] D.K. Dubey, D. Pardasani, A.K. Gupta, M. Palit, P.K. Kanaujia, V. Tak, J. Chromatogr. A 1107 (2006) 29.
[26] K.E. Rasmussen, S. Pedersen-Bjergarrd, M. Krogh, H.G. Ugland, T. Grønhaug, J. Chromatogr. A 873 (2000) 3.
[27] T.G. Halvorsen, S. Pedersen-Bjergarrd, K.E. Rasmussen, J. Chromatogr. A 909 (2001) 87.
[28] L.S. De Jager, A.R.J. Andrews, Analyst 126 (2001) 1298.
[29] X. Wen, C. Tu, H.K. Lee, Anal. Chem. 76 (2004) 228.
[30] K.E. Rasmussen, S. Pedersen-Bjergaard, Trac-Trends Anal. Chem. 23 (2004) 1.
[31] J.B. Quintana, R. Rodil, T. Reemtsma, J. Chromatogr. A 1061 (2004) 19.
[32] T.S. Ho, J.L.E. Reubsaet, H.S. Anthonsen, S. Pedersen-Bjergaard, K.E. Rasmussen, J. Chromatogr. A 1072 (2005) 29.
[33] F.J.M. Santana, A.R.M. Oliveira, P.S. Bonato, Anal. Chim. Acta 549 (2005) 96.
[34] A. Leinonen, K. Vuorensola, L.M. Lepola, T. Kuuranne, T. Kotiaho, R.A. Ketola, R. Kostiainen, Anal. Chim. Acta 559 (2006) 166.
[35] T. Kuuranne, T. Kotiaho, S. Pedersen-Bjergaard, K.E. Rasmussen, A. Leinonen, S. Westwood, R. Kostiainen, J. Mass Spectrom. 38 (2003) 16.
[36] P. Liang, L. Guo, Y. Liu, S. Liu, T.Z. Zhang, Microchem. J. 80 (2005) 19.
[37] S. Pedersen-Bjergaard, K.E. Rasmussen, J. Chromatogr. B 817 (2005) 3.
[38] N. Vora-adisak, P. Varanusupakul, J. Chromatogr. A 1121 (2006) 236.
[39] M. Thevis, H. Schmickler, W. Schänzer, Anal. Chem. 74 (2002) 3802.
[40] M. Thevis, W. Schänzer, J. Am. Soc. Mass Spectrom. 14 (2003) 658.
[41] A.A. Boyd-Boland, J. Pawliszyn, J. Chromatogr. A 704 (1995) 163.
[42] C.C. Chou, M.R. Lee, Anal. Chim. Acta 538 (2005) 49.
[43] R. Herráez-Hernández, P. Campins-Falco, A. Sevillano-Cabeza, J. Chromatogr. 582 (1992) 181.
[44] M.R. Lee, Y.S. Song, B.H. Hwang, C.C. Chou, J. Chromatogr. A 896 (2000) 265.

Available online at www.sciencedirect.com

ScienceDirect

Talanta 75 (2008) 817–823

Talanta

www.elsevier.com/locate/talanta

Detection of clindamycin by capillary electrophoresis with an end-column electrochemiluminescence of tris(2,2′-bypyridine)ruthenium(II)

Jingwu Wang [a,*], Zhibing Peng [a], Jia Yang [b], Xiaoxia Wang [c], Nianjun Yang [d,**]

[a] *Department of Chemistry, Nanchang University, Nanchang 330031, China*
[b] *Tecom Science and Technology Corp. Ltd., Nanchang 330029, China*
[c] *Graduate School of Engineering, University of Fukui, Fukui, Japan*
[d] *Diamond Research Center, National Institute of Advanced Industrial Science and Technology, Umezono 1-1-1, Tsukuba, Japan*

Received 13 November 2007; received in revised form 17 December 2007; accepted 17 December 2007
Available online 26 December 2007

Abstract

Coupled capillary electrophoresis (CE) with end-column electrogenerated chemiluminescence (ECL) was adopted for the quantitative detection of clindamycin. Clindamycin enhanced ECL intensity of tris(2,2′-bypyridine)ruthenium(II) ($Ru(bpy)_3{}^{2+}$) as a *coreactant*. Under the optimized conditions, the ECL intensity was linear with the concentration of clindamycin over the range from 5.0×10^{-7} to 1.0×10^{-4} M with a detection limit of 1.4×10^{-7} M. The proposed CE–ECL was successfully applied for the detection of clindamycin in pharmaceutical and clinic samples. The interaction of clindamycin with hemoglobin was also investigated. The binding constant of clindamycin with hemoglobin was estimated to be 3.6×10^3 M^{-1}.

Keywords: Capillary electrophoresis; End-column electrochemiluminescence; Clindamycin; Tris(2,2′-bypyridine)ruthenium(II); Drug analysis

---

1. Introduction

Capillary electrophoresis (CE), based on the separation of charged molecules through a small capillary under the influence of an electric field, has emerged as a powerful and popular analytical separation technique for the determination of numerous analytes from organic molecules to macromolecules such as DNA and proteins [1,2] during the last two decades. The main attractive features cover high resolving power and small sample volume [3]. Therefore, it has been widely utilized nowadays as an excellent complement to high-performance liquid chromatography for the daily assays. Coupling capillary electrophoresis with other techniques (e.g. UV–vis spectrometry [4], mass spectrometry [5], electrochemistry [6], chemiluminescence/electrochemiluminescence (ECL) [7–20], and fluorescence) marries the advantages of nice sensitivity and selectivity, high efficiency, possible microminiaturization/integration, and reduced cost, and thus has been developed widely and been utilized remarkably in recent years [12–20]. Among them, CE–ECL has been paid considerable attention. For example, Huang et al. utilized CE–ECL for the detection of chloroquine phosphate and for the study on the interaction of chloroquine phosphate with human serum albumin [12]. Wang and co-workers applied CE–ECL detection system for the detection of various drugs [16]. Dickson et al. [17] employed CE–ECL for the separation and detection of biologic samples. Forbes et al. [18] separated and detected ß-blockers by CE–ECL method. Wang and Bobbitt [19] designed in suit ECL cell to analyze various amino acids. Whang and co-workers [20] proposed a wall-jet CE–ECL detector by use of a disk-like ITP electrode as working electrode.

Clindamycin, a lincosamide antibiotic, of which chemical structure is shown in Fig. 1, is highly efficient against Gram-positive and Gram-negative anaerobic pathogens as well as Gram-positive aerobes by inhibition of bacterial protein synthesis [21] and has been widespread used as an antimicrobial in pregnant and non-pregnant patients. Several methods, including spectrophotometry [22], gas chromatography [23,24], micellar electrokinetic chromatography (MEKC) [25], high-performance liquid chromatography (HPLC) with UV detection [26–28],

---

[*] Corresponding author. Tel.: +86 791 803 3020.
[**] Corresponding author. Tel.: +81 29 861 5080.
E-mail addresses: wangjingwu@ncu.edu.cn (J. Wang), nianjun-yang@aist.go.jp (N. Yang).

0039-9140/$ – see front matter © 2007 Elsevier B.V. All rights reserved.
doi:10.1016/j.talanta.2007.12.019

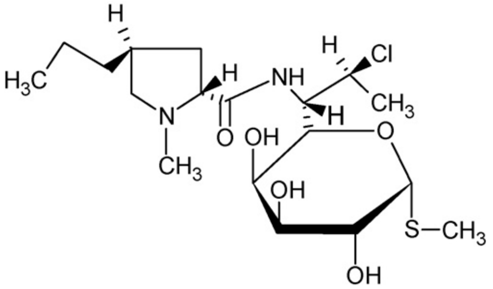

Fig. 1. Chemical structure of clindamycin.

electrospray tandem mass spectrometry [29], and chemiluminescence [30], have thus been reported for the determination of clindamycin in bulk drug, dosage forms and biological fluids. These methods offered sensitive detection, however, always need long analysis time. Also organic solvents are always used.

Since clindamycin contains a tertiary amine group in the molecular structure, it is promising to enhance ECL intensity [14] as a *coreactant* during its oxidation. This paper, therefore, aims at proposing a novel monitoring route of clindamycin by the combined end-column CE–ECL. Tri (2, 2′-bipyridyl) ruthenium(II) based ECL system was chosen due to its high ECL efficiency and stability in aqueous media [12–20]. The experimental optimum for the measurements of clindamycin in real samples was also performed. Furthermore, like many other drugs, clindamycin may undergo some degree of reversible binding to plasma proteins, a process which might significantly affect its distribution in body and the elimination rate. The distribution and the effect of the drug in the human body are undoubtedly related with the content of unbond drug in our body. Therefore, the interaction of protein with clindamycin was also conducted.

2. Experimental

2.1. Chemical and solutions

Hemoglobin (bovine red cells) and clindamycin were purchased from Worthington Biochemical Corporation (NJ, USA). Tris(2, 2′-bipyridyl)ruthenium(II) chloride hexahydrate was obtained from J&K Chemical Company (HK, China), Other chemicals used are of analytical grade. The double-distilled water was used throughout experiments and the solutions were filtered through 0.22 μm membrane before measurements. The stock solution of 0.01 M clindamycin was prepared by dissolving 0.2572 g clindamycin hydrochloride in 50 mL water and stored at 4 °C in a refrigerator and the stock solution of $Ru(bpy)_3{}^{2+}$ was prepared by use of 50 mM pH 7.5 phosphate buffer solutions. The mixtures of the diluted $Ru(bpy)_3{}^{2+}$ solutions with clindamycin hydrochloride solutions were used for measurements. The pH values of the mixtures were varied as the experiments required. Before measurements, the solution was diluted with water to prepare standard solutions with a series of concentrations for the construction of calibration curve, the study of reproducibility and recovery.

2.2. Apparatus

The MPI-B CE–ECL instrument was purchased from Xi'an Remax Electronic Science-Tech Co. (Xi'an, China) and consists of a high-voltage power supplier for separation and injection, a potential control system, a chemiluminescence detection system, and a data processor. An uncoated fused-silica capillary (25 μm i.d., 375 μm o.d.) with the length of 42 cm bought from Yongnian Optical Conductive Fiber Plant (Hebei, China) was set between two buffer reservoirs and employed to separate clindamycin from other pharmaceuticals. The electrophoresis was driven by the high potential apparatus and high voltage was applied at the injection end. This high potential apparatus provides a separation voltage across the capillary to drive the sample by electro-migration injection at definite time.

The end-column ECL cell was conducted in a three-electrode system, which was composed of a Pt working disk electrode (300 μm in diameter), an Ag/AgCl reference electrode (KCl saturated), and a Pt wire counter electrode. The detection cell has a volume of about 300 μL and is fixed in a dark detection chamber. The capillary and the Pt working electrode were screwed in an opposite direction inside the ECL cell. The reference electrode and counter electrode were inserted into the cell from punched holes of the upper side of the cell. To avoid blocking photo detection by the photomultiplier tube (PMT), the reference electrode and counter electrode were inserted into the solution just above the working electrode. An optical glass was adopted as ECL detection window and put directly at the top of a PMT. The glass slide and PMT were fixed in the chamber in order to keep the same distance between the working electrode and PMT photo detector. The outlet of the capillary was grounded by a stainless tube which fixed on the capillary by epoxy. A Model CHI600 voltammetric analyzer (CH Instruments, Austin, TX, USA) was used to supply the potential for the redox reaction of $Ru(bpy)_3{}^{2+}$ on the Pt working electrode. The detection cell was placed directly above PMT. The output of ECL intensity was amplified and recorded with MPI-B software by a computer. 250 μL of $Ru(bpy)_3{}^{2+}$ solution in 50 mM pH 7.5 phosphate buffer solution was added into the reservoir and refreshed every 2 h. Before each run, the capillary was flushed with the corresponding running buffer until the baseline was stable.

2.3. Experimental procedure

Prior to electrochemical measurements, the Pt disc working electrode was polished with 0.3 and 0.05 μm Al_2O_3 powder, cleaned with water in an ultrasonic cleaner, and then carefully put on an opposite position to the capillary outlet end. Elimination of the oxide layer on the Pt electrode was always performed *via* scanning the potential of the Pt disc electrode from −0.5 to 0.0 V for ten cycles. In order to make CE effluent contact the electrode surface directly, the distance between Pt working electrode and the outlet of the capillary was controlled strictly in the range of 70 ± 5 μm with the aid of an optical microscope. 250 μL of $Ru(bpy)_3{}^{2+}$ solution was added into the reservoir before analysis, and replaced every 2 h to eliminate depletion effect or potential interference from reaction during the analysis. The capillary is always flushed with 0.1 M sodium hydroxide for overnight followed by rinsing with distilled water for 30 min at the first use. Before each run, the capillary was flushed with distilled water and the corresponding running buffer until the baseline of ECL is flat. A series of extraction procedures was done before electrophoresis to eliminate the influence of ionic strength in sample and obtain clear electrophoretic profile. Then the sample solutions were injected and their ECL emission was recorded.

For the interaction of clindamycin hydrochloride with hemoglobin, 200 μL of 0.01 M clindamycin and 50 μL of 100 μM hemoglobin were injected into a dialysis bag (21 mm diameter, molecular weight cutoff 8000–14,400), which was incubated in 2 mL 50 mM pH 7.5 phosphate buffer solution at 37 °C. The ECL intensity of clindamycin outside the dialysis bag was detected every half an hour until no remarkable changes in ECL intensity was found, indicating that the equilibrium of the interaction of clindamycin with hemoglobin has been reached because the dialysis bag keeps big protein molecules (e.g. hemoglobin) inside but releases small-sized molecules (e.g. clindamycin). After the equilibrium, 100 μL of the solution inside the dialysis bag was injected into 2 mL 50 mM pH 7.5 phosphate buffer solution. The mixture was then inspected by the UV–vis spectrophotometer to confirm the interaction of clindamycin with hemoglobin. As control experiments, the UV–vis spectra of (1) clindamycin hydrochloride and hemoglobin without incubation (100 μL of 0.01 M clindamycin and 20 μL of 200 μM hemoglobin dissolving in 2 mL 50 mM pH 7.5 phosphate buffer solution, of (2) clindamycin hydrochloride only (100 μL of 0.01 M clindamycin dissolving in 2 mL 50 mM pH 7.5 phosphate buffer solution), and of hemoglobin only (40 μL of 200 μM hemoglobin dissolving in 2 mL 50 mM pH 7.5 phosphate buffer solution) were also recorded.

2.4. Sample treatment

Three batches of drug capsules of clindamycin hydrochloride were purchased from Henan Tianfang Pharmaceutical Co. Ltd. (Henan, China). A number of capsules were dissolved in 50 mL water for 10 min with the help of an ultra-sonic cleaner. The solution was filtered through a 0.22 μm membrane and diluted 1000-fold before injection. The content of clindamycin hydrochloride was detected with standard calibration curve.

Another kind of sample solutions was prepared by adding certain amounts of clindamycin into 1 mL urine of healthy people and alkalinized with 100 μL 0.1 M sodium hydroxide solution. 5 mL ethyl acetate was then added to each sample and the tubes were capped. The samples were vortex mixed for 10 s, and then centrifuged at 3500 $r\,\mathrm{min}^{-1}$ for 15 min, the top organic layer was separated and transferred into a clean set of centrifugation tubes. This procedure was repeated twice. The organic layer obtained at the second time was also transferred into the same tubes and evaporated to dryness under a gentle stream of nitrogen at 40 °C. The residue was reconstituted in 0.5 mL of filtered water and vortex mixed for about 60 s. Finally, the sample solution was injected into the electrophoresis system by electromigration for the content measurement of clindamycin. CE was adopted here to separate some interference in urine which may affect ECL response.

3. Results and discussion

3.1. Enhanced ECL of $Ru(bpy)_3{}^{2+}$ by clindamycin

In Fig. 2, cyclic voltammogram of 5.0 mM $Ru(bpy)_3{}^{2+}$ (curve b) dissolving in 50 mM pH 7.5 phosphate buffer solution on a Pt electrode shows a couple of reversible redox waves with almost equal peak current. It is distinctly different from cyclic voltammogram of the Pt electrode in a blank solution without $Ru(bpy)_3{}^{2+}$ (curve a). Curve (c) represents cyclic voltammogram of the mixture of 5.0 mM $Ru(bpy)_3{}^{2+}$ and 2.5 mM clindamycin in 50 mM pH 7.5 phosphate buffer solution. The anodic current was enhanced while the cathodic one became weak, indicating the participation of clindamycin during electrochemical oxidation of $Ru(bpy)_3{}^{2+}$ as a *coreactant*. According to the earlier reports [14,31,32], the possible mechanism for the enhanced ECL emission might occur in the steps of (i) oxidation of $Ru(bpy)_3{}^{2+}$ into $Ru(bpy)_3{}^{3+}$; (ii) oxidation of clindamycin to generate strong reducing species; (iii) reduction of part of $Ru(bpy)_3{}^{3+}$ with generated strong reducing species to form radicals of $Ru(bpy)_3{}^{2+*}$; (iv) light emission of $Ru(bpy)_3{}^{2+*}$ and returning to the ground state $Ru(bpy)_3{}^{2+}$. Part of $Ru(bpy)_3{}^{3+}$ is reduced into $Ru(bpy)_3{}^{2+}$ on the Pt electrode and this reaction results in cathodic peak current.

3.2. Optimization of experimental conditions

The experimental conditions affected the light intensity of ECL were then studied, including the potential applied at the working electrode, pH value and salt concentration of buffer solutions in detection reservoir, pH value of running buffer solutions, injection time, and injection voltage.

3.2.1. Effect of applied potential

The potential applied to the working electrode is in charge of the reaction rate of ECL reagent, which will decide essentially

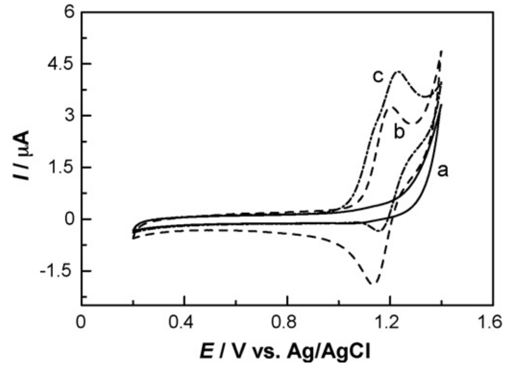

Fig. 2. Cyclic voltammograms on a Pt electrode in solutions of (a) 50 mM pH 7.5 phosphate buffer solution, (b) 5 mM Ru $(bpy)_3{}^{2+}$ in 50 mM pH 7.5 phosphate buffer solution, and (c) 5 mM Ru $(bpy)_3{}^{2+}$ and 2.5 mM clindamycin in 50 mM pH 7.5 phosphate buffer solution at a scan rate of 50 mV s^{-1}.

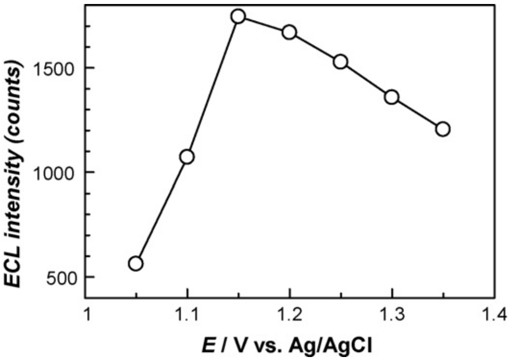

Fig. 3. Variation of ECL intensity with the applied potential on the Pt electrode. Experimental conditions: the concentration of clindamycin, 1.0×10^{-4} M; injection voltage, 10 kV; injection time, 10 s; running buffer solution, 10 mM pH 8.0 phosphate buffer solution; separation voltage, 15 kV; ECL cell, 5.0 mM $Ru(bpy)_3{}^{2+}$ + 50 mM pH 8.0 phosphate buffer solution; photomultiplier tube (PMT) voltage, −800 V.

the intensity of the emitted light [33]. Therefore, the influence of the applied potential on the ECL intensity was studied and the experimental results were shown in Fig. 3 where the applied potential varied over the range from 1.05 to 1.35 V. An increase in the applied potential from 1.05 to 1.15 V resulted in an enhancement in the ECL intensity while further increase in the potential, on the contrary, reduced the ECL intensity. The decrease in ECL intensity at higher potential than 1.20 V possibly results from the passivated effect of the oxidation of water. Hence, in the following experiments the applied potential was fixed at 1.15 V.

3.2.2. Effect of pH and buffer concentration

The ECL reaction of $Ru(bpy)_3{}^{2+}$ with alkylamine has been well-known as a pH-dependent process and the maximum emission has been observed under a slightly basic condition [34]. Fig. 4 shows the variation of ECL intensity with the pH values of buffer in detection reservoir. As expected, the maximum ECL intensity was obtained in a slight basic solution (pH 7.5). The buffer concentration in the detection cell was also found to affect the ECL intensity. The maximum ECL intensity was noticed when the concentration was 50 mM. It has to be noted here that, the running buffer also has great effect on the ECL intensity since the pH-dependant reaction of $Ru(bpy)_3{}^{2+}$ with alkylamine strongly influences electro-osmotic flow (EOF). The maximum ECL value was obtained when the pH value of running buffer was 7.5. Thus, 50 mM phosphate buffer solution with a pH value of 7.5 was used in detection reservoir and also as the running buffer.

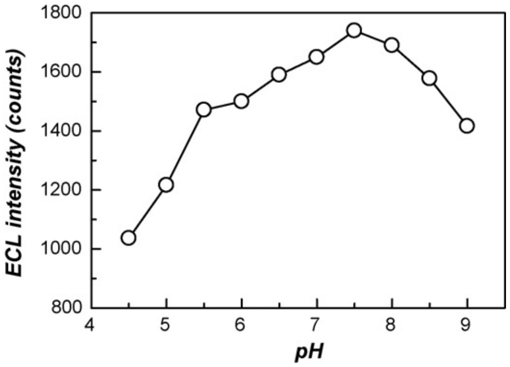

Fig. 4. Effect of pH value of the phosphate buffer solutions in the detection cell on the ECL intensity. Experimental conditions: detection voltage, 1.15 V; other conditions, the same as in Fig. 3.

One point we have to mention here is that the data presented in Fig. 4 might not reveal the true pH dependency of the ECL reaction of clindamycin with $Ru(bpy)_3{}^{2+}$, but shows a combination of the effect of pH and reduction of $Ru(bpy)_3{}^{3+}$ due to degradation at alkaline solutions, because we performed these experiments by dissolving $Ru(bpy)_3{}^{2+}$ and clindamycin in the same buffer solution. It has been proved that the ECL intensity will be enhanced on the occurrence of the de-protonization of the tertiary amine, which requires the pH value of solution is at or above the log(pK_a) of amines. Higher pH values of solutions would be indicated and more hydroxyl ions will be generated in the solutions. On the other side, hydroxyl ion will react with $Ru(bpy)_3{}^{3+}$ ions generated from electrochemical oxidation of $Ru(bpy)_3{}^{2+}$ and produce ECL emission. Although previous studies [35,36] have successfully isolated these effects allowing the true pH dependence to be determined, we paid more attention in this work on the application of the resultant systems for the analytical applications and will carry out these experiments in the near future.

3.2.3. Effect of injection voltage and injection time

Investigation on the influence of the injection voltage on the ECL intensity was also performed and the results were shown in Fig. 5(a), where the injection voltage increased from 4 to 16 kV while the injection time was fixed at 10 s. The number of theoretical plates (N) was also calculated according to the equation:

$$N = 5.54\left(\frac{t_m}{W_{1/2}}\right)^2 \quad (1)$$

where t_m is the migration time and $W_{1/2}$ is the width at half height of the electrophoretic peak. One can see that the ECL intensity increases but N decreases with an increase in the injection voltage. The similar trend is noticed in Fig. 5(b), where an increase in injection time results in an increase in ECL intensity but a reduction in N. It has been known that the ECL intensity is dependent on the concentration of analyte in the diffusion layer on the working electrode surface, where the chemiluminescence reaction occurs. At higher injection voltage and long injection time, more analyte can enter the diffusion layer and higher ECL signal will be produced. However, the dispersion of the analyte may also lead to broaden the peak and to decrease the number of N. Analogous phenomena have been also noticed on other types of detection. For example, even using a UV detector, higher intensities (to a certain point) will be obtained but with wider peaks when the injected amount is increased. In order to gain a higher ECL signal with a larger N, the injection voltage of 10 kV and the injection time of 10 s were chosen in the following experiments.

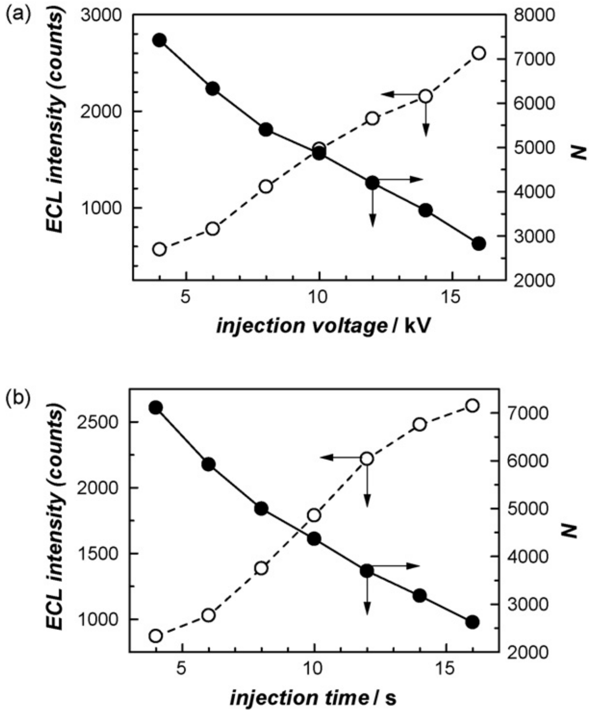

Fig. 5. (a) Effect of injection voltage on the ECL intensity (○) and on the number of theoretical plate (●); (b) effect of injection time on the ECL intensity (○) and on the number of theoretical plate (●). Experimental conditions: detection voltage, 1.15 V; 50 mM pH 7.5 phosphate buffer solution in the detection cell; running buffer, 50 mM pH 7.5 phosphate buffer solution; other conditions, the same as in Fig. 3.

3.3. Calibration curve of clindamycin hydrochloride

Under the optimized experimental conditions (separation capillary, 42 cm length, 25 μm i.d.; sample injection, 10 s at 10 kV; separation voltage: +15 kV; running buffer, 50 mM pH 7.5 phosphate buffer solution; detection voltage, 1.15 V; concentration of $Ru(bpy)_3^{2+}$, 5.0 mM), ECL response for a series of concentrations of clindamycin hydrochloride was detected. The ECL intensity linearly increased with the concentration of clindamycin hydrochloride in the range from 5.0×10^{-7} to 1.0×10^{-4} M. The linear regression equation is $Y = 19.618c + 33.696$ ($R = 0.9992$), where Y is the ECL intensity (counts) and c is the concentration of clindamycin hydrochloride (μM). The detection limit was 1.4×10^{-7} M according to IUPAC regulation. The relative standard deviation (R.S.D.) of the ECL intensity of 1.0×10^{-5} M clindamycin hydrochloride is 1.9% ($n = 6$).

3.4. Separation of clindamycin from other pharmaceuticals

It is well-known that CE–ECL detection system is powerful and effective to separate complex mixture; the separation of clindamycin from other similar pharmaceuticals was then studied. Dextromethorphan and chlorphenamine, which have a tertiary amine group and might affect the detection of clindamycin, were selected to be mixed with clindamycin. The mixture was injected into the capillary under the optimized conditions for the detection of clindamycin. The ECL response as a function of migration time is shown in Fig. 6. Under the optimized conditions, dextromethorphan (peak a), chlorphenamine (peak b), and clindamycin (peak c) were separated clearly. The migration times were 165.2, 169.4, and 192.7 s for dextromethorphan (peak a), chlorphenamine (peak b), and clindamycin (peak c), respectively. The separation factor, which is defined as the ratio of the difference of migration time of clindamycin from the interference to the migration time of clindamycin, was calculated to be 0.14 and 0.12 for dextromethorphan and chlorphenamine, respectively. The separation resolutions, defined as the ratio of the difference of immigration time of clindamycin from that of co-existed species to the half of the summation of the width of their migration peaks, were estimated to be 6.08 and 3.98 for the separation of clindamycin from dextromethorphan and from chlorphenamine, respectively. These results indicate good separation of clindamycin from other pharmaceuticals.

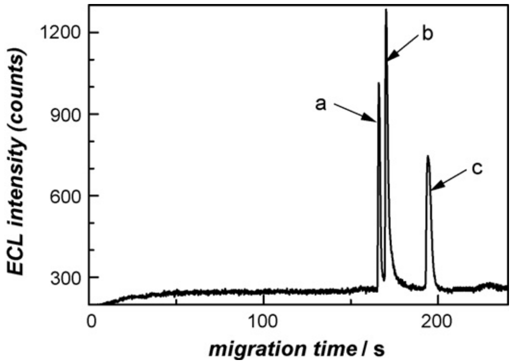

Fig. 6. The electropherogram of three pharmaceuticals: 5 μM dextromethorphan (a), 8 μM chlorphenamine (b) and 35 μM clindamycin (c). Experimental conditions: detection voltage, at 1.15 V; 50 mM pH 7.5 phosphate buffer solution in the detection cell; running buffer, 50 mM pH 7.5 phosphate buffer solution; other conditions, the same as in Fig. 3.

3.5. Determination of clindamycin in samples

The proposed CE–ECL method was applied for the monitoring of clindamycin hydrochloride in pharmaceutical and clinic samples. Table 1 shows the measured results of the content of clindamycin hydrochloride in pharmaceutical samples, which are very close to the labeled value in every batch. The R.S.D. was in the range of 1.9–2.2%. Table 2 shows the recovery efficiencies for known amounts of clindamycin hydrochloride in human urine. The recovery was higher than 95% and the R.S.D. for these measurements was in the range of 2.1–2.7%. These results indicate this CE–ECL is sensitive enough for the measurement of clindamycin in pharmaceuticals and urine samples.

Table 1
Determination of clindamycin hydrochloride in drug capsules

Sample number	Labeled (mg/capsule)	Found (mg/capsule)	R.S.D. (%) ($n = 5$)
050320860	150	143.1	2.0
051120250	150	141.4	2.2
051121180	150	146.5	1.9

Table 2
Analytical results of clindamycin in human urine samples

Samples	Added (M)	Found (M)	Recovery (%)	R.S.D. (%) ($n = 5$)
Urine 1	1.0×10^{-5}	9.5×10^{-6}	95.4	2.3
Urine 2	5.0×10^{-5}	4.8×10^{-5}	96.4	2.1
Urine 3	7.5×10^{-5}	7.3×10^{-5}	96.8	2.7

3.6. Interaction of hemoglobin with clindamycin hydrochloride

According to the procedure in experimental Section 2.4, the interaction of hemoglobin with clindamycin hydrochloride was inspected under the selected experimental conditions by use of UV–vis spectroscopy as well as CE–ECL. Fig. 7 shows UV–vis spectra of clindamycin (curve a), hemoglobin (curve b), the mixture of clindamycin and hemoglobin (curve c), and the solution inside the dialysis bag in 50 mM pH 7.5 phosphate buffer solution after incubation (curve d). There was remarkable difference of curve (d) for the solution inside the dialysis bag after incubation from curve (c) for the mixture of clindamycin and hemoglobin before incubation. The peaks in curve (d) are also different from those in curve (a) for clindamycin and from curve (b) for hemoglobin. These facts confirm the interaction of clindamycin with hemoglobin.

The interaction of clindamycin with hemoglobin was further investigated by CE–ECL detection system. Different volumes of clindamycin solution were mixed with 100 μL of 200 μM hemoglobin solutions in a series of dialysis bags and the dialysis bags were incubated in 2 mL phosphate buffer solution at 37 °C. The ECL intensity of injected clindamycin was measured and defined as I_1. After the equilibrium, the intensity of the outside solution of dialysis bags was detected and defined as I_2, which is owing to unbound clindamycin and can be used to estimate its concentration (c_{unbound}). I_1 was always larger than I_2. This fact confirms the binding of clindamycin with hemoglobin. Moreover, the bound clindamycin concentration (c_{bound}) can be obtained from c_{injected} to c_{unbound}, where c_{injected} stands for the concentration of injected clindamycin. It has to be noted that the relative ECL intensity, defined as the ratio of the ECL intensity from outside solutions after reaching equilibrium to the total ECL intensity once clindamycin was injected, was adopted here to minimize the possible incidental error of the apparatus. Fig. 8 shows the variation of the relative ECL intensity and the bound clindamycin with the injected clindamycin concentration. The binding curve was then fitted to estimate the binding constant and the maximum binding amount of clindamycin hydrochloride with hemoglobin. The binding coefficient, θ, can be evaluated from the binding amount of clindamycin (α_c, mol) and its maximum value ($\alpha_{\max}$, mol) in the form of

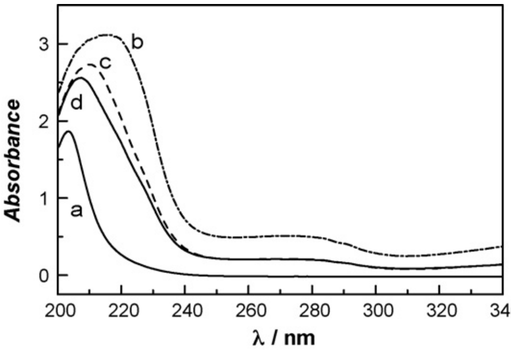

Fig. 7. The UV–vis spectra of (a) 100 μL of 0.01 M clindamycin, (b) 40 μL of 200 μM hemoglobin, (c) 100 μL of 0.01 M clindamycin + 20 μL of 200 μM hemoglobin, and (d) 100 μL of the solution inside the dialysis bag in 2 mL 50 mM pH 7.5 phosphate buffer solution.

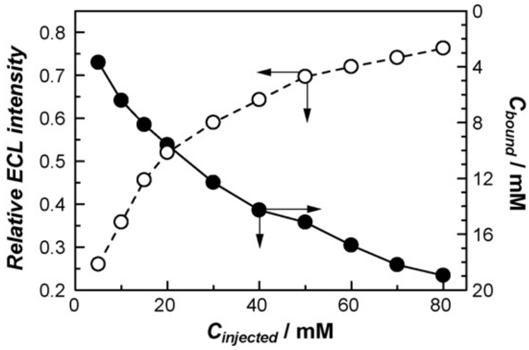

Fig. 8. Variation of the relative ECL intensity outside the dialysis bag (○) and variation of the bound clindamycin concentration (●) with the concentration of injected clindamycin.

$$\theta = \frac{\alpha_c}{\alpha_{\max}} \tag{2}$$

On the other hand, it is known that at the given hemoglobin concentration, Langmuir isotherm equation is efficient for the interaction [37],

$$q = \frac{Kc}{1 + Kc} \tag{3}$$

where K is the binding constant and c is the concentration of clindamycin. Combining of Eqs. (2) and (3) results in:

$$\alpha_c = \frac{Kc\alpha_{\max}}{1 + Kc} \tag{4}$$

The bound clindamycin in Fig. 7 was non-linearly fitted using Eq. (4) as:

$$\alpha_c = \frac{2.40 \times 0.36c}{1 + 0.36c} \tag{5}$$

The maximum binding amount and the binding constant were then estimated to be 2.40×10^{-4} M and 3.6×10^{3} M^{-1}, respectively.

4. Conclusion

Coupled capillary electrophoresis (CE) with end-column electrogenerated chemiluminescence (ECL) was introduced to detect clindamycin successfully. Clindamycin acts as a *coreactant* to enhance tris(2,2′-bypyridine)ruthenium(II) based electrochemiluminescent intensity on a Pt electrode. The interaction of clindamycin with hemoglobin was also confirmed by CE–ECL as well as UV–vis spectroscopy. Further studies related with enhanced ECL intensity and the possibly improved detection limits by larger-sized capillaries are currently undergoing in our lab. The proposed CE–ECL method for the detection of clindamycin is efficient, simple, reproducible, and sensitive. Owing to the coupling of CE with ECL, the great advantage of this method is to have nice selectivity towards clindamycin. This method is potential to be utilized as an official route for the qualitative control of clindamycin hydrochloride in pharmaceutical and clinic samples.

References

[1] J.Z. Xing, J. Lee, S.A. Leadon, M. Weinfeld, X.C. Le, Methods 22 (2000) 157–163.
[2] M. Ye, S. Hu, W.W.C. Quigley, N.J. Dovichi, J. Chromatogr. A 1022 (2004) 201–206.
[3] J.M. Harnly, T.C. O'Haver, Anal. Chem. 53 (1981) 1291–1298.
[4] C. Vogt, J. Vogt, A. Becker, E. Rohde, J. Chromatogr. A 781 (1997) 391–405.
[5] G. Boatto, M. Nieddu, G. Dessì, P. Manconi, R. Cerri, J. Chromatogr. A. 1159 (2007) 198–202.
[6] X. Sun, W. Cao, X. Bai, X. Yang, E. Wang, Anal. Chim. Acta 442 (2001) 121–128.
[7] B. Huang, J. Li, L. Zhang, J. Cheng, Anal. Chem. 68 (1996) 2366–2369.
[8] M. Hashimoto, K. Tsukagoshi, R. Nakajima, K. Kondo, J. Chromatogr. A 832 (1999) 191–202.
[9] K. Tsukagoshi, Y. Okumura, R. Nakajima, J. Chromatogr. A 813 (1998) 402–407.
[10] C. Kuyper, R. Milofsky, Trends Anal Chem. 20 (2001) 232–240.
[11] X. Huang, Z. Fang, Anal. Chim. Acta 414 (2000) 1–14.
[12] Y. Huang, W. Pan, M. Gao, S. Yao, J. Chromatogr. A 1154 (2007) 373–378.
[13] W.-Y. Lee, T.A. Nieman, J. Chromatogr. A 659 (1994) 111–118.
[14] J.B. Noffsinger, N.D. Danielson, Anal. Chem. 59 (1987) 865–868.
[15] N.A. Al-Arfaj, Talanta 62 (2004) 255–263.
[16] X. Sun, J. Liu, W. Cao, X. Yang, E. Wang, Y.S. Fung, Anal. Chim. Acta 470 (2002) 137–145.
[17] J.A. Dickson, M.M. Ferris, R.E. Milofsky, HRC-J. High Res. Chromatogr. 20 (1997) 643–646.
[18] G.A. Forbes, T.A. Nieman, J.V. Sweedler, Anal. Chim. Acta 347 (1997) 289–293.
[19] X. Wang, D.R. Bobbitt, Anal. Chim. Acta 383 (1999) 213–220.
[20] M.-T. Chiang, M.-C. Lu, C.-W. Whang, Electrophoresis 24 (2003) 3033–3039.
[21] G.N. Rechberger, G. Fauler, W. Windischhofer, H. Köfeler, W. Erwa, H.-J. Leis, Rapid Commun. Mass Spectrom. 17 (2003) 135–139.
[22] F.A. El-Yazbi, S.M. Blai, Analyst 118 (1993) 573–576.
[23] G.J. Flaherty, J. Bubp, J. White, M. Borin, J. Gambertoglio, J. Antimicrob. Agents Chemother. 37 (1993) 1137–1143.
[24] L.W. Brown, J. Pharm. Sci. 63 (1974) 1597–1600.
[25] P. Dehouck, A. Van Schepdael, E. Roets, J. Hoogmartens, J. Chromatogr. A 932 (2001) 145–152.
[26] J.A. Orwa, K. Vandenbempt, S. Depuydt, E. Roets, J. Hoogmartens, J. Pharm. Biomed. Anal. 20 (1999) 745–752.
[27] D.J. Platzer, B.A. White, J. Pharm. Biomed. Anal. 41 (2006) 84–88.
[28] G.C. Batzias, G.A. Delis, M. Koutsoviti-Papadopoulou, J. Pharm. Biomed. Anal. 35 (2004) 545–554.
[29] H. Zhou, Z. Zheng, S. Wu, Y. Tai, X. Cao, Y. Pan, J. Pharm. Biomed. Anal. 41 (2006) 1116–1123.
[30] X. Shao, X. Xie, Y. Liu, Z. Song, J. Pharm. Biomed. Anal. 41 (2006) 667–670.
[31] H. Qiu, J. Yan, X. Sun, J. Liu, W. Cao, X. Yang, E. Wang, Anal. Chem. 75 (2003) 5435–5440.
[32] R.D. Gerardi, N.W. Barnett, S.W. Lewis, Anal. Chim. Acta 378 (1999) 1–41.
[33] K.E. Haapakka, J.J. Kankare, Anal. Chim. Acta 138 (1982) 263–275.
[34] S.N. Brune, D.R. Bobbitt, Talanta 38 (1991) 419–424.
[35] Y. Chi, Y. Dong, G. Chen, Electrochem. Commun. 9 (2007) 577–583.
[36] Y. Chi, J. Xie, G. Chen, Talanta 68 (2006) 1544–1549.
[37] X.C. Fu, W.X. Shen, T.Y. Yao, Physical Chemistry, forth ed., High Education Press, Beijing, China, 1989.

Available online at www.sciencedirect.com
ScienceDirect
Talanta 75 (2008) 666–670
Talanta
www.elsevier.com/locate/talanta

Electrochemical surface plasmon resonance detection of enzymatic reaction in bilayer lipid membranes

Jianlong Wang, Fuan Wang, Hongjun Chen, Xiaohua Liu, Shaojun Dong*

State Key Laboratory of Electroanalytical Chemistry, Changchun Institute of Applied Chemistry, Changchun Jilin 130022,
Graduate School of the Chinese Academy of Sciences, Beijing 100039, China

Received 7 September 2007; received in revised form 23 November 2007; accepted 26 November 2007
Available online 14 January 2008

Abstract

In this paper, electrochemical surface plasmon resonance (SPR) method was first used to detect enzymatic reaction in bilayer lipid membrane (BLM) based on immobilizing horseradish peroxidase (HRP) in the BLMs supported by the redox polyaniline (PAn) film. By SPR kinetic curve in situ monitoring the redox transformation of PAn film resulted from the reaction between HRP and PAn, the enzymatic reaction of HRP with H_2O_2 was successfully analyzed by electrochemical SPR spectroscopy. The results show that this BLM supported on PAn film cannot only preserve the bioactivity of HRP immobilized in the membrane, but also provide a channel for the transfer of electrons between HRP and PAn on electrode surface. These characteristics enabled the development of SPR biosensor for sensitively detecting H_2O_2. H_2O_2 has been detected by electrochemical SPR spectroscopy in the concentration range of 5×10^{-5} M to 2×10^{-3} M. After each of detections, the SPR sensor surface was completely regenerated by electrochemically reducing the oxidized PAn to its reduced state. This method provides a novel route for enhancing the detection of small ligand of enzymatic reaction in BLM by electrochemical SPR spectroscopy.

Keywords: Electrochemical surface plasmon resonance; LBM; Enzymatic reaction

1. Introduction

Optical surface plasmon resonance spectroscopy is a powerful tool for in situ real-time characterization of solid/liquid interfaces [1]. This technology has been widely used for the study of interactions of biological molecules because of its characters as a rapid, label-free, high selective and high sensitive assay method [2–7]. However, these researches mainly focus on studying the binding process between the large biomolecules, the reaction process between the large biomolecules and their small ligands are seldom detected by SPR spectroscopy, because the changes in the refractive index resulted from the binding of small ligand are very small. Some methods have been used to improve the sensitivity of SPR for detecting the reaction of these small ligands or other small molecules. The first method employed polymers with high molecular weights as a transduction layer to increase the changes in the refractive index at the sensing interface triggered by small molecules [8]. The second method utilized the optoelectronic response of inorganic material to enhance SPR signal for detection of small biomolecules [9,10]. The third method reported in literature utilized the conformational change of macromolecules or proteins switched by small molecules to amplify the change of SPR signal [11,12]. The fourth method was the use of a high molecular weight ligand that competing with the small molecular weight analyte for receptor binding [13]. Here, we propose a novel way by utilizing electrochemical SPR spectroscopy [14] to detect an enzymatic reaction in BLM.

As well known, HRP is able to oxidize PAn film without requiring the intervention of any additional mediator species [15]. This enabled the development of electrochemical biosensor for detecting H_2O_2. A serious problem in the application of this system is how to immobilize enzyme on the surface of electrode with high stability and enzymatic activity. It has been confirmed that modification of electrode by lipid can substantially preserve the bioactivity of enzyme and improve the sensitivity and stability of a biosensor because of the characteristic of BLMs [16]. The heme proteins have been embedded in

---

* Corresponding author. Tel.: +86 431 85262101; fax: +86 431 85689711.
E-mail address: dongsj@ns.ciac.jl.cn (S. Dong).

0039-9140/$ – see front matter © 2007 Elsevier B.V. All rights reserved.
doi:10.1016/j.talanta.2007.11.062

BLMs and the corresponded biosensors have been constructed [17]. However, these biosensors were mainly characterized by electrochemistry, electrochemical SPR spectroscopy has never been used to detect the capability of these biosensors constructed by embedding enzyme in BLMs for the binding of small ligands with the enzyme. Herein, we prepared a BLM containing HRP on a SPR gold substrate modified by PAn film, and investigated the preparation process of this composite film by SPR spectroscopy. Furthermore, we evaluated the enzymatic reaction between HRP and H_2O_2 by electrochemical SPR spectroscopy.

2. Experimental

2.1. Reagents

Aniline (Beijing Chemical, 99.7%) was used after distillation, citric acid (99.5%) and H_2O_2 (30%) (Beijing Chemical) were used without further purification. Horseradish peroxidase (HRP) was purchased from Beijing Dingguo Biotechnology Development Center. 1,2-Distearoyl-sn-glycerol-3-phosphoglycerol, sodium salt (DSPG) was obtained from sigma and was used as received. Stock solutions of H_2O_2 with different concentrations were freshly prepared each day. All solutions were made with deionized water, which was purified with a Milli-Q system (Millipore).

2.2. Preparation of the enzyme membranes

PAn film was deposited by cycling the potential between −0.2 and 0.9 V with a scan rate of 0.02 V/s in 0.05 M aniline of 0.1 M H_2SO_4 solution. After a cyclic potential was performed, another cyclic scan was followed and the anodic limit was adjusted to 0.8 V to lower the production of unwanted byproducts. The thickness of PAn film measured was 10.5 nm. Vesicles doped with HRP were prepared by dissolving HRP into the 0.50 mg/ml DSPG vesicle solution with a final concentration of 2 mg/ml. The dispersion obtained was coated over the PAn film in a Teflon cuvette at room temperature for 2 h. Finally, the resulted enzyme membrane was washed with acetate buffer solution of pH 5.4, and stored in the buffer solution.

2.3. In situ SPR electrochemical measurements

SPR measurements were performed with a home-built electrochemical SPR system [18]. The SPR-active substrates were prepared by sputtering of gold (∼42.7 nm) to the surface of glass slide that was modified with an underlayer of chromium (∼1.5 nm). For further experiments, SPR-active gold film cleaned through piranha solution was pressed onto the base of a half-cylindrical lens via index matching oil. The gold surface of the glass slide mounted against the Teflon cell with use of a Kalrez O-ring was used as SPR sensor surface and also a working electrode (the apparent electrode area was 0.38 cm^2). The Teflon cell allowed for simultaneous recording of SPR and electrochemical data and applying of a voltage to the sample.

2.4. Electrochemical experiments

Electrochemical experiments were carried out with a CHI800 electrochemical system in a Teflon cell. The Teflon cell was provided with a saturated Ag/AgCl reference electrode and a platinum counter electrode. Electrochemical measurements were all recorded and reported vs. the KCl-saturated Ag/AgCl reference electrode. All experiments were done at room temperature. Buffers were purged with highly purified nitrogen for at least 20 min prior to a series of experiments.

3. Results and discussion

3.1. Electrochemical SPR spectroscopy characterization of the enzyme membrane preparation

In our previous work, we have confirmed that conducting polymer film can be served as a strong support for s-BLM [19]. Here, we further utilized electrochemical SPR spectroscopy to detect enzymatic reaction in BLM based on electron communication between the enzyme immobilized in BLM and PAn. The configuration of enzyme membrane and the reaction mechanism of this enzymatic reaction were shown in Fig. 1. In detail, PAn film was firstly electrodeposited on the surface of SPR gold film. And then, the DSPG bilayer lipid membrane containing HRP was formed on the surface of PAn film by vesicles fusion.

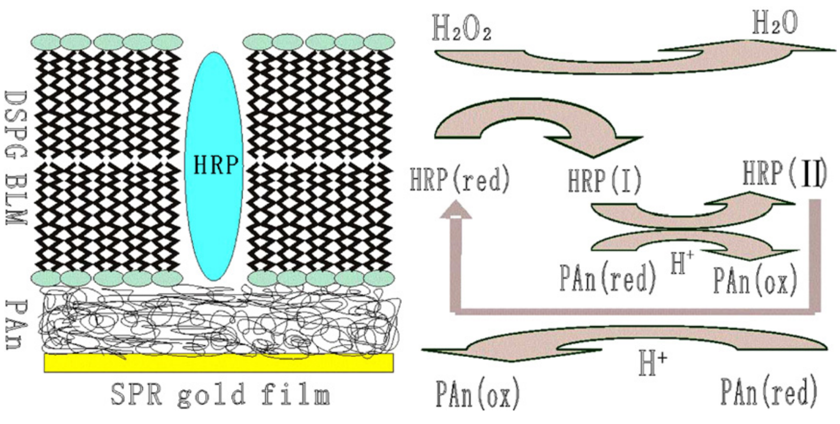

Fig. 1. The configuration and the reaction mechanism of this biosensor for detecting surface enzymatic reaction.

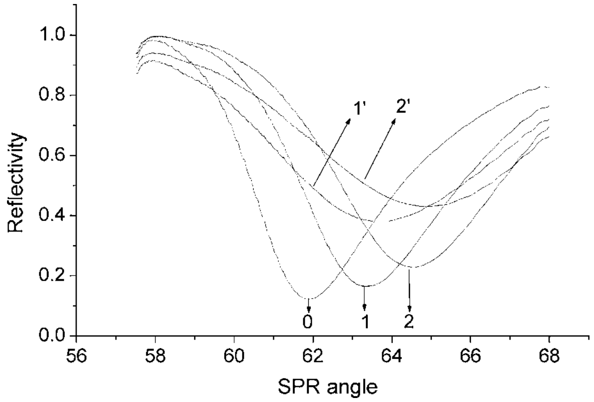

Fig. 2. SPR reflectivity and minimum reflectivity angle curves in situ recorded after various surface modification steps. (0) The bare SPR gold film. (1) The *R*–*θ* curve of the PAn film at reduced state. (1′) The *R*–*θ* curve of the PAn film at oxidized state. (2) The changes of SPR *R*–*θ* curve after BLM containing HRP were deposited on the surface of PAn film (at reduced state). (2′) The changes of SPR *R*–*θ* curve after BLM containing HRP were deposited on the surface of PAn film (at oxidated state).

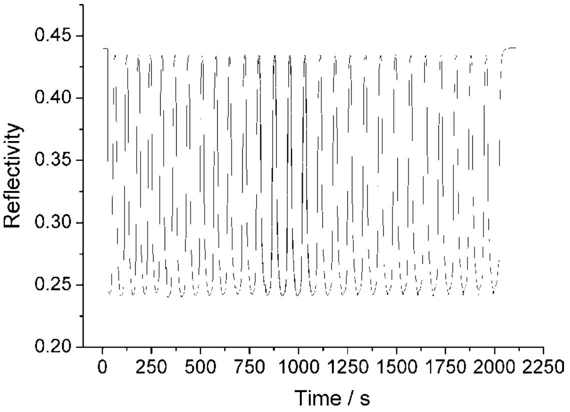

Fig. 3. The change of SPR kinetic curve during continuously electrochemically scanning in pH 5.0 acetate buffer. The angle of incidence was fixed at 65°.

The preparation process of the enzyme membrane was in situ monitored by SPR *R*–*θ* curves. As shown in Fig. 2, the *R*–*θ* curve of bare Au was recorded as curve 0. The minimum of the *R*–*θ* curve shifts to higher angle after PAn film was electrodeposited on SPR gold film. The *R*–*θ* curves of the PAn film before and after electrochemical oxidation were recorded as curve 1 and curve 1′, respectively. Compared curve 1 and curve 1′, the SPR *R*–*θ* curve for the oxidized PAn film shows a slight shift to higher angle relative to that of the reduced PAn film, but a very distinct change occurs in the resonance depth of SPR curve. This change should be ascribed to the change of PAn film in the optical property resulting from the conductivity change of the PAn film. Many works had discussed the conductivity change of PAn film with potential in a buffer solution of pH 5, and demonstrated that there exists a fast and reversible transition in the conductivity around +0.28 V corresponding to a redox transition between a conducting state, emeraldine, and an insulating state, pernigraniline [20]. Curve 2 shows the change of SPR *R*–*θ* curve after BLM containing HRP was deposited on the surface of PAn. The SPR angle increased about 0.88° obtained by the Software fitting. In order to confirm the formation of BLM, we further simulated the thickness of BLM by nonlinear least-squares method. At a wavelength of 670 nm, the refractive index values used for the SPR modeling calculations are 1.61 and 1.3301 for BaK4 lens and water, respectively. The real part of the refractive index used for bulk gold film is 0.1288, and the imaginary part of the refractive index is 3.8627. The thickness of bulk gold film is estimated as 42.7 nm. The optical constants PAn film is known as 1.51 [21] and its thickness is estimated as 10.5 nm. The refractive index of the lipid is about 1.45 [22]. Based on these parameters, the thickness of BLM is estimated as 9.5 nm. This value is larger than the predicted thickness for a planar bilayer (roughly 5 nm thick). The main reason is originated from the mixed morphology of the lipid structure deposited on the surface of PAn film. According to the results reported by Cheng et al. [23], the composite structure consisting of a bilayer, vesicle fragments, and lipid junctions can be formed on some patterned pocket or substrate. The thickness of BLM possessing this structure is larger than a general BLM, and this BLM is not highly insulating. We also observed this character in our experimental results by electrochemical SPR spectroscopy through analyzing the redox change of PAn film before and after BLM deposited. Curve 2 and curve 2′ are the SPR *R*–*θ* curve for the reduced and oxidated PAn after BLM containing HRP was deposited. In general, the formation of close packed BLM would strongly block the transfer of electrons and protons between the substrate electrode and solution. So the number of protons needed under the redox change of PAn film would be limited by the ion transfer ability of BLM deposited on the surface of PAn film. Thus, the change of SPR reflectivity minimum between the reduced and oxidized PAn film would disappear if a close packed BLM was formed. However, we can see an obvious change of SPR reflectivity minimum in curve 2 and curve 2′. This change is slightly smaller than that of the value at simple PAn film shown in curve 1 and curve 1′. This minor change in the resonance depth maybe results by an increase in the extinction coefficient *k*, a measure for the absorptivity of a medium. Since the BLM are non-absorbing at 670 nm, we attribute the apparent increase in *k* to scattering effects [22]. This is likely caused by the insertion of HRP into the membrane. These results confirmed that this composite film is not highly insulating. This low-insulating character can be also observed from the SPR kinetic curves during the modulation process between the state of the reduced and oxidized PAn film. Fig. 3 is the change of SPR kinetic curve during continuously electrochemically scanning in acetate buffer of pH 5.0. We can see that the reflectivity is changed from 0.24 to 0.44 with the potential scanning from 0 to 0.34 V. It shows that the proton communion between PAn film and solution is produced during the process of potential scanning. We can also find amplitude of potential-modulated reflectivity minimum does not change during the process of scanning. It means this mixed membrane supported on PAn film surface is rather stable, and the SPR sensor surface was completely regenerated by electrochemically reducing the oxidized PAn to its reduced state.

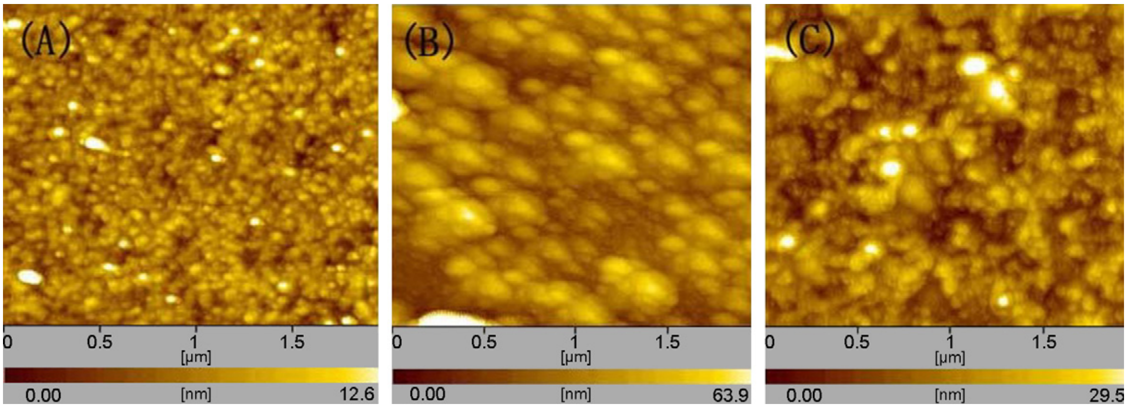

Fig. 4. Typical AFM images of the bare gold (A), the electropolymerized PAn layer (B) and PAn supported BLM containing HRP (C).

3.2. AFM characterization of the enzyme membrane morphology

Except for SPR method, AFM was also used to character the formation process of this enzyme membrane. As convinced by AFM, the gold surface seemed to be smooth with a low RMS roughness (about 1.179 nm) in Fig. 4A. The RMS roughness was increased to 10.08 nm as PAn film with a globular morphology was formed on the surface of gold substrate (Fig. 4B). The increase of rms roughness mainly comes from the uneven growing of PAn film. On the other hand, the self-assembly of DSPG induced a smoother topography than that of the PAn film with rms roughness decreasing from 10.08 to 5.213 nm (Fig. 4C), showing the deposition of BLM onto the PAn surface across the PAn film.

3.3. Electrochemical SPR detection of enzymatic reaction between HRP and H_2O_2

Previous works demonstrated that HRP could reconstitute into lipid bilayer and showed its expected bioactivity for electrocatalyzing H_2O_2. However, this process is difficult to be detected by SPR spectroscopy because the refractive index change in the reaction process between HRP and H_2O_2 is quite small. Therefore, in our case, PAn film is used as underlying substrate for supporting BLM. If HRP is reconstituted into the BLM and contacts with PAn film, the enzymatic reaction of HRP with H_2O_2 should be observed by detecting the redox transformation of PAn film resulting in the electron exchange between HRP and PAn [15]. SPR kinetics curve is used to investigate the catalytic responses of this enzyme substrate to H_2O_2 in solution. In order to confirm the change of SPR response is resulted from the enzymatic reaction between HRP and PAn in the presence of H_2O_2, the comparison experiments containing the reactions of PAn film with H_2O_2 and PAn film supported BLM with H_2O_2 were carried out, respectively. The angle shifts in R–θ curves were not observed in these two experimental conditions (the curves were not shown). Fig. 5 depicts the SPR kinetics curves at different H_2O_2 concentrations. In the presence of H_2O_2, the reflectivity remains unchanged because no redox transformation of PAn film occurred. After adding H_2O_2, the reflectivity would change with the concentrations of H_2O_2. When a lower concentration of H_2O_2 is used, a smaller slope of SPR kinetics curve is obtained, and it means a smaller transformation rate. From Fig. 5, we also observe the response time of the enzymatic reaction for H_2O_2. It should be pointed out that the response time (∼350 s) in present system is slower than the results reported by Iwasaki et al. (∼100 s). This is because the number of protons needed by the redox change of PAn film is limited by the ion transfer ability of BLM deposited on the surface of PAn film. Although this BLM is none highly insulating, it produce a block effect for proton transfer between PAn and solution. That is why the response time of the SPR biosensor is longer than the other SPR biosensors. From another point of view, this longer response time is in favor of extracting the accurate slope of SPR kinetic curves. A good linear relation between H_2O_2 concentrations and the slope of SPR kinetic curves is obtained. As shown in the inset of Fig. 5, H_2O_2 was successfully detected in the concentration range of 5×10^{-5} M to 2×10^{-3} M. After each of detections, the SPR sensor surface was completely regenerated by electrochemically reducing the oxidized PAn to its reduced state. These results demonstrate that SPR technology combined with electrochemical method is a good technique to investigate enzymatic reaction.

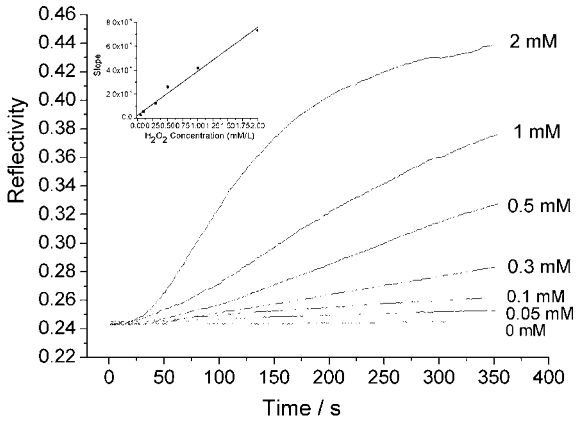

Fig. 5. SPR kinetics curves at various concentration of H_2O_2. The angle of incidence was fixed at 65°. Inset: calibration plot of H_2O_2 concentration with the slope of SPR kinetics curves.

4. Conclusions

We described in this paper an effective method for detecting enzymatic reaction of enzyme with small molecules by electrochemical SPR spectroscopy. This method utilizes the optoelectronic switch of redox polyaniline to amplify the SPR signal. Particularly, we have analyzed the catalytic reaction between H_2O_2 and HRP immobilized in BLM and successfully detected the concentration of H_2O_2 by SPR. These results show the BLM supported by PAn film is a proper substrate for detection of enzymatic reaction by electrochemical SPR method. Furthermore, this electrochemical SPR method provides a potential application for detecting proton transition in BLMs.

Acknowledgements

This work was supported by special funds for major state basic research of China (No. 2002CB713803) and the National Nature Science Foundation of China (No. 20427003).

References

[1] X.F. Kang, Y.D. Jin, G.J. Cheng, S.J. Dong, Langmuir 18 (2002) 1713.
[2] F. Deckert, F. Legay, Anal. Biochem. 274 (1999) 81.
[3] D.R. Shankaran, K.V.A. Gobi, N. Miura, Sens. Actuators: B 121 (2007) 158.
[4] S. Vutukuru, S.R. Bethi, R.S. Kane, Langmuir 22 (2006) 10152.
[5] Y. Dong, K.S. Phillips, Q. Cheng, Lab on a Chip 6 (2006) 675.
[6] A. Brecht, P. Gauglitz, Anal. Chim. Acta 347 (1997) 219.
[7] R. Georgiadis, K.P. Peterling, A.W. Peterson, J. Am. Chem. Soc. 122 (2000) 3166.
[8] Y. Iwasaki, T. Horiuchi, O. Niwa, Anal. Chem. 73 (2001) 1595.
[9] M. Zayats, S.P. Pogorelova, A.B. Kharitonov, O. Lioubashevski, E. Katz, I. Willner, Chem. Euro. J. 9 (2003) 6108.
[10] O.A. Raitman, E. Katz, I. Willner, V.I. Chegel, G.V. Popova, Angew. Chem. Int. Ed. 40 (2001) 3649.
[11] H. Sota, Y. Hasegawa, Anal. Chem. 70 (1998) 2019.
[12] J.E. Gestwicki, H.V. Hsieh, J.B. Pitner, Anal. Chem. 73 (2001) 5732.
[13] D.R. Shankaran, K.V. Gobi, T. Sakai, K. Matsumoto, K. Toko, N. Miura, Biosens. Bioelectron. 20 (2005) 1750.
[14] S. Koide, Y. Iwasaki, T. Horiuchi, O. Niwa, E. Tamiya, K. Yokoyama, Chem. Commun. 9 (2000) 741.
[15] P.N. Bartlett, P.R. Birkin, J.H. Wang, Anal. Chem. 70 (1998) 3685.
[16] P.T. Kissinger, J.B. Hart, R.N. Adams, Brain Res. 55 (1973) 209.
[17] J. Szebeni, E.E. Di Iorio, H. Hauser, K.H. Winterhalter, Biochemistry 24 (1985) 2827.
[18] J.L. Wang, F.A. Wang, X.Q. Zou, Z.A. Xu, S.J. Dong, Electrochem. Commun. 9 (2007) 343.
[19] Y. Shao, Y.D. Jin, J.L. Wang, L. Wang, F. Zhao, S.J. Dong, Biosens. Bioelectron. 20 (2005) 1373.
[20] V. Chegel, O. Raitman, E. Katz, R. Gabai, I. Willner, Chem. Commun. 10 (2001) 883.
[21] X.F. Kang, G.J. Cheng, S.J. Dong, Electrochem. Commun. 3 (2001) 489.
[22] T. Wilkop, D.K. Xu, Q. Cheng, Langmuir 23 (2007) 1403.
[23] Z.Z. Wang, T. Wilkop, Q. Cheng, Langmuir 21 (2005) 10292.

Available online at www.sciencedirect.com
ScienceDirect

Talanta 75 (2008) 636–641

Talanta

www.elsevier.com/locate/talanta

Review

In vivo glucose monitoring: Towards ‘Sense and Act’ feedback-loop individualized medical systems

Joseph Wang*

Biodesign Institute, Departments of Chemical Engineering and Chemistry and Biochemistry, Arizona State University, Tempe, AZ 85287-5001, USA

Received 13 February 2007; accepted 11 October 2007
Available online 22 October 2007

Abstract

Glucose biosensors are key components of closed-loop glycaemic control (insulin delivery) systems for effective management of diabetes. By providing a fast return of the analytical information in a timely fashion, such sensors offer direct and reliable assessment of rapid changes in the glucose level, as desired for making optimal and timely therapeutic interventions in cases of hypo- and hyperglycemia. The majority of sensors used for continuous glucose monitoring are amperometric enzyme electrodes. The successful realization of closed-loop glycaemic control requires innovative approaches for addressing major challenges of biofouling, inflammatory response, calibration, stability, selectivity, power, miniaturization, common to other remote sensor systems. The goal of this review article is to demonstrate how these challenges are being addressed towards achieving reliable continuous subcutaneous monitoring of glucose. While the concept is presented here in connection to the management of diabetes, such loop-based individualized integrated (sensing/release) medical systems should lead to a fine-tune drug therapy and should have an enormous impact upon the treatment and management of different diseases.

Keywords: Glucose; Enzyme electrodes; Closed-loop system; Diabetes; Drug delivery; Remote sensing

Contents

1. Introduction

Diabetes affects about 200 million people worldwide. The growing global demands for managing diabetes make glucose the most commonly tested analyte in clinical diagnostics. Tight glucose monitoring is an essential component of modern diabetes management. Commonly used blood-glucose fingerstick self-testing is limited by the number of tests per day it permits, hence resulting in a poor approximation of blood glucose variations. Continuous monitoring is thus highly desired for detecting sharp changes in the glucose level and triggering proper corrective action in cases of hypo- and hyperglycemia [1,2]. By providing a fast return of the analytical information in a timely fashion, such monitoring capability offers direct and reliable assessment of the trends and patterns of the blood glucose level.

---

* Tel.: +1 480 727 0399; fax: +1 480 727 0412.
E-mail address: joseph.wang@asu.edu.

0039-9140/$ – see front matter © 2007 Elsevier B.V. All rights reserved.
doi:10.1016/j.talanta.2007.10.023

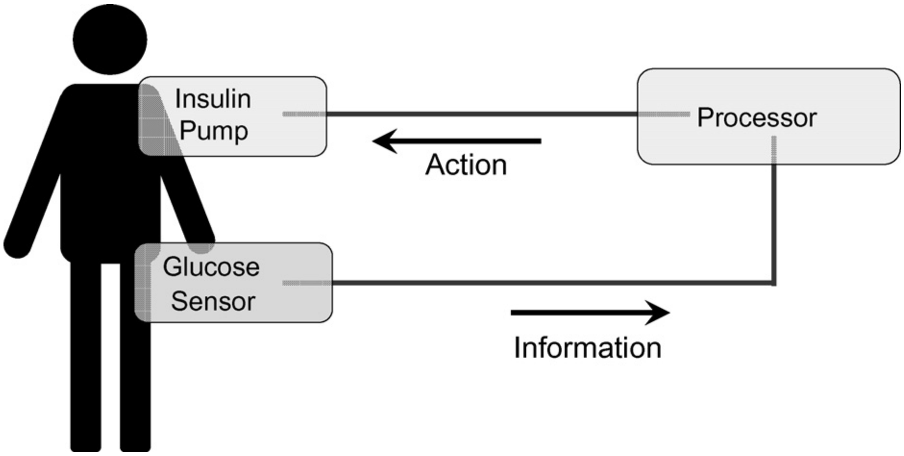

Fig. 1. Key components of closed-loop diabetes management system using the ‘Sense and Act’ approach for optimal insulin delivery. The sensor relays the analytical information to the insulin pump, and a computer algorithm controls the amount of insulin delivered.

Modern closed-loop glycaemic control systems, currently being developed by various organizations across the globe, integrate the glucose-sensing element with an insulin-delivery feedback loop (along with a data processing and energy source) for optimal dose of insulin (Fig. 1). Such integrated diabetes management systems rely on the ‘Sense and Act’ feedback-loop approach to enable appropriate corrective action via optimal and timely dosing. The sensor thus relays the information to the pump that dispenses the right amount of insulin. The information will also be transmitted by telemetry to a remote desktop at the user’s physician office. This sense/release glycaemic control system represents the first example of an individualized drug administration system for optimal therapeutic intervention [3,4]. Such response to distinct changes in the body chemistry of each person offers unique opportunity to deliver personalized medical care. The development of such responsive drug-delivering systems is expected to dramatically change patient monitoring, in general, and diabetes management, in particular. One can envisage a time when the release of different potent drugs could be controlled by a microprocessor, in response to information fed back from a biosensor, though there are many technological challenges to be overcome before this attractive therapeutic route becomes a reality.

Glucose biosensors are key components of closed-loop glycaemic control systems, essential for optimal frequency and dose of insulin. Minimally invasive amperometric enzyme electrodes offer the greatest promise for tight management of diabetes. Similar to other remote sensor systems (discussed in this special issue), implantable in vivo biosensors can be regarded as remote sensors as they cannot be directly accessed, and must operate reliably and continuously under harsh conditions. In vivo glucose biosensors thus share similar issues and challenges as other remote sensors, including long-term stability, inflammatory (biofouling) processes, calibration, selectivity, oxygen dependence, miniaturization, communication, and power requirements. While conventional electrochemical measurements of glucose in the laboratory environment rely on short electrode-sample exposure times, along with convenient quantitation (via standard additions), and replacement of the electrode (in connection to a benchtop analyzer), continuous in vivo sensing must overcome major technical difficulties (associated with the continuous exposure to the biological fluid) and rely on miniaturized instrumentation and implantable power.

The goal of this article is to demonstrate how these challenges can be addressed towards reliable continuous monitoring of glucose. It is not a comprehensive review on in vivo glucose biosensors, but rather an article discussing solutions to the key obstacles for such continuous subcutaneous monitoring and towards effective closed-loop glycaemic control. While the discussion is focused on subcutaneously implantable in vivo glucose sensors, it has broad implications to a wide range of enzyme electrodes for continuous in vivo monitoring and upon the management of other diseases in connection to responsive drug delivery systems.

1.1. Subcutaneous glucose monitoring

A wide range of possible in vivo glucose biosensors has been designed as important tools in maintaining glucose levels close to normal. The majority of these glucose sensors are amperometric enzyme electrodes based on the glucose-oxidase (GOx)-catalyzed oxidation of glucose by oxygen [2,5]:

$$\text{glucose} + \mathrm{O_2} \xrightarrow{\text{glusoce oxidase}} \text{gluconic acid} + \mathrm{H_2O_2} \qquad (1)$$

and upon amperometric (anodic) detection of the hydrogen peroxide product:

$$\mathrm{H_2O_2} \xrightarrow{\text{electrode}} \mathrm{O_2} + 2\mathrm{H^+} + 2e^- \qquad (2)$$

Most in vivo devices rely on such mediatorless-based detection of hydrogen peroxide due to potential leaching and toxicity of the mediator. The first application of such devices for in vivo glucose monitoring was demonstrated by Shichiri et al. in 1982 [6]. Shichiri’s needle biosensor relied on a platinum anode held at +0.6 V (vs. a silver cathode), which was used to monitor the enzymatically produced hydrogen peroxide. The enzyme (GOx) entrapment was accomplished in connection with a cellulose-diacetate/heparin/polyurethane coating. However, due to major challenges (particularly biocompatibility, discussed below) most recent activity towards continuous glucose monitoring has shifted to the development of subcutaneously implantable needle-type electrodes [1,2]. The subcutaneous tissue is minimally invasive and its glucose level has been shown to correlate with the blood glucose concentration. Such implantable devices track blood glucose levels by measuring the glucose concentration in the interstitial fluid of the subcutaneous tissue (assuming the ratio of the blood/tissue levels is constant). Subcutaneously implantable biosensors rely on insertion of a short needle into the skin (in the abdomen or upper arm), yield a reading every 1–2 min, and provide an alarm when glucose levels become too low or too high. The implanted device, designed to function for about 3–5 days between replacements, is small enough to be painlessly replaced by the user. Success in this direction has reached the level of short-term human implantation [7–9]; continuously functioning devices, possessing adequate (>1 week) stability, are expected in the near future. Such devices would enable a swift and appropriate corrective action (through a closed-loop insulin delivery system), in connection to advanced computer algorithms. Such algorithms correct also for the transient discrepancies (short time lag) between blood and tissue glucose concentrations when the blood glucose concentration rapidly increases rapidly or decreases.

1.2. *What are the requirements and limitations?*

The major requirements of clinically accurate in vivo glucose sensors have been discussed in several review articles [2,10]. The ideal sensor would be one that provides a reliable real-time continuous monitoring of glucose with high selectivity, speed, and stability. The major challenges for meeting these demands include of rejection of the sensor by the body, miniaturization, long-term stability of the enzyme, and transducer, oxygen deficit, in vivo calibration, short stabilization times, baseline drift, safety, power, and convenience. Potential errors in the measured glucose concentration (due to biofouling and oxygen or electroactive interferences) can have an adverse effect upon the right therapeutic intervention (i.e. optimal insulin dose).

The sensor must be of a shape and small size that allows convenient implantation and results in minimal discomfort. Sensors with outer diameter smaller than 450 μm (i.e., needles smaller than 26-gauge) are essential to meet these demands. Such miniaturization of in vivo sensors is not trivial. The fabrication of subcutaneously implanted needle-type sensors commonly involve controlled deposition of an inner permselective coating, followed by the enzyme layer, and an outer layer that renders a biocompatible interface and mass transport control (Fig. 2). Such placement of the sensor on the needle shaft (rather than at the tip) facilitates the membrane coating.

1.2.1. *Inflammatory and biofouling processes*

Implanted glucose sensors are subject to undesirable interactions between the sensor surface and biological medium that cause deterioration of the sensor performance, and proved to be the major barriers to the development of reliable implantable devices. These adverse effects include both the material (sensor) and host (tissue) response. The inflammatory 'foreign-body' response is characterized with problems such as bacterial adhesion and scar tissue formation. Such build-up of tissue around the sensor, as a result of its implantation, affects diffusion to the sensor and changes the glucose concentration in the immediate vicinity of the sensor. Prolonged operations in complex biological fluids are complicated also by surface fouling by co-existing macrobiomolecules (e.g., serum albumin) that suppresses the glucose response.

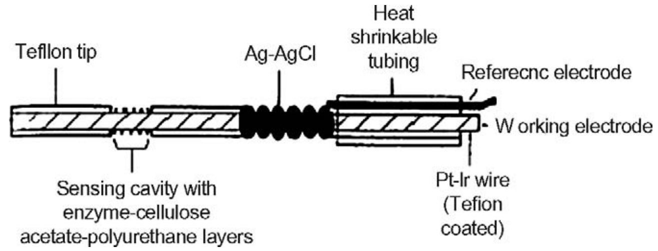

Fig. 2. Schematic diagram of a subcutaneously implanted needle-type sensor: (a) Teflon-coated Pt–Ir wire; (b) Teflon tip; (c) sensing cavity; (d) Ag/AgCl reference electrode; (e) heat-shrinkable tubing; (f) reference electrode terminal; (g) working electrode terminal (from Ref. [11], with permission).

Recent avenues for improving the biocompatibility of in vivo glucose sensors focused on designing interfaces that resist biofouling [2,12]. These include a controlled release of nitric oxide (NO) [12–14], use of outer coatings (such as polyethyleneglycols or Nafion) that exhibit low protein adsorption [15,16], or co-immobilization of the anticoagulant heparin [17]. The former is attributed to the discovery that NO is an effective inhibitor of platelet and bacterial adhesion. Despite of these developments, most glucose biosensors still lack the biocompatibility necessary for reliable prolonged operation in whole blood, and hence rely on alternative sensing sites, particularly the subcutaneous tissue.

1.2.2. *Selectivity*

The amperometric measurement of the hydrogen-peroxide product of the GOx reaction (Eq. (2)) requires application of a potential at which co-existing reducing species, such as ascorbic, and uric acids and some drugs (e.g., acetaminophen), are also electroactive. The anodic contributions of these and other oxidizable endogenous constituents can compromise the selectivity and hence the overall accuracy of measurement (and the optimal insulin delivery). Considerable efforts have thus been devoted to minimizing the interference of co-existing electroactive compounds.

One useful strategy for minimizing electroactive interferences is to use a permselective coating that minimizes the access of these constituents towards the transducer surface. Different polymers, multi-layers and mixed layers, with transport properties based on charge, size or polarity, have been particularly useful for excluding co-existing electroactive compounds [16,18–20]. Such films exclude also surface-active macromolecules, hence protect the surface and impart higher stability. Electropolymerized films, particularly poly(phenelendiamine) and overoxidized polypyrrole, have been shown to be very effective for imparting high selectivity (based on size exclusion) while confining GOx onto the surface [18,19].

1.2.3. Calibration

A critical issue in continuous glucose sensing, and all in vivo biosensors, is the calibration of the system. This is particularly crucial when the data form the basis for triggering a rapid therapeutic intervention. The challenge of calibrating in vivo glucose biosensors is not a trivial process and involves transformation of the time-dependent current signal $i(t)$ into an estimation of glucose concentration at time t, $C_G(t)$. This can be accomplished through one- or two-point calibration procedures [20,21]. A "one-point" in vivo calibration can be used for highly selective sensors, having a zero output current at zero glucose concentration [20]. In the one-point calibration procedure, the sensor sensitivity S is determined from a single blood glucose determination as the ratio between the current signal i and the blood glucose concentration C_G. Subsequently, the glucose concentration can be estimated at any time from the current i as $C_G(t) = i(t)/S$. Such one-point calibration protocol has been shown useful even when glucose concentration changes rapidly. However, if the intercept i_0 is not negligible, a two-point calibration procedure is essential [21]. The two-point calibration involves estimate of two parameters: the sensor sensitivity S, expressed in nA/(mg/dl), and the intercept i_0, corresponding to the sensor output (current, expressed in nA) axis, observed in the absence of glucose. Addition of another (non-enzyme) electrode was also suggested for estimated the exact background current i_0 [22].

1.2.4. Oxygen dependence

Another key issue in the practical utility of GOx-based in vivo enzyme electrodes is the dependence of the response upon the level of the oxygen cofactor. Such oxygen demand can lead to major errors due to fluctuations in oxygen tension and the stoichiometric limitation of oxygen (Eq. (1)). These errors result in fluctuations in sensor response and a reduced upper limit of linearity. This limitation, known as the "oxygen deficit", reflects the fact that normal oxygen concentrations are about one order of magnitude lower than the physiological level of glucose.

Several avenues have been proposed for addressing this oxygen limitation. These include proper coverage that improves the availability of oxygen to the enzyme region (relative to glucose) [23,24], or designing oxygen-rich biocomposite electrode materials [25].

In particular, Gough's group [23] developed a two-dimensional sensor design, with an outside silicone rubber, which is impermeable to glucose but highly permeable to oxygen. This provides a two-dimensional oxygen supply the enzyme region (both radial and axial) but only one dimensional supply of glucose. Zhang and Wilson [24] designed a membrane coverage that improves the relative surface availability of oxygen by presenting a diffusion barrier to the substrate.

The second route for minimizing the oxygen limitation relies on oxygen-rich electrodes to provide an internal supply of oxygen. Carbon-paste enzyme electrodes based on oxygen-rich fluorocarbon-oil pasting liquids have been particularly useful for this task [25]. Such oxygen-rich biocomposites act as an internal source of oxygen and can support the enzymatic reaction under severe oxygen-deficit conditions, including oxygen-free solutions.

1.2.5. Integration and power source

The sensing and delivery system must couple its high performance with minimal space and power requirements. Modern closed-loop glycaemic control systems, e.g., of Minimed Medtronic or Abbott Inc., integrate the glucose sensing element with a data processing and energy source for optimal delivery of insulin (Fig. 1). The pager-sized glucose monitor thus transmits its data straight to the insulin pump, that uses a computer algorithm to calculate the rate and timing of insulin release for optimal therapeutic intervention. Such systems offer a 3–5-day period of subcutaneous glucose monitoring, with measurement of tissue glucose every 3–5 min. An alarm capability is included to alert the individual of very low or high glucose levels. One attractive approach to implement such closed-loop system is to use two easily replaceable communicating patches (on the skin), one with the implanted sensor–amplifier–transmitter and the second with the RF receiver, insulin reservoir, a pump, battery, and subcutaneously implanted drug implant [3] (Fig. 3).

While substantial progress has been made towards shrinking the electronic package, reducing the size of the power source remains a major challenge. Miniaturized power sources, such as biofuel cells or batteries, currently being developed for addressing this challenge, offer an attractive approach for powering the autonomous sensor-transmitter system [26]. Heller's group has engineered a tiny membraneless glucose–oxygen biofuel cell,

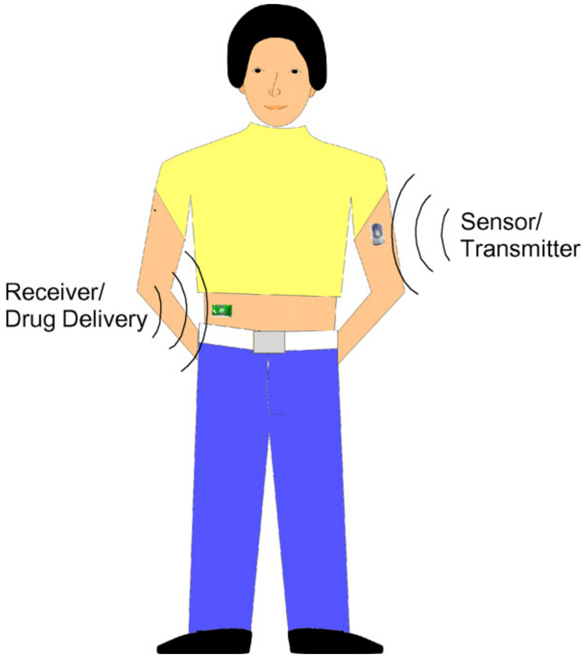

Fig. 3. Future sense/release glycaemic control feedback-loop medical system based on two easily replaceable communicating patches on the skin, one with the implanted glucose biosensor–amplifier–transmitter and the second with the RF receiver, insulin reservoir, a pump, battery, and subcutaneously implanted drug implant.

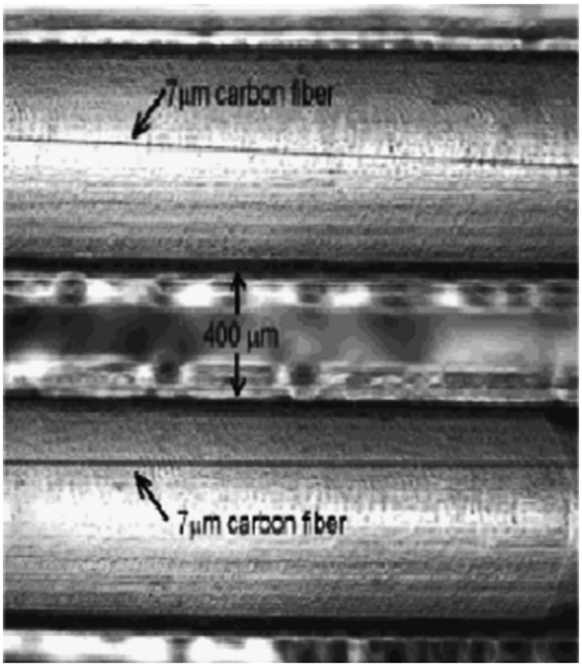

Fig. 4. Segment of a miniature biofuel cell, consisting of mediated enzymes immobilized on 7-µm diameter carbon fibers (from Ref. [27], with permission).

based on implantable 7 µm carbon fiber anode and cathode, coated with GOx and laccase or bilirubin oxidase, respectively, and wired with osmium-based redox hydrogels [27]. The photograph of Fig. 4 shows portion of the anode and cathode of such miniature biofuel cell (Fig. 4). Unlike conventional fuel cells, the selectivity of the enzyme catalysts eliminates the need for separating the biocatalytic electrodes from the physiological fluid. The toxic and corrosive components of batteries require special attention in connection to potential in vivo use of such implantable power sources [26]. Commonly used batteries are much larger than the glucose sensor itself, and often rely on a large case. Case-less miniature Zn–AgCl batteries (with anode diameters down to ca. 100 µm) were developed by Shin et al. [28]. The power source, the implanted sensor, and related circuitry would eventually be packaged in a miniature disposable unit [29]. Such implantable power can benefit other implantable devices (e.g., cardiac pacemakers) for other life-threatening diseases.

Such next-generation of implantable glucose sensors will give continuous readout that can be read from remote desktops at the clinic or hospital, compared to the patient's record, and allows the physician to follow closely changes in the patient's health.

2. Conclusions

This article discusses solutions to the key obstacles for continuous subcutaneous glucose monitoring towards effective closed-loop glycaemic control. In vivo glucose sensors are truly remote devices, in that they cannot be directly accessed and are subject to similar issues of long-term stability, biocompatibility, calibration, communications, and power, common to other remotely deployed analytical devices. A major progress has been made over the past two decades for addressing successfully these challenges to reliable glucose monitoring and towards integrating these devices with an insulin-delivery feedback loop. Such advances should minimize short-term crises and long-term complications of diabetes and would lead to improved quality and length of life for people with diabetes. In addition to minimally invasive subcutaneous glucose monitoring, efforts continue toward the development chronically implanted devices (aimed at functioning reliably for periods of 6–12 months) and towards non-invasive glucose sensing. This non-invasive route for continuous glucose monitoring is expected to eliminate the challenges associated with implantable devices. Different routes for "collecting" the glucose through the skin are currently being examined by various groups and companies in connection to such non-invasive glucose testing. The wearable glucose monitor (GlucoWatch Biographer), based on the coupling of reverse iontophoretic collection of glucose and amperometric biosensor functions [30] represents an attractive route in this direction.

The 'Sense and Act' route for diabetes management system represents the first example of an individualized drug administration system for optimal therapeutic intervention [3,4]. Such drug-delivering medical feedback loop systems are expected to revolutionize patient monitoring by enabling personalized medicine in connection to different diseases and conditions. Though there are still many technological challenges to be overcome before this becomes a reality, one can envisage a time when the release of a potent drug could be controlled by a microprocessor, in response to information fed back from a biosensor.

References

[1] C. Henry, Anal. Chem. 70 (1998) 594A.
[2] G.C. Wilson, R. Giffortd, Biosens. Bioelectr. 20 (2005) 2388.
[3] A. Heller, AIChE J. 51 (2005) 1054.
[4] S. Deo, E. Moschou, S. Peteu, S. Daunert, P. Eisenhardt, M. Madou, Anal. Chem. 75 (2003) 207A.
[5] J. Wang, Electroanalysis 13 (2001) 983.
[6] M. Shichiri, Y. Yamasaki, N. Hakui, H. Abe, Lancet 2 (1982) 1129.
[7] T.M. Gross, T.M. Diabetes, Technol. Ther. 2 (2000) S19–S26.
[8] B. Cho, B. Feldman, P. Le, F. Mao, C. Thomas, Diabetes 52 (2003) A91.
[9] D. Schmidtke, A. Freeland, A. Heller, R. Bonnecaze, Proc. Natl. Acad. Sci. U.S.A. 95 (1998) 294.
[10] S. Jaffari, A.P. Turner, Physiol. Meas. 16 (1995) 1.
[11] D. Bindra, Y. Zhang, G.S. Wilson, R. Sternberg, D.R. Thevenot, D. Moatti, G. Reach, Anal. Chem. 63 (1991) 1692.
[12] M. Frost, M.E. Meyerhoff, Anal. Chem. 78 (2006) 7370.
[13] R. Gifford, M.M. Batchelor, Y. Lee, G. Gokulrangan, M.E. Meyerhoff, G.S. Wilson, J. Biomed. Mater. Res., Part A 75A (2005) 755.
[14] B.K. Oh, M.E. Robbines, B.J. Nablo, M.H. Schoenfisch, Biosens. Bioelectr. 21 (2005) 749.
[15] R.G. Chapman, E. Ostuni, M.N. Liang, G. Meluleni, E. Kim, L. Yan, G. Pier, H.S. Warren, G.M. Whitesides, Langmuir 17 (2001) 1225.
[16] F. Moussy, D.J. Harrison, D.W. O'Brien, R.V. Rajotte, Anal. Chem. 65 (1993) 2072.
[17] J. Wang, L. Chen, S.B. Hocevar, B. Ogorevc, Analyst 125 (2000) 1431.
[18] S. Emr, A. Yacynych, Electroanalysis 7 (1995) 913.
[19] C. Malitesta, F. Palmisano, L. Torsi, P. Zambonin, Anal. Chem. 62 (1990) 2735.
[20] E. Csoregi, C.P. Quinn, D.W. Schmidtke, S.E. Lindquist, M.V. Pishko, I. Katakis, J.A. Hubbel, A. Heller, Anal. Chem. 66 (1994) 3131.

[21] B. Aussedat, V. Thome-Duret, G. Reach, F. Lemmonier, J. Klein, Y. Hu, G.S. Wilson, Biosens. Bioelectr. 12 (1997) 1061.

[22] R. Jeong, J.Y. Hwang, S. Joo, T.D. Chung, S. Park, S.K. Kang, W.Y. Lee, H.C. Kim, Biosens. Bioelectr. 19 (2003) 313.

[23] D. Gough, J. Lucisano, P. Tse, Anal. Chem. 57 (1985) 2351.

[24] Y. Zhang, G. Wilson, Anal. Chim. Acta 281 (1993) 513.

[25] J. Wang, F.J. Lu, Am. Chem. Soc. 120 (1998) 1048.

[26] A. Heller, Anal. Bioanal. Chem. 385 (2006) 469.

[27] T. Chen, S. Calabrese Barton, G. Binyamin, Z. Gao, Y. Zhang, H. Kim, A. Heller, J. Am. Chem. Soc. 123 (2001) 8630.

[28] W. Shin, J.W. Lee, Y. Kim, H. Steinfink, A. Heller, J. Am. Chem. Soc. 127 (2005) 14590.

[29] A. Pothukuchy, N. Mano, G. Georgiou, A. Heller, Biosens. Bioelectr. 22 (2006) 678.

[30] M. Tierney, H. Kim, J. Tamada, R. Potts, Electroanalysis 12 (2000) 666.

Available online at www.sciencedirect.com

ScienceDirect

Talanta 75 (2008) 642–650

Talanta

www.elsevier.com/locate/talanta

Nitric oxide-releasing/generating polymers for the development of implantable chemical sensors with enhanced biocompatibility

Yiduo Wu, Mark E. Meyerhoff*

Department of Chemistry, The University of Michigan, Ann Arbor, MI 48109-1055, USA

Received 5 February 2007; accepted 13 June 2007
Available online 28 June 2007

Abstract

The development of reliable *in vivo* chemical sensors for real-time clinical monitoring of blood gases, electrolytes, glucose, etc. in critically ill and diabetic patients remains a great challenge owing to inherent biocompatibility problems that can cause errant analytical results upon sensor implantation (e.g., cell adhesion, thrombosis, inflammation). Nitric oxide (NO) is a well-known inhibitor of platelet activation and adhesion, and also a potent inhibitor of smooth muscle cell proliferation. In addition, NO mediates inflammatory response and promotes angiogenesis. Polymers that release or generate NO at their surfaces have been shown to exhibit greatly enhanced thromboresistance *in vivo* when in contact with flowing blood, as well as reduce inflammatory response when placed subcutaneously, and thus have the potential to improve the biocompatibility of implanted chemical sensors. Locally elevated NO levels at the surface of implanted devices can be achieved by using polymers that incorporate NO donor species that can decompose and release NO spontaneously when in contact with physiological fluids, or NO-generating polymers that possess an immobilized catalyst that decompose endogenous *S*-nitrosothiols to generate NO *in situ*. The potential use of such NO-releasing/generating materials for preparing *in vivo* sensors implanted either intravascularly or subcutaneously, is examined in this review.

Keywords: Implantable sensors; Biocompatibility; Nitric oxide; Platelet activity; Inflammatory response

1. Introduction

The care of critically ill hospitalized patients requires frequent and accurate measurements of arterial blood gases (pH, PO_2, PCO_2), electrolytes (Na^+, K^+, Ca^{2+}) and glucose/lactate levels in undiluted whole blood. To date, such values are usually obtained from *in vitro* tests using discrete blood samples drawn intermittently from patients and analyzed on benchtop instruments or smaller point-of-care devices [1–3]. However, intermittent sampling can miss events that can be life-threatening to the patient. Indeed, isolated measurements are not able to provide the desired real-time monitoring of minute-to-minute physiological changes that can occur in unstable critically ill patients [2]. Therefore, continuous intravascular sensing of clinically important species would be of great value to improve the quality of health care for such patients.

At the same time, reliable *in vivo* monitoring of glucose concentrations in blood or the interstitial fluid could significantly enhance the quality of life for millions of non-hospitalized patients with diabetes mellitus. A successful implantable glucose sensor must: (i) be small enough to be placed intravascularly or subcutaneously; (ii) provide long-term stable analytical signals so that re-calibration can be minimized; (iii) yield accurate measurements of glucose that correlate well with *in vitro* tests based on discrete blood samples so that therapeutic action can be taken based on the measured values (e.g., infusion of insulin); (iv) be compatible with the biological environment in which it is implanted (i.e., 'biocompatible').

Advances in the miniaturization of optical and electrochemical sensors for blood gases, electrolytes and glucose/lactate have made it possible to place such devices within blood vessels or under the skin. However, despite significant efforts toward developing implantable intravascular and/or subcutaneous chemical

---

* Corresponding author at: 930 N. University Ave., The University of Michigan, Ann Arbor, MI 48109-1055, USA Tel.: +1 734 763 5916; fax: +1 734 647 4865.
E-mail address: mmeyerho@umich.edu (M.E. Meyerhoff).

0039-9140/$ – see front matter © 2007 Elsevier B.V. All rights reserved.
doi:10.1016/j.talanta.2007.06.022

sensors suitable for continuous *in vivo* monitoring, the routine clinical use of such devices has not yet been realized. The major challenge to be overcome for success in this area is the erratic analytical results obtained from sensors implanted *in vivo*. Errant analytical results are generally attributed to the adverse biological responses to such implanted devices [2–5], which usually relates to the lack of biocompatibility of the implanted optical or electrochemical probes.

The biocompatibility of an implantable medical device refers to the ability of the device to perform its intended function, with the desired degree of incorporation within the host, without eliciting any undesirable local or systemic effects in that host [6]. The biological response to implanted sensors depends largely on the site of implantation. Intravascular placement is the most desirable for blood chemistry measurements. The biocompatibility problems associated with sensors implanted intravascularly have been reviewed previously [1–3,7]. When an intravascular sensor is in contact with blood, the initial biological response is the rapid adsorption of plasma proteins (e.g., fibrinogen, fibronectin and von Willebrand's factor (vWF)) onto the surface, followed by the adhesion and activation of platelets (see Fig. 1a) [8]. Once activated, platelets undergo shape change and secretion of their granular contents. The activated platelet is a key player in the coagulation cascade and will ultimately lead to the formation of a blood clot on the surface of the device [9]. Such biofouling of the sensing membrane can restrict the diffusion of analyte to the sensor surface [10]. Moreover, the metabolic activities of adhered cells consume oxygen and glucose while producing carbon dioxide, thus changing the local concentration of blood gases and glucose levels sensed by the implanted device [5]. Fig. 1b illustrates the typical patterns of deviation for sensors implanted intravascularly. Even a monolayer of cells adhered onto the sensor surface is sufficient to produce the behavior illustrated in Fig. 1b.

Similar patterns of deviation can also be observed when blood flow is reduced in the blood vessel where the sensor is placed, or when the sensor touches the wall of blood vessels where inherent metabolism of endothelial cells can affect sensor performance in the same way as adhered blood cells ("wall effect") [2,5]. Moreover, thrombus formation in patients can occur randomly

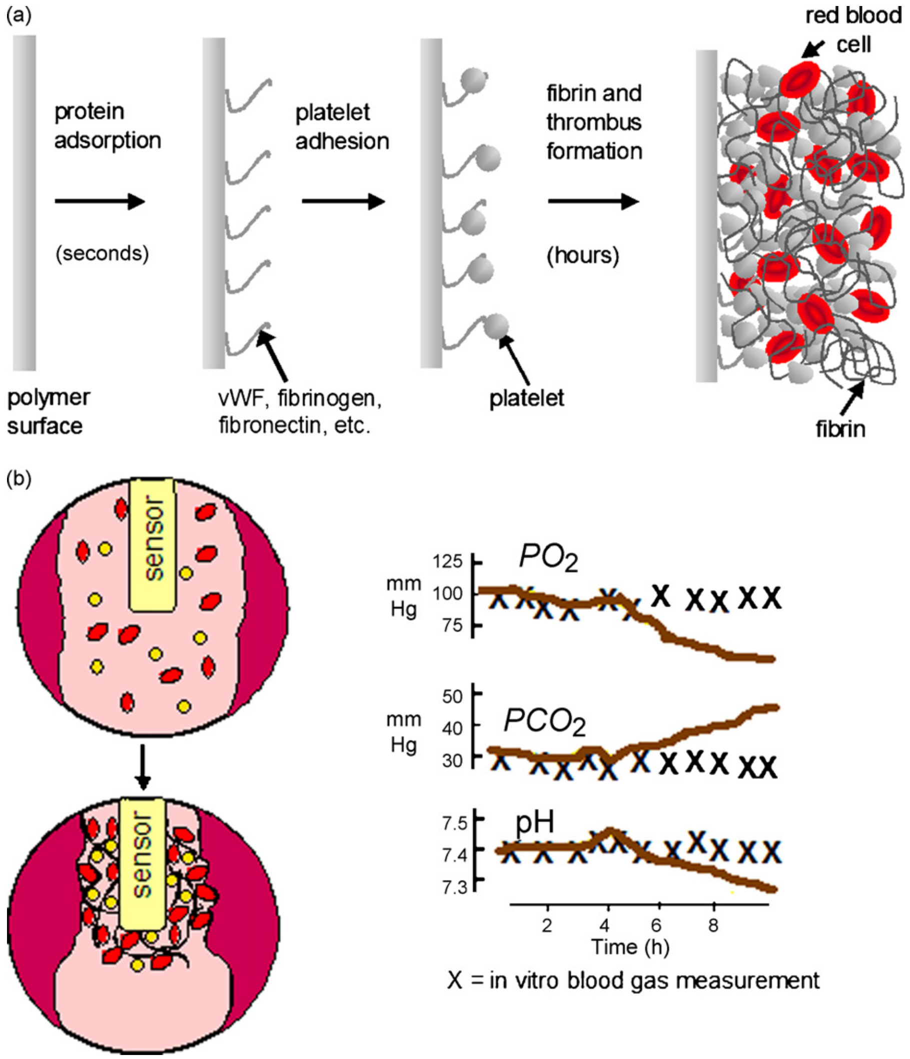

Fig. 1. (a) Sequence of events leading to thrombus formation on surface of intravascularly implanted sensor and (b) subsequent deviations in implanted sensor measurements of blood gases/pH due to cell adhesion and/or low blood flow at implant site.

since it also depends on factors such as the native coagulation propensity of a particular patient and the velocity of blood-flow within the lumen of the vessel in which the sensor is placed. The unpredictability of intravascular sensor performance due to these biological factors makes the resulting measurements unreliable, preventing timely therapeutic intervention.

Sensors implanted under the skin (subcutaneous measurements), such as those often developed for monitoring glucose levels, do not encounter the same issues of platelet activation and thrombus formation. However, such sensors are subject to their own biocompatibility problems, primarily from inflammatory responses that can affect their accuracy. The size, shape and physical/chemical properties of the implanted devices contribute to variations in the intensity and time duration of the inflammatory and wound-healing process [11]. Acute inflammatory response starts immediately after sensor implantation as fluids, plasma proteins and inflammatory cells migrate to the implant site [12]. The first event that occurs is protein adsorption, followed by the attack of phagocytic cells (neutrophils, monocytes and macrophages) on the implanted sensor, attempting to destroy it. However, since the sensor is large, only ‘frustrated phagocytosis’ occurs [11,12]. Acute inflammatory response (24–48 h) is characterized by the predominance of neutrophils, which are later replaced by macrophages, monocytes and lymphocytes during the chronic inflammation stage [12]. Ultimately, fibrous encapsulation of the subcutaneously implanted device by primarily macrophages and fibrin indicates the end-stage of the wound-healing process.

The fibrous capsule can change the analyte levels in the vicinity of the sensor through metabolic activities (e.g., faster glucose consumption). It also can affect the transport of analyte to the sensor surface as well as that between the blood and the interstitial fluid. This can lead to significant changes in the calibration curve (i.e., lowering the sensitivity) as well as affecting the lag time of the sensor's response to the fluctuations of glucose levels in bulk blood for both optical [13,14] and electrochemical sensors [4,11,15]. Angiogenesis around the site of tissue injury caused by implanted sensor is also part of the wound-healing process. Since more blood vessels around the implanted sensors will facilitate the diffusion of the analyte from blood to the subcutaneous fluids (so interstitial fluid levels of the analyte more closely resemble blood levels), the degree of angiogenesis after implantation will also influence the output of sensors placed subcutaneously [16].

2. Strategies toward improving biocompatibility

2.1. Surface modifications

The surface of an implanted device is thought by many to be of critical importance in determining the *in vivo* performance of any implant. Surface modification strategies employed to address biocompatibility issues have been reviewed by Wisniewski et al. [10]. These approaches include hydrogel overlays, phospholipid-based biomimcry, flow-based systems, Nafion coatings, surfactants, covalent attachments, diamond-like carbons, and topology treatments. Surfaces with high water content are found to be more inert to protein adsorption and cell adhesion as a result of low interfacial energy [17]. Hydrogels and other hydrophilic surface modifications are aimed at minimizing protein adsorption, since such adsorption initiates a series of biological responses [8,12]. Biomaterials with the surface immobilized biological molecules, such as albumin [18], heparin [19], thrombomodulin [20], prostacyclin [21] and hyaluronic acid [22] have all been shown to exhibit some effectiveness in enhancing biocompatibility.

2.2. Potential for utilizing nitric oxide (NO) with in vivo sensors

Unfortunately, hydrophilic surfaces by themselves may retard, but do not completely prevent the adsorption of proteins on surfaces *in vivo*. Eventually, the proteins that can initiate platelet adhesion/activation or those that mediate inflammatory responses will still adsorb onto the surface of the implanted sensor, leading to thrombus formation and/or inflammation. The biological environments in which the sensors are implanted involve a myriad of activities besides the cell surface expression of certain molecules. In the case of the vascular endothelium, that lines the inner walls of all blood vessels (and is known to be the best example of a completely non-thrombogenic surface), a number of active molecules such as thrombomodulin, prostacyclin, heparan sulfate, and nitric oxide (NO) are either expressed at the surface or are continuously being secreted to mediate the biological responses underlining biocompatibility [9].

Over the past 20 years, NO has received considerable interest from the pharmacological and biomedical research communities owing to its diverse physiological functions as a protective, regulatory and signaling molecule involved in the regulation of blood pressure, clotting, neurotransmission and immune response. Indeed, NO is widely recognized as a key anti-platelet, anti-inflammatory and vasodilating agent [23–27]. In addition, NO is also known to inhibit bacterial growth [28,29] and promote angiogenesis [30].

Nitric oxide is produced endogenously from L-arginine and oxygen by enzymes known as nitric oxide synthases (NOS) [31]. NO exerts its vasodilation and anti-platelet function by binding to the heme iron of soluble guanylate cyclase and subsequently increasing the production and intracellular concentrations of cyclic guanosine monophosphate (cGMP), a secondary messenger [32]. The endogenous concentration of NO as a dissolved gas is very low (~3 nM) [33]. Under physiological conditions, oxidized NO (in the form of NO^+ or N_2O_3) reacts with thiol groups in cysteine or cysteine-containing peptides and proteins (e.g., glutathione, albumin and hemoglobin) to yield *S*-nitrosothiols (RSNOs) [34,35]. RSNOs act as carriers of NO in the body and are thought to be responsible for the storage and bioavailability of NO [33,36].

Vasoconstriction can occur at the site where the intravascular sensor is implanted as a biological response to reduce bleeding at the implant site. Meanwhile, platelets are activated and recruited to repair the vascular injury [37]. NO is synthesized in the endothelial cells that line the wall of healthy blood vessel and diffuses in all directions. When NO reaches the underlying vascular smooth muscle cells, NO stimulates cGMP production and, in turn, decreases the Ca^{2+} levels in the smooth muscle cells, leading to vascular relaxation [38]. Muscle relaxation allows the blood vessel to dilate and lowers the blood pressure. NO also diffuses into circulating platelets, especially when they approach the surface of the endothelium. Platelet activation is also Ca^{2+} dependent [39] and is thus inhibited by NO [27,40]. The lifetime of NO in whole blood is very short (<1 s) due to its reaction with heme-containing compounds such as oxyhemoglobin [41]. Therefore the anti-platelet effect occurs only locally when platelets are in close proximity to the endothelium, as the presence of red blood cells would block the NO transfer to platelets. It has been estimated that the endothelial derived NO flux is in the range of 0.5×10^{-10} to 4.0×10^{-10} mol cm^{-2} min^{-1} [42]. Therefore, if the surface of an intravascular sensor can release or generate NO at or above this range of fluxes, it is expected to display enhanced thromboresistance. Furthermore, the released NO will be effective only locally at the blood/polymer interface, which is ideal for biocompatibility purposes. Owing to the low NO fluxes, the small dimension of the intravascular sensor, and the very short half-life of NO in blood, the locally released NO is unlikely to cause any systemic effect that may lead to cytotoxicity or hemorrhage.

Nitric oxide also is involved in virtually every step of the inflammatory process [43]. In fact, NO plays a crucial role in wound healing and down regulates mediators of inflammatory response. Low concentrations of NO can inhibit adhesive molecule expression, cytokine and chemokine synthesis as well as leukocyte adhesion and transmigration [43]. Nitric oxide also promotes angiogenesis and disruption of the NOS-based NO generation pathway is known to impair neovascularization [30]. Subcutaneous implantation also brings the risk of infection, which can also be inhibited by NO [29]. Therefore, an active surface that can continuously release or generate NO in the interstitial fluid may also benefit greatly from a locally enhanced level of NO, with respect to reducing inflammatory cell migration and promotion of neovascularization that could increase the exchange of glucose and other analytes into the subcutaneous fluid adjacent to the implanted sensor.

3. Implantable sensors with NO-releasing/generating coatings

3.1. NO-releasing materials

Since the discovery of the anti-thrombogenic role of NO, the possibility of improving biocompatibility by incorporating NO-releasing/generating function into biomedical polymers has been explored by several research groups. Ramamurthi and Lewis [40] used the direct infusion of gaseous $NO_{(g)}$ (0.1 ppm) through a semi-permeable membrane to produce surface NO fluxes ranging between 3×10^{-8} to 6.6×10^{-8} mol cm^{-2} min^{-1}. These low levels of NO were shown to inhibit platelet adhesion by as much as 87%. However, it would be quite difficult to deliver gaseous NO (from reservoir of NO gas) to the surface of an implanted sensor, once it was placed in an artery/vein or under the skin. Fortunately, a number of NO donor compounds have been developed to deliver NO *in vivo* and study its biological effects [44]. For implantable sensor applications, the NO donors must be incorporated in the polymer either as a thin outer coating or into the bulk polymer from which the medical sensor is made (e.g., polymeric tubing for certain catheter style sensors). The duration of NO release should match the implant lifetime of the device itself. In addition, it is critical that the NO release rate be controllable, as excess exposure to the NO donor, NO and any reaction products can be cytotoxic, mutagenic or carcinogenic.

To date, the two most widely investigated NO donors for biomedical applications are *S*-nitrosothiols (RSNO) and *N*-diazeniumdiolates (so-called NONOates). *S*-Nitrosothiols can be prepared by reacting thiols with nitrous acid. *S*-Nitrosoglutathione (GSNO) and *S*-nitroso-*N*-acetyl-cysteine (SNAC) have been blended into various polymers (e.g., poly(vinyl alcohol), poly(vinyl pyrrolidone), poly(ethylene glycol)) by de Oliveira and coworkers for targeted delivery of NO and parent RSNOs [45–47]. Bohl and West demonstrated that *S*-nitrosocysteine (CysNO) immobilized within a poly(ethylene glycol) hydrogel reduced platelet adhesion and smooth muscle cell proliferation *in vitro* [48].

A *N*-diazeniumdiolate is an NO adduct with secondary amines [49]. One equivalent of amine reacts with two equivalents of NO to form the corresponding diazeniumdiolate under high $NO_{(g)}$ pressure (e.g., 80 psi). The NO release from diazeniumdiolates is proton-driven and follows pseudo-first order kinetics at physiological pH [50]. The chemistry of NO release from dibutylhexyldiamine diazeniumdiolate ($DBHD/N_2O_2$) is depicted schematically in Fig. 2a. Three general procedures have been used in the preparation of diazeniumdiolate-based NO-releasing polymers: (1) dispersion of small amine-based diazeniumdiolate molecules into polymer matrices (e.g., $DBHD/N_2O_2$) [51]; (2) diazeniumdiolation of covalently linked amine sites on pendant polymer side chains, or on the polymer backbone [52,53]; (3) covalent binding of diazeniumdiolate groups to micro- or nano-particles, and use of such particles as polymer fillers [54]. The half-life of NO release can be modulated by selecting different secondary amine structures [55] and the NO fluxes can be tuned by changing the diazeniumdiolate dopant amount, hydrophobicity of the polymer matrices or by applying topcoats of polymers to control the diffusion of water into the layer containing the NONOate. The leaching of non-covalently bound small molecule diazeniumdiolates can be greatly reduced by using highly lipophilic diazeniumdiolates blended into the polymer matrix [51].

A key assumption with respect to potentially using NO-release polymers to prepare implantable sensors is that the NO release chemistry does not interfere with the sensing chemistry of the device. Since NO is a redox active species, it is necessary to establish that the initial NO donors and the released NO from the outer coating does not interfere with the analyte measurement by significantly changing the sensitivity, selectivity or lifetime of the implantable chemical sensor, especially electrochemical devices.

Initial work with NO releasing chemical sensors focused on using a small molecule NO donor, dimethylhexane diamine

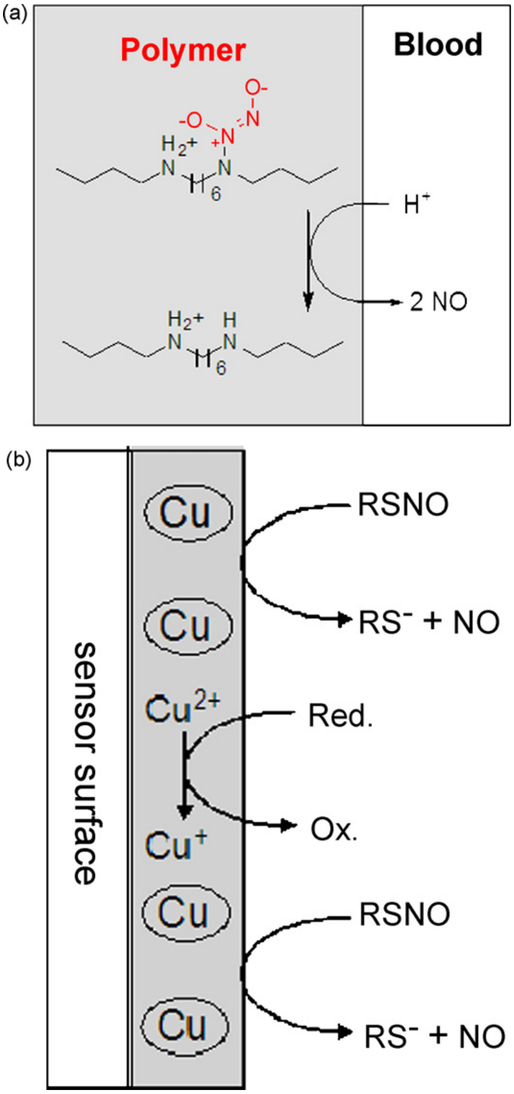

Fig. 2. Schematic of (a) NO-release from DBHD/N_2O_2 and (b) NO generation by immobilized Cu catalyst.

diazeniumdiolate (DMHD/N_2O_2), dispersed into plasticized poly(vinyl chloride) (PVC) and polyurethane (PU) membranes for the purpose of preparing NO releasing potentiometric ion-selective sensors. Indeed, Espadas-Torre et al. reported that pH and K^+ sensors prepared with the NO-releasing polymer membranes (doped also with the appropriate ion-selective ionophores (tridodecylamine (TDDA) or valinomycin) for sensing purposes) exhibit similar potentiometric response sensitivities and selectivities towards H^+ and K^+ as control sensors without NO release [56]. The NO-releasing ion-selective polymer films also exhibit greatly reduced platelet adhesion and activation compared to control films without NO release when tested *in vitro* using platelet-rich sheep plasma. Mowery et al. further demonstrated that two other NO donors, diazeniumdiolated linear polyethylenimine and diazeniumdiolated methoxymethylpiperazine PVC, can also be used to prepare potentiometric sensing membranes [57]. They also extended the application of (DMHD/N_2O_2) to a Clark-style amperometric oxygen sensor and proved that NO release does not affect the sensor's amperometric response [57]. Frost et al. utilized the diazeniumdiolated diaminoalkyltrimethoxylsilane (DACA/N_2O_2) crosslinked polydimethylsiloxane (PDMS) to coat the outer walls of a potentiometric CO_2 sensing catheter [58]. The NO-releasing CO_2 sensors exhibited comparable Nernstian response slopes as the control sensors without NO release chemistry. Apparently, the low fluxes of NO released from such coatings do not have a significant impact on the analytical performance of these devices.

Nitric oxide release has also been employed to enhance the biocompatibility of optical sensors. Schoenfisch et al. reported a dual-layer fluorescence-based oxygen sensor configuration with the underlying NO-releasing layer made from DACA/N_2O_2 crosslinked silicone rubber (SR) covered by a second polymeric layer containing the pyrene/perylene fluorescent indicators [59]. The NO-releasing sensors yielded identical responses to oxygen as conventional sensors without NO release. Further, Schoenfisch and coworkers developed a NO-releasing xerogel-based optical pH sensor and demonstrated its improved blood compatibility through an *in vitro* platelet adhesion study [60].

To further confirm that NO-releasing polymers can improve biocompatibility, separate *in vitro* platelet adhesion studies using platelet-rich plasma have been carried out [56,61]. More quantitative studies on the reduction of *in vitro* platelet adhesion on plasticized PVC with varying fluxes of NO was recently conducted using a novel lactate dehydrogenase (LDH) assay [62]. Reduced platelet adhesion was correlated with the increase in NO fluxes. Platelet adhesion was effectively reduced from $14.0 \pm 2.1 \times 10^5$ cells cm^{-2} on the control polymer, to $2.96 \pm 0.18 \times 10^5$ cells cm^{-2} on polymers with an NO flux of $7.05 \pm 0.25 \times 10^{-10}$ mol cm^{-2} min^{-1}.

The initial proof-of-concept that NO release can improve the biocompatibility of devices implanted intravascularly were performed by implanting sham catheters coated with diazeniumdiolated methoxymethylpiperazine PVC into canine carotid arteries for 6 h [57]. The catheters coated with NO-releasing polymer showed greatly reduced platelet activation and adhesion compared to conventional PVC implanted in the same animal. These experiments indicated that low levels of NO release did in fact inhibit thrombus formation on the surface of implanted intravascular devices within the complex and dynamic environment of flowing blood.

The first *in vivo* evaluation of NO-releasing intravascular chemical sensors was reported by Schoenfisch et al. [63]. In this study, DMHD/N_2O_2 dispersed in cross-linked silicone rubber (SR) was coated over the outer SR gas-permeable tubing of a Clark-style amperometric oxygen-sensing catheter to impart NO release. These sensors were implanted in canine arteries for up to 23 h without systemic anti-coagulation. During the course of the experiments, the oxygen levels monitored by the NO-releasing sensors tracked more closely with *in vitro* blood gas analysis of PO_2 levels performed on discrete blood samples drawn from the animal, as compared to non-NO release control oxygen sensors implanted within the same animal (e.g., more accurate results). At the end of each animal study, the sensors were carefully explanted from the arteries and examined by scanning electron microscopy (SEM). The NO-releasing catheters consistently showed a marked decrease in platelet adhesion under SEM, with no gross thrombus formation. On the other hand, gross thrombus formation was routinely observed on the control catheters which were covered by adhered platelets, fibrin and entrapped red cells.

These encouraging results suggested the potential of using NO-releasing polymers to enhance the biocompatibility and concomitant analytical performance of intravascular chemical sensors. However, it was found that the small molecule NO donor (DMHD/N_2O_2) could leach out of the polymer coating and a significant amount of NO was released from by the decomposition of the donor outside of the polymer coating matrix [61]. This poses potential risks as the decomposition product, free dimethylhexane diamine, could react with labile nitrogen oxide species and form a *N*-nitrosamine, which is carcinogenic. In addition, the leaching of NO donor into the aqueous phase would reduce the effectiveness of locally released NO to inhibit platelet adhesion/activation at the polymer/blood interface (i.e., less NO being locally released at sensor/blood interface).

To address the leaching problem, Zhang et al. developed the DACA-SR/N_2O_2 material where the diazeniumdiolate groups are anchored on a diamine silane crosslinker and thus the leaching of the parent diamine from the polymer matrix is eliminated [64]. Frost et al. applied this covalently attached diazeniumdiolated DACA-SR/N_2O_2 coating (~100 μm thickness) on the surface of Clark-style oxygen-sensing catheters and evaluated the performance of these devices in porcine carotid and femoral arteries for 16 h [65]. The blood oxygen levels determined by the NO-releasing sensors ($N = 9$) were statistically identical to the standard *in vitro* blood gas measurements, while the control sensors ($N = 9$) implanted in the same animals showed statistically significant deviations (negative values) at 95% confidence interval in oxygen measurements after 10 h of implantation. Furthermore, the NO-releasing catheters were found to be relatively thrombus-free after explantation, while the control catheters without NO-release exhibited largely varied degrees of biological response, ranging from very few adhered platelets to a complete coverage of the surface by blood clots. Such variation in biological response is typically observed with implanted sensors, and it is precisely this variability that makes measurements with conventional sensors so unreliable.

As mentioned above, another approach to create NO release polymeric coatings is to use a more lipophilic parent diamine compound with longer alkyl side-chains so that extraction into aqueous phase is minimized [51]. Replacing the methyl side groups in DMHD with butyl groups enhances the partition coefficient of the diamine into the organic polymer phase by 10^4. In another study, the resulting diazeniumdiolated dibutylhexyldiamine (DBHD/N_2O_2) was dispersed into SR, together with potassium tetrakis(4-chlorophenyl) borate (KTpClPB) which buffers the pH in the organic phase to maintain a more constant longer term NO release. Biocompatibility evaluations of NO-releasing catheters with outer SR coatings containing DBHD/N_2O_2 in the porcine artery model yielded similar results to other NO-releasing sensor studies, with more accurate blood oxygen measurements and less platelet adhesion and activation observed [58].

NO-releasing polymers containing DBHD/N_2O_2 have also shows improved biocompatibility when used as outer coatings for preparation of needle-type subcutaneous glucose sensors. Gifford et al. prepared glucose sensors with a thin PU/PDMS coating (~10 μm thick) doped with the DBHD/N_2O_2 NO donor and implanted them in rats together with control sensors [66]. Histological evaluation of neutrophil infiltration revealed that inflammatory response was greatly reduced during the first 24 h at implant sites where the NO release sensors were placed versus control sites in the same animals. However, the NO release from the polymer coating could only last ca. 16 h, owing the very thin coating necessary to prevent a dramatic decrease in the flux of glucose to the underlying glucose oxidase enzyme layer of the sensor. Therefore, although the sensors remained functional *in vivo* for several days, the reduction of inflammatory response was not maintained for an extended implant period (3 days). Increasing the coating thickness is not an option as it would change the membrane permeability and adversely affect the sensitivity and response time of the glucose sensor. To circumvent the limitation of NO donor reservoir in the NO-releasing coating, alternative NO-generating approaches have been pursued to immobilize catalysts onto the polymer surface that can decompose endogenous RSNOs, an NO carrier, to generate NO *in situ* at the polymer/blood interface.

3.2. NO-generating materials

As discussed above, polymer coatings containing NO donors on the surfaces of implantable sensors will eventually be depleted, and thus these sensors are likely to eventually lose the biocompatibility advantage offered by NO release. The concept of “NO generation” coatings is to utilize the endogenous RSNO species that exist in the physiological fluids as a continuously replenishing NO donor to generate enhanced NO levels at the blood/polymer interface. RSNOs are regarded as a reservoir and carrier of NO in the body. The most abundant endogenous RSNOs are *S*-nitrosoalbumin (AlbSNO) and GSNO. Transnitrosation reactions occur *in vivo* so that the nitroso-group can be transferred from one thiol to another [34,36]. The cleavage of S-NO bond in RSNOs to release NO can occur by three well-established mechanisms [67]. First, copper ion mediated catalytic decomposition requires Cu^{2+} to first be reduced to Cu^+. Copper(I) reacts with RSNO to liberate NO by transferring an electron, and thus forms a thiolate anion and regenerates Cu^{2+}. Under physiological conditions, ascorbate and thiolate anions are sufficient reducing agents to convert Cu^{2+} to Cu^+. The second RSNO decomposition pathway is through the reaction with high concentrations (>1 mM) of ascorbate to release NO and produces thiolate and dehydroascorbate [68]. The third decomposition mechanism of RSNOs is the homolytic cleavage of the S–NO bond by light at characteristic absorbance bands of 330–350 or 550–600 nm, yielding NO and the disulfide of the parent thiols [69]. Further, Hou et al. reported that glutathione peroxidase (GPx) and other seleno compounds (e.g., selenocystamine) can also catalyze RSNO decomposition [70]. Recent research using organotellurium compounds indicate that they also possess similar catalytic activities towards RSNO decomposition [71].

The potential advantage of the NO-generation approach *in vivo* is the utilization of circulating RSNOs as an unlimited supply of NO at the polymer/blood interface. Duan et al. explored the possibility of generating NO by transnitrosation from endogenous RSNOs to L-cysteine immobilized on polymer surfaces [72]. They covalently attached L-cysteine to PU and polyethylene terephthalate (PET) and these L-cysteine modified polymers reduce *in vitro* platelet adhesion by more than 50% when tested in plasma, but not with a platelet suspension in phosphate buffer. The suggested mechanism was through the transnitrosation of NO^+ from endogenous RSNOs (e.g., Alb-SNO) to the cysteine moiety on the polymer surface to yield immobilized CysNO. CysNO is relatively unstable and can thus decompose to release NO locally at the polymer interface.

Oh et al. developed a lipophilic Cu(II)–cyclen-type complex to generate NO from RSNO and nitrite under physiological conditions [73,74]. PVC and PU films doped with this Cu(II) complex generated NO in the presence of reducing agents (e.g., ascorbate, cysteine, glutathione). It was demonstrated such polymers can generated NO with an apparent surface flux as high as $8 \times 10^{-10}\,\mathrm{mol\,cm^{-2}\,min^{-1}}$ from physiological levels (1 μM) of GSNO. The same polymer was also shown to generate NO from nitrite under physiological conditions in the presence of ascorbate. A material that is capable of locally and continuously generating NO from endogenous RSNOs and nitrite could be used to tackle the biocompatibility problems for not only implantable sensors, but even long-term implants, such as stents and vascular grafts.

Wu et al. recently evaluated the biocompatibility of NO-generating polymeric coatings *in vivo* on intravascular oxygen-sensing catheters using the aforementioned porcine artery model for up to 20 h [75]. The NO-generation was achieved using small metallic copper particles of two different sizes (3 μm and 80 nm), doped within a thin outer coating of an appropriate polymer applied to the surface of the oxygen sensing catheter. Corrosion of metallic copper provides the copper ions required for RSNO decomposition (see Fig. 2b). The 3 μm Cu^0 particles were dispersed in a polymer blend of RTV-3140 SR and Tecophilic SP-60D-60 hydrophilic PU (SR:PU = 2:1), while the 80 nm Cu^0 particles were dispersed in Tecoflex SG-80A PU with an underlying adhesion promoter layer to ensure tight adhesion to the SR tubing used to construct the catheter. It was demonstrated that such coatings can generate NO surface fluxes of more than $2 \times 10^{-10}\,\mathrm{mol\,cm^{-2}\,min^{-1}}$ at physiological GSNO levels. Further, the incorporation of Cu^0 particles does not alter the sensitivity and stability of the sensor, nor does it cause any significant leaching of Cu ions due to corrosion. On average, the NO-generating sensors ($N = 12$ for the 3-μm group and $N = 6$ for the 80-nm group) showed improved biocompatibility along with more accurate PO_2 measurements when compared to control sensors without Cu^0 particles. The average percent deviations of PO_2 measured by NO-generating and control sensors as compared with standard blood gas machine results (considered 100% accurate) are plotted in Fig. 3. On average, values from NO-generating sensors showed closer agreement with *in vitro* blood gas measurements, while control sensors yielded consistent false-negative values due to thrombus formation. Nine out of 12 control sensors in the 3 μm group developed mature blood clot as determined after explantation, while only 3 out of the 12 NO-generating sensors had evidence of surface clot. Similar results were obtained with the 80-nm particle group—3 out of the 6 control sensors had surface clot and only 1 out of the 6 NO-generating sensors had thrombus formed over the surface.

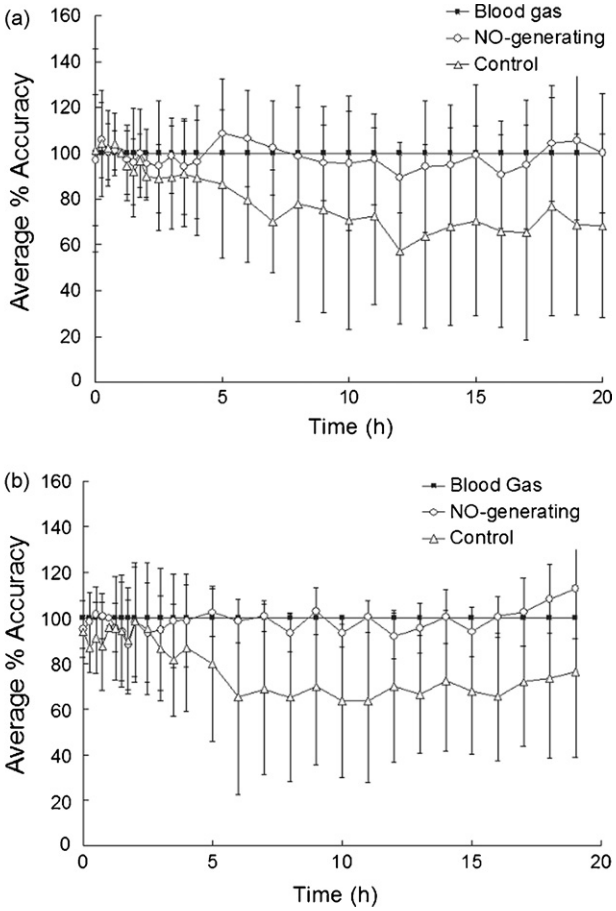

Fig. 3. Plots of the average percent accuracy of (a) NO-generating sensors based on 3 μm Cu^0 particles and control sensors ($N = 12$ each) and (b) NO-generating sensors based on 80 nm Cu^0 particles and control sensors ($N = 6$ each), as compared to *in vitro* blood gas analyzer results (from Ref. [75], with permission).

Fig. 4 shows the representative images of NO-generating and control sensors from each group after explantation. It is clear that the NO generating sensor has less thrombus at the sensing tip. An LDH assay [62] was used to quantify the degree of thrombus formation on the sensor surfaces. The average LDH content in the biolayer on the control sensor surfaces is ~8 times greater than the LDH content of the biolayer covering the NO-generating sensors, further indicating the presence of more adhered cells on control sensors. The thrombus formation on some of the NO-generating sensors might be attributed to the low endogenous RSNO levels in particular animals so that there might be insufficient NO generated at the surface. Indeed, the question of normal RSNO levels in blood is still under debate and the reported values in the literature range from 15 nM to 7 μM [33,76]. There might

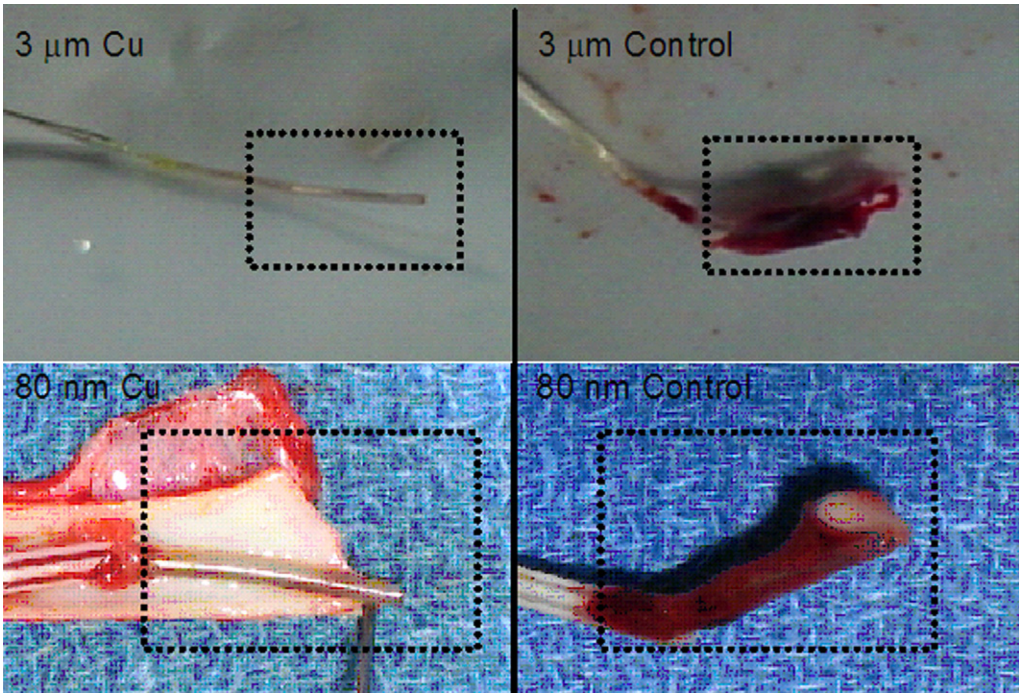

Fig. 4. Images of two representative pairs of NO-generating (left) and control sensors (right) after *in vivo* studies. The portions within the dotted boxes were exposed to blood (from Ref. [75], with permission).

also be a considerable animal-to-animal variation in endogenous RSNO concentrations, giving rise to the difference in biological response seen in the animals. To overcome the limitation of basal RSNO levels, it might be necessary to provide a bolus of naturally occurring RSNO each day, to ensure that blood RSNO levels are adequate to create elevated levels of NO at the sensor/blood interface. Use of newly developed electrochemical RSNO sensors [77,78] to monitor blood RSNO concentrations will likely to help sort out whether such action would be necessary to implement the NO generation approach to enhance the biocompatibility of the implanted sensors.

4. Future prospects

The routine use of implantable chemical sensors is highly dependent on the reliability of their analytical results. To date, the analytical functionality of such devices is still hampered by the adverse biological responses, which render the analytical results not reliable enough to make therapeutic/clinical decisions. As outlined above, it has been recently shown that the local release/generation of biologically active species such as NO is capable of reducing thrombus formation as well as inflammatory responses for intravascular and subcutaneous sensors, making the output signals from such devices potentially more useful. However, NO alone is unlikely to be the solution for the entire biocompatibility problem. Indeed, the vascular endothelium is a perfectly non-thrombogenic surface due to a number of molecules working synergistically to maintain vascular homeostasis. A biomimetic approach to create an 'artificial endothelium' will likely provide the most promising approach for the development of truly biocompatible sensors. NO release/generating polymers are the first step in this direction. Further, surface immobilization of heparin and thrombomodulin, used in conjunction with continuous release of a variety of naturally occurring anti-thrombogenic species (including NO and prostacyclin), may render implanted sensors even greater biocompatibility than NO release/generation alone. A dual-functional polymeric coating with surface-immobilized active heparin and NO-release has recently been reported [79]. In addition, it has been found that surface bound thrombomodulin co-immobilized with heparin on NO-releasing polymers both retain their biological functions and might be a promising candidate for future development of implantable sensors [80].

References

[1] E. Fogt, Clin. Chem. 36 (1990) 1573.
[2] C.K. Mahutte, Clin. Biochem. 31 (1998) 119.
[3] M.C. Frost, M.E. Meyerhoff, Curr. Opin. Chem. Biol. 6 (2002) 633.
[4] N. Wisniewski, F. Moussy, W.M. Reichert, Fresenius' J. Anal. Chem. 366 (2000) 611.
[5] M. Frost, M.E. Meyerhoff, Anal. Chem. 78 (2006) 7370.
[6] D. Williams, Med. Device Technol. 14 (2003) 10.
[7] M.E. Meyerhoff, Trends Analyt. Chem. 12 (1993) 257.
[8] J.D. Andrade, V. Hlady, Adv. Polym. Sci. 79 (1986) 1.
[9] R.W. Colman, Cardiovasc. Pathol. 2 (1993) 23.
[10] N. Wisniewski, M. Reichert, Colloids Surf. B Biointerf. 18 (2000) 197.
[11] G.S. Wilson, R. Gifford, Biosens. Bioelectron. 20 (2005) 2388.
[12] J.M. Anderson, Cardiovasc. Pathol. 2 (1993) 33.
[13] R. Ballerstadt, C. Evans, A. Gowda, R. McNichols, Diab. Technol. Ther. 8 (2006) 296.
[14] P.W. Barone, R.S. Parker, M.S. Strano, Anal. Chem. 77 (2005) 7556.
[15] M. Gerritsen, J.A. Jansen, J.A. Lutterman, Neth. J. Med. 54 (1999) 167.
[16] U. Klueh, D.I. Dorsky, D.L. Kreutzer, Biomaterials 26 (2005) 1155.
[17] R.A. Latour, J. Biomed. Mater. Res. A 78A (2006) 843.

[18] Y. Marois, N. Chakfe, R. Guidoin, R.C. Duhamel, R. Roy, M. Marois, M.W. King, Y. Douville, Biomaterials 17 (1996) 3.

[19] V.L. Gott, J.D. Whiffen, R.C. Dutton, Science 142 (1963) 1297.

[20] A. Kishida, Y. Akatsuka, M. Yanagi, T. Aikou, I. Maruyama, M. Akashi, ASAIO J. 41 (1995) M369.

[21] C.D. Ebert, E.S. Lee, S.W. Kim, J. Biomed. Mater. Res. 16 (1982) 629.

[22] R. Barbucci, A. Magnani, R. Rappuoli, S. Lamponi, M. Consumi, J. Inorg. Biochem. 79 (2000) 119.

[23] P.L. Feldman, O.W. Griffith, D.J. Stuehr, Chem. Eng. News 71 (1993) 26.

[24] L.J. Ignarro, G.M. Buga, K.S. Wood, R.E. Byrns, G. Chaudhuri, Proc. Natl. Acad. Sci. U.S.A. 84 (1987) 9265.

[25] J.G. Diodati, A.A. Quyyumi, N. Hussain, L.K. Keefer, Thromb. Haemost. 70 (1993) 654.

[26] C.M. Maragos, D. Morley, D.A. Wink, T.M. Dunams, J.E. Saavedra, A. Hoffman, A.A. Bove, L. Isaac, J.A. Hrabie, L.K. Keefer, J. Med. Chem. 34 (1991) 3242.

[27] K. Wong, X.B. Li, Transfus. Apheresis Sci. 30 (2004) 29.

[28] J. MacMicking, Q.-W. Xie, C. Nathan, Annu. Rev. Immunol. 15 (1997) 323.

[29] B.J. Nablo, H.L. Prichard, R.D. Butler, B. Klitzman, M.H. Schoenfisch, Biomaterials 26 (2005) 6984.

[30] J.P. Cooke, Atheroscler. Suppl. 4 (2003) 53.

[31] W.K.C. Alderton, E. Chris, Knowles, G. Richard, Biochem. J. 357 (2001) 593.

[32] L.J. Ignarro, J. Card. Surg. 17 (2002) 301.

[33] J.S. Stamler, O. Jaraki, J. Osborne, D.I. Simon, J. Keaney, J. Vita, D. Singel, C.R. Valeri, J. Loscalzo, Proc. Natl. Acad. Sci. U.S.A. 89 (1992) 7674.

[34] N. Hogg, Free Radic. Biol. Med. 28 (2000) 1478.

[35] J. Stamler, D. Singel, J. Loscalzo, Science 258 (1992) 1898.

[36] D. Jourd'heuil, K. Hallen, M. Feelisch, M.B. Grisham, Free Radic. Biol. Med. 28 (2000) 409.

[37] A. Schober, C. Weber, Antioxid. Redox Signal. 7 (2005) 1249.

[38] C.A. Gruetter, B.K. Barry, D.B. McNamara, D.Y. Gruetter, P.J. Kadowitz, L.J. Ignarro, J. Cyclic Nucleotide Res. 5 (1979) 211.

[39] P. Massini, R. Kaserglanzmann, E.F. Luscher, Thromb. Haemost. 40 (1978) 212.

[40] A. Ramamurthi, R.S. Lewis, Ann. Biomed. Eng. 26 (1998) 1036.

[41] J.P. Wallis, Transfus. Med. 15 (2005) 1.

[42] M.W. Vaughn, L. Kuo, J.C. Liao, Am. J. Physiol. (Heart Circ. Physiol.) 43 (1998) H2163.

[43] T.J. Guzik, R. Korbut, T. Adamek-Guzik, J. Physiol. Pharmacol. 54 (2003) 469.

[44] P.G. Wang, M. Xian, X.P. Tang, X.J. Wu, Z. Wen, T.W. Cai, A.J. Janczuk, Chem. Rev. 102 (2002) 1091.

[45] S.M. Shishido, M.G. de Oliveira, Photochem. Photobiol. 71 (2000) 273.

[46] A.B. Seabra, L.L. Da Rocha, M.N. Eberlin, M.G. De Oliveira, J. Pharm. Sci. 94 (2005) 994.

[47] S.M. Shishido, A.B. Seabra, W. Loh, M.G. de Oliveira, Biomaterials 24 (2003) 3543.

[48] K.S. Bohl, J.L. West, Biomaterials 21 (2000) 2273.

[49] R.S. Drago, Br. Karstett, J. Am. Chem. Soc. 83 (1961) 1819.

[50] K.M. Davies, D.A. Wink, J.E. Saavedra, L.K. Keefer, J. Am. Chem. Soc. 123 (2001) 5473.

[51] M.M. Batchelor, S.L. Reoma, P.S. Fleser, V.K. Nuthakki, R.E. Callahan, C.J. Shanley, J.K. Politis, J. Elmore, S.I. Merz, M.E. Meyerhoff, J. Med. Chem. 46 (2003) 5153.

[52] D.J. Smith, D. Chakravarthy, S. Pulfer, M.L. Simmons, J.A. Hrabie, M.L. Citro, J.E. Saavedra, K.M. Davies, T.C. Hutsell, D.L. Mooradian, S.R. Hanson, L.K. Keefer, J. Med. Chem. 39 (1996) 1148.

[53] M.C. Frost, M.M. Reynolds, M.E. Meyerhoff, Biomaterials 26 (2005) 1685.

[54] H.P. Zhang, G.M. Annich, J. Miskulin, K. Stankiewicz, K. Osterholzer, S.I. Merz, R.H. Bartlett, M.E. Meyerhoff, J. Am. Chem. Soc. 125 (2003) 5015.

[55] J.A. Hrabie, L.K. Keefer, Chem. Rev. 102 (2002) 1135.

[56] Espadas-Torre, V. Oklejas, K. Mowery, M.E. Meyerhoff, J. Am. Chem. Soc. 119 (1997) 2321.

[57] K.A. Mowery, M.H. Schoenfisch, N. Baliga, J.A. Wahr, M.E. Meyerhoff, Electroanalysis 11 (1999) 681.

[58] M.C. Frost, M.M. Batchelor, Y.M. Lee, H.P. Zhang, Y.J. Kang, B.K. Oh, G.S. Wilson, R. Gifford, S.M. Rudich, M.E. Meyerhoff, Microchem. J. 74 (2003) 277.

[59] M.H. Schoenfisch, H.P. Zhang, M.C. Frost, M.E. Meyerhoff, Anal. Chem. 74 (2002) 5937.

[60] K.P. Dobmeier, G.W. Charville, M.H. Schoenfisch, Anal. Chem. 78 (2006) 7461.

[61] K.A. Mowery, M.H. Schoenfisch, J.E. Saavedra, L.K. Keefer, M.E. Meyerhoff, Biomaterials 21 (2000) 9.

[62] Y. Wu, Z.R. Zhou, M.E. Meyerhoff, J. Biomed. Mater. Res. A 81A (2007) 956.

[63] M.H. Schoenfisch, K.A. Mowery, M.V. Rader, N. Baliga, J.A. Wahr, M.E. Meyerhoff, Anal. Chem. 72 (2000) 1119.

[64] H.P. Zhang, G.M. Annich, J. Miskulin, K. Osterholzer, S.I. Merz, R.H. Bartlett, M.E. Meyerhoff, Biomaterials 23 (2002) 1485.

[65] M.C. Frost, S.M. Rudich, H.P. Zhang, M.A. Maraschio, M.E. Meyerhoff, Anal. Chem. 74 (2002) 5942.

[66] R. Gifford, M.M. Batchelor, Y. Lee, G. Gokulrangan, M.E. Meyerhoff, G.S. Wilson, J. Biomed. Mater. Res. A 75A (2005) 755.

[67] D.L.H. Williams, Acc. Chem. Res. 32 (1999) 869.

[68] A.J. Holmes, D.L.H. Williams, J. Chem. Soc. Perkin Trans. 2 (2000) 1639.

[69] R.J. Singh, N. Hogg, J. Joseph, B. Kalyanaraman, J. Biol. Chem. 271 (1996) 18596.

[70] Y.C. Hou, Z.M. Guo, J. Li, P.G. Wang, Biochem. Biophys. Res. Commun. 228 (1996) 88.

[71] S. Hwang, M.E. Meyerhoff, J. Mater. Chem. 17 (2007) 1462.

[72] X.B. Duan, R.S. Lewis, Biomaterials 23 (2002) 1197.

[73] B.K. Oh, M.E. Meyerhoff, J. Am. Chem. Soc. 125 (2003) 9552.

[74] B.K. Oh, M.E. Meyerhoff, Biomaterials 25 (2004) 283.

[75] Y. Wu, A.P. Rojas, G.W. Griffith, A.M. Skrzypchak, N. Lafayette, R.H. Bartlett, M.E. Meyerhoff, Sens. Actuators B 121 (2007) 36.

[76] D. Giustarini, A. Milzani, R. Colombo, I. Dalle-Donne, R. Rossi, Clin. Chim. Acta 330 (2003) 85.

[77] W. Cha, Y. Lee, B.K. Oh, M.E. Meyerhoff, Anal. Chem. 77 (2005) 3516.

[78] W. Cha, M.E. Meyerhoff, Langmuir 22 (2006) 10830.

[79] Z.R. Zhou, M.E. Meyerhoff, Biomaterials 26 (2005) 6506.

[80] B. Wu, B. Gerlitz, B.W. Grinnell, M.E. Meyerhoff, Biomaterials 28 (2007) 4047.